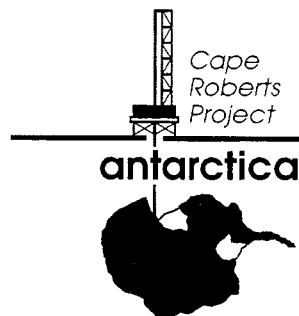


Volume 6, Number 1/2 - 1999

Studies from the Cape Roberts Project
Ross Sea, Antarctica
Initial Report on CRP-2/2A

GUEST EDITORS

Christopher R. Fielding & Michael R.A. Thomson



Editorial Policy

TERRA ANTARTICA (ISSN 1122-8628) - established in 1994 - aims to favour the exchange of ideas and results in the field of Antarctic Earth Sciences. Contributions to the development of Antarctic Geology, Geophysics, Glacial Geology, and Glaciology from related areas, bordering Sciences, and technological advancement are expected. The Journal is open to the international community and is distributed worldwide. It publishes two issues per year. Additional thematic issues, devoted to specific topics and meetings, can also be published.

Publications should be in the form of articles, short notes, letters, and summary reports. Review papers on relevant topics may be accepted.

The Editorial Advisory Board will undertake the responsibility of refereeing procedure for the manuscripts. Guest-editors will undertake the responsibility of refereeing procedure for manuscripts for thematic issues.

The two issues will appear the first within the end of June and the second within the end of December. Instructions for contributors are reported on the inside back cover.

Subscription rates

1999

	<i>UE countries</i>	<i>Other countries</i>
Professionals	27 Euros	32 Euros
Students	15 Euros	20 Euros
Institutions	80 Euros	85 Euros

Overcharge for air mail despatch: 8 Euros/year

Orders for subscriptions should be sent to *Terra Antartica Publication* (see address below). Back issues are still available (except Volume 1); prices are the same as 1999.

The price of one single issue is 40 Euros.



**Terra Antartica
Publication**

Museo Nazionale dell'Antartide '*Felice Ippolito*'
Sezione Scienze della Terra - Università degli Studi di Siena
Via del Laterino 8, 53100 Siena (Italia)

e-mail terranta@mna.unisi.it

fax ++39-0577-233817

**Studies from the Cape Roberts Project
Ross Sea, Antarctica
Initial Report on CRP-2/2A**

Contents

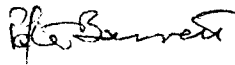
	Page
Foreword - P.J. Barrett & C.A. Ricci.....	V
Cape Roberts Project Personnel.....	VII
Studies from the Cape Roberts Project, Ross Sea, Antarctica - Initial Report on CRP-2/2A	
Cape Roberts Science Team.....	1
1 - Introduction.....	3
<i>Background and Geological Setting</i>	
<i>Drill Site Observations (Sea Ice, Weather, Drilling Operations)</i>	
<i>Core Management and Sampling</i>	
<i>Pliocene-Quaternary Strata in CRP-2</i>	
2 - Core Properties and Down-Hole Geophysics.....	27
<i>Fracture Arrays</i>	
<i>Physical Properties from On-Site Core Measurements</i>	
<i>Down-Hole Logging</i>	
<i>Correlation of Seismic Reflectors with CRP-2/2A</i>	
3 - Lithostratigraphy and Sedimentology.....	49
<i>Introduction</i>	
<i>Description of Sequence</i>	
<i>Facies Analysis</i>	
<i>Sequence Stratigraphy</i>	
<i>Sedimentology</i>	
<i>Diagenesis</i>	
<i>Deformation</i>	
4 - Petrology.....	89
<i>Introduction</i>	
<i>Basement Clasts</i>	
<i>Volcanic Clasts</i>	
<i>Clay Mineralogy</i>	
<i>X-Ray Mineralogy</i>	
<i>Sand Grains</i>	
<i>Organic Geochemistry</i>	

5 - Palaeontology.....	107
<i>Introduction</i>	
<i>Siliceous Microfossils</i>	
<i>Foraminifera</i>	
<i>Calcareous Nannofossils</i>	
<i>Palynology</i>	
<i>Macropalaeontology</i>	
6 - Palaeomagnetism.....	145
<i>Introduction</i>	
<i>Methods</i>	
<i>Results</i>	
<i>Discussion</i>	
<i>Additional Work</i>	
7 - Summary of Results.....	156
<i>Introduction</i>	
<i>Methods</i>	
<i>Results</i>	
<i>Discussion</i>	
References.....	169

Foreword

This volume is the third of several special issues of *Terra Antarctica* to present the results of the Cape Roberts Project, in which the Antarctic programmes of Australia, Britain, Germany, Italy, New Zealand, and the United States of America are collaborating to take a series of cores off the Antarctic coast. The coring is being carried out with a drilling rig set on the fast sea-ice to investigate climatic and tectonic history of the region (Barrett & Davey, 1992; International Steering Committee, 1994). The first season's drilling in 1997 was curtailed at a depth of 148 mbsf (metres below sea floor) after an unusual storm-generated ice break-out, but the results obtained have wide implications for the regional geological history and are reported in both the Initial Report on CRP-1 (Cape Roberts Science Team, 1998) and a series of papers comprising the Scientific Report on CRP-1 (Hambrey & Wise, editors, in press).

Here we report on the successful drilling of CRP-2/2A to a depth of 624 mbsf, continuing the sampling of strata beneath those cored in CRP-1 last year. Sea-ice conditions were good and the refurbished sea riser functioned well, but drilling conditions were difficult in the boulder bed 5 m thick just below the sea floor and in the loose sand beds at several levels down to 550 mbsf. Nevertheless the problems were overcome with skill, experience and persistence of the drilling team. The Cape Roberts Science Team of 60 scientific, technical and support staff also had its challenges in describing, sampling and reporting on core from one of the most complex depositional settings on earth, and to a tight publication deadline. We thank all of those who took part in the project for their commitment to producing and reporting on the core in a timely way. We also look forward in late 1999 to the next Cape Roberts special issue, the Scientific Report, with a more detailed analysis of results of the 1998 drilling.



Peter Barrett



Carlo Alberto Ricci

ACKNOWLEDGEMENTS

The Cape Roberts Project has been made possible through the financial and logistical support of the national Antarctic programmes of Germany, Italy, New Zealand, United Kingdom, the United States of America, and for Australia the James Cook University/University of Queensland consortium. In addition, DMT, Essen, Germany, helped to support the project by providing access to the CoreScan® and software at reduced rates. We are grateful to Dr G. Rafat, DMT, for his time in setting up the CoreScan® at the Drill Site laboratory. We also thank Lisa Peters and Rich Esser, New Mexico Geochronology Research Laboratory, New Mexico Tech, Socorro, USA, for their help in the accelerated processing of the samples for $^{40}\text{Ar}/^{39}\text{Ar}$ analysis.

We are grateful to Steve Kottmeier, and Robbie Score and her staff for the excellent support provided for the Crary Science & Engineering Center operation at McMurdo Station. Thanks also to Jay Burnside and the science construction staff. The help of divers from CSEC (Rob Robbins, Christian MacDonald and minder Robbie Score) for installing and recovering the air bags under the sea ice beneath the drill rig was also appreciated. Murray Knox carried out the levelling of the sea ice at the drill site and John Alexander interpreted the data. John Alexander, as Scott Base Liaison Officer, also smoothed the communications and logistics path between McMurdo Station, Scott Base and Cape Roberts. We also thank Pat Cooper and his drilling team for persevering until success was achieved, and Jim Cowie, Alex Pyne and support staff for their difficult work in the WINFLY period, maintenance of Cape Roberts camp and supplies, and for the checking maintenance and storage for the next drilling season. Andy Archer (ASA, Denver) processed DMSP satellite images, and Bob Onstott (ERIM) processed SAR images of the early season sea ice for Cape Roberts Project operations.

Cape Roberts Project Personnel

INTERNATIONAL STEERING COMMITTEE

Professor Maria Bianca Cita
Dipartimento di Scienze della Terra
Università degli Studi di Milano
Via L. Mangiagalli 34, I 20133 Milano
ITALY
e-mail: cita@imiucca.csi.unimi.it

Dr Fred Davey
Institute of Geological & Nuclear Sciences Ltd
P O Box 30368, Lower Hutt
NEW ZEALAND
e-mail: f.davey@gns.cri.nz

Dr Franz Tessensohn
Bundesanstalt für Geowissenschaften und Rohstoffe
Stilleweg 2, D-30655 Hannover
GERMANY
e-mail: Franz.Tessensohn@bgr.de

Dr Mike Thomson
British Antarctic Survey
High Cross, Madingley Road, Cambridge CB3 0ET
UNITED KINGDOM
e-mail: m.thomson@bas.ac.uk

Professor Peter Webb
Department of Geological Sciences
Ohio State University
Columbus, Ohio 43210
UNITED STATES OF AMERICA
e-mail: webb.3@osu.edu

Dr Ken Woolfe
School of Earth Sciences
James Cook University
Townsville, Queensland 4811
AUSTRALIA
e-mail: ken.woolfe@jcu.edu.au

OPERATIONS/LOGISTICS MANAGEMENT GROUP

Ms Gillian Wratt (Convener)
Antarctica NZ
Private Bag 4745
Christchurch
NEW ZEALAND

Mr Erick Chiang
Office of Polar Programs
National Science Foundation
4201 Wilson Boulevard
Arlington, Virginia 22230
UNITED STATES OF AMERICA

Dr Ken Woolfe
School of Earth Sciences
James Cook University
Townsville, Queensland 4811
AUSTRALIA

Dr John Dudeney
British Antarctic Survey
High Cross Madingley Road
Cambridge CB3 0ET
UNITED KINGDOM

Dr Mario Zucchelli
ENEA
Via Anguillarese, 3301 - Roma
00100 Roma AD
ITALY

Professor Dieter Fütterer
Alfred-Wegener-Institut
Postfach 12 01 81
D-27516 Bremerhaven
GERMANY

ADVISOR

Dr Scott Borg
National Science Foundation
4201 Wilson Boulevard
Arlington, Virginia 22230
UNITED STATES OF AMERICA

SCIENCE PARTICIPANTS

Professor Peter Barrett
Chief Scientist
School of Earth Sciences
Victoria University of Wellington
P O Box 600, Wellington
NEW ZEALAND
e-mail: Peter.Barrett@vuw.ac.nz

Professor Peter Webb
 Crary Lab Science Leader
 Department of Geological Sciences
 Ohio State University
 Columbus Ohio 43210
 UNITED STATES OF AMERICA
 e-mail: webb.3@osu.edu

Dr Fulvia Aghib
 Sedimentologist
 Dipartimento di Scienze della Terra
 Università degli Studi di Milano
 Via Mangiagalli 34, 20133 Milano
 ITALY
 e-mail: f.aghib@e35.gp.terra.unimi.it

Dr Mauro Alberti
 Graphic Artist
 Museo Nazionale dell'Antartide
 Via del Laterino 8, 53100 Siena
 ITALY
 e-mail: alberti@mna.unisi.it

Ms Jo Anderson
 Core Processing Technician
 School of Earth Sciences
 Victoria University of Wellington
 P O Box 600, Wellington
 NEW ZEALAND
 e-mail: jo.anderson@vuw.ac.nz

Dr Pietro Armienti
 Petrologist
 Dipartimento di Scienze della Terra
 Università degli Studi di Pisa
 Via Santa Maria 53, 56126 Pisa
 ITALY
 e-mail: armienti@dst.unipi.it

Dr Rosemary Askin
 Palynologist
 Byrd Polar Research Center
 Ohio State University
 Columbus, Ohio 43210
 UNITED STATES OF AMERICA
 e-mail: askin.1@osu.edu

Mr Cliff Atkins
 Sedimentologist
 School of Earth Sciences
 Victoria University of Wellington
 P O Box 600, Wellington
 NEW ZEALAND
 e-mail: cliff.atkins@vuw.ac.nz

Dr Stephen Bannister
 Geophysicist
 Institute of Geological & Nuclear Sciences Ltd
 P O Box 30368, Lower Hutt
 NEW ZEALAND
 e-mail: s.bannister@gns.cri.nz

Mr Steven Bohaty
 Palaeontologist (siliceous microfossils)
 Department of Geosciences
 University of Nebraska - Lincoln
 Lincoln, Nebraska 68588-0340
 UNITED STATES OF AMERICA
 e-mail: sbohaty@unlgrad1.unl.edu

Mr Jason Brink
 Downhole Logging Specialist
 Department of Geology & Geophysics
 University of Utah
 Salt Lake City, Utah
 UNITED STATES OF AMERICA
 e-mail: jdbrink@mines.utah.edu

Ms Sonia Bryce
 Core Processing Technician
 Department of Geology
 James Cook University
 Townsville, Q 4811
 AUSTRALIA
 e-mail: sonya.bryce@jcu.edu.au

Dr Christian Bucker
 Downhole Logging
 Geowissenschaftliche Gemeinschaftsaufgaben
 Stilleweg 2, D-30655 Hannover
 GERMANY
 e-mail: c.buecker@gga-hannover.de

Mr Edward Butler
 Core Processing Technician
 School of Earth Sciences
 Victoria University of Wellington
 P O Box 600, Wellington
 NEW ZEALAND
 e-mail: Edward.Butler@vuw.ac.nz

Dr Michele Claps
 Sedimentologist
 Istituto di Scienze del Mare
 Università degli Studi di Ancona
 Via Breccie Bianche, 60131 Ancona
 ITALY
 e-mail: cli@dns.unife.it

Mr Matthew Curren
 Assistant Core Curator
 Antarctic Marine Geology Research Facility
 Department of Geological Sciences, Florida State Univ.
 Tallahassee, Florida 32306-4100
 UNITED STATES OF AMERICA
 e-mail: curator@gly.fsu.edu

Dr Michael Hannah
 Palynologist
 School of Earth Sciences
 Victoria University of Wellington
 P O Box 600, Wellington
 NEW ZEALAND
 e-mail: michael.hannah@vuw.ac.nz

Dr Fred Davey
 Marine Geophysicist
 Institute of Geological & Nuclear Sciences Ltd
 P O Box 30368, Lower Hutt
 NEW ZEALAND
 e-mail: f.davey@gns.cri.nz

Dr Stuart Henrys
 Marine Geophysicist
 Institute of Geological & Nuclear Sciences
 P O Box 30368, Lower Hutt
 NEW ZEALAND
 e-mail: s.henrys@gns.cri.nz

Mr Rusty Divine
 Diatom Technician
 Department of Geosciences
 University of Nebraska - Lincoln
 Lincoln, Nebraska 68588-0340
 UNITED STATES OF AMERICA
 e-mail: 82770@bigred.unl.edu

Mr Nick Jackson
 Core Processing Technician
 School of Earth Sciences
 Victoria University of Wellington
 P O Box 600, Wellington
 NEW ZEALAND
 e-mail: Nick.Jackson@vuw.ac.nz

Dr Werner Ehrmann
 Sedimentologist
 Martin-Luther-Universität,
 Institut für Geologische Wissenschaften
 Domstrasse 5, D-06108 Halle/Saale
 GERMANY
 e-mail: ehrmann@geologie.uni-halle.de

Dr Thomas Janecek
 Core Curator
 Antarctic Marine Geology Research Facility
 Department of Geological Sciences, Florida State Univ.
 Tallahassee, Florida 32306-4100
 UNITED STATES OF AMERICA
 e-mail: curator@gly.fsu.edu

Dr Chris Fielding
 Sedimentologist
 Department of Earth Sciences
 University of Queensland
 Brisbane, QLD 4072
 AUSTRALIA
 e-mail: chrisf@earthsciences.uq.edu.au

Professor Richard Kettler
 Organic Geochemist
 Department of Geosciences
 University of Nebraska - Lincoln
 Lincoln, Nebraska 68588-0340
 UNITED STATES OF AMERICA
 e-mail: rkettler@unlinfo.unl.edu

Dr Fabio Florindo
 Palaeomagnetist
 Istituto Nazionale di Geofisica
 Via di Vigna Murata 605, 00143 Roma
 ITALY
 e-mail: florindo@ing750.ingrm.it

Dr Conrad Kopsch
 Physical Properties Technician
 Alfred-Wegener-Institut
 Postfach 12 01 81, 27516 Bremerhaven
 GERMANY

Dr Hannes Grobe
 Data Management
 Alfred-Wegener-Institut
 Postfach 12 01 81
 D-27516 Bremerhaven
 GERMANY
 e-mail: grobe@awi-bremerhaven.de

Professor Lawrence Krissek
 Sedimentologist
 Department of Geological Sciences
 Ohio State University
 Columbus, Ohio 43210
 UNITED STATES OF AMERICA
 e-mail: krissek@mps.ohio-state.edu

Dr Mark Lavelle
Sedimentologist
British Antarctic Survey
High Cross, Madingley Road, Cambridge CB3 0ET
UNITED KINGDOM
e-mail: m.lavelle@bas.ac.uk

Ms Barbara McLeod
Photography Technician
Department of Fine Arts
Louisiana State University
129 Vicarro Dr, Baton Rouge, LA 70802
UNITED STATES OF AMERICA

Dr Jaap van der Meer
Sedimentologist
Fysisch Geografisch en Bodemkundig Laboratorium
University of Amsterdam, Nieuwe Prinsengracht 130
1018 VZ Amsterdam
THE NETHERLANDS
e-mail: j.j.m.meer@frw.uva.nl

Dr Tim Naish
Sedimentologist/Stratigrapher
Institute of Geological & Nuclear Sciences
P O Box 30 368, Lower Hutt
NEW ZEALAND
e-mail: t.naish@gns.cri.nz

Dr Frank Niessen
Physical Properties Specialist
Alfred-Wegener-Institut
Postfach 12 01 81, 27516 Bremerhaven
GERMANY
e-mail: fniessen@awi-bremerhaven.de

Ms Sandra Passchier
Micropalaeontology Technician/Sediment Deformation
Byrd Polar Research Center
Ohio State University
Columbus, Ohio 43210
UNITED STATES OF AMERICA
e-mail: passchier.1@osu.edu

Dr Timothy Paulsen
Structural Geologist
Byrd Polar Research Center
Ohio State University
Columbus, Ohio 43210
UNITED STATES OF AMERICA
e-mail: paulsen.9@osu.edu

Mr Eric Plankell
Core Scanning Technician
Byrd Polar Research Center
Ohio State University
Columbus, Ohio Y3210
UNITED STATES OF AMERICA
e-mail: plankell.2@osu.edu

Ms Kerstin Polozek
Sedimentologist
Martin-Luther-Universität,
Institut für Geologische Wissenschaften
Domstrasse 5, D-06108 Halle/Saale
GERMANY
e-mail: polozek@geologie.uni-halle.de

Professor Ross Powell
Sedimentologist
Department of Geology
Northern Illinois University
DeKalb, Illinois 60115
UNITED STATES OF AMERICA
e-mail: ross@geol.niu.edu

Mr Alex Pyne
Sea Ice Specialist
School of Earth Sciences
Victoria University of Wellington
P O Box 600, Wellington
NEW ZEALAND
e-mail: alex.pyne@vuw.ac.nz

Dr Ghodrat Rafat
Core Scanning Technician
DMT - GeoTec
Franz-Fisher-Weg 61, D-45307 Essen
GERMANY
e-mail: rafat@geotec.dmt-fp.cubis.de

Dr Ian Raine
Palaeontologist (terrestrial palynomorphs)
Institute of Geological & Nuclear Sciences
P O Box 30 368, Lower Hutt
NEW ZEALAND
e-mail: i.raine@gns.cri.nz

Dr Andrew Roberts
Palaeomagnetist
School of Ocean & Earth Science, Univ. of Southampton
Southampton Oceanography Centre
European Way, Southampton SO14 3ZH
UNITED KINGDOM
e-mail: arob@mail.soc.soton.ac.uk

Dr Leonardo Sagnotti
 Palaeomagnetist
 Istituto Nazionale di Geofisica
 Via di Vigna Murata 605, 00143 Roma
 ITALY
 e-mail: sagnotti@mart.e.ingrm.it

Mr Michael Tabecki
 Rock Section Technician
 British Antarctic Survey
 High Cross, Madingley Road, Cambridge CB3 0ET
 UNITED KINGDOM
 e-mail: mgta@bas.ac.uk

Ms Sonia Sandroni
 Editorial Assistant
 Dipartimento di Scienze della Terra
 Università degli Studi di Siena
 Via del Laterino 8, 53100 Siena
 ITALY
 e-mail: sandroni@unisi.it

Dr Franco Talarico
 Petrologist
 Dipartimento di Scienze della Terra
 Università degli Studi di Siena
 Via del Laterino 8, 53100 Siena
 ITALY
 e-mail: talaf@dst.unisi.it

Dr Reed Scherer
 Palaeontologist (siliceous microfossils)
 Department of Earth Sciences - Quat. Geol.
 Villavägen 16 Uppsala University
 S-752 36, Uppsala
 SWEDEN
 e-mail: Reed.Scherer@natgeog.uu.se

Dr Marco Taviani
 Palaeontologist (macrofossils)
 Istituto di Geologia Marina, CNR
 Via Gobetti 101, I-40129 Bologna
 ITALY
 e-mail: taviani@boigm2.igm.bo.cnr.it

Mr Erich Scholz
 Downhole Logging Technician
 Department of Geology & Geophysics
 University of Utah
 Salt Lake City, Utah
 UNITED STATES OF AMERICA

Dr Mike Thomson
 Editor
 British Antarctic Survey
 High Cross, Madingley Road, Cambridge CB3 0ET
 UNITED KINGDOM
 e-mail: m.thomson@bas.ac.uk

Mr John Simes
 Palynology Technician
 Institute of Geological & Nuclear Sciences
 P O Box 30 368, Lower Hutt
 NEW ZEALAND
 e-mail: j.simes@gns.cri.nz

Ms Elizabeth Trummel
 Teacher, Experiencing Antarctica
 Husmann Elementary School
 131 Paddock Street
 Crystal Lake, IL 60014
 UNITED STATES OF AMERICA
 e-mail: boop82@aol.com

Dr John Smellie
 Petrologist
 British Antarctic Survey
 High Cross, Madingley Road
 Cambridge CB3 0ET
 UNITED KINGDOM
 e-mail: j.smellie@bas.ac.uk

Professor Kenneth Verosub
 Palaeomagnetist
 Department of Geology
 University of California
 Davis, California 95616
 UNITED STATES OF AMERICA
 e-mail: verosub@geology.ucdavis.edu

Dr Percy Strong
 Palaeontologist (foraminifera)
 Institute of Geological & Nuclear Sciences
 P O Box 30 368, Lower Hutt
 NEW ZEALAND
 e-mail: p.strong@gns.cri.nz

Dr Giuliana Villa
 Palaeontologist (calcareous nannofossils)
 Dipartimento di Scienze della Terra
 Università degli Studi di Parma
 Parco Area delle Scienze 157A, 43100 Parma
 ITALY
 e-mail: geol01@ipr.univ.cce.unipr.it

Dr David Watkins
 Palaeontologist (calcareous nannofossils)
 Department of Geosciences
 University of Nebraska
 Lincoln, Nebraska 68588-0340
 UNITED STATES OF AMERICA
 e-mail: dwatkins@unlinfo.unl.edu

Dr Gary Wilson
 Palaeomagnetist
 Department of Earth Sciences
 University of Oxford
 Parks Road, Oxford, OXI 3PR
 UNITED KINGDOM
 e-mail: wilsons@geology.ohio-state.edu

Dr Graeme Wilson
 Palynologist
 Institute of Geological & Nuclear Sciences
 P O Box 30-368, Lower Hutt
 NEW ZEALAND
 e-mail: graeme.wilson@gns.cri.nz

Dr Terry Wilson
 Structural Geologist
 Byrd Polar Research Center
 Ohio State University
 Columbus, Ohio 43210
 UNITED STATES OF AMERICA
 e-mail: twilson@mps.ohio-state.edu

Dr Thomas Wonik
 Downhole Logging Specialist
 Bundesanstalt für Geowissenschaften
 Stilleweg 2, D-3000 Hannover 51
 GERMANY
 e-mail: wonik@bgr.de

Dr Ken Woolfe
 Sedimentologist
 School of Earth Sciences
 James Cook University
 Townsville, Q 4811
 AUSTRALIA
 e-mail: ken.woolfe@jcu.edu.au

PROJECT STAFF

Mr Jim Cowie
 Project Manager
 Antarctica NZ
 Private Bag 4745
 Christchurch
 NEW ZEALAND
 e-mail: j.cowie@antarcticanz.govt.nz

Mr Alex Pyne
 Science Support Manager
 School of Earth Sciences
 Victoria University of Wellington
 P O Box 600, Wellington
 NEW ZEALAND
 e-mail: alex.pyne@vuw.ac.nz

Mr Pat Cooper
 Drilling Manager
 Rapid Creek, Waimangaroa
 Westport
 NEW ZEALAND

Mr John Alexander
 Cape Roberts Liaison Officer
 P O Box 314
 Queenstown
 NEW ZEALAND

WINFLY TEAM

Jim Cowie	Project Manager
Alex Pyne	Science Support Manager
Brian Howat	Plant Operator
Murray Knox	Plant Operator
Colleen Clarke	Camp Manager/Paramedic
Brian Reid	Electrician
Jeremy Ridgen	Mechanic
Peter Sinclair	Carpenter
Kevin Conaglen	Carpenter/Field Assistant

CAMP SUPPORT

Dennis Skinner	Chef
Kath Varcoe	General Duties
Dave Bryce	Field Assistant
Steve Brown	Carpenter

DRILLERS

Pat Cooper	Drilling Manager
Malcolm Macdonald	Driller
John Marcussen	Driller
Frank Tansey	Driller
Michael Avey	Assistant Driller
Chris Collie	Assistant Driller
David Eaton	Assistant Driller
Tony Kingan	Assistant Driller
Todd Symons	Assistant Driller
Sam Woodford	Assistant Driller
Leon Holloway	Drilling consultant

Studies from Cape Roberts Project Initial Report on CRP-2/2A, Ross Sea, Antarctica

Cape Roberts Science Team*

Abstract - The site for CRP-2, 14 km east of Cape Roberts (77.006°S; 163.719°E), was selected to overlap the early Miocene strata cored in nearby CRP-1, and to sample deeper into the east-dipping strata near the western margin of the Victoria Land Basin to investigate Palaeogene climatic and tectonic history. CRP-2 was cored from 5 to 57 mbsf (metres below the sea floor) (core recovery 91%), with a deviation resulting in CRP-2A being cored at the same site. CRP-2A reached down to 624 mbsf (recovery 95%), and to strata with an age of c. 33-35 Ma. Drilling took place from 16 October to 25 November 1998, on 2.0-2.2 m of sea ice and through 178 m of water.

Core fractures and other physical properties, such as sonic velocity, density and magnetic susceptibility, were measured throughout the core. Down-hole logs for these and other properties were run from 63 to 167 mbsf and subsequently from 200 to 623 mbsf, although density and velocity data could be obtained only to 440 mbsf because of hole collapse. Sonic velocity averages c. 2.0 km s⁻¹ for the upper part of the hole, but there is a sharp increase to c. 3.0 km s⁻¹, and also a slight angular unconformity, at 306 mbsf, corresponding most likely to the early/late Oligocene boundary (c. 28-30 Ma). Velocity then increases irregularly to around 3.6 km s⁻¹ at the bottom of the hole, which is estimated to lie 120 m above the V4/V5 boundary. The higher velocities below 306 mbsf probably reflect more extensive carbonate and common pyrite cementation, in patches, nodules, bedding-parallel masses and as vein infills. Dip of the strata also increases down-hole from 3° in the upper 300 m to over 10° at the bottom. Temperature gradient is 21° km⁻¹. Over 2 000 fractures were logged through the hole. Borehole televiewer imagery was obtained for the interval from 200 to 440 mbsf to orient the fractures for stress field analysis.

Lithostratigraphical descriptions on a scale of 1:20 are presented for the full length of the core, along with core box images, as a 200 page supplement to this issue. The hole initially passed through a layer of muddy gravel to 5.5 mbsf (Lithological Sub-Unit or LSU 1.1), and then into a Quaternary diatom-bearing clast-rich diamicton to 21 mbsf (LSU 2.1), with an interval of alternating compact diamicton and loose sand, and containing a rich Pliocene foraminiferal fauna, to 27 mbsf (LSU 2.2). The unit beneath this (LSU 3.1) has similar physical properties (sonic velocity, porosity, magnetic susceptibility) and includes diamictites of similar character to those of LSU 2.1 and 2.2, but an early Miocene (c. 19 Ma) diatom assemblage at 28 mbsf (top of LSU 3.1) shows that this sub-unit is part of the older section.

The strata beneath 27 mbsf, primary target for the project, extend from early Miocene to perhaps latest Eocene age, and are largely cyclic glacial-marine nearshore to offshore sediments. They are described as 41 lithological sub-units and interpreted in terms of 12 recurrent lithofacies. These are 1) mudstone, 2) inter-stratified mudstone and sandstone, 3) muddy very fine to coarse sandstone, 4) well-sorted stratified fine sandstone, 5) moderately to well-sorted, medium-grained sandstone, 6) stratified diamictite, 7) massive diamictite, 8) rhythmically inter-stratified sandstone and mudstone, 9) clast-supported conglomerate, 10) matrix-supported conglomerate, 11) mudstone breccia and 12) volcanoclastic sediment.

Sequence stratigraphical analysis has identified 22 unconformity-bounded depositional sequences in pre-Pliocene strata. They typically comprise a four-part architecture involving, in ascending order, 1) a sharp-based coarse-grained unit (Facies 6, 7, 9 or 10), 2) a fining-upward succession of sandstones (Facies 3 and 4), 3) a mudstone interval (Facies 1), in some cases coarsening upward to muddy sandstones (Facies 3), and 4) a sharp-based sandstone-dominated succession (mainly Facies 4). The cyclicity recorded by the strata is interpreted in terms of a glacier ice margin retreating and advancing from land to the west, and of rises and falls in sea level. Analysis of sequence periodicity awaits a firmer chronology. However, a preliminary spectral analysis of magnetic susceptibility for a deep-water mudstone within one of the sequences (from 339 to 347 mbsf) reveals ratios between hierarchical levels that are similar to those of the three Milankovitch orbital forcing periodicities.

The strata contain a wide range of fossils, the most abundant being marine diatoms. These commonly form up to 5% of the sediment, though in places the core is barren (notably between 300 and 412 mbsf). Fifty samples out of 250 reviewed were studied in detail. The assemblages define ten biostratigraphical zones, some of them based on local or as yet undescribed forms. The assemblages are neritic, and largely planktonic, suggesting that the sea floor was

* F. Aghib, M. Alberti, J. Anderson, P. Armienti, R. Askin, C. Atkins, S. Bannister, P.J. Barrett, S. Bohaty, J. Brink, S. Bryce, C. Bucker, E. Butler, M. Claps, P. Cooper, M. Curren, F. Davey, R. Divine, W. Ehrmann, C. Fielding, F. Florindo, H. Grobe, M. Hannah, S. Henrys, N. Jackson, T. Janecek, R. Kettler, C. Kopsch, L. Krissek, M. Lavelle, B. McLeod, J. van der Meer, T. Naish, F. Niessen, S. Passchier, T. Paulsen, E. Plankell, K. Polozek, R. Powell, A. Pyne, G. Rafat, I. Raine, A. Roberts, L. Sagnotti, S. Sandroni, R. Scherer, E. Scholz, J. Simes, J. Smellie, P. Strong, M. Tabecki, F. Talarico, M. Taviani, M. Thomson, E. Trummel, K. Verosub, G. Villa, D. Watkins, P. Webb, G. Wilson, G. Wilson, T. Wilson, T. Wonik, K. Woolfe

mostly below the photic zone throughout deposition of the cored sequence. Calcareous nannofossils, representing incursions of ocean surface waters, are much less common (72 out of 183 samples examined) and restricted to mudstone intervals a few tens of metres thick, but are important for dating. Foraminifera are also sparse (73 out of 135 samples) and represented only by calcareous benthic species. Changing assemblages indicate a shift from inshore environments in the early Oligocene to outer shelf in the late Oligocene, returning to inshore in the early Miocene. Marine palynomorphs yielded large numbers of well-preserved forms from most of the 116 samples examined. The new *in situ* assemblage found last year in CRP-1 is extended down into the late Oligocene and a further new assemblage is found in the early Oligocene. Many taxa are new, and cannot as yet contribute to an improved understanding of chronology or ecology. Marine invertebrate macrofossils, mostly molluscs and serpulid tubes, are scattered throughout the core. Preservation is good in mudstones but poor in other lithologies.

Climate on land is reflected in the content of terrestrial palynomorphs, which are extremely scarce down to c. 300 mbsf. Some forms are reworked, and others represent a low growing sparse tundra with at least one species of *Nothofagus*. Beneath this level, a significantly greater diversity and abundance suggests a milder climate and a low diversity woody vegetation in the early Oligocene, but still far short of the richness found in known Eocene strata of the region. Sedimentary facies in the oldest strata also suggest a milder climate in the oldest strata cored, with indications of substantial glacial melt-water discharges, but are typical of a colder climate in late Oligocene and early Miocene times. Clast analyses from diamictites reveal weak to random fabrics, suggesting either lack of ice-contact deposition or post-depositional modification, but periods when ice grounded at the drill site are inferred from thin zones of *in-situ* brecciated rock and soft-sediment folding. These are more common above c. 300 mbsf, perhaps reflecting more extensive glacial advances during deposition of those strata.

Erosion of the adjacent Transantarctic Mountains through Jurassic basalt and dolerite-intruded Beacon strata into basement rocks beneath is recorded by petrographical studies of clast and sand grain assemblages. Core below 310 mbsf contains a dominance of fine-grained Jurassic dolerite and basalt fragments along with Beacon-derived coal debris and rounded quartz grains, whereas the strata above this level have a much higher proportion of basement-derived granitoids, implying that the large areas of the adjacent mountains had been eroded to basement by the end of the early Oligocene.

There is little indication of rift-related volcanism below 310 mbsf. Above this, however, basaltic and trachytic tephra are common, especially from 280 to 200 mbsf, from 150 to 46 mbsf, and in Pliocene LSU 2.2 from 21 to 27 mbsf. The largest volcanic eruptions generated layers of coarse (up to 1 cm) trachytic pumice lapilli between 97 and 114 mbsf. The thickest of these (1.2 m at 112 mbsf) may have produced an eruptive column extending tens of km into the stratosphere. A source within a few tens of km of the drill site is considered most likely.

Present age estimates for the pre-Pliocene sequence are based mainly on biostratigraphy (using mainly marine diatoms and to a lesser extent calcareous nannofossils), with the age of the tephra from 112 to 114 mbsf (21.44 ± 0.05 Ma from 84 crystals by Ar-Ar) as a key reference point. Although there are varied and well-preserved microfossil assemblages through most of the sequence (notably of diatoms and marine palynomorphs), they comprise largely taxa either known only locally or as yet undescribed. In addition, sequence stratigraphical analysis and features in the core itself indicate numerous disconformities. The present estimate from diatom assemblages is that the interval from 27 to 130 mbsf is early Miocene in age (c. 19 to 23.5 Ma), consistent with the Ar-Ar age from 112 to 114 mbsf. Diatom assemblages also indicate that the late Oligocene epoch extends from c. 130 to 307 mbsf, which is supported by late Oligocene nannofossils from 130 to 185 mbsf. Strata from 307 to 412 mbsf have no age-diagnostic assemblages, but below this early Oligocene diatoms and nannofossils have been recovered. A nannoflora at the bottom of the hole is consistent with an earliest Oligocene or latest Eocene age.

Magnetostratigraphical studies based on about 1 000 samples, 700 of which have so far undergone demagnetisation treatment, have provided a polarity stratigraphy of 12 pre-Pliocene magnetozones. Samples above 270 mbsf are of consistently high quality. Below this, magnetic behaviour is more variable. A preliminary age-depth plot using the Magnetic Polarity Time Scale (MPTS) and constrained by biostratigraphical data suggests that episodes of relatively rapid sedimentation took place at CRP-2 during Oligocene times (c. 100 m/My), but that more than half of the record was lost in a few major and many minor disconformities. Age estimates from Sr isotopes in shell debris and further tephra dating are expected to lead to a better comparison with the MPTS.

CRP-2/2A has recorded a history of subsidence of the Victoria Land Basin margin that is similar to that found in CIROS-1 70 km to the south, reflecting stability in both basin and the adjacent mountains in late Cenozoic times, but with slow net accumulation in the middle Cenozoic. The climatic indicators from both drill holes show a similar correspondence, indicating polar conditions for the Quaternary but with sub-polar conditions in the early Miocene-late Oligocene and indications of warmer conditions still in the early Oligocene. Correlation between the CRP-2A core and seismic records shows that seismic units V3 and V4, both widespread in the Victoria Land Basin, represent a period of fluctuating ice margins and glacial marine sedimentation. The next drill hole, CRP-3, is expected to core deep into V5 and extend this record of climate and tectonics still further back in time.

1 - Introduction

BACKGROUND AND GEOLOGICAL SETTING

BACKGROUND

The aim of the Cape Roberts Project is to obtain continuous core through c. 1 200 m of strata on the western side of McMurdo Sound, Antarctica, in order to investigate the Cenozoic climatic and tectonic history of the region. The project is named after Cape Roberts, the staging point for the offshore drilling and a small promontory 125 km northwest of McMurdo Station and Scott Base (Fig. 1.1).

The project is designed to address two questions:

- did ice sheets grow and decay on Antarctica, with attendant changes in global sea level, prior to 34 Ma ago, when it is widely believed the first extensive ice formed on the continent?
- at what time did the continent begin to rift to form the Ross Sea and the Transantarctic Mountains?

A further important goal of the project is to determine the age and environmental significance of seismic reflectors that have been traced basin-wide beneath the western Ross Sea.

This volume records the first work carried out on the CRP-2/2A drill holes, completed on 30 November 1998

(Tab. 1.1). The first section outlines the geological setting of the drill holes and reports on the operating environment (climate and sea ice), the drilling activity, and the thin Quaternary/Pliocene sediments that mantle the older Cenozoic sequence. It also outlines the core processing and management schemes at the CRP-2 drill site, Cape Roberts Laboratory and at the Crary Science & Engineering Center at McMurdo Station. The remainder of the report presents the first results and a preliminary interpretation of the data from both the core and logging within the hole itself.

GEOLOGICAL SETTING

McMurdo Sound lies at the southwestern corner of the Ross Sea between the Transantarctic Mountains in southern Victoria Land and volcanic Ross Island (Fig. 1.2), and at the southern end of the Victoria Land Basin (VLB), one of four major extensional basins forming the Ross continental shelf (Houtz & Davey, 1973; Cooper & Davey, 1985, 1987). The VLB is a trough filled with sediment of Cenozoic and possibly older age, at least 400 km long and c. 150 km wide, immediately seaward of the Transantarctic Mountains. It is separated from the early Palaeozoic

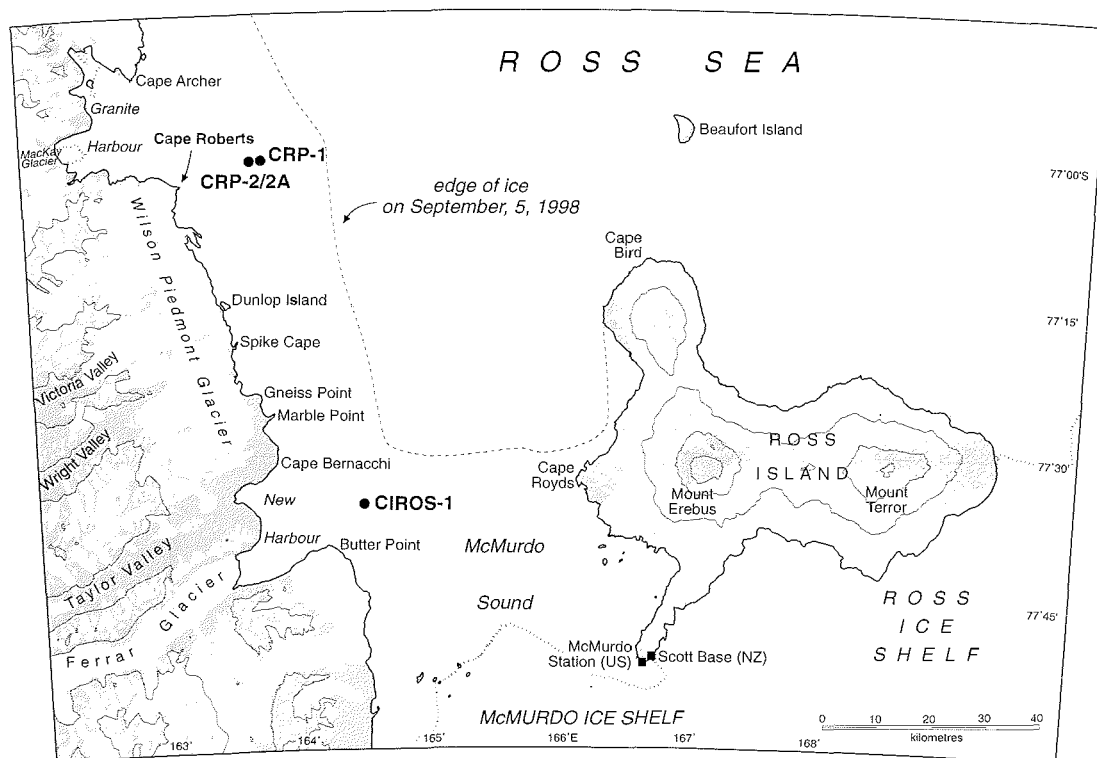


Fig. 1.1 - Map of the south west corner of the Ross Sea, showing the locations of Cape Roberts, CRP-1, CRP-2/2A and CIROS-1, and McMurdo Station/Scott Base, the main staging point for the project. The edge of the fast sea-ice, which provides the drilling platform is also shown.

Tab. 1.1 - Site data for CRP-2/2A.

Position:	14.2 km at 096° true from Cape Roberts	921 m at 284° true from CRP-1	
Latitude:	77.006°S	Longitude:	163.719°E
Water depth from msl:	177.94 m	Sea-ice thickness:	2.0 m (1 Oct) to 2.2 m (23 Nov)
First core:	07.30, 16 October	Last core:	14.20, 25 November
Sea riser embedded to:	13.03 mbsf	Lateral ice movt:	9.87 m to east from 17 Oct to 23 Nov
HQ core to:	199.31 mbsf		
NQ core to:	624.15 mbsf		
Recovery from:			
CRP-2	5.47 to 57.39 mbsf	47.26 m (91%)	
CRP-2A	13.03 to 45.97 mbsf	11.29 m (34%)	partially following CRP-2
CRP-2A	45.97 to 624.15 mbsf	548.67 m (95%)	new hole
Deepest core-lithology:	hard sandy siltstone	Deepest core-age:	earliest Oligocene (c. 33 Ma on diatoms, nannofossils and dinoflagellates)

Note: two holes were drilled at the same location, CRP-2 from the initial embedding of the sea riser (the outer float-supported casing) at 5 mbsf, and CRP-2A, which was cored from 12.20 mbsf after CRP-2 had reached 57.39 mbsf. CRP-2A deviated slightly from CRP-2 after the sea riser was successfully embedded to a depth of 13 mbsf.

basement rocks of the mountains by a major fault system, known as the Transantarctic Mountain Front, which parallels the present coast and represents the western edge of the VLB. Strata in the middle of the basin reach a thickness of 10-14 km, the oldest being interpreted as early rift-related volcanic rocks (Fig. 1.2, V6). Above these lie the older sedimentary seismic sequences, V5 and V4. Through uplift and erosion along the basin margin they now dip at between 2 and 5° eastward, and lie just beneath the sea floor on Roberts ridge, a bathymetric high about

12-20 km off Cape Roberts. The younger sequences (V1-V3) are 5 km thick in the middle of the basin but thin to c. 300 m on Roberts ridge.

Two main crustal thinning events have formed the basins of the Ross Sea, but they are not well constrained in time. The first, an essentially non-magmatic rifting event over most of the Ross Sea, is probably related to the break-up of Gondwana in this region (late Mesozoic). The second event, which was associated with volcanic activity, was largely confined to the VLB, and an Eocene

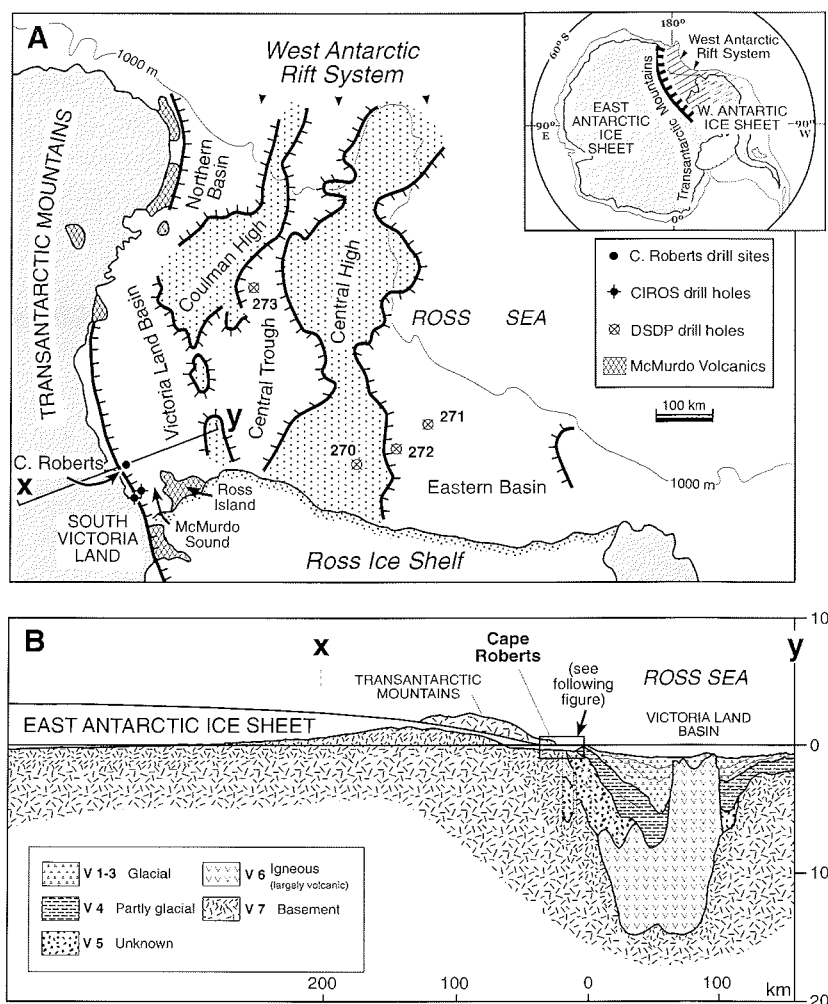


Fig. 1.2 - Map of the Ross continental shelf (A) and cross-section through the edge of the West Antarctic Rift System (B), showing the East Antarctic ice sheet, the Transantarctic Mountains and the Victoria Land Basin.

and younger age has been proposed (Cooper & Davey, 1987).

The main structural trend of the VLB is NNW, parallel to the axis of the Transantarctic Mountains. Northwest-trending, seismically defined faults demarcate presumed late Mesozoic half-grabens in the basin floor, and have been interpreted as terminating upward in the sedimentary section (Cooper & Davey, 1987). NNE- and ENE-trending faults have also been recognized in the mountains along the rift margin, and interpreted as having been formed, or have been reactivated, during transtension in more recent times (Wilson, 1995). Similar fault trends have been interpreted from seismic data from the basin margin off Cape Roberts (Hamilton et al., 1998).

Seismic sections have been interpreted as showing faults cutting through the sedimentary section and reaching the sea floor in one or two places (e.g. Fig. 5, Barrett et al., 1995), suggesting relatively recent tectonic activity. However, the age and facies of strata in the area of Roberts ridge indicate only minor vertical movement of this part of the rift floor in Neogene times. Water depths for the early Miocene strata in CRP-1 are inferred to have been less than 100 m below sea level (mbsl) for much of the period (Harwood et al., 1998; Taviani et al., 1998), suggesting that the ridge has sunk less than 200 m net in the last 20 million years.

The great east-facing scarp of the Transantarctic Mountains, which forms the backdrop for the drilling off Cape Roberts has a youthful appearance, but it too may have changed little in Neogene times. The dominance of basement clasts in strata of Neogene age in CRP-1 (Talarico & Sandroni, 1998) suggests that the adjacent mountains may have been deeply eroded and perhaps even

approaching their present elevation by the early Miocene. The continuation of this erosional record back into the earliest Oligocene is being investigated with results from CRP-2/2A.

The sea floor off Cape Roberts has been the focus of a number of geophysical surveys, which have been reviewed by Barrett et al. (1995), the Cape Roberts Science Team (1998) and Hamilton et al. (1998). One of the more unusual features is the large positive magnetic anomaly surveyed by Bozzo et al. (1997) and modelled as fragments of a stratiform basic igneous body close to the sea floor several kilometres northwest of CRP-2/2A. The outline of the magnetic bodies at a depth of 1 km is shown in figure 1.3, along with simplified bathymetry of the sea floor off Cape Roberts, and the main track lines used in establishing the seismic stratigraphy of the area.

The chronology of the seismic sequences of the VLB had been deduced through correlation of seismic reflectors (notably the reflector separating V3 and V4), eastward from Roberts ridge into the VLB and then south to the CIROS-1 drill hole (Fig. 1.1). There, the reflector was traced to an unconformity thought to separate a deeper water early Oligocene sequence from a shallow water late Oligocene sequence (Barrett et al., 1995; Bartek et al., 1996). However, in the first drill hole of this project, CRP-1 (Fig. 1.4), the lowest strata of V3 were found to be early Miocene, ranging in age from c. 18 Ma from 43 metres below the sea floor (mbsf) to between 20 Ma and 22 Ma at 148 mbsf. These ages are well established from a range of techniques, including diatom biostratigraphy (Harwood et al., 1998), Sr isotope analysis (Lavelle, 1998), and Ar-Ar analysis on volcanic debris (McIntosh,

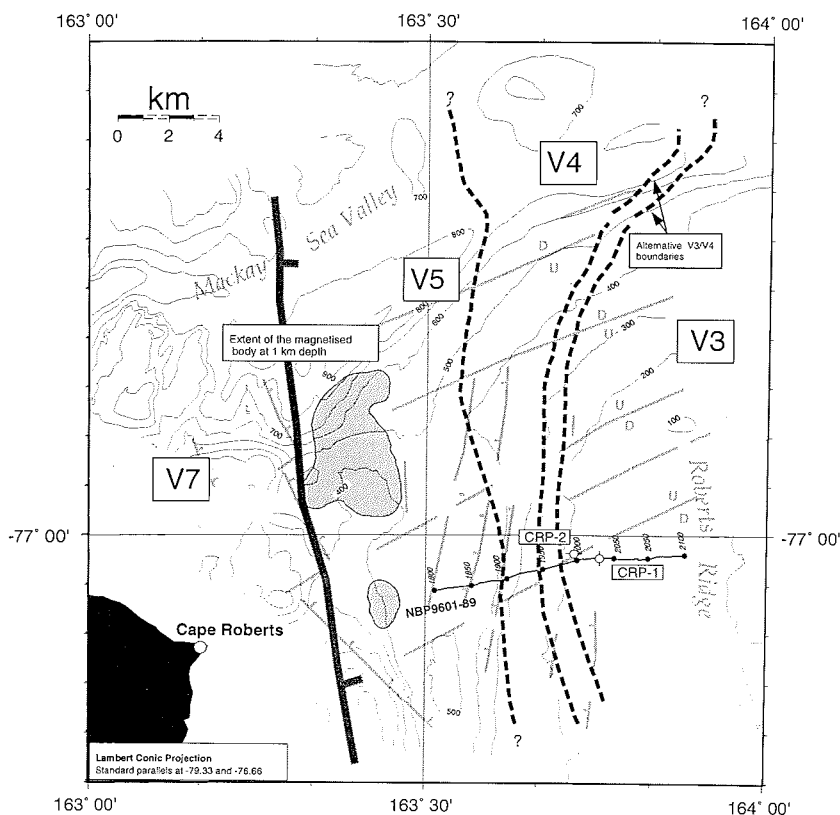


Fig. 1.3 - Map of the area off Cape Roberts (bathymetric contours in 50 metre intervals), showing the location of Roberts ridge, lines from key seismic surveys (dotted), the survey line on which the drill holes are based (solid, with drill sites) and the distribution of the older sedimentary sequences (V3, V4, V5) beneath the sea floor (dashed lines). The major fault inferred by Henrys et al. (1998) and the more complex fault systems interpreted by Hamilton et al. (1998) are also shown.

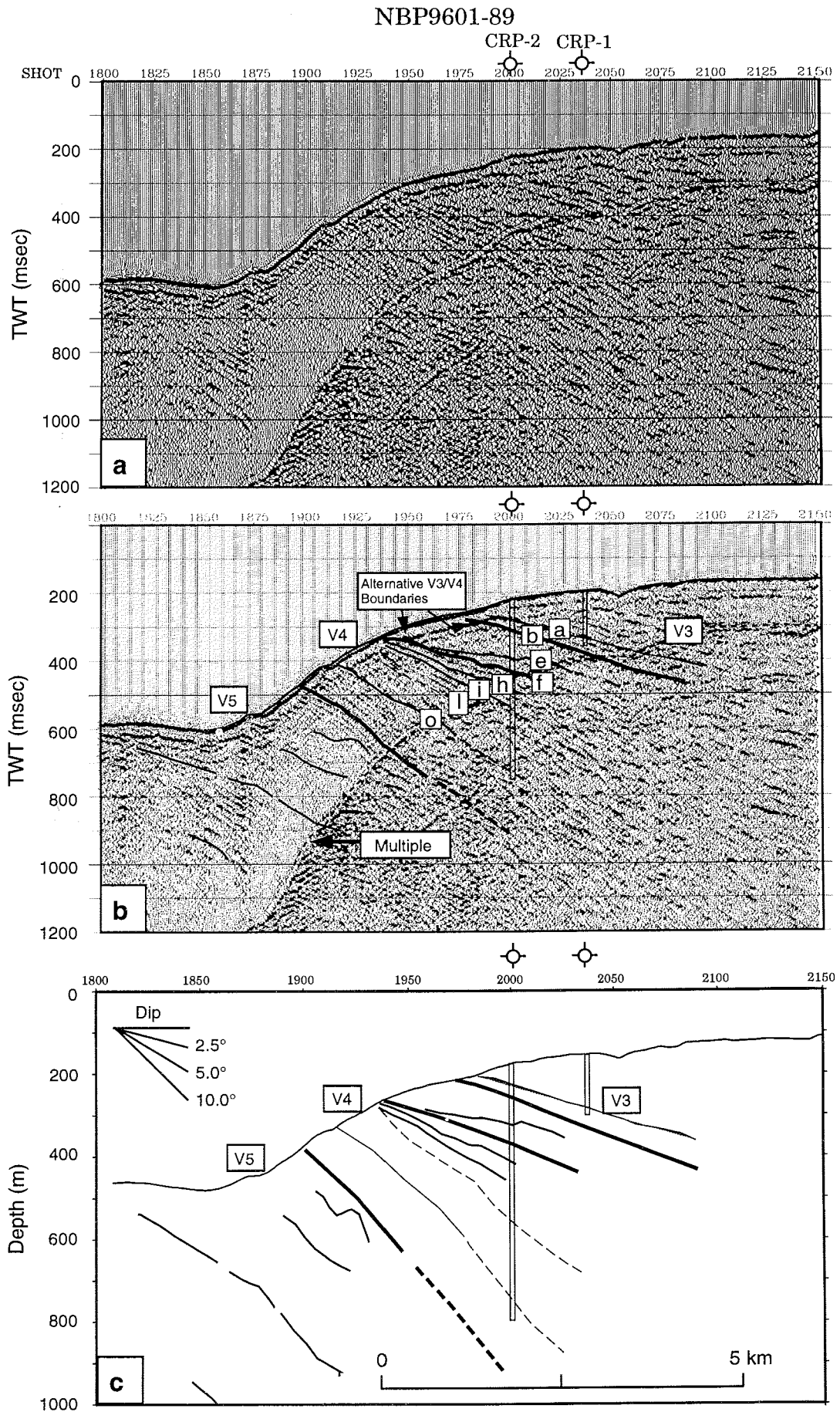


Fig. 1.4 - Seismic section NBP9601-89 (a), with interpretation in terms of two way travel time (b) and of depth (c). Major reflectors are identified by letter, and more fully described in table 2.1. Chronology is not yet well established but best estimates for the present are that reflector a is c. 20 Ma, alternative reflectors for the V3/V4 boundary straddle the Oligocene/Miocene boundary (23.5 Ma), which lies at 130 mbsf in the drill hole; reflector i corresponds to the late/early Oligocene boundary (c. 30 Ma), and reflector o is c. 33 Ma (close to the Oligocene/Eocene boundary).

1998), with some refinement using magnetostratigraphy (Roberts et al., 1998). It was plain, therefore, that the Cape Roberts sequence represented a record from perhaps 15 Ma and older (allowing for the 200 m of younger strata east of CRP-1 and not cored) rather than the 30 Ma and older strata that had been expected.

CRP-2/2A represents a second record of the period from *c.* 21 to *c.* 33 Ma from the area (the first being from CIROS-1 70 km to the south). This provides an excellent opportunity for comparing the two records in order to distinguish local from regional depositional, climatic and tectonic events. Both sites (CRP-2/2A and CIROS-1) are about the same distance seaward (10 km) of the main fault forming the present margin of the VLB, and both sites lie close to the mouths of outlet glaciers (Ferrari and Mackay, Fig. 1.1) draining the East Antarctic Ice Sheet. In addition, the strata imaged seismically above V4 (sequences N to Q in the more detailed stratigraphical scheme of Bartek et al., 1996) give a picture of locally channelled but extensive sheets of sediment persisting laterally for many tens of kilometres along the basin margin.

The pages that follow present not only the first primary data from CRP-2/2A but also the first attempts at correlation by age and lithology with CIROS-1, the necessary first step in identifying regional events with global implications, such as ice-sheet, sea-level, and rift-margin history. They also report on serendipitous discoveries, such as the striking volcanic ash layers in early Miocene strata from 109 to 114 mbsf, and the less obvious but nonetheless useful ash-rich layers as far down as 280 mbsf.

Detailed core descriptions (on a scale of 1:20 or 4 m to the page), and images of each core box (4 boxes to a page) are published separately as a supplement to this issue.

DRILL SITE OBSERVATIONS (SEA ICE, WEATHER, DRILLING OPERATIONS)

SEA-ICE OBSERVATIONS

Each winter a fringe of fast sea-ice (abbreviated to "fast ice") forms around the southern and western margins of McMurdo Sound, and extends north along the Victoria Land coast past Cape Roberts (Fig. 1.1). In most years it grows to a thickness of between 1.7 and 2.0 m, providing a safe platform for movement of heavy equipment and drilling operations (Pyne, 1986). In 1997, however, its thickness only just exceeded the minimum operational requirement of 1.5 m by early October (Cape Roberts Science Team, 1998).

In 1998, satellite imagery showed that the fast ice was forming by the end of March, and that it remained stable through April with an ice edge extending for *c.* 23 km off Cape Roberts. The ice grew steadily through the winter, and the first set of ice thickness observations showed that it had already reached 1.8 m in the proposed area for CRP-2 by 7 September 1998. Figure 1.5 compares satellite images from April, June and September, showing how little the ice edge changed through the winter, in contrast to the previous year (Cape Roberts Science Team, 1998, p. 8). By 7 October, as the rig was being set up, the ice thickness was greater than 2.0 m and continued to grow marginally into November, reaching a thickness about 2.2 m near the drill rig by 24 November, just before drilling ended (Tab. 1.2). On 20 November the ice surface at the drill site showed the initial signs of reaching isothermal condition but rapid decay of the ice surface in the immediate vicinity of the drill rig and mud huts only occurred during the

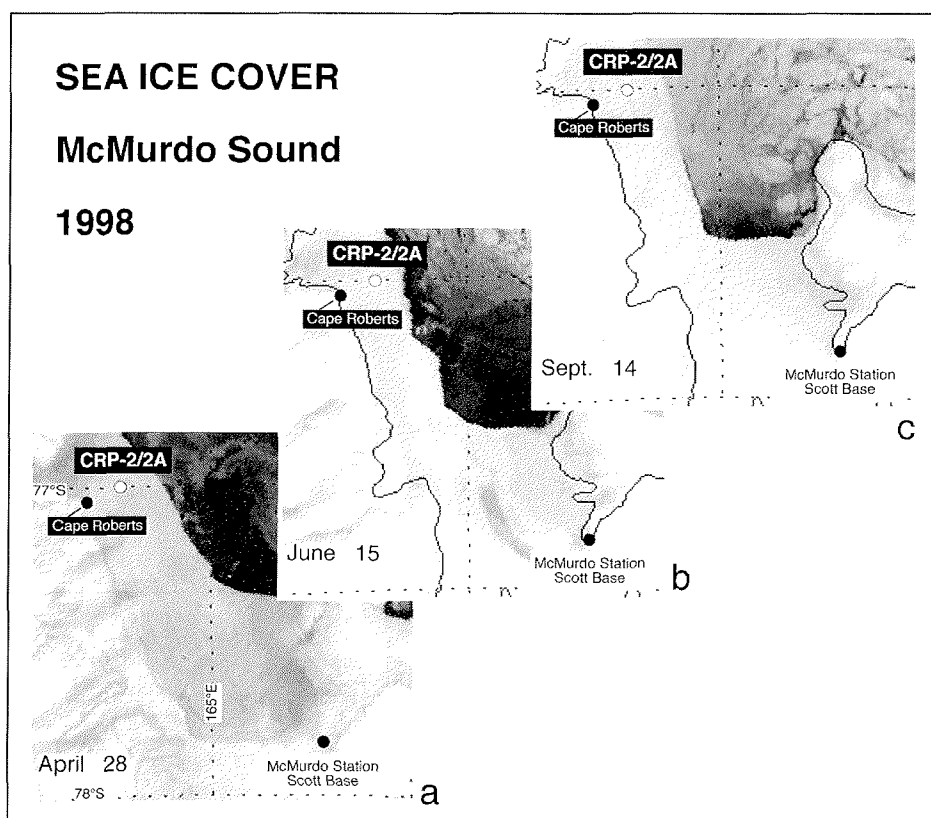


Fig. 1.5 - Satellite images of McMurdo Sound, showing the extent of the fast ice on 28 April, 15 June and 14 September, and the stability of the ice margin over this period.

period 30 November to 4 December when recovery of the drill site was completed.

In the past, the weight of the drilling system (around 55 tonnes with rig, supported casing and drill rods, and drilling fluid in tanks) has been supported almost entirely by the ice, resulting in progressive depression of the ice surface as drilling proceeded. This year, two air bags with a total lift of up to 10 tonnes (two 5 tonne bags) were placed under the ice immediately beneath the drill rig to compensate partially for the ice loading caused by the 17 tonne drill rig. Table 1.3 shows the depression of the ice surface through time, measured by levelling with reference to an arbitrary datum about 300 m east of the rig. The results of these levelling surveys are influenced not only by the drill rig but other distributed static loads such as the mud huts/generator complex and mobile loads (short term static) such as the bulldozers and sea riser/drill rod sledges. A measure of the local deflection under the drill rig is the amount of "freeboard" in the drilling ice hole, *i.e.* the height of the ice surface above sea level. Freeboard measurements were made daily by the drill crew. The initial freeboard before loading is taken as 10% of ice thickness. This year it was reduced by just 20 mm when drilling ended on 25 November, in contrast to a reduction of 170 mm when drilling ended on 24 October 1997, when no air bags were installed and the sea ice was significantly thinner and weaker (warmer).

Lateral movement of the fast ice was recorded using GPS equipment with decimeter accuracy at the drill site and three other locations within a distance of 300 m. The total movement of the rig during the period from the sea riser spud-in to the end of coring (15 October to 25

Tab. 1.2 - Growth in ice thickness at the site for CRP-2.

Date	Thickness (m)
7 September	1.81
12 September	1.78-1.85
25 September	1.82-1.97
8 October	~ 2.10
24 November	2.18

Tab. 1.3 - Deflection resulting from the load of the drilling system during the occupation of site CRP-2 using a datum on the sea-ice surface 300 m from the rig as a reference level.

Date	Peg D (mm)	Peg H (mm)
30 September	0	0
16 October	-16	-36
26 October	-7	-40
24 November	-13	-38

Note: 30 September is given an initial value of zero because it predates the loading of sea ice at the drill site. Pegs D and H were sites within 30 m of the rig and on either side.

Tab. 1.4 - Cumulative movement of sea-ice platform at CRP-2 from 17 October 1998.

Date	25 Oct	2 Nov	10 Nov	18 Nov	Nov 23
Distance (North)	-0.06 m	-0.70 m	0.60 m	0.10 m	1.17 m
Distance (East)	1.68 m	4.39 m	5.80 m	9.13 m	9.80 m
Distance (Total)	1.68 m	4.45 m	5.83 m	9.13 m	9.87 m

November) was about 10 m and was consistently offshore in an easterly direction (Tab. 1.4). This is well within the theoretical tolerances of operating stress for the sea riser deployed in water 178 m deep, although corrective measures were made after 18 November to restrain the

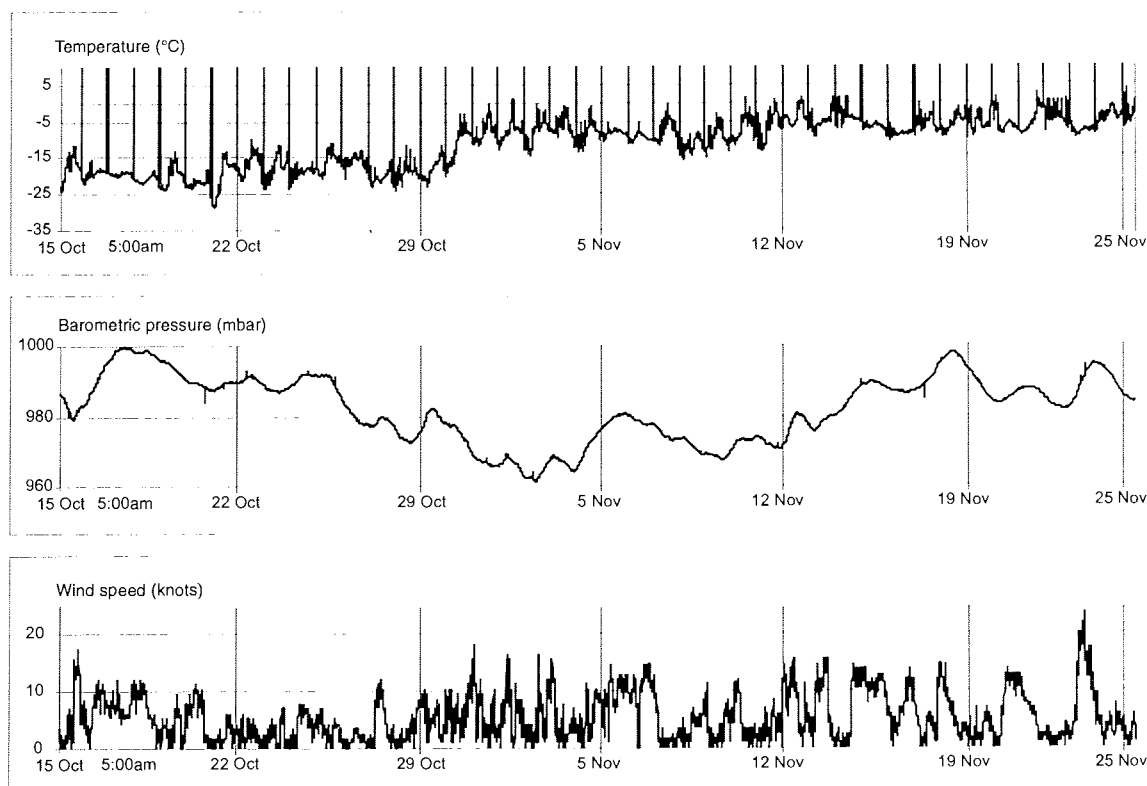


Fig. 1.6 - Temperature, wind and barometric pressure at Cape Roberts camp during the drilling period (15 October - 25 November 1998).

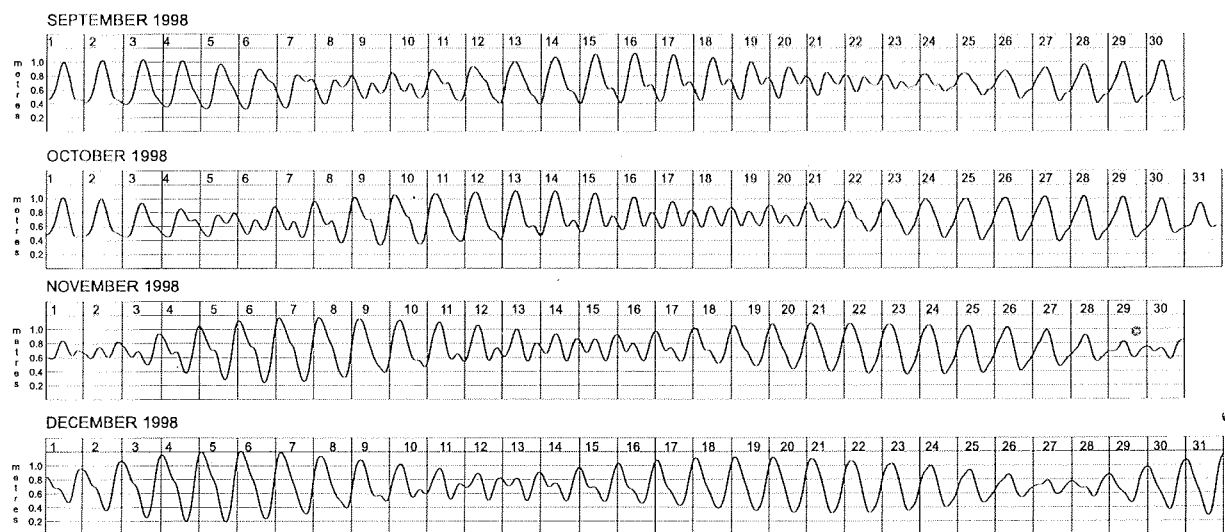


Fig. 1.7 - Tidal predictions for Cape Roberts from September to December 1998.

rotation of the riser at the drill rod entry point (top). This rotation was consistent in direction with that caused by an easterly offset of the sea ice platform. The other monitoring points within the drill site area also showed a consistent rate and direction of movement with that of the drilling rig over the same time period.

WEATHER OBSERVATIONS

During the drilling phase of the project from 15 October to 25 November, weather observations (temperature, wind speed, direction and barometric pressure) were recorded at the Cape Roberts Camp at five minute intervals (Fig. 1.6). The season was characterized by generally light winds and mostly clear skies. Snow fell on only a few days and was typically associated with light northerly winds. No drilling days were lost to weather, and conditions were good enough for flying on all but two shift changes during the 42 days of 24 hour per day operations that helicopters were scheduled.

Average daily temperatures rose from *c.* -25°C at the start of drilling in early October to *c.* -5°C at the end of drilling in late November. Maximum temperatures occurred during calm conditions regardless of time of day. Observed temperatures ranged from -33°C to +4.5°C.

Winds were generally light and from southerly quarters. The maximum measured wind gust at Cape Roberts Camp was 32 knots. However, hourly, 10-minute-mean wind

speeds only once exceeded 20 knots, and were below 10 knots for more than of 60% of the drilling period.

FACTORS AFFECTING DRILLING OPERATIONS (TIDES AND CURRENTS)

The drilling operation is influenced not only by the thickness and lateral movement of the sea ice but also tides and currents in the water column. The tides have two effects on the drilling: moving the sea ice through a vertical range varying from 0.3 during neap tides to 1.0 m during spring tides, and generating currents that drag the outer casing and flotation system (sea riser) in the water column. Tidal predictions (Fig. 1.7) were made on the basis of 12 months of records from the Cape Roberts tide gauge in 1996, and using a tidal prediction program from the University of Hawaii Sea Level centre. Observations through the drilling period showed that tides at Cape Roberts, and at CRP-2 14 km offshore, were synchronous, and generally similar in vertical range.

Current velocity and direction were recorded at CRP-2 using an S4 current meter in order to establish baseline data for deploying the sea riser, and to provide data for ensuring correct tension on the sea riser during peak current flows. The instrument was deployed through a hole in the sea ice, about 300 m south of the drill site from 24 September to 30 September, and then later in the Video Hut hole within 8 m of the drill rig (Tab. 1.5), during various stages of the

Tab. 1.5 - Summary of current meter deployments at the CRP-2 drill site. Full profile: 0 to 178 mbsl.

Name	Depth	Sampling rate	Period	Date
CRP2-98A	full profile	continuous	30 min	24 Sep
CRP2-98B	64 m	1 min averaged every 5 min	4 days	25 to 28 Sep
CRP2-98C	64 m	1 min averaged every 5 min	2 days	29 Sep to 1 Oct
CRP2-98D	full profile	continuous	30 min	30 Sep
CRP2-98E	40 m	1 min averaged every 5 min	1 day	9 to 10 Oct
CRP2-98F	20 m	1 min averaged every 5 min	2 days	11 to 13 Oct
CRP2-98G	20 m	1 min averaged every 5 min	no data held	14 Oct
CRP2-98H	full profile	continuous	1 hr	20 Oct
CRP2-98I	30 m	1 min averaged every 5 min	4 days	22 to 26 Oct

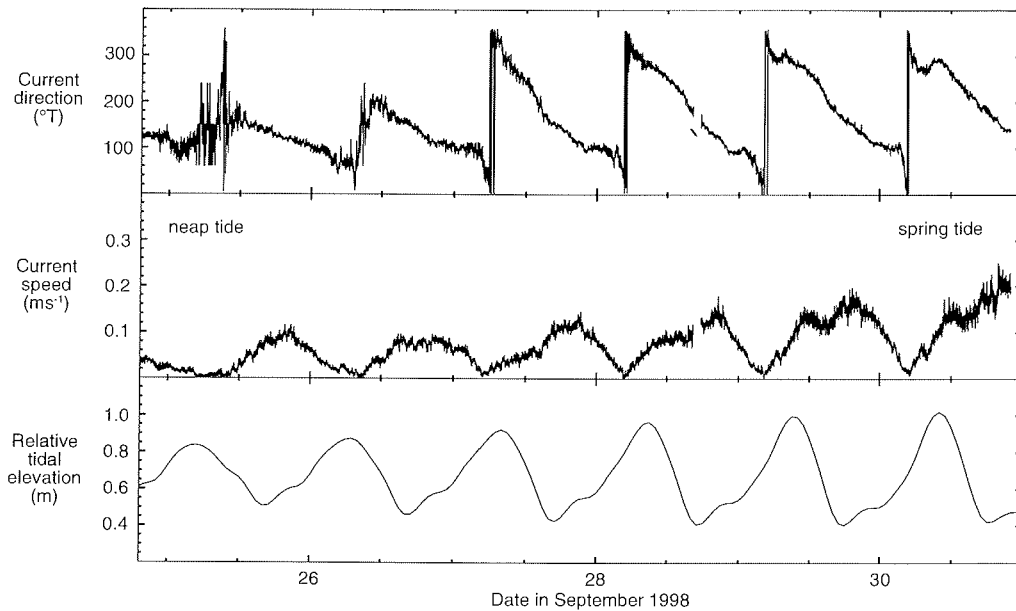


Fig. 1.8 - Current direction and speed compared with tidal movement for the period from 25 to 30 September 1998 at the site of CRP-2.

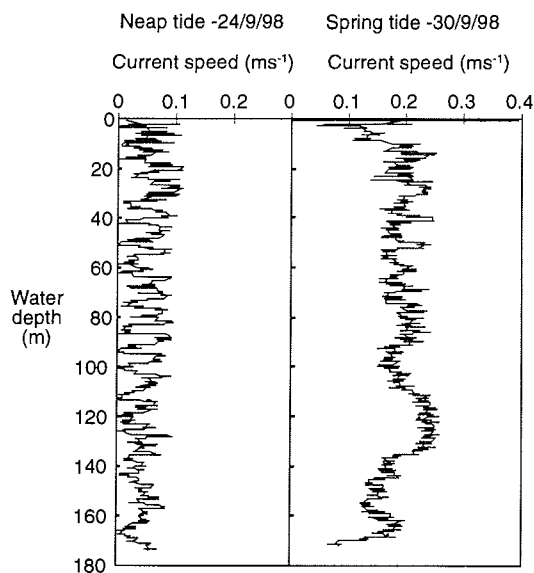


Fig. 1.9 - Current speed through the water column for a neap tide and a spring tide at the site of CRP-2.

spring-neap tidal cycle. Three of the deployments were to take vertical profiles through the entire water column of 178 m, and eight were static deployments at set depths for periods of time ranging from one to four days.

Spring tides were of greatest concern because of the high tidal currents associated with them. Figure 1.8 shows a plot of current speed, direction and predicted tidal variation in sea level, over a neap to spring tide period. The highest current speeds (0.25 ms^{-1} at c. 64 mbsl) occur during spring tides at the main low water of the day and on the smaller high water of the day. During spring tides the currents move in an anti-clockwise direction, swinging full circle during a 24 hour period. Current direction varies continuously between northwest at high water, through west to southeast at low tide and then to east during the smaller rising tide. For neap tides, however, current velocities are typically less than 0.1 ms^{-1} , and flow direction lies mostly within the southeasterly quarter.

Current speeds in the water column are low (from c. 0.1 to 0.05 ms^{-1}) during neap tides (Fig. 1.9). At spring

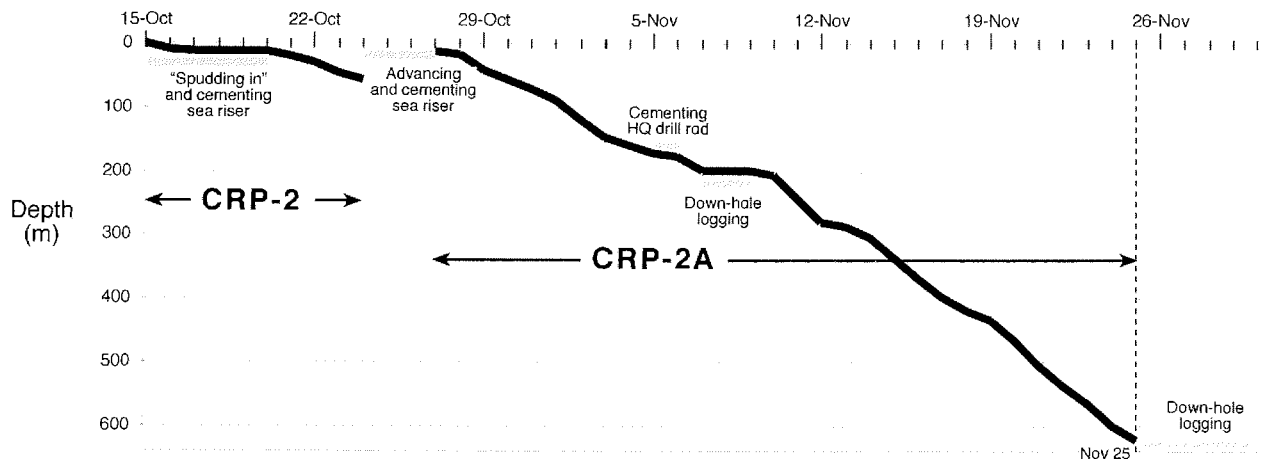


Fig. 1.10 - Plot of down-hole progress in CRP-2/2A.

tides (during the smaller high water of the day) current speeds rise sharply from almost zero at the base of the ice to between 0.16 and 0.20 ms⁻¹ at 10 mbsl. Speeds then change little until the interval from 105 to 135 m, where they rise to c. 0.24 ms⁻¹, before declining to c. 0.05 ms⁻¹ just above the sea floor.

DRILLING OPERATIONS

Core recovery began on 16 October and finished on 25 November at a depth of 624.15 mbsf. Down-hole progress is shown in figure 1.10, and details of times and recovery of each run in table 1.6.

The drilling was carried out by a Longyear 44HD wireline diamond drilling system and Q series drill rod. The first coring drill string (HQ), with core barrel and diamond bit at the bottom, is rotated inside 5 inch OD casing, supported by rigid flotation collars and inflatable air bags in the upper part of the casing string (termed the sea riser, Fig. 1.11). The HQ drill string cuts a 96 mm diameter hole and 61 mm diameter core. The second coring string (NQ), is rotated within the HQ once the latter is cemented into the formation as casing. The NQ string cuts a hole 76 mm diameter and 45 mm diameter core (Fig. 1.12). In both drill strings the core “slides” passively into a non-rotating “inner tube”, 3 (or 6) m long, which latches inside the core barrel as the drill bit penetrates into the formation. The inner tube itself is lined with two thin half-round steel sections (“splits”), which hold the core. After drilling for up to 3 (or 6) m, the inner tube is retrieved by a wire cable, termed the “wireline”, and the core pumped out on a bench still inside the “splits”. It is then transferred to the core-processing lab for description, measurement of physical properties and fractures, splitting and boxing.

The core cuttings are cleared from the hole and the walls stabilized by the drilling fluid, to which a range of additives are mixed to ensure the correct balance of density, viscosity and chemistry for these tasks. The additives are either naturally occurring in sea water (KCl) or biodegradable (Tab. 1.7). This hole required more drilling fluid additives than expected because of the time required to seat the sea riser properly, and the mud loss as a consequence of encountering loose sand beds and fractured formation at several levels down to 190 m. Firm ground was encountered at this level and the hole cased with the HQ drill rod to seal off the fluid loss zones above. Drilling proceeded quickly below this until more loose sand at 290 m led to further mud loss. The interval was small, and further similar sands were encountered briefly down to a depth of 550 m. In all, a total of 41 tonnes of additives were used in the drilling at CRP-2.

The various elements of the drilling system and camp were on site by 5 October and the rig assembled and in position by 7 October, when the ice hole for the drill rig was drilled. Two holes 1.1 m in diameter were then cut in the ice, one for the sea riser and the other for deploying the submarine video camera system (Fig. 1.11). Two cylindrical airbags (1.5 m diameter and 3 m long), each with 5 tonne lift capacity, were positioned by Crary Science & Engineering Center divers under the rig to reduce the effect of the 17 tonne drill rig depressing the

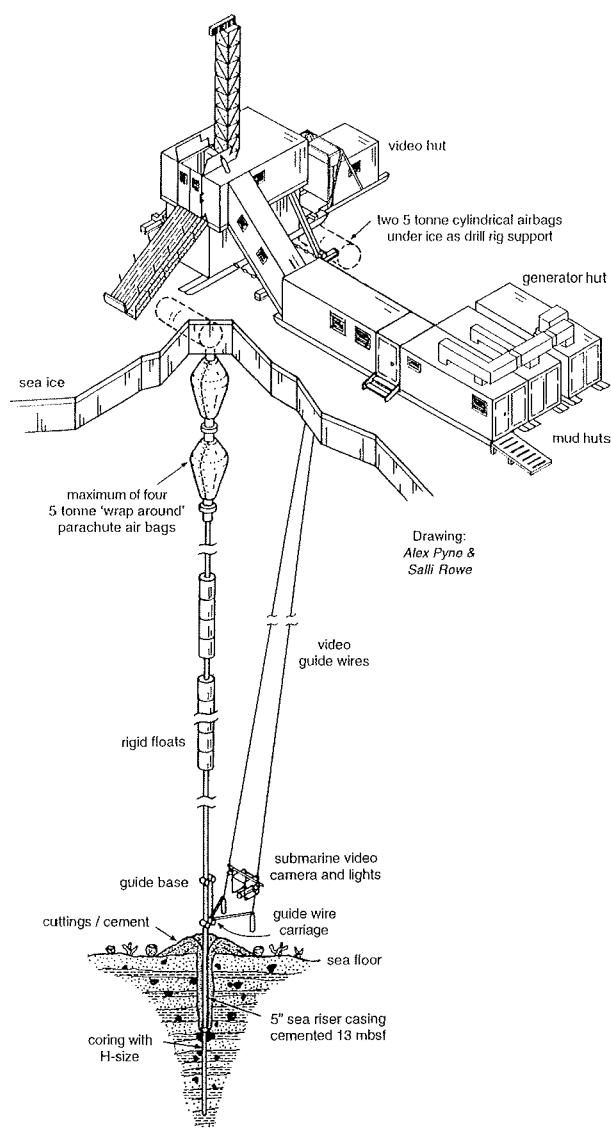


Fig. 1.11 - The drilling system used for CRP-2/2A, showing the rig, mud hut, video hut and the sea riser. Sketch: Alex Pyne & Salli Rowe.

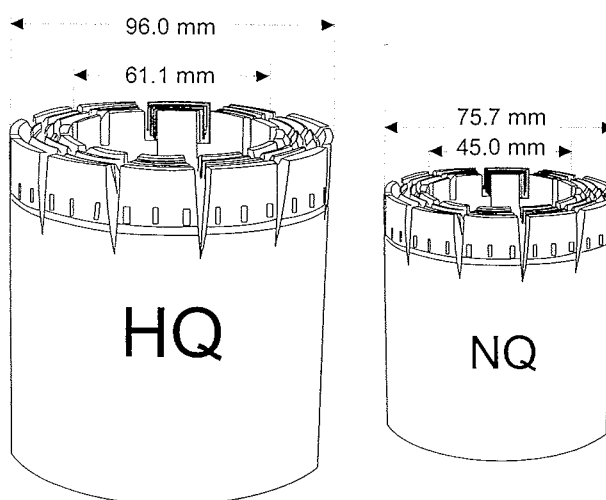


Fig. 1.12 - Main features and sizes of HQ and NQ coring bits. The bit is lubricated and cleared of cuttings by drilling fluid that is pumped down inside the drill string and through holes to the bit face, returning to the surface via the annulus between the drill rod and the hole wall (or the casing, where it has been set).

Tab. 1.6 - Data on down-hole progress and core recovery.

		Core Runs				Core Recovery						Core Runs				Core Recovery			
Run	Day	Time	Start	End	Length		Cumul		Run	Day	Time	Start	End	Length		Cumul			
			(mbsf)	(mbsf)	m	%	(m)	(%)				(mbsf)	(mbsf)	m	%	(m)	(%)		
1	Oct	0730	5.47	6.63	0.87	75	0.87	75	24		1620	54.56	55.54	0.85	87	3.08	100		
2	16	1045	6.61	7.69	1.05	97	1.92	86	25		1830	55.54	57.01	1.25	85	4.33	95		
3		1445	7.69	9.51	1.89	104	3.81	94	26		1940	57.01	57.64	0.58	92	4.91	95		
4		1640	9.51	12.03	2.50	99	6.31	96	<i>Drilled 17.63 m Rec'd 12.61 m (72%)</i>										
		<i>Drilled</i>	<i>6.56 m</i>	<i>Rec'd</i>	<i>6.31 m</i>	<i>(96%)</i>													
5	Oct	1242	12.21	14.21	1.98	99	8.29	95	27	Oct	0010	57.64	59.99	1.26	54	6.17	82		
6	21	1404	14.21	15.41	1.14	95	9.43	95	28	31	0230	59.99	60.61	0.74	119	6.91	85		
7		1640	15.41	17.11	1.59	94	11.02	95	29		0415	60.61	61.36	0.65	87	7.56	85		
8		1823	17.11	20.16	3.04	100	14.06	96	30		0550	61.36	62.21	0.85	100	8.41	86		
		<i>Drilled</i>	<i>7.95 m</i>	<i>Rec'd</i>	<i>7.75 m</i>	<i>(97%)</i>													
9		2150	20.16	21.86	1.40	82	15.46	94	31		0720	62.21	62.71	0.50	100	8.91	87		
10	Oct	0130	21.86	22.95	0.75	69	16.21	93	32		0945	62.71	63.08	0.37	100	9.28	87		
11	22	1100	22.95	23.41	0.00	0	16.21	90	33		1130	63.08	64.29	1.21	100	10.49	89		
12		1400	23.41	25.59	2.07	95	18.28	91	34		1425	64.29	66.13	1.86	101	12.35	90		
13		1607	25.59	25.94	0.29	83	18.57	91	35		1600	66.13	67.46	1.33	100	13.68	91		
14		1700	25.94	27.18	0.80	65	19.37	89	36		1730	67.46	68.53	1.05	98	14.73	92		
		<i>Drilled</i>	<i>7.02 m</i>	<i>Rec'd</i>	<i>5.31 m</i>	<i>(76%)</i>													
15		2030	27.18	28.46	0.81	63	20.18	88	37		1930	68.53	69.72	1.06	89	15.79	91		
16		2120	28.46	30.26	1.86	103	22.04	89	38		2145	69.72	70.56	0.76	90	16.55	91		
17		2350	30.26	32.49	2.06	92	24.10	89	39	Nov	0001	70.56	71.86	1.30	100	17.85	92		
18	Oct	0230	32.49	34.26	1.70	96	25.80	90	40	1	0300	71.86	73.31	0.76	52	18.61	89		
19	23	0400	34.26	35.58	1.09	83	26.89	89	41		0410	73.31	74.98	1.65	99	20.26	90		
20		0615	35.58	37.68	1.64	78	28.53	89	42		0550	74.98	77.46	2.41	97	22.67	91		
21		0900	37.68	39.41	1.66	96	30.19	89	43		0650	77.46	78.66	1.18	98	23.85	91		
22		1140	39.41	40.41	0.92	92	31.11	89	44		0930	78.66	80.26	1.52	95	25.37	91		
23		1215	40.41	40.66	0.58	232	31.69	90	45		1135	80.26	82.42	1.98	92	27.35	91		
24		1430	40.66	42.41	1.71	98	33.40	90	46		1310	82.42	83.42	1.19	119	28.54	92		
25		1605	42.41	43.81	0.36	26	33.76	88	47		1600	83.42	85.99	2.57	100	31.11	93		
26		1740	43.81	45.41	1.60	100	35.36	89	48		1830	85.99	88.57	2.51	97	33.62	93		
27		1900	45.41	46.56	1.05	91	36.41	89	<i>Drilled 18.85 m Rec'd 17.83 m (95%)</i>										
28		2000	46.56	46.86	0.40	133	36.81	89	49		2000	88.57	90.21	1.60	98	35.22	93		
		<i>Drilled</i>	<i>19.68 m</i>	<i>Rec'd</i>	<i>17.44 m</i>	<i>(89%)</i>													
29		2130	46.86	47.81	0.89	94	37.70	89	50		2130	90.21	92.76	2.55	100	37.77	94		
30		2310	47.81	49.31	1.50	100	39.20	89	51		2300	92.76	95.01	2.25	100	40.02	94		
31	Oct	0100	49.31	50.73	1.42	100	40.62	90	52	Nov	0020	95.01	96.71	1.70	100	41.72	94		
32	24	0245	50.73	52.37	1.64	100	42.26	90	53	2	0225	96.71	99.45	2.74	100	44.46	95		
33		0430	52.37	54.17	1.84	102	44.10	91	54		0400	99.45	102.56	3.10	100	47.56	95		
34		0630	54.17	55.56	1.30	94	45.40	91	55		0600	102.56	105.66	3.03	98	50.59	95		
35		0800	55.51	57.43	1.86	97	47.26	91	56		0920	105.66	108.69	3.06	101	53.65	95		
		<i>Drilled</i>	<i>10.57 m</i>	<i>Rec'd</i>	<i>10.45 m</i>	<i>(99%)</i>													
End of CRP-2 on 24 October 1998, at 57.43 mbsf; start of CRP-2A on 18 October 1998, at 12.20 mbsf.										57		1100	108.69	111.69	3.00	100	56.65	96	
1	Oct	1710	12.20	13.46	0.47	37	0.47	37	58		1310	111.69	114.69	3.00	100	59.65	96		
2	28	1837	13.46	14.75	1.29	100	1.76	69	59		1430	114.69	117.11	2.40	99	62.05	96		
3		2000	14.75	15.59	0.75	89	2.51	74	60		1650	117.11	120.11	2.97	99	65.02	96		
		<i>Drilled</i>	<i>3.39 m</i>	<i>Rec'd</i>	<i>2.51 m</i>	<i>(74%)</i>													
4		2230	15.59	16.61	0.41	40	2.92	66	61		1740	120.11	120.66	0.51	93	65.53	96		
5	Oct	0030	16.61	18.61	0.65	33	3.57	56	62		1930	120.66	121.16	0.52	104	66.05	96		
6	29	0215	18.61	20.21	1.40	87	4.97	62	63		2120	121.16	123.57	2.41	100	68.46	96		
7		0400	20.21	21.01	0.33	41	5.30	60	64	Nov	0020	123.57	126.60	3.03	100	71.49	96		
8		0540	21.01	22.31	0.57	44	5.87	58	65	3	0210	126.60	129.71	3.10	100	74.59	97		
9		0630	22.31	23.36	0.20	19	6.07	54	66		0400	129.71	132.71	3.00	100	77.59	97		
10		0810	23.36	24.76	0.80	57	6.87	55	67		0535	132.71	135.74	3.03	100	80.62	97		
11		1035	24.76	25.23	0.23	49	7.10	54	68		0945	135.74	138.74	2.88	96	83.50	97		
12		1215	25.23	27.14	0.97	51	8.07	54	69		1135	138.74	141.74	3.06	102	86.56	97		
13		1830	27.14	39.13	0.92	8	8.99	33	70		1315	141.74	144.74	2.87	96	89.43	97		
14		2000	39.13	40.01	0.88	100	9.87	35	71		1430	144.74	145.91	0.89	76	90.32	97		
		<i>Drilled</i>	<i>24.42 m</i>	<i>Rec'd</i>	<i>6.95 m</i>	<i>(28%)</i>													
15		2145	40.01	41.06	0.78	74	10.65	37	72		1600	145.91	146.65	0.78	105	91.10	97		
16		2315	41.06	42.81	0.69	39	11.34	37	73		1800	146.65	147.65	1.00	100	92.10	97		
17	Oct	0415	42.81	47.17	1.20	28	12.54	36	74		1955	147.65	148.52	0.87	100	92.97	97		
18	30	0550	47.17	48.16	0.82	83	13.36	37	<i>Drilled 27.86 m Rec'd 27.44 m (98%)</i>										
19		0900	48.16	48.93	0.69	90	14.05	38	75		2305	148.52	150.36	1.41	77	94.38	96		
20		1045	48.93	50.97	2.09	102	16.14	42	76	Nov	0030	150.36	151.30	0.85	90	95.23	96		
21		1215	50.97	52.46	1.43	96	17.57	42	77	4	0200	151.30	151.90	0.61	102	95.84	96		
		<i>Drilled</i>	<i>40.26 m</i>	<i>Rec'd</i>	<i>17.10 m</i>	<i>(42%)</i>													
22		1345	52.46	53.68	1.30	107	1.30	107	78		0310	151.90	152.71	0.71	88	96.55	96		
23		1450	53.58	54.56	0.93	95	2.23	106	79		0805	152.71	153.01	0.26	87	96.81	96		
									80		1030	153.01	154.46	1.28	88	98.09	96		
									81		1330	154.46	155.14	0.60	88	98.69	96		
									82		1800	155.14	157.73	2.47	95	101.16	96		
									83		1915	157.73	157.91	0.14	78	101.30	96		
		<i>Drilled</i>	<i>13.17 m</i>	<i>Rec'd</i>	<i>11.87 m</i>	<i>(90%)</i>													
									84		2300	157.91	159.36	1.49	103	102.79	96		
									85	Nov	0400	159.36	162.55	3.00	94	105.79	96		
									86	5	0600	162.55	165.61	3.09	101	108.88	96		
									87		1130	165.61							

Tab. 1.6 - Continued.

Core Runs				Core Recovery				Core Runs				Core Recovery									
Run	Day	Time	Start	End	Length	Cumul	Run	Day	Time	Start	End	Length	Cumul								
			(mbsf)	(mbsf)	m	% (m) (%)				(mbsf)	(mbsf)	m	% (m) (%)								
88		1400	168.61	171.61	3.00	100	114.71	96	148	2100	366.54	368.62	1.13	54	305.04	97					
	<i>Drilled</i>	<i>13.70 m</i>	<i>Rec'd</i>	<i>13.41 m</i>	<i>(98%)</i>				149		2300	368.62	371.62	2.07	69	307.11	96				
Drilling ceased for downhole logging.																					
89	<i>Nov</i>	1620	171.61	174.61	2.71	90	117.42	96	150	<i>Nov</i>	0030	371.62	374.62	2.54	85	309.65	96				
90	<i>6</i>	1845	174.61	177.36	2.91	106	120.33	96	151	<i>17</i>	0245	374.62	377.62	2.55	85	312.20	96				
	<i>Drilled</i>	<i>5.75 m</i>	<i>Rec'd</i>	<i>5.62 m</i>	<i>(98%)</i>				152		0400	377.62	380.62	2.64	88	314.84	96				
91		2140	177.36	180.31	3.08	104	123.41	97	153		0511	380.62	383.62	2.82	94	317.66	96				
92		2340	180.31	183.21	2.85	98	126.26	97	154		0645	383.62	386.62	2.87	96	320.53	96				
93	<i>Nov</i>	0140	183.21	186.11	2.80	97	129.06	97	155		0825	386.62	387.40	0.70	90	321.23	96				
94	<i>7</i>	0230	186.11	186.86	0.61	81	129.67	96	156		1015	387.40	387.56	0.16	100	321.39	96				
95		0415	186.86	188.05	1.19	100	130.86	97	157		1345	387.56	390.37	2.81	100	324.20	96				
96		0530	188.05	189.17	1.00	89	131.86	96	158		1525	390.37	393.37	2.95	98	327.15	96				
97		0730	189.17	189.74	0.57	100	132.43	96	159		1700	393.37	395.42	1.75	85	328.90	96				
98		1200	189.74	192.67	2.30	78	134.73	96	160		1930	395.42	397.42	1.49	75	330.39	96				
99		1345	192.67	192.97	0.16	53	134.89	96	<i>Drilled 30.88 m Rec'd 26.48 m (86%)</i>				162		2100	397.42	398.94	1.33	88	331.72	96
100		1700	192.97	195.97	2.89	96	137.78	96	163		2250	398.94	401.62	2.02	75	333.74	96				
101		1930	195.97	198.79	2.87	102	140.65	96	164	<i>Nov</i>	0000	401.62	404.54	1.81	62	335.55	95				
102		2100	198.79	199.39	0.52	87	141.17	96	165	<i>18</i>	0200	404.54	407.62	3.09	100	338.64	95				
	<i>Drilled</i>	<i>22.03 m</i>	<i>Rec'd</i>	<i>20.84 m</i>	<i>(95%)</i>				166		0400	407.62	410.62	3.05	102	341.69	95				
End of HQ hole; start of NQ hole.																					
103	<i>Nov</i>	0510	199.39	201.02	1.46	90	142.63	96	167		0530	410.62	412.97	2.29	97	343.98	95				
104	<i>10</i>	1754	201.02	207.02	6.07	101	148.70	96	168		1055	412.97	415.97	3.04	101	347.02	96				
	<i>Drilled</i>	<i>7.63 m</i>	<i>Rec'd</i>	<i>7.53 m</i>	<i>(99%)</i>				169		1300	415.97	417.96	1.22	61	348.24	95				
105		2230	207.02	213.07	5.81	96	154.51	96	170		1530	417.96	418.56	0.60	100	348.84	95				
106	<i>Nov</i>	0200	213.07	219.03	5.87	98	160.38	96	171		1630	418.56	418.92	0.33	92	349.17	95				
107	<i>11</i>	0630	219.03	225.05	5.97	99	166.35	96	<i>Drilled 21.50 m Rec'd 18.78 m (87%)</i>				172	<i>Nov</i>	0315	418.92	419.62	0.69	99	349.86	95
108		1050	225.05	231.00	6.10	103	172.45	97	173	<i>19</i>	0500	419.62	422.62	1.24	41	351.10	95				
109		1415	231.00	237.09	5.99	98	178.44	97	174		0615	422.62	425.17	1.84	72	352.94	95				
110		1830	237.09	243.09	6.03	101	184.47	97	175		0830	425.17	426.75	1.17	74	354.11	95				
	<i>Drilled</i>	<i>36.07 m</i>	<i>Rec'd</i>	<i>35.77 m</i>	<i>(99%)</i>				176		0925	426.75	428.14	0.93	67	355.04	95				
111		2230	243.09	249.09	6.00	100	190.47	97	177		1110	428.14	430.58	1.88	77	356.92	94				
112	<i>Nov</i>	0230	249.09	255.09	6.06	101	196.53	97	178		1500	430.58	433.06	0.55	22	357.47	94				
113	<i>12</i>	0645	255.09	261.09	5.99	100	202.52	97	179		1800	433.06	435.20	2.23	104	359.70	94				
114		1055	261.09	267.09	6.00	100	208.52	97	<i>Drilled 16.28 m Rec'd 10.53 m (65%)</i>				180		2210	435.20	437.56	2.26	96	361.96	94
115		1455	267.09	273.09	6.02	100	214.54	97	181	<i>Nov</i>	0000	437.56	440.62	3.08	101	365.04	94				
116		1800	273.09	279.09	5.98	100	220.52	97	182	<i>20</i>	0200	440.62	443.62	2.99	100	368.03	94				
	<i>Drilled</i>	<i>36.00 m</i>	<i>Rec'd</i>	<i>36.05 m</i>	<i>(100%)</i>				183		0415	443.62	446.62	3.02	101	371.05	94				
117		2038	279.09	281.22	1.30	61	221.82	97	184		0630	446.62	449.62	3.01	100	374.06	94				
118		2330	281.22	282.77	1.01	65	222.83	97	185		0835	449.62	452.64	3.03	100	377.09	94				
119	<i>Nov</i>	0430	282.77	285.24	0.50	20	223.33	96	186		1005	452.64	455.64	2.97	99	380.06	94				
120	<i>13</i>	1140	285.24	288.22	2.92	98	226.25	96	187		1155	455.64	458.64	3.01	100	383.07	94				
	<i>Drilled</i>	<i>9.13 m</i>	<i>Rec'd</i>	<i>5.73 m</i>	<i>(63%)</i>				188		1345	458.64	461.64	2.98	99	386.05	94				
121	<i>Nov</i>	1100	288.22	290.58	2.18	92	228.43	96	189		1530	461.64	464.64	3.00	100	389.05	94				
122	<i>14</i>	1330	290.58	293.58	2.98	99	231.41	96	190		1725	464.64	467.64	3.00	100	392.05	94				
123		1510	293.58	296.62	3.09	102	234.50	96	<i>Drilled 32.44 m Rec'd 32.35 m (100%)</i>				191		2030	467.64	470.64	2.93	98	394.98	94
124		1642	296.62	299.62	3.00	100	237.50	96	192		2240	470.64	473.62	3.03	102	398.01	95				
125		1815	299.62	302.62	2.95	98	240.45	96	193	<i>Nov</i>	0015	473.62	476.62	2.80	93	400.81	95				
	<i>Drilled</i>	<i>14.40 m</i>	<i>Rec'd</i>	<i>14.20 m</i>	<i>(99%)</i>				194	<i>21</i>	0130	476.62	479.61	3.06	102	403.87	95				
126		2010	302.62	305.62	3.03	101	243.48	96	195		0315	479.61	482.62	3.05	101	406.92	95				
127		2250	305.62	308.62	2.97	99	246.45	96	196		0445	482.62	485.62	2.97	99	409.89	95				
128	<i>Nov</i>	0100	308.62	311.62	3.02	101	249.47	96	197		0630	485.62	488.62	3.04	101	412.93	95				
129	<i>15</i>	0360	311.62	314.62	2.99	100	252.46	96	198		0910	488.62	491.64	3.04	101	415.97	95				
130		0545	314.62	317.62	3.00	100	255.46	96	199		1100	491.64	494.64	3.02	101	418.99	95				
131		0630	317.62	320.62	2.99	100	258.45	96	200		1225	494.64	497.64	3.08	103	422.07	95				
132		0925	320.62	323.62	3.09	103	261.54	97	201		1350	497.64	500.79	3.11	99	425.18	95				
133		1105	323.62	326.62	2.97	99	264.51	97	202		1625	500.79	503.84	2.98	98	428.16	95				
134		1325	326.62	329.62	2.94	98	267.45	97	203		1810	503.84	506.84	2.96	99	431.12	95				
135		1540	329.62	332.62	2.87	96	270.32	97	<i>Drilled 39.20 m Rec'd 39.07 m (100%)</i>				204		2245	506.84	509.65	2.86	102	433.98	95
136		1810	332.62	335.62	3.10	103	273.42	97	205	<i>Nov</i>	0120	509.65	512.59	2.45	83	436.43	95				
	<i>Drilled</i>	<i>15.00 m</i>	<i>Rec'd</i>	<i>14.97 m</i>	<i>(100%)</i>				206	<i>22</i>	0310	512.59	515.62	3.11	103	439.54	95				
137		2030	335.62	338.62	3.01	100	276.43	97	207		0530	515.62	518.62	2.96	99	442.50	95				
138		2330	338.62	341.62	2.99	100	279.42	97	208		0930	518.62	521.64	3.05	101	445.55	95				
139	<i>Nov</i>	0150	341.62	344.62	3.02	101	282.44	97	209		1205	521.64	524.64	3.04	101	448.59	95				
140	<i>16</i>	0400	344.62	347.62	3.00	100	285.44	97	210		1400	524.64	527.64	3.00	100	451.59	95				
141		0659	347.62	350.62	2.98	99	288.42	97	211		1555	527.64	530.64	2.79	93	454.38	95				
142		0900	350.62	353.62	3.02	101	291.44	97	212		1735	530.64	533.64	2.62	87	457.00	95				
143		1030	353.62	356.64	2.94	97	294.38	97	213		1935	533.64	536.64	1.							

Tab. 1.6 - Continued.

Run	Day	Time	Core Runs		Core Recovery				Run	Day	Time	Core Runs		Core Recovery			
			Start (mbsf)	End (mbsf)	Length (m)	%	Cumul (m)	(%)				Start (mbsf)	End (mbsf)	Length (m)	%	Cumul (m)	(%)
219		0900	551.61	553.93	1.80	78	472.26	94	234		1555	591.11	594.12	3.01	100	512.41	95
220		1155	553.93	554.63	0.31	44	472.57	94	235		1735	594.12	597.12	3.00	100	515.41	95
221		1258	554.63	557.31	3.07	115	475.64	94	236		1920	597.12	600.12	3.00	100	518.41	95
222		1515	557.31	560.34	3.03	100	478.67	94	Drilled 33.78 m Rec'd 33.71 m (100%)								
223		1725	560.34	563.34	3.06	102	481.73	94	237		2240	600.12	603.00	2.88	100	521.29	95
224		1930	563.34	566.34	2.97	99	484.70	94	238		0115	603.00	606.08	3.08	100	524.37	95
Drilled 29.70 m Rec'd 25.91 m (87%)									239		0315	606.08	609.07	2.99	100	527.36	95
225		2140	566.34	568.04	1.64	96	486.34	94	240		0510	609.07	612.04	2.97	100	530.33	95
226		2330	568.04	570.02	1.99	101	488.33	94	241		0715	612.04	615.09	3.05	100	533.38	95
227	Nov	0107	570.02	573.04	3.06	101	491.39	94	242		0925	615.09	618.07	2.98	100	536.36	95
228	24	0300	573.09	576.04	2.95	100	494.34	94	243		1140	618.07	621.10	3.03	100	539.39	95
229		0440	576.02	579.06	3.02	99	497.36	94	244		1420	621.10	624.15	3.05	100	542.44	95
230		0640	579.06	582.09	3.02	100	500.38	95	Drilled 24.03 m Rec'd 24.03 m (100%)								
231		0920	582.09	585.09	3.00	100	503.38	95	End of hole CRP-2A.								
232		1130	585.09	588.09	3.00	100	506.38	95									
233		1410	588.09	591.11	3.02	100	509.40	95									

ice. The sea riser was then lowered to the sea floor with the video camera guide wire carriage positioned below the rigid floats installed on 5.5 m lengths of casing. The inflatable float system was then strapped to the top of the riser. The sea riser finally penetrated the sea floor (was "spudded-in") at 1000 NZDT on 15 October (Fig. 1.11).

The sea floor was covered with a layer about 0.8 m thick of sponge mat and sandy mud. Beneath this lay a stiff coarse gravelly mud. The sea riser was initially advanced to resistance at 1.7 mbsf, and a hole drilled to around 5.5 mbsf. Coring in H size (61 mm) then proceeded to 12 mbsf, revealing that the gravelly bed extended only to 5.5 mbsf, beneath which lay a firm sandy diamicton. The sea riser was then advanced further but could not be moved beyond 5.5 mbsf on account of a boulder (Fig. 1.13). Cementing followed over the next 3 days, but with little success on account of the low temperatures (-1.8°C) at the sea floor. Coring began again on 20 October, reaching 57 mbsf by 24 October, but continued mud loss to the sea floor required a further effort to embed the sea riser deeper into the sea floor.

Further embedment of the sea riser involved "spike-loading" (lifting and dropping the casing several centimetres with the main winch) into the firm diamicton, and then deployment of an under-reamer for widening the hole ahead of the casing. The under-reamer was only partially successful in widening the hole for around 2 m beneath the bottom of the casing. In addition, it became loose and detached itself, possibly after catching on a large clast. Although it was subsequently recovered, it was considered too much of a risk to deploy again in this inhomogeneous formation. Progress continued by spike-loading the sea riser to a depth of 13 mbsf, when a boulder was encountered. The sea riser was successfully cemented at this level.

Coring in H then proceeded from 13 mbsf. However in the embedment process the base of the sea riser had moved out of CRP-2, resulting in a new hole being cored. This has been termed CRP-2A. At 18 mbsf the bit returned to CRP-2, but after either fully or partially following the old hole it veered off again at around 30 mbsf and continued down in entirely new ground. Some core was recovered from the interval from 18 to 30 mbsf, showing the wall of

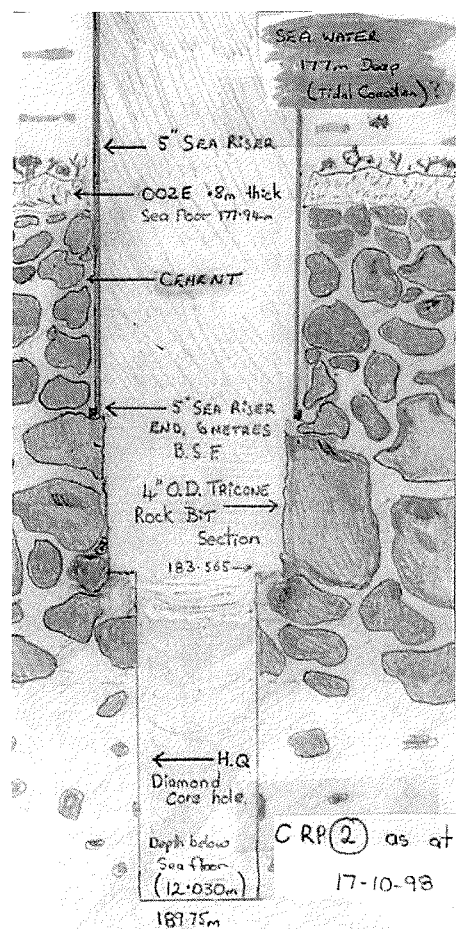


Fig. 1.13 - Impression of the sea riser as it was initially embedded into the sea floor. Sketch: Pat Cooper.

CRP-2. Progress continued at a rate of about 20 m/day, until further loose sand was encountered at around 150 mbsf, and continuous full mud loss indicated that the hole would need to be cased as soon as sound formation was encountered. Because the hole seemed not to be caving much, it was decided to make time for logging in the open hole. This was done for the interval from 62 mbsf (above which there was a higher likelihood of

Tab. 1.7 - Additives used in CRP-2/2A for the drilling fluid.

SEA RISER INSTALLATION													
Date	Depth (mbsf)	Metres Cored	KCl ~ 40kg	Guar 25 kg	XCD 25 kg	Pac-R 25kg	Mica 25kg	Cement 40kg	CaCl 25kg	Barites 25kg	Mixes (1800 l)	Vol (cu.m)	Cement (litres)
13/10/98			3	1									
14/10/98			3	1							1	1.8	
15/10/98			70	13							23	41.4	
16/10/98								30	0.6		0.33	0.594	600
17/10/98													
18/10/98			2										
19/10/98			4					15	0.6				300
20/10/98			21	1	4	2					13	23.4	
25/10/98			16	3							6	10.8	
26/10/98			4	4				10	0.6		7	12.6	200
TOTAL (SEA RISER)			4.92	0.575	0.1	0.05		2.2	0.05		50.33	90.59	
(additives in tonnes)													
HQ CORING													
15/10/98	5.47											(cu.m)	(litres)
16/10/98	12.03	6.56	42	8							14	25.2	
20/10/98	12.21	0.18											
21/10/98	22.95	10.74	37.5		8	6					25	45	
22/10/98	32.49	9.54			12	11					46	82.8	
23/10/98	49.31	16.82	68		9	7					48	86.4	
24/10/98	57.42	8.11	16	4					1		8	14.4	
27/10/98	13.46	13.46											
28/10/98	16.61	3.15			3	3					14	25.2	
29/10/98	42.81	26.20			4	4	3				22	39.6	
30/10/98	57.64	14.83			3	4	4				17	30.6	
31/10/98	70.56	12.92	44		2	2					18.5	33.3	
1/11/98	95.01	24.45	52.5		5	4	16		1		27	48.6	
2/11/98	123.57	28.56	24		5	4	5		1		24	43.2	
3/11/98	150.36	26.79	22		5	5	2		2		26	46.8	
4/11/98	159.36	9.00	31	4	3	4					31	55.8	
5/11/98	171.61	12.25	10		2	2					11	19.8	
6/11/98	183.22	11.61	20		3	4					20	36	
7/11/98	199.31	16.09	23		2	2		6	1		19	34.2	120
TOTAL (HQ)			19.28	0.4	1.65	1.55	0.75	0.24	0.15		210.5	378.9	
(Additives in tonnes)													
NQ CORING													
9/11/98	199.31		22		1	1				3	6	10.8	
10/11/98	213.07	13.76	16		2	3	1				10	18	
11/11/98	249.11	36.04	19		3	3	5				19	34.2	
12/11/98	282.77	33.66	12		2	2	4				12	21.6	
13/11/98	288.22	5.45	24	2	1	2					11	19.8	
14/11/98	311.62	23.40	20		1	2					10	18	
15/11/98	341.62	30.00	15	1	2	1					11	19.8	
16/11/98	371.62	30.00	3						1		3	5.4	
17/11/98	404.54	32.92	4	1							4	7.2	
18/11/98	418.92	14.38	6		1						3	5.4	
19/11/98	440.62	21.70	6	1	1						6	10.8	
20/11/98	476.62	36.00	7	1	1						7	12.6	
21/11/98	509.65	33.03	5		1						5	9	
22/11/98	542.62	32.97	5	1	1						5	9	
23/11/98	570.02	27.40	13	1	1						7	12.6	
24/11/98	602.92	32.90	7	1	1						7	12.6	
25/11/98	624.15	21.23	3								1	1.8	
TOTAL (NQ)			7.48	0.225	0.475	0.35	0.25	0.00	0.03	0.08	102	183.6	
(Additives in tonnes)													
HOLE COMPLETION (30/11/98)							0.20						
TOTAL FOR CRP-2/2A			31.68	1.2	2.23	1.95	1.00	2.64	0.22	0.08	332.5	598.5	1385
TOTAL FOR ALL ADDITIVES				41	Tonnes								

Notes on the additives:

KCl - Potassium chloride, constituent of sea-water and used for controlling density of drilling fluid;

Guar - Guar gum, extract from guar seed. Used for increasing viscosity and conditioning the hole;

XCD - XCD polymer. Also used for increasing viscosity and conditioning the hole;

Pac-R - Used as a filtrate to reduce loss of drilling fluid;

Mica - muscovite flakes. Used to reduce loss of drilling fluid in highly porous intervals;

CaCl - Calcium chloride. Used as an accelerant for cementing.

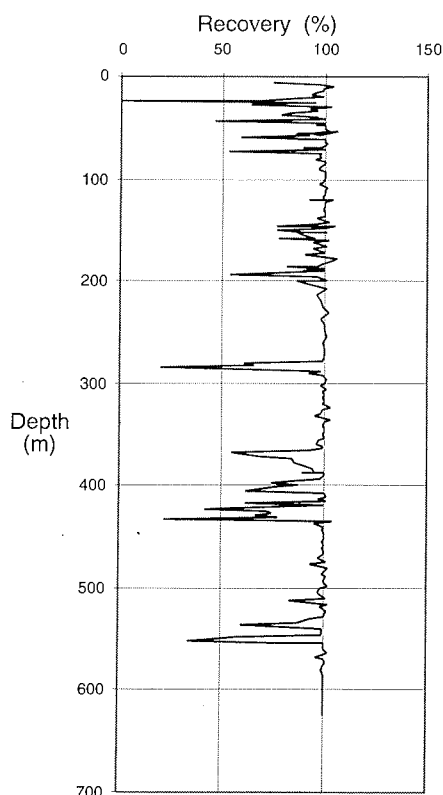


Fig. 1.14 - Core recovery plotted against depth for CRP-2/2A.

the hole collapsing) to the bottom of the hole at 162 mbsf. Drilling continued and firm ground was found below 180.00 mbsf. The hole was cased with the H rod at 199.34 mbsf.

Coring in N proceeded quickly, using the 6 m inner tube, to 290 mbsf, when further loose sand slowed coring, and the 6 m core barrel was replaced with a 3 m barrel. From this point, coring progressed a little more slowly but consistently at c. 30 m/day to 25 November. At this point we had passed a significant geological target, and met the coring requirements of the project for the season. We also wanted to ensure that the down-hole logging could be completed successfully in time to allow for the safe decommissioning the drilling system and camp. Coring ceased at 14.40 hours on 25 November and the hole was prepared for logging. Recovery for the hole averaged 95%, with most of the loss coming from intervals of loose sand a few metres thick (Fig. 1.14).

The logging process was successful for the first six runs, at which time it bridged off at 441 mbsf. Three further runs were successful to this depth. It was then decided to attempt to clear the bridge, but these were unsuccessful and caused further difficulties and loss of a Shelby coring tool. The HQ casing was then cut at 80 mbsf, and a little further logging carried out before the hole was cemented, and the sea riser severed about 1.5 m below the sea floor. All tubulars apart from that cemented into the sea floor were recovered. The drilling system and buildings were then moved by sledge back to Cape Roberts for winter storage on land.

CORE MANAGEMENT AND SAMPLING

DRILL SITE AND CAPE ROBERTS CAMP

Initial core curation began at the drill site. Upon core recovery, down-hole depths were measured on the core to the nearest centimetre and expressed as metres below the sea floor (mbsf).

The core was first cut into one-metre lengths and then longitudinally into an Archive Half and a Working Half using a rotary diamond saw. The Archive and Working halves were placed in separate core boxes (3 m per box for HQ size core and 4 m per box for NQ size core). Yellow plastic separators, with the mbsf depth written on them, were placed at one-metre intervals within the core box. Any voids in the core box were filled with foam blocking to minimize movement of the core during transport.

Sampling of the core began at the drill site. A 10 cm section of the Working Half was taken at approximately 20 m intervals. This "fast-track" sample was sent the same day by helicopter to the palaeontologists at McMurdo Station for age determination. In addition to the "fast-track" sample, fifteen 10- to 20-cm long whole-core sections were removed from the core for clast fabric and shape studies.

TRANSPORTATION

Core Boxes From Cape Roberts Drill Site to McMurdo Helicopter Pad. Insulated, vinyl-covered carrying cases, with a capacity of three or four core boxes each, were used to transport the core via helicopter between the Cape Roberts Drill Site and the Cape Roberts Camp, and then on to McMurdo Station. The carrying cases were placed inside the helicopter to protect the core from freezing. Two to four carrying cases (6-16 core boxes) were transported each day along with a "fast-track" sample. The Working and Archive halves of the core were sent on alternate days as a safety measure.

Core Boxes to Core Storage Facility (CSEC-CSF). The cases containing the core arrived at the McMurdo helicopter pad between 20.00 and 24.00 hrs each day and were transported, by truck, from the helicopter pad to the Crary Science and Engineering Center-Core Storage Facility (CSEC-CSF). The insulated cases were carried into the CSEC-CSF where the individual core boxes were removed from the carrying cases, logged in, and placed on shelving. The Archive and Working halves were placed in separate areas of the Facility. The CSEC-CSF was maintained at a temperature of 4°C and at a relative humidity of 60%.

SEQUENCE OF EVENTS IN THE CSEC CORE LABORATORY

Core Laboratory, McMurdo. A core laboratory was set up in room 201 of the CSEC. The walls, the floor, the benches, and all equipment in the room were thoroughly cleaned prior to the core arrival at the laboratory and at the end of each sampling session to minimize the potential for

contamination of the core. The temperature of the room was maintained at 18°C. The relative humidity of room 201 was low (40%), despite the addition of two humidifiers operating 24 hrs/day. The laboratory contained 10 m of bench space covered with an easily cleaned surface. Fluorescent lighting was augmented by high-intensity halogen lighting to enhance the viewing of the core.

The morning following the arrival of the core at McMurdo Station, the core boxes were repackaged into the insulated cases and carried by hand to the Core Laboratory in the CSEC. The core boxes were removed from the carrying cases and placed on the laboratory benches in depth sequence.

Initial Core Appearance. In general, the core arrived from the Cape Roberts Camp in excellent condition. The core was moist, with a sheen of water on the cut surface of the sediment. Occasionally, minor longitudinal shifting had occurred within the individual metre-long sections. The cores were misted with filtered water on a regular basis to counteract the dehydration effects of the low humidity in the room.

Core Logs Rechecked, Photography and Viewing of the Core. Each day 18 to 24 m of the Working Half of the core were logged and photographed by the sedimentologists, and the core logs received from the Cape Roberts Camp were checked for discrepancies against the core. Upon completion of core logging, the sedimentologists provided a short briefing and a tour of the displayed core to the Cape Roberts science group.

Selecting Sample Intervals. On average, 18 to 24 m of core were available for sampling each day. The investigators selected their sample intervals by placing disposable sample "flags" (a toothpick with an adhesive label wrapped around it) alongside the core. The palaeomagnetic investigators marked their samples by placing 4 x 7 mm slips of paper over their requested intervals.

Disputed Sample Intervals. Overlaps between investigators requesting the same interval were resolved through discussions with the on-ice parties involved, the curators, and the Cape Roberts Sample Committee (Fielding, Smellie, Villa, Wilson).

Data Entry. The curators entered the sample interval data into a relational database (4th Dimension). These data included: the investigator, hole number (CRP-2 or CRP-2A), box number (1-155), top interval of sample (mbsf), bottom interval of sample (mbsf), volume of the sample (cubic centimetres), date, and comments. The comments section recorded the type of sample taken (e.g. sediment, fossil, or clast) and the discipline and type of analysis to be performed on each sample (e.g. petrology-thin section or palaeontology-diatoms). This sample information and other coring information can be accessed through the WWW sites of the curatorial facilities at the Antarctic Marine Geology Research Facility, at the Florida State University in Tallahassee, Florida (www.art.fsu.edu) and the Alfred-Wegener-Institute for Polar and Marine Research in Bremerhaven, Germany (www.pangaea.de).

SAMPLING

General Sampling. The core curators carried out the routine daily sampling, with over 5 600 samples taken for on-ice investigation. Common laboratory spatulas, small scoops, and forceps were used to remove samples from un lithified core. A diamond saw was used cut the more lithified material, as well as the large clasts. All of these tools were cleaned prior to the beginning of the sampling session and between the sampling of different intervals. At no time was any tool used more than once before it was cleaned. The sampling tools were washed with hot water and a laboratory detergent, rinsed with clean water, and then given a final rinse with filtered water. The tools were allowed to air dry to minimize the potential for contamination by paper or cloth fibre. The voids left in the core following extraction of the samples were filled with cut foam blocks to stabilize the core. Upon completion of sampling, the core was misted with filtered water and then returned to the CSEC-Core Storage Facility. The benches, the floor, and all sampling equipment were washed in preparation for the next shipment of core.

Palaeomagnetic Sampling. The Palaeomagnetists conducted their own sampling. To avoid contamination of the core, orientated, coherent sections were removed from the core box, placed on a carrying tray, and taken to the palaeomagnetic sampling lab (a separate building located on the loading dock of CSEC room 201). A diamond drill was used to remove the sample and the remaining core section was replaced in the core box in the proper orientation.

CORE SHIPMENT

The core was re-examined in the CSEC-CSF prior to packaging for shipment to the core repositories in Florida and Germany. Additional foam blocking was added where needed and the core was misted with filtered water again before the core-box lids were taped into place.

The core boxes were placed into specially constructed wooden boxes that contained nine separate compartments holding four boxes each. The containers were marked with arrows pointing to the upright position and with signs designating the correct temperature for transport (4°C/40°F). The wooden boxes were shipped in a refrigerated container via the cargo ship *Greenwave* to Lyttleton, New Zealand. The Working Halves of the core were off-loaded for ocean transport to Germany. The Archive Halves continued aboard the *Greenwave* to California where they were off-loaded and transported overland via refrigerated truck to Florida.

PLIOCENE-QUATERNARY STRATA IN CRP-2

INTRODUCTION

In CRP-2, a c. 27 m succession of Pliocene-Quaternary (mainly) glacial sediments overlies the late Paleogene-early Neogene succession on the Ross Sea Unconformity. The sequence is mainly described from CRP-2, because in

CRP-2A recovery was less. At nearby CRP-1, 43 m of Quaternary sediments overlie the unconformity and *in situ* Pliocene sediments were not encountered. The Pliocene-Quaternary sediments are unconsolidated and cannot be distinguished easily from underlying rock on lithological or sedimentological grounds. Precise dating of the boundaries has not been achieved, but palaeontologically they can be established with reasonable precision. There are three Lithostratigraphical Sub-Units (LSU 1.1, 2.1, 2.2) in the sequence, of which the first one has not been recovered; LSU 2.1 and 2.2 are divided in a number of smaller units with gradational boundaries.

In the following discussion, the two lithostratigraphical units will be described and their characteristics summarised on the basis of the 1:20 scale logs, given in section 1 in the supplement to this issue. This is followed by a brief, preliminary interpretation. Although the sandy beds could possibly be interpreted in a non-glacial context, the intricate architecture of the sands and diamictos suggest that they all relate to the same glacial events. However, because of the time involved intermediate erosion may have removed large parts of the sequence before emplacement of the next diamicton.

PHYSICAL PROPERTIES

In LSU 2.1 (Quaternary) and 2.2 (Pliocene) core-physical property data were obtained for magnetic susceptibility and wet-bulk density (WBD)/porosity below 12.25 mbsf. The uppermost part of the core (above 12.25 mbsf) was not available for whole-core measurements because of drilling operational problems. Core P-wave velocities were not measured above 14.03 mbsf because the unconsolidated and partially broken character of the core did not permit sufficient sound transmission.

The Quaternary (LSU 2.1) is characterized by a susceptibility of about 200 (10^{-5} SI). Magnetic susceptibility must be corrected for loop sensor and core diameter. Wet-bulk density and the calculated fractional porosity vary between 1.9 and 2.1 g cm^{-3} and 0.3 to 0.5, respectively. The

velocity data are sparse and vary from 1.8 to 2.0 km s^{-1} . At 15 mbsf there is a major peak to low susceptibility and high WBD (low porosity) caused by a large clast. In Unit 2.1 the relative high degree of dispersion is probably caused by diamicton lithology. Dispersion is common in the core property data of CRP-1 diamicton units (Cape Roberts Science Team, 1998). In CRP-2, Unit 2.1, susceptibility is similar to that in the upper Quaternary units of CRP-1 (2.1 and 2.2) but significantly higher than in the lower Quaternary units (2.3 - 4.1) of CRP-1. The fractional porosity of the CRP-2 Quaternary sediments is lower by about 0.2 than in the upper part of CRP-1. However, velocities in Quaternary sediments in CRP-1 and CRP-2 are similar (*cf.* Cape Roberts Science Team, 1998).

Core-physical property data at the upper and lower boundary of the Pliocene are lacking. However, LSU 2.2 (Fig. 1.15) of Pliocene age, has slightly higher density (lower porosity) and significantly lower susceptibility compared to the overlying Quaternary units. Compared to the underlying Miocene, differences are minor or indistinct. The low susceptibility values in the Pliocene unit gradually increase into the upper part of the Miocene (Fig. 1.15). Density/porosity and velocity show similar values to those of the uppermost part of the Miocene LSU 3.1 (Fig. 1.15).

In conclusion, the core-physical property characteristics of Quaternary and Pliocene are not distinctly different from Miocene units. Therefore, possible unconformities at the Miocene/Pliocene and Pliocene/Quaternary boundaries are not obvious in the records. The lower porosity at the top of CRP-2 may suggest stronger consolidation compared to the top unit of CRP-1. There are no obvious correlations between the Quaternary of CRP-1 and CRP-2 based on core-physical properties alone.

Down-hole logging of Quaternary and Pliocene sediments took place on 29 November 1998. Above 12.5 mbsf, density and spectral gamma-ray logs were run within the sea riser. Between 12.5 and 23/28 mbsf (tool dependent) all tools measured formation properties in the open borehole. Below this depth, the data presented in figure 1.16 and section 4 in the supplement to this issue were collected within HQ casing. The spectral gamma-ray

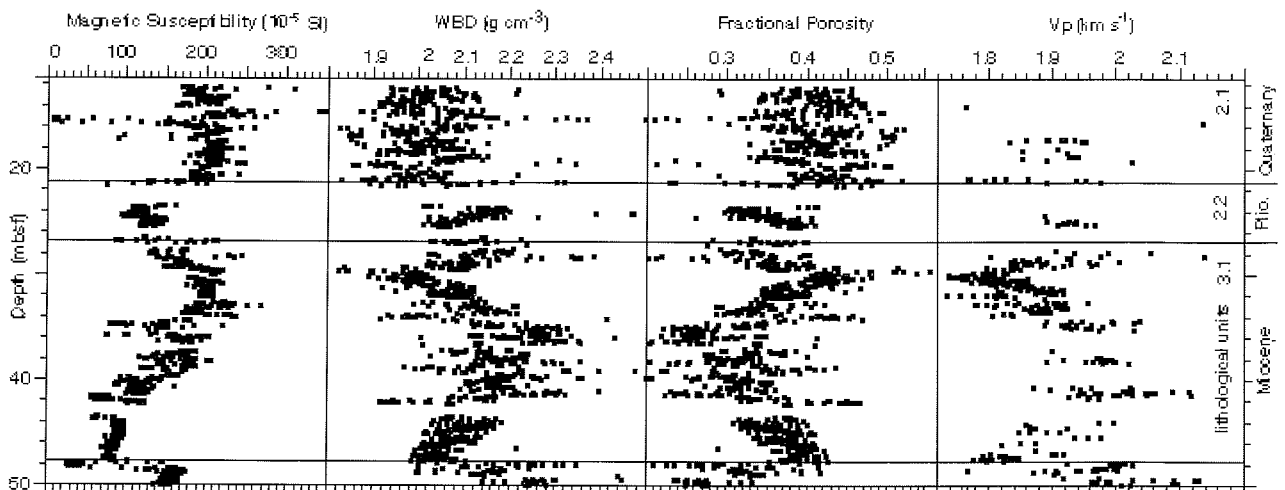


Fig. 1.15 - Core physical properties in the top 50 mbsf of CRP-2.

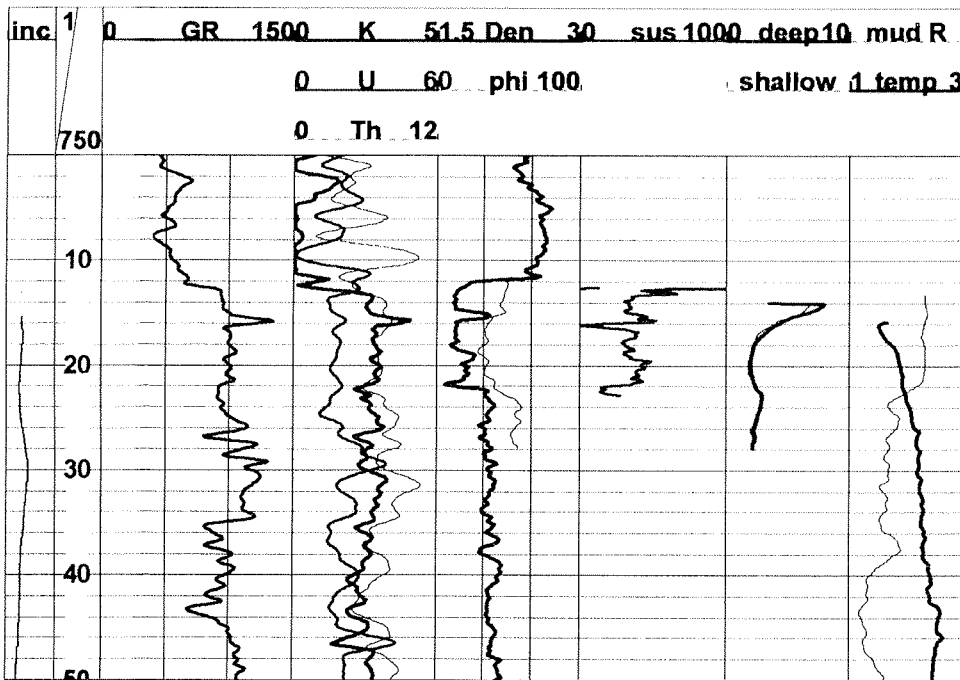


Fig. 1.16 - Composite plot of down-hole measurements. The columns from left to right are showing the following parameters: inclination of the drill hole (inc) (1-2°); logging depth (mbsf); gamma-ray GR (0-150 API); potassium (K) (0-5%); thorium (Th) (0-12 ppm); uranium (U) (0-6 ppm); density (den) (1.5-3 g/cm³); neutron porosity (phi) (0-100%); susceptibility (sus) (0-100 x 10⁻⁴ SI); electrical resistivity (Rlong) (0-10 Ohmm) and (Rshort) (0-10 Ohmm); mud resistivity (mud R) (0-20 Ohmm); temperature (temp) (1-3°C).

and density values are corrected for the attenuation effects caused by HQ casing, but not for the sea riser.

There are no major changes in well-log based physical properties at the lower boundary between the interpreted Pliocene and Miocene boundary at 27 mbsf. The change from Quaternary to Pliocene sediments at 21 mbsf is accompanied by a decrease in density (2.1 to 1.7 g/cm³) and by an increase in susceptibility (20x10⁻⁴ to 40x10⁻⁴ SI). However, the changes in spectral gamma-ray values across this boundary are negligible. The low values in density may be related to wash-outs in the drill hole. Caliper measurements, which detect wash-outs, were avoided in this interval due to difficult drill hole conditions. A large clast at 16 mbsf is detected by high potassium and density values, and low-susceptibility values. There is a strong correlation between down-hole logging data and core-based physical properties for the Quaternary-Pliocene sediments.

LITHOSTRATIGRAPHY AND SEDIMENTOLOGY

Facies Analysis

Two interbedded facies can be recognized, although most transitions are gradational. The first facies is a diamicton, which is compact to massive, locally stratified or laminated with ill-defined boundaries, and which is very poorly sorted; there are several zones of *in situ* brecciation, some of which show a fine fabric. It is interpreted as a probable basal till, produced during glacial overriding of the CRP-2 drill site. The second facies is a ? stratified, moderate to well-sorted fine to coarse sand, which occurs interbedded with the diamicton. Although these sands may be completely unrelated (the lower boundaries have invariably not been recovered), they may also be interpreted as clast-free to clast-poor parts of the diamict.

Description of Sequence

Lithostratigraphical Sub-Unit 1.1 (0.00?-5.54 mbsf), ?

The only material recovered from this interval was a single 7 cm dolerite clast, indicated as drilling wash.

Lithostratigraphical Sub-Unit 2.1 (5.54-21.16 mbsf), diamicton. Recovery of CRP-2 starts at 5.54 mbsf and down to 21.16 mbsf the strata are believed to be Quaternary on micropalaeontological grounds (Fig. 1.17).

Quaternary strata of Unit 2.1 are described as unconsolidated, massive, locally weakly stratified, very poorly sorted, clast-rich sandy diamicton. Clasts are up to boulder size (40 cm+), and are mainly angular to subrounded. There is no preferred clast orientation. The clasts are composed of granitoids, dolerite, quartz, feldspar and volcanic rocks, locally diamictite and possibly also Tertiary sedimentary rocks, including sandstone. There are traces of volcanic glass, sponge spicules and calcareous microfossils. The upper part of the diamicton is weakly laminated to thinly bedded at intervals, while between 5.54 and c. 11 mbsf, it possesses a brecciated fabric, mainly consisting of small, subrounded aggregates (Fig. 1.18a). Below 12.2 mbsf there are local variations in clast content on a scale of 10 to 30 cm, with textural grading between. Both normal and reversed grading occur throughout the unit. Most boundaries are gradational. As in CRP-1, *in situ* brecciation has been observed in the lower, more compact parts of the diamicton, especially in the interval between 13 and 16 mbsf, where the enclaves are larger than in the upper brecciated zone (Fig. 1.18b).

The diamict probably represents glacial overriding of the CRP-2 drill site, because its characteristics are compatible with those of basal tills: multimodal in grain size, vague lamination, zones that differ in clast content and *in situ* brecciation. This interpretation is supported by the clast characteristics. But, because none of these characteristics are diagnostic, the sequence could also

hornblende monzogranite, dolerites, basalts and sedimentary rocks (mainly diamictite, quartzose sandstone, siltstone). The proportion of granitoid clasts shows two peaks at *c.* 11 and 15 mbsf and there is a slight decrease above. Dolerite clasts show a similar abundance pattern but become more abundant than granitoids between 17 and 20 mbsf. By contrast, sedimentary clasts, the most abundant lithologies after granitoids, show marked fluctuations in abundance and a significant upward increase. Basalt clasts are rare and restricted to the *c.* 9-10 mbsf interval.

LSU 2.2 is very similar to LSU 2.1 but contains a higher content of granitoids and basalt clasts. The latter are restricted to *c.* 24-25 mbsf. Five volcanic pebbles 0.8-3 cm in diameter were examined petrographically. They are probably basaltic to trachytic in composition, are vesicular and sub-aphyric, and most contain plagioclase microphenocrysts. The basaltic clasts consist largely of scoriaceous tachylite. The close petrographical similarity between granitoid clasts in CRP-1 and CRP-2 (*cf.* Cape Roberts Science Team, 1998; Talarico & Sandroni, 1998), in particular the abundance and petrographical features of the monzogranites, suggest that the Cambro-Ordovician Granite Harbour Intrusive Complex is the most likely and most important source unit for the Quaternary and Pliocene sections of CRP-2. However, there was also a significant contribution of clasts from the Jurassic Ferrar Group and from sedimentary sequences of probable Tertiary age. Tertiary sediments are presently not exposed in the Transantarctic Mountains, although they are common as erratics on the Ross Ice Shelf (Wilson, 1967). The basaltic and trachytic volcanic clasts were probably derived from outcrops of the Cenozoic McMurdo Volcanic Group. They are much larger than volcanic clasts of similar appearance observed in CRP-1 (Cape Roberts Science Team, 1998).

X-Ray Mineralogy

The bulk mineralogy of one fast-track sample from the Pliocene-Quaternary section of CRP-2/2A was examined using a Rigaku Miniflex+ X-ray diffraction (XRD) system at the Cray Science and Engineering Center. The interval sampled was 11.93-12.03 mbsf, and the sample was analysed using procedures described in the Initial Report volume for CRP-1 (Cape Roberts Science Team, 1998, p. 84-85). Quartz and plagioclase feldspar are the dominant phases in this sample, with lesser amounts of K-feldspar. Other minerals appear to be present in low abundances, including illite/muscovite, clinopyroxene, and diopside. The relative abundances of total feldspar, K-feldspar, and quartz were estimated from the intensity ratios of mineral-specific XRD peaks, and indicate that this sample has high abundances of total feldspar and K-feldspar relative to quartz. This composition is consistent with the relative abundance ratios in the immediately underlying pre-Pliocene section of CRP-2/2A, and suggests that the input of recycled, fine-grained, quartzose Beacon Supergroup material was relatively small compared to the input from more feldspar-rich source rocks (such as the McMurdo Volcanic Group).

Sand Grains

Sand grains were examined petrographically in 13 smear slides, and 'empirical detrital modes' (as defined later, see Sand Grains section in Petrology chapter) were determined on two samples from each lithostratigraphical unit. There are no mineral or rock fragments unique to the Quaternary strata. The different grain types and their likely provenance are described more fully in the section on sand grains (Petrology chapter), and the grain proportions are included in table 4.3. All of the samples are quartzo-feldspathic, with mean values for quartz plus feldspar of about 85-90% (range: *c.* 49-98%). K-feldspar and albitic plagioclase are most common among the feldspars, but calcic plagioclase (labradorite-bytownite) is also generally present. Most of the remainder of each sample consists of colourless to translucent green clinopyroxene (12-15%) and a variable proportion (4-15%) of opaque grains (comprising opaque oxide, oxidised volcanic glass and probable clinopyroxene, and a variety of fine-grained sub-opaque lithic fragments of uncertain origin). Minor amphibole (mainly green hornblende, rarely brown) is ubiquitous (1-2%), as are trace amounts of biotite (brown, rarely green). There are few noticeable differences between LSU 2.1 and 2.2. However, accessory garnet and zircon are characteristic of LSU 2.1 (absent in 2.2) and volcanic glass occurs mainly in trace amounts (<1%; range 0-4%), whereas in LSU 2.2 glass typically forms 8-10% (range 1-17%). Most of the glass is brown, but colourless glass is also present in many of the samples examined. The glass is poorly to non-vesicular, completely unaltered and unabraded.

Apart from a more restricted range of accessory minerals, the new results show no significant differences compared with those described in previous studies of sand grains in Quaternary sediments cored in McMurdo Sound (MSSTS-1 and CRP-1; Barrett et al., 1986; Smellie, 1998). A source area predominantly composed of granitoids, dolerite and contemporaneous mafic and evolved volcanic rocks is indicated. The relatively high abundance of fresh volcanic glass in LSU 2.2 suggests that volcanism was more active during the depositional period of that unit compared to LSU 2.1. The presence of brown (mafic) and colourless (evolved) glass and trace amounts of strongly coloured ferromagnesian minerals, such as aenigmatite, suggest that the volcanic activity had a bimodal alkaline composition similar to that of the Cenozoic McMurdo Volcanic Group.

Organic Geochemistry

Pliocene-Quaternary samples from CRP-2 contain little organic or inorganic carbon (Tab. 1.8): TOC values range from 0.051 to 0.19%, whereas inorganic carbon values range from 0.07 to 0.22%. Much of the inorganic carbon apparently occurs as siderite or another refractory carbon phase. Ratios of TOC:TN decrease down-hole from values of 13 at 6.00-6.02 mbsf to 1.3 at 26.55-26.57 mbsf. These values are consistent with an interpretation that the aquatic contribution to the preserved organic matter has decreased since the Pliocene.

Tab. 1.8 - Measured organic carbon in Pliocene-Quaternary units.

Sample in mbsf	%TC	%TOC _{HS}	%TOC _{HT}	%TN	%TS
2-6.00-6.02	0.18	0.18	0.092	0.0070	0.038
2-9.85-9.87	0.26	0.21	0.13	0.010	0.036
2-15.09-15.11	0.16	0.16	0.077	0.0078	0.036
2-20.02-20.04	0.41	0.28	0.19	0.014	0.032
2-24.28-24.30	0.078	0.12	0.051	0.0077	0.024
2-26.55-26.57	0.065	0.14	0.0087	0.0067	0.022

Clast Shape and Fabric

The Plio-Quaternary interval of the CRP-2/2A drill core consists of several clast-rich units. Five fall-back (collapse into open well) samples and two 20-cm long whole-round core sections were collected from this interval for shape and fabric analysis. The original stratigraphical position of clasts in the fall-back samples is poorly constrained but the whole round core sections are from 19.30-19.50 mbsf and 25.68-25.88 mbsf in LSU 2.1 and 2.2 respectively. Lithology of each clast was determined and roundness estimated using the Krumbein visual roundness chart which divides the clasts into nine roundness

categories. Clasts were also examined for other features such as facets, and for surface features such as striations. In addition, three-dimensional fabric analysis was made on the whole-round core sections by systematically disaggregating the core and measuring the trend and plunge of the a-axis (long axis). None of these samples was oriented with respect to north.

Shape. All the samples show broad roundness distributions with a mean Krumbein roundness ranging between 0.35 and 0.41 (subrounded) and with standard deviation ranging between 0.09 and 0.14.

All samples contain between 19% and 51% of faceted clasts. Striated clasts are present in several samples although they typically comprise less than 10% of the total number of clasts in the sample. The development of these features depends largely on clast lithology but, if present, they provide good evidence of basal glacial transport. Dolerite, granitoid and sedimentary clasts are dominant in these samples with volcanic and metamorphic clasts making up the remainder. Striations occur only on fine-grained dolerite and sedimentary clasts. Up to three cross-cutting sets are preserved on a single facet and one particularly clear example from 11.64 mbsf in CRP-2 displays three sets of

Tab. 1.9 - Diatoms and ebridians in unconsolidated sand, 21.60-23.5 mbsf.

Marine diatoms	Age
<i>Actinocyclus actinochilus</i>	Pliocene-Recent (3.1 to 0.0 Ma**)
<i>Actinocyclus ingens</i>	Middle Miocene-Recent (16.2 to .66 Ma**)
<i>Actinocyclus karstenii</i>	Pliocene
<i>Actinocyclus</i> sp. (fragments of large valves)	Late Miocene?
<i>Chaetoceros</i> sp.	Not diagnostic
<i>Coscinodiscus</i> spp.	Not diagnostic
<i>Denticulopsis maccollumii</i> (?) (fragment)	Lower to Middle Miocene (~17 to 14.4 Ma*)
<i>Eucampia antarctica</i>	Middle Miocene-Recent
<i>Fragilariopsis obliquecostata</i> (fragment)	Pliocene?-Recent
<i>Hyalodiscus</i> sp. A	Not diagnostic
<i>Isthmia</i> sp. (fragment)	Not diagnostic
<i>Paralia sulcata</i>	Not diagnostic
<i>Stellarima microtrias</i>	Not diagnostic
<i>Stephanopyxis</i> sp.	Not diagnostic
<i>Thalassiosira fasciculata</i> (?) (fragment)	Late Pliocene-early Pleistocene
<i>Thalassiosira complicata</i>	Early Pliocene (4.3 to 3.3-3.1 Ma*)
<i>Thalassiosira elliptipora</i>	Late Pliocene-early Pleistocene (2.3 to .70 Ma**)
<i>Thalassiosira inura</i>	Pliocene (4.9 to 1.9 Ma**)
<i>Thalassiosira lentiginosa</i>	Pliocene-Recent (4.2 to 0.0 Ma**)
<i>Thalassiosira oestrupii</i>	Pliocene-Recent (5.6 to 0.0 Ma**)
<i>Thalassiosira oliverana</i>	Miocene - Recent
<i>Thalassiosira torokina</i> early form	Late Miocene-early Pliocene
<i>Thalassiosira torokina</i> late form	Late Pliocene-early Pleistocene
<i>Thalassiosira tumida</i> (fragments)	Pliocene-Recent (4.2 to 0.0 Ma**)
<i>Thalassiosira vulnifica</i>	Pliocene (3.2 to 2.3 Ma**)
<i>Thalassiothrix antarctica</i> group	
<i>Trinacria excavata</i>	
Ebridians	
<i>Pseudammodochium lingii</i>	Paleogene-lower Miocene
<i>Pseudammodochium sphericum</i>	Paleogene-lower Miocene
Non-marine diatom	
<i>Luticola</i> spp.	Pliocene?-Recent
<i>Melosira charcotii</i>	Pliocene?-Recent
<i>Navicula peraustralis</i>	Pliocene?-Recent
<i>Navicula quaternaria</i>	Pliocene?-Recent
<i>Navicula</i> sp. B (CRP-1)	?
<i>Nitzschia westii</i>	Pliocene?-Recent
<i>Stauroneis anceps</i>	Pliocene?-Recent

Note: * = Berggren et al. (1985) time scale; ** = Berggren et al. (1995) time scale.

striae with the dominant set parallel to the long axis of the clast.

Fabric. Trend and plunge of the a-axis of clasts from the whole-round core sections were plotted on Schmidt equal area, lower hemisphere stereonet projections. The data display a broad scatter with no obvious preferred orientation. Normalized eigenvalues (S_1 , S_2 and S_3) summarize fabric strength or degree of clustering about the mean orientation axes or eigenvectors (Dowdeswell et al., 1985). The sample from 19.30-19.50 mbsf yields an S_1 value of 0.445 and S_3 value of 0.232 and the sample from 25.68-25.88 mbsf yields values of 0.462 and 0.254 respectively. The eigenvalue analysis of these samples indicates a random orientation. Although this is characteristic of ice-rafted diamictites according to Domack & Lawson (1985), it should be realized that clast fabric is not diagnostic.

Summary. The clasts from fall-back and whole-round core samples from the Pliocene-Quaternary interval of CRP-2/2A show a broad roundness range with the average being subrounded. A significant percentage of clasts are faceted and several samples display striated clasts. This is characteristic of clasts which have experienced subglacial transport. Three dimensional fabric analysis of clasts in whole-round sections of core indicates no preferred orientation.

PALAEONTOLOGY

Diatoms

Twenty eight samples from the Pliocene to Quaternary section of CRP-2, including samples ranging from the uppermost sample at 6.25 mbsf down to 26.79 mbsf, were examined for diatoms. All samples were examined as

strewn slides, using standard methods. Additionally, selected samples were sieved at 10 μm , and some were floated in sodium polytungstate to recover material with specific gravity less than 2.2.

Most samples are barren or contain trace quantities of generally unidentifiable diatom fragments. Samples within an unconsolidated and poorly recovered sand unit, 21.6-23.5 mbsf (the upper part of LSU 2.2), contain a diatom assemblage of mixed ages, including diatoms representing initial deposition during the late Miocene, early Pliocene and latest Pliocene-earliest Pleistocene (Tab. 1.9). We suggest that all of the diatoms in the sand may be allochthonous.

A maximum age for the subunit is indicated by the occurrence of *Thalassiosira elliptipora*, which has a well-established stratigraphical range of 2.4 - 0.70 Ma. This is one of the key diatom marker taxa present in the Quaternary carbonate unit of CRP-1 (LSU 3.1). The occurrence of *T. elliptipora* fragments, among other late Pliocene/Pleistocene diatoms (Fig. 1.19), and in the absence of *Thalassiosira antarctica*, indicates that the sand unit was deposited in the latest Pliocene to earliest Pleistocene, above *in situ* Pliocene sediments, as indicated by foraminifera.

This sand unit in CRP-2 also contains common extant non-marine diatoms, all of which are known to range back at least to the late Pliocene, based on their occurrence in CIROS-2. There is no evidence of contamination by modern McMurdo Sound diatoms. The Pliocene-lower Miocene unconformity is recognized by a marked change from poorly-fossiliferous sediments in the Pliocene LSU 2.2 to sediments rich in lower Miocene diatoms in the underlying unit. Samples directly above the unconformity at 26.8 mbsf contain common lower Miocene diatoms interpreted as reworked from below.

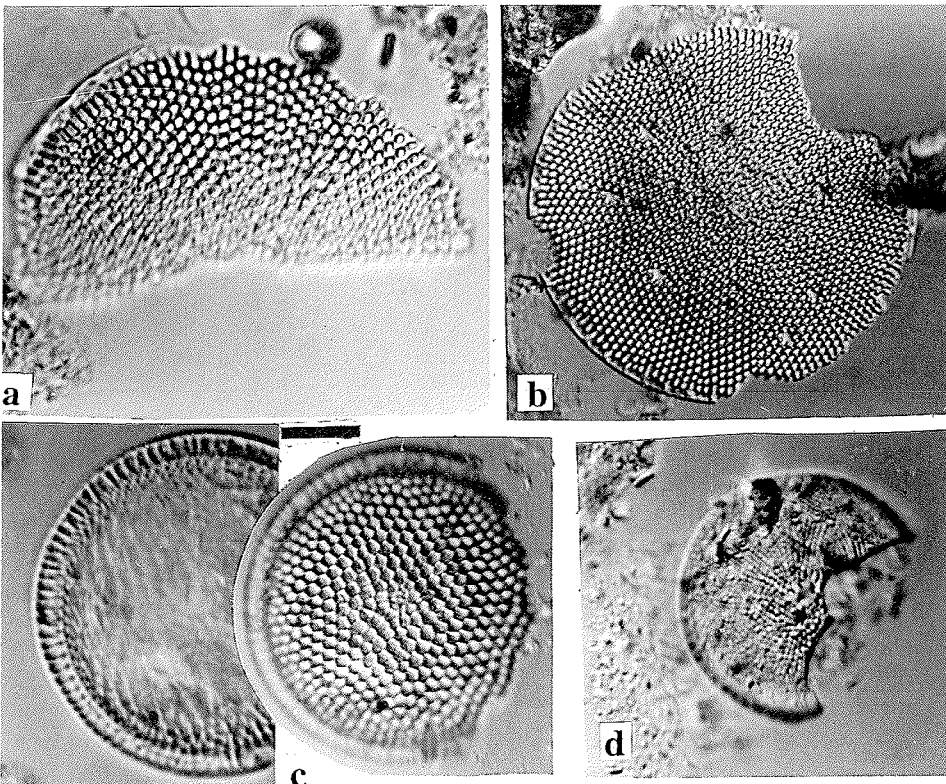


Fig. 1.19 - Diatoms in sand unit, 21.60 - 23.5 mbsf.

a) *Thalassiosira elliptipora*,
 b) *Thalassiosira vulnifica*,
 c) *Thalassiosira torokina* (late form), two levels of focus,
 d) *Thalassiosira complicata*.
 Scale bar = 10 μm .

1974; Webb & Strong, 1998a, b) is present in all five samples from the sub-unit. Twenty-two species of foraminifera were documented in five of seven samples from LSU 2.2 taken from the interval 21.19-25.80 mbsf (Tab. 1.10). A sample from 25.42 mbsf, near the base of Unit 2.2, contains the most diverse assemblage at 12 species. Two samples from the 26.37-26.68 mbsf interval, near the base of LSU 2.2, were barren. This unit is correlated with the Pliocene Pecten Gravels (Wright Valley) and Pliocene of DVDP-10 (Taylor Valley). A number of taxa documented in CRP-2/LSU 2.1 and 2.2 are known to range through both the Pliocene and Quaternary. In the case of CRP-2, the Pliocene and Quaternary faunal elements may be separated on the basis of poorer preservation, larger size and a yellow-orange staining. Further work may indicate the need to propose two new varieties or species of Pliocene foraminifera. The first is a small, inflated and less spinose variant of *Ehrenbergina glabra*, referred to here as an obese variety of *Ehrenbergina glabra*; the second is a large inflated variety of *Rosalina globulosa*. *In situ* Pliocene sediments were not documented in the CRP-1 succession and Pliocene foraminifera in CRP-1/Unit 2.1-3.1 (Quaternary) were considered to have been transported to Roberts ridge from a far distant source, presumably by ice-rafting (Webb & Strong, 1998a, b). The recovery of a ~5 m *in situ* Pliocene succession at CRP-2 indicates that a local source for recycled Pliocene microfossils might need to be considered. Similar Pliocene assemblages have been reported from a variety of coastal and fjordal settings with bathymetric ranges from littoral down to no more than 200 m.

Terrestrial Palynology

The Pliocene-Quaternary interval is barren or effectively barren of terrestrial palynomorphs. Three samples of nine contain single specimens each of the pollen *Nothofagidites lachlaniae* (in a clast at 15.75-15.76 mbsf), *Tricolpites* sp.a (21.18-21.19 mbsf) and *Podocarpidites* sp.b (22.33-22.34 mbsf). These are probably reworked from older strata, although it is noted that all three species are characteristic of the Sirius Group (e.g. Askin & Markgraf, 1986; Wilson et al., 1998), and the possibility that the *Podocarpidites* sp.b specimen is contemporaneous with deposition of the upper Pliocene unit cannot be discounted.

Marine Palynology

Only rare marine palynomorphs were recorded (Tab. 1.10), dominantly phycoma of prasinophyte algae assignable to *Cymatiosphaera* and the acritarch *Leiosphaeridae*. Dinoflagellate cysts are rare, the majority occurring in a single clast sample (15.75-15.76 mbsf).

Macrofossils

Macrofossils are sparse and poorly preserved in the Quaternary part of CRP-2 between 9.13 and 20.51 mbsf. They consist mostly of small fragments of unidentified marine bivalves, rare bryozoans, serpulid worm tubes and

Tab. 1.11 - Macrofossils encountered in CRP-2.

Quaternary	
9.13- 9.14 mbsf:	unidentified macrofossil
10.12-10.13 mbsf:	unidentified mollusc fragment(s)
10.14-10.15 mbsf:	unidentified bivalve fragment(s)
10.28-10.29 mbsf:	unidentified bivalve fragment(s)
10.46-10.47 mbsf:	unidentified bivalve fragment(s)
15.15-15.16 mbsf:	unidentified bivalve fragment(s) (pectinid ?)
16.30-16.38 mbsf:	bryozoan and bivalve fragment(s) echinoid spines
19.84-19.90 mbsf:	serpulid fragment(s), echinoid spines
20.50-20.51 mbsf:	unidentified bivalve fragment(s)
?Quaternary-Pliocene	
22.05-22.06 mbsf:	bivalve (pectinid ?) fragment(s)
22.12-22.13 mbsf:	pectinid (? <i>Chlamys</i> sp.) fragment(s)
23.90-23.19 mbsf:	bivalve (pectinid?) fragment(s)
24.49-24.51 mbsf:	pectinid ? fragment(s)

echinoid spines (Tab. 1.11). No age assessment can be directly derived from such macrofauna. The fauna is obviously normal marine but offers no clues regarding palaeobathymetry.

The core interval between 22.05 and 24.51 mbsf contains a few bivalve fragments, mostly of pectinids. Although Pliocene pectinids (*Chlamys*) are known to be different from Quaternary pectinids (*Adamussium*) in Antarctica, the fragmentary state of the fossils encountered and the abrasion of diagnostic shell features (such as ribs) make it difficult to establish for certain whether or not the pectinid fragment found at 22.12 mbsf belongs to *Chlamys* sp. Reworking of such calcitic fossils cannot be ruled out. However, the occurrence of calcareous fossils throughout this part of CRP-2 core is encouraging for making a better assessment using Sr-dating.

MAGNETOSTRATIGRAPHY

The goal of the palaeomagnetic investigations was to develop a magnetic polarity zonation for CRP-2. The Pliocene-Quaternary interval comprises diamictos, sands and sandy diamictos. Coarse-grained sediments are usually not suitable for palaeomagnetic analysis. However, in previous palaeomagnetic studies of sedimentary units from the Victoria Land Basin, strong and stable magnetizations have been recorded and even coarse-grained units have proved suitable for palaeomagnetic analysis (Wilson et al., 1998; Roberts et al., 1998). We attribute the stability of the magnetizations to the presence of fine magnetite particles within the fine-grained sediment matrix in these otherwise coarse-grained units (cf. Sagnotti et al., 1998a, b; Wilson et al., 1998; Roberts et al., 1998).

The unconsolidated Pliocene-Quaternary sediments were sampled with plastic cubes (6.25 cm³) and were analysed in the palaeomagnetic laboratory at the University of California, Davis. The samples were measured on an automated, pass-through cryogenic magnetometer and were subjected to in-line stepwise alternating field (AF) demagnetization up to peak fields of 60 mT.

Almost all of the samples from the Pliocene-Quaternary interval are stably magnetised and characteristic remanence components are clearly defined from vector component diagrams (Fig. 1.20). All 22

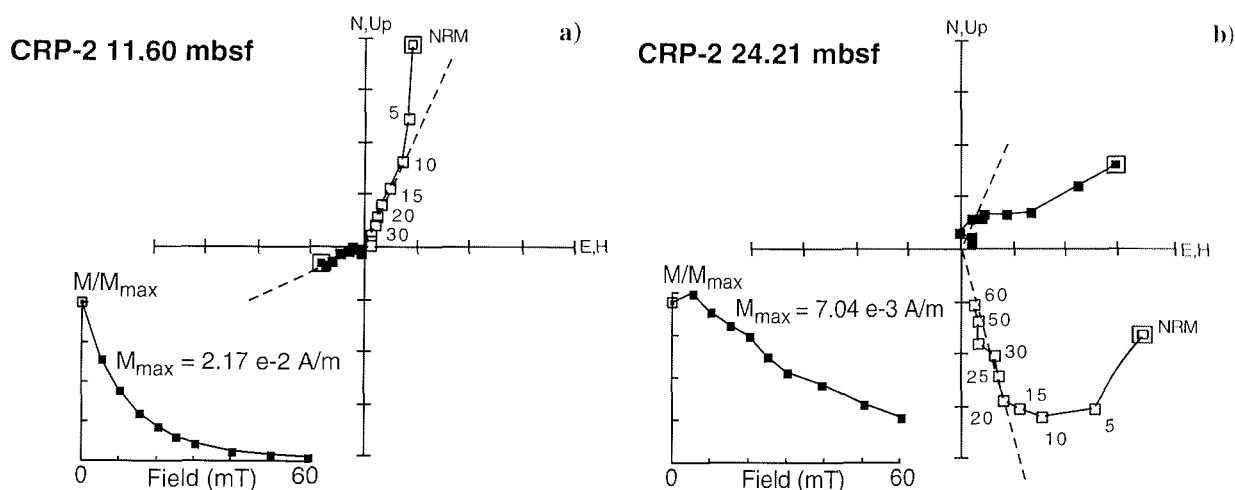


Fig. 1.20 - Vector component diagrams (with normalized intensity decay plots) for samples from the normal polarity Quaternary (CRP-2 11.60 mbsf, a) and reversed polarity Pliocene (CRP-2 24.21 mbsf, b) magnetozones. Open (closed) symbols represent projections onto the vertical (horizontal) plane. The dashed lines represent linear regression fits which indicate the characteristic remanence component. The core is not azimuthally oriented, therefore declination values are not meaningful.

samples from the Quaternary interval (LSU 2.1) display normal polarity (between 7.32 and 21.12 mbsf). These samples are variably influenced by a near-vertical, drilling-induced magnetic overprint that is removed by AF demagnetization at 5-20 mT (Fig. 1.20a). Drilling-induced overprints are common in palaeomagnetic studies associated with drilling projects and were routinely observed in the CIROS-1 and CRP-1 cores (Wilson et al., 1998; Roberts et al., 1998). Such overprints can be extremely useful when they are easily removed by stepwise demagnetization because they provide evidence that the cores or the samples have not been inadvertently flipped during handling and sampling.

Owing to poor core recovery and lack of suitable material, it was possible to collect only three samples from the Pliocene interval (within LSU 2.2), of which two were stably magnetized (between 23.64 and 26.30 mbsf). The two stably magnetized Pliocene samples have reversed polarity directions (Fig. 1.20b). The normal (Quaternary) and reversed polarity (Pliocene) samples have inclinations that are close to those expected at the latitude of the site (77°S ; $I_{\text{exp}} = 83.4^{\circ}$), which confirms that any secondary magnetizations have been successfully removed by stepwise demagnetization (Fig. 1.21).

It is relatively straightforward to define a magnetic polarity zonation for the Pliocene-Quaternary interval (Fig. 1.21). The Quaternary normal polarity magnetozon most likely represents the Brunhes Chron (C1n). It is not possible to determine, on the basis of polarity, which part of the last 780 ky is represented by this unit (all age estimates for polarity boundaries are based on the timescale of Cande & Kent (1995)).

The Pliocene reversed polarity magnetozon is less easy to correlate with the magnetic-polarity timescale. There are two long periods of dominantly reversed polarity in the Pliocene, including the late Gilbert Chron (C2Ar; 4.18-3.58 Ma) and the early Matuyama Chron (C2r; 2.58-1.95), as well as several short reversed polarity subchrons

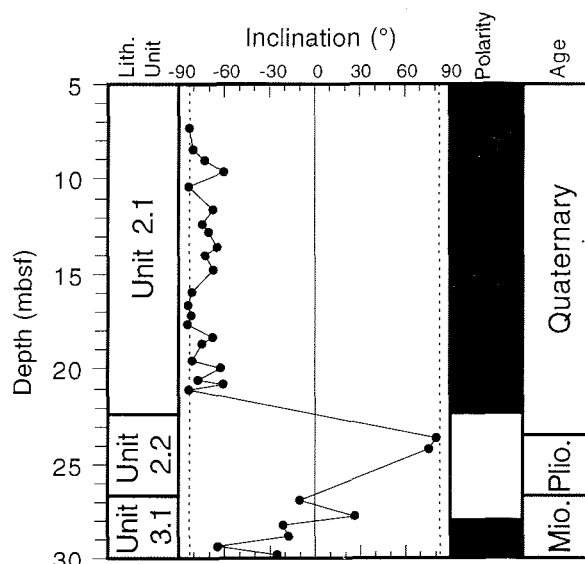


Fig. 1.21 - Plot of palaeomagnetic inclination (determined by linear regression fitting of data from several demagnetization levels) with respect to depth for the Pliocene-Quaternary interval of the CRP-2 core. Dashed lines are plotted to indicate the expected inclinations ($\pm 83.4^{\circ}$) for reversed and normal polarity at the site latitude (77.0°S). Black (white) indicates normal (reversed) polarity on the polarity log.

in the middle Gilbert Chron and in the Gauss Chron. The Pliocene age of lithostratigraphical Unit 2.2 is based on its foraminiferal content (see Palaeontology section, this chapter), which does not constrain precise correlation of the reversed polarity magnetozon with the magnetic polarity timescale. The break between Pliocene and Quaternary sediments lies beneath the boundary between LSU 2.1 and 2.2 (see Palaeontology section, this chapter). Lack of suitable material for palaeomagnetic sampling prevented precise identification of the position of the polarity boundary with respect to the break between the Pliocene and Quaternary sediments.

2 - Core Properties and Down-Hole Geophysics

FRACTURE ARRAYS

INTRODUCTION

Systematic logging of fractures in the core and the drill hole walls of CRP-2/2A is being undertaken to document the brittle deformation patterns and crustal stress regimes associated with rifting along the Transantarctic Mountains Front at Cape Roberts. Because the Cape Roberts Project drill sites are located along the Transantarctic Mountains - Victoria Land rift basin structural boundary, abundant fracturing of the sedimentary strata was expected. The objectives of the fracture analysis are to acquire an age-controlled structural record of the kinematic and dynamic history along the Transantarctic Mountains Front and to obtain the first information on the contemporary *in situ* stress field within Antarctica.

Fracture logging of core was completed for CRP-2 and CRP-2A cores. A large population of fractures was present and a total of 2 017 core fractures were logged. In the more indurated portion of the cored sequence, fracture surface features were well developed, yielding kinematic and dynamic data. A range of both natural fractures and induced fractures were identified based on these surface fractographic features and on morphological characteristics of the core fractures. Preliminary descriptions of the core fractures are provided below. Down-hole logging using bore hole televiwer and dipmeter tools was completed for portions of the drill hole (see section on Down-Hole Logging) and will be used to map fractures in the drill hole walls, to search for any drill hole break-outs, and to provide orientation for portions of the CRP-2/2A core.

FRACTURE STUDY PROCEDURES

Fracture logging was carried out on the whole core at the Drill Site science laboratory. Core fractures were numbered sequentially downward from core top and depths to the top and base of each fracture were recorded. Dip angle and direction were measured with respect to an arbitrarily placed red line scribed along the length of the core. Where sequential core runs could be fitted together directly, the red scribe line was matched between runs. For HQ core, c. 10% of the core runs could be fitted together, whereas 56% of the NQ core runs could be matched. The number of consecutive core runs that could be fitted together increased down core, culminating in a 42 m interval between 576 and 618 mbsf that was fitted and scribed continuously. Core fracture logging included observation and photography of fracture morphology, fracture surface features, fracture fill material, fracture terminations, and cross-cutting and abutting relations between fractures. Procedures for logging fractures in

cores and criteria used for distinguishing natural and induced fractures generally followed Kulander et al. (1990).

After fracture logging was completed, the whole core was scanned using CoreScan® equipment leased from DMT, Germany. The CoreScan® obtains digital images of the entire core circumference by rotating the whole core on rollers, line-scanning, and digitally joining these into 'unrolled' core images up to a maximum of 100 cm in length. Due to the poor induration of core material, it was only possible to carry out whole-core scanning of c. 2% of the CRP-2/2A sequence down to 83 mbsf. There were sufficiently coherent sections of the core between 83 and 200 mbsf to allow c. 60% of the whole core to be scanned. Between 200 and 624.15 mbsf, 82% of the whole core was scanned. The slabbed face of the entire working half of the core was also scanned after the core was split and placed in the core boxes. For Box 30 only, the archive half of the split core was scanned instead of the working half.

In CRP-2A, down-hole logging with dipmeter was completed from 65 to 170, 200 to 255, and 280 to 624 mbsf and with bore-hole televiwer from 64.7 to 163.7 (unoriented) and from 200 to 441 mbsf (oriented). All the dipmeter logs were oriented. Analysis of these down-hole logs will be used to map fractures in the drill hole walls and will also be used to orient the CRP-2A core by matching drill hole wall and core fractures (*cf.* Nelson et al., 1987). In particular, we will match the bore hole televiwer images of the drill hole walls with the whole-core scan images to provide core orientation (*e.g.* Schmitz et al., 1989; Weber, 1994). A single attempt to orient the core directly using a core orienting tool was unsuccessful. We will use core intervals oriented by matching with bore hole televiwer imagery to test whether orientation of core based on palaeomagnetic vectors is reliable for CRP-2/2A core and, if so, the palaeomagnetic data will be used to orient additional core intervals, as was done for CRP-1 (Paulsen & Wilson, 1998). Here we provide an example of orienting core based on comparison of bore hole televiwer and CoreScan® imagery. Until further analyses can be carried out, however, the fracture data obtained from the core is only oriented with respect to an "arbitrary north" defined by the red scribe line, which differs between unmatched core runs.

FRACTURE DISTRIBUTION AND DENSITY

Fractures are present in all portions of the core. Fracture density, plotted as fractures/m, is shown in figure 2.1. Note that breaks in the histogram with no fractures reflect intervals where no core was recovered. Fracture densities in the Quaternary/Pliocene section average 2.29 fractures/m and range from 1 to 4 fractures/m. In the Miocene section, fracture densities range from 1 to 9 fractures/m and average

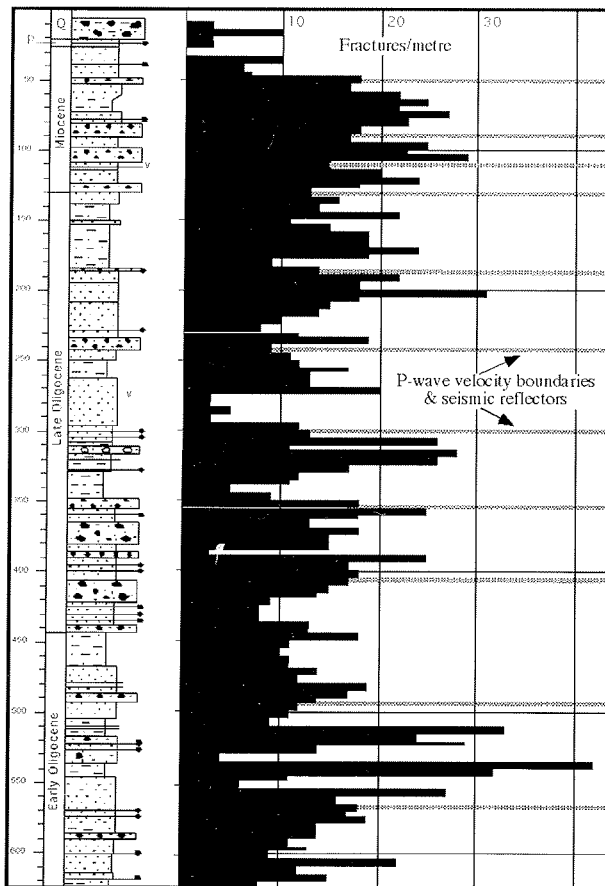


Fig. 2.1 - Fracture density plot showing the number of fractures per 5 m intervals of core with relation to depth and lithological and age boundaries within the CRP-2A core. P-wave velocity boundary modified from figure 2.25.

about 3.55 fractures/m. In the upper Oligocene section, fracture densities range from 1 to 10 fractures/m and average about 2.93 fractures/m. In the lower Oligocene section, fracture densities range from 0 to 10 fractures/m and average about 3.21 fractures/m.

The marked increase in fracture density across the contact between Pliocene and Miocene strata is only partly attributable to increased induration, as much of the upper Miocene section is also poorly indurated. Fractures commonly occurred in well-indurated diamictites, sandstones, and siltstones, and less commonly in conglomerate units and unlithified sand intervals. Fracture density commonly increases across P-wave velocity boundaries that have been correlated with seismic reflectors, suggesting that fracturing was influenced by mechanical differences between rock types and/or related to degree of induration. Further analysis of fracture density vs lithology and grain size will reveal any consistent relations within the core. Pronounced peaks in fracture density occur at 520 and 540 mbsf and mark intervals containing abundant normal faults and veins.

FRACTURE TYPES IN CRP-2/2A CORE

To interpret the mode of origin and significance of CRP-2/2A core fractures, it is essential to differentiate

natural fractures from induced fractures. Natural fractures are those that existed in the crust prior to drilling and were intersected by coring. Natural fractures in the CRP-2A core include microfaults, veins, clastic dykes, and possible sub-vertical joints. Other types of natural deformation, including soft-sediment folding, brecciation, and glacial shearing, are treated elsewhere in this volume (see section on Deformation). Induced fractures form in response to drilling- or coring-related perturbations of the stress field, or due to subsequent handling of the core. In some cases such induced fractures are indicative of the contemporary maximum and minimum horizontal stress directions in the crust. CRP-2/2A core contains abundant drilling-, coring-, and handling-induced fractures.

Natural Fractures

Microfaults. Several varieties of microfaults occur in the CRP-2A core. Only discrete fault planes inferred to be of brittle origin are described here. Open, brittle microfaults with approximately down-dip slickenlines and in some cases having polished slickenside surfaces, occur sporadically through the core between 51 and 549 mbsf (Fig. 2.2). Dips of these faults typically range between 55 and 75° and, where offset can be observed, they have normal-sense displacement. With greater depth, fault planes are typically sealed by mm-scale bands of material, some of which is as yet unidentified. Sealed microfaults appear at c. 300 mbsf and are abundant in intervals from c. 310 to 325 mbsf and c. 510 mbsf to the base of the cored interval. In the vast majority of cases where offset of either bedding or veins was observed, the faults have normal-sense displacement (Fig. 2.3). Some rare reverse-sense faults are also present. Although not restricted to any particular lithology, closed microfaults are abundant in strata showing

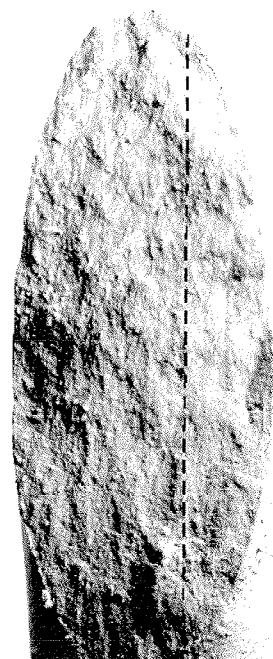


Fig. 2.2 - Brittle microfault with down-dip slickenlines. Fault dip 68°, depth = 480.36-480.47 mbsf, core diameter = 45 mm.

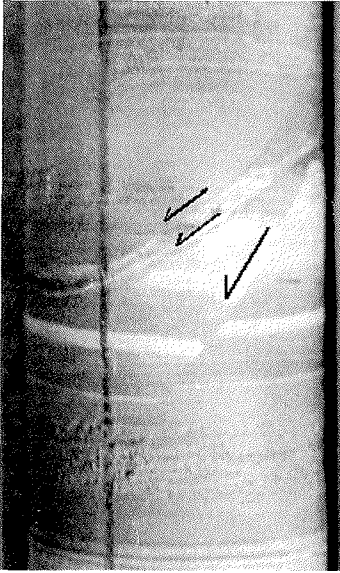


Fig. 2.3 - Closed microfaults with normal-sense offset of bedding. Fault dips = 55 and 58°, depth = 315.90 to 316.00 mbsf, core diameter = 45 mm.

evidence of substantial soft-sediment disruption, suggesting a possible genetic relationship. The closed microfaults typically have dips ranging from *c.* 60 to 80°, although a few lower-angle faults are present. In many portions of the core, the fault planes have a conjugate geometry, with approximately equal and opposite dips (Fig. 2.4). In several cases, clear cross-cutting relations



Fig. 2.4 - Veins on 'unrolled' Corescan® image of whole core. Negative image shows hairline white calcite veins as thin black lines (outlined by thin white dash lines). Note conjugate geometry (equivalent strike and opposite dips) and normal-sense offset of one vein by a second. This vein-filled normal fault also displaces bedding. Vein dips are 65 and 72°. The vertical lines on the core image are the scribed reference lines. Depth = 542.88 - 543.18 mbsf, unrolled core circumference = *c.* 142 mm.

between members of the conjugate sets indicate they are coeval (Fig. 2.4).

Based on macroscopic observation, the material filling the fault planes appears to be of several different types. Dark bands along surfaces that truncate and offset bedding are common in core below about 350 mbsf. One such surface parted, revealing well-developed surface polish and slickenlines within the dark fault zone material, indicating a brittle-shear origin. The dark bands thus may consist of cataclastically crushed material formed due to fault surface shearing. It is also possible that some of these bands lack shear movement and instead represent injected fine-grained sedimentary material. A second type of fault fill material is pale grey in colour with a granular appearance, and appears to be sedimentary material lining the fault surfaces. Carbonate cementation along normal fault planes occurs in sandstone intervals and in places appears similar to the grey sedimentary fill material. The cement either forms continuous sub-planar zones of grey cement or forms patches or spheres of cement aligned along the fault planes (Fig. 2.5). Vein material, consisting of thin calcite veins or layered calcite and pyrite, is also common along normal fault planes (Fig. 2.4). Future thin-section examination of the materials along fault planes will be used to clarify their type and origin and to identify any textures of kinematic significance.

Veins. Mineralized veins were first identified at *c.* 332 mbsf and become abundant deeper in the sequence, beginning at *c.* 440 mbsf. The veins commonly contain calcite and many also contain pyrite. Swarms of very thin, hairline calcite veins occur at several levels below *c.* 520 mbsf. Although vein dips range from sub-horizontal to sub-vertical, the vast majority of the veins have dips between 60 and 80° (*e.g.* Fig. 2.4). As discussed above, some calcite veins follow normal fault planes with conjugate geometry and show mutual offsets (Fig. 2.4). In other cases, veins with similar steep dips are compound,

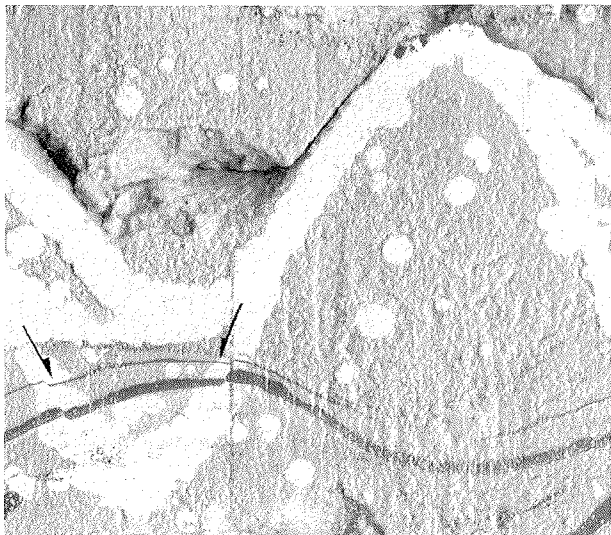


Fig. 2.5 - Cemented normal fault on 'unrolled' Corescan® image of whole core. Note carbonate cement along normal fault planes that displace bedding and distributed spherules of the same cement. Normal fault dips 70°, depth = 511.49 - 511.62 mbsf, unrolled core circumference = *c.* 142 mm.

consisting of multiple, thin strands, and have *en echelon* segments that overlap or coalesce. This type of geometry is characteristic of opening-mode tension veins. At present it is not possible systematically to differentiate veins following shear planes from tensile veins, but mineral textures determined from thin-section examination may help to clarify this key issue.

Clastic Intrusions. Several planar clastic dykes with thicknesses of 1-2 cm occur in the core between *c.* 337 and 600 mbsf (see also section on Deformation). These dykes typically have pale rims of carbonate cement and some associated pyrite mineralization (Fig. 2.6). Clastic dykes range in dip angle from 75 to 86°. Additional mm-scale sedimentary intrusions also occur and, as noted above,

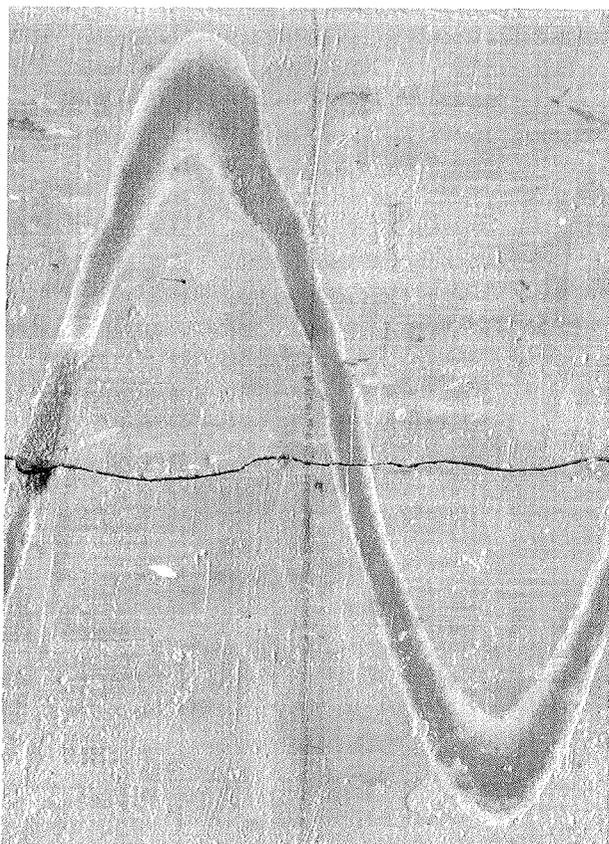


Fig. 2.6 - Clastic dyke on 'unrolled' Corescan® image of whole core. Note pale rim of carbonate cement. Dyke dips 75°, depth = 337.68 - 337.87 mbsf, unrolled core circumference = *c.* 142 mm.

locally follow normal fault planes. These planar to anastomosing, thin sedimentary veins are particularly common between *c.* 315 and 365 mbsf.

Induced Fractures

Petal and Petal-Centreline Fractures. Petal and petal-centreline fractures form below the drill bit in response to stress induced when the weight on the bit temporarily increases (Lorenz et al., 1990; Li & Schmitt, 1997). These induced fractures have curving shapes that follow the stress trajectories radiating below the bit and this distinctive curvilinear geometry allows them to be confidently identified in core (Kulander et al., 1990). Over 100 curvilinear fractures interpreted as petal and petal-centreline fractures are present in the CRP-2/2A core and occur at all depths between *c.* 19 and 587 mbsf. Although not restricted to a particular lithology, the petal-centreline fractures most commonly occur in fine-grained strata. In cemented strata the petal-centreline fracture surfaces displayed distinctive fractographic features including hackle plumes and arrest lines that indicate down-core fracture propagation directions. A sub-population of this fracture set formed shallow, scoop- or spoon-shaped flakes along the core margins and had sub-vertical dips (Fig. 2.7). Such fractures are common at the top of core runs, suggesting they formed as the drill string 'tagged' the bottom at the start of a new core run, consistent with models for the genesis of petal-centreline fractures (Kulander et al., 1990; Lorenz et al., 1990; Li & Schmitt, 1997). Significantly, preliminary examination of the bore hole televiewer imagery reveals sub-vertical fractures in the drill hole walls over the same depth intervals as some of the petal-centreline fractures logged in the core. This will allow us to obtain orientation for the petal-centreline fractures and map the maximum horizontal stress direction in the crust, which has been shown to parallel the strike of petal-centreline fractures (Plumb & Cox, 1987; Kulander et al., 1990).

Disc Fractures. Disc fractures form normal to the core axis when unloading produces axial tension within the core. Sub-horizontal to low-angle (<30° dip) fractures are abundant in CRP-2/2A core. In many cases these fractures nucleated on fossils or limestones that served as stress concentrators (Fig. 2.8). Some of these fractures have

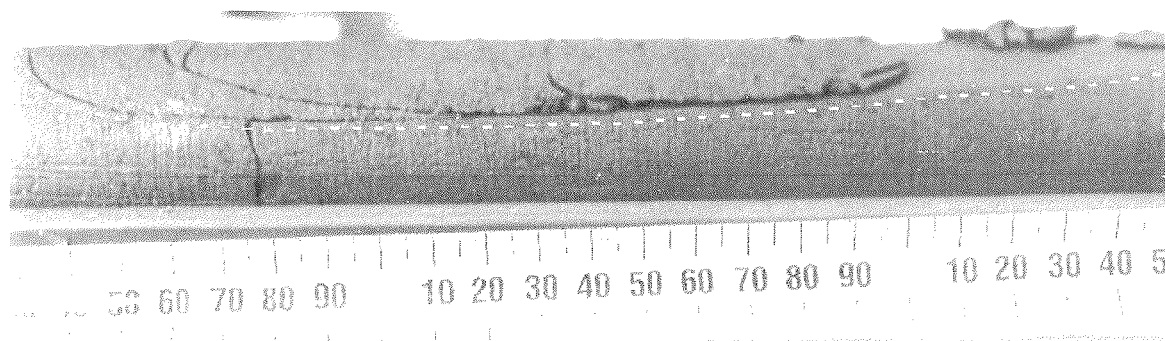


Fig. 2.7 - Petal-centreline fracture at depth 258.17 - 258.45 mbsf. Note sub-vertical dip and curvilinear, 'spoon' shape of fracture. Second petal fracture curves to merge with the main petal-centreline fracture.

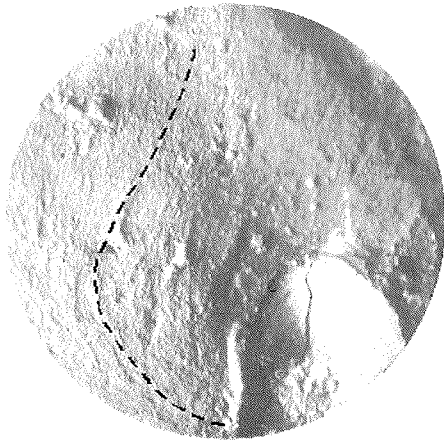


Fig. 2.8 - Disc fracture nucleated on macrofossil. Note origin point at fossil margin and hackle plume radiating across fracture face (dash line). These features demonstrate an induced, tensile origin for this horizontal fracture. Depth = 448.26 mbsf, core is 45 mm diameter.

distinctive curvilinear 'saddle' shapes typical of disc fractures formed in areas where the horizontal stresses are anisotropic (Bankwitz & Bankwitz, 1995; Bell, 1996). Below *c.* 200 mbsf, these core fractures, where developed in fine-grained lithologies, commonly showed surface fractographic features including origin points, hackle plumes and twist hackle along core margins (Fig. 2.8), proving an induced, tensile fracture origin. Measurements of plume axis trends were taken and, in some core intervals, the plumes showed consistent trends. This suggests that the plume axes on the disc fractures may have formed parallel to the trend of the maximum horizontal compressive stress direction, as demonstrated elsewhere (Kulander et al., 1990).

Other Induced Fractures. Planar to irregular induced fractures in the core formed due to a variety of other factors. Sub-horizontal tensile fractures formed due to the upward pull on the drill string exerted when the hydraulic system elevated the chuck during a coring run, when the core lifter mechanism latched on to the base of the core, and when the drillers broke the core from the bedrock at the end of a run. These types of fractures commonly had well-developed hackle plume structures characteristic of tensile fracture propagation. Another type of fracture formed at or close to the bit during drilling when the core was broken off along a subhorizontal plane and then spun when the drill bit re-engaged, producing finely etched circular lines and grooves on interlocking surfaces, resembling bowls shaped on a potter's wheel. Torsion fractures, consisting of irregular or helical breaks where the core was twisted, occurred sporadically in the core. They were most common near the base of core runs in clay-rich lithologies, where the core resisted sliding and the slow entry into the core barrel subjected the core to torque from the rotating drill bit. In some cases, up to 30 cm of core at the base of the run would be pervasively broken by wavy gaping tension fractures arranged in *en echelon* patterns consistent with the clockwise torque exerted by the rotating drill bit. Handling-induced fractures of many varieties developed during core processing and transport. Some such fractures mimic the geometry of

fracture types previously described and may have nucleated on incipient drilling- or coring-induced fractures that had not propagated completely through the core.

FRACTURES IN BORE HOLE TELEVIEWER IMAGERY

Fractures present in the drill hole walls must either be pre-existing natural fractures or drilling-induced fractures, such as petal-centrelines types that propagate into the rock proximal to the drill bit. Coring- and handling-induced fractures will not be present. Thus comparison of fractures logged in core with those visible in the televiewer imagery can constrain interpretations of fracture origin. The oriented televiewer images allow fracture attitudes to be determined, with dip calculated from the amplitude of the sine wave and dip direction given by the orientation of the wave trough. In addition, where fractures can be matched between core and televiewer images, segments of the core can be oriented and true geographic coordinates can be assigned to measurements made with respect to the arbitrary core reference lines. Much of the fracture mapping and core orientation based on the bore hole televiewer imagery will be carried out when high-resolution digital images are obtained from the original analogue televiewer data. As an example, however, figure 2.9 shows televiewer data from the drill hole between *c.* 327 to 331 mbsf, consisting of a sequence of merged Polaroid photos taken at 1 m intervals for on-site interpretations. The same depth interval of core reconstructed in digitally 'stitched' scan images of the unrolled circumference of the core, resized and reoriented to match the drill hole image, is also shown in figure 2.9. A set of steep SE-dipping fractures is clearly imaged on the televiewer log and can be matched directly to steep core fractures interpreted as being induced petal-centrelines fractures. Steep NW-dipping core fractures, also probable induced petal-centrelines fractures, are only barely discernible on the televiewer imagery. Natural fractures, consisting of faults and clastic intrusions, dip at moderate to low angles to the NW. These are present, though not as sharp, on the televiewer imagery. Coring-induced and handling-induced fractures, visible on the scanned core, are not seen on the bore hole televiewer imagery. Overall the match between fractures in the drill hole wall and in the core is excellent in this interval.

INTERPRETATION OF FRACTURES AND STRESS REGIMES

The abundant brittle deformation features in CRP-2/2A core are consistent with the tectonic setting adjacent to the Transantarctic Mountains Front. The CRP-2/2A microfault arrays have a conjugate geometry and offset sense which demonstrate a vertical maximum compressive stress during deformation. Sub-vertical, tensile veins and clastic dykes in the core are also consistent with this stress orientation. A stress regime with vertical maximum compressive stress is characteristic of a continental rift regime and these structures most likely reflect tectonic deformation of the Cape Roberts area. Preliminary examination of televiewer and CoreScan® imagery of equivalent depth intervals indicates that some normal faults strike NE-SW

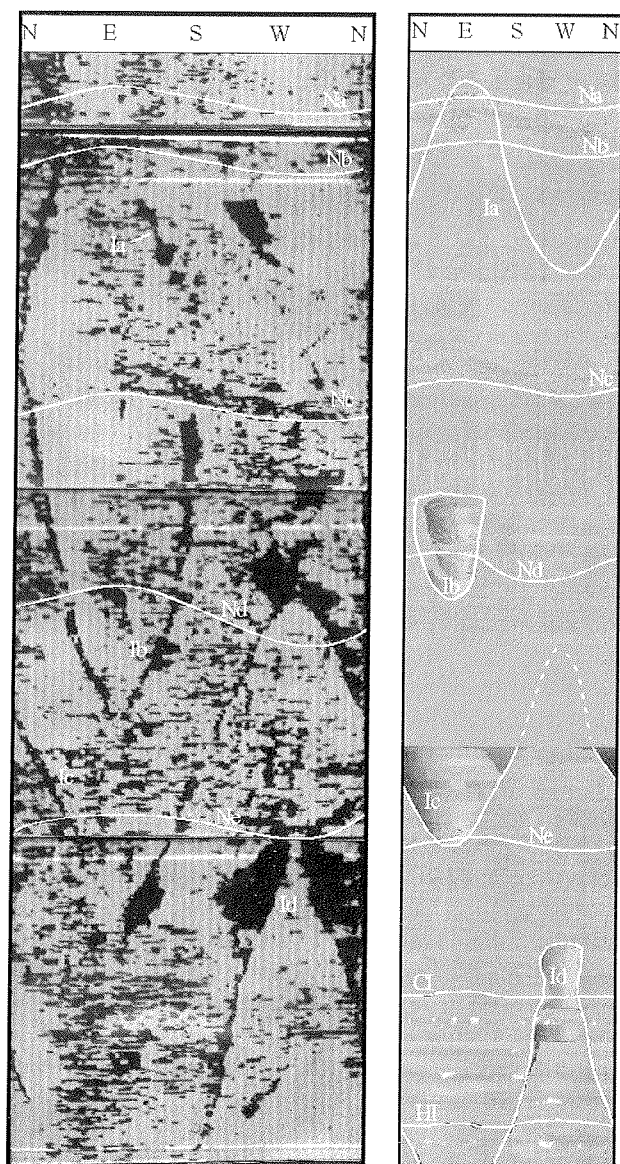


Fig. 2.9 - Example of oriented drill hole televiwer imagery of the drill hole wall (left) and digitally 'stitched' Corescan® image of the whole core (right). The Corescan imagery has been reoriented by matching fractures in the oriented televiwer imagery. Note that steep fractures appear over a greater depth interval on the televiwer imagery because the drill hole diameter is substantially larger than the core diameter. Natural fractures are labeled 'N' and induced fractures are labeled 'I'; 'a' to 'e' denote matching fractures on the televiwer and Corescan imagery. Note that coring-induced (CI) and handling-induced (HI) fractures in the core are not present in the drill hole walls. CRP-2A depth interval = c. 327 - 331 mbsf. There is a gap in the Corescan imagery from 330.00 to 330.18 mbsf resulting from fractured core which could not be scanned.

and dip either to the SE or NW. This is comparable to fault orientations in CRP-1 determined from core intervals oriented using palaeomagnetic vectors. These orientations also are similar to brittle faults mapped in bedrock outcrops along the coast of southern Victoria Land (Wilson, 1995). When more extensive oriented core is available it will be possible to determine whether these trends are consistently developed, or if there are changes in fault trends, and therefore stress directions, through time.

Although more detailed analysis of fault distribution vs depth and mechanical properties of the strata is required, there are clearly more highly faulted intervals that may possibly mark discrete deformation episodes. The apparent association of faulting and intense soft-sediment deformation of strata could possibly indicate fault-related seismic activity in the region.

The large population of petal-centrelines fractures, some of which are clearly visible in the oriented bore hole televiwer images, will provide one indicator of the regional maximum horizontal stress direction. The example presented of oriented bore hole televiwer imagery shows that induced petal-centrelines fractures strike NE-SW, consistent with strikes of petal-centrelines fractures in CRP-1 core oriented palaeomagnetically. Preliminary examination of the televiwer imagery suggests that steep fractures in CRP-2/2A consistently show this orientation. If borne out by further analysis, it should be possible to obtain statistically significant results demonstrating the maximum horizontal stress direction of the contemporary stress field. Analysis of plume patterns on disc fractures may also indicate the *in situ* stress directions. Finally, any drill hole break-outs determined from analysis of the bore hole televiwer and/or dipmeter data may also provide further stress constraints. It will thus be possible to provide a more robust estimate of the *in situ* contemporary stress directions along the Transantarctic Mountains Front in the Cape Roberts area than was possible from CRP-1.

PHYSICAL PROPERTIES FROM ON-SITE CORE MEASUREMENTS

INTRODUCTION

Whole-core physical properties provide easy-to-measure data with a very high vertical resolution. CRP-2 on-site core measurements were carried out in a similar way to CRP-1. For the CRP-1 core, physical properties were used to define and interpret stratigraphical patterns, including a comparison between lithology and sequences (Cape Roberts Science Team, 1998; Niessen & Jarrard, 1998; Niessen et al., 1998). For example, grain-size has an effect on porosity calculated from wet-bulk density (WBD). In particular sequences were reflected by the cyclic pattern of magnetic susceptibility (MS) in the lower part of the CRP-1 core but were overprinted by volcanic debris derived from the McMurdo volcanic province in the upper part of the core. Porosity exhibited a strong down-core decrease indicative of secondary overprint on consolidation such as overcompaction by ice and cementation. The P-wave velocity (V_p) was used to calculate acoustic travel time which is essential for the correlation of the core with seismic profiles. The velocity-porosity relationship of CRP-1 deviated from global models, the reason for which remains uncertain. This question will be addressed further using whole-core physical property data obtained during CRP-2. An additional goal of CRP-2 was, for the first time in records from the Victoria Land Basin, to compare *in situ* physical conditions recorded by down-hole logging with

core-physical properties. In addition, both down-hole and core-physical property data from CRP-2/2A can be used to correlate the cores of the sites CRP-1 and CIROS-1, in order to improve the correlation of strata in space and time and to calibrate further the seismic stratigraphy of the region.

METHODS

Measurements at the drill-site laboratory included non-destructive, near-continuous determinations of wet-bulk density (WBD), P-wave velocity (V_p), and magnetic susceptibility (MS) at 2-cm intervals. The Multi Sensor Core Logger (MSCL, GEOTEK Ltd., UK) was used to measure core temperature, core diameter, P-wave travel time, gamma-ray attenuation and MS. The technical specifications of the MSCL system are summarized in table 2.1. The cores were logged in plastic carriers (Fig. 2.10a) to avoid destruction of non-consolidated rock material. Core carriers had inside diameters to fit either HQ (61.1 mm diameter) or NQ (45 mm diameter) cores and were non-magnetic. The orientation of the P-wave and gamma-ray sensors was vertical. Data were logged in continuous intervals of 3 to 12 m (6 m on average) long core sections. Prior to each of these logging intervals, a calibration piece of 0.4 m length was logged, including a 0.3 m blank carrier, plus 0.1 m cylindrical plastic standard for both HQ and NQ size in order to monitor the accuracy of WBD and V_p values.

MS was measured in terms of SI units, using a Bartington MS-2 meter and a loop sensor of 80 mm internal diameter. The sensor was tested using the Bartington sensor-specific core-calibration piece. No offset was observed. Data are corrected for loop-sensor and core diameter as follows:

$$MS (10^{-5} \text{ SI}) = \text{measured value} (10^{-5} \text{ SI}) / K\text{-rel} \quad (i)$$

K-rel is a sensor-specific correction calculated from the diameter of the core over the diameter of the loop

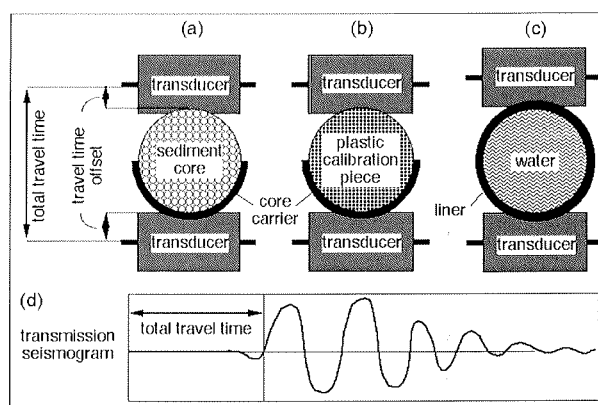


Fig. 2.10 - Vertical orientation of rotational transducers, different settings for logging and calibration, and definition of total travel time and offset. a) Logging of cores on carriers, b) logging of standard plastic cylinder on carrier, c) test-liner filled with water, d) transmission seismogram.

sensor according to the correction instructions for the Bartington MS2 sensor systems (Tab. 2.1). The geometry of the loop sensor does not allow a direct determination of volume MS. Data corrected for loop-sensor and core diameter can be converted roughly to volume MS by multiplication by about 1.4 (Niessen et al., 1998). The whole-core MS data presented here are corrected only with respect to equation (i) and thus directly comparable to the whole-core physical property data presented in the CRP-1 Initial Report (Cape Roberts Science Team, 1998).

V_p was measured using Acoustic Rolling Contact Transducers (ARC, GEOTEK Ltd., UK). The transducers were rolling along the top of the core (upper transducer) and the bottom outside of the carrier (lower transducer), respectively. Whole-core P-wave velocities were calculated from the core diameter and travel time after subtraction of the P-wave travel time through the core carrier wall, transducer, and electronic delay. This travel-time offset was determined in two steps of which the laboratory settings are illustrated in figure 2.10. First, cylindrical

Tab. 2.1 - Multi-Sensor-Core Logger (MSCL-25) specifications for CRP-2/2A.

P-wave Velocity and Core Diameter	
Transducer	Acoustic Rolling Contact Transducer (GEOTEK Ltd.)
Transmitter pulse frequency	230 kHz
Transmitted pulse repetition rate:	100 Hz
Received pulse resolution	50 ns
P-wave travel-time offset	18.14 μ s (HQ), 18.8 μ s (NQ)
Wet Bulk Density	
Gamma ray source	Cs-137
Source activity	356 MBq
Source energy	0.662 MeV
Counting time	10 s
Collimator diameter	5 mm (HQ), 2.5 mm (NQ)
Gamma detector	NaI-Scintillation Counter (John Count Scientific Ltd.)
Magnetic Susceptibility	
Loop sensor type	MS-2B (Bartington Ltd.)
Loop sensor diameter	80 mm
Alternating field frequency	0.565 kHz
Sensitivity mode	1 s (HQ), 10 s (NQ)
Magnetic field intensity	approx. 80 A/m RMS
Loop sensor correction coefficient K-rel	1.54

plastic standards of NQ and HQ core size were used to measure the travel time through the carrier wall by placing the cylinders bare and on carriers between the transducers (Fig. 2.10b). Then, a full liner, from which the core carriers were made, was used filled with water to determine the travel time through the transducers plus electronic delay (Fig. 2.10c). The arrival time of the P-wave pulse was detected using the second zero-crossing of the received waveform (Fig. 2.10d). P-wave velocities (V_p) were normalized to 20°C using the temperature logs:

$$V_p = V_{pm} + 3 * (20 - t_m) \quad (ii)$$

where:

V_{pm} = P-wave velocity at measured temperature, and t_m = measured temperature.

Core temperature was measured by a calibrated infrared sensor. P-wave-logging of standard plastic cylinders gave a mean of 2.35 km s⁻¹ (true V_p = 2.37 km s⁻¹) with a standard deviation of 0.04.

In addition to the standard V_p -detection system of the GEOTEK Multi-Sensor-Core-Logger (MSCL) a laboratory-built p-wave registration apparatus was used. Depth control and the P-wave signal were imported from the GEOTEK system by a controller (used to trigger and calibrate the system to real core depth equivalent to the depth registered by the MSCL). Each individual transmission seismogram was digitised using a high speed ADC board T3012 (30 MHz, 12 bit, National Instruments) placed into an industrial PC (Dolch, 233 MHz). Sampling intervals are 50 ns over a total of 200 μ s per seismogram. Data were stored for further post-drilling analysis. In addition to the core-thickness detection system provided by the MSCL, a laser beam was used to determine core thickness. Laser thickness was digitised by the same ADC board used for data acquisition of the seismograms.

WBD was determined from attenuation of a gamma-ray beam transmitted from a radioactive source (¹³⁷Cs). Beam collimators of 5 mm and 2.5 mm were used for HQ and NQ core size, respectively. The beam was focused through the core-centre and the underlying carrier into a gamma detector. To calculate density from gamma counts non-attenuated (zero) counts were measured through the carrier prior to each logging run of 6 m core sections (on average). The output of the gamma detector was calibrated using aluminium, carbon and water of known densities. Quantification of WBD was carried out according to the following formula:

$$WBD = a + b * (1/\mu * d) * \ln(I/I_0) \quad (iii)$$

where

a, b = system-specific variables to correct for count-rate dependent errors as described by Weber et al. (1997);

d = core diameter;

μ = specific mass-attenuation coefficient for gamma rays, and

$\ln(I/I_0)$ = natural logarithm of the ratio of attenuated (core on carrier) over non-attenuated (bare carrier) gamma counts per second.

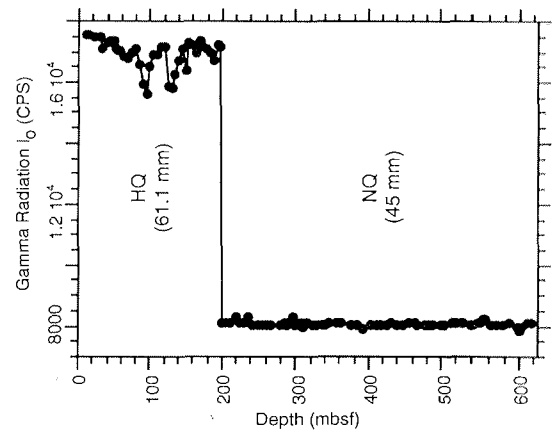


Fig. 2.11 - The stability of the gamma-ray detector monitored for non-attenuated radiation (I_0) as a function of depth in core. Core depth refers to the run of core from that depth prior to which the monitoring was carried out.

Porosity was calculated from the WBD as follows:

$$POR = (dg - WBD) / (dg - dw) \quad (iv)$$

where:

dg = grain density (2.7 g cm⁻³), and

dw = pore-water density (1.03 g cm⁻³).

The gamma detector output was calibrated at the beginning of CRP-2 coring activity for the HQ settings and recalibrated for NQ prior to the first run with smaller (NQ) diameter core (199.49 mbsf). The initial calibration piece was used to monitor the stability of the gamma detector during the measuring process. With increasing core depth, the I_0 radiation decreased significantly for HQ settings due to the higher radiation of the 5 mm beam on the detector over time (Fig. 2.11). An instability of the same magnitude was not observed for NQ settings. However, there is a linear relationship between the measured non-attenuated gamma radiation (HQ) and the detected deviation from the density of the plastic calibration cylinders (Fig. 2.12). This linear regression was used to correct the WBD of each individual core-logging run. The

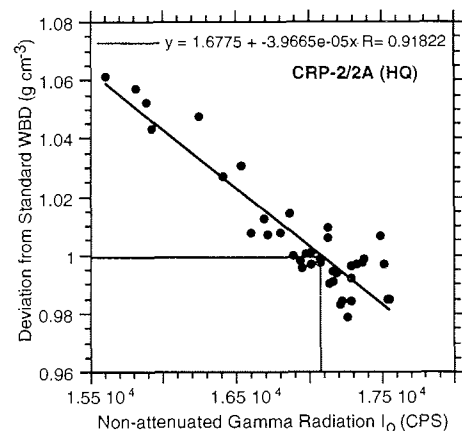


Fig. 2.12 - Deviation from standard WBD as a function of non-attenuated gamma radiation (I_0) measured in the same calibration runs.

mean density of the HQ standard cylinders (true density = 1.408 g cm^{-3}) improved from 1.399 to 1.408 g cm^{-3} and the standard deviation improved from 0.030 to 0.014 (39 HQ calibration runs). In comparison, the NQ standard revealed a density mean value of 1.388 g cm^{-3} . The standard deviation was 0.028 (128 NQ calibration measurements). There was no opportunity to improve the deviation for NQ WBD because no correlation between I_0 and standard density was observed. This can be explained by the low level of radiation through the 2.5 mm collimator, relative to the background noise from the detector. Thus, measuring at higher radiation level is more precise if detector drift is corrected. This is demonstrated in figure 2.13 where the total range of HQ and NQ densities measured in the core are compared to the corrected HQ and uncorrected NQ standard density measurements, respectively.

Down-core logs comprise nearly complete data sets for all lithological units. Only for those depth intervals where major disturbances were observed (gaps or heavily crumbled core) were data eliminated. In particular in the upper part of the core to a depth of *c.* 60 mbsf , the transmission of the P-wave pulses through the core was insufficient in places. In such cases unrealistic high ($>8 \text{ km s}^{-1}$) or low ($<1.4 \text{ km s}^{-1}$) values were determined from the background noise of the MSCL Vp-detection system. Such Vp values were removed from the data.

DISTRIBUTION OF CORE-PHYSICAL PROPERTY DATA

Magnetic susceptibilities range over a large scale from nearly 1 to more than 1000 (10^{-5} SI). Most WBD range from about 1.7 to 2.7 g cm^{-3} (Fig. 2.13). Extreme low and high WBD were observed in some unconsolidated pumice (1.3 to 1.5 g cm^{-3}) and large basement clasts (up to 3.1 g cm^{-3}), respectively. The corresponding porosities calculated after equation (iv) range from *c.* -0.2 to 0.8 . The assumption of constant grain density of 2.7 g cm^{-3} (equation iv) results in negative porosities for clasts of higher density. A similar observation was made in the CRP-1 core (Niessen & Jarrard, 1998).

Velocities range from *c.* 1.6 to more than 6 km s^{-1} (Fig. 2.13). In CRP-2/2A, the distribution of Vp is strongly negative-skewed compared to WBD. There is a nearly normal distribution of WBD in the upper HQ-size of the core (0 - 199.49 m) and slightly negative-skewed distribution of WBD in the lower NQ-part of the core. None of these observations can be attributed to sensor drift or errors which were monitored by standards (Fig. 2.13).

TRANSMISSION SEISMOGRAMS

Seismograms recorded from the P-wave pulse through the core exhibit a broad range of different shapes and frequency distribution. Detailed post-processing and analysis of the seismograms will reveal the potential use of seismograms as proxies for variations in lithology (defined by grain size and/or diagenetic effects). Here, three seismograms (Fig. 2.14) are selected in order to demonstrate the variability and to show the potential of this relatively new method in whole-core physical investigation. The first is typical for a cemented sandstone

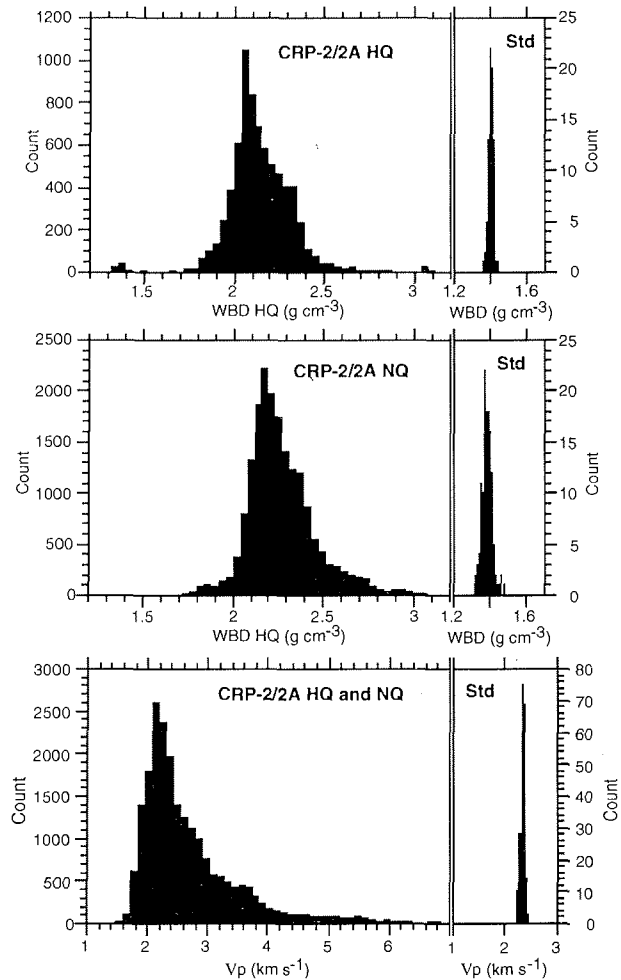


Fig. 2.13 - Distribution of all WBD and Vp in the core (left) and in the standard cylinders (right) used to monitor sensor drift during the logging campaign. Note that core data and standard data are plotted on the same lateral scale.

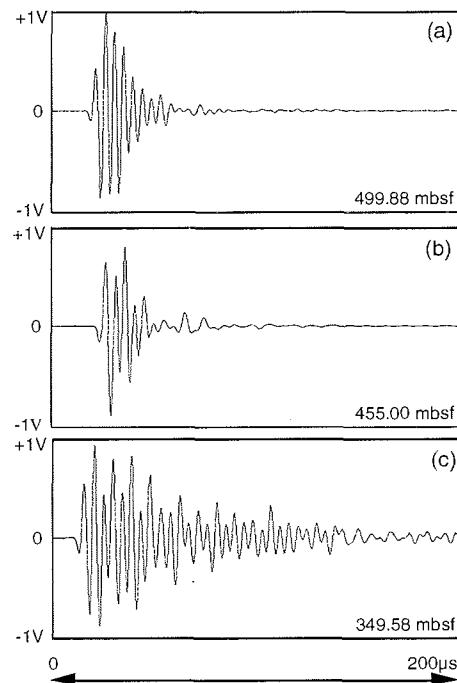


Fig. 2.14 - Transmission seismograms from different lithologies and depths. a) Sandstone, LSU 13.1; b) mudstone, LSU 13.1; c) dolerite clast, LSU 12.1.

unit (Fig. 2.14a); those from mudstones (Fig. 2.14b) exhibit consistent differences from sandstones. For example, mudstone seismograms are characterized by a maximum negative amplitude at the end of the first sine, and by a different shape of the envelope compared to that of sand and sandstone. Sandstone and mudstone seismograms are very different from the transmission signal recorded through large clasts. For example, acoustic pulses through dolerite clasts create distinct oscillations on the entire length of 200 μ s of the recorded seismogram (Fig. 2.14c). The large variability of terrestrial-derived sediments cored at CRP-2/2A plus the effects of cementation offer a unique opportunity for a comprehensive study of transmission seismograms.

LINKING CRP-2 AND CRP-2A USING MAGNETIC SUSCEPTIBILITY

In the upper 50 mbsf, core-physical property data are more complete in CRP-2 than in CRP-2A. The high-resolution MS record was used to link core-physical properties measured in CRP-2 and CRP-2A (Fig. 2.15). The envelope indicating major down-core shifts in CRP-2 MS (Fig. 2.15) was superimposed on the much more sparse data of CRP-2A MS. Generally, the down-core trend is similar. Dispersion of single data points in both records can be explained by individual clasts which reveal different magnetic signatures. The records were matched using a large granite clast at 15.4 mbsf (Fig. 2.15). Linking the pattern of MS at about 52 mbsf shows a vertical displacement between the two cores of about 0.2 m. In order to combine data sets from both cores, the sets were cut at a depth of 52.80 mbsf (CRP-2A). At that depth little down-core variation in physical properties was observed (Fig. 2.15). The core-physical property data presented here are from CRP-2 above 52.80 mbsf and CRP-2A below 52.80 mbsf.

STRATIGRAPHY OF CORE-PHYSICAL PROPERTIES

An overview of the down-core pattern of MS, WBD and V_p is presented in figure 2.16. The data are compared with the sequence-stratigraphy boundaries. The sequence stratigraphy is described in more detail in the Lithostratigraphy and Sedimentology chapter. All single data-points deviating from the general down-core trend of core-physical properties were removed from the data. Thus, strong scatter caused by large clasts is not visible. By combining all three records together, four major units (A - D) can be distinguished (Fig. 2.16).

Unit A extends from the top of the core to about 130 mbsf and is defined by relatively high MS and stronger noise level in all three properties compared to the underlying interval B. The minimum WBD observed at about 110 mbsf is caused by pumice layers. The boundary with the underlying unit B is relatively sharp. MS shows distinct offsets at the base of some sequence boundaries (e.g. Sequence 4 and 6). In the WBD and V_p record distinct offsets are seen at bottom of Lithostratigraphical Units (LU) 7 and 8.

Unit B (c. 130 - 330 mbsf) exhibits minimum noise in MS, WBD and V_p . The susceptibilities decrease cyclically to less than 20 (10^{-5} SI) at the bottom of unit B. The

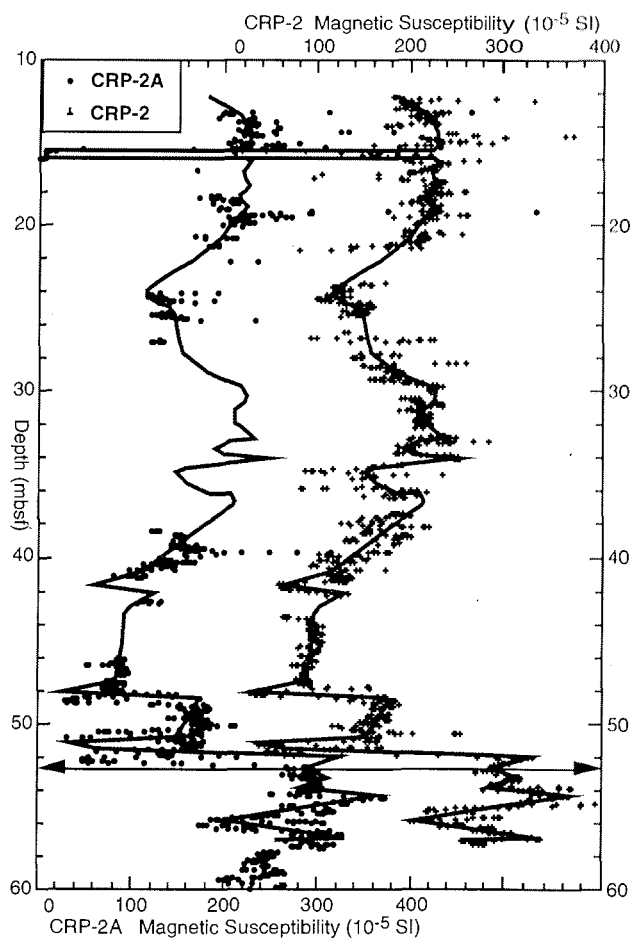


Fig. 2.15 - Magnetic susceptibility correlation of CRP-2 and CRP-2A. The envelope of CRP-2 data (right) was superimposed on the CRP-2A data (left) to match the cores.

transition to the underlying unit C is more gradual, depending on which physical property is chosen to define a major shift. Here it is suggested placing the boundary at c. 330 mbsf (base of LU 12), which is the end of a low-MS interval. However, using amplitude and noise as criteria, the WBD and V_p suggest a down-core change already at a depth of c. 290 mbsf. Within unit B there is good agreement with minor boundaries and/or cycles seen in the physical properties and lithostratigraphical units. In particular, this is evident in the MS log. A distinct MS offset at the bottom of LU 10 suggests an unconformity.

Unit C (c. 330-530 mbsf) is defined by strong shifts in magnetic susceptibilities from as low as 10 to well above 500 (10^{-5} SI). Both noise and amplitudes are increased in WBD and V_p logs compared to the overlying unit B. The boundary to the underlying unit D is sharp. It is defined by major decreases in amplitudes of MS, WBD and V_p observed at the bottom of sequence 20. The pattern of lithostratigraphical units agrees well with that of MS. Most lithostratigraphical units onset with strata high in MS with a gradual decrease towards the top. Correspondence with lithostratigraphical units is less obvious in the WBD and V_p logs except for the bottom of LU 18 and 20.

Unit D (c. 530 mbsf to the end of the core) is characterized by a lower MS compared to Unit C. The pattern of MS is cyclic. In contrast with Unit C, the onsets

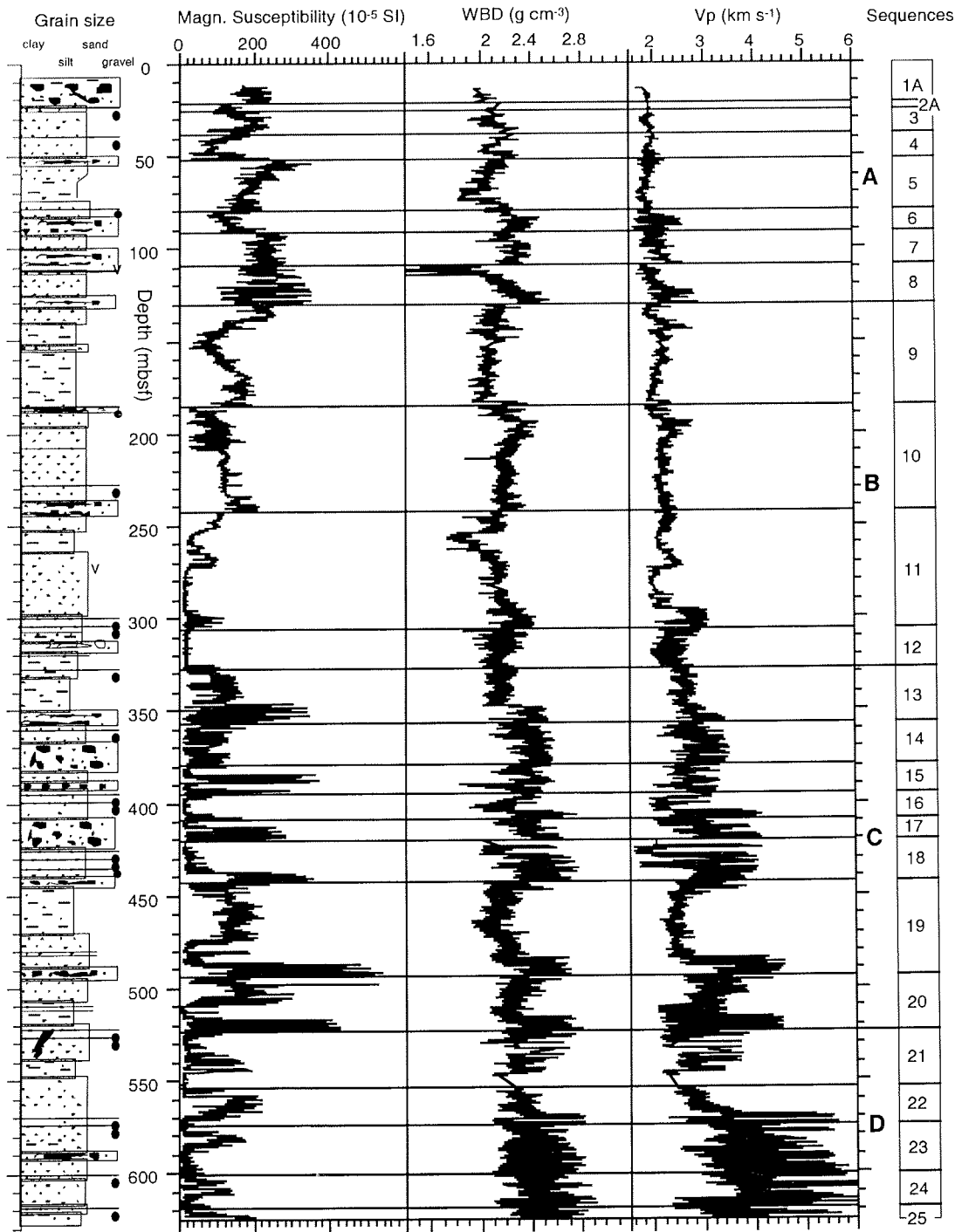


Fig. 2.16 - Summary log of core-physical property data with extreme high and low isolated data-points (clasts) excluded. Horizontal lines represent sequence boundaries. A, B, C and D are major physical property Units distinguished in the core-physical property data.

of most sequences seem to correlate with minima in MS. WBD and Vp exhibit a major down-core variations from medium to very high amplitudes. In particular, Vp values increase to above 5 km s⁻¹ which is significantly higher than in the upper units of the core.

Two logs of higher vertical resolution are presented (0-325 and 325-625 mbsf, Figs. 2.17 & 2.18 respectively). Here the core-physical properties include dispersed data from clasts. This data set is compared with the lithostratigraphical units. In the detailed logs, calculated porosity

is plotted instead of WBD. It is evident that some major changes of core-physical properties match lithological unit boundaries. Many lithological boundaries are characterized by gradual rather than sharp changes in the physical property data, but even so some general trends can be observed.

In general, diamictite units exhibit lower porosities, higher Vp, and large dispersion in all three parameters. In particular, LSU 4.1, 6.2, 7.1, 9.1 and 10.1 are characterized by this pattern (Fig. 2.17). By contrast, sandstones and mudstones exhibit higher porosity and lower Vp and less

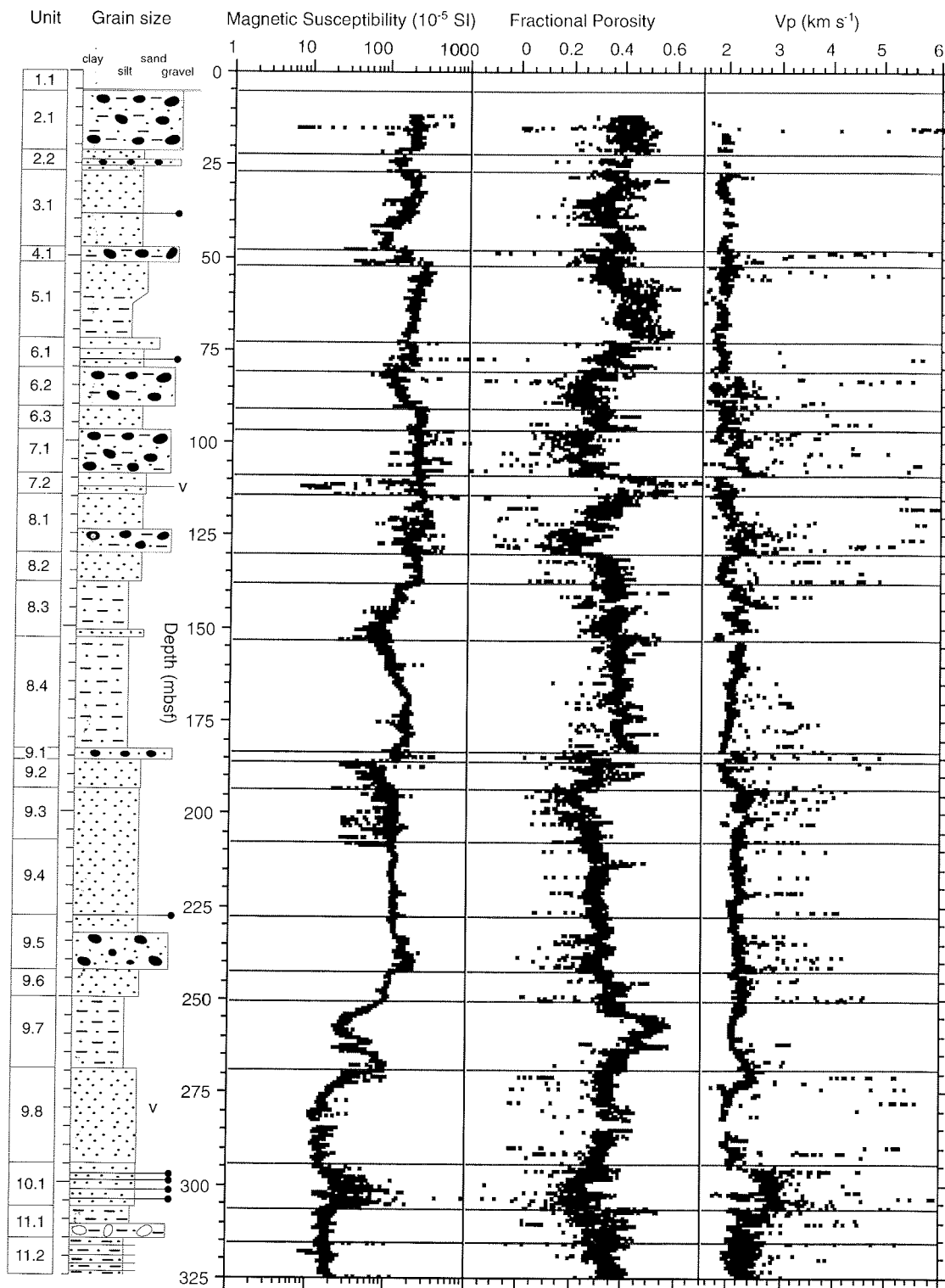


Fig. 2.17 - Log of all core-physical property data in the upper part of CRP-2/2A. Horizontal lines represent boundaries of lithostratigraphical units.

noise in the data. This is particularly evident in the mudstone LSU 9.7, 8.4 and 11.3 (Figs. 2.17 & 2.18). A similar observation was made for the core-physical properties of CRP-1 (Cape Roberts Science Team, 1998).

Different grain-sizes help to explain the four major core-physical property Units A-D described above. In Unit A (LSU 1.1 to 8.1) more gravel is present than in the LSU 8.2 to 11.3 of Unit B which are more dominated by sandstone and mudstone. In the upper part of LSU 12.1

to 12.4) the core-physical property data appear very noisy. These lithostratigraphical units have higher gravel content which may cause the larger dispersion in the data.

The pattern is different in the lower part of Units C and Unit D. Here strong down-core fluctuations in the data persist, even though the lithology is dominated by sandstone (LSU 13.1 to 15.6) with larger amounts of gravel in only a few units. This effect may be explained by variability in cementation which is evident in some of the lower sandstone

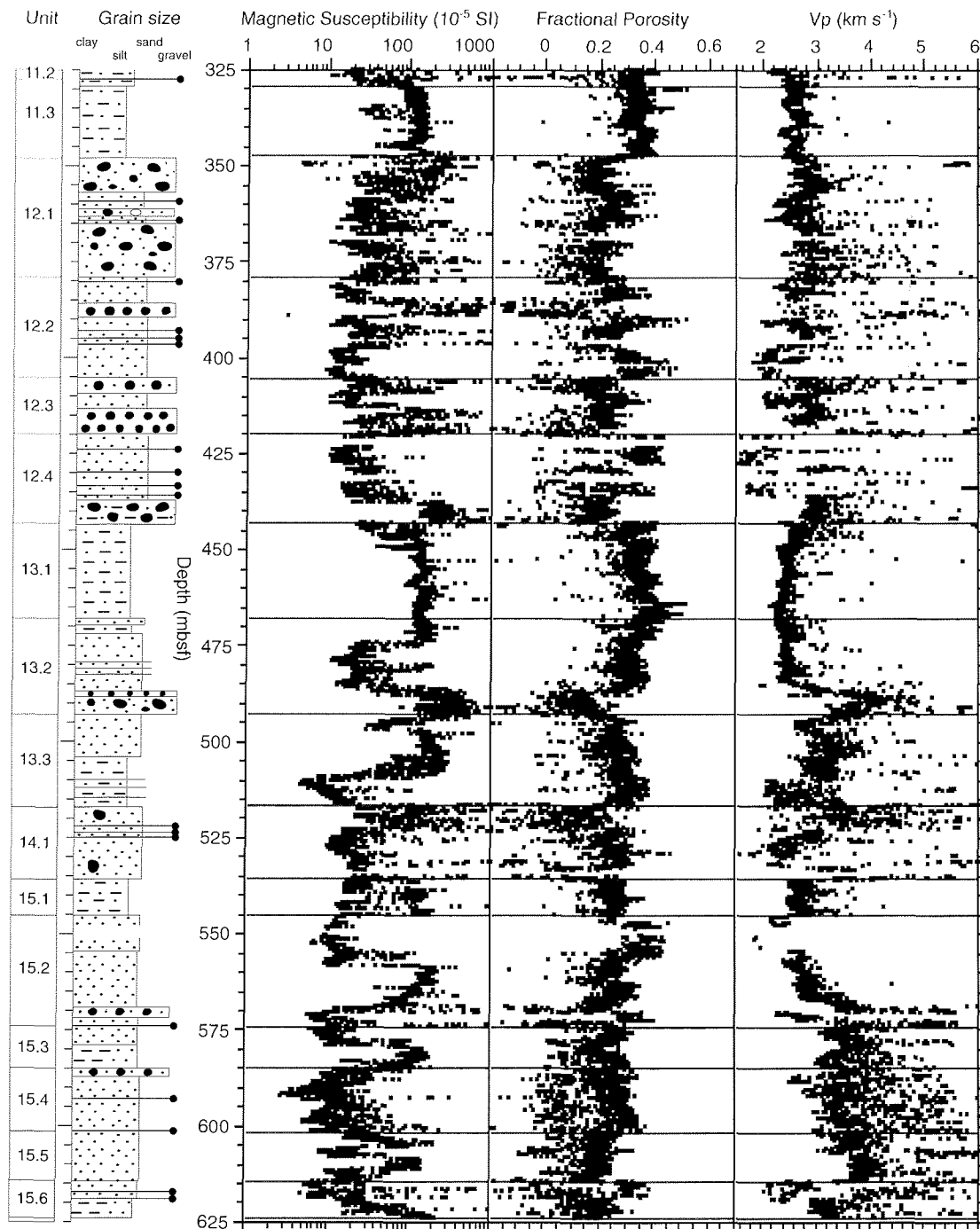


Fig. 2.18 - Log of all core-physical property data in the lower part of CRP-2/2A. Horizontal lines represent boundaries of lithostratigraphical units.

units. In the core-physical properties, cementation is indicated by a strong increase of V_p compared to only minor decrease in porosity. The reason is that cementation can have a major affect on rigidity and thus V_p , without causing a large decrease in porosity. This effect also explains the skewness in the V_p distribution compared to that of WBD (Fig. 2.13). Some well-cemented lithological units are characterized by very high V_p up to 6 km s^{-1} . These include LSU 13.2, 14.1 and 15.2 - 15.5. Cementation may also partly explain the larger degree of dispersion in the lower part of the core in general (below about 330 mbsf). Cementation is described in more detail in the Lithostratigraphy and Sedimentology chapter.

DOWN-HOLE LOGGING

INTRODUCTION

Down-hole logs from CRP-2A provide a representative record of *in situ* physical properties of formations adjacent to the drill hole. Interpretation of continuous measurements in the drill hole provide detailed lithological, stratigraphical, geophysical and mineralogical information. At the Cape Roberts drill site, the down-hole tools (Tab. 2.2) were lowered individually into the drill hole on a four-conductor cable (diameter 4.7 mm). Table 2.2 lists vertical resolution, logging speed, and the

sampling interval for individual measurements which is variable and tool dependent.

Down-hole logging was carried out in three phases: phase I covered the section from 65 to 172 mbsf, phase II from 200 to 625 mbsf, and phase III from 13 to 27 mbsf. Phase I logging took place from 5 to 6 November, while phases II and III began on 25 November and were completed on 29 November 1998.

TOOL DESCRIPTION

A brief description of the logging tools run is given in the following sections. For a detailed explanation of logging tool principles and applications see, for example, Serra (1984) and Rider (1996).

Spectral Gamma-Ray Tool

The spectral gamma-ray (SGR) tool measures the natural radioactivity of the formation. The amounts of the radioactive isotopes of potassium (K), uranium (U), and thorium (Th) are measured quantitatively by a Bismuth-Germanium - scintillation detector. The computer software subdivides the entire incident gamma-ray spectrum into discrete energy windows for isotope analysis. Temperature changes within the drill hole may cause a shift in the gamma-ray spectrum. During the logging run, the software controls the shift in the spectrum by comparing it to a calibrated spectrum to provide the total abundance of K, U, and Th.

The SGR tool is often used to distinguish between sandstone and mudstone because naturally occurring radioactive minerals are generally more abundant in fine-grained sediments. However, radioactivity may also be high in mineralogically immature sandstones and in sediments containing volcanic material.

The gamma-ray tool may be run in a cased drill hole, although, attenuation effects caused by the casing have to be corrected by data processing after the log is run.

Density Tool

The density (Den) tool measures the energy flux at given distances from a caesium-137 gamma-ray source (activity about 3.6 GBq). The attenuation of gamma-rays is caused mainly by Compton scattering. The density of the rock formation (wet-bulk density) is computed from this energy flux by assuming that the atomic weight of most rock-forming elements up to iron (Fe) is approximately twice the atomic number. Because this is not the case for hydrogen, found in water, the tool response was calibrated in holes with known densities.

The radioactive source and two NaI-detectors are placed in the tool that is pressed against the drill hole wall by a bowspring arm. Excessive roughness of the hole or break-outs will cause some drilling fluid to infiltrate between the detectors and the formation, resulting in density readings that can be artificially low. Approximate corrections can be made by comparing density data with calliper data.

Neutron Porosity Tool

A minitron accelerator within the neutron porosity (ϕ) tool emits neutrons with 14 MeV 17 times a second, resulting in production of 10^8 neutrons per second. The emitted neutrons collide with other atoms in the formation. The highest energy loss occurs when neutrons collide with hydrogen nuclei, which have nearly the same mass as the neutron. The number of neutrons that rebound off larger atoms is recorded by two He-3 counters spaced 0.18 m from each other. If the hydrogen concentration is small, as in low-porosity formations, neutrons can travel farther before being captured. The opposite effect occurs when the water content is high, as in high-porosity formations. However, hydrogen bound in minerals, such as clays, also contribute to the measurements, often resulting in over-estimated raw porosity data. By taking the ratio of the detected neutrons from the far and the near detector, the raw porosity can be calculated.

Sonic Velocity Tool

The sonic velocity (sonic) tool uses one acoustic transmitter (piezo sparker) and two acoustic receivers to measure the time required for sound waves to travel over source-receiver distances of 0.8 and 1.2 m. The differences in travel time are then converted into compressional-wave velocities. Full sonic waveforms are stored for post-field analysis of shear-wave and compressional-wave velocities and possibly rheological parameters.

Porosity and degree of lithification are the main controls on compressional-wave velocity. A decrease in porosity or an increase in lithification results in a velocity increase. Density and velocity values can be combined to produce an impedance log which is the base input for a synthetic seismogram that may be compared with seismic-reflection profiles.

Vertical Seismic Profiling

The vertical seismic profiling (VSP) tool records acoustic signals generated by a seismic source (*e.g.* explosives). A retractable arm presses the tool, which contains a three component geophone, against the drill hole wall with a force of 800 N. Measurements are taken at discrete depth intervals.

The eigenfrequency of the geophone is 14 Hz. The frequency range varies from 2 to 400 Hz and the dynamic range is 120 dB. The data are recorded for 1 024 ms and are digitised at an interval of 0.5 ms. A geophone of the same type, set up close to the drill hole mouth, detects the direct wave.

VSP data allow the calculation of interval and average velocities *versus* depth, a time-depth conversion, and a correlation with surface seismic profiles. The tool records downgoing waves and reflected waves, even if the reflector is below the position of the tool.

Bore Hole Televiewer

The bore hole televiewer (BHTV) incorporates a piezoelectric crystal which rotates 3 times per second

Tab. 2.2 - Tool table with important technical parameters and logged intervals. Cen = centralised tool; eccen = eccentric tool.

Tool Abbreviation	Tool Name	Units	Diameter (mm)	Speed (m/min)	Sample Interval (m)	Vertical Resolution (m)	Phase I depths (mbsf)	Phase II depths (mbsf)	Phase III depths (mbsf)	Total Metres Logged
SGR	Spectral Gamma Ray (GR, Potassium (K), Uranium (U), Thorium (Th))	API, %, ppm, ppm	52	1	0.1	0.3	0 - 172	139 - 624	12 - 23	624
Den	Density	gcm ⁻³	48 eccen	4	0.1	0.25		0 - 445	12 - 27	460
phi	Neutron Porosity	%	42	3	0.1	0.5	64 - 167	140 - 620	12 - 24	568
Sonic	P-wave Velocity	kms ⁻¹	42 cen	4	0.1	0.4	63 - 167	200 - 440		344
VSP	Vertical Seismic Profiling		48	na	7.5				0 - 127	127
BHTV	Borehole Televiwer		40 cen	1			65 - 164	200 - 440		339
aind	Array Induction (Resistivities: RLong, RShort)	Ohmm	52	4	0.1	0.6	63 - 170	200 - 623	12 - 29	547
Dip	Borehole Geometry (Inclination & Azimuth), 4-pad Conductivity, 4-arm Caliper, Magnetic Field (deltaZ)	degrees, degrees, pad units, mm, nT	52	3	0.005	0.02	63 - 160	200 - 623		520
Sus	Magnetic Susceptibility	10 ⁻⁴ SI	42	5	0.04	0.4	63 - 167	200 - 623	12 - 25	540
Salet	Mud Temperature (Temp), Mud Resistivity (mud R)	°C, Ohmm	40	10	0.1	0.2	17 - 162	17 - 624		607

around a central shaft and fires a pulse approximately 1 800 times per second (Zemanek et al., 1970). The pressure pulse generated by the crystal travels through the drill hole fluid and is reflected from the drill hole wall. The signal, which returns to the crystal, provides a measure of the amplitude and travel-time for each pulse. The crystal is oriented magnetically. During logging, a photograph is taken every metre which allows for in-field interpretations. See Barton et al. (1991) for further details of the processing and analysis of BHTV data.

During logging phase I, the BHTV was operated in 'mark' mode instead of the normally used 'compass' mode due to operational complications. As a result, the BHTV images from 64.7 to 163.7 mbsf are not oriented with respect to geographical coordinates. However, during phase II, the BHTV was successfully operated in 'compass' mode and thus the drill hole image is oriented from 200 to 441 mbsf.

Analysis of these images allows detection and orientation of break-outs, fractures and faults, and bedding planes. In a bore hole drilled in a region in which the two horizontal stresses are unequal, break-outs will develop due to the drill hole stress concentration at the orientation of the least horizontal stress. Fractures, faults, and bedding planes that intersect the drill hole can be detected primarily because they are mechanically weaker or softer. The BHTV may also identify locations of large lonestones. The lonestones are denser than the surrounding sediments and consequently have a high impedance contrast and greater sonic reflectivity. High-resolution BHTV images will be available for interpretation after the analogue data are digitised.

Magnetic Susceptibility Tool

The magnetic susceptibility tool (Sus) is based on electromagnetic propagation of waves: a transducer coil emits electromagnetic waves with a frequency of 1 kHz into the formation. The induced electromagnetic field depends on the formation susceptibility and conductivity. An induced voltage is recorded by the receiver coil, located 0.2 m above the transducer.

The tool is calibrated with rock samples of known susceptibility.

Induction Tool

The induction tool (aind) operates on the same principles as the magnetic susceptibility tool in order to evaluate the formation electrical conductivity. Different frequencies are emitted by the transducer coil: 10, 20, and 40 kHz. Four receiver coils are located 0.5, 0.75, 1.1, and 1.5 m from the transducer coil. The configuration of source and receiver coils allow the measurement of formation conductivity at 0.5 and 1 m vertical spacing (shallow and deep), this spacing limits the influence of the mud resistivity.

Water content, salinity, and drill hole temperatures are the most important factors that control the electrical properties of rocks. According to Archie's Law, resistivity is proportional to the inverse square root of porosity. Archie validated this law for sandstones, and thus porosity may be calculated from resistivity measurements in sand sections of the drill hole. However, porosities may also be computed in other lithologies based on empirically derived assumptions. Another factor controlling formation resistivity is the concentration of hydrous minerals, including clays, which are conductive. Metallic minerals and the geometry of interconnected pore space also affect the formation resistivity.

Dipmeter Tool

The dipmeter (Dip) tool consists of four orthogonal pads that are pressed against the drill hole wall and measure high-resolution conductivity variations of the formation. The conductivity traces provide details for sedimentological and structural interpretations. Cross-correlation of the four conductivity traces can provide measurements of dip and azimuth of bedding and fractures.

An inclinometer is included in the dipmeter tool for spatial orientation of the pad readings. This orientation provides the deviation of the drill hole from vertical. The tool is oriented with respect to the earth's magnetic field using a three-axis flux-gate magnetometer. Since the drill

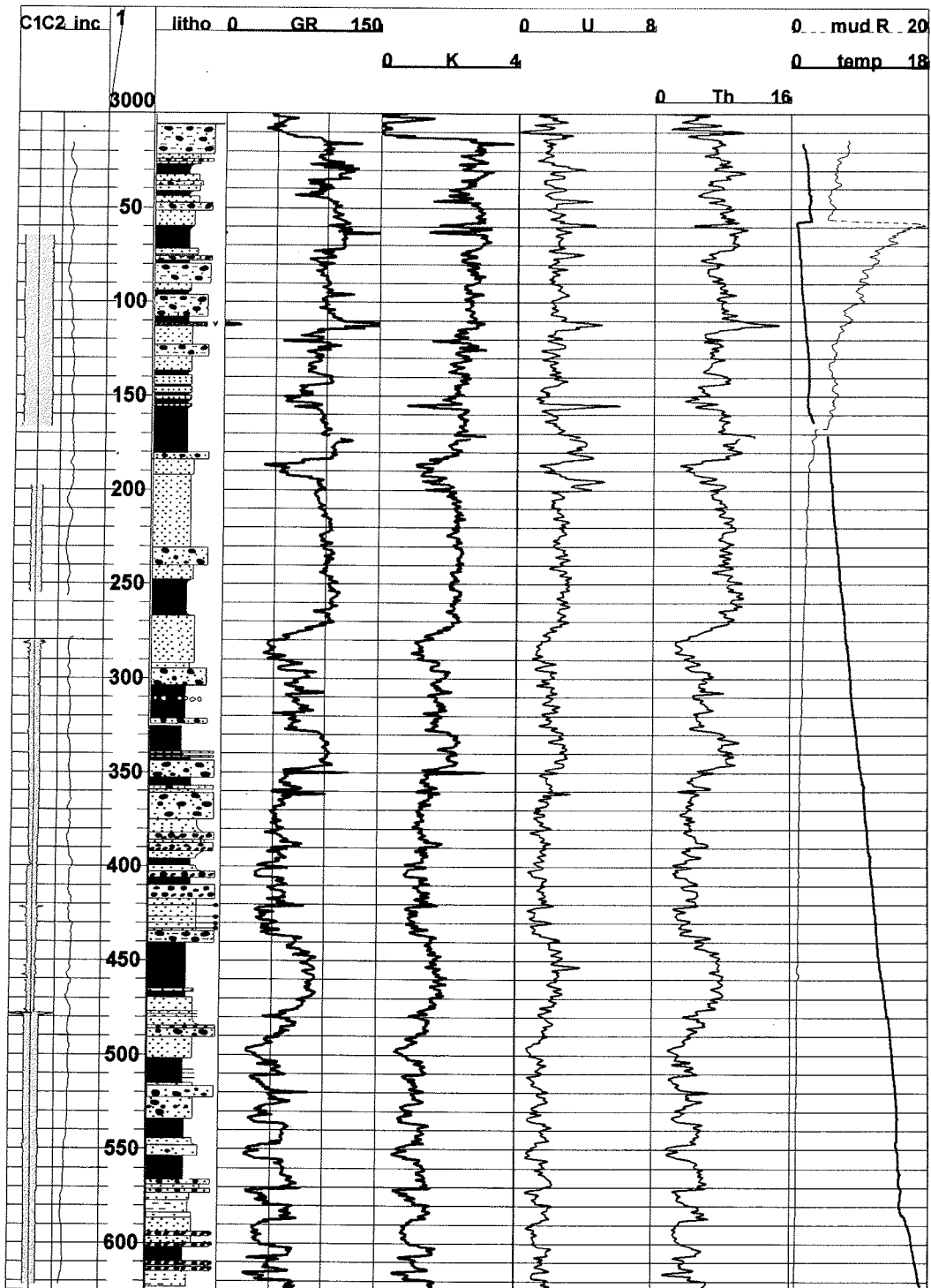


Fig. 2.19 - Composite plot of down-hole measurements. The columns from left to right show the following parameters: drill hole calliper (C1 and C2) (60-120 mm); inclination of the drill hole (inc) (1-2°); logging depth (mbsf); simplified core-based lithology; gamma-ray (GR) (0-200 API); potassium (K) (0-4%); thorium (Th) (0-20 ppm), uranium (U) (0-8 ppm); sonic velocity (sonic) (1.5-4.5 kms⁻¹); density (den) (1-3 gm⁻³); neutron porosity (phi) (0-100%); susceptibility (sus) (0-150 x 10⁻⁴ SI); vertical magnetic anomaly (deltaZ) (-500 - 500 nT); electrical resistivity (deep) (0-10 Ohmm) and (shallow) (0-10 Ohmm); mud resistivity (mud R) (0-20 Ohmm); temperature (temp) (0-18°C). Some sections of the borehole were measured through the casing by various tools (see Tab. 2.2). All data are corrected for casing effects (except for the sea-riser from 0-12.3 mbsf).

site is less than 1 200 km away from the magnetic pole, the magnetic declination can change dramatically and suddenly. Therefore, a magnetic-field station at the surface was used to record the natural variations of the earth's magnetic field during down-hole logging.

Temperature and Salinity Tool

A type Pt100 electrical thermometer records mud temperature (Temp) with a precision of 0.1°C. The drilling process disturbs the temperature field in the drill hole.

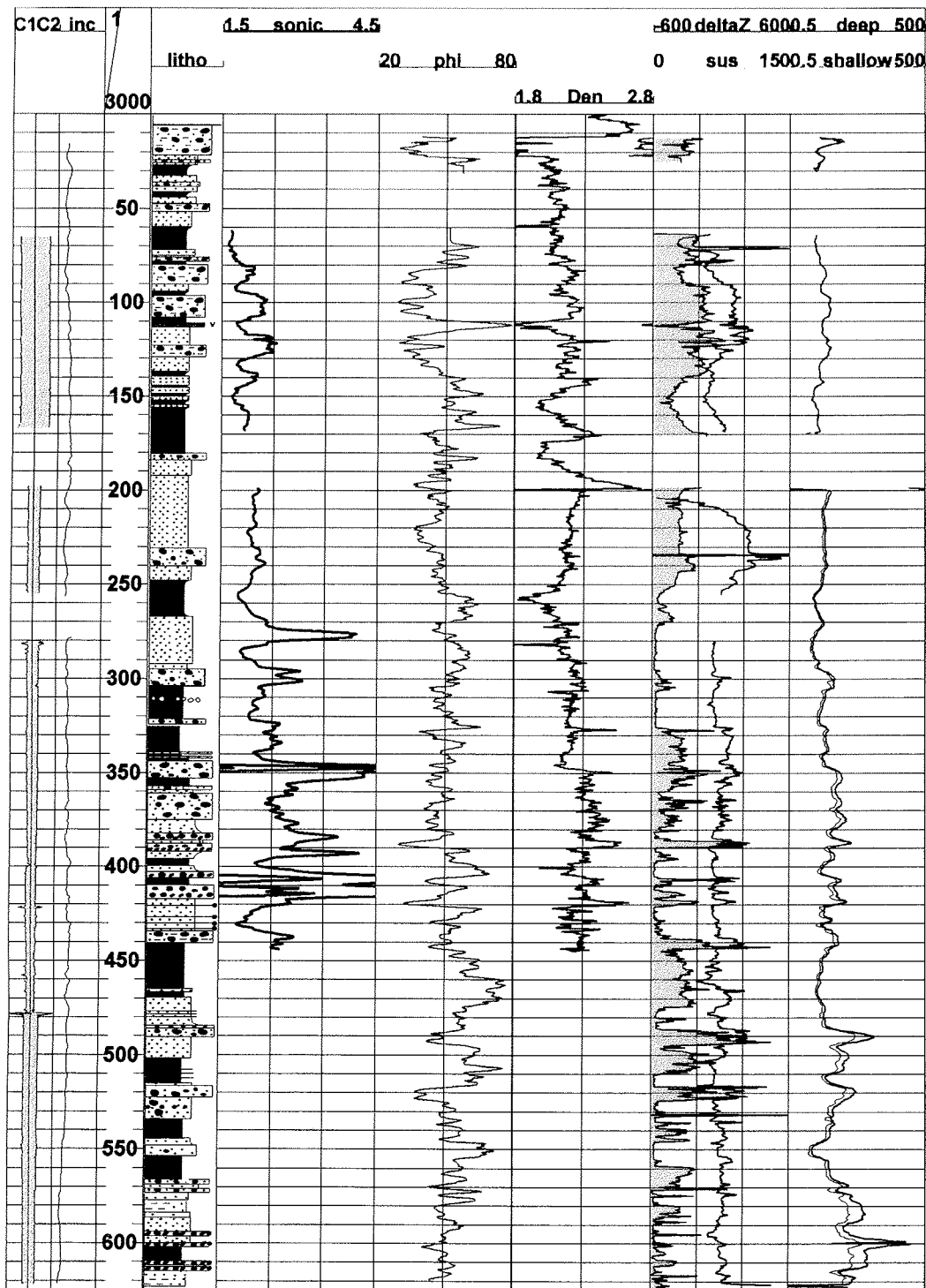


Fig. 2.19 - Continued.

According to Bullard (1947), the time necessary for a drill hole to attain temperature equilibrium is at least as long as the time required for drilling. However, temperature changes measured shortly after drilling completion may indicate water movement in the drill hole or in the formation, or changes in lithology. The same tool also records mud electrical conductivity with two adjacent electrodes. The mud is free to pass by the electrodes in the tool. All electrodes are isolated in a metallic housing to prevent any external electric influence from the formation. This effect

is also minimized by restricting the distance of the two source electrodes to 50 mm from the receiver electrodes. The tool is calibrated with water samples of known temperature and conductivity.

LOG DATA ANALYSIS

All down-hole data for CRP-2A, except dipmeter and VSP, are plotted in figure 2.19 and in section 4 in the supplement to this issue. Certain tools were not run in the

hole when casing was present or when drill hole bridging prevented further measurements. A list of data gaps is given in table 2.2. Those tools run within casing (SGR and Den) and are corrected for the attenuation caused by the casing, except for the section in the sea riser above 12.3 mbsf. All depths listed are logging depths which may be offset from core depths, because the drilling rig moved up and down due to tidal fluctuations. Therefore, individual tools were levelled to a datum on the sea riser. A brief analysis of log data is given below.

The calliper data (Fig. 2.19 and section 4 in the supplement to this issue) indicate that the diameter of the CRP-2A drill hole is generally even. The diameter of the drill hole decreases below 200 mbsf, because of a change in the size of drill bit, from 96 to 75 mm. Large break-outs or wash-outs are evident at 150, 282, 422, and 477 mbsf. The largest wash-out recorded in the drill hole, 160 mm, is located at 477 mbsf. Caution must be exercised in the interpretation of down-hole data in the areas containing large wash-outs. The inclination of the drill hole is generally less than 2° from vertical.

In general, the total gamma-ray values, as well as the individual amounts of K and Th, decrease down the drill hole. This trend is most evident in the K content and does not appear in the U content. Potassium chloride was an additive to the drilling mud but is unlikely to have caused this downward trend. The gamma-ray log can be divided into three main sections. In the upper section of the drill hole, from sea floor to 275 mbsf, the gamma-ray values are consistently high (100 API), in the middle section, from 275 - 480 mbsf, the values range from 50 - 100 API, and in the bottom section, from 480 - 625 mbsf, displays low gamma-ray values from 20 - 80 API. This bottom section displays a pattern of cyclicity (Cyclostratigraphy section in Lithostratigraphy and Sedimentology chapter).

Over the length of the drill hole, there is no obvious correlation between gamma-ray values and lithology, although, diamicts tend to show the lowest gamma-ray values. A U peak at 110 mbsf is attributable to a volcanic ash layer, and a decrease in drill hole temperature at 155 mbsf is correlated with a U high (see below).

Formation velocities range from 1.7 to 2.5 kms⁻¹ down to 275 mbsf, with an average velocity of 2.0 kms⁻¹. There is a sharp peak in velocity from 275 to 280 mbsf correlated with highly cemented sandstone. Below this peak, the average sediment velocity changes to 2.8 kms⁻¹. Velocities up to 6 kms⁻¹ are highly correlated to diamicts and may be caused by individual limestones (*e.g.* at 348 - 355 mbsf and 408 - 420 mbsf).

The average bulk density between sea floor and 445 mbsf increases from 2.05 to 2.30 gcm⁻³. Maxima in density values are evident in diamict units which have values up to 2.5 gcm⁻³. A density minimum of 1.7 gcm⁻³ is detected within a volcanic ash layer from 110 to 114 mbsf. The density peak at 200 mbsf is artificial and caused by the tool entering the bottom of the HQ casing.

The average neutron porosity (ϕ) value throughout the drill hole is 50%. The high porosity values may represent an influence from hydrous minerals such as

clays. Neutron porosity is correlated negatively with density and sonic velocity values suggesting that porosity is the main control for all three logs.

During the logging operations a magnetometer, stationed 50 m east of the drill site, monitored the Earth's magnetic field. The dipmeter tool measured the vertical intensity of the earth's magnetic field. The ΔZ curve (Fig. 2.19) was derived by subtracting the average vertical intensity of the earth's magnetic field (-63 000 nT) from the measured vertical component. The susceptibility and ΔZ are similar in character. This similarity implies that the overall nature of magnetisation in the sediments is induced rather than remnant. A strong anomaly in the ΔZ curve at 235 mbsf may be because of the remnant magnetisation of a limestone.

From the sea floor to 325 mbsf the susceptibility curve is smooth with values greater than 20×10^{-4} SI. Below this depth, the values fluctuate from 0 to 150×10^{-4} SI. The susceptibility values above 325 mbsf may be strongly influenced by the influx of clasts from the McMurdo Volcanic Group (Sedimentology, Clast Variability section). In some sedimentary environments magnetic minerals are concentrated in the finest grained sediments. This may also be the case for sediments below 325 mbsf. The cyclicity observed in the gamma-ray values below 500 mbsf is also observable in the susceptibility record.

The seismic source for CRP-2A VSP measurements was an explosion of 400 g of primer 'Anzomex P' using No. 8 submarine detonators 15 m below the sea ice, and 105 m south of the drill site. The seismic detonator lead was connected to a SIE blaster which in turn was linked by shot-firing cable to the seismic-recording equipment. The reference geophone was positioned 2.6 m west of the drill hole. VSP measurements were taken every 7.5 m, between sea floor and 127 mbsf, in the HQ casing.

As a result of a frequency analysis, high frequency noise with maxima at 177 - 185, 280 - 285, and 324 - 330 Hz are recognized. These noise levels are probably associated with tube wave energy generated by compressional wave to tube wave conversions on the drill string. The down-going waves, initiated by the seismic source, include low-frequency noise, between 5 and 15 Hz. A bandpass filter (13-17-110-120 Hz) was applied for the initial processing. Tests look promising for wavelet deconvolution.

Separation of up-going and down-going waves was carried out using a polygonal mute in the frequency-wave number (f-k) domain. However, the effectiveness of this filtering is limited by the low number of traces and the poor resolution in the f-k domain.

Figure 2.20 shows the current status of the processed seismic data. The vertical axis is in one-way travel-time and the horizontal axis is the depth of the geophone. This figure shows the up-going (reflection) energy, following the f-k filtering described above. Coherent up-going energy is visible at around 181, 275, 352, 490, 562, 652, and 889 ms. The most coherent arrivals are the 181 and 889 ms arrivals.

The inverse of electrical conductivity, resistivity, is plotted in figure 2.19. The shallow and deep resistivity values are nearly equal down to 275 mbsf. Below this

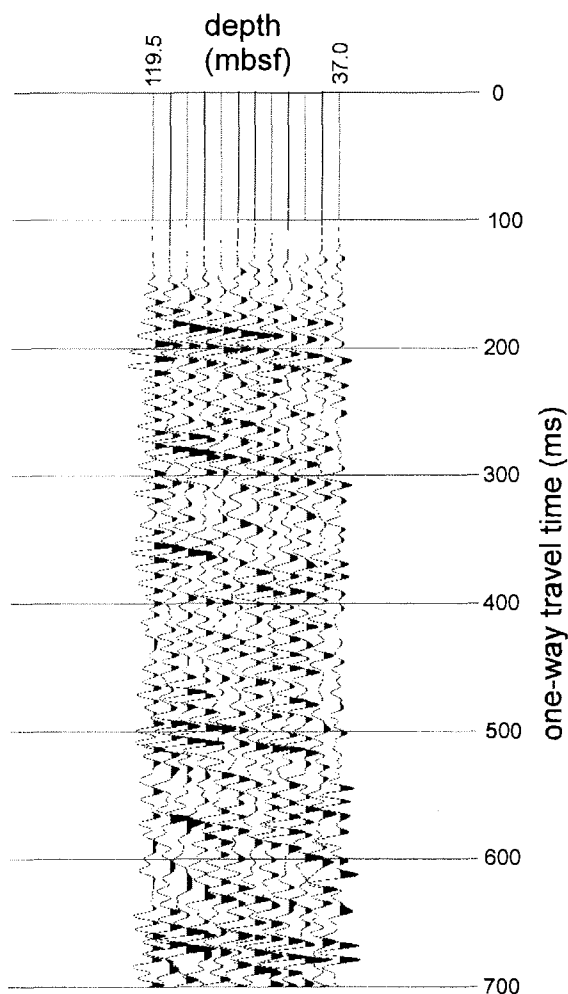


Fig. 2.20 - Plot of vertical seismic profile (VSP) after applying an f-k filter to enhance the up-going waves. The vertical scale is one-way travel time in ms; the horizontal scale is mbsf. Up-going waves can be traced down to a reflector at 706 mbsf.

depth the shallow resistivities are lower than deep resistivities due to infiltration of conductive mud into the formation. The depth of this infiltration zone is limited by formation permeability and porosity. Drill hole resistivity values are correlated with diamicts which often contain large resistive clasts.

Mud temperature and resistivity were measured, in phase I and II, shortly after drilling activities ceased, so that drill hole-temperature equilibrium was not reached. The average temperature gradient for the entire drill hole is 28 Kkm⁻¹, with a bottom hole temperature of 17.2°C. A change in the temperature gradient to 50 Kkm⁻¹ occurs below 585 mbsf (Fig. 2.21). Other drill hole-temperature anomalies may indicate zones of cold seawater influxes. From 140-160 mbsf and from 550-585 mbsf, the drill hole temperature suddenly drops by 1 K. These sudden drops in temperature coincide with a decrease in calculated salinity of drill hole fluids. Salinity is calculated as NaCl equivalent from the measured mud conductivity.

Figures 2.22 to 2.24 highlight special features of the CRP-2A drill hole. Figure 2.22 displays the logging results

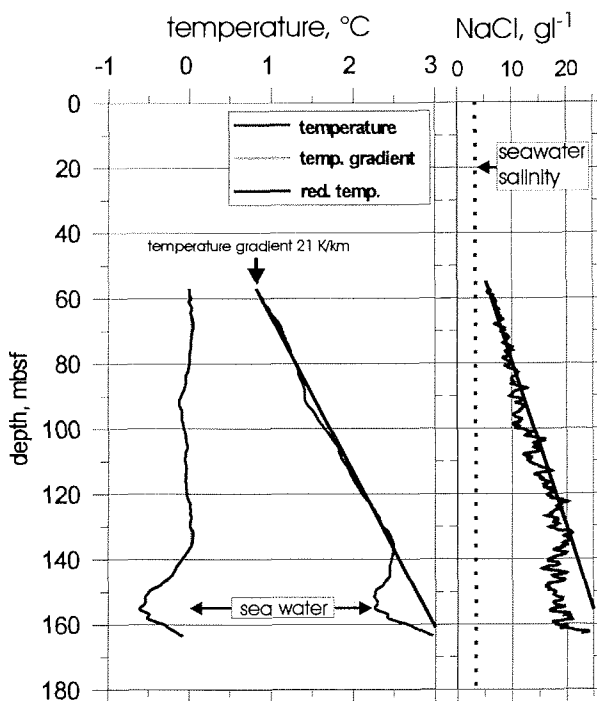


Fig. 2.21 - Plot of the temperature profile in the loose sand section between 143 and 155 mbsf, showing a marked change in temperature. This temperature change may be caused by an influx of cold seawater into the drill hole. The salinity of mud (>10 gl⁻¹) is greater than that of sea water (3 gl⁻¹), thus the decrease of salinity is attributable to a seawater influx.

for the interval from 110 to 114 mbsf where a volcanic ash layer was drilled. The ash layer is characterized by an increase in gamma-ray and porosity values, and a decrease in density values. However, there is no evident change in velocity values. An increase in abundance of magnetized particles in the volcanic ash is indicated by anomalies in the magnetic susceptibility and the vertical intensity of the magnetic field.

Loose sands at 143-155 mbsf presented several problems for the drilling operation (Fig. 2.23). This section is characterized by a decrease in gamma-ray, sonic, density, resistivity, susceptibility, and temperature values and an increase in porosity. A U enrichment, up to 8 ppm, at 155 mbsf may be caused by the leaching of seawater flowing through the sand layer. The underlying, less permeable mudstone provides a barrier to the downward flow of seawater. The relative lows in the magnetic susceptibility may be caused by dispersion of magnetic minerals in the sand.

Figure 2.24 shows cyclic changes in gamma-ray and susceptibility values corresponding to sequence boundaries (Sequence Stratigraphical Interpretation). The gamma-ray values oscillate between 30 and 70 API, and the sequence boundaries are located in the steep gradient of these changes. Coarsening- and fining-upward sequences are also visible in the gamma-ray and susceptibility data.

The overall quality of data is good, despite difficulties caused by logging in a narrow drill hole which had a tendency to form bridges. Further investigation of the

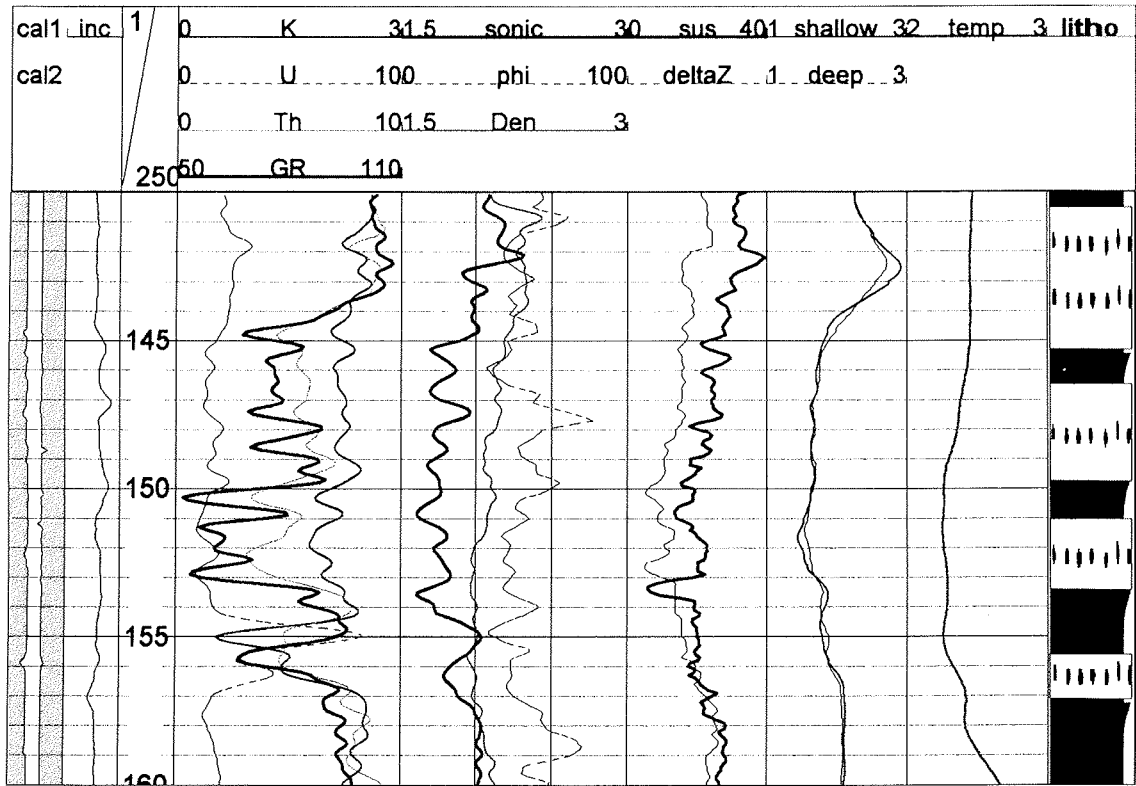


Fig. 2.22 - Composite plot of the drilled ash-bearing layers between 105 and 125 mbsf. The physical property abbreviations are as in figure 2.19. Note the high gamma-ray and porosity values and decreasing velocity, density and electrical resistivity values in the ash layer.

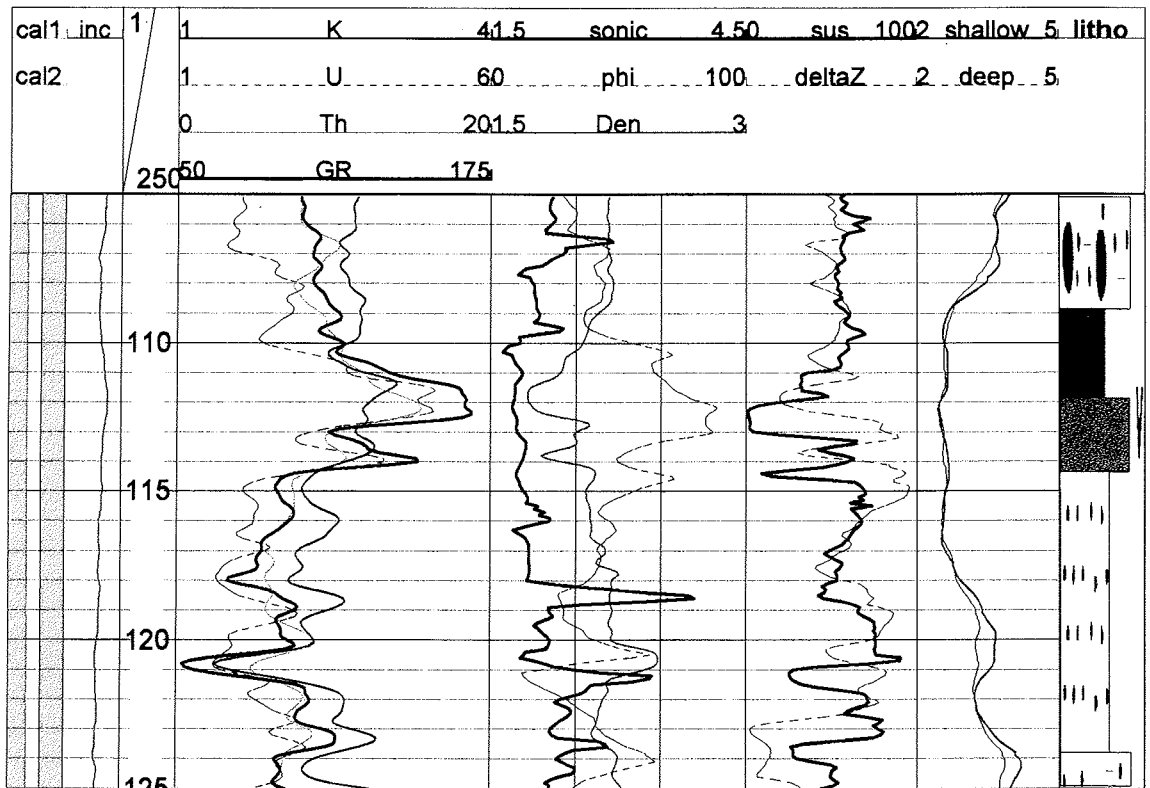


Fig. 2.23 - Composite plot of a sand layer between 143 and 155 mbsf. This sand zone is characterized by low gamma-ray values, densities, and velocities, and high porosities. The negative temperature anomaly may be related to cold seawater influx. The loose sands caused severe drilling problems. The physical property abbreviations are as in figure 2.19.

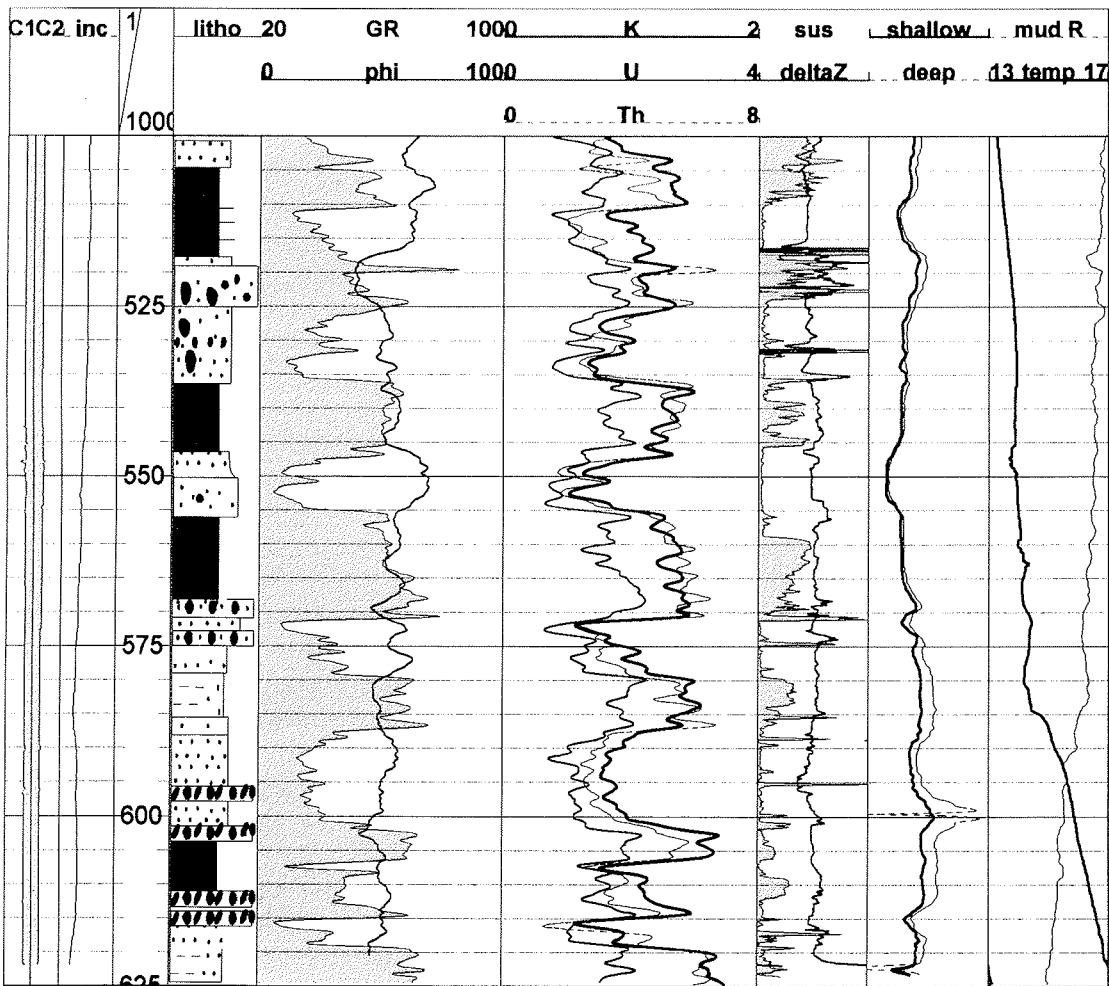


Fig. 2.24 - Composite plot showing cyclicity in gamma-ray and susceptibility values below 500 mbsf. These cycles also correspond to sequence boundaries. Some coarsening and fining upward sequences are also visible (e.g. from 555 to 570 mbsf). The physical property abbreviations are as in figure 2.19.

down-hole data will provide a better understanding of the geological history of the area.

CORRELATION OF SEISMIC REFLECTORS WITH CRP-2/2A

Drill holes CRP-2 and 2A are located 300 m north of seismic line NBP9601-89 (Fig. 1.3, shot point 1998), a W-E line across Roberts ridge. CRP-2/2A reached a depth of 624.15 mbsf, equivalent to 525 ms twt bsf (Fig. 1.4). At least 15 seismic events can be identified at this depth or above, and can be related to the cored section (Fig. 2.25). These are summarized in table 2.3.

The seismic stratigraphy of the Victoria Land Basin was established by Cooper & Davey (1985), who identified a number of major seismic units (V1-V5) separated by basin-wide reflectors. We sought to sample and calibrate stratigraphically two critical seismic reflectors, one separating V3 from V4 and the other V4 from V5; for the V3/V4 reflector, there were two possible depth interpretations. CRP-2/2A sampled the sedimentary

sequences from just above the upper alternative V3/V4 boundary, penetrated the lower alternative V3/V4 boundary and terminated c. 120 m above the presumed position of the V4/V5 boundary, at a depth of about 624 mbsf. We have taken the logs of sonic velocity and density from the whole-core logging and used these to derive a time-depth relationship. We have then converted the seismic travel times to depth, and thus derived a down-hole reflectivity profile. This profile has then been used to link the seismic data with the lithological logs (Fig. 2.25).

A re-evaluation of the correlation of seismic reflection data from the central Victoria Land Basin to the CRP drill sites (Henrys et al., 1998) suggested that the interpreted correlations are not unequivocal. However, it should be noted that uncertainty in the association of a strong reflector with a particular named interface does not mean that there is any uncertainty in the existence of that reflector as a physical feature. The interpretation here will be limited to an analysis of the major units; detailed linkages are uncertain because of the low resolution of the seismic signal (wavelength ~ 30 m). However, reflection coefficient data and changes in physical properties that extend over

Tab. 2.3 - Correlation between seismic reflectors, reflectivity and velocity values from measurements on the core, and lithostratigraphical units in CRP-2/2A.

Seismic Reflector	Twt bsf (ms)	Lithostratigraphical correlation and depth	Comments and inferences
a*	50	LSU 4.1 at 48 - 52 mbsf	Gently dipping reflector at a 4-m-thick diamict; corresponds to minor velocity and impedance change. Correlates to CRP-1.
b*	83	Boundary between LSU 6.2 and 6.3 at 90 mbsf	Significant impedance and velocity change; 8-m-thick diamictite. Upper alternative for V3/V4.
c	110	Boundary between LSU 7.1 and 7.2 at 109 mbsf	Major impedance change between thick diamictite (7.1) and an ash-bearing unit with a 1.2-m-thick ash bed. Reflection not strong.
d	145	Near the base of LSU 8.1 at 125-130 mbsf	Velocity increase within lower part of a diamictite; Oligocene-Miocene boundary placed at 130 m on biostratigraphical evidence. Minor reflector.
e*	180/ 190	Boundary between LSU 9.1 and 9.2 at 183 mbsf or between LSU 9.2 and 9.3 at 194 mbsf	Sharp increases in velocity in diamictite and sandstone, respectively; appear to correspond to weak seismic reflectors.
f*	215	Boundary within LSU 9.4 at 220 mbsf	Reflector «f» does not correspond to an identifiable velocity change. Lower alternative for V3/V4.
<i>Sea-floor multiple intersects CRP-2A at 220 ms bsf. Below this, interpretation of reflectors is more difficult.</i>			
g	241	Possibly boundary between LSU 9.5 and 9.6 at c. 240 mbsf	
h	265	Middle of LSU 9.8 at c. 276 mbsf	Velocity fall and increased reflection coefficient.
i*	290	LSU 10.1 at 296 - 306 mbsf	Sharp velocity increase at top of unit, associated with impedance changes; an equally sharp decrease velocity at the base of LSU 10.1 corresponds to a major impedance change and angular unconformity.
**	315	Base of LSU 11.2 at c. 328 mbsf	Slight velocity increase.
j*	350	Boundary within LSU 12.1 at c. 365 or boundary between LSU 12.1 and 12.2 at 378 mbsf	Velocity increase and significant change in reflectivity; marks the beginning of a zone of highly variable physical properties down to 420 mbsf.
k	380	LSU 12.3 at 420 mbsf	LU 12 contains several thick diamictites of varying impedance and velocity, but only that in the base of LSU 12.3 corresponds to a step of significant duration.
l*	405	LSU 12.4 to 13.1 at 437 - 443 mbsf	Top of 6-m-thick diamictite corresponds to major velocity change and to a reflector extrapolated through the sea-floor multiple.
m*	440	Boundary between LSU 13.2 and 13.3 at 495 mbsf	Corresponds to significant velocity change and a reflector.
<i>Second sea-floor multiple intersects CRP-2A at 440 ms bsf. Below this, interpretation of reflectors is much more difficult.</i>			
n	460/ 475	Boundary between LSU 13.3 and 14.1 at 516 mbsf	Corresponds to a significant velocity change and a faint reflector.
o*	490/ 520	Base of LSU 15.2 at 570 mbsf	Lowest significant velocity change in CRP-2A, within well-cemented sandstone; corresponds to a major reflector traced to a 100-m wide bench on the sea floor at c. 570 mbsf.

Note: *strongest and most persistent reflectors, **not seen on large scale near-trace plot.

about 20 m have been used to improve correlations. We also note that diamictites do not always correspond to a significant velocity or impedance change (e.g. at 230 mbsf), and in some cases strong and continuous reflectors have no associated change in velocity (see reflector f at 220 msec TWT bsf in Fig. 2.25).

A major lithological change (diamictite to mudstone), sampled at about 142 mbsf in CRP-1, is correlated with the

base of a 4-m thick Early Miocene diamictite forming Lithostratigraphical Sub-Unit (LSU) 4.1 in CRP-2 at a depth of about 52 mbsf; this is consistent with the correlation from CRP-1 to CRP-2 using seismic reflection data.

Table 2.3 summarizes the correlation between seismic reflectors from line NBP9601-89 and lithostratigraphical units in CRP-2/2A. Down-hole logging data and synthetic seismograms will be included in the Scientific Report.

3 – Lithostratigraphy and Sedimentology

INTRODUCTION

This chapter presents the results of a lithostratigraphic subdivision of the CRP-2/2A core, and of a variety of sedimentological investigations. In the first section, the core is divided into informal lithostratigraphical units and sub-units, and the lithologies in each are described. In the following section, a facies analysis provides a process and environmental interpretation of the core, from which a preliminary depositional model is developed. This is in turn followed by a sequence stratigraphic interpretation of the succession encountered in the hole, a brief discussion of clast variability, clast shape and fabric, an initial exploration of potential, small-scale cyclicity in the core, and a description and a preliminary interpretation of diagenetic and deformational features.

A detailed core description is shown at a scale of 1:20 as section 1 in the supplement to this issue, with core images shown as section 2 and a summary description at a scale of 1:500 shown as section 3.

The core has been divided into 15 lithostratigraphical units, based on major changes in lithology recognised by the scientific team at the Cape Roberts Camp during the drilling of CRP-2/2A. The division draws attention to prominent lithologies such as major diamictite bodies and an interval rich in volcanic tephra. The major units are in turn divided into a total of 41 sub-units, based on smaller-scale lithological changes. The Quaternary and Pliocene intervals are described in the Introduction chapter, while pre-Pliocene units and sub-units are considered here.

Twelve recurrent lithofacies have been recognised in the CRP-2/2A core based on lithology or associations of lithologies, bedding contacts and bed thicknesses, texture, sedimentary structures, fabric and colour. The entire facies assemblage is interpreted to record marine environments of deposition, from the abundance of marine macro- and microfossils, and absence of any indicators of emergence. Facies 1 (mudrocks) is interpreted as mainly suspension fallout deposits of relatively quiet, offshore marine environments, while Facies 2 (thinly interstratified mudrocks and very fine- to fine-grained sandstones) is interpreted to reflect the increasing influence of current activity, and in some instances, waves. The implication of this is that the facies may in some cases record sediment deposition in quite deep water, while in others reflect shallow, protected bays or lagoons. Facies 3 (poorly sorted, muddy fine-grained sandstones) is interpreted as the product of low-concentration sediment gravity flows across the sea floor, while Facies 4 (moderately sorted, clean fine-grained sandstones) is believed to record sediment deposition from dilute water currents and waves in a shallow marine setting which locally at least was above storm wave base. Facies 5 (moderately to well-sorted, clean, medium-grained sandstones) is interpreted to represent deposition from aqueous currents in shallow marine environments subjected to a high rate of sediment supply.

Facies 6 (stratified diamictites) and Facies 7 (massive diamictites) are interpreted to reflect a variety of depositional processes in ice-contact, marine proglacial (and possibly subglacial) environments. Facies 8 (rhythmically interbedded sandstones and siltstones) is interpreted as resulting from suspension settling from turbid plumes ("cyclopsam") in ice-proximal glacial marine environments. Facies 9 (clast-supported conglomerate) and Facies 10 (matrix-supported conglomerate) are both interpreted to record coarse-grained sediment deposition from sediment-charged, aqueous currents in shallow-water, proximal outflow systems. Facies 11 (intraformational clast breccia) is interpreted to arise from sediment gravity flows across the submarine surface following destabilization of the substrate by some (unknown) mechanism. Finally, Facies 12 (volcaniclastics) is interpreted as arising from tephra accumulation by both direct suspension settling and reworking on the sea floor, following explosive volcanic eruptions nearby.

In a preliminary sequence stratigraphic analysis, 24 unconformity-bounded, glacial marine depositional sequences have been recognised, spanning the early Oligocene to Quaternary. The analysis is based on the recognition of repetitive vertical arrangements of the lithofacies summarised above. Each sequence is bounded by sharp erosion surfaces (Sequence Boundaries) that mark abrupt, landward dislocations in facies and hence interpreted environment of deposition. Sequences typically comprise a four-part architecture involving, in ascending order, 1) a sharply-based, coarse-grained unit (Facies 6, 7, 9 or 10), interpreted as a combined Lowstand and early Transgressive Systems Tract deposit, 2) a fining-upward succession of sandstones (Facies 3 and 4) into sandy mudstones (Facies 1), interpreted as a Transgressive Systems Tract, 3) a mudstone interval (Facies 1), commonly fossiliferous and in some cases coarsening upward into muddy sandstones (Facies 3), interpreted as a Highstand Systems Tract, and 4) a sharply-based, sandstone-dominated succession (principally Facies 4), interpreted as a Regressive Systems Tract. Initial constraints on the time period recorded by the CRP-2/2A core and observations on the overall stratigraphic stacking pattern permit some preliminary speculations as to the geological factors responsible for the cyclical facies pattern.

Studies of lithology, abundance, size and distribution of coarse clasts within the CRP-2/2A core are summarised in a short section of this chapter, but detailed elsewhere in full (see Petrology Chapter, Basement Clasts and Volcanic Clasts section). Seven major varieties of coarse clasts have been recognised, their relative abundances allowing initial interpretation of changes in sediment provenance within the cored succession. Major changes in clast character were noted across sequence boundaries and lithostratigraphical unit boundaries.

Three-dimensional fabric analysis of clasts from selected, whole core samples of gravel-rich lithologies has

revealed broad scatter in most samples, with very weak preferred orientations to random orientations dominating. Two alternative explanations are offered for these fabrics: 1) that subglacial deposits are not recorded within the examined samples, or 2) that any subglacial deposits have suffered post-depositional modification which has removed any pre-existing directional fabric. Studies of clast shape on the same samples has revealed some differences between lithofacies. Diamictites studied show broad roundness distributions, with averages in the range subrounded to subangular, show on average 23% faceted clasts and one striated clast. These properties suggest that clasts in those diamictites have experienced some subglacial transport. Pebbly sandstones also show an average roundness of subangular, but with more rounded to well-rounded clasts, suggesting a strong element of fluvial reworking, while the conglomerates studied displayed a number of angular clasts and one striated clast, suggesting only limited fluvial working of those sediments.

A pilot study to investigate the potential for recognising small-scale facies cyclicity has been conducted on a laminated, fine-grained interval from Lithological Unit 11.3 (329.30-347.31 mbsf). Magnetic susceptibility data (see Chapter 2, Core Properties and Down-Hole Geophysics section) from this interval have been subjected to a spectral analysis, which has revealed strong patterns of cyclicity. The frequency lines in the derived power spectrum identify ratios between hierarchical levels of cycles that show close similarity to those of the Milankovitch orbital forcing periodicities computed for the Cenozoic. The success of this experiment suggests that much potential exists for elucidating evidence of cyclicity from laminated facies within the CRP-2/2A core.

Preliminary investigations into diagenesis of the CRP-2/2A core have revealed a variety of diagenetic features, many of which can be readily identified in hand specimen. Prominent among these are carbonate cementation, mineral fills of fractures, veins and tension gashes, and pyrite cementation. Carbonate cementation takes a variety of forms, including diffuse patches in many cases surrounding fossil shell material, small spherical nodules, larger ovoid nodules and stratiform layers. Carbonate cements are rare within the uppermost 150 m of the core but increase down-hole and become extensive below 400 mbsf. Many fractures and veins noted within the core are lined or filled by mineral material, notably carbonates and pyrite (in a few cases both types within the same fracture). Pyrite is also present as a cementing phase, most commonly found filling burrows or as diffuse patches in dark-coloured siltstones below 250 mbsf.

In a complementary study, deformational features, notably zones of brecciated rock, soft-sediment folding and other deformation, shear zones and microfaults were also described from the core. Such features are common, and are interpreted to record some combination of glaciotectonic and tectonic deformation. In the absence of other reliable diagnostic criteria, structures at macroscopic and microscopic scales may provide critical evidence of subglacial conditions in the core. As structures of interpreted glaciotectonic origin have been recognised in CRP-1, the documentation of deformational structures is

therefore of critical importance to palaeoenvironmental interpretation of CRP-2/2A. Above 297 mbsf, deformation is confined to discrete intervals within the core, including a number of brecciated zones with a jigsaw-fit fabric termed "crackle breccias". Below 297 mbsf, *in situ* brecciation is rare, but microfaulting, clastic intrusions and other soft-sediment deformation, and possible zones of shearing are common as far as the terminal depth of the hole.

The research reported in this section provides important documentation and useful first interpretations of depositional environments recorded in the CRP-2/2A core. Future work will undoubtedly reveal further details of the geological history of the Cape Roberts area.

DESCRIPTION OF SEQUENCE

The sedimentary sequence recovered in CRP-2/2A is shown graphically in figure 3.1. The pre-Pliocene portion of that sequence has been divided into 13 major lithostratigraphical units, with many of those major units further divided into lithostratigraphical sub-units. Each lithostratigraphical subdivision is described here. Preliminary interpretations of these rocks are given in Facies Analysis section, where the sedimentary facies, and their interpreted depositional environments, are discussed in detail.

LITHOSTRATIGRAPHICAL SUB-UNIT 3.1 (26.79-47.79 mbsf), SAND

LSU 3.1 is composed predominantly of compact, muddy fine to medium-grained sands, with low and variable abundances of dispersed clasts. Above 36 mbsf, the muddy fine sandstone grades locally to sandy mudstone. Two minor associated lithologies are present: thin beds of massive, poorly sorted, very coarse sandy granule gravel, and thin beds of compact, massive clast-poor sandy diamicton. The compact, muddy fine- to medium-grained sandstones are dark grey (N3) to olive grey (5Y 3/2) in colour, and generally have clast abundances of 1 to 3%. Dominant clast types include dolerite, granitoid, and (less commonly) diamictite. Bedding thicknesses in the sands range from 10 cm to approximately 2.5 m, with most beds being internally massive. However, stratification, ranging from crude to laminated, is developed locally in intervals up to 30 cm thick. Lithostratigraphical Unit 3.1 is sparsely fossiliferous, with molluscs and octacorals present; the latter occur between 35.85 and 36.50 mbsf. Carbonate cement is present in discrete zones or nodules, particularly between 40.00 and 44.00 mbsf. The upper 3 m of this unit display evidence of *in situ* brecciation, with fine sandstone intraclasts set within a matrix of soft muddy sand. Similar features, combined with evidence of soft-sediment deformation, also occur in discrete intervals up to 60 cm thick between 37.80 and 44.00 mbsf. From 44.95 mbsf to the base of LSU 3.1, thin-bedded muddy fine sand is interstratified with thin-bedded siltstone; some portions of this interval are strongly brecciated, exhibit steep dips, and show evidence of imbrication along low-angle thrust surfaces. LSU 3.1 has a sharp lower boundary.

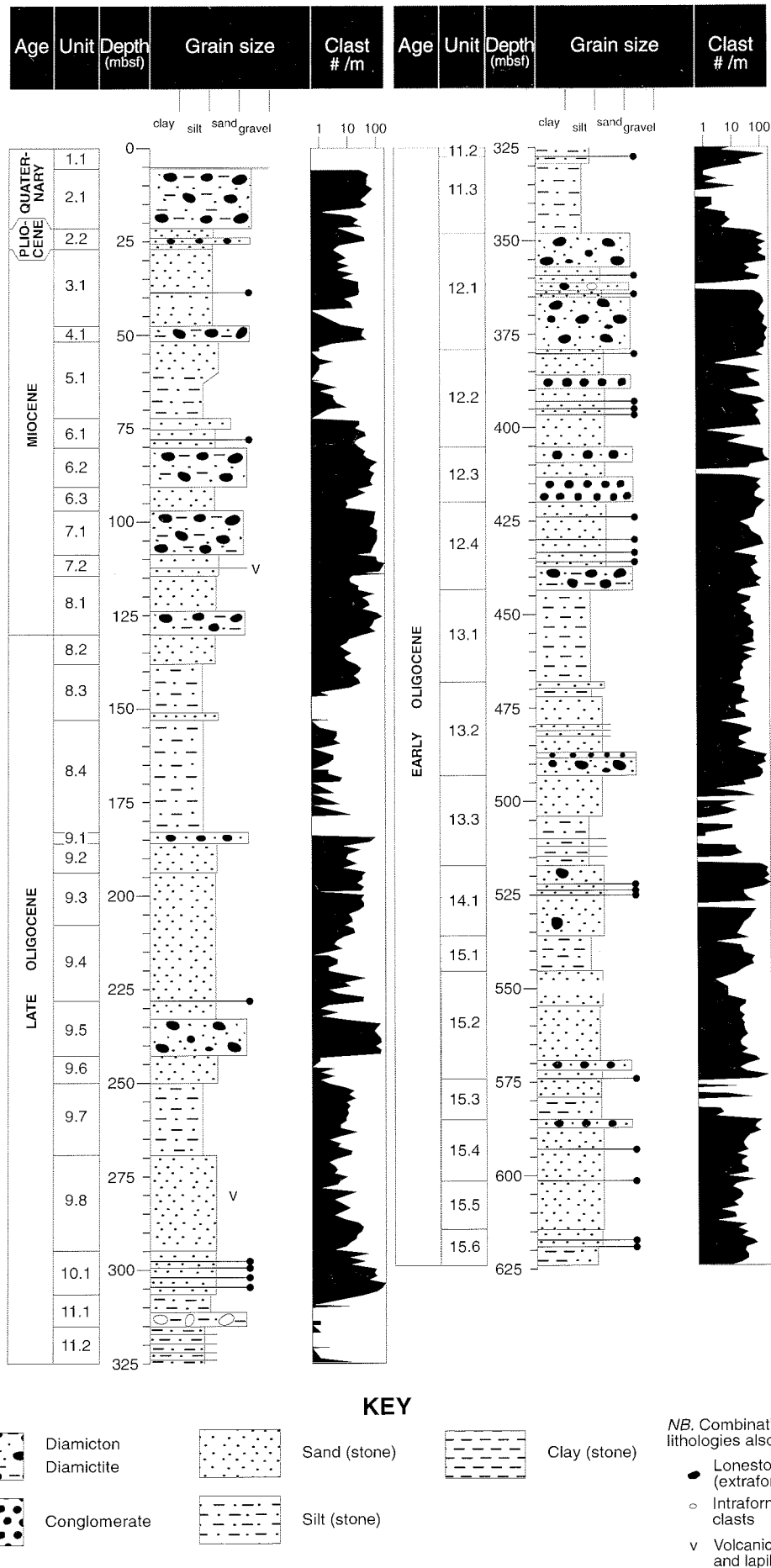


Fig. 3.1 - Graphical log of the sedimentary sequence recovered in CRP-2/2A, showing lithostratigraphical subdivisions. The clast count data are plotted logarithmically in order to highlight abundances in clast-poor intervals.

LITHOSTRATIGRAPHICAL SUB-UNIT 4.1

(47.79-51.95 mbsf in CRP-2; 48.00-52.36 mbsf in CRP-2A),
DIAMICTON

LSU 4.1 grades downward from a thin, compact, weakly laminated muddy fine to medium sand with very dispersed clasts to a compact, massive, clast-poor fine- to medium- sandy diamicton. Clasts range from 1% to 3% in abundance and from angular to rounded in shape, with an average shape of subrounded. Granitoid and dolerite clasts are most common, with granitoid clasts up to 9 cm in diameter. Diamictite clasts are also present, although in very low abundance. Matrix composition is estimated at c. 55% quartz, 15% feldspar, 3% volcanic fragments, 20% clay, 5% pyroxene and hornblende, 2% volcanic glass, and traces of diatoms and sponge spicules. The abundance of carbonate cement increases downcore, so that LSU 4.1 grades locally to diamictite. As a result of this cementation, thin irregular fractures are also evident in this diamictite. The lower contact of LSU 4.1 is sharp.

LITHOSTRATIGRAPHICAL SUB-UNIT 5.1

(52.36-72.84 mbsf), MUDSTONE AND SANDSTONE

LSU 5.1 gradually fines down-core, from muddy very fine sandstone with very fine sandstone laminae above 57.33 mbsf, to very fine sandy mudstone between 57.33 and 59.00 mbsf, and to massive mudstone with a few thin fine sandstone beds below 59.00 mbsf. The muddy very fine sandstone is black (N3 to N4), and contains laminae of very fine sandstone at 55.68-55.85 mbsf that are soft-sediment deformed but show evidence of ripple cross-lamination. The very fine sandy mudstone and the massive mudstone are also black. In addition, the massive mudstone contains thin beds of very fine sandstone, which commonly have sharp upper and lower contacts and show evidence of soft-sediment deformation. Very dispersed clasts and shell fragments are present in low abundances through LSU 5.1; the latter, however, are more abundant at 55.79-56.50 mbsf and at 68.73-70.42 mbsf. The most notable fossil is a bivalve fragment at 56.03 mbsf. The composition of the massive mudstone is estimated as: 30-40% quartz, 5-10% feldspar, 2-5% rock fragments, 40-45% clay, 3-5% pyroxenes and hornblende, 3-5% volcanic glass, 2-5% diatoms, and traces of sponge spicules. Carbonate cement is distributed irregularly through Unit 5.1, but the effects of brecciation are evident throughout this interval. Brecciation is relatively pervasive above 64.00 mbsf, but is concentrated in discrete horizons below that level. The lower contact of LSU 5.1 is relatively gradational.

LITHOSTRATIGRAPHICAL SUB-UNIT 6.1

(72.84-80.70 mbsf), SAND

LSU 6.1 comprises medium sand with dispersed to common clasts above 75.11 mbsf, and fine to muddy fine sand below that level. The interval dominated by fine to muddy fine sand also contains two minor lithologies: a 78 cm-thick bed of sandy diamicton, and a 65 cm-thick bed of very sandy mudstone with dispersed clasts. The medium sand, found in the upper 2.27 m of LSU 6.1, is

compact, massive to weakly stratified, poorly sorted, and contains limited evidence of soft-sediment deformation. The fine to muddy fine sand occurs in beds varying from 20 to 90 cm in thickness; these beds are internally massive. Composition of the medium sand and the fine to muddy fine sand is approximately 40% quartz, 10-15% feldspar, 2-15% rock fragments, 5-40% clay, 3-10% pyroxenes and hornblende, 3-15% volcanic glass, trace-2% diatoms, and traces of sponge spicules. The diamicton is a compact, massive, very poorly sorted sandy diamicton, with granitoid, dolerite, and quartzite as the dominant clast lithologies, whereas the mudstone with dispersed clasts is locally weakly stratified and brecciated. Shell fragments occur within the uppermost 50 cm and the lowermost 70 cm of this unit. LSU 6.1 has a sharp lower contact.

LITHOSTRATIGRAPHICAL SUB-UNIT 6.2

(80.70-90.67 mbsf), DIAMICTITE

LSU 6.2 is an olive grey (5Y 3/2) massive, poorly sorted, clast-rich to clast-poor sandy diamictite. It exhibits weak stratification in the interval from 81.10 to 81.86 mbsf through the presence of thin beds of very fine sandstone; some of these beds also show evidence of soft-sediment deformation. The sandy matrix contains approximately 50% quartz, 15-20% feldspar, 5% rock fragments, 10-20% clay, 10% pyroxene and hornblende, and up to 5% volcanic glass. Clast abundances range from 5% to 25%, with dolerite, granitoid, quartz and feldspar as the major clast lithologies. The clasts average subrounded in shape, and are up to 16 cm in diameter. Carbonate cement occurs as discrete irregular bodies, and the diamictite is brecciated locally. The lower contact of LSU 6.2 is gradational, set at the lowest occurrence of abundant clasts.

LITHOSTRATIGRAPHICAL SUB-UNIT 6.3

(90.67-96.85 mbsf), SAND/SANDSTONE

Above 92.42 mbsf, LSU 6.3 is composed of massive, poorly sorted fine to medium sand with dispersed very coarse sand and granules, interstratified with well-sorted fine sand. These two lithologies originally were well-stratified with sharp contacts, but all of the original stratification has now undergone soft-sediment deformation. Below 92.42 mbsf, the unit is composed of three interbedded lithologies: massive medium to coarse sand with dispersed very coarse sand and granules, massive muddy fine sand with dispersed very coarse sand and granules, and very fine sandstone. Bedding thicknesses of these lithologies range from 10 cm to 1 m. One bed, at 94.81-94.96 mbsf, is composed of fine sandstone and contains high-angle cross-stratification. Composition of this unit is approximately 40-45% quartz, 15% feldspar, 10% rock fragments, 5-10% clay, 20-25% volcanic glass (brown, yellow, and colourless), traces to 5% pyroxene and hornblende, and traces of diatoms and sponge spicules. Unit 6.3 is sparsely fossiliferous, with shell fragments distributed throughout its extent. Carbonate cement is distributed in irregular, discrete zones through Unit 6.3, producing some sandstone horizons. The cemented zones exhibit limited amounts of fracturing and contain calcite-

filled veins; the core is brecciated in two intervals, each approximately 60 cm thick, between 91.00 and 95.00 mbsf.

LITHOSTRATIGRAPHICAL SUB-UNIT 7.1
(96.85-109.07 mbsf), DIAMICTITE

LSU 7.1 comprises a compact, very poorly sorted, clast-rich to clast-poor, pumice-bearing, sandy diamictite. The diamictite locally is weakly stratified, and its clast population is dominated by subangular to rounded (average subrounded) pieces of granitoid, dolerite, quartz, feldspar, and pumice. Minor lithologies in this unit include one thin interbed (<10 cm thick) each of mudstone, fine sandstone, and fine to medium sandstone. Pumice lapilli are present throughout the diamictite, and become a relatively common constituent below 99 mbsf. Carbonate cement is present as discrete irregular zones; most are 3-15 cm in diameter, but the largest zone is 69 cm in length.

LITHOSTRATIGRAPHICAL SUB-UNIT 7.2
(109.07-114.21 mbsf), SANDSTONE AND LAPILLISTONE

LSU 7.2 is composed of two major lithologies: stratified, poorly sorted fine sandstone with dispersed pumiceous lapilli, and stratified, moderately sorted pumiceous lapillistone and ash. The fine sandstone with dispersed pumiceous lapilli is greyish black (N2) in colour and occurs in beds 3-60 cm thick, within which are locally stratified intervals of thick laminations to thin beds. Abundances of dispersed lapilli within the fine sandstone range from 5% to 10%. This lithology dominates the upper 1.54 m of LSU 7.2, and locally exhibits evidence of soft-sediment deformation. In the interval 110.61-112.77 mbsf, the fine sandstone with dispersed pumiceous lapilli is interbedded with stratified pumiceous lapillistone in two distinct styles: 1) the two lithologies are interstratified at the scale of thick laminae to thin beds, with sharp-based layers and local development of parallel stratification and ripple cross-lamination in the fine sandstones, and 2) thicker beds (10 cm to 1.22 m thick) of lapillistone are interbedded with massive sandstone. The basal 10-20 cm of the thickest lapillistone bed are reversely graded; the remainder of that bed and the other thick lapillistone beds are massive. Below 112.77 mbsf, LSU 7.2 is dominated by massive fine lithic sandstone in beds 10-30 cm thick; however, parallel laminated and ripple cross-laminated fine lithic sandstone is interbedded with massive mudstone at 113.37-113.66 mbsf. In the latter interval, soft-sediment deformed zones, 5-20 cm thick, indicate disturbance of the interbedded lithologies. The basal bed in LSU 7.2 is a sharp-based, 24 cm-thick, weakly thin-bedded fine lapillistone and coarse to very coarse ash.

LITHOSTRATIGRAPHICAL SUB-UNIT 8.1
(114.21-130.27 mbsf), SANDSTONE AND DIAMICTITE

LSU 8.1 is composed primarily of stratified to massive, well- to poorly sorted, fine to medium sandstone above 123.78 mbsf; below that level, the fine to medium sandstone is interbedded with very poorly sorted, clast-rich to clast-poor sandy diamictite. Bed thicknesses within the sandstone

range from 10 cm to 1.2 m; internally, the beds vary from massive to weakly thinly bedded. Below 123.78 mbsf, diamictite beds one to two metres thick are separated by 40 cm to 2.2 m of massive to weakly stratified, muddy to well-sorted, fine to medium sandstone, generally with dispersed clasts. The diamictites are massive to locally weakly stratified, clast-poor, and sandy, with granitoid, dolerite, feldspar, and quartz as the predominant clast types, but with minor amounts of obsidian(?) and orthoquartzite clasts. The majority of beds throughout LSU 8.1 have sharp bases, and some of the sandstone beds, as well as one of the diamictite beds, exhibit soft-sediment deformation. Important minor lithologies include: a deformed interval of interstratified muddy very fine sandstone, clast-rich sandy to muddy diamictite, and very poorly sorted fine sand with dispersed clasts at 121.79-122.59 mbsf, and intervals of very poorly sorted gravel to sandy conglomerate at 122.74-122.82 mbsf and at 125.11-125.65 mbsf. The sandstone is locally fossiliferous, especially with shell fragments at 117.00-118.00 mbsf and at 121.00-122.00 mbsf, and a layer of shell debris at 117.76 mbsf. Some of the sandstones have been weakly bioturbated. Irregular zones of carbonate cement are present but rare in LSU 8.1. Also noteworthy is a dolerite boulder at 120.51-121.36 mbsf, which has deformed the sediment beneath it for an interval of 10-20 cm. LSU 8.1 has a gradational lower contact.

LITHOSTRATIGRAPHICAL SUB-UNIT 8.2
(130.27-137.79 mbsf), SANDSTONE

LSU 8.2 is composed of several closely related types of sandstone: poorly sorted fine sandstone, muddy very fine sandstone, and poorly sorted fine sandstone with dispersed coarse to very coarse sand and granules. The composition of these sandstones is estimated at 45% quartz, 15% feldspar, 5% rock fragments, 10% clay, 10% pyroxene and hornblende, 15% volcanic glass, and traces of diatoms and sponge spicules. Beds of these lithologies are massive through most of LSU 8.2, but laminated to thinly bedded intervals are dominant between 133 and 135.50 mbsf. The entire unit has been weakly to moderately bioturbated, and shell fragments occur at 134.52-136.24 mbsf and 137.18-137.27 mbsf. Soft-sediment deformational features are evident, but not pervasive, throughout LSU 8.2, and carbonate cement is sparsely distributed in discrete irregular zones.

LITHOSTRATIGRAPHICAL SUB-UNIT 8.3
(137.79-153.39 mbsf), MUDSTONE AND SANDSTONE

Above 142 mbsf, LSU 8.3 is composed of fine sandy mudstone with soft-sediment deformed laminae and thin beds of poorly sorted fine sandstone. At 142 mbsf, the fine sandy mudstone grades into very poorly sorted fine sandstone with dispersed coarse to very coarse sand and clasts, which then extends downcore to 144.28 mbsf. Below 144.28 mbsf, LSU 8.3 comprises interbedded very poorly sorted fine sandstone and massive to laminated very fine sandy mudstone. Locally, thin sharp-based intervals (1-4 cm thick) of the fine sandstone interbeds are

laminated. The interval below 144.28 mbsf is also deformed to varying extent, with brecciation relatively common. The brecciated zones also contain multiple, complex, sandstone-filled sedimentary dykes. Below 144.28 mbsf, the thicker, poorly cemented sandstone beds also have been disturbed and washed during drilling. Small pyritic nodules are present in the mudstones, and carbonate cement forms sparse irregular bodies.

LITHOSTRATIGRAPHICAL SUB-UNIT 8.4
(153.39-183.85 mbsf), MUDSTONE

LSU 8.4 is dominated by olive-grey (5Y 4/1), massive to weakly laminated mudstone. Above 163.05 mbsf, the mudstone is interbedded with thin, sharp- and scour-based, parallel-laminated to ripple cross-laminated fine to medium sandstone. Bioturbation is locally evident in this portion of Unit 8.4. The interval below 163.05 mbsf is composed almost entirely of pervasively bioturbated, weakly laminated to massive, very fine sandy mudstone with dispersed clasts; only a few very thin sandstone laminae are present below 163.05 mbsf. LSU 8.4 is sparsely fossiliferous, primarily containing shell fragments throughout its extent. Taxa present include pteropods and serpulid tubes, and an articulated bivalve is present at 180.18 mbsf. Discrete irregular patches of carbonate cement occur throughout this unit, and thin brecciated zones are located at approximately 154.00 and 163.60 mbsf. Micro-faulting, soft-sediment deformation, and vertical fracturing are concentrated in the interval 176-180 mbsf. LSU 8.4 has a sharp, inclined lower contact.

LITHOSTRATIGRAPHICAL SUB-UNIT 9.1
(183.35-185.96 mbsf), SANDSTONE AND DIAMICTITE

LSU 9.1 grades down-core from poorly sorted, fine to medium sandstone with common clasts to clast-poor sandy diamictite. The sandstone is medium dark grey (N4), with disturbed moderate to thin bedding above 184.03 mbsf, but it is weakly stratified to massive from 184.03 to 184.72 mbsf. Massive to moderately stratified, very poorly sorted, clast-poor to clast-rich sandy diamictite is present below 184.72 mbsf, and contains some evidence of soft-sediment deformation. Shell fragments and patchy carbonate cement are present in low abundances throughout LSU 9.1. The base of LSU 9.1 is gradational, from the base of the lowest large clast to underlying massive (drilling disturbed?), slightly muddy, fine to medium sandstone.

LITHOSTRATIGRAPHICAL SUB-UNIT 9.2
(185.96-193.64 mbsf), SANDSTONE

LSU 9.2 is composed predominantly of sandstone, but grades from poorly sorted muddy fine sandstone above 190.75 mbsf to moderately sorted, fine- to medium-sandstone below that level. Thin pebble-rich intervals form a minor lithology throughout LSU 9.2. The poorly sorted muddy fine sandstone, which grades locally to muddy fine sandstone with dispersed clasts, contains faint flat to slightly inclined stratification, and grades to a thin pebble conglomerate at 187.65 mbsf. The moderately

sorted fine-medium sandstone that occurs below 190.75 mbsf has abundant flat stratification, grades locally to thin (<1 cm thick) pebbly layers, and is bioturbated. Shell fragments are present at 186.63 mbsf and in the interval 191.00-191.59 mbsf. Vesicular, glassy lapilli are concentrated in the interval 193.37-193.47 mbsf. LSU 9.2 has a sharp lower contact.

LITHOSTRATIGRAPHICAL SUB-UNIT 9.3
(193.64-207.76 mbsf), PEBBLY SANDSTONE

LSU 9.3 is dominated by massive to weakly stratified muddy fine sandstone with dispersed clasts, which grades locally into more clast-rich intervals of clast-poor to clast-rich sandy diamictite. These two lithologies are thinly interbedded at 193.64-196.65 mbsf and 198.55-199.25 mbsf, but form thicker beds through the remainder of this unit (20-40 cm thick for the diamictite, 70 cm to 4 m thick for the sandstone). The sandstone is dark greenish grey (5G 4/1), and contains faint lamination, flat stratification, and possible ripple cross-lamination. Composition of the sandstone is estimated at 60% quartz, 5% feldspar, 5% rock fragments, 15% clay, 10% pyroxene and hornblende, 5% volcanic glass, and traces of diatoms. The diamictite is dark grey to grey (N4 to N6), massive to weakly stratified, poorly sorted, clast-poor to clast-rich, and sandy. The predominant clast types are volcanic, granitoid, dolerite, and sedimentary lithologies. Shell fragments are distributed throughout LSU 9.3, but an articulated bivalve is present at 195.48 mbsf. An impression of woody debris, 1 cm long, is located at 195.40 mbsf. The fine sandstone is bioturbated, whereas the diamictite is not; because the fine sandstone forms more of the section downcore, the overall abundance of bioturbation also increases downcore. Soft-sediment deformation structures and brecciation are present to common above 199 mbsf. LSU 9.3 has a very gradational lower contact.

LITHOSTRATIGRAPHICAL SUB-UNIT 9.4
(207.76-227.33 mbsf), SANDSTONE

LSU 9.4 is composed almost entirely of dark greenish grey (5G 4/1), poorly sorted muddy fine sandstone, with only very minor occurrences of thin mudstone and thin coarse sand to granule layers. The sandstone varies from massive to well stratified, with inclined parallel stratification particularly well developed in the interval 218.25-227.28 mbsf. This interval also contains minor occurrences of ripple cross-lamination, and a package of convex-up laminations at 218.90-219.00 mbsf is suggestive of hummocky cross-stratification. The composition of the sandstone is approximately 65% quartz, 5% feldspar, 4% rock fragments, 10% clay, 8% pyroxene and hornblende, 8% volcanic glass, and traces of diatoms and sponge spicules. Shelly fossils and fossil fragments are relatively common through this unit; especially noteworthy are the occurrences of serpulid tubes and a possible *in situ* mollusc at 210.22-210.31 mbsf, articulated bivalves at 224.17 and 227.27 mbsf, and gastropod fragments at 217.74 and 225.96 mbsf. Evidence of bioturbation is common in this unit, and carbonate cement occurs as widely separated

zones of intense cementation. The lower boundary of LSU 9.4 is sharp and irregular.

LITHOSTRATIGRAPHICAL SUB-UNIT 9.5
(227.33-242.70 mbsf), DIAMICTITE AND SANDSTONE

LSU 9.5 is composed of a thin upper, clast-poor muddy diamictite, a middle zone of muddy fine sandstone, and a lower clast-poor sandy diamictite. The clast-poor muddy diamictite is 73 cm thick, dark greenish grey (5G 4/1), and massive, with angular to subangular granitoid, dolerite, volcanics, feldspar, and quartz clasts. The lower contact of this diamictite is gradational, a result of decreasing clast and mud contents. The muddy fine sandstone, which is 5.67 m thick, is dark greenish grey (5G 4/1), weakly laminated, poorly sorted, locally bioturbated, and fossil-bearing, with rare weak ripple cross-lamination. The muddy fine sandstone has a gradational lower contact, placed at the top of the highest occurrence of underlying clasts. The clast-poor sandy diamictite is 10.97 m thick, and massive, with angular to subrounded clasts of granitoid, dolerite, quartz, feldspar, and volcanic(?) lithologies. The sandy diamictite also contains a few thin beds (approximately 10 cm thick) of weakly laminated fine sandstone. Carbonate cement is relatively sparse in LSU 9.5, occurring as three thin, weakly cemented intervals. LSU 9.5 has a sharp lower contact.

LITHOSTRATIGRAPHICAL SUB-UNIT 9.6
(242.70-250.40 mbsf), SANDSTONE

Faintly laminated to massive, poorly sorted, dark greenish grey (5G 4/1) muddy very fine to fine sandstone is the dominant lithology in lithostratigraphical LSU 9.6. Laminated, moderately sorted, dark grey (N3) mudstone, interstratified with sharp-based siltstone and fine sandstone laminae, is the only minor lithology, and is present in the interval 245.45-245.54 mbsf. The very fine to fine sandstone is locally moderately bioturbated, and contains dispersed shell fragments above 245.00 mbsf; a shell bed of articulated bivalves is present at 249.61-249.77 mbsf. In general, LSU 9.6 fines downward by both a decrease in the mean sand size and an increase in mud content of the matrix. Vertical fractures up to 2 m long occur within this unit. The base of LSU 9.6 is gradational, marked by increased mud content and carbonate cementation.

LITHOSTRATIGRAPHICAL SUB-UNIT 9.7
(250.40-262.90 mbsf), MUDSTONE

LSU 9.7 is composed of two major lithologies: dark greenish grey (5G 4/1), weakly laminated, poorly sorted sandy mudstone with dispersed small clasts above 252.30 mbsf, and massive, locally weakly stratified to moderately bioturbated, poorly to moderately sorted mudstone with dispersed small clasts below 252.30 mbsf. Very fine sandstone laminae form the only minor lithology, and are widely spaced through this unit. LSU 9.7 is fossiliferous below 254.00 mbsf, with an articulated bivalve at 255.01 mbsf. Pyritic burrow fills are also common below 252.30 mbsf. Sparse carbonate cement occurs in this unit. The basal contact of LSU 9.7 is gradational over c. 1 m.

LITHOSTRATIGRAPHICAL SUB-UNIT 9.8
(262.90-295.58 mbsf), SANDSTONE

LSU 9.8 is composed almost entirely of muddy fine sandstone to fine sandstone, which changes from dark greenish grey (5G 4/1) to dark grey (N3) down-core. The sandstone is massive to weakly stratified, and weakly bioturbated. Small pyritic bodies are dispersed through this interval, commonly within burrow-fills. Three minor lithologies are present within LSU 9.8: 1) massive to weakly laminated mudstone, which grades downward to muddy fine sandstone in the interval 262.90-264.45 mbsf, 2) fine sandstone, which occurs as a few, widely spaced thin laminae above 270.10 mbsf, and 3) sandy silty clay, which occurs as a single laminated interval at 285.59-285.61 mbsf. Volcanic ash and isolated lapilli are present, although in low abundance, between 269.74 and 280.13 mbsf. Unit 9.8 is very sparsely fossiliferous, with a gastropod fragment at 290.66 mbsf and bivalve fragments at 294.07-294.13 mbsf. Clasts occur in low abundances throughout this unit, with granitoid, dolerite, volcanic, sandstone, and green metamorphic/volcanic lithologies observed. Thin zones of strong carbonate cementation are relatively common, some of which subsequently have been fractured and then healed with additional calcite precipitation. The lower contact of LSU 9.8 is sharp, and is placed on top of the highest underlying pebble layer.

LITHOSTRATIGRAPHICAL SUB-UNIT 10.1
(295.58-306.65 mbsf), DIAMICTITE AND SANDSTONE

LSU 10.1 contains a number of basic lithologies, interbedded and deformed at a variety of scales. Basic lithologies include: 1) muddy to sandy, clast-poor to clast-rich diamictite, 2) muddy fine sandstone, locally with dispersed clasts, 3) very fine sandy mudstone, and 4) moderately sorted fine to very coarse sandstone, with and without dispersed clasts. All of these lithologies are dark greenish grey (5GY 4/1) in colour. Identifiable beds of a single lithology are relatively rare in LSU 10.1. The remainder of this interval is composed of thinly bedded to lamina-scale interstratification of two or more of these lithologies, with variable amounts of soft-sediment deformation overprinting the interbedding. The most common lithological associations include: 1) thinly interbedded very fine sandy mudstone and poorly sorted, muddy very fine sandstone, 2) interlaminated to thinly interbedded very fine sandy mudstone, muddy very fine sandstone, and moderately sorted silt laminae, and 3) diamictite interbedded with one or more of the very fine sandy mudstone, muddy very fine sandstone, and fine sandstone. Sedimentary structures present include laminae deformed beneath lonestones in the sandy mudstone and muddy very fine sandstone, weak parallel stratification to lamination in the muddy very fine sandstone and fine sandy mudstone, and ripple cross-lamination to cross-bedding in fine to very coarse sandstone. Clasts, both those in the diamictite and those dispersed in the other lithologies, are mainly granitoid, dolerite, feldspar, quartz, and volcanic rocks. Soft-sediment deformation affects more than half of LSU 10.1, and rare microfaults are also

present. Carbonate cementation is minimal in this interval. LSU 10.1 has a sharp lower contact.

LITHOSTRATIGRAPHICAL SUB-UNIT 11.1
(306.65-315.52 mbsf) MUDSTONE AND SANDSTONE

LSU 11.1 contains four basic lithologies, interbedded at a variety of scales and ranging from soft-sediment deformed to completely brecciated. The basic lithologies include: 1) dark grey to medium dark grey (N3 to N4) massive mudstone to silty claystone, 2) massive to normally graded and ripple cross-laminated, moderately sorted, very fine to medium sandstone, 3) greenish black to dark greenish grey (5G 2/1 to 5G 4/1), massive, poorly sorted muddy very fine sandstone, and 4) dark greenish grey to light olive-grey (5GY 4/1 to 5Y 5/2), massive to thinly laminated and ripple cross-laminated siltstone. The interval above 311.02 mbsf is composed of these lithologies, both as monolithological beds 5-50 cm thick and as zones of thin interbeds. This interval has been overprinted by soft-sediment folding, microfaulting, and minor brecciation. Below 311.02 mbsf, the same lithologies and interbedding styles are evident, but are present as randomly oriented clasts within a matrix of muddy very fine to medium sandstone. This interval, below 311.02 mbsf, is a sedimentary breccia, rather than a product of *in situ* brecciation.

LITHOSTRATIGRAPHICAL SUB-UNIT 11.2
(315.52-327.43 mbsf), MUDSTONE, SANDSTONE AND DIAMICTITE

LSU 11.2 is composed of silty claystones and clayey siltstones, muddy sandstones, and diamictites, which are interbedded and interstratified at a range of scales and are overprinted by soft sediment deformation, microfaulting, and clastic intrusions to varying degrees. The upper 2.47 m of LSU 11.2 are composed of interstratified clayey siltstone, silty claystone, and muddy sandstone, and are significantly disturbed by folding, faulting, soft sediment deformation, and clastic dyke emplacement. The majority of LSU 11.2, 317.99-326.16 mbsf, comprises moderately well-bedded to well-laminated partially consolidated sand, sandstone, and mudstone. Bed boundaries vary between sharp and weakly gradational, and some beds exhibit fining-up or coarsening-up trends. Microfaults, clastic dykes, and load structures are common in this interval. Ripple cross-lamination is present in a few of the very fine sandstones. Well-defined beds of massive to weakly stratified clast-rich sandy diamictite are present between 326.16 and 327.43 mbsf, with dolerite, granitoid, volcanic, and metamorphic lithologies, plus quartz and feldspar, as the major clast types. The base of LSU 11.2 is sharp, and is placed at the base of the lowest diamictite.

LITHOSTRATIGRAPHICAL SUB-UNIT 11.3
(327.43-347.31 mbsf), MUDSTONE

LSU 11.3 is composed almost entirely of mudstone and sandy mudstone, grading locally to fine sandy siltstone. The only minor lithologies observed are in deformed

zones, specifically: discontinuous laminae and zones of very fine to fine sandstone, siltstone, and conglomerate incorporated in deformed mudstone at 327.43-329.30 mbsf, a thin bed of mudstone breccia (331.96-331.98 mbsf), and widely spaced sedimentary dykes throughout the remainder of the unit. The mudstone is dark grey (N3) to dark greenish grey (5GY 4/1), massive to locally stratified, and weakly to moderately bioturbated, and has low abundances of dispersed clasts. Microfaults and microload casts are present, as are fossils. The latter, most of which are serpulid tubes, are especially common from 340.60 to 345.00 mbsf. Weak carbonate cementation, in the form of discrete irregular cemented zones, is sparsely present through this unit. The base of LSU 11.3 is sharp and irregular.

LITHOSTRATIGRAPHICAL SUB-UNIT 12.1
(347.31-379.00 mbsf), DIAMICTITE

The predominant lithology in LSU 12.1 is dark grey (N3) and medium-dark grey (N4) clast-rich to clast-poor sandy diamictite; less important lithologies are medium sandstone and mudstone, and a variety of sandstones (muddy fine sandstone, muddy medium to coarse sandstone with common clasts, well-sorted medium to coarse sandstone, poorly sorted coarse sandstone with dispersed clasts). Diamictites dominate the intervals 360.36-362.80 mbsf and 364.30-379.02 mbsf, and form less abundant interbeds in the other portions of LSU 12.1. The diamictites occur as beds 14 cm - 6 m thick, and vary internally from massive to weakly laminated. Clasts within the diamictite are dominated by dolerite, but include granitoid, quartz, feldspar, and sandstone. A diamictite bed at 360.93-362.80 mbsf contains stratified and deformed mudstone clasts up to cobble size. Faulting, soft-sediment deformation, and clastic dykes are common in the diamictites. The second most common lithology in LSU 12.1 comprises a variety of sandstones, which occur as monolithological beds up to 1.84 m thick, and as interstratified intervals up to a few decimetres thick. Most of these sandstones are internally massive or weakly laminated, but a few contain ripple cross-lamination. The sandstones are also affected locally by soft-sediment deformation and clastic dykes. The other accessory lithology, light grey (N7) medium sandstone and very dark grey (N3) mudstone, forms an interval at 347.31-347.78 mbsf that has been disrupted severely by soft-sediment deformation, faulting, and syndepositional loading. Carbonate cementation is rare in LSU 12.1, occurring as widely separated irregular bodies. The lower contact of LSU 12.1 is sharp, placed at the base of the lowest large clast in the thick diamictite.

LITHOSTRATIGRAPHICAL SUB-UNIT 12.2
(379.00-405.20 mbsf), SANDSTONE

A wide variety of sandstones are present in LSU 12.2, and interlaminated to interstratified combinations of various sandstones form the majority of this unit. Minor lithologies include clast-poor muddy diamictite, poorly sorted, matrix-supported pebble conglomerate, and massive mudstone.

Above 397 mbsf, the sandstones are present as interbedded to interlaminated muddy very fine sandstone, fine to muddy fine sandstone, and moderately to poorly sorted medium to coarse sandstone. Parallel laminations and ripple cross-lamination are preserved locally in these sandstones. Five discrete diamictites occur above 397 mbsf, and range in thickness from 26 cm to 1.02 m. These are clast-poor to clast-rich sandy diamictites, containing angular to subrounded clasts of dolerite, granitoid, quartz, feldspar, and very fine sandy mudstone. Pebble conglomerates are also present above 397 mbsf, ranging from a 19 cm-thick, massive, clast-supported pebble gravel to a 3.44 m-thick, matrix- to clast-supported, pebble to cobble conglomerate. Clasts in the thicker conglomerate are angular to well rounded (averaging subrounded); dolerites dominate the clast population, with lesser abundances of granitoids, quartz, feldspar, sandstone, and siltstone. The sandstone component coarsens below 397 mbsf, with interlaminations to interbeds of poorly sorted fine to medium sandstone and poorly sorted medium to very coarse sandstone with dispersed granules and pebbles. Massive mudstone is a minor lithology below 397 mbsf, occurring as one discrete bed and as thin interbeds within the sandstones. Soft-sediment deformation is evident through most of LSU 12.2, and microfaults are present but rare. Nodular carbonate cement is distributed sparsely through this unit. The basal contact of LSU 12.2 is sharp.

LITHOSTRATIGRAPHICAL SUB-UNIT 12.3
(405.20-419.88 mbsf), DIAMICTITE

LSU 12.3 is dominated by clast-poor to clast-rich sandy diamictites, which range from massive to internally weakly stratified. The diamictites occur both as discrete beds up to 3 m thick and as thinner interbeds within sequences of diamictite, muddy fine to coarse sandstone, and poorly sorted, matrix-supported granule to pebble conglomerate. Clasts within the diamictites are angular to well-rounded, averaging subangular to subrounded, and are dominated by dolerites; granitoid, quartz, feldspar, sandstone, and volcanic clasts are present in subordinate amounts. A few intervals, consisting only of interbedded sandstones up to 60 cm in thickness, are also present in LSU 12.3, and the basal 1.42 m of this unit comprise a clast-supported pebble to boulder conglomerate. Shell fragments are common at 413-418 mbsf, and carbonaceous debris is present at 417.22 mbsf. Below 411.00 mbsf, soft-sediment deformation features and clastic dykes are common. LSU 12.3 has a sharp basal contact.

LITHOSTRATIGRAPHICAL SUB-UNIT 12.4
(419.88-442.99 mbsf), SANDSTONE AND DIAMICTITE

The upper 18 m of lithostratigraphical LSU 12.4 are composed of a variety of sandstone types (medium to fine sandstone, often with dispersed granules, muddy fine sandstone, and massive medium to very coarse sandstone, often with dispersed granules) interbedded with massive and laminated clast-poor to clast-rich muddy and sandy diamictite. Sandstone beds and interbedded sandstone intervals are 1-3 m thick, and lie between diamictite beds

that are 40-80 cm thick. The sandstones range from massive to ripple cross-laminated and cross-bedded. A clast-poor, sandy to muddy diamictite forms the basal 5.12 m of this unit; clasts are rounded to angular (averaging subrounded) and dominated by dolerite, with subordinate amounts of granitoids, quartz, feldspar, orthoquartzite, carbonate and mudstone. LSU 12.4 is sparsely fossiliferous, and contains sparse to common nodular carbonate cement. Much of the interval 420.90-432.50 mbsf was disturbed, washed, and/or lost during drilling.

LITHOSTRATIGRAPHICAL SUB-UNIT 13.1
(442.99-468.00 mbsf), MUDSTONE AND DIAMICTITE

LSU 13.1 is composed of clast-poor muddy diamictite and/or muddy fine sandstone with dispersed clasts, grading both locally and down-core to poorly sorted fine sandy mudstone with dispersed clasts. Local transitions between the diamictite and/or muddy fine sandstone and the sandy mudstone are highly gradational, with no visible stratification. The down-core transition to sandy mudstone with dispersed clasts is also gradational, and occurs between 456 and 458 mbsf. Clasts throughout LSU 13.1 are dominated by dolerite, with minor amounts of granitoid, volcanics, quartz, and feldspar. Bioturbation is common throughout this interval, as are fossils. Some of the fossils include primary shell material, but most are preserved as moulds. Microfaults, soft-sediment deformation features, and clastic dykes are distributed sparsely through LSU 13.1. Carbonate cementation varies from weak to locally strong, and pyrite- and calcite-filled veins are common locally. The lower contact of LSU 13.1 is gradational.

LITHOSTRATIGRAPHICAL SUB-UNIT 13.2
(468.00-493.00 mbsf), SANDSTONE

The dominant lithologies in LSU 13.2 are muddy very fine to fine sandstone with dispersed clasts, and moderately sorted medium to fine sandstone. Less common lithologies include clast-poor to clast-rich muddy to sandy diamictite, massive fine sandy mudstone with dispersed clasts, and clast-supported pebble conglomerate. The sandstones dominate this unit above 487 mbsf, whereas the diamictite and the pebble conglomerate dominate the interval below 487 mbsf. The sandstones occur as monolithological beds up to 4 m thick, but also occur in an interbedded form. When interbedded, the moderately sorted medium to fine sandstones form sharp-based beds 2-90 cm thick (locally with loading structures along the base), overlain by the muddy very fine to fine sandstone. The transition from the moderately sorted sandstones to the muddy fine sandstones is commonly deformed and/or bioturbated. Thin diamictites and fine sandy mudstones occur as interbeds within the sandstone-dominated portion of LSU 13.2. Sedimentary structures within the sandstones include parallel laminations, inclined wispy lamination, ripple cross-lamination, rare cross-bedding, and load casts. Possible coal fragments form thin laminae in sandstones below 484 mbsf. The sandstones and minor sandy mudstones are bioturbated and contain minor amounts of fossil material, with the exception of a relatively fossiliferous interval at

482-484 mbsf. Below 487 mbsf, the sequence is dominated by the pebble conglomerate and by a 5 m-thick interval of interbedded and deformed clast-rich sandy diamictite and poorly sorted fine to coarse sandstone with common clasts. Throughout LSU 13.2, the clasts are dominated by dolerite and granitoid, with lesser abundances of quartz, feldspar, volcanic rocks, and sandstone. Soft-sediment deformation, microfaults, and clastic dykes are also distributed sparsely throughout LSU 13.2. Irregular, large-scale nodular carbonate cementation is relatively common, and a few thin horizons also contain small (cm-scale) spherical carbonate-cemented nodules. LSU 13.2 has a sharp base.

LITHOSTRATIGRAPHICAL SUB-UNIT 13.3
(493.00-516.40 mbsf), SANDSTONE AND MUDSTONE

LSU 13.3 contains three basic lithologies, interbedded to interlaminated at a variety of scales. Basic lithologies include: 1) medium sandstone, ranging from moderately sorted to poorly sorted with dispersed granules and clasts, 2) muddy fine to very fine sandstone, and 3) clayey siltstone. The medium sandstone is present in forms from laminae to beds *c.* 2 m thick; these intervals range from massive to parallel laminated or ripple cross-laminated, and usually have sharp bases. The muddy fine to very fine sandstone occurs as lenses within the clayey siltstone, but also forms laminae to thin beds. Internally, these sandstones are massive, bioturbated, parallel laminated, or ripple cross-laminated, with possible wave-formed ripples and hummocky cross-stratification at 509-510 mbsf. The clayey siltstone is present as discrete laminae and thin beds, and also as lenses within some of the fine sandstones. These three basic lithologies occur in three associations: 1) the medium sandstone and the fine/very fine sandstone, either as discrete thin to thick beds, or interbedded, with the sharp-based medium sandstone gradationally overlain by the fine/very fine sandstone. This association dominates LSU 13.3 above 504.44 mbsf. 2) The fine/very fine sandstone interlaminated to interbedded with the clayey siltstone. This association occurs at 504.44-508.40 mbsf. 3) Thinly interbedded to interlaminated medium sandstone, fine/very fine sandstone, and clayey siltstone. This association dominates the sequence below 508.40 mbsf. In addition to the sedimentary structures listed above, load casts, flame structures, and possible dish-and-pillar structures are present below 504.44 mbsf. Soft-sediment deformation has affected the upper 1 m and the lower 15 m of this unit. Possible plant debris is present at 504.71 mbsf, and carbonaceous grains are concentrated in sparse laminae throughout LSU 13.3. Below 513 mbsf, sandstones commonly are stained with an "oily" overprint within 1 cm of mudstone intervals. Nodular carbonate cement is present throughout LSU 13.3, and small spherical carbonate-cemented nodules are present in the upper 3 m and the lower 6 m of the unit. LSU 13.3 has a sharp lower contact.

LITHOSTRATIGRAPHICAL SUB-UNIT 14.1
(516.40-535.46 mbsf), SANDSTONE

LSU 14.1 is composed of a variety of sandstones, ranging from medium to very fine, but all with dispersed

to abundant clasts. The sandstones grade locally to thin beds of matrix-supported pebble conglomerate. Above 523.33 mbsf, the unit consists of massive medium sandstone with abundant clasts, grading locally to matrix-supported pebble conglomerate, with minor interbeds of muddy very fine and moderately sorted medium sandstone. Clasts are mainly dolerite and granitoid, but include volcanic rocks, sandstones, metamorphic rocks, and coal. The interval 523.33-527.66 mbsf comprises interbedded to interlaminated fine sandstone, muddy fine sandstone, and medium sandstone, with the latter grading to pebbly conglomerate and sandstone with abundant clasts in zones 20-30 cm thick. Below 527.66 mbsf, LSU 14.1 is composed of a thick bed of massive to cross-bedded, poorly sorted fine to medium sandstone with dispersed clasts; the clasts include a dolerite boulder that occupies 43 cm of the core. The majority of these sandstones are dark grey (N3) to dark greenish grey (5GY 4/1) in colour, but greyish olive-green (5GY 3/2) is common below *c.* 526 mbsf. Granules and coal are present in laminae within the sandstones. Nodular carbonate cement and small spherical carbonate-cemented nodules are present throughout the unit; the latter are especially common at 532.00-534.00 mbsf. Microfaulting and fracturing are important locally. LSU 14.1 has a sharp lower contact.

LITHOSTRATIGRAPHICAL SUB-UNIT 15.1
(535.46-545.16 mbsf), MUDSTONE

LSU 15.1 is composed of consolidated, bioturbated, moderately to poorly sorted fine sandy clayey siltstone with rare clasts. Weak stratification is developed in some intervals, but most of LSU 15.1 is disturbed by pervasive microfaulting and soft-sediment deformation. This unit is medium grey (N5) to medium light grey (N6) in colour. Clasts are dominated by volcanic rocks and dolerite, with minor amounts of granitoid and quartz. Fossil fragments are common at 540.40-540.80 mbsf and 544.20-544.80 mbsf. Nodular carbonate cement is distributed sparsely through LSU 15.1, but calcite- and pyrite-filled veins are common. LSU 15.1 has a sharp lower contact.

LITHOSTRATIGRAPHICAL SUB-UNIT 15.2
(545.16-574.20 mbsf), SANDSTONE AND MUDSTONE

LSU 15.2 is composed primarily of poorly sorted muddy very fine sandstone and moderately to poorly sorted medium to coarse sandstone; sandy mudstone, clast-poor sandy diamictite, and matrix- to clast-supported granule to pebble conglomerate are minor lithologies. The core is disturbed by drilling at 548.5-550.6 mbsf. Above 568.87 mbsf, the muddy very fine sandstones and the medium to coarse sandstones occur both as discrete beds, up to 1.5 m thick, and as weakly interstratified beds, up to 12 m thick. Siltstone laminae/thin beds form a small proportion of the sequence, but generally have sharp upper and lower contacts and display soft-sediment deformation. Below 568.87 mbsf, coarse-grained components are more abundant, including a 2 m-thick clast-poor sandy diamictite and decimetre-thick clast concentrations within the sandstone; locally, the decimetre-thick clast concentrations

grade to granule to pebble conglomerate. A 37 cm-thick, massive, clast-supported large pebble conglomerate occurs at the base of LSU 15.2. Clasts are subangular to rounded, and composed of volcanic rocks, dolerite, sandstone, mudstone, and granitoid. Bioturbation is evident in the sandstones, including well-developed *Zoophycos* at 559 mbsf. This unit is sparsely fossiliferous. Carbonaceous debris is present, as are "oily" overprints on sandstones. Nodular carbonate cement, microfaulting, calcite-filled veins, and soft-sediment deformation all become more abundant below 555 mbsf, whereas small spherical carbonate-cemented nodules are restricted to 552.80-554.60 mbsf and 572.00-574.20 mbsf. The base of LSU 15.2 is sharp and irregular.

LITHOSTRATIGRAPHICAL SUB-UNIT 15.3
(574.20-584.75 mbsf), SANDSTONE AND MUDSTONE

Well-sorted fine to very fine sandstone dominates LSU 15.3; massive to planar laminated mudstone is present in lesser amounts. Colours are dark greenish grey (5GY 3/1) to greenish grey (10Y 5/1). The sandstone is well sorted, occurring either in discrete beds 10 cm to 1 m thick, or as interlamination and thin interbeds within the mudstone. The sandstone beds and interbeds display cross-bedding, and parallel and cross-lamination. Hummocky cross-stratification is present in a sandstone at 578.00-578.20 mbsf, and carbonaceous debris is concentrated along laminations within the sandstones. Within the interbedded intervals, the thin sandstones have sharp bases, often with load casts, and bioturbation mixes the sandstone with the overlying mudstone. Within one thick bed, at 579.00-581.00 mbsf, the muddy very fine sandstone and the mudstone are interlaminated in a distinctive wispy style, giving an appearance similar to that of microflaser bedding; however, the origin of this appearance, either as a result of original deposition or as a result of post-depositional processes, is unknown at present. Deformation, in the form of soft-sediment folding, is present at 578-579 mbsf, but intensifies below 581 mbsf, where fluid escape and fluidisation structures accompany the soft-sediment deformation. Nodular carbonate cement and small spherical carbonate-cemented nodules are common above 579 mbsf. LSU 15.3 has a sharp lower contact.

LITHOSTRATIGRAPHICAL SUB-UNIT 15.4
(584.75-601.53 mbsf), SANDSTONE AND CONGLOMERATE

LSU 15.4 is dominated by two lithologies: massive to well-stratified, poorly sorted muddy fine to coarse sandstone, and matrix- to clast-supported pebble conglomerate. Clast-poor sandy diamictite forms a minor lithology in LSU 15.4, occurring discontinuously in the upper 4 m of the unit. Sandstones are the most abundant lithology, varying from muddy fine sandstone to medium or coarse sandstone. Bed thicknesses range from 2 to 170 cm, and most beds are internally massive. A few of the stratified sandstone beds are monolithological, but most contain thin interbeds of two or more sandstone types. The sandstone interval 590.05-597.23 mbsf is weakly stratified

by the presence of clast-rich zones approximately 40 cm thick. The pebble conglomerates are massive, matrix- to clast-supported, and form beds 5-74 cm thick. Clasts are predominantly volcanic in composition, but also include dolerite, granitoid, sandstone, coal, quartz, feldspar, and mudstone lithologies. The pebble conglomerates occur above 588.10 mbsf and below 600.00 mbsf. Fossil fragments are present throughout LSU 15.4, and are common in the interval 596.30-600.01 mbsf. Carbonaceous debris is common in the sandstones, where it often occurs as discrete laminae. Both nodular carbonate cement and spherical carbonate-cemented mininodules are common. LSU 15.4 has a sharp lower contact.

LITHOSTRATIGRAPHICAL SUB-UNIT 15.5
(601.53-614.56 mbsf), SANDSTONE

LSU 15.5 comprises muddy fine to medium sandstone, grading locally to fine sandy mudstone with rare clasts. These lithologies form beds 10 cm to 2 m thick, which are composed either entirely of sandstone, or of fine interlamination to interbeds of these two lithologies. Within the interval 607.48-610.76 mbsf, the muddy very fine sandstone and the mudstone are interlaminated in a distinctive wispy style, giving an appearance similar to that of microflaser bedding. However, the origin of this appearance, either as a result of original deposition or as a result of post-depositional processes, is unknown at present. The sandstones are massive to stratified, with the stratified intervals exhibiting flat lamination and ripple cross-lamination. One possible example of hummocky cross-stratification is present, at 612.14-612.24 mbsf. Load casts, flames, and possible ripple cross-lamination are present, but rare, in the interstratified intervals. Carbonaceous debris is relatively common in the sandstones, and an "oily" overprint is common around thicker mudstones. Soft-sediment deformation features, microfaults, pyrite- and calcite-filled veins, nodular carbonate cement, and small spherical carbonate-cemented nodules are all common in LSU 15.5. This unit has a sharp lower contact.

LITHOSTRATIGRAPHICAL SUB-UNIT 15.6
(614.56-624.15 mbsf), SANDSTONE AND CONGLOMERATE

LSU 15.6 is composed of a wide range of lithologies, which generally occur in two associations: 1) sharp-based, massive to bedded, moderately sorted pebble conglomerate and coarse sandstone, overlain by fine sandstone, and 2) interlaminated and interbedded intervals of poorly sorted, muddy very fine sandstone with dispersed clasts, moderately sorted fine sandstone, and massive mudstone with dispersed clasts. The first association occurs from the top of Unit 15.6 to 618.88 mbsf, with beds 50 cm to 2.5 m thick. The second association occurs from 618.88 mbsf to the base of LSU 15.6. In the interval 621.78-622.65 mbsf, the muddy very fine sandstone and the mudstone are interlaminated in a distinctive wispy style, giving an appearance similar to that of microflaser bedding. However, the origin of this appearance, either as a result of original deposition or as a result of post-depositional processes, is

unknown at present. Clasts in the conglomerates include volcanics, dolerite, granitoid, sandstone, and mudstone; clasts in the other lithologies include these, as well as feldspar and coal. Deformational features are prominent below 620.00 mbsf, and include evidence of soft sediment deformation, microfaults, and a 20 cm-long clastic dyke, now mineralized, at the base of the hole. Nodular carbonate cementation is present throughout this unit, and small spherical carbonate-cemented nodules are common above 619.00 mbsf.

FACIES ANALYSIS

Twelve lithofacies are recognised within the Miocene and Oligocene section of CRP-2A and are defined using lithologies or associations of lithologies, bedding contacts and bed thicknesses, texture, sedimentary structures, fabric and colour. After further sedimentological analyses provide more details of sediment characteristics, additional subdivision of these lithofacies is likely. Terminology used here refers to lithified forms but some Miocene lithologies are unlithified.

FACIES 1 - MUDSTONE

Facies 1 consists of massive very fine sandy mudstone and mudstone. Locally, the mudstone may be laminated to thinly bedded, as shown both by colour changes and by inclusion of siltstone and very fine sandstone laminae (Fig. 3.2a). The facies includes silty claystone and clayey siltstone and locally grades to sandstone over tens of centimetres. Generally, bioturbation is weak but locally the mudstones are strongly bioturbated and some intervals lack evidence of primary original stratification. Where stratified, this facies shows soft-sediment deformation structures in discrete intervals, and locally that deformation is intense (see Deformation section). Dispersed clasts are included in many occurrences of this facies and they vary from less than 1% to increasing quantities such that the mudstone locally grades into muddy diamictite. Intraformational mudstone clasts are also present in some beds and are locally sufficiently concentrated as to form the mudstone breccia of Facies 11 described below. Mudstones are commonly interbedded with massive to normally graded, moderately sorted and ripple cross-laminated very fine to medium sandstone, massive, poorly sorted, muddy very fine sandstone and massive to thinly laminated and ripple cross-laminated siltstone. Some thick mudstone beds near the bottom of the core are very dark grey to black represents concentrations of organic carbon probably dominated by coal material (see Organic Geochemistry section). Marine mollusc shells and their fragments are commonly scattered through mudstone facies and serpulid worm tubes are locally abundant.

Facies 1 mudstones represent the quietest water conditions within the CRP-2/2A sequence. These are thought to be hemipelagic sediment which due to their high silt content, probably had their main contributions from fluvially-derived turbid plumes. These sediments also had contributions from distal or dilute sediment

gravity flows in the form of very fine sand and silt laminae and from icebergs contributing limestones.

FACIES 2 - INTERSTRATIFIED SANDSTONE AND MUDSTONE

Very fine and fine to locally medium sandstone and very fine sandy mudstone are commonly interstratified with sharp lower contacts and sharp or gradational upper contacts; these comprise Facies 2 (Fig. 3.2b & c). The sandstone is either massive or normally graded and locally includes ripple cross-lamination, some of which appears to have been wave-influenced (Fig. 3.2c), and planar lamination in the upper, finer-grained intervals of the sandstone beds. Interstratification is on a scale that ranges from lamination to beds a few metres thick, and when laminated, units may include siltstone laminae. Intervals of interstratified clayey siltstone, silty claystone and muddy very fine sandstone occur locally. Thin diamictite beds are included in some intervals. Where bioturbation occurs it is commonly within the finer-grained intervals, especially the mudstones, and passes down into the underlying sandstone. Dispersed limestones locally deform laminae beneath them and are interpreted as dropstones. Intervals may fine upward through an increasing proportion of mudstone strata, with a concomitant increase in bioturbation upward, or they may coarsen upward through an increasing number of sandstone beds. Soft-sediment deformation is common within depositional intervals or may occur on a slightly larger scale to include several intervals; clastic dykes occur locally. Marine macrofossils occur commonly and there are local occurrences of plant fragments.

Bioturbation and marine macrofossils indicate a submarine environment of deposition for this facies. That being the case, the trend of normal grading including parallel laminated and ripple cross-laminated sandstones passing up to massive to laminated mudstones is characteristic of a range of current types from combined wave and current action to that of low to moderate density sediment gravity flows. Common soft-sediment deformation and clastic dykes imply the succession's pore water pressure was at times high and that sediments were rapidly deposited.

FACIES 3 - POORLY SORTED (MUDDY) VERY FINE TO COARSE SANDSTONE

Varieties of poorly sorted sandstones characterize Facies 3 (Fig. 3.2d). The facies varies from fine- to coarse-grained sandstones that are massive to parallel laminated or bedded; some beds are normally graded but very locally they show reverse grading. The muddy, very fine and fine sandstone may be locally ripple cross-laminated and include mudstone laminae. Siltstone laminae are boudinaged and exhibit soft-sediment folding. Coarse to very coarse sand and clasts are dispersed throughout, and locally, where clasts are abundant in the medium to coarse sandstones, they may be sufficiently concentrated to form matrix-supported conglomerate or they may exhibit coarse tail fining-upward trends. In addition, conglomerates occur locally at the base of beds, generally above sharp contacts.



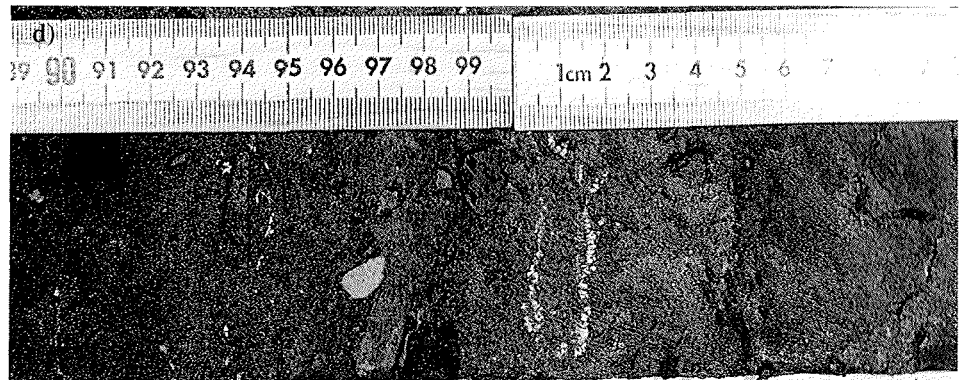
Fig. 3.2 - Core images of examples of the sedimentary facies in CRP-2/2A. Orientation is with the top of the hole to the upper left and bottom to lower right.

a) Mudstones of Facies 1 at 464.00-466.00 mbsf, which locally contain well-preserved, articulated modioloid bivalves, are bioturbated and contain scattered small gravel.

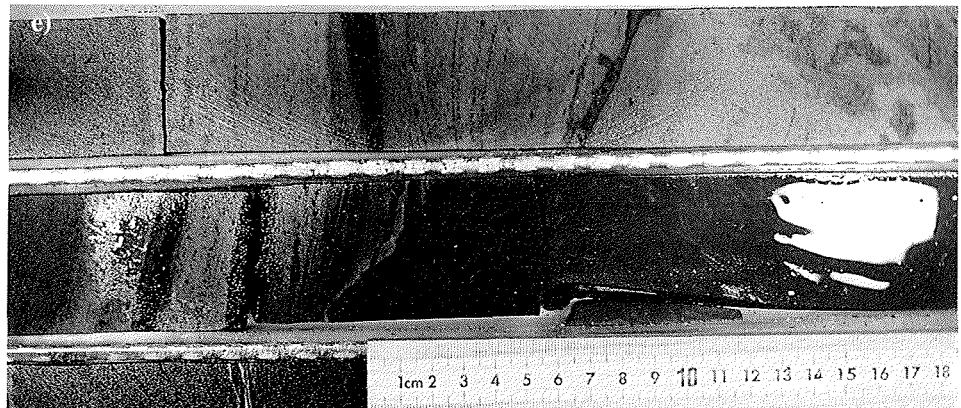
b) Interlaminated and thinly interbedded siltstones and very fine- to fine-grained sandstones of Facies 2 at 315.74-319.74 mbsf, showing rhythmic inter-bedding, sharp-bounded and some normally graded sandstone beds, well-developed extensional microfaulting (lower right of photo), low-angle shear planes (upper right of photo), diffuse patches of carbonate cementation (upper centre of photo) and soft-sediment deformation including prominent load casts and load balls (column above ruler).

c) Interlaminated and thinly interbedded very fine- to fine-grained sandstones of Facies 2 (upper 2 core sections) overlying well-sorted, medium-grained sandstones of Facies 5 (lower 2 core sections) - 508.52-512.32 mbsf. Note the variable thickness of Facies 2 sandstone laminae and beds, the thoroughly bioturbated nature of some thicker sandstone beds (4th column from top), the delicately ripple cross-laminated and lenticular bedded nature of some thinner sandstone beds (including some ripple form sets suggestive of combined current-wave flow). Note also the distribution of small, circular carbonate nodules and micro-faults (one of which is heavily carbonate-cemented) in the Facies 5 sandstones.

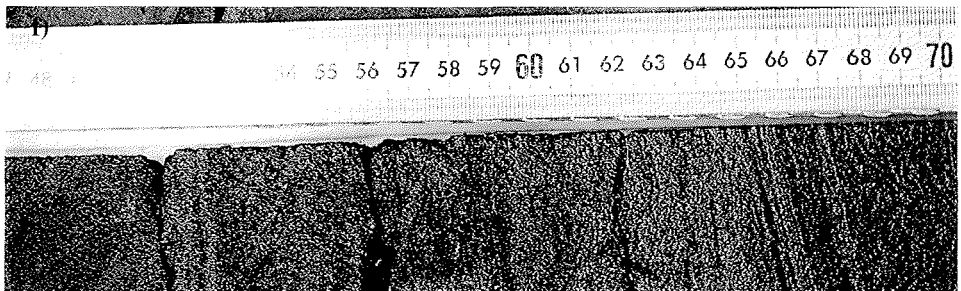
d) Poorly sorted, muddy, vaguely stratified fine- to coarse-grained sandstones of Facies 3 at 36 mbsf. Note the common fossil debris (including a coral at 1 cm on ruler), and scattered coarse debris including pebbles of vesicular (McMurdo Volcanic Group) basalt (e.g. at 99 cm on ruler).



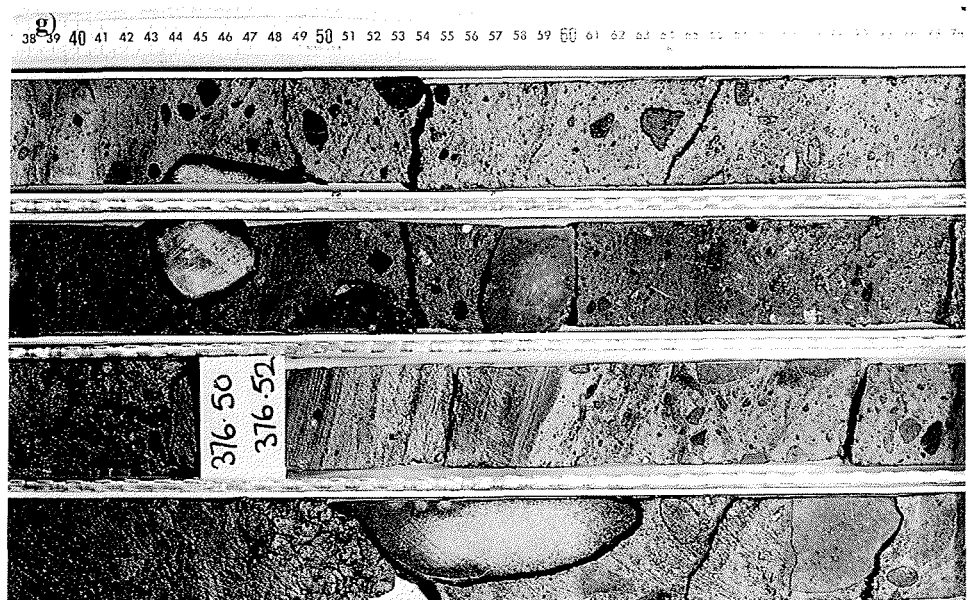
e) Well-sorted, delicately laminated fine-grained sandstones of Facies 4 at 577.90-579.00 mbsf, in microfaulted contact with underlying, very fine-grained, sandstones from 579.00 to 579.18 mbsf. Note the flat laminated and low-angle cross-bedded nature of the sandstones, including development of curved, convex-upward lamination reminiscent of small-scale hummocky cross-stratification (middle of top section). Small black particles are detrital coal, possibly reworked from the Beacon Supergroup.



f) Well-sorted, well-stratified medium-grained sandstones of Facies 5 at 302.49-302.71 mbsf, showing well-developed small-scale cross-bedding.

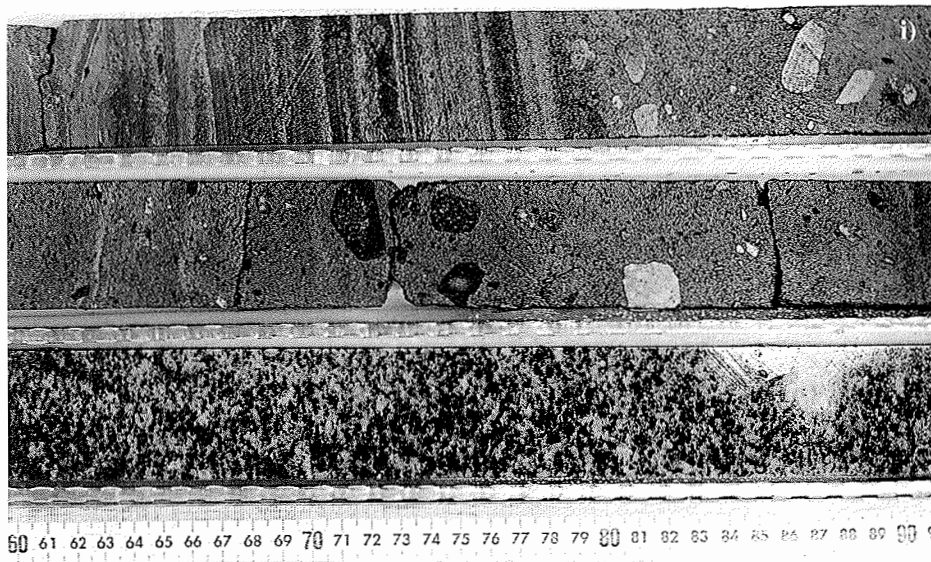


g) Clast-rich, vaguely stratified, sandy matrix diamictite of Facies 6 at 374.38-377.75 mbsf, with a short flat stratified sandstone parting from 376.52-376.62 mbsf.

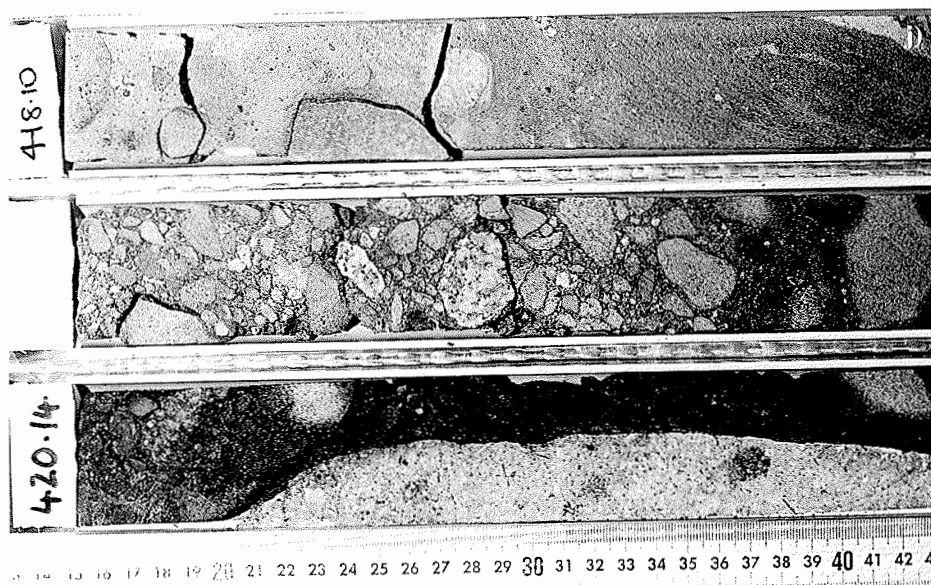




h) Clast-poor, massive, sandy matrix diamictite of Facies 7 at 98.85-101.20 mbsf, showing some vague textural/colour variations that could be interpreted as fluid injection structures.

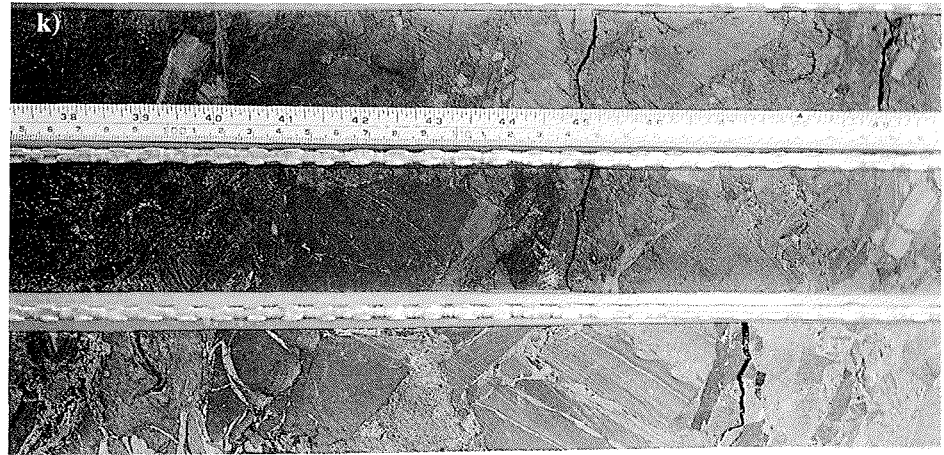


i) Clast-rich to clast-poor, sandy matrix diamictites of Facies 6 and 7, overlain by flat-stratified, rhythmically interbedded siltstone and fine- to coarse-grained sandstones of Facies 8 (347.58-349.89 mbsf).

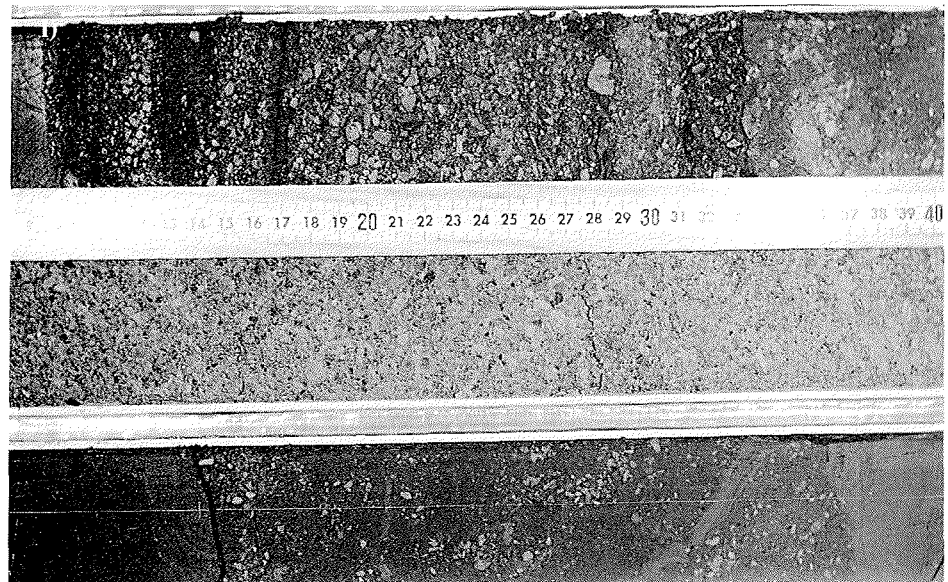


j) Clast- and matrix-supported (sand matrix) conglomerates of Facies 9 and 10 at 418.10-420.45 mbsf. Note the presence of clasts up to boulder grade, and locally moderately well-sorted texture of the pebble-grade intervals.

k) Intraformational clast breccia of Facies 11 at 313-315 mbsf. Note the clast-packed fabric, apparently unstratified nature and sand matrix of the breccia. Clasts are exclusively composed of siltstone and interlaminated siltstone/very fine-grained sandstone, lithologies which are preserved *in situ* immediately beneath the breccia unit.



l) Pumice lapillistones (volcaniclastics) of Facies 12 at 111.06-113.38 mbsf, showing three different types of bed: 1) stratified lapillistone (upper section), 2) massive clast-packed lapillistone (middle section) and 3) matrix-supported mud-rich lapillistone with dispersed pumice lapilli (lower section).



Commonly, when the sandstones are massive the beds are amalgamated, whereas stratified intervals may be produced by changing mud proportions causing colour variations. These muddy sandstones may be interbedded with Facies 4 and even locally Facies 5 sandstones; they grade into mudstone or locally exhibit fining trends in the sands from fine to very fine-grained with a concomitant increase in mudstone. Soft-sediment deformation is apparent only locally. Facies 3 is weakly to moderately bioturbated and marine macrofossils are rare to common; one interval has a concentrated bed of infaunal mussels still *in situ*, and another preserves a coral.

Those units containing marine macrofauna exhibit grading trends in both sand and gravel sizes, indicative of medium- to high-density sediment gravity flow deposits. Some of the thicker massive beds of very fine to fine sandstone may include contributions from very rapid deposition from highly sediment-charged suspended turbid plumes originating from fluvial discharges.

FACIES 4 - MODERATELY TO WELL-SORTED STRATIFIED FINE SANDSTONE

Moderate- to well-sorted fine sandstones which exhibit low-angle cross-bedding and cross-lamination or are planar

thin bedded to laminated characterize Facies 4 (Fig. 3.2e). This facies includes possible hummocky cross stratification (HCS) where laminae have a similar convex upward shape (Fig. 3.2e). Compositionally, these sandstones are rich in quartz and locally contain coal grains dispersed along laminae or constituting distinct laminae. Very fine, medium and coarse sand occurs locally. Dark massive or laminated mudstone is locally interstratified with the sandstones and where it does occur, bituminous material is dispersed locally in the juxtaposed sandstones. Some intervals exhibit major penecontemporaneous soft-sediment folding and microfaulting. Facies 4 sandstone is also locally weakly bioturbated, mainly in mudstone partings.

The delicate lamination preserved in this facies are indicative of dilute tractional currents with quiescent periods represented by mudstone. Their association with other marine facies and the presence of possible HCS infers a marine setting within or about wave base.

FACIES 5 - MODERATELY SORTED STRATIFIED OR MASSIVE MEDIUM TO COARSE SANDSTONE

Facies 5 represents moderately sorted medium sandstone (Fig. 3.2c & f) which is locally fine or coarse-grained. Beds are commonly planar- or cross-stratified but

they may also appear massive. They have dispersed to abundant very coarse sand and clasts, some of them being angular. Some massive beds are amalgamated and may have conglomerate marking lower contacts which are everywhere sharp. Facies 5 sandstone is also locally weakly to moderately bioturbated and contains marine macrofossils. These sandstones contain isolated intervals of soft-sediment deformation.

Marine currents are the most likely mechanism for this facies perhaps on a shoreface, with local hiatuses marked by gravelly layers. The facies may appear massive because of uniformity of grain size rather than due a lack of primary sedimentary structure. The environment was under the influence of icebergs due to the presence of lonestones and perhaps some of the massive beds maybe from iceberg turbation.

FACIES 6 - STRATIFIED DIAMICTITE

Stratified diamictite comprising Facies 6 is clast-rich to clast-poor, sandy or muddy and most commonly exhibits no apparent clast orientation, although clast a-axes are locally aligned with stratification (Fig. 3.2g). The stratification style is most commonly laminated and thin bedded which varies from being weakly- to well-defined. Stratification is formed by mudstone, siltstone and very fine to very coarse sandstone strata which vary in their mud content. Strata are also produced by increasing mean sand size from being fine in the diamictite matrix to being medium-grained in the laminae, or by varying proportions of mud. Clasts are angular to rounded and locally are all of one lithology, for example, dolerite. Facies 6 commonly grades into or out of massive diamictite and thinner beds of the facies are locally interstratified with conglomerates, sandstones, massive diamictites and mudstones. Soft-sediment deformation is locally strong. Stratified diamictites are not bioturbated but some include marine macrofossils.

The poorly sorted character and presence of outsized clasts in some areas allows alternative interpretations of this facies. The diamictic character may originate from debris flow deposition combined with ice-rafting processes introducing clasts as well. Some units, especially those that grade into and out of massive diamictites may be from direct rain-out of debris from ice that is being acted on by currents to produce lamination of the matrix. Alternatively, subglacial tills can exhibit these types of structures.

FACIES 7 - MASSIVE DIAMICTITE

Massive diamictite of Facies 7 is more common than stratified diamictite but it too varies from being clast-rich to clast-poor and may be sandy or muddy (Fig. 3.2h & i). When the matrix is sandy, the diamictite locally grades into sandstone by decreasing clast proportions, whereas, when the matrix is muddy, the diamictite locally grades through pebbly mudstone into mudstone by decreasing clast proportions. Locally the mud content of sandy diamictite increases with the decrease in clast proportions. At the other extreme, clasts rarely increase in proportion and the diamictite locally grades into conglomerate which

is commonly matrix-supported. Where the diamictite facies does not grade from underlying units, the lower contact is sharp and commonly loaded or soft-sediment deformed. Most commonly, clasts have no apparent orientation but rarely a-axes have an apparent preferred sub-horizontal orientation. Clasts range from angular to rounded and at one location a clast rests on top of a crack in an underlying one. Thinner beds of this facies commonly are interstratified with mudstones, sandstones and stratified diamictites. Marine macrofossil and pumiceous lapilli are included in sediments of this facies but they are very local.

Of all of the facies this one is the most likely to be of subglacial origin. However beds that show gradations into other types of facies may be more likely attributed to rain-out processes from floating ice or amalgamated debris flow deposits. Some of the intervals do contain marine macrofossils and locally lapilli, and they are commonly bounded by sequences that also contain evidence of submarine deposition.

FACIES 8 - RHYTHMICALLY INTERSTRATIFIED SANDSTONE AND SILTSTONE

Very fine and fine sandstone occurs rhythmically interstratified with mudstone where the sandstones are most commonly massive and have sharp upper and lower contacts (Fig. 3.2i). As Facies 2, these sediments may grade into mudstone which may include discrete siltstone laminae that range from one grain thick up to 1 mm thick with sharp contacts. Lonestones are present and locally they deform laminae beneath, but outsized clasts may also occur locally as one-grain-thick granule laminae. Commonly, Facies 8 is either included within intervals of Facies 6/7 or occurs above or below them, and diamictites are also locally thinly interbedded with them. Soft-sediment deformation occurs within many intervals.

This facies is intimately associated with marine sequences and its rhythmicity in sandstone-mudstone and mudstone-siltstone couplets is indicative of plume cyclopsam and cyclopel deposits (Mackiewicz et al., 1985; Cowan et al., 1997). They have a close association with diamictites, commonly in intervals overlying them. These have been found to originate from suspension settling from turbid plumes under highly sediment-charged conditions.

FACIES 9 - CLAST-SUPPORTED CONGLOMERATE

The clast-supported conglomerate of Facies 9 is massive and poorly sorted with a matrix of poorly sorted, very fine- to coarse-grained sand (Fig. 3.2j). Generally there appears to be no preferred clast orientation and some units include angular clasts among the more common subangular to subrounded debris. Units of this facies most commonly have sharp lower contacts but locally grade up from sandstones through to matrix-supported conglomerate into the clast-supported conglomerate. However, this facies commonly grades upward into matrix supported conglomerate mostly by decreasing clast proportions. Internally, Facies 9 may grade normally from cobble to small pebble conglomerate.

The coarse nature and presence of angular clasts indicate these deposits were deposited close to fluvial discharges. This facies may be submarine by association with marine sequences and may have been in suspension transport in turbulent subglacial conduit discharges. Alternatively, it could represent high density mass flows or redeposited conglomerates, especially where it grades into matrix supported types. Ice rafting could have contributed the angular clasts.

FACIES 10 - MATRIX-SUPPORTED CONGLOMERATE

Facies 10 is matrix-supported conglomerate which is commonly massive and very poorly sorted (Fig. 3.2j). Its characteristics are similar to those of Facies 9 but clasts are fewer and are dispersed within matrix sand. The conglomerates appear to have higher proportions of angular clasts than do clast supported varieties. As described under Facies 9, this facies may grade to clast-supported conglomerates and arise transitionally from sandstone by increasing clast proportions.

The dispersed nature of clasts in a sandy matrix, and grading trends indicate this facies was deposited from high-density mass flows or sediment-charged aqueous currents, and may have been redeposited in shallow marine waters close to a source of fluvial outwash. Alternatively, they may have been deposited from suspension after transport in turbulent subglacial conduit discharges.

FACIES 11 - MUDSTONE BRECCIA

A facies that occurs at several different intervals and notably in one bed over 4 m thick, is intraclastic mudstone breccia which is defined as Facies 11 (Fig. 3.2k). The massive penecontemporaneous breccia has clasts of massive mudstone, laminated silty claystone and muddy very fine sandstone included in a matrix of muddy very fine to medium sandstone. The clasts are dominantly angular but some are subangular to subrounded; they have no apparent preferred orientation and the breccia is clast-supported. Upper and lower contacts are sharp and this facies most frequently occurs in sequences that are soft-sediment folded and microfaulted.

Several inferences can be made on the origin of this facies. The thinner intervals are most likely redepositional events by sediment mass flow processes. The thickest interval may also be from a large scale mass flow event perhaps related to tectonism. However, alternative explanations may be from glacier over-riding or glacier pushing in marine sediments.

FACIES 12 - VOLCANICLASTIC

Several types of volcaniclastic sedimentary rocks occur in the core and they are grouped into Facies 12 (Fig. 3.2l). The most striking type of this facies is massive, reversely or normally graded pumiceous lapillistone, which in one bed is 1.22 m thick. Volcaniclastic material also occurs within lithic, massive and laminated fine and medium sandstone as dispersed ash and lapilli. The pumiceous interval of this facies occurs interstratified with massive

fine to medium sandstones and fining-upward fine sandstone. Other volcaniclastic material occurs most commonly as a dark volcanic glass forming ash laminae or is locally dispersed.

From its particle size and inclusion with marine sediments, this facies is thought to be volcanic air fall debris deposited through water. Some units may be concentrated by marine currents or may have been redeposited in mass flows. The influence of ice in concentrating the material before its fall through water is unknown; however, extraformational debris is absent indicating an absence of glacial ice.

DISCUSSION

The sequence recovered in CRP-2/2A is dominated by facies representative of shallow marine settings as is indicated by the sporadic occurrence of marine fossils through the core. Characteristic lithofacies complement these conclusions from fossils, such as:

- the mudstone of Facies 1, indicative of hemipelagic sedimentation,
- the interstratified sandstone and mudstone of Facies 2, indicative of either dilute marine currents such as from wave action or sediment gravity flows,
- the poorly sorted sandstone of Facies 3, deposited by sediment gravity flows or settling from turbid plumes,
- the stratified fine sandstones of Facies 4, with possible hummocky cross-stratification, indicative of wave-base settings,
- the common gradational contacts of the diamictites in Facies 6 and 7 and the interbedding of some intervals with other marine facies, indicative of proximal glacial marine redeposition and rain-out processes,
- the rhythmic sandstones and siltstones of Facies 8 that are interpreted as cyclopsams and cyclopels from highly sediment-charged glacial streams in the sea,
- the volcaniclastic rich Facies 12, which includes evidence of falling through water and being reworked by dilute currents and sediment gravity flows.

From the individual facies and their sequences, the shallow marine settings appear to have varied from the shoreface to wave base and beyond, but they also appear to include deltaic and/or grounding-line fan settings with large fluvial discharges and their associated delta/fan front and prodeltaic/fan sediment gravity flow deposits as well as cyclopels and cyclopsams. The fan setting and perhaps the deltaic setting too, are associated with ice-contact and ice-proximal environments. The intimate association of the fan sediments with debris flow diamictites and major penecontemporaneous sediment deformation are common grounding-line associations. Indeed, the volume of sediment associated with melt-water influx and the apparent nature of rapid deposition with consequent slumping and redistribution indicate a polythermal to temperate glacial condition, especially in the older strata of Oligocene age. The deformation in the sequence may also be associated with glacial over-riding and, although the fabric analyses thus far indicate no strong subglacial till fabric, some of the diamictites may also be subglacially derived. If sub-glacial deposition has

occurred, then based on the marine character of the sequence, the most logical inference would be for the glacier to have been grounded in the sea. During periods when the glacier advanced into the sea the relatively flat shoreface and shelf may have relief produced by grounding line deposits in the form of morainal banks, sufficient to produce mass flow and sediment redeposition. Isolated banks may have also created restricted circulation conditions on their shoreward side during some time periods as is indicated by some macrofossil assemblages and some of the darker Facies 1 mudstones which represent distal glacial marine and paraglacial conditions. Independent of the glacial and marine settings, nearby volcanic eruptions contributed volcanic ash of various composition and most of it subsequently was reworked in the marine environment. The volcanism is a reminder of the active tectonism that may have accompanied deposition of the whole sequence, but as yet, the influence of that tectonism on facies variations is not well understood.

SEQUENCE STRATIGRAPHY

Preliminary results of a sequence stratigraphic analysis of CRP-2/2A core, presented here, identify 24 unconformity-bound, glacial marine, depositional sequences spanning the early Oligocene to Quaternary (Fig. 3.3). Traditional facies analysis is used here as the basis for the interpretation of palaeoenvironments for all parts of the depositional sequences. Our analysis follows the approach applied by Fielding et al. (1998) to the CRP-1 core, and is based on the premise that changes in grain-size reflect changes in depositional energy, and therefore, broadly correspond to changes in palaeobathymetry. Such a contention is also supported by interpretation of the depth palaeoecology of constituent macrofaunal assemblages (M. Taviani, pers. comm.).

VERTICAL ORGANISATION OF FACIES

The recognition of vertically-stacked cyclical facies successions bounded by sharp erosion surfaces, that mark prominent lithological dislocations, allows the cored interval to be subdivided readily into sequences. Sequences typically comprise a four-fold lithological architecture, which includes the following elements in ascending stratigraphical order (Fig. 3.4):

- 1) a sharp-based, poorly sorted coarse-grained unit (2-20 m thick) comprising diamictite/diamiction, pebbly sandstone and/or conglomerate (Facies 6, 7, 9, 10),
- 2) a fining upwards interval (up to 25 m thick) of sandstone (Facies 3, 4) which passes up-section into fine sandy mudstone (Facies 1, 2),
- 3) a mudstone (up to 30 m thick; Facies 1), that is often marked at the base by a condensed fossiliferous interval passing gradationally upwards into a muddy sandstone (Facies 3) to a sandstone-dominated facies assemblage (Facies 4; up to 20 m thick), and
- 4) a sharp-based well sorted massive, to cross-bedded sandstone (Facies 5) and/or interbedded/interlaminated sandstones and siltstones (Facies 2; 2-10 m thick).

SEQUENCE BOUNDARIES

Hiatal surfaces bounding CRP-2/2A sequences are sharp, unweathered, planar surfaces that cut across mudstone or sandstone facies of the underlying sequences, and mark abrupt facies dislocations between these underlying strata and superjacent diamictites and conglomerates (Fig. 3.5A). It is suggested here that sequence boundaries coincide with *glacial surfaces of erosion* (GSE), which record periods of local glacial advance across the sea-floor during glacio-eustatic sea-level fall (e.g. Fielding et al., 1998). In contrast to the traditional Exxon definition of the sequence boundary, which was developed from studies of non-glaciated continental margins (e.g. Vail, 1987), GSEs do not necessarily mark a basinward migration and downward shift of the shoreline during falling relative sea-level. Rather, they are the product of erosion caused by either debris flows spilling off the front of proglacial grounding line fans and/or the direct grounding of advancing glacier ice onto the sea-floor. The latter process in many cases removes proglacial deposits. Thus we interpret most of the sequence boundaries as GSEs produced by ice contact with the sea floor. It is important to note that both processes of sequence boundary formation can also occur independently of glacio-eustatic sea-level oscillations and produce an unconformity of only local areal extent.

Notwithstanding these added complications inherent in glacio-marine basin margins, we view the sequence boundaries recorded in the cored interval (Fig. 3.3) as primarily reflecting glacier advance in concert with a eustatic drawdown of base-level. Such a contention is supported by the recognition of faunal and sedimentological evidence for palaeobathymetric deepening and shallowing cycles within sequences. That grounded ice passed periodically through the site of CRP-2/2A is consistent with the location of the drill site in the palaeo-Mackay Valley close to the western margin of the West Antarctic Rift Systems.

Because the lower portions of many of the diamicts exhibit characteristics that are compatible with basal tills: multimodal grain size, vague lamination, and *in situ* brecciation (see Deformation section), and overlie sharp erosional surfaces, we interpret twenty-two of the twenty-four sequence-bounding unconformities and basal diamicts to have formed in a setting that was probably landward of the glacial maximum ice front. In this type of setting, scouring by advancing grounded ice may remove substantial parts of the subjacent sequences. Consequently, CRP-2/2A sequences display various degrees of top-truncation. The preservation of shallow water regressive facies in the upper parts of twelve of the twenty-four sequences implies that glacial erosion may have occurred within close proximity to the contemporary shoreline.

The basal portions of Sequences 3 and 21 represent positions marginally basinward of the glacial-maximum grounding line, but above storm wave base. These sequences display sharp erosional lower boundaries, but comprise a shallow-water sand facies instead of diamictite immediately above the sequence boundary. The absence of diamictite and the occurrence of a well-sorted sharp-based sandstone leads us to interpret these

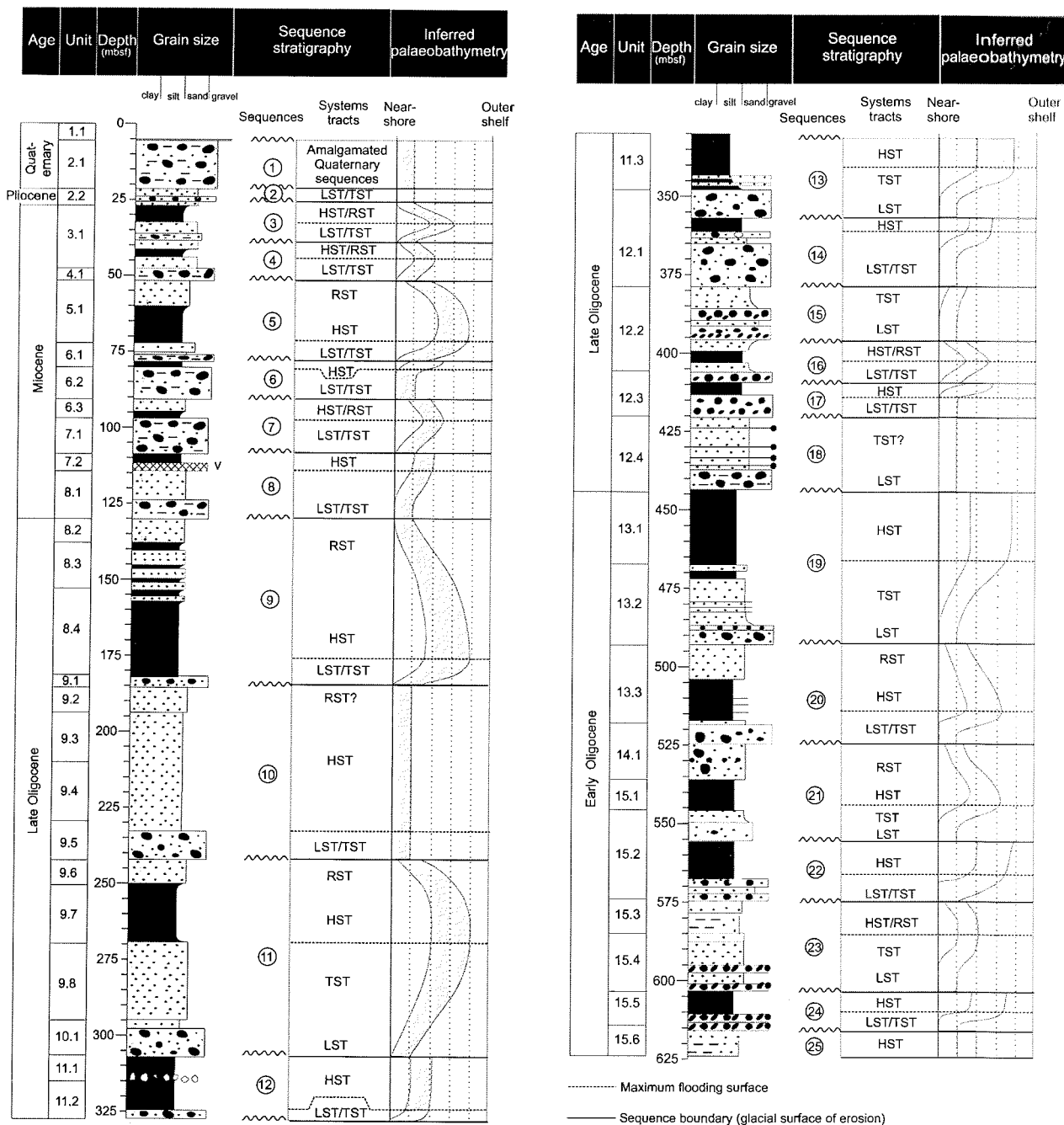


Fig. 3.3 - Composite stratigraphic log of the CRP-2/2A core showing sequence stratigraphic architecture and an inferred palaeobathymetric curve for sequences.

sequence boundaries as current-scoured surfaces formed immediately offshore from a subglacial stream or clastic shoreline. They, therefore, may represent regressive surfaces of erosion cut towards the end of sea-level fall, and/or ravinement surfaces associated with landward passage of the shoreface during the ensuing transgression.

LOWSTAND AND TRANSGRESSIVE SYSTEMS TRACTS

The coarse-grained basal units of the sequences comprise massive (Facies 7) and stratified (Facies 6)

diamictite together with clast- (Facies 9) and matrix- (Facies 10) supported conglomerate. The diamictic facies are consistent with a combination of glacio-marine processes including subglacial entrainment during ice advance, melt-out and rainout during ice withdrawal, and proglacial debris-flow deposition with ice rafting. Conglomerate facies are also consistent with ice proximal glacio-marine sedimentation and probably represent deposition from subglacial streams, short flow fluvial deposition, and redeposited fluvial conglomerates. Distinguishing sub-glacial tills deposited during ice advance from proglacial tills deposited during retreat is inherently difficult, as the sedimentological characteristics

IDEALISED SEQUENCE MOTIF

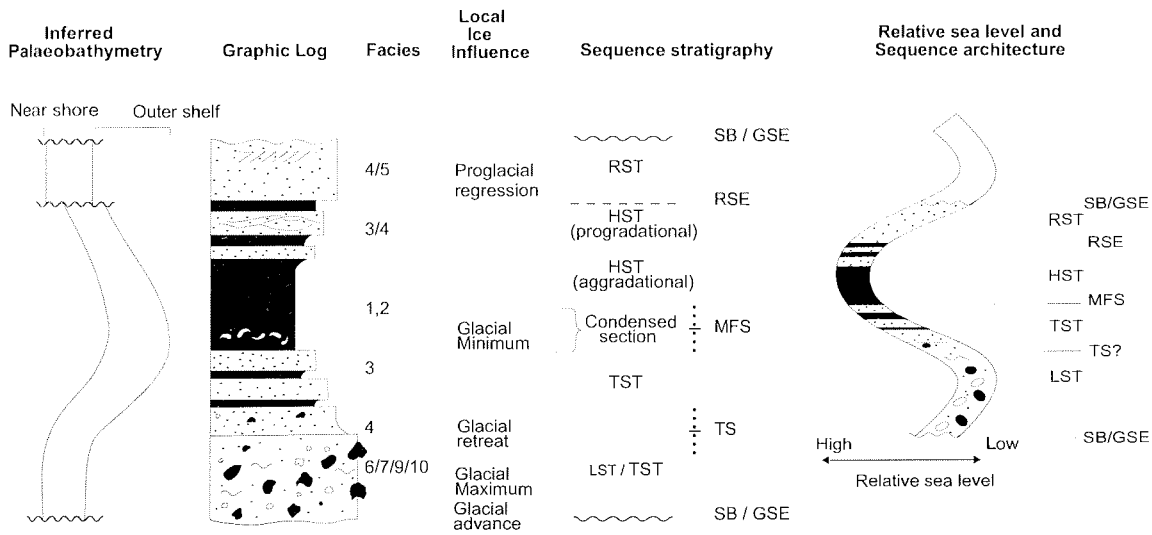


Fig. 3.4 - Typical motif of depositional sequences.

of these deposits are not well-understood in modern glacial environments. Therefore, the coarse-grained basal facies are considered to have a polyphase origin representing ice-proximal deposition during advance and withdrawal of glacier ice within a shallow marine setting.

Consequently, basal diamictite and conglomerate facies are assigned to both the *lowstand systems tract* (LST) and the *transgressive systems tract* (TST). It is generally not possible to identify the LST/TST boundary. However, given the paucity of facies that could be readily interpreted as subglacial origin, it is suggested that the basal diamictites

comprise a predominantly transgressive record of glacial retreat. Typically, diamictite clast fabrics are weakly oriented or random, suggesting a large component of rainout debris which, in many cases, may have been remobilized in subsequent gravity flows as evidenced by syn-depositional soft sediment deformation structures, intraclasts, and clastic intrusion features. Stratified diamictite facies are interpreted as representing waterlain glacio-marine sediments. Upper portions of TSTs display clear fining-upwards trends and are mostly capped by a fossiliferous unit interpreted as the *condensed section* corresponding to a zone of maximum water depth and lowest sedimentation rate in a cycle.

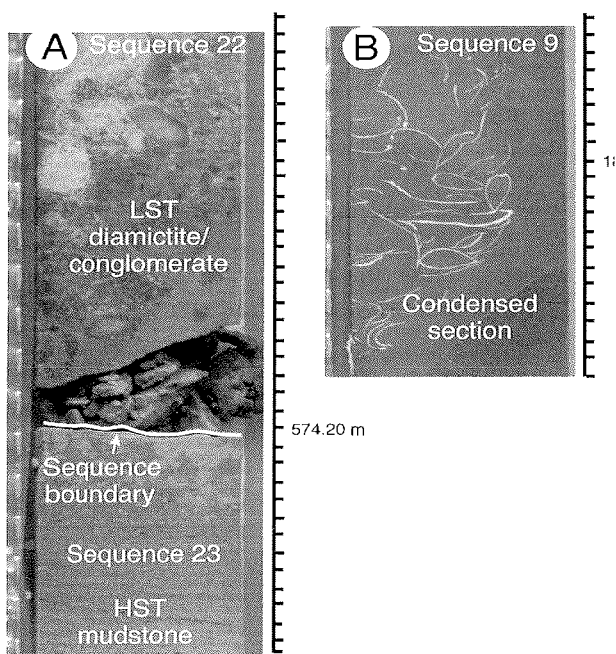


Fig. 3.5 - (A) View of sequence boundary separating diamictite in the lower part of Sequence 22 from mudstone in the upper part of Sequence 23; (B) fossiliferous condensed section shellbed of Sequence 9. Scale is graduated in 1 cm intervals.

HIGHSTAND SYSTEMS TRACTS

The base of the mudstone units is typically fossiliferous (Fig. 3.5A) and contains molluscan fauna indicative of maximum water depths in sequences (M. Taviani, pers. comm.). A lower interval (up to 30 m) of massive to weakly laminated/bedded, bioturbated, sparsely fossiliferous mudstone (Facies 1 and 2) typically passes upwards into a muddy sandstone to sandstone facies (Facies 3 and 4). Micro- and macrofaunal determinations show little or no change in water depth up-section in this lower interval. Sediments that gradually overlie mudstone facies appear markedly more progradational, shoaling to probable inner shelf water depths. It is suggested that this regressive mudstone to sandstone interval results from sediment infilling during the highstand and/or early fall of sea-level. Accordingly, this facies succession is assigned to the *highstand systems tract* (HST).

Highstand systems tract deposits are interpreted as forming during the late rise, stillstand and early fall of a relative sea-level cycle (e.g. Vail, 1987; Posamentier et al., 1988). In offshore locations the *downlap surface* (DLS) marks the base of an HST, which is broadly

coincident with the level of maximum palaeo-water depth termed the *maximum flooding surface* (MFS). At seismic scale the MFS represents a change from retrogradational to progradational cross-sectional stratal geometries (e.g. van Wagoner, 1988, 1990). In CRP-2/2A core sequences it is not possible to evaluate downlap. Nevertheless, the TST/HST boundary is placed at an abruptly gradational transition between fining-upwards sand facies and massive mudstone facies in most sequences. The base of the HST is typically fossiliferous (Fig. 3.5A) and contains molluscan fauna and lithofacies indicative of maximum water depths (M. Taviani, pers. comm.).

REGRESSIVE SYSTEMS TRACTS

Twelve of the twenty-four CRP-2/2A sequences include in their upper parts a sharp-based shallow-marine facies succession of probable innermost shelf to shoreface origin. These facies include moderately to well-sorted, stratified fine sandstone (Facies 4), and moderately sorted, stratified or massive medium to coarse sandstone (Facies 5). They display a variety of tractional sedimentary structures including planar bedding and lamination, hummocky and swaley cross-stratification, high-angle cross-stratification, and low-angle cross-stratification, collectively indicative of shallow, shoreface environments. Additionally, some occurrences of Facies 2 ripple cross-laminated mudstone and sandstone (with small-scale wave- and combined flow-generated ripple structures) may reflect estuarine conditions. The occurrence of sharp-based shallow-marine sands at the top of sequences, the strongly progradational character of the succession, and the subsequent truncation by overlying GSEs, are all consistent with sediments deposited during a period of falling relative sea-level, or forced regression (Fig. 3.4). We tentatively interpret these regressive sandstones as forming in a proglacial deltaic depositional environment seaward of the advancing ice front. In all cases the upper portions of sequences appear to be overrun and severely truncated by the subsequent advancing glacier.

Strata deposited during gradual or stepwise forced regression accumulate as a basinward-descending and offlapping series of wedges, bounded below by an abruptly gradational (e.g. Naish & Kamp, 1997) or erosional downlap surface (e.g. Plint, 1988) and above by a subaerial unconformity (often removed by marine ravinement), which corresponds to the sequence boundary. Naish & Kamp (1997) have referred to this distinctive stratal package as the *regressive systems tract* (RST), and view it as the logical counterpart to the transgressive systems tract. In many cases, it is not possible to locate the lower boundary of the RST precisely, where the contact with the underlying highstand systems tract is gradational, but typically it corresponds to an abruptly gradational transition from mudstone to sandstone. Regressive systems tract sediments are markedly more progradational than those of the HST, and step down or are inclined towards the basin. The upper bounding surface of the RST, the subaerial unconformity which is often marked by fluvial channel incision or delta abandonment, passes into a correlative submarine

unconformity landward of the lowstand shoreline, where it marks the base of the lowstand systems tract (LST). In CRP-1 and CRP-2/2A the upper bounding unconformity of the RST is marked by the GSE.

FREQUENCY AND AMPLITUDE OF SEDIMENTARY CYCLICITY AND IMPLICATIONS FOR ANTARCTIC GLACIAL HISTORY

Twenty-four cycles of local advance and retreat of the Mackay Glacier during the Oligocene to Quaternary can be identified on basis of the preliminary facies and sequence stratigraphic analysis of the CRP-2/2A core. The Quaternary and Pliocene intervals, Sequences 1 and 2 respectively, most probably comprise a series of amalgamated sequences recording a cryptic and very incomplete glacial history of the last 5 Ma. That the Quaternary record lies within a normal polarity interval interpreted as Bruhnes Chron, suggests that high amplitude climatic variations characteristic of the last 700 ka may have driven major glacial episodes, destroying much of the earlier Plio-Pleistocene stratigraphic record. The recognition of a thin interval of Pliocene glacial/interglacial stratigraphy in CRP-2/2A is important as significant fluctuations in the size of the Antarctic ice sheet have been inferred from studies of the onland "Pliocene" Sirius Formation (Webb & Harwood, 1991; Wilson, 1995).

Although punctuated by significant unconformities, the Oligocene-Miocene section of the core is relatively more complete with 6 sequences preserved in the Miocene and 16 sequences representing the Oligocene. Noteworthy is that some of these sequences (notably 8, 14, 18) may be the amalgamated product of several severely truncated sequences. Broad constraints on the amplitudes of palaeobathymetric fluctuations reveal cyclical changes in water depth from upper shoreface to outer shelf water depths, perhaps of 50 to 100 m magnitude. Bathymetric changes throughout a sedimentary cycle are controlled by three independent variables: rate of eustatic sea-level change, rate of subsidence, and rate of sediment accumulation. Basin subsidence and eustatic sea-level combine to cause changes in relative sea-level, which in turn control the net accommodation space available for sediment. The rate of generation and loss of accommodation, together with the rate of sediment accumulation produce changes in bathymetry, which control the facies architecture of the resulting depositional sequence.

The isolation of the eustatic sea-level component from a continental-margin sedimentary succession is inherently difficult to achieve. Even with high-resolution information about the nature of intra-cycle changes of water depth, and first order approximations of subsidence and sedimentation rates, uncertainty remains about the amount of the sea-level lowstand strata lost at the bounding unconformities. At this stage it is not possible to estimate the amplitude of any glacio-eustatic component, but changes in water depth of up to 100 m are consistent with eustatic water depth changes inferred for the Oligo-Miocene from seismic records (Haq et al., 1988), and

deep ocean oxygen isotope records (Zachos et al., 1997; Vitor & Anderson, 1998).

Evaluating the frequency of sedimentary cyclicity is complicated and depends on 2 factors: 1) the time represented by sediment, and 2) the time contained in inter-sequence unconformities. Frequency analysis of these types of records requires a high-resolution time model which allows age constraints to be put on hiatuses and can be used to determine variations in sedimentation rate. Such time models generally require a magnetostratigraphy that is robustly calibrated to the timescale with biostratigraphic and numeric age datums. At the time of writing, a high-resolution integrated chronology was not available for CRP2-2/A. A high degree of floral and faunal endemism and a paucity of low-latitude index taxa in the cored interval has hampered calibration of the magnetostratigraphy. However, numerical ages on two tuffaceous intervals and strontium isotopic analyses currently being undertaken should help to better constrain the time model for CRP-2/2A.

Preliminary magnetostratigraphic results imply a thick interval of normal polarity in the late Oligocene which may span up to 9 sequences, implying that individual depositional sequences in certain parts of the core may correspond to Milankovitch orbital frequencies (eccentricity). Such an interpretation has several important implications, notably 1) that the cored interval contains an incomplete record of the Oligocene-Quaternary of western Ross Sea with large periods of time represented at sequence-bounding unconformities, and 2) where sequences are preserved, they may represent an important ice-proximal record of orbital control on the dynamics of the Antarctic ice sheet, which has significant implications for understanding the origin of Oligocene-Neogene global eustatic sea-level change.

Alternatively, the frequency of sequence cyclicity may be of a longer duration similar to that of the 3rd order (0.5-2 Ma) eustatic cyclicity reported on the Haq et al. (1988) sea-level curve, and the composite Cenozoic oxygen isotope curve of Vitor & Anderson (1997). A plot of cycle thickness vs depth (Fig. 3.6) reveals a longer term cycles of sequence stacking, perhaps of c. 15 Ma duration, which may reflect extrabasinal tectonic influences related to the uplift history of the Transantarctic Mountains, or differential movement of individual fault blocks in the vicinity of the drillsite. Further chronostratigraphic analyses must be undertaken for the CRP-2/2A Scientific Report volume in order to evaluate the stratigraphic frequencies inherent in this important ice-proximal Antarctic record.

SEDIMENTOLOGY

CLAST VARIABILITY

20 503 clasts, ranging in dimension from granule to boulder grade, were logged and counted on the basis of both approximate grain-size and lithology in the Miocene-Oligocene section of CRP-2/2A core.

The clast population is composed of seven major lithological groups which document a varied but local

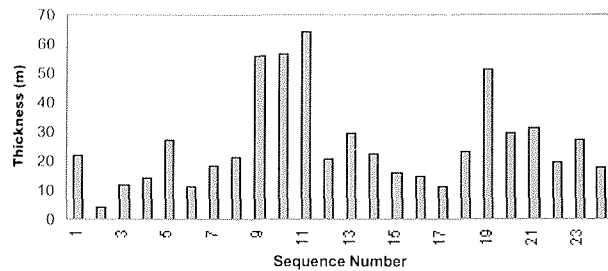


Fig. 3.6 - Plot of cycle thickness vs depth highlights long-duration, cyclical stacking pattern of sequences.

provenance (see Basement Clasts section), including: Cambro-Ordovician granitoids, Ferrar dolerite, McMurdo Volcanic Group alkaline basalts, Koettlitz Group Ca-silicate rocks, Kirkpatrick basalts, McMurdo Volcanic Group pumice and sedimentary rocks (including both intraformational and Beacon Supergroup sedimentary rocks).

This section focuses on the main patterns of clast variability as derived from major variations in concentration and grain-size throughout the Miocene-Oligocene strata. Further information on the distribution pattern and preliminary petrological data on the various clast lithologies are reported in Basement Clasts section of this report. The total number of clasts, here preferred to clast percentages which are strongly influenced by the size of single clasts, are plotted against the lithostratigraphical log in figure 3.1. Most lithological boundaries, as well as sequence boundaries, in the core are marked by significant variations in clast content. In particular there is a strong correlation between high clast concentrations and diamict units, a pattern already observed in CRP-1 (Cape Roberts Science Team, 1998b, 1998c).

Moreover, significant variations occur in the relative proportions of the main lithologies and/or the appearance or disappearance of particular lithologies (see Basement Clasts section) across lithological and sequence stratigraphical boundaries. Minor to significant fluctuations in both the clast content and relative proportions among the different rock types also occur within each single litho-stratigraphical unit, in particular in the more clast-rich units. A detailed analysis of these small-scale compositional trends is in progress, whereas a broader subdivision of the whole clast population into seven petrofacies is proposed and discussed later in this report (Basement Clasts section).

In diamict units the clast content averages 50-100 clasts per metre, with values very close to 200 in Lithostratigraphical Unit 12.1. In mud- or sand-dominated units the clast content is distinctly lower and usually <10, grain-size typically ranges from granule (the most abundant) to pebble. In diamict units, grain size ranges from granule to boulder (the latter very few and restricted to Units 12.1 and 13.1), with granules and fine to coarse pebbles forming the most represented grain-size classes. A slight increase in grain-size within the pebble class and in the number of cobbles can be observed moving down-core, particularly below c. 300 m.

CLAST FABRIC

Introduction and Method

Clast fabric has been used by many workers to assist in the interpretation of clast-rich sediments, particularly in glacial environments, specifically to infer origins of deposits and define glacial flow directions (Domack & Lawson, 1985; Dowdeswell et al., 1985). Ten whole round (unslabbed) sections of core ranging between 18 and 31 cm long were collected from the Miocene/Oligocene interval of the CRP-2/2A core for the purpose of three-dimensional fabric analyses. Eight were from sandy diamictite units and two from poorly sorted sandstones with clasts. All of these samples are from just above interpreted sequence boundaries (see section on Sequence Stratigraphic Interpretation). The analysis was achieved by securing the core in an upright position in a simple supporting apparatus with a horizontal stage that was lowered over the core. The core was systematically disaggregated and the trend and plunge of the a-axis (long axis) of each clast measured and recorded on the stage. The number of measurements in each sample depended on the clast concentration but ranged from 13 to 30 clasts. None of the samples was oriented with respect to north, because no azimuth could be determined at the drill site.

The trend and plunge data were plotted on Schmidt equal area, lower hemisphere stereonet projections. The data were then contoured using a small circle area of 1% and contour intervals at 2.0, 5.0, 10.0 and 15.0%. Also, the Eigenvalue analysis method of Mark (1973) was applied to the data. This produces three orthogonal vectors (eigenvectors, V_1 , V_2 and V_3). V_1 refers to the direction of maximum clustering and V_3 the direction of minimum clustering. Associated with these vectors are normalized eigenvalues (S_1 , S_2 and S_3) which represent the degree of clustering around the corresponding vector and essentially summarise fabric strength. S_1 measures the strength of clustering about the mean axis V_1 , and S_3 represents the clustering about the V_3 axis. These data are displayed in figure 3.7. Interpretation of eigenvalues requires great care if the data are multimodal, as vectors can plot between modes and interpretation is best when made in conjunction with other evidence.

Results

The stereonet plots display broad scatter in most samples and eigenvalues suggest only very weak preferred orientations and even random orientation. Principle eigenvalues (S_1) range from 0.423 in the sandy diamictite sample at 441.22-441.52 mbsf to a maximum of 0.617 in the deformed sandy diamictite sample at 490.10-490.39 mbsf. Typical S_1 values lie between 0.50 and 0.60. Figure 3.8 shows a plot of S_1 against S_3 and compares data from CRP-2/2A with fields defined by Dowdeswell et al. (1985). This helps distinguish fabrics from different mechanisms of deposition. The samples from CRP-2/2A all show relatively low S_1 values and moderate to high S_3 values. Random orientations are characteristic of ice-

rafted diamictons (Domack & Lawson, 1985) and plot in the waterlain glaciogenic sediment field. Weak fabrics are suggestive of sediment flows and can be induced in waterlain sediment that has undergone post-depositional slumping or flowage (Dowdeswell et al., 1985). No strong fabrics, indicative of lodgement or melt-out tills, are present in the data.

The dominance of random and weakly oriented fabrics, and the absence of any obvious subglacial fabric signature in these samples, despite close proximity to the sequence boundaries where evidence of grounded ice might be expected, can be interpreted in one of two ways. Firstly, if the unit was deposited by grounded ice, any original subglacial fabric may have been modified and weakened by post-depositional deformation. Alternatively, it may indicate that subglacially formed deposits from grounded ice are not preserved in these intervals and that the samples represent either waterlain sediment (sample 441.22-441.52 mbsf), or soft-sediment deformed waterlain deposits and sediment flows (all other samples). Both of these possibilities are consistent with the clast shape data, which indicates most of the sediment has experienced subglacial transport but does not distinguish whether final deposition was from ice-rafting or grounded ice.

CLAST SHAPE

Introduction and Method

Clast shape can be expressed in terms of three independent properties: form, roundness and surface texture (Barrett, 1980). These have been widely used in the analysis of clast-rich sediments and are considered good indicators of transport mechanisms. The Miocene and Oligocene interval of the CRP-2/2A core contains many clast-rich intervals, including conglomerates and diamict units suitable for clast shape analysis. Ten whole-round core samples ranging in length from 12 to 31 cm and one bulk sample were removed, one from each of the major clast-rich units. All samples are from just above interpreted sequence boundaries (see section on Sequence Stratigraphic Interpretation). Samples from 48.60-48.80, 101.67-101.85, 232.80-233.04, 351.37-351.67, 372.15-372.46, 406.80-407.09, 441.22-441.52 and 490.10-490.39 mbsf are from sandy diamictite units. Samples at 121.59-121.79 and 518.32-518.62 mbsf are from clast-rich sandstone units and finally samples at 124.92-125.92 (bulk sample) and 387.02-387.32 mbsf are clast- to matrix-supported conglomerates. These samples were systematically disaggregated to obtain whole (uncut by coring) clasts. The lithology of each clast greater than 0.5 cm in diameter was determined and grouped into broad categories. For whole clasts, the length of the three orthogonal axes (a, b and c) was measured. Roundness was assessed using the Krumbein visual roundness chart, which provided mean roundness and percentages of clasts in each of nine roundness classes. Clasts were also examined for surface features such as facets and striations. The number of observations varied depending on clast concentration and ranged between 13 and 50.

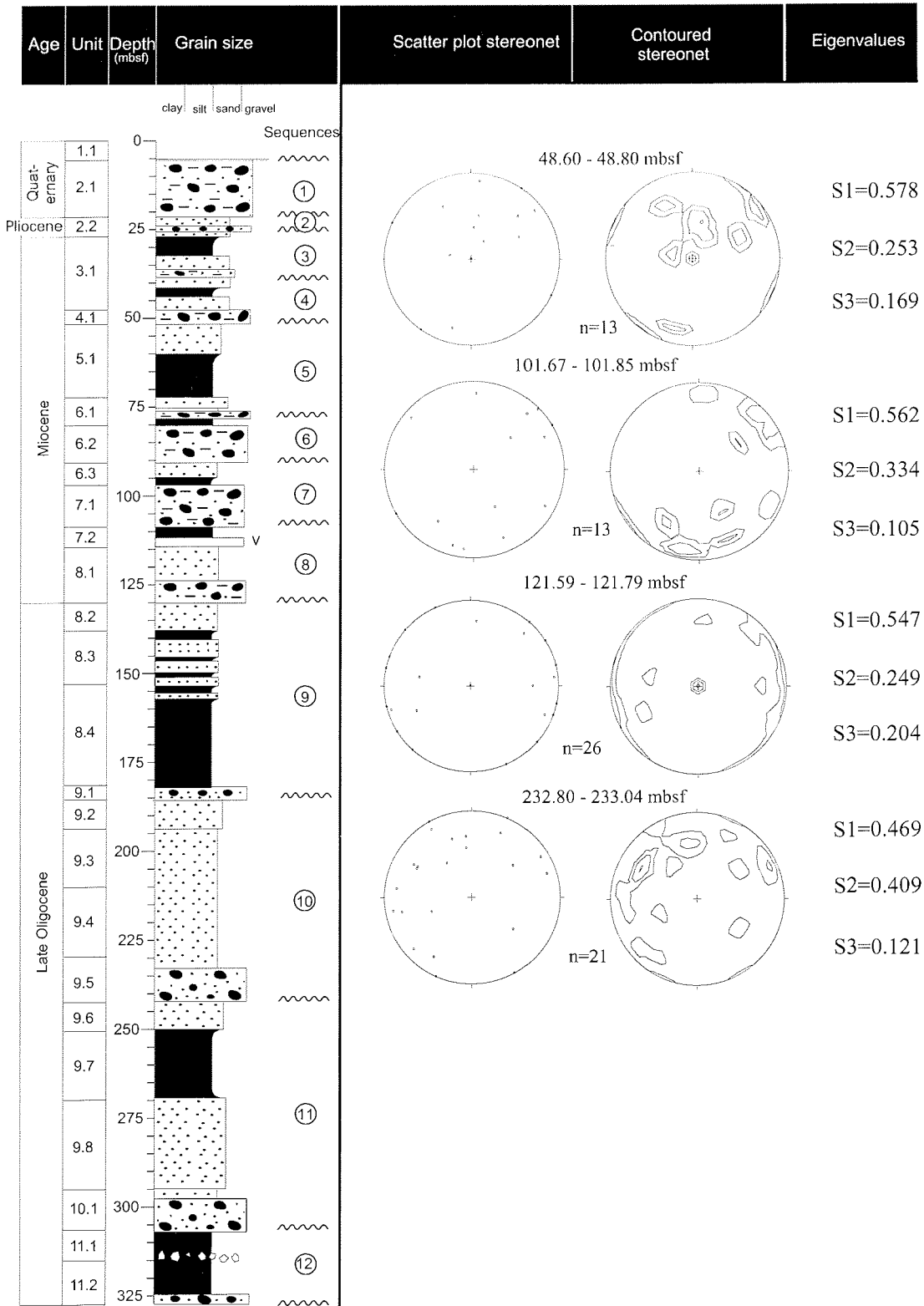


Fig. 3.7 - Core log of CRP-2/2A showing equal area, lower hemisphere stereonet projections of trend and plunge of a-axis (long axis) of each clast (scatter and contoured) and eigenvalues for each sample.

Roundness

Roundness is presented as histograms in figure 3.9. Krumbein roundness values correspond to Powers roundness classes as follows: very angular 0.0-0.17; angular 0.17-0.25; subangular 0.25-0.35; subrounded 0.35-0.49;

rounded 0.49-0.7; well rounded 0.7-1.0. The sandy diamictite samples 48.60-48.80 and 101.67-101.85 mbsf, in Lithostratigraphical Units 4.1 and 7.1 respectively, show broad distributions and the latter has a distinct peak in the 0.3 class. The poorly sorted, fine-to coarse-grained sandstone with clasts at 121.59-121.79 mbsf in LSU 8.1

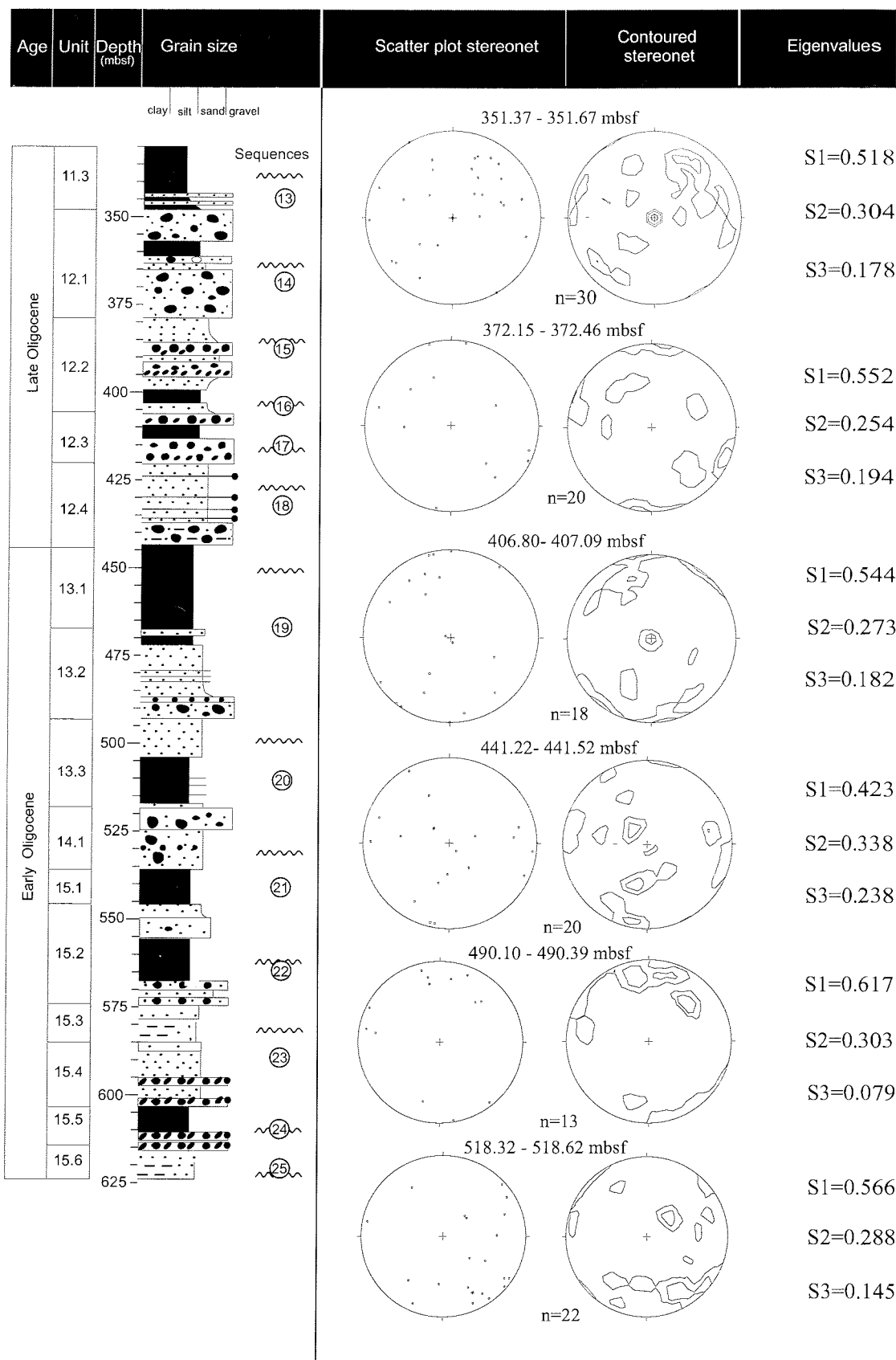


Fig. 3.7 - Continued.

displays an unusual roundness distribution. Over 50% of the clasts are in the angular and very-angular class. This gives a low mean roundness of 0.29 but the distribution also displays a high standard deviation of 0.16 due to the

distinctive rounded tail with one clast with a roundness value of 0.8. This indicates that there may be components of supraglacial material and also fluviually reworked clasts in the deposit. Also from LU 8 is the sandy conglomerate

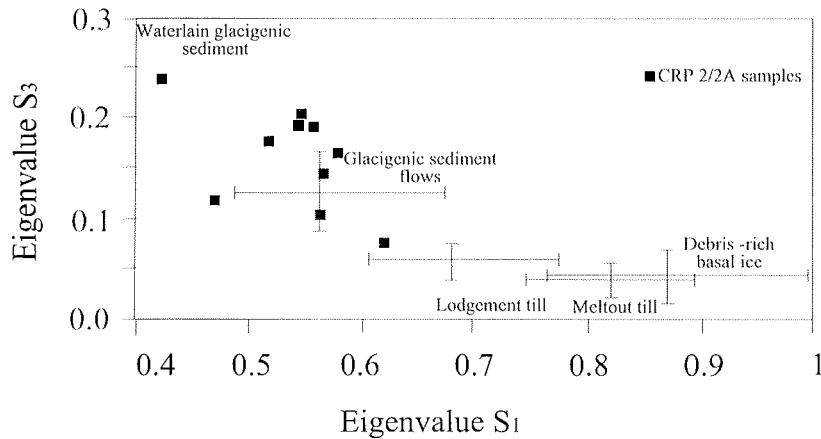


Fig. 3.8 - Plot of Eigenvalues S_1 and S_3 for CRP-2/2A core samples and environmental fields determined by Dowdeswell et al. (1985) from Svalbard tillites.

sample 124.92-125.92 mbsf. The broad distribution is bimodal with peaks in the 0.2 and 0.4 classes and mean roundness of 0.32, which is comparable with that in the diamictite units. The sandy diamictite samples 351.37-351.67, 372.15-372.46 and 490.10-490.39 mbsf show deformation features and interestingly have slightly higher mean roundness values than the undeformed sandy diamictites. The conglomerate at 387.02-387.32 mbsf has the most normal distribution, with all roundness classes up to 0.6 represented. The deepest sample at 518.32-518.62 mbsf is a poorly sorted, fine- to coarse-grained sandstone and shows a marked peak in the subangular class similar to the pebbly sandstone sample at 121.59-121.79 mbsf.

Lithology, Facets and Surface Features

Lithology is displayed as histograms in figure 3.9. These clearly illustrate the dominance of granite and dolerite in all samples. The most marked trend is the change in dominance of these lithologies down the core. The samples from the top sample at 48.60-48.80 down to and including the conglomerate sample at 124.92-125.92 mbsf in LSU 8.1 are dominated by granitoid lithologies (at least 65%) with dolerite second most frequent. Sample 121.59-121.79 mbsf in LSU 8.1 contains 19% volcanic clasts. This contrasts with samples in the lower interval which are dominated by dolerite (>60%). Sedimentary and metamorphic clasts appear in several samples, typically less than 5%.

The presence of surface features, such as striations, can provide good evidence of basal glacial transport. However, the development of striae is strongly dependent on lithology (Kuhn et al., 1993). A total of only three striated clasts were found in the samples, all fine grained, indurated mudstone. These were in the deformed sandy diamictite sample at 351.37-351.67, the conglomerate at 387.02-387.32 and the sandy diamictite at 406.80-407.09 mbsf. It is interesting to note that sample 387.02-387.32 mbsf is a conglomerate, suggesting that this material may be reworked glacial sediment.

Facets are present on all lithologies in all samples, typical of sediment that has experienced subglacial transport. Percentages of faceted clasts range from a low of 23% in the sandy diamictite sample at 101.67-101.85 to

a maximum of 50% in the sandstone sample at 518.32-518.62 mbsf. The conglomerate samples from 124.92-125.92 and 387.02-387.32 mbsf show a high percentage of faceted clasts, 44% and 40% respectively, further suggesting that the sediment contains glacial material and that any fluvial rounding is limited.

Summary

The shape data from clasts in the eleven samples of sandy diamictite, poorly sorted, fine- to coarse-grained sandstone and conglomerate generally display broad roundness distributions and have average roundness values between subangular and subrounded. Granitoid lithologies dominate above 200 mbsf and dolerite dominates below this depth. The sandy diamictites have broad roundness distributions and have at least 23% faceted clasts, typical of subglacially derived sediment. The deformed sandy diamictites have a slightly higher mean roundness and one of these samples contains a striated mudstone clast. These characteristics suggest that these deposits have experienced subglacial transport and were deposited either by ice-raftering or grounded ice.

The sandstone samples have peaks in the subangular class and at least 27% faceted clasts. The sample at 121.59-121.79 mbsf also has several clasts in the rounded and well-rounded classes and suggests the deposit contains a mix of glacial (supraglacial) and fluvially influenced sediment, and is probably sourced from ice-raftered debris. The conglomerate samples show a broad range of roundness values but the sample at 124.92-125.92 mbsf has a low mean roundness. This suggests that only moderate (if any) fluvial influence and the sample at 387.02-387.32 mbsf contains one of the striated mudstone clasts indicating the sediment has a probable glacial component that has been little affected by reworking.

HIGH-FREQUENCY CYCLICITY IN THE MAGNETIC SUSCEPTIBILITY RECORD FROM UNIT 11.3

Introduction

This section will address the search for periodicities that might have controlled deposition of the CRP-2/2A

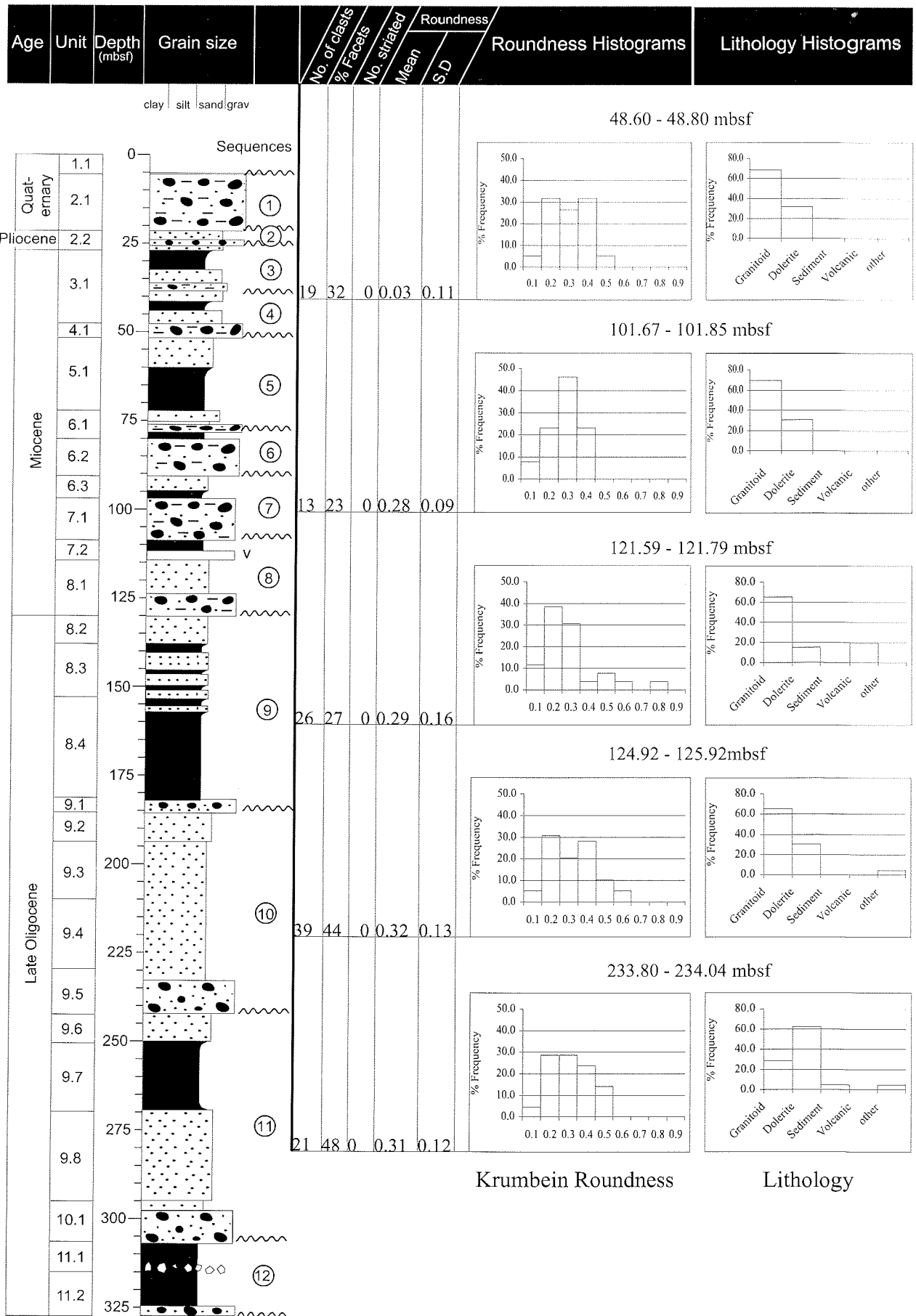


Fig. 3.9 - Core log of CRP-2/2A showing summary shape statistics, roundness histograms and lithology histograms.

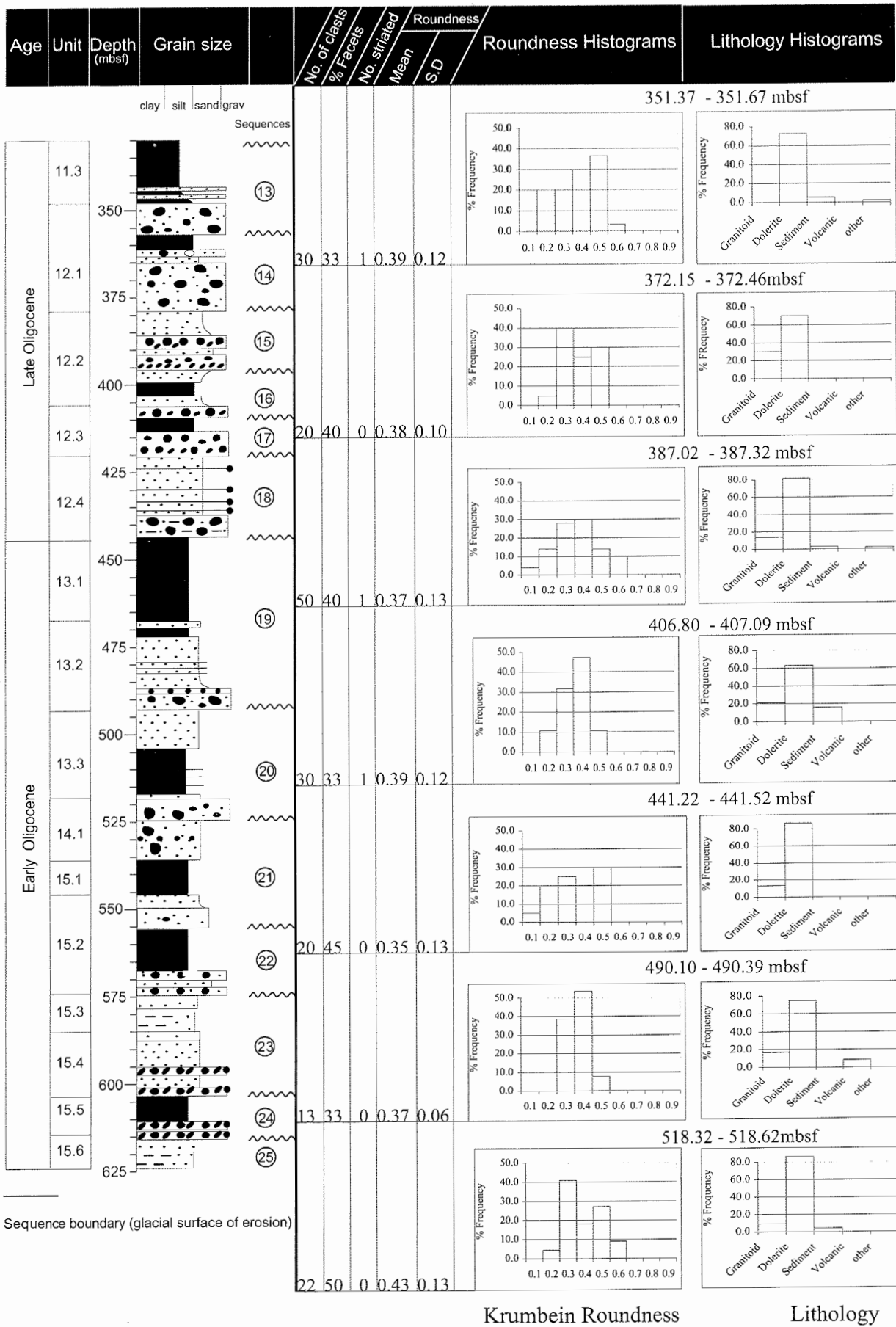


Fig. 3.9 - Continued.

sequence and been recorded in the core. Cyclicity recorded in sedimentary successions is very important since it may give insight into the occurrence of periodic changes in depositional environment, as a possible response to external forcing (Fischer et al., 1990; Fischer & Bottjer, 1991). At the time of writing a complete set of data is not available (such as physical properties series, sequence of sedimentological rhythms). Therefore, the results presented here are a pilot study to explore the possibility of a further search for cyclicity through the entire CRP-2/2A succession in a more continuous and complete fashion. Some spectral analysis techniques (Pestiaux & Berger, 1984; Fischer et al., 1990) were applied to a short array of data extracted from the low-field magnetic susceptibility analysis of the core. This set of analytical data demonstrates that magnetic susceptibility analysis is very appropriate and suitable for this purpose (Arai et al., 1996).

Time Series

The magnetic susceptibility was measured continuously along the core at the Drill Site laboratory, with an average sampling interval of 2 cm, using a Bartington MS-2 magnetic susceptibility metre and a loop sensor of 80 mm internal diameter. The values were later corrected for loop-sensor and core diameter to obtain a normalized data series. The time series analysed in this study covers the magnetic susceptibility data for mudstone Sub-Unit 11.3 (329.30-347.31 mbsf).

Sub-Unit 11.3 constituted a continuous sequence of mudstone and very fine to fine sandy mudstone, with local fine and very fine sandy beds from mm to cm-scale. Bioturbation affected the succession only locally and at a small scale. Clasts (mostly basalt and granitoid) were rarely present. The character of the sedimentation appeared to be quite uniform throughout the entire interval, and weak carbonate cementation occurred only in a few places. Sedimentological evidence, such as absence of re-sedimentation events and the continuity in the depositional style, suggests that no important hiatuses were likely to be present down the sequence. Considering the uniform lithology and the depositional characteristics of the mudstone interval, it is possible to argue that the sedimentation rate has remained relatively constant throughout, at least to a significant extent.

In the few cases where the analysed segment showed irregularities due to fractures, unconsolidation or poor recovery of the core, the magnetic susceptibility was somewhat altered or measured with uncertainty, and thus some values were extrapolated through linear interpolation of the closest ones. Small basalt and granitoid clasts might have altered the original magnetic susceptibility signal, thereby introducing anomalously high values. Before any mathematical treatment of the time series, these spurious peaks were subtracted from the data set and the series was resampled with a constant rate. This results in a sequence of 901 equispaced data points covering the entire stratigraphical thickness of the unit.

Before the processing, a visual assessment of the magnetic susceptibility data suggested that periodic

components might be recorded in the time series. This is clearly shown in figure 3.10 by the existence of various orders of long and short wavelength cyclicity bundled together in a more complex hierarchy.

Spectral Analysis

The best strategy in performing time series analysis on a stratigraphical data set is to apply a combination of different spectral algorithms, each one performing a specific task with particular advantages (Pestiaux & Berger, 1984; Hinnov & Goldhammer, 1991; Reijmer et al., 1994). Following this procedure, problems concerning the treatment of stratigraphical data can be tested and a better control against possible mathematical artefacts of the time series analysis can be obtained.

To avoid any predictable alteration of the signal amplitude in parts of the function, and to obtain a high level of precision during processing, some conditions must be checked before running the appropriate algorithms. First, the statistical properties of the time series should remain unaltered by shifts in the sampled interval origin (stationary condition). Then, the effect of long-term trends, which can cause a shift of the real amplitude in parts of the series, should be compensated for and eventually subtracted (linear trend and mean correction) (Diggle, 1990). Finally, the time series requires to be normally distributed statistically.

Because each processing routine is sensitive to a specific character of the time series, this approach permits a better resolution of the major properties of the original signal. The time series is processed using two spectral estimators: the Blackman-Tukey (BT) and the Maximum Entropy algorithms (ME) (see Paillard et al., 1996). Using these techniques in conjunction allows a better reconstruction of the most important spectral features and therefore ensures a high degree of significance when interpreting the results.

One of the most powerful and simple algorithms is the ME (Press et al., 1989), a routine designed to fit the sharp spectral peaks in the signal, giving a high-frequency resolution within the range of autoregressive models selected in the analysis together with a good control on the regularity of the *quasi*-periodic frequency. These advantages are sometimes diminished by the lack of statistical confidence estimate and some non-linearity in the evaluation of spectral lines, and can therefore produce undesirable spurious results. To test the statistical significance of the spectral values, the ME method is used here in conjunction with the BT, a very stable procedure for processing time series (Blackman & Tukey, 1958). This algorithm estimates the autocorrelation function from the data series, weighted by a Tukey window to discard possible bias, and computes the Fourier transform to obtain the power spectrum. Its design enables an estimation of some *a priori* random-noise models, like those originating by low-order autoregressions (Hinnov & Goldhammer, 1991), which are likely to be incorporated into the time series when sampling stratigraphical data. The spectral peaks were tested against two orders of

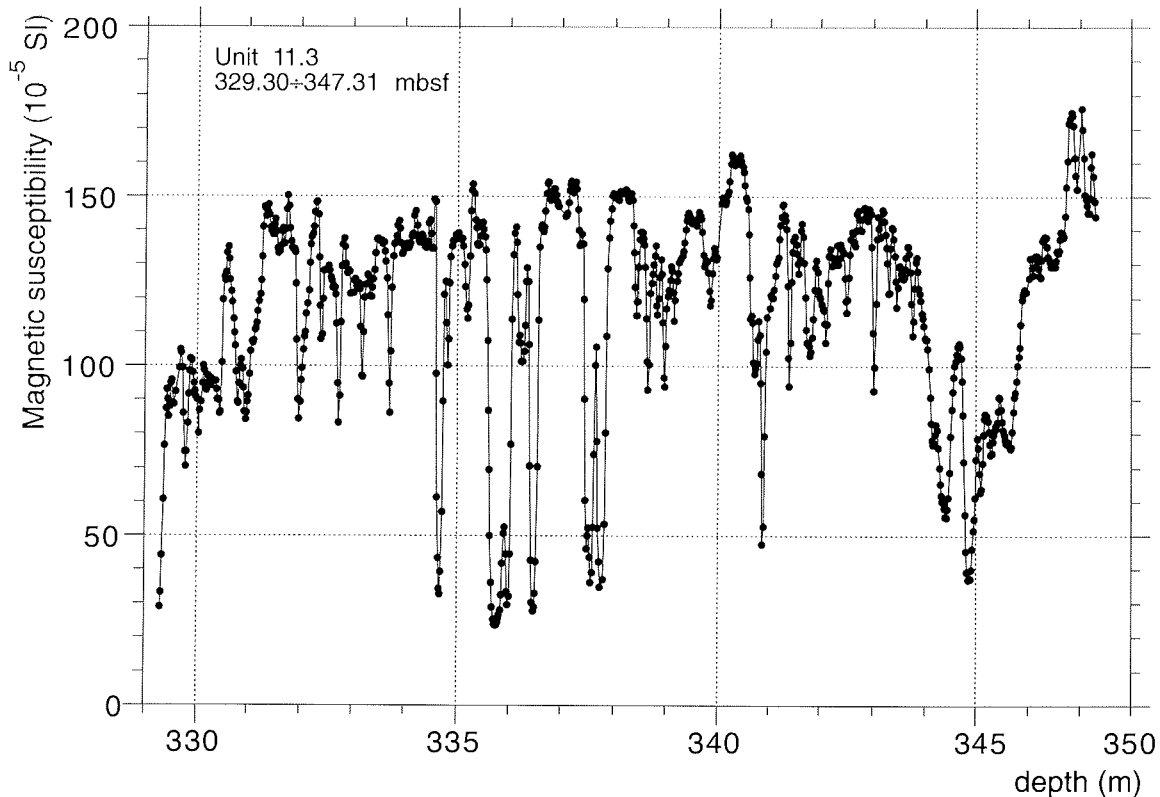


Fig. 3.10 - The low-field magnetic susceptibility of mudstone Unit 11.3, plotted *versus* depth. The high values of magnetic susceptibility induced by the presence of granitoid and basalt clasts are subtracted and the corresponding values linearly interpolated. The resultant time series was tested for periodicity by Blackman-Tukey and Maximum Entropy spectral analysis.

autoregression and only the values passing the two noise levels were taken into consideration. Therefore the combination of the two techniques will ensure a good degree of validity in the following interpretation.

Interpretation of the Spectral Peaks

In the spectra analysed, the values on the y-axis indicate the spectral power (expressed in arbitrary units) while the x-axis refers to frequencies in cycles/metre, from low-frequency (left) to high-frequency (right) periodicities. Peaks that were statistically significant (passing the 95% confidence level) and which exceeded the noise levels (given by the two first orders of autoregression) were converted in length of periodicity in cm and thus labelled with the appropriate value, while the others remained statistically meaningless and were disregarded. The results of the analysis carried out on the analysed unit displayed three major groups of periodicities.

Using the Blackman-Tukey algorithm with a short length of the autocovariance series (15%) the highest power peaks can be easily estimated (Fig. 3.11a). The most prominent peaks above the noise levels were at 426 cm, around 110 cm, and 60 cm. These values were similarly present when the same time series was processed by the Maximum Entropy routine (with the autocovariance series set at 7.5%, Fig. 3.11b): a dominant periodicity at 423 cm and then, with progressively less spectral power, peaks at 107 cm and 60 cm. A very weak peak was present

at 26 cm, but fell below the noise levels and therefore was regarded as no real periodicity, but as the product of highly-periodic *quasi*-random noise.

The presence of these frequency lines was confirmed when the time series was processed with the same routines but with higher values of autocovariance, providing additional spectral information on these periodicities. In the BT spectra, run at 50% of the autocovariance series (Fig. 3.11c), some of the broad peaks displayed in the previous analysis were split into two components, as for the periodicities at 165 cm and 102 cm, and at 62 and 55 cm. The strongest spectral line remained relatively constant at 441 cm. Similar components were resolved when the autocovariance was increased in the ME processing as well (to the value of 15%, Fig. 3.11d), revealing peaks at the corresponding values: 441 cm, 156 cm and 94 cm, and a single peak at 59 cm. As before, a broad group of frequencies (around 26 cm) did not pass the noise levels, and was not taken into account in the spectral interpretation.

Since the BT algorithm enables to test the spectral lines against the noise levels but lacks good resolution, which is conversely ensured by the ME, and since in the spectra many of peaks occurred at very similar frequencies, it is possible to summarize the most remarkable spectral features of the magnetic susceptibility in the mudstone Unit 11.3. Cyclic oscillations occurred with the following periodicities: 423-441 cm, 156-94 cm and 60-57 cm.

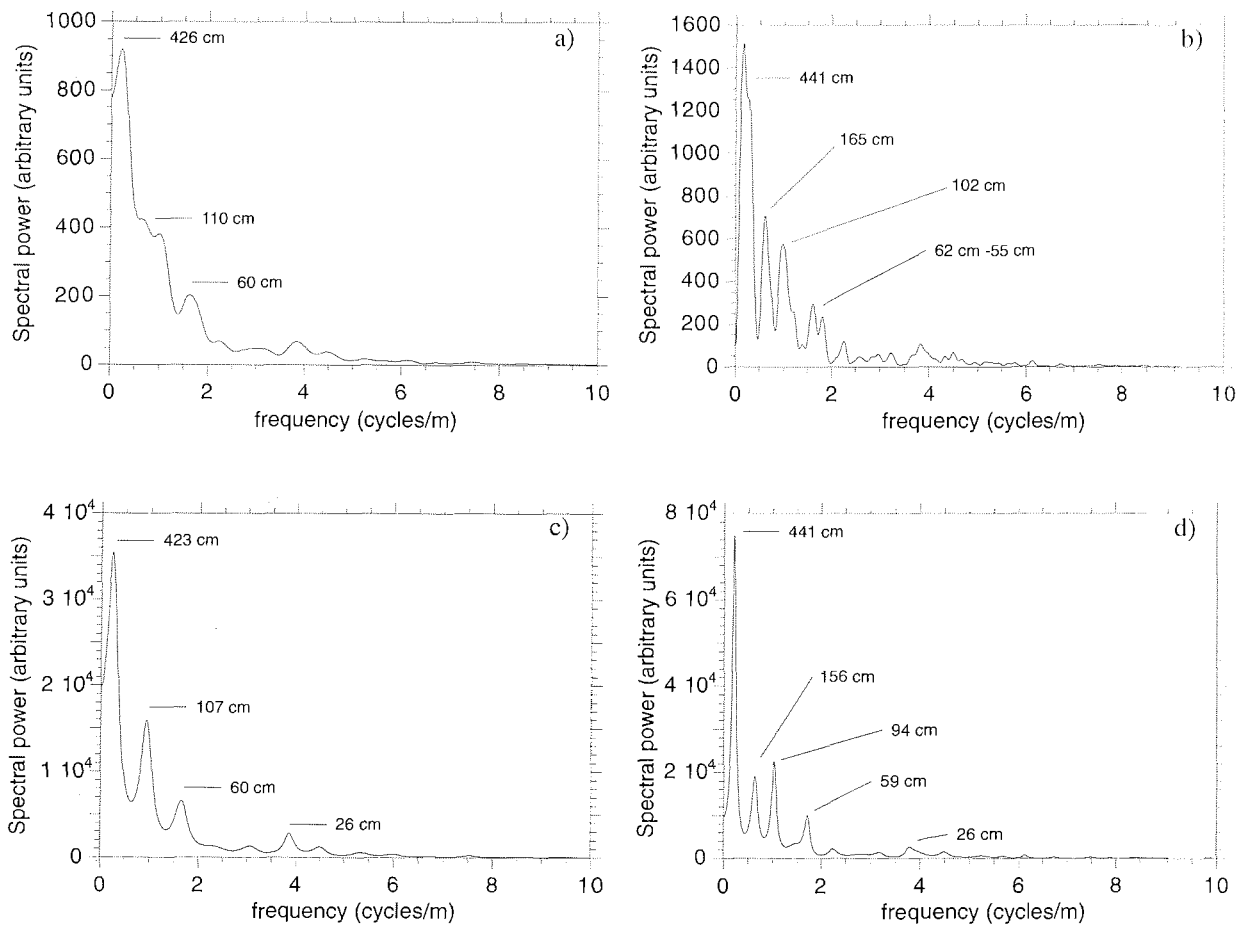


Fig. 3.11- a) Blackman-Tukey spectral analysis of the magnetic susceptibility time series (length of the autocovariance series is 15%). The peaks indicate the statistically significant broad groups of periodicities above the noise levels, and are expressed in cm by the corresponding labels. b) Maximum Entropy spectral analysis of the magnetic susceptibility series (length of the autocovariance series is 7.5%). This method provides a high resolution estimate of the spectral energy: the labelled peaks point to the most powerful single frequency lines. c) Blackman-Tukey spectral analysis of the magnetic susceptibility series (length of the autocovariance series is 50%). As in figure 3.11a the labelled peaks indicate only the statistically significant frequencies above the levels of noise. d) Maximum Entropy spectral analysis of the magnetic susceptibility series (length of the autocovariance series is 15%). The labelled peaks refer to the strongest single frequency peaks.

Discussion and Conclusion

Spectral analysis techniques were applied to the low-field magnetic susceptibility from mudstone Unit 11.3 of CRP-2/2A to test the possibility of the existence of a cyclic signature within this interval. This methodology (Pestiaux & Berger, 1984; Fischer et al., 1990; de Boer & Smith, 1994) proves clearly the existence of a regular and strong cyclic pattern in the magnetic susceptibility record of this interval and allows us to discard a stochastic mechanism as controlling its fluctuations. This should stimulate questions on the nature of the periodic forcing mechanism. The periodicities expressed in cm are compared each against the other and the relative ratios are calculated. In particular, when the major peaks are normalized to the highest frequency, the obtained ratios refer to hierarchies of decreasing wavelength from low to high frequency. The resulting relationships are summarized as follows.

wavelengths	441-423 cm	156-94 cm	60 cm
ratios	7.3-7.0	2.6-1.6	1

The application of this method is of considerable significance because the frequency lines in the power

spectrum now identify the ratios between the hierarchic levels of the cycles (Claps & Masetti, 1994).

A very high degree of similarity exists between these ratios and those obtained from the Milankovitch orbital forcing periodicities (short term eccentricity, obliquity and precession cycles) and their main components, computed for the Cenozoic (Berger, 1984; Berger & Loutre, 1994). These are tuned to the precession orbital cycle and reported as follows.

Milankovitch orbital cycles	eccentricity	obliquity	precession
duration	123-95 ky	54-41 ky	23-19 ky
ratios	6.5-4.2	2.8-1.8	1

While the obliquity/precession ratio matches precisely with the peaks identified at 156-94 cm, it should be pointed out that the eccentricity/precession ratio appears slightly lower than the ratio relative to the highest spectral peak. This may be induced by relatively small changes in the sedimentation rate occurring during the deposition of the mudstone interval. The presence of the three clear and significant groups of spectral lines with a very low level of noise and the positive relationship with the Milankovitch orbital ratios suggests that the

magnetic susceptibility signal might have been controlled by orbital forcing.

This quantitative approach suggests that the fluctuations of the magnetic susceptibility provide a very sensitive tool for recording high-frequency periodicities. Further detailed analysis applied on other intervals of the CRP-2/2A, and cross-correlated with cyclicity in the sedimentary facies, could offer a broader understanding of the effect of external forcing mechanisms on the magnetic and sedimentary signals.

DIAGENESIS

INTRODUCTION

This section describes the main diagenetic features recorded throughout the core from the CRP-2/2A drill hole. The goal of this preliminary investigation is to provide a comprehensive description of carbonate patches, carbonate-cemented concretions/nodules, veins, mineralization in fractures, in sedimentary dykes and burrows.

Macroscopic observations and some preliminary investigations on thin-sections and smear slides (using a petrographical microscope) were carried out on 122 samples selected to show both lithological and diagenetic variation. Results from these studies are summarized below. The distribution of these main diagenetic features (over 625 m interval) is recorded in the summary lithological log (100 m/page in section 3 in the supplement to this issue).

DESCRIPTION OF

MACROSCOPIC DIAGENETIC FEATURES

Lithostratigraphical Sub-Unit 2.1 (5.54-21.16 mbsf), Sub-Unit 2.2 (21.16-26.80 mbsf). No cementation patterns were recognized in Quaternary strata consisting of "unconsolidated, massive, locally weakly stratified, very poorly sorted, clast-rich sandy diamicton". The sparse fractures are open and do not show any mineralization. Pliocene strata consisting of diamicton and sand are unconsolidated and uncemented.

Lithostratigraphical Sub-Unit 3.1 (26.80-47.79 mbsf). This unit contains few weakly carbonate-cemented patches in its lower part below 33.50 mbsf. Carbonate cementation occurs within the *in-situ* brecciated interval in the lower part of the unit, below 37.80 mbsf.

Lithostratigraphical Sub-Unit 4.1 (47.79-51.94 mbsf). The unit described as diamicton shows only sparse, weakly carbonate-cemented patches.

Lithostratigraphical Sub-Unit 5.1 (51.94-72.84 mbsf). This unit is locally carbonate-cemented and intensely brecciated between 54.59 and 55.20 mbsf and in the lower part of the unit. Samples from 55.12, 56.07 and 68.18 mbsf, consisting of mudstones and muddy fine sandstones, show a moderate degree of carbonate cementation and contain fossil fragments (pectinids, serpulid tubes) which show some dissolution patterns on the shells.

Lithostratigraphical Sub-Unit 6.1 (72.84-80.70 mbsf), Sub-Unit 6.2 (80.70-90.67 mbsf), Sub-Unit 6.3 (90.67-96.85 mbsf). Unit 6.1 shows no evidence of carbonate

cementation. A sample at 80.10 mbsf prepared for fossil examination appears locally strongly carbonate-cemented and contains partially corroded shell fragments. Unit 6.2 contains scattered carbonate cemented patches and a prominent carbonate-cemented nodule at a depth of 89.38-89.52 mbsf showing an increase in cementation upwards. Unit 6.3 shows locally moderately carbonate-cemented zones and a calcite-filled hairline fracture composed of finely crystalline calcite cement at a depth of 95.27 mbsf. Units 6.1 and 6.3 are strongly brecciated and contain fossil debris.

Lithostratigraphical Sub-Unit 7.1 (96.85-109.07 mbsf), Sub-Unit 7.2 (109.07-114.21 mbsf). No macroscopic evidence of diagenesis was noted in these units which consist of volcanoclastic lithologies.

Lithostratigraphical Sub-Unit 8.1 (114.21-130.27 mbsf), Sub-Unit 8.2 (130.27-137.79 mbsf), Sub-Unit 8.3 (137.79-153.38 mbsf), Sub-Unit 8.4 (153.38-183.85 mbsf). A large carbonate-cemented nodule was recorded at 117.89-118.09 mbsf, a few centimetres below a horizon of shell debris. Diffuse carbonate cementation occurs at 126.32 and 128.00 mbsf. The incipient carbonate diagenesis is marked by the development of microcrystalline calcitic cements occurring as patches (117.88, 132.27 mbsf) and as infilling in hairline fractures (137.22 mbsf). Unit 8.2 consists of fine sandstones, carbonate cementation is diffuse, a 4 cm carbonate nodule occurs at 132.27 mbsf and hairline calcite-filled fractures occur in the lower part below 132.21 mbsf. In Unit 8.3 at a depth of 144.26-147.65 mbsf within the brecciated interval fractures are mostly open, some show calcite mineralization; a siltstone-filled sedimentary dyke was recorded at 146.88 mbsf and mineralization occurs along a microfault at 152.46 mbsf. In Unit 8.4 the fractures are partially mineralized as recorded at a depth of 153.87, 163.12, 163.19, 173.42 and 176.22 mbsf; carbonate cementation occurs as patches around serpulid tubes in the lower part at 178.04-183.35 mbsf.

Lithostratigraphical Sub-Unit 9.1 (183.35-185.94 mbsf), Sub-Unit 9.2 (185.35-193.61 mbsf), Sub-Unit 9.3 (193.61-250.40 mbsf), Sub-Unit 9.4 (250.40-262.00 mbsf). No carbonate cementation has been recorded in Unit 9.1. In Unit 9.2 carbonate patches, focused around shell debris, occur at 187.40 and 191.42 mbsf. In Unit 9.3 a few mineralized fractures occur at a depth of 195.17 and 195.59 mbsf; carbonate cementation in patches and concretions was recorded at 202.94, 210.20, 241.70, 244.80, 245.50 and 249.65 mbsf. A sample from 210.20 mbsf consists of a pale coloured carbonate-cemented siltstone containing a few fragments of moderately-preserved shells and several moulds of large molluscan and serpulid tubes. The moulds seem to be filled by fine to drusy calcitic cements. The sample from 241.70 mbsf is a diamictite showing varying amounts of carbonate cementation within the muddy matrix. At 244.80 mbsf muddy sandstones appear carbonate-cemented and contain preserved bivalve debris. At 245.50 mbsf a few carbonate patches occur in laminated siltstones. At 249.65 mbsf cemented patches are developed within thick shell debris of well-preserved bivalves. Linings from some open fractures in siltstones were sampled at 247.90 and 248.02 mbsf in order to check

the occurrence of mineralization; the composition seems to reflect the surrounding poorly lithified lithologies. Abundant pyrite infillings in burrows are present in sandy siltstones at different depths from 253.80 to 271.00 mbsf in association with some moderate carbonate-cemented patches. Carbonate cementation was recorded throughout the siltstones; strong carbonate cementation at 272.57, 274.36, 277.92, 281.92, 285.24, 291.46, 294.16 mbsf (usually around shells) and a centimetric nodule at 280.92 mbsf. Shells show different degrees of preservation; the large gastropods from samples at 285.24, 291.46 mbsf seem to be partially dissolved.

Lithostratigraphical Sub-Unit 10.1 (295.58-306.65 mbsf). No diagenetic features were recorded in the upper part, from 295.58 to 297.01 mbsf. From 297.01 to 306.65 mbsf within a strongly deformed sequence of siltstones/diamictites a few carbonate cemented patches are present at 297.42, 302.37 and 306.32 mbsf.

Lithostratigraphical Sub-Unit 11.1 (306.65-315.59 mbsf), Sub-Unit 11.2 (315.59-347.29 mbsf). Moderately-cemented carbonate patches were noted at 308.30, 310.80 and 315.85 mbsf within a strongly disrupted sequence of different lithologies. A centimetric-wide sedimentary dyke at 315.66 mbsf contains pyrite mineralization. From 329.30 to 347.29 mbsf in a dark grey siltstone/sandstone sequence containing abundant shell debris, serpulid tubes and burrows, carbonate cementation occurs at 337.70, 341.86, 342.00 and 342.11 mbsf around partially dissolved shells. Hairline vein-fills are common and pyrite was recorded throughout the sequence and as infilling in sedimentary dyke at 337.46 mbsf.

Lithostratigraphical Sub-Unit 12.1 (347.29-442.99 mbsf). Complex interbedded sandy diamictites contain diffuse carbonate patches recorded at 357.28, 364.50, 365.60, 373.90, 379.68, 380.62, 385.70, 397.30, 401.47, 404.54, 405.10, 407.91, 408.12, 420.82, 423.13, 423.78, 426.66, 430.14, 432.51, 435.17 and 435.69 mbsf. The carbonate cement seems to be developed as fringes around grains and within the matrix. Some open fractures, containing brownish linings, and calcite and mineral-filled (not calcite) fractures were recorded at a variety of depths throughout the sequence.

Lithostratigraphical Sub-Unit 13.1 (442.99-516.40 mbsf). The upper part of the sequence (from 442.99 to 484.10 mbsf) mostly consists of siltstone/sandstone lithologies, containing abundant bivalves and gastropods, some in growth position. Shells show different degrees of preservation from well-preserved to moulds showing only some relicts of the original shell and the development of fine to drusy calcitic cementation (444.10, 446.30, 449.32 and 471.06 mbsf). Carbonate cementation occurs in patches at different depths at 450.70, 460.20, 460.43 and 462.20 mbsf, increasing in size and degree of lithification below 467.80 mbsf; below this depth carbonate cementation increases forming (besides sparse patches) discrete well-cemented layers up to a few cm thick (at 469.06, 471.39, 474.59, 475.08, 482.34). A calcite-filled sedimentary dyke occurring at 511.32 mbsf shows different generations of carbonate cementation. Burrows are abundant and some show pyrite infilling (at 446.00, 468.66, 471.73 mbsf). Pyrite mineralization (associated with calcite cement)

within several mm-thick sedimentary dykes occurs at depths of 446.00, 449.34 and 459.58 mbsf. Below 484.10-516.40 mbsf, carbonate cementation is strongly developed in sand/sandstone lithologies and forms millimetric and centimetric nodules. The millimetric nodules are up to 4 mm in size, poorly indurated and consist of carbonate-cemented sand grains. The centimetric nodules range in size from 1 to 2 cm and show different stages of cement development. The millimetric carbonate-cemented nodules occur within loose coarse sands at 484.65, 485.62, 496.70, 497.52, 501.05, 501.90 and 504.00 mbsf. The carbonate-cemented nodules (up to 2 cm) gradually increase in size and coalesce to form coherent layers as recorded at 486.96, 496.89, 497.10, 501.20, 501.71 and 504.32 mbsf. Within the well-lithified sandstones, micronodules are poorly defined.

Lithostratigraphical Sub-Unit 14.1 (516.40-535.45 mbsf). This unit is a complex sequence of pebble conglomerates/sandstones/sandy siltstones showing patchy carbonate cementation within the upper part of the conglomerate and well developed carbonate-cemented nodules within sandstone lithologies in the lower part at 525.28, 532.11, 532.77-535.45 mbsf. Sandstones at 528.40-531.20 mbsf show an unusual greenish colour related to the occurrence of chlorite formed by deuteric alteration of mafic volcanic rocks.

Lithostratigraphical Sub-Unit 15.1 (535.45-545.16 mbsf), Sub-Unit 15.2 (545.16-574.20 mbsf), Sub-Unit 15.3 (574.20-584.75 mbsf), Sub-Unit 15.4 (584.75-601.53 mbsf), Sub-Unit 15.5 (601.53-614.56 mbsf), Sub-Unit 15.6 (614.56-624.15 mbsf). The upper muddy sandstones (from 535.45 to 545.16 mbsf) are mostly deformed and contain diffuse carbonate and/or pyrite mineralizations within fractures and along faults (at 536.18, 536.25 and 538.09 mbsf); some appear cut and displaced by later faults, reflecting multiple phases of deformation (at 539.07, 542.83 and 543.13 mbsf). Carbonate patches are common and pyrite micronodules, probably of biogenic origin, are dispersed within the matrix. The sequence appears strongly carbonate-cemented: coherent layers 4-8 cm thick, several hairline calcite-filling fractures and abundant calcite mineralizations were all recorded. Mineral-fillings are often cut and displaced by faults (579.28, 599.83, 602.27, 602.82 and 619.98 mbsf) and seem to be composed of fine to blocky to drusy calcite crystals (563.78, 565.70, 559.83, 602.82, 604.14 and 606.08 mbsf); some mineralization is within wide carbonate cemented patches (602.27 mbsf). Pyrite occurs in fractures at different depths (596.90, 602.20 mbsf), and is associated with a fringe of carbonate cement at 606.11 and 618.98 mbsf.

SUMMARY OF RESULTS

Carbonate cementation. Carbonate cementation is rare in the upper 150 mbsf of the core where it occurs as light-coloured centimetric patches, especially in coarse lithologies. Below this depth, carbonate cementation increases with lithification and becomes more extensive below 400 mbsf in all lithologies. It occurs in fossiliferous concretions/nodules containing shell debris; the incipient

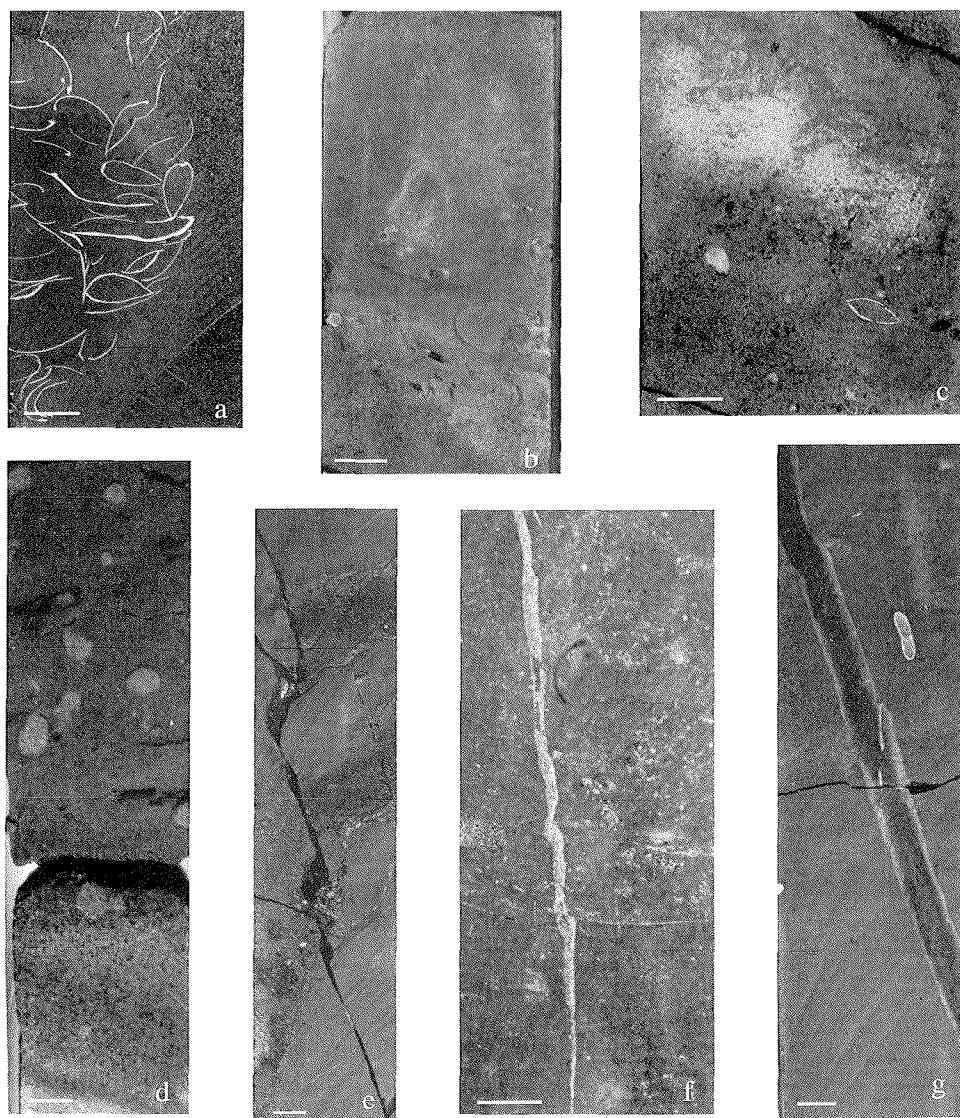


Fig. 3.12 - Close-ups from CRP-2/2A core showing some macroscopic diagenetic features (scale bar 1 cm). *a*) shell debris of preserved and many still articulated bivalves (coquina, 249.70 mbsf); *b*) large carbonate concretions containing pectinid shells, serpulid polychaete tubes and gastropod moulds, partially cemented by fine to drusy carbonate (210.20 mbsf); *c*) diffuse patchy carbonate cementation containing an articulated bivalve (195.40 mbsf); *d*) calcite-fills developed along microfaults (447.18 mbsf); *e*) open fracture in siltstone/sandstone sequence (338.20 mbsf); *f*) sedimentary dyke showing pyrite-fills associated with a thin light-coloured calcite rim (337.70 mbsf).

diagenesis is indicated by corrosion and partial dissolution of the biogenic tests. Bivalves, gastropods and serpulid polychaete tubes show a wide variety of preservation stages ranging from well preserved, to partially dissolved, to solution moulds cemented by calcite (Fig. 3.12a, b & c). Heavily corroded tests may be internally cemented by blocky crystals of calcite; in some cases, the moulds are filled by fine drusy calcitic cement (solution-cavity fill).

Millimetric and centimetric carbonate-cemented nodules were observed within coarse sand/fine-medium sandstone lithologies (Fig. 3.12d). The sandy millimetric nodules are a few millimetres in size and poorly indurated. In preliminary observations of thin-sections they seem to be entirely composed of carbonate-cemented well-washed sand grains and do not show any internal texture. They might be formed in areas of high-energy, as suggested by the sedimentary structures (see Description of Sequence), where sedimentation rates are low, but the origin of the

carbonate has yet to be clarified. Centimetric carbonate-cemented nodules show preserved radiaxial textures around detrital grains consisting of tiny coal particles. Coal might act as nucleus for their formation, as previously recorded in glacio-lacustrine/glacimarine deposits where the formation of carbonate concretions are related to organic carbon-carbonate diagenesis (Lamothe et al., 1983).

Mineral-fills. In the upper 150 mbsf, where carbonate cementation is rare, fractures within the brecciated intervals are open; some show a thin soft brownish lining reflecting the same composition of the surrounding poorly consolidated matrix (Fig. 3.12e). Very thin calcite-filled veins (hairline) first occur below 90 mbsf and vary in orientation from horizontal to vertical with respect to bedding, ranging in size from less than 1 to 10 mm wide. They were observed especially in fine-grained lithologies, and are composed of finely microcrystalline calcite cement. Below 300 mbsf, calcite mineral-fills are intensely

developed along fractures and microfaults (Fig. 3.12f); below 500 mbsf calcite mineralization appears to be composed of different generations of cementation.

Pyrite. Pyrite is present as infilling in burrows (below 250 mbsf) in siltstone lithologies and is moderately abundant in the intervals 251.80-271.00 mbsf, 446.00-472.15 mbsf, 535.45-560.00 mbsf, 597.00 mbsf and 602.20 mbsf. Pyrite also occurs as infilling associated with a thin light-coloured calcite rim in 1 cm-wide sedimentary dykes in silt/sand lithologies (Fig. 3.12g). Irregular patches and zones of pyrite-fills were recorded at different depths below 310 mbsf, within disrupted intervals.

Detailed investigations of the texture, ultratexture and composition of selected samples from CRP-2/2A drill hole will provide the necessary information to better understand the diagenetic processes affecting the sequence.

Previous studies described the diagenetic features of samples from the CRP-1 drill hole, located 800 m east of CRP-2/2A hole (Baker & Fielding, 1998) and from the CIROS-1 drill hole on the western edge of the Victoria Land Basin (Bridle & Robinson, 1990). Carbonate cementation associated with shell material occurring in all lithologies suggests a relationship between selective dissolution of aragonitic shells and precipitation of authigenic carbonate (Fig. 3.12a, b & c) as previously described in the core from CRP-1 drill hole by Claps & Aghib (1998). Calcite cementation occurring as mineral-fills in veins and fractures might be related to the migration of carbonate-rich waters, especially within disrupted/brecciated intervals, and subsequent cementation (Fig. 3.12d). Carbonate precipitation might have a mixed marine-meteoric origin due to the infiltration of meteoric waters during period of glacial advance over the CRP-2/2A drill hole as suggested in the Miocene sequence from CRP-1 core (Baker & Fielding, 1998). Pyrite mineral-fills recorded below 300 mbsf in the CRP-2/2A core may represent an early stage in diagenesis as previously reported at DSDP Site 603 in the eastern Atlantic Ocean, along the continental rise (von Rad & Botz, 1983). Pyrite recorded in dark mudstones (below 250 mbsf) as infilling burrows and as micronodules in palaeontological preparations may be related to bacterially-mediated redox reactions in organic-rich sediments (Berner, 1984).

DEFORMATION

INTRODUCTION

Structural features, such as brecciation, soft-sediment folding and shear zones, were described from the sample half of the CRP-2/2A core prior to sampling, to obtain an overview of the down-core distribution and style of natural brecciation and soft-sediment deformation. In CRP-1 brecciated intervals below massive diamictites, commonly accompanied by soft-sediment deformation, were interpreted as the effect of grounded ice (Passchier et al., 1998). The identification of ice-grounding events is important, because it indicates the location of possible major erosion episodes, which form hiatuses in the stratigraphical record, and it contributes to the palaeo-

climate record of the area. In addition, a representation of the deformation history of the core will improve the accuracy of palaeontological datums, since deformation is associated with variable degrees of transport and reworking of sediments. An attempt was made to distinguish between deformation caused by drilling, large-scale tectonic processes and glaciotectonics.

In the core, both ductile and brittle sediment deformation features occur. Brittle deformation can take place in consolidated and in unconsolidated sediments. In unconsolidated sediments, ductile deformation is indicative of a water-saturated state of the sediment. The presence of visible deformation is caused by low strain of the sediment. At high strain the sediment will be homogenised to a degree that deformation can only be observed in thin section (van der Meer, 1993). The presence of primary sedimentary structures facilitates the identification of deformation features (sediments that were structureless when deposited, will still look structureless when deformed). The absence of macroscopic structural features, therefore, does not exclude deformation of the sediment.

CRP-2/2A is located in a tectonically active rift-margin setting in a glacially dynamic environment, which suggests both large-scale tectonic and glaciotectonic processes could cause deformation of the sediment. Typical environments where low strain deformation occurs are tectonically unstable sloping environments with high pore water pressures in the sediment, proglacial ice-contact or subglacial environments with a thick deforming bed (Boulton, 1996). High strain deformation is localized in thin zones and is recognized as extensive shearing of sediment. Shearing takes place in faults and in thin deforming beds beneath glaciers (Alley et al., 1997).

In addition to the deformation features, clastic dykes are present in the core. Clastic dykes are described from both extensional tectonic (*e.g.* Bergman, 1982), terrestrial subglacial (*e.g.* Larsen & Mangerud, 1992) and glacial marine environments (*e.g.* Von Brunn & Talbot, 1986).

PROCEDURES

Breccia types, microfaults, soft-sediment deformation features and shear zones were identified on the cut core face and described. In claystones, brecciation may be obscured by clay being smeared on the cut surface of the core (*e.g.* ~94 mbsf). Extra care was taken in examining claystones to identify deformation. Drilling-induced deformation was also recognized and eliminated from the analysis. In the core, concentric grooves on horizontal fracture surfaces point to spinning of segments of core around a vertical axis. Rotation of segments of core is also likely to be the cause of some loose rubbly intervals within brecciated segments. In this case, the breccia is a geological feature and the rubble is the result of drilling.

Breccias (Fig. 3.13) were classified according to the definitions presented in Passchier et al. (1998). Both normal and reverse microfaults were observed in the core, normal faults being more abundant (Fig. 3.14). Soft-sediment deformation features described are: folding, rotated clasts, convolute bedding and chaotic sediment mixing. Three types of shear zones were recognized:



Fig. 3.13 - Brecciated fine sandstone at ~45 mbsf. The brecciation is of chaotic type (see Passchier, 1998).

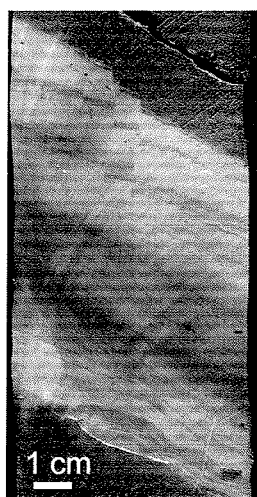


Fig. 3.14 - Normal microfaulting between ~76.2 and 176.35 mbsf. Note soft-sediment deformation at the bottom of microfaulted zone.

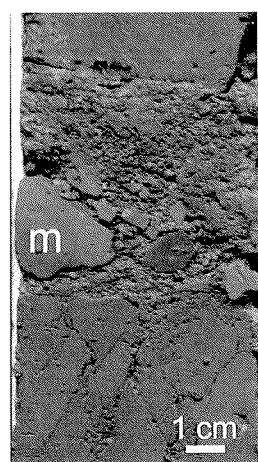


Fig. 3.15 - Small-scale cataclastic shear-zone, with a large intraclast of a microlaminated facies (m) and other intraformational pebbles and granules at 66.76-66.83 mbsf. The microlaminated facies is not present above or below the shear zone. Note *in situ* crackle breccia below the shear zone and the sharp contact with the host rock.

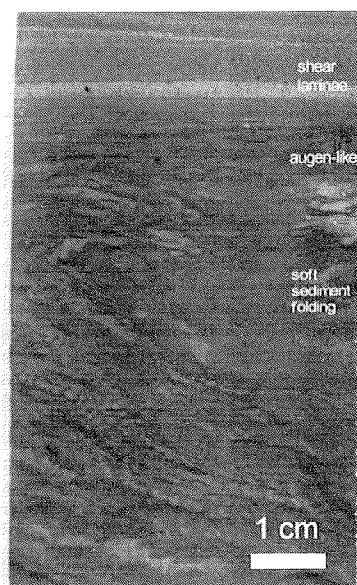


Fig. 3.16 - Possible shear zone in very fine sandstone at ~581.4 mbsf. Note increasing strain upward in the picture, expressed by a transition from soft-sediment folding at the bottom to horizontal shear laminae at the top.

1) small-scale cataclastic shear zones consisting of intraformational abraded pebbles and granules within cemented fine sandstones (Fig. 3.15), 2) soft-sediment folding progressing into bedding attenuation (Fig. 3.16), and 3) augen-like structures in lithified very fine-grained sandstones.

DESCRIPTION OF DEFORMATION ABOVE ~297 mbsf

Above ~297 mbsf, deformation is confined to discrete intervals. The uppermost record of localised *in situ* brecciation in the core is at ~11 mbsf, in a Quaternary diamicton. The strata above this level contain cemented intraclasts, of which some are subrounded, possibly indicating transport. Below the Quaternary, brecciation of the CRP-2/2A core occurs, similar to CRP-1, mainly in

sandstones and siltstones. Brecciation intensifies at ~38 mbsf and decreases below ~150 mbsf. Soft-sediment deformation and microfaults are common throughout the core below ~40 mbsf.

Between 44.91 and 47.87 mbsf chaotic breccias, folds and thrusts point to extensive deformation of the sediment (Fig. 3.16). Between ~50 and ~71 mbsf the sediments are heavily fractured. Breccia textures can be described as jigsaw-puzzle fit (crackle breccias), interrupted by chaotic and rubbly zones. Fractures are mainly open, but SEM studies of open fractures from CRP-1 have shown that a thin fill may be present which cannot be identified with the unaided eye (Baker & Fielding, 1998). A small-scale cataclastic shear zone consisting of a ~5 cm wide interval of abraded material was identified at 66.76-66.83 mbsf

(Fig. 3.15). The breccia is developed in mudstone and sandstone below a massive, clast-poor diamicton. The bottom of the diamicton is dissected by sandstone- and siltstone-filled veins with a subhorizontal to inclined orientation. The core is locally fractured between ~71 and ~93 mbsf, but these fractures may be induced by coring.

The sediment is again deformed between 93.85 and 98.64 mbsf. Deformation consists of crackle breccias in mudstone and zones of subangular fine sandstone clasts in a fine sandstone matrix. Laminae in a diamictite below this brecciated zone are possibly a result of soft-sediment folding (tectonic lamination).

Another deformed interval of core occurs between 120.15 and 135.74 mbsf. The deformation consists of crackle breccias with angular clasts and soft-sediment deformation. Planar fractures with steep dips occur within this interval. Between 120.15 and ~131 mbsf the deformation is discontinuous and consists mainly of soft-sediment folding alternating with bioturbated zones. Between ~131 and ~132 mbsf *in situ* fracturing of the core has resulted in a jigsaw puzzle fit of large angular clasts. Another brecciated zone begins at 134.74 and abruptly terminates at 135.74 mbsf.

Further breccias occur between ~145 and ~150 mbsf. The textures are chaotic and associated with clastic intrusions of sands into fractured mudstone. At the bottom of this interval is a >5 cm wide sandstone dyke, whose true width cannot be determined because it is cut by the edge of the core. The infill is a partly cemented, structureless, poorly sorted fine to medium sand with dispersed coarse to very coarse sand. The mudstone is brecciated along a near-vertical contact with the sandstone dyke.

Local decimetre-thick crackle breccias occur between ~150 and ~163 mbsf. These await further work to determine whether they are natural breccias or drilling-induced. Between 176.2 and 196.9 mbsf isolated microfaults, zones of soft-sediment deformation and clastic intrusions are present.

Between 183.35 to 185.95 mbsf is a shear zone identified from the presence of folded laminae and a pressure shadow behind a clast (Fig. 3.17). The shear zone developed in a mudstone and has sharp contacts with the overlying mudstone and the underlying partly stratified diamictite.

Vertical fractures are a further interesting feature below a diamictite at ~245 mbsf. Apart from these fractures, the interval between ~245 and ~298 mbsf shows minimal deformation.

DEFORMATION OF SEDIMENT BELOW ~297 mbsf

The character and intensity of deformation of the core changes markedly at ~297 mbsf. *In situ* brecciation is scarce below this level, but microfaulting, clastic intrusions and other soft-sediment deformation are common throughout the lower part of the core. A clastic dyke cross-cuts a calcite-cemented patch at ~297.4 mbsf and a cemented patch is faulted at ~468.7 mbsf.

The uppermost deformed interval extends from ~297 to 308 mbsf. The diamictites at the top of this interval show folding and tectonic lamination, whereas the sandstones



Fig. 3.17 - Sheared medium sandstone at ~183 mbsf. Note sharp contact at the top of the sandstone and the pressure shadow to the left of the clast.

are deformed in a brittle fashion with abundant steeply dipping normal microfaults and some breccia. At ~306 mbsf the bottom of a diamict contains a diamict intraclast and is sheared below it (Fig. 3.18). The underlying mudstone is brecciated with rubble breccia grading down into *in situ* brecciation. At ~311 to 315 mbsf a thick sedimentary mudstone breccia occurs. Between ~315 and 327 mbsf microfaults and clastic dykes are abundant through a complex of interbedded lithologies. From ~327 to ~501 mbsf, deformation in mudstone units is limited to microfaulting. The diamictites and sandstones show signs of soft-sediment folding, sometimes overprinting of two folding events can be recognised (*e.g.* ~382 mbsf). A possible shear zone is present at the bottom of a diamictite at ~362 mbsf, associated with a clastic dyke with a diamict infill. Partly pyritized sandy mudstone dykes occur at ~447 mbsf (Fig. 3.19). These dykes range in width from several mm to about one cm and the walls are lined with finer-grained material.

The bottom part of the core between ~501 and 614.15 mbsf includes structures described as convolute bedding, load casting, mineral-filled veins, some local brecciation and shear planes. Some clastic dykes are offset by faults (*e.g.* ~535-540 mbsf). Abundant microfaults, pebbles with rotational structures, breccias and many clastic injections occur between ~524-527 mbsf and between ~543 and 552 mbsf. A very fine sandstone between 579.02 and 580.99 mbsf is strongly lithified and shows mm-scale augen-like structures, which cannot be explained by any sedimentological process. The same type of augen-like structures occurs between 608.7 and 610.7 mbsf and between ~614 and ~614.2 mbsf. The sandstones are folded and sheared, with clastic intrusions and microfaults in this lowermost interval of deformed

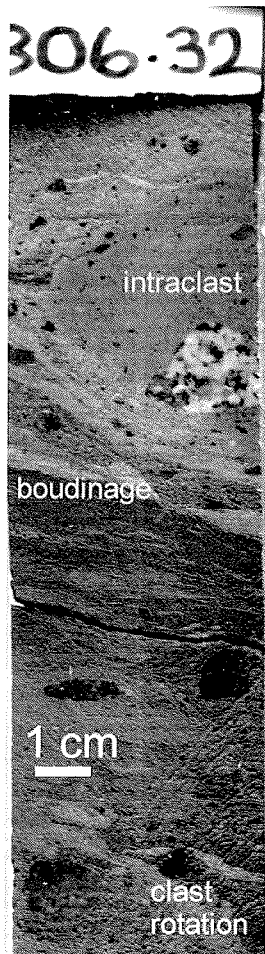


Fig. 3.18 - Sheared diamictite at ~306 mbsf. Note rotated clast at the bottom of the picture, boudinage and intraclast at the top.

sediment running from ~578 mbsf to the bottom of the hole at 624.15 mbsf.

DISCUSSION

Sandstones at the bottom of the hole may be highly sheared between ~614 and ~614.2 mbsf, between 608.7 and 610.7 mbsf, and between ~579 and ~581 mbsf (Fig. 3.16). Thin-section analysis of the structures is expected to reveal what process caused the augen-like structures in these intervals. In general, between ~297 and ~614.15 m, deformation of the sediments resulted in soft-sediment folding in the diamictites and brittle deformation of sandstones and mudstones. Diamictites have low permeability, retain water, and therefore behave ductilely under stress, whereas sandstones and mudstones (mostly siltstones) show brittle failure due to lower pore-water pressures. The deformation of diamictites, sandstones and mudstones may have occurred at the same time, but the differences in competence of the materials resulted in different deformation styles. This mechanism is illustrated by structures between ~306 and ~308 mbsf, where increasing strain upward towards the bottom of the diamictite suggest that a connection may exist between soft-sediment shearing of a diamictite and brecciation of the underlying mudstone. This arrangement of structures



Fig. 3.19 - Clastic dykes at ~447 mbsf. Note textural difference between material along wall and in the centre of the large dyke.

could be the result of grounded ice overriding the diamictite.

A fault cross-cuts a calcite cemented patch at ~468.7 mbsf, and a clastic dyke cuts through a cemented part of the core at ~297.4 mbsf, suggesting that some brittle deformation postdates the lithification of the sediments. At this point it is not possible to interpret the origin of all microfaults. Possibly at least two deformation episodes affected the strata below 297 mbsf: an early episode when the sediment was still unconsolidated, and another episode when the sediments were lithified. Possible processes, which could result in deformation of unconsolidated sediments and clastic intrusions include mass-movement, iceberg calving and scouring, and subglacial deformation beneath grounded ice. Faulting and clastic intrusions into extension fractures in lithified material may be caused by tectonics associated with uplift of the rift margin and the development of the basin.

The shear zone at 183.35 mbsf (Fig. 3.17) may be a result of either mass-movement or subglacial shearing. Either way, it is most likely that sediment has been removed and that there is a gap in the record. The clastic dyke associated with brecciation at ~145 to ~149 mbsf is overlain by a massive fine-grained sandstone with dispersed clasts. The brecciated fabric of the mudstone and the sandstone infill of the dyke suggest that high fluid pressures in the sand caused the mudstone to fracture. Possibly the injection was a single short-lived event, because there is no apparent stratification of the infill and some rip-up clasts from the mudstone are still nearly in place. Similar structures have been described from extensional tectonic (Bergman, 1982), glacio-marine (Von Brunn & Talbot, 1986) and subglacial environments (Larsen & Mangerud, 1992).

Fractured core between 130 and 131 mbsf may be attributed to grounded ice, although fractures between 134.74 and 135.74 mbsf may be drilling induced. A

diamictite is present above the brecciated sandstone with a gradational contact between the two at 130.27 mbsf. The brecciated intervals at ~93-98, ~50-71 and 44.91-47.87 mbsf show similarities to breccias observed in CRP-1, which were interpreted as the result of grounded ice (Passchier et al., 1998).

SUMMARY

The preliminary description of deformed intervals of core suggests that soft-sediment shearing and brecciation occurs at least down to 552 mbsf. Sheared and brecciated strata are also present at ~44-47, ~50-71, ~93-98, ~130, ~183-185, ~306-308, ~362, ~382 and ~524-527 mbsf. Augen-like structures suggest that more shear zones may occur at ~580, ~609 and ~614 mbsf. Emplacement of clastic dykes includes rapid multiple event injections resulting in graded or laminated infills, and single event injections of sand.

Some deformation is associated with grounded ice close to or over-riding the location of the drill-site. However, especially in the lower part of the core deformation is complicated by multiple deformation events. It is also possible that, for certain intervals of the core, extensional tectonics in the basin coincided with ice-grounding events. The cross-cutting relationships between diagenetic features, faults and soft-sediment deformation need to be evaluated in more detail using Corescan images of the cut surface to determine the sequence and style of deformation events. Perhaps, orientation of the core will lead to a reconstruction of stress fields, using the strike and dip of fractures and faults as determined from whole-core scans. Thin-section studies of possible shear zones and sheared diamictites will help to define the stress regime during deformation, and the grain-size, fabric, and composition of the clastic material in dykes. Both types of data will help to constrain interpretations of the deformation features in the core.

4 - Petrology

INTRODUCTION

Preliminary petrological characterization of the Lower Miocene to Lower Oligocene(?) sedimentary sequence of CRP-2/2A is aimed at detecting the most relevant features related to the evolution of a basin which previous studies have shown received discharge mainly from the adjacent region of the Transantarctic Mountains (TAM) through local polar outlet glaciers (Barrett et al., 1981; Barrett et al., 1995; Armienti et al., 1998; Bellanca et al., 1998; Smellie, 1998).

Distinctive markers for the history of the sediment transport into the basin are represented by the relative abundance of detritus coming from the crystalline basement, sandstones of the Beacon Supergroup, Ferrar dolerites and Kirkpatrick basalts and alkaline rocks from the McMurdo Volcanic Group (MVG). All these possible sources were easily detectable in the sedimentary sequence with the limited analytical techniques available during the drilling phase. The methods which were adopted include counting and identifying all clast types, microscopic examination of rock thin-sections and smear slides of sandstones, characterization of organic compounds and X-Ray Diffraction analysis of the silt and clay fractions. These methods have allowed us to reach some general conclusions which, although needing further confirmation from more detailed studies, seem to offer a coherent description of the evolution of the sedimentary pile.

Mineral ratios were measured in fast-track whole-rock samples to look for variations related to provenance. Preliminary data on tectosilicate ratios are presented in the section on X-Ray Mineralogy, and a section on Clay Mineralogy is devoted to the origin of clay minerals and their relations with possible sources and climatic evolution. The section on Organic Geochemistry deals with the content of organic matter in relation to zones of high primary productivity and reworking of detrital coal. The modal compositions of sandstone layers are discussed in a section on Sand Grains.

Granitoids of the Granite Harbour Intrusive Complex (GHIC) are dominant in the crystalline basement (Allibone et al., 1993b) and green hornblende is their most abundant mafic phase. Since this mineral is almost entirely supplied by the GHIC, it was carefully checked throughout the core (Sand Grains section). Appraisal of the variation in exposure of the source units during the erosion of the TAM, the recycling of (Cenozoic?) sedimentary units, and the input from younger volcanic rocks was undertaken by counting clasts larger than 2 mm (Basement Clast section).

Volcanic debris from the MVG may have been carried to the sedimentation site by a variety of processes, including

direct air-fall, current transport, or as debris incorporated in local glaciers discharging close to Cape Roberts. Dating of volcanic ash levels from CRP-2/2A confirms that Cenozoic volcanism in the area is older than was previously thought from data on land (Sand Grain section). The discovery of tephra layers up to 1.2 m thick, dated isotopically by the $^{40}\text{Ar}/^{39}\text{Ar}$ method, provides potentially important time markers for the region. The age obtained (21.44 ± 0.05 Ma) represents the oldest and most precise isotopic age for any tephra in the Ross Sea region (see Chronology section, Summary chapter).

BASEMENT CLASTS

The term "basement clast" is used here in a broad sense, to refer to the granule to boulder clast population which was probably derived from the pre-Tertiary basement presently exposed in the Transantarctic Mountains west of the CRP drill sites. Clast variability data describing down-core content and grain-size variations of clasts from the Miocene-Oligocene strata of CRP-2/2A are summarized in the Clast Variability section. This section will focus on a preliminary petrographical characterization of the crystalline and other basement rocks and on the most significant variations in clast type and relative proportions among the different lithological groups. Sampling, macroscopic observations and preliminary petrographical analyses were performed following the same procedure and sample management adopted for the CRP-1 core (Cape Roberts Science Team, 1998c, 1998d).

RESULTS

Petrographical and distribution pattern data were collected on 20 503 clasts. Each was described on the basis of both dimension and lithology (see Clast Variability section). The clast population is dominated by granules and fine to coarse pebbles, but also includes minor cobbles and rare boulders. The pebbles become slightly coarser and the proportion of cobbles increases down-core, particularly below *c.* 300 mbsf.

A major change in the distribution pattern of the clast types also occurs at *c.* 310 mbsf, with granitoid-dominated clasts above and mainly dolerite clasts below (Fig. 4.1). Moreover, compositional and modal data suggest a further division into seven main detrital assemblages or petrofacies (P1 to P7). The main compositional features and trends within each petrofacies are summarized below. Relevant preliminary petrographical data on granitoids and rare clasts of metamorphic rocks are also included (see Volcanic Clasts section).

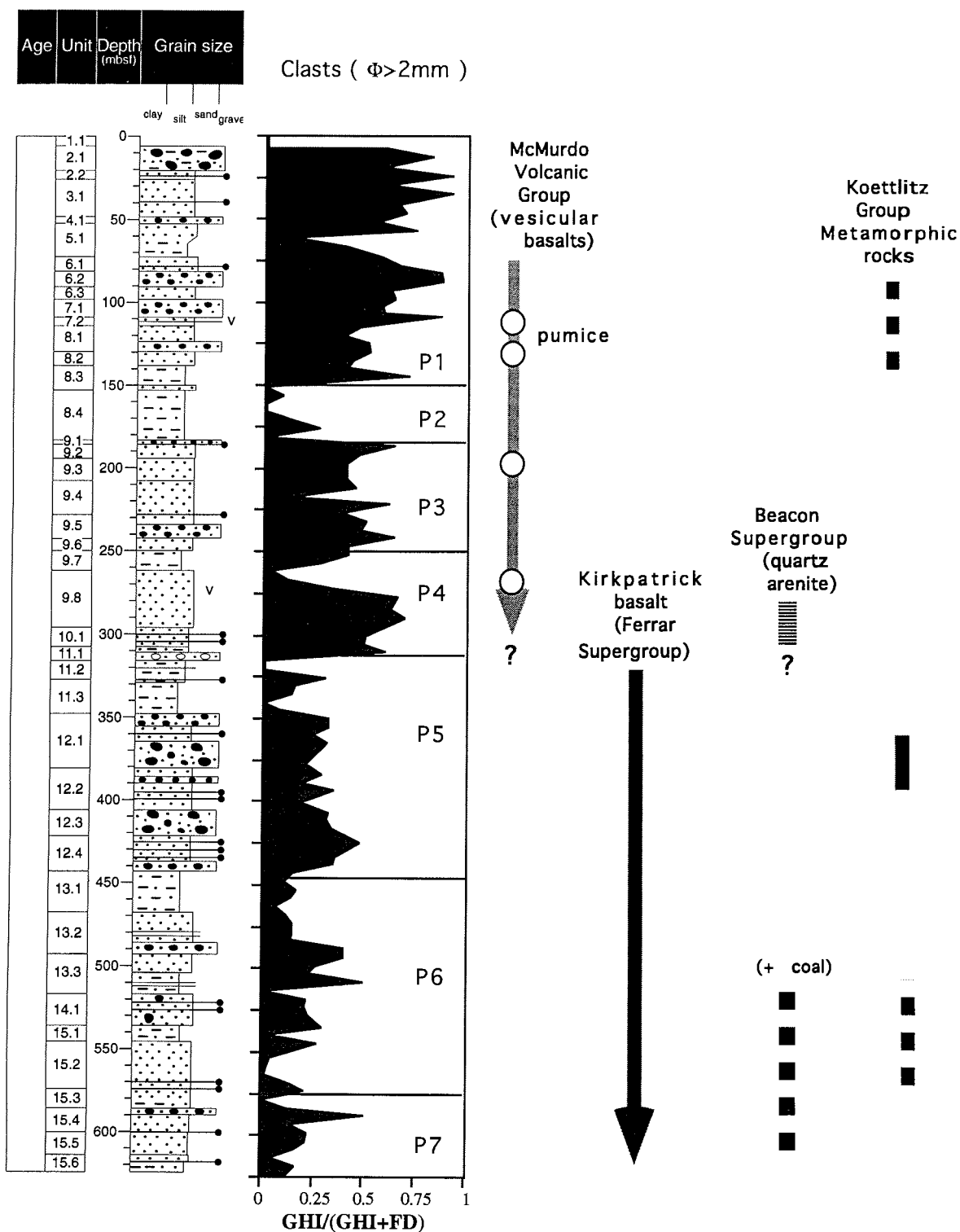


Fig. 4.1 - Proportion of major clast types (Granite Harbour Intrusive Complex, GHI, and Ferrar Supergroup dolerites, FD) plotted against depth. P1-P7 = main detrital assemblages or petrofacies. The first occurrence and distribution of minor lithologies are also shown.

P1 (26.70 to c.150 mbsf). In this petrofacies, granitoids are generally more common than dolerite (c. 80-60%), but the proportion of dolerite increases slightly with depth. Other lithologies are distinctly much less common and impersistent. They include: vesicular basalts (six occurrences: at c. 36, 77-80, 94, 122, 132 and 140-144 mbsf), pumice (forming the only clast type at 109-114 mbsf (Volcanic Clasts section),

but also occurring as a few scattered clasts at c. 101, 116, 122, 132 and 141-143 mbsf) and rare metamorphic rocks, mainly very fine-grained, thinly layered Ca-silicate rocks (at c. 79, 88, 115, 124 and 142 mbsf). A preliminary petrographical examination of P1 granitoids indicates that they consist mainly of grey medium to coarse-grained biotite monzogranite, fine- to medium-grained quartz-diorite and quartz-

monzonite, minor leucocratic biotite granite, biotite-hornblende granodiorite and rare granitic porphyry.

P2 (from c. 150 to c. 185 mbsf). The second assemblage is characterized by low clast concentrations, with dolerite forming the dominant lithology and a very low proportion of granitoids. The only additional rock types are represented by a few clasts of intraformational sedimentary rocks (quartz-rich sandstone, black volcanoclastic siltstone).

P3 (from c. 185 to c. 250 mbsf). The third petrofacies has subequal proportions of dolerite and granitoids (mainly pink biotite monzogranite), but it also includes minor vesicular basalt (at c. 178, 194, 198 mbsf) and pumice clasts (at c. 194 mbsf).

P4 (from c. 250 to c. 310 mbsf). At c. 250 mbsf, there is a sharp lithological and modal change. Down-core, the assemblage shows a slight increase in the proportion of granitoid clasts and a decrease in dolerite. P4 granitoids are mainly pink monzogranite, minor grey monzogranite and rare pink granitic porphyry. Vesicular basalt and sedimentary rocks are also major components; they are persistent but abundances fluctuate sharply. The sedimentary rocks are mainly intraformational clasts of grey and black siltstone, but also include a few possible Beacon Supergroup sedimentary rocks (well consolidated black siltstone with calcite veins at c. 292, and quartz arenite at c. 293 mbsf). Rare pumice clasts also occur between c. 259 and 265 mbsf.

P5 (from c. 310 to c. 440 mbsf). Excluding a very clast-poor section between c. 330 and 345 mbsf (Lithostratigraphical Sub-Unit 11.3), the clast assemblage in P5 is similar to P3, but contains dissimilar scarce and impersistent volcanic clasts of non-vesicular, olivine-free basalts (Jurassic Kirkpatrick basalts, see Volcanic Clasts section) and rare clasts of gneiss and Ca-silicate (at c. 360 and c. 385 mbsf). Clasts of intraformational black siltstone or sandstone are also present. Granitoid pebbles in P5 consist mainly of pink or grey biotite monzogranite but pink to orange microgranite and granitic to monzonitic porphyry are also widespread and abundant, particularly below 362 mbsf.

P6 (from c. 440 to c. 575 mbsf). This petrofacies is characterized by a broad peak in granitoid clast abundances at c. 475-500 mbsf (with potential for further subdivision into two sub-assemblages), and a highly variable content of non-vesicular Kirkpatrick basalts (mainly concentrated at c. 530-540 and 560-570 mbsf). Rare clasts of Ca-silicate rock and gneiss occur at c. 524, 559, 565 and 570 mbsf. Sedimentary clasts present include intraformational siltstone, minor Beacon Supergroup(?) quartz arenite (at c. 562, 566 and 573 mbsf) and dispersed coal (mainly occurring below c. 486 mbsf). P6 granitoid clasts are mainly grey to pale-pink biotite monzogranite and minor biotite-hornblende granodiorite. Pink to orange felsic porphyry is also present throughout P6.

P7 (from c. 575 to 625 mbsf). This assemblage shows significant fluctuations in the proportions of granitoids (mainly grey and pink monzogranites) and dolerite clasts, although the granitoids generally decrease down-core antithetic to the proportions of non-vesicular Kirkpatrick basalts, and a few sedimentary clasts (mainly coal and Beacon Supergroup(?) quartz arenite).

PROVENANCE

Similar to previous drill holes (MSSTS-1, CIROS-1, CRP-1) on the western edge of the Victoria Land Basin (Barrett, 1986, 1989; George, 1989; Hambrey et al., 1989; Cape Roberts Science Team, 1998a, 1998d; Talarico & Sandroni, 1998), the CRP-2/2A drill hole provides evidence of a multi-component source for the supply of granule to boulder clasts to the Tertiary sedimentary sequences in the McMurdo Sound. This varied provenance closely resembles the present-day on-shore rocks of the Transantarctic Mountains in southern Victoria Land, which include: 1) granitoid and amphibolite facies metasediments of the Early Palaeozoic Ross Orogen, 2) quartz arenites, minor black siltstones and coaly strata of the Devonian-Triassic Beacon Supergroup, 3) dolerite sills and lavas (Kirkpatrick basalt) of the Jurassic Ferrar Supergroup, and 4) alkaline volcanic rocks of the Cenozoic McMurdo Volcanic Group.

Preliminary petrographical characterization of CRP-2/2A clasts indicates that all these major geological units contributed clasts to the Miocene-Oligocene strata. As in the Quaternary-Pliocene sequence (see Introduction chapter), most of the crystalline basement pebbles were derived from the Cambro-Ordovician Granite Harbour Intrusive Complex, which is the dominant component in the local basement (Gunn & Warren, 1962; Allibone et al., 1993a, 1993b). The Miocene-Oligocene strata also contain metamorphic rocks (e.g. Ca-silicate rocks) which are known to be a common metasedimentary lithology in the amphibolite facies Koettlitz Group south of Mackay Glacier (Grindley & Warren, 1964; Findlay et al., 1984; Allibone, 1992).

Compositional and modal data indicate the presence of significant fluctuations in the relative proportions of the main lithologies (in decreasing order of abundance: granitoids, Ferrar dolerites, McMurdo Volcanic Group basalts, Kirkpatrick basalts, Beacon sedimentary rocks). In particular they point to an important lithological change at c. 310 mbsf indicating a relatively abrupt change from a mainly crystalline basement source to one dominated by Ferrar Supergroup lithologies.

The presence of significant modal and compositional variations down-core provide a clear evidence of an evolving provenance. When these data are integrated with additional provenance information obtained from concurrent geochemical, petrological and sedimentological investigations, the distinction of the seven main detrital clast assemblages has significant implications for unravelling the complex interplay between tectonic, volcanic and glaciomarine sedimentary processes during the formation of the Victoria Land Basin and uplift of the Transantarctic Mountains in Oligocene-Miocene time.

VOLCANIC CLASTS

Volcanic clasts thought to be related to activity of the Cenozoic McMurdo Volcanic Group (MVG) were collected from levels above 280 mbsf. They are generally vesicular and vary in composition from alkali basalts to

trachytes, although a few fragments of syenitic composition are also present. By contrast, below 320 mbsf, aphyric or sub-aphyric volcanic clasts become abundant. However, they are all non-vesicular basalts containing pigeonite and abundant quench-crystallized ilmenite and they are considered to be related to lava flows of Jurassic age (Kirkpatrick basalts). Volcanic clasts of both types were taken for chemical analysis to investigate their compositional variations throughout the CRP-2/2A core.

Volcanic clasts of the McMurdo Volcanic Group were examined in more detail because of their relationship with the development of the Ross Sea rift. They derive from alkaline magmas and are readily recognised by the occurrence of olivine in the groundmass of mafic lavas and strongly-coloured ferromagnesian phases (aegirine, arfvedsonite) in evolved rocks. The samples vary in size from 1 to 5 cm. Bulk sediments enriched in tephra, and hand-picked pumice fragments, were also collected for chemical investigation. Volcanic glass and mineral grains are particularly common throughout LSU 7.2 (see below), and at 193.45 and at 280.10 mbsf.

Petrographical examination of 10 representative clasts reveals the occurrence of lavas varying in composition from alkali basalt to trachyte, but alkali basalt and hawaiite are most common. Alkali basalt (CRP-2/2A 203.75 mbsf) is characterized by the presence of olivine phenocrysts, completely altered to bowlingite, and bytownitic plagioclase microphenocrysts. This clast also contains partly resorbed xenocrysts of quartz with a clinopyroxene reaction rim, a textural feature that is commonly observed in MVG basic rocks. The complete alteration of olivine in this sample may account for the scarcity of olivine in CRP-1 (Smellie, 1998) and CRP-2/2A sediments. Hawaiite and mugearite lavas mostly have fluidal textures with plagioclase and augite phenocrysts. The optically determined composition of plagioclase (labradorite) matches that of crystals derived from the MVG to the sand fraction of CRP-1 (Armienti et al., 1998). One basaltic clast shows an outer rim of tachylitic glass with small plagioclase microcrystals. The rim closely resembles opaque fragments found in the uppermost 280 m of CRP-2/2A and throughout CRP-1 (Cape Roberts Science Team, 1998b, p. 47, Fig. 12f). Felsic varieties (trachyte and syenite) differ in the degree of crystallinity. They are characterized by the occurrence of sanidine and/or anorthoclase microphenocrysts commonly accompanied by zoned green aegirine-augite microphenocrysts; fayalitic olivine also occurs in a syenite clast at 258.88 mbsf.

Parts of the sequence are rich in volcanic components (e.g. LSU 7.2, LSU 9.2 at 193.45 mbsf and LSU 9.8 at c. 280 mbsf). They contain abundant fresh, crystal-poor glass that is commonly highly vesiculated pumice. Glass is generally associated with grains of a wide variety of volcanic rocks.

LSU 7.2 - TEPHRA LAYERS

Special attention was devoted to LSU 7.2, between 108 and 114 mbsf, that contains seven main layers of tephra (Fig. 4.2). Four samples were taken at different

levels for $^{40}\text{Ar}/^{39}\text{Ar}$ isotopic dating. Individual pumice fragments from different layers were also hand-picked for whole-rock chemical analyses to establish any compositional variation.

Tephra are scattered throughout LSU 7.2. Thin beds of fine sandstone and siltstone separate pumice-rich beds. Some layers have dispersed pumice with a very variable concentration. Many of the pumice lapilli, including some in the 1.2 m-thick layer, are well rounded. The 1.2 m-thick layer and the layer at bottom of LSU 7.2 (Fig. 4.2), contain a high proportion of fine glassy tuff matrix.

Four samples were examined petrographically: Sample CRP-2/2A 111.28 mbsf is a poorly bedded, poorly sorted lapillistone formed of pumice lapilli that range in size from about 10 mm to less than 1 mm, together with 5% admixed lithic clasts. The pumice lapilli consist of colourless glass and are supported by a fine-sand matrix of quartz and feldspar fragments with abundant brown glass shards, green hornblende and pyroxene. Sponge spicules and diatoms are common.

Samples CRP-2/2A 111.77, and 112.25 mbsf (from the 1.2 m-thick bed) and CRP-2/2A 114.12 mbsf come from beds of tephra dominated by poorly sorted pumice lapilli (70-80%) set in a matrix of very fine grained vitric ash. The lapilli are almost crystal-free, highly vesiculated and colourless. The deposits also contain scattered crystals of alkali feldspar, aegirine-augite and sporadic Na-amphibole (arfvedsonite). The paucity of comagmatic plagioclase feldspar, the sporadic occurrence of angular quartz (from the basement of the volcano?) and association with anorthoclase, aegirine-augite and arfvedsonite suggest that the pumices have a peralkaline trachytic or phonolitic composition, like other rocks commonly found in MVG and in CRP-1 core (Armienti et al., 1998). Small accessory fragments (<1 mm) of altered volcanic rocks and holocrystalline trachyte are also common.

Origin of Tephra Layers in LSU 7.2

The absence of detrital sand grains, that would occur within the matrix if the layer had suffered redeposition within the basin, suggests that the 1.2 m-thick layer (Samples CRP-2/2A 111.77, 112.25 mbsf) and that at 114.12 mbsf are not reworked deposits. However, at the very top of the 1.2 m-thick bed, small pockets of silt-size crystals and brown glass suggest that it is slightly reworked or redeposited. In the remaining bulk of the layer, the proportion of ash matrix is high (20 to 30%) for a water-deposited tephra and is possibly due to the high vesiculation of pumice that made it sink as slowly as the ash. Preservation of delicate grading within these ash-rich tephra layers also argues against its redeposition after mobilisation in the sedimentary basin. Similar arguments also apply to the layer at the bottom of LSU 7.2.

Some subdivisions proposed in the 1:20 core log for the 1.2 m-thick layer, on the basis of grading and grain-size variations, could be simply linked to different settling velocity of larger particles in the water column more than to pulsation in eruptive activity. The rounded shapes of some lapilli suggest that the pumice fragments spent some time as floating rafts prior to sinking.

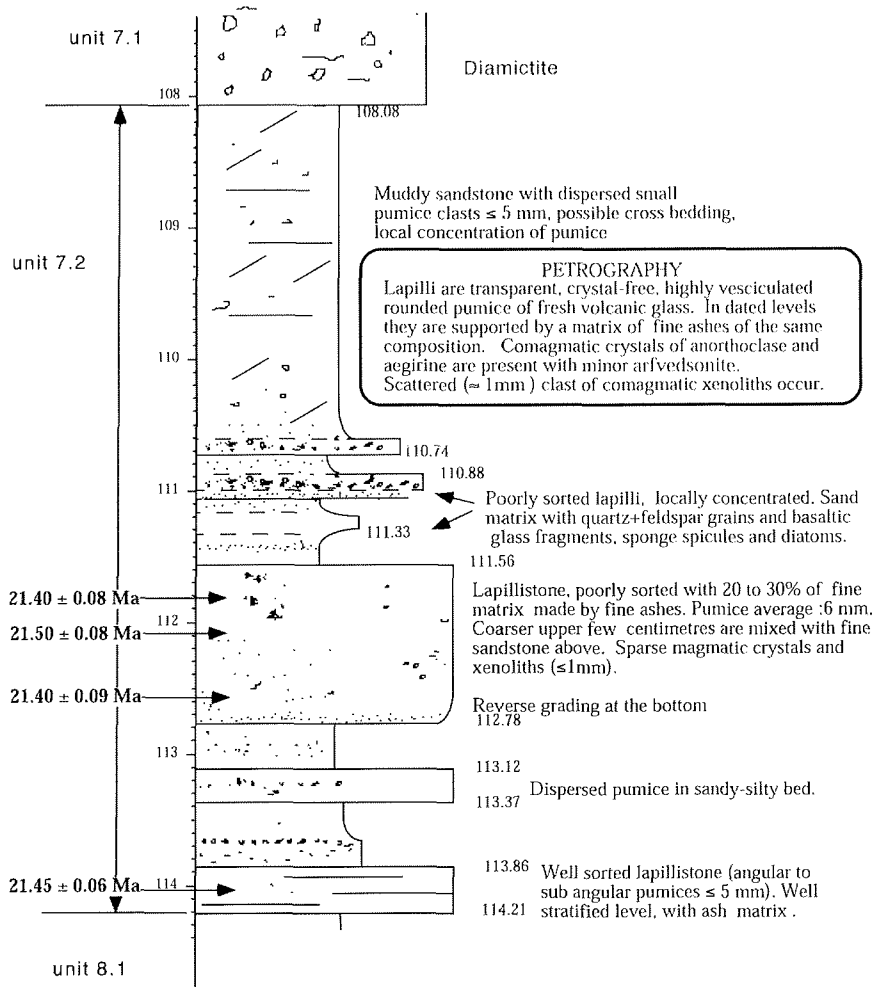


Fig. 4.2 - Stratigraphical log of ash-rich LSU 7.2, with petrographical and geochronological information.

Evaluation of the Height of Eruptive Column of the 1.2 m-Thick Layer

Calculations were performed to estimate the height of the eruptive column able to disperse pumice particles found in the 1.2 m-thick tephra layer, using a model of advection and diffusion of volcanic particles (Armienti et al., 1988; column-heights calculated by Gianni Macedonio, Osservatorio Vesuviano, Naples, Italy). A horizontal transport distance of 120 km was postulated - *i.e.* the distance to the nearest known volcanic centre on land of comparable age (Mount Morning area; Kyle, 1990). Particles were assumed to be of spherical shape and wind velocity was kept constant. Two typical sizes found at the base of the layer were taken into account: 1 mm and 2 mm, with settling velocities of 7.74 m s⁻¹ and 11.0 m s⁻¹, respectively. Larger particles may have floated longer before sinking to the sea floor and, moreover, they would require unrealistic column heights or wind speed for the assumed distance of 120 km. The results of the calculations are shown in figure 4.3, where the heights of release from an eruptive column of the two particle sizes are plotted as a function of the wind speed. Shorter travel distances imply an almost linear decrease of the column height (for a distance of 60 km we can expect approximately the same column height needed for a wind of double the speed). A

tentative estimate of column height, for a distance between 60 and 120 km and wind speed of 100 km h⁻¹, is between 33 and 17 km for 1 mm lapilli. Note that a high wind speed may constrain deposition of tephra to a narrow region focused along the plume dispersal axis. Some transport of pumice on the sea surface seems to be implied by the

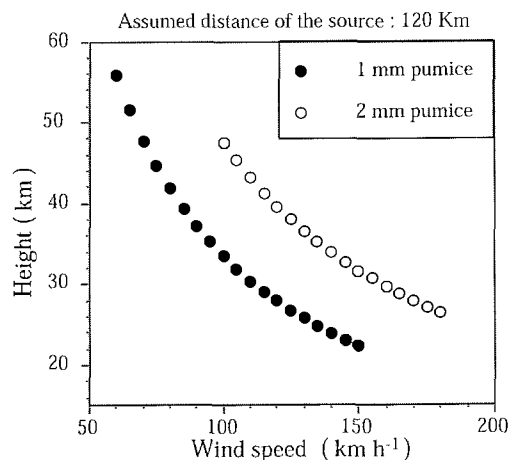


Fig. 4.3 - Effects of wind speed on the height of release required to transport pumice particles of 1 and 2 mm diameter for a distance of 120 km.

rounded shape of the pumice fragments. Moreover, the large abundance of particles of about 6 mm of diameter in the bulk of the layer suggests that a much lower column was responsible of the deposition of the tephra layer. This implies that the volcanic source was even closer than our calculations based on smaller pumice sizes suggest. An unknown volcanic centre may have been responsible for the activity, possibly within 60 km of Cape Roberts drilling site.

Age of LSU 7.2 Tephra Layers

A total of 98 single feldspar crystals were extracted from four samples from LSU 7.2, from depths between 111.58 and 114.15 mbsf (Fig. 4.2). Following neutron irradiation at Texas Agricultural and Mechanical Nuclear Science Center, samples were analyzed by W.C. McIntosh and L. Peters using the $^{40}\text{Ar}/^{39}\text{Ar}$ laser fusion method in the New Mexico Geochronology Research Laboratory at New Mexico Institute of Mining and Technology. Procedures were the same as those described by McIntosh & Chamberlin (1984). All ages were determined relative to the Fish Canyon Tuff sanidine inter-laboratory standard with an assigned age of 27.84 Ma (Deino & Potts, 1990). Of the 98 crystals analysed, ten were found to be older xenocrysts. After rejecting those and an additional four crystals which gave poor data, the remaining 84 crystals yielded precise, tightly grouped age data with high radiogenic yield, typically 99% or higher (Fig. 4.4). Mean ages calculated from analysis of those 84 crystals are as follows (all errors quoted at $\pm 2\sigma$):

CRP-2/2A-111.58-111.75	n=18	21.40 \pm 0.08 Ma
CRP-2/2A-112.19-112.34	n=11	21.50 \pm 0.07 Ma
CRP-2/2A-112.61-112.77	n=27	21.40 \pm 0.09 Ma
CRP-2/2A-114.03-114.15	n=28	21.45 \pm 0.06 Ma
CRP-2/2A-111.58-114.15 (mean)	n=84	21.44 \pm 0.05 Ma

The ages of all four samples overlap at $\pm 2\sigma$ and are considered to be analytically indistinguishable. The early Miocene mean age of 21.44 \pm 0.05 Ma is considered to be an accurate age determination for the eruption, or series of eruptions, that produced these tephra layers. There is no obvious source for the rejected much older crystals, whose ages range between 159 and 393 Ma. Their source(s) may have been of Palaeozoic age, with partial age resetting due to incorporation of the small crystals in a hot magmatic column.

SUMMARY

The study of volcanic clasts and tephra layers in the CRP-2/2A sequence allows us to suggest that:

- volcanic clasts above 280 mbsf belong to the activity of some volcanic centre of the McMurdo Volcanic Group. Volcanic clasts from below 350 mbsf are derived from Kirkpatrick basalt lava flows;
- volcanic tephra layers in LSU 7.2 (at 111.56-112.78 and 113.86-114.21 mbsf) are not reworked, and their isotopic age (21.44 \pm 0.05 Ma) is a likely age for their eruption and deposition;
- the height of the eruptive column responsible for the deposition of the tephra was probably less than 17 km. A local source is suggested, possibly within 60 km of the drilling site.

CLAY MINERALOGY

X-ray diffraction (XRD) analyses of clay minerals were performed on 29 fast-track samples distributed throughout the CRP-2 and CRP-2A cores (Tab. 4.1). After sieving the samples through a 63 μm mesh, the clay fraction was isolated from the silt fraction in large settling tubes by the Atterberg method with the settling time based

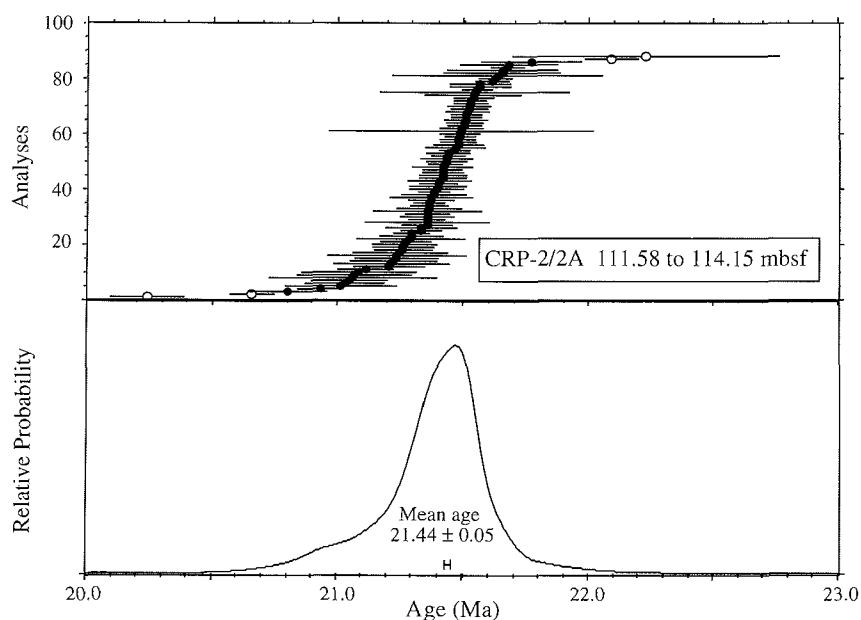


Fig. 4.4 - Probability distribution diagram of single-crystal laser-fusion analyses from CRP-2/2A-111.58-114.15 mbsf feldspars. Upper panel shows individual analyses with $\pm 1\sigma$ error bars; lower panel shows cumulative probability distribution curve. Hollow symbols denote analyses rejected from mean age calculations. (Analyses by W.C. McIntosh, New Mexico Geochronology Research Laboratory).

Tab. 4.1 - Estimates of the relative abundance of the main clay mineral groups smectite, illite, chlorite and kaolinite in the clay fraction of sediments from CRP-2/2A core.

Sample (mbsf)	Smectite	Illite	Chlorite	Kaolinite
28.90	x x x x	x x x x x x x x x x x	x x x	x
36.24	x x x x x	x x x x x x x x x x	x x x x	x
47.41	x x x x	x x x x x x x x x x x	x x x x	(x)
57.32	x x x x x	x x x x x x x x x x x	x x x	x
71.13	x x x	x x x x x x x x x x x	x x x x	x
75.60	x x x x x x	x x x x x x x x x x	x x x x	(x)
96.71	x x x x x	x x x x x x x x x x	x x x x	x
130.73	x x x x x	x x x x x x x x x x x	x x x	x
158.38	x x x x x	x x x x x x x x x x x	x x x x	x
177.89	x x x x	x x x x x x x x x x x	x x x x	x
195.57	x x x x	x x x x x x x x x x x	x x x x	x
215.60	x x x x x	x x x x x x x x x x x	x x x	x
236.25	x x x x	x x x x x x x x x x x	x x x x x	x
260.04	x x x	x x x x x x x x x x x	x x x x x	x
292.09	x x x x x x x x x x	x x x x x x x	x x x	x
316.44	x x x x x x x x x x	x x x x x x x	x x x	x
338.82	x x x x x x	x x x x x x x x x	x x x x	x
358.24	x x x x	x x x x x x x x x x x	x x x x	x
390.25	x x x x x	x x x x x x x x x x x	x x x x	(x)
412.25	x x x x x x x x x	x x x x x x x x	x x x	x
444.78	x x x x x x x x x	x x x x x x x	x x x x	x
465.06	x x x x x	x x x x x x x x x	x x x x x x	(x)
486.19	x x x x	x x x x x x x x x	x x x x x x	x
524.41	x x x x	x x x x x x x x x	x x x x x x	x
543.87	x x x x	x x x x x x x x x x x	x x x x x	x
564.58	x x x x x x	x x x x x x x x x	x x x x	x
584.48	x x x x x x x x x x	x x x x x x x	x x x	x
604.50	x x x x x x x x x x x	x x x x x	x x x x	x
623.67	x x x x x x x x x x x x	x x x x	x x x x	x

Note: the number of crosses is proportional to the abundance of the clay minerals.

on Stoke's Law. 5-10 ml of a 50% MgCl₂ solution was added to the clay suspension (up to 5 litres) in order to charge the clay minerals and make them sink by agglomeration. Subsequently, excess ions were removed by double centrifuging in de-ionised water.

The clay fraction was then dispersed in about 15-20 ml water. The clays were mounted as texturally orientated aggregates by dropping about 1 ml of the clay suspension onto cardboard discs and evaporating the water. The cardboard discs were then mounted with double-sided adhesive tape into aluminium sample holders. The mounted clays were solvated with ethylene-glycol vapour for about 18 hrs immediately before the X-ray analyses.

The XRD measurements were conducted on a Rigaku Miniflex automated diffractometer system with CuK_α radiation (30 kV, 15 mA). The samples were X-rayed in the range 2-30 °2θ in steps of 0.01 °2θ with a measuring time of two seconds per step. The X-ray diffractograms were evaluated on an Apple Macintosh Personal Computer using the "MacDiff" software (Petschick, unpublished freeware).

The study concentrated on the presence and abundance of the main clay mineral groups smectite, illite, chlorite and kaolinite, based on the integrated areas of their basal reflections at c. 15-17 Å (smectite), 10 Å (illite), 7 and 3.54 Å (chlorite), and 7 and 3.57 Å (kaolinite). Only rough estimates, rather than precise percentages are given, because the separation of the clay fraction and the textural orientation of the clay aggregates on the mounts were incomplete.

In general, the clay mineral assemblages of the CRP-2/2A core are dominated by illite, with chlorite and smectite being common and kaolinite occurring in trace amounts (Tab. 4.1). Non-clay minerals, quartz, plagioclase feldspar

and K-feldspar are present in high concentrations in the clay fraction of all samples; amphibole concentrations, however, are low. Such an assemblage also dominates the lower Miocene sediments of core CRP-1 (Ehrmann, 1998b) and long intervals within the Oligocene-lower Miocene sediments of cores from CIROS-1 and MSSTS-1 (Ehrmann, 1997, 1998a).

Illite and chlorite are typical detrital clay minerals. They cannot form in the normal marine environment but are the products of physical weathering and glacial scour. Illite and chlorite are therefore typical of the recent high latitudes. They are derived particularly from crystalline rocks, such as those that are widespread on the East Antarctic craton and in the Transantarctic Mountains. Chlorite is a characteristic mineral for low-grade, chlorite-bearing metamorphic and basic rocks, but is not resistant against chemical weathering and transport. Illite tends to be derived from more acidic rocks and is relatively resistant (Biscaye, 1965; Griffin et al., 1968; Windom, 1976). Both clay minerals could also be derived from the sedimentary rocks of the Beacon Supergroup (La Prade, 1982), which overlie the basement in the western part of the Transantarctic Mountains.

In general, high smectite concentrations are mostly a product of chemical weathering and form by hydrolysis under climatic conditions between warm-humid and cold-dry, in environments characterized by very slow movement of water (Chamley, 1989). Therefore, smectite formation in the recent Antarctic environment is usually only a subordinate process. However, another source for smectite is the weathering of volcanic rocks and thus, high smectite concentrations have been reported from glaci-marine sediments in areas with volcanic rocks in the hinterland

(Ehrmann et al., 1992; Ehrmann, 1998b), showing that those rocks can provide considerable amounts of smectite, even under a polar climate.

In the case of the CRP-2/2A sediments, the smectite probably is derived from a source local to McMurdo Sound, which is characterized by basaltic volcanic rocks that occur over a wide area between Ross Island and Mount Morning (McMurdo Volcanic Group). The oldest known surface samples of this area are dated at 19 Ma (Kyle, 1990). According to magnetic surveys, many more volcanic centres of similar size but unknown age exist on the present Ross Sea continental shelf, beneath the Ross Ice Shelf and the West Antarctic ice sheet (Behrendt et al., 1994, 1995), and could have contributed to the CRP-2/2A smectites. Weathering of Ferrar dolerite or Kirkpatrick basalt in the Transantarctic Mountains is a further possible origin for the smectite in the CRP-2/2A sediments.

The clay mineral assemblages in the upper c. 290 m of core CRP-2/2A show only minor down-core fluctuations (Tab. 4.1). Generally, illite is the dominant clay mineral with concentrations of roughly 50-60%, whereas both chlorite and smectite concentrations fluctuate probably between 15% and 25%. Such an assemblage is typical for a sediment source in the Transantarctic Mountains, where physical weathering of basement rocks and sedimentary rocks of the Beacon Supergroup provide large amounts of both illite and chlorite. Such a source therefore seems to have dominated throughout the time represented by the upper c. 290 m of the CRP-2/2A core.

Below c. 290 mbsf, the clay mineral record allows a subdivision into two major assemblages. One assemblage is the illite-dominated assemblage described above. The other assemblage is characterized by distinctly enhanced smectite concentrations but relatively low illite concentrations. Two short intervals with enhanced smectite concentrations can be identified at c. 290-320 mbsf and c. 410-450 mbsf (Tab. 4.1). In these intervals the smectite contents seem to increase to c. 40-45%, at the expense mainly of illite but also of chlorite. At the moment, it is not clear what caused the increase. Theoretically it could be caused by the enhanced input of smectite from a source in the McMurdo Volcanic Group to the south, either by ice or by suspension in ocean currents. Similarly, in the core from CIROS-1, two upper Oligocene intervals with high smectite concentrations were also ascribed to a southerly source (Ehrmann, 1998a). However, the investigations of the gravel and sand fractions showed no major input of volcanic components from the McMurdo Volcanic Group below c. 290 mbsf. A source in the Ferrar dolerites and Kirkpatrick basalts in the Transantarctic Mountains is also possible, if that source is not strongly diluted by weathering products of the crystalline basement and the sedimentary sequences of the Beacon Supergroup, which mainly provide illite and chlorite. Ferrar dolerite and Kirkpatrick basalt are constituents of the gravel and sand fraction of the sediments. Theoretically, the enhanced smectite concentrations could also indicate somewhat warmer and more humid conditions on the Antarctic continent, resulting in more intense chemical weathering, although diamictites and other glaciomarine sediments were deposited at the drill site during that time.

The biostratigraphical investigations (see Palaeontology chapter) indicate that the CRP-2/2A core penetrated into lowermost Oligocene sediments, but did not reach the Eocene/Oligocene boundary. If our rough and preliminary data on the clay mineral assemblages are correct, then they could support this biostratigraphical dating. Thus, in the lowermost part of CRP-2/2A, below 560 mbsf, the smectite concentrations steadily increase from c. 20% to c. 55%.

Just above the Eocene/Oligocene-boundary a very distinct change in the clay mineral composition from an older smectite-dominated to a younger illite-dominated assemblage is well documented in the deep-sea record of the Southern Ocean (Ehrmann & Mackensen, 1992; Ehrmann et al., 1992) and also in the core from CIROS-1 (Ehrmann, 1997, 1998a). In the deep sea, that transition can be dated to 33.7-32.7 Ma (time scale of Berggren et al., 1995). The higher smectite concentrations in the lowermost Oligocene and Eocene sediments of the CIROS-1 core and of deep-sea cores were interpreted to reflect chemical weathering under a temperate and humid climate on the Antarctic continent, when large parts of East Antarctica were probably ice-free, but several glaciers reached the coast of McMurdo Sound and icebergs calved into the sea and contributed to the glaciomarine sedimentation. However, it is also acknowledged that the smectite maximum observed in the lowermost part of the CRP2/2A core could be caused by a change in the source area.

X-RAY MINERALOGY

In order to provide a general characterization of the bulk mineralogy of pre-Pliocene sediments from CRP-2/2A, 26 "fast-track" samples were analyzed using a Rigaku Miniflex+ X-ray diffraction (XRD) system at the Crary Science and Engineering Center. The materials were analysed, and the diffraction patterns were processed with JADE 3+ software, using procedures described in the Initial Report volume for CRP-1 (Cape Roberts Science Team, 1998c, p. 84-85).

Sample locations and the minerals identified in each sample are listed in table 4.2. Quartz and plagioclase feldspars are the dominant phases in each sample, with lesser amounts of K-feldspars present in most samples. The occurrence and diversity of K-feldspars decrease down-core, however. Other minerals show low intensity peaks on the XRD patterns, suggesting low abundances, and occur discontinuously in the pre-Pliocene section; these include some expected detrital phases (illite/muscovite, augite, diopside), and other phases that are identified with less confidence and may be products of *in situ* alteration (analcime, phillipsite).

The data generated by these analyses cannot be used quantitatively to determine the abundances of the various minerals present. However, comparing the intensities of two XRD peaks (one chosen for each mineral of interest) can provide a useful qualitative indicator of the variations in relative abundances of those two phases through a stratigraphical section. The same peak area ratios have been calculated for samples from CRP-2/2A as were used

Tab. 4.2 - Minerals identified by X-ray diffraction analysis in bulk samples from CRP-2/2A.

Depth (mbsf)	Minerals Present
28.89	quartz, albite, anorthite, anorthoclase, orthoclase, microcline, augite, diopside
71.23	quartz, albite, anorthite, microcline, sanidine, orthoclase, augite, diopside
96.77	quartz, albite, anorthite, anorthoclase, microcline, augite, muscovite
130.80	quartz, albite, anorthite, anorthoclase, microcline, augite, muscovite/illite
158.48	quartz, albite, anorthite, microcline, orthoclase, diopside
177.90	quartz, albite, anorthite, microcline, sanidine, Augite, diopside, muscovite/illite
195.68	quartz, albite, anorthite, anorthoclase, microcline, sanidine, orthoclase, muscovite/illite
215.70	quartz, albite, anorthite, sanidine, microcline, muscovite
236.25	quartz, albite, anorthite, sanidine(?), orthoclase, muscovite
260.00	quartz, albite, anorthite, microcline, sanidine(?), orthoclase, muscovite
292.30	quartz, albite, anorthite, microcline, sanidine, muscovite
316.45	quartz, albite, anorthite, microcline, orthoclase, muscovite/illite, gismondine(?)
339.98	quartz, albite, anorthite, anorthoclase, microcline, orthoclase, muscovite
358.35	quartz, albite, anorthite, microcline, anorthoclase(?), muscovite, diopside
390.21	quartz, albite, anorthite, anorthoclase, muscovite/illite
412.27	quartz, albite, anorthite
444.76	quartz, albite, anorthite, microcline, orthoclase, muscovite/illite, gismondine(?)
465.04	quartz, albite, anorthite, microcline, muscovite/illite, gismondine(?)
486.32	quartz, albite, anorthite, anorthoclase(?), muscovite
507.81	quartz, albite, anorthite, muscovite/illite, gismondine(?), chabazite(?)
524.39	quartz, albite, anorthite, muscovite/illite, gismondine(?)
543.85	quartz, albite, anorthite, muscovite/illite, gismondine(?)
564.68	quartz, albite, anorthite, muscovite/illite, gismondine(?)
584.59	quartz, albite, anorthite, microcline, muscovite/illite, gismondine(?), phillipsite(?), analcime(?)
604.46	quartz, albite, anorthite, muscovite(?), gismondine(?), analcime(?)
623.63	quartz, albite, anorthite, orthoclase, muscovite/illite(?), gismondine(?)

to determine total feldspar/quartz and K-feldspar/quartz ratios for the Initial Report of CRP-1 (Cape Roberts Science Team, 1998c, p. 84-85). The resulting stratigraphical profiles of feldspar/quartz and K-feldspar/quartz peak intensity ratios are shown in figures 4.5 and 4.6, respectively.

The general structures of the feldspar/quartz ratio profile (Fig. 4.5) and the K-feldspar/quartz ratio profile (Fig. 4.6) are similar, with values decreasing down-core to relatively low and uniform values below c. 300 mbsf. One potential reason for these compositional variations is a change in sediment grain-size, since feldspar/quartz ratios tend to decrease as grain-size decreases (Blatt, 1992). Such a grain-size control does not appear to have been a major influence on these curves, however, because all of the samples were taken from the finest lithologies available: muddy fine sandstones, sandy mudstones, and the matrix of muddy to fine sandy diamictites. As a result, the grain-size of the bulk sediment analyzed does not appear to vary significantly between samples, thereby minimizing the possibility that the patterns observed in

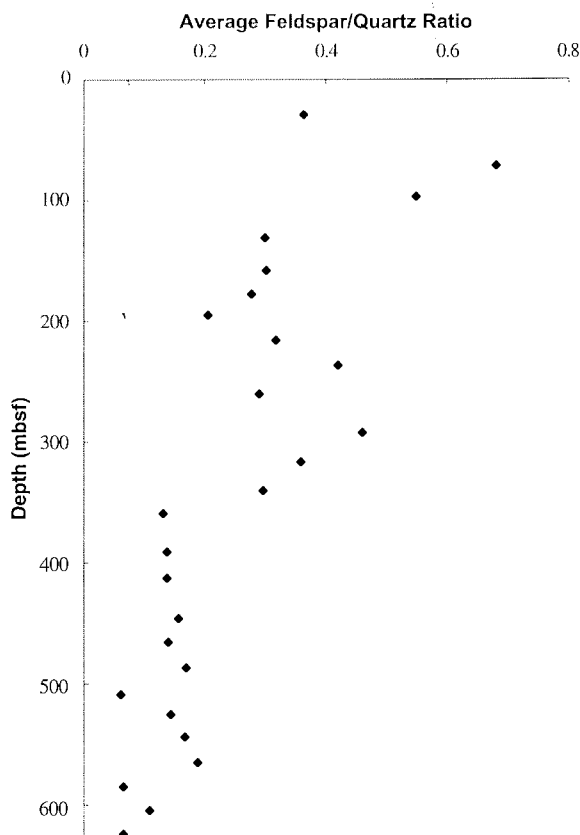


Fig. 4.5 - Stratigraphical profile of feldspar/quartz XRD peak intensity ratios for bulk sediments from CRP-2/2A. Each ratio plotted is the average of three separate peak intensity ratios. The feldspar considered in these ratios is predominantly plagioclase.

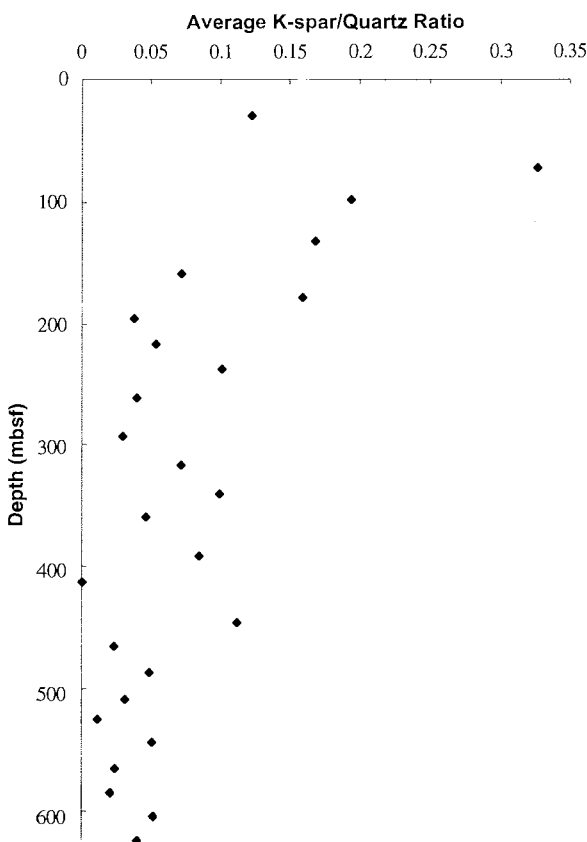


Fig. 4.6 - Stratigraphical profile of K-feldspar/quartz XRD peak intensity ratios for bulk samples from CRP-2/2A. Each ratio plotted is the average of four separate peak intensity ratios.

figures 4.5 and 4.6 are primarily a result of grain-size changes down-core.

A second possible explanation for the patterns seen in figures 4.5 and 4.6 is a change in sediment provenance during the period of deposition. The possible role of changing source contributions can be evaluated by comparing the variations in bulk mineralogy, sand fraction composition (see Sand Grains section) and coarse clast composition (see Basement Clasts section) down-core. This comparison indicates relatively consistent patterns of variation in all three compositional indicators, which aids in interpretation of the bulk mineralogical data. Above *c.* 300 mbsf, both the feldspar/quartz and the K-feldspar/quartz ratios are relatively large, although decreasing down-core. For most of this interval (to *c.* 280 mbsf), the sand fraction consistently contains components derived from the McMurdo Volcanic Group (MVG), as well as green hornblende, interpreted as being derived from the Granite Harbour Intrusive Complex (GHIC). The coarse clasts in this interval support the latter interpretation, as material derived from the GHIC is generally more abundant than other clast types. As a result, the high total plagioclase abundances and the high K-feldspar abundances relative to quartz in the bulk sediment are consistent with a sediment provenance dominated, through most of this interval, by two feldspar-rich sources (the MVG and the GHIC). At *c.* 285 - *c.* 300 mbsf, however, the absence of MVG-derived sand suggests that the GHIC are the sole source of feldspars. In addition, the predominance of plagioclase over K-feldspars in the bulk sediment is consistent with plagioclase supply from both the MVG and the GHIC, whereas K-feldspars are derived primarily from the GHIC.

Below *c.* 300 mbsf, all three compositional indicators (bulk mineralogy, sand composition, and coarse clast composition) show a consistent pattern of change. Both the total feldspar/quartz ratio and the K-feldspar/quartz ratio decrease and remain relatively uniform, green hornblende and MVG detritus are replaced by Kirkpatrick basalt and/or fine-grained dolerite in the sand fraction, and Ferrar dolerite clasts are generally more abundant than GHIC clasts. These changes all point to a shift in sediment provenance, from crystalline basement and the MVG to Beacon Supergroup sources. Recycling of quartz-rich Beacon Supergroup sedimentary rocks supplied detritus with lower total feldspar/quartz and K-feldspar/quartz ratios. That signal of Beacon sedimentary recycling is probably more evident in the bulk mineralogy (and sand grain population) than in the coarse clasts because of strength differences between Beacon sedimentary rocks and the Kirkpatrick basalt/Ferrar dolerite.

SAND GRAINS

This section describes the results of an initial investigation of the sand fraction in CRP-2A samples. It was undertaken to determine the range of sand-size mineral and lithic grains present, to estimate their relative proportions, and to provide initial information on

provenance and temporal variations. Previous studies in the area described sand grains and provenance of samples from the MSSTS-1 and CIROS-1 drill holes, both situated *c.* 80 km to the south, and CRP-1, situated about 800 m east of CRP-2/2A (Barrett et al., 1986; George, 1989; Smellie, 1998). These investigations reported a varied provenance resembling the local rocks of the Transantarctic Mountains in southern Victoria Land, including granitoid and metamorphic rocks of an Upper Precambrian-lower Palaeozoic 'basement', quartzose sedimentary rocks of the Devonian-Triassic Beacon Supergroup, sills, dykes and lavas of the Ferrar dolerite and Kirkpatrick basalt, and alkaline volcanic rocks of the Cenozoic McMurdo Volcanic Group.

METHODS

The study is based on examination of *c.* 130 unstained, covered smear slides, obtained at *c.* 5 m intervals in the CRP-2/2A core. Unlike the investigation of samples in CRP-1 (Cape Roberts Science Team, 1998b), CRP-2/2A samples were neither washed nor ground prior to smearing, thus minimising the secondary crushing of grains and avoiding unsystematic loss of biotite. However, sandstones below *c.* 500 mbsf were found to be strongly cemented and were difficult to sample in some cases without causing extensive breakage of detrital grains. The types and proportions of the major sand grains present initially were estimated visually. Seventy one samples were then selected for modal point counts, and 100 grains per sample were counted, exclusive of matrix. The point-count data are summarized in table 4.3. Both sets of modal estimates were used in the treatment of the data set, although more reliance was placed on the point-counted data for interpretations, and only those data are used in the diagrams accompanying this section. The point-counted results described here are not true detrital modes (*cf.* the Gazzi-Dickinson method; Dickinson, 1970) and the data should be regarded as qualitative.

Unlike CRP-1 samples, the CRP-2/2A samples examined are predominantly very fine- and fine-grained sandstones (60% of the sample set), with 30% of sandy siltstones/very silty sandstones and only about 10% of coarser samples (to medium sand size). Because detrital modes were not obtained on any of the siltstones or very matrix-rich very fine sandstones, the grain size of the majority of samples was more or less uniform (*i.e.* 85% of counted samples were very fine and fine sandstone), and undesirable effects of grain size variation were avoided (*cf.* Ingersoll et al., 1984; Smellie, 1998).

The different mineral and lithic grain types recognised and their inferred provenance are described in Cape Roberts Science Team (1998b, p. 46). For the visual estimates, the mineral grains were divided into simple petrographical types (*e.g.* colourless grains (quartz and feldspar), pyroxene, amphibole, volcanic glass, opaque grains), whose proportions could be determined relatively easily and reliably. For the modal counts, quartz and feldspar were separately identified, and there were also separate counts for brown and colourless glass. The opaque grain category

is a mixture of several grain lithologies, including: opaque oxide (*e.g.* (?) magnetite), extensively oxidised glass and lithic grains, feldspar densely charged with opaque 'dust', and coaly fragments.

RESULTS

The samples are dominated by colourless grains of quartz and feldspar, whose total proportion varies between 65 and 92%. The grains are variably abraded, mainly sub-angular/sub-rounded, but rounded grains are also commonly present and show a significant increase in abundance below *c.* 300 mbsf. Orthoclase is the commonest feldspar present, and other K-feldspars are minor. They are commonly charged with very fine opaque 'dust' that either gives crystals a reddish coloration or the grains are largely opaque. Plagioclase is also ubiquitous, mainly sodic in composition (albite-andesine) but accompanied by calcic plagioclase (labradorite-bytownite) and showing minor sericitic clay alteration.

Among the coloured mineral grain population, two pyroxene minerals are commonly present: 1) abraded translucent green pyroxene (augite, pigeonite and hypersthene) with prominent cleavage, a variable proportion of exsolved opaque oxide and/or fine parallel exsolution lamellae, and 2) angular grains of transparent very pale green or colourless clinopyroxene (augite). Although often petrographically distinctive, the two types grade in appearance into one another and no attempt was made to distinguish them quantitatively. They are rarely accompanied by trace amounts of titanite and aegirine or aegirine-augite. Amphibole is also ubiquitous, mainly a green to brownish green pleochroic hornblende, but including trace amounts of brown hornblende, (?)kaersutite and very rare (?)aenigmatite. Mica grains are represented by brown or rarely green biotite with a distribution mirroring that of amphibole (see below). The pyroxenes are a major component of most samples and typically form 7-20% of the mode. Amphibole varies between 0 and 4%, whereas biotite mainly occurs in trace amounts.

Volcanic glass is common above *c.* 280 mbsf, almost disappearing below that depth; it last appears in a sample at 469 mbsf. It is mainly poorly to non-vesicular, with blocky shapes and is fresh (very rarely (?)palagonite-altered) and predominantly angular; abraded glass is conspicuous in a few samples. Brown (basaltic?) and colourless (evolved - trachytic?) glass are ubiquitous; red glass is also present but less common. Glassy lapilli composed of very finely vesicular, colourless long-tube pumice are common and conspicuous in LSU 7.1 and 7.2 (note: all subsequent unit references are to lithostatigraphical sub-units), and form a thin 'layer' at *c.* 280 mbsf. The pumice is essentially identical in appearance to that forming the tephra layers in LSU 7.2 (Volcanic Clasts section).

Opaque grains are present but are very poorly characterized owing to extensive opaque oxide alteration. They are mostly sub-rounded. After quartz, feldspar and pyroxene grains, they are the next most common grain type, usually varying between 2 and 12% in the mode, and

reaching a maximum of 22%. In addition to detrital coal and (?) magnetite, grains of tachylite glass, partly glassy to holocrystalline lavas, dolerite and granitoids were also identified (although granitoids were counted as their constituent minerals; *cf.* Dickinson, 1970). The opaque grain total counts also include pyroxene and K-feldspar grains almost totally replaced by opaque oxide. Lava grains above *c.* 280 mbsf are predominantly unaltered, although grains of altered lava occur to the base of the cored sequence.

Common accessory minerals include pink garnet, zircon and sphene, and rare epidote, zeolite and detrital calcite. Silicic microfossils (diatoms and sponge spicules) are ubiquitous down to *c.* 350 mbsf, but are virtually absent below that depth in the samples examined.

Most of the sandstone samples contain less than 20% matrix or cement and some are essentially matrix-free. Cements are common and include micritic carbonate, coarser carbonate (especially in diagenetic nodules; see Diagenesis section), and (below *c.* 510 mbsf) tentatively identified gypsum and anhydrite.

MODAL VARIATIONS

Quartz (Q) contents are relatively low and variable above *c.* 100 mbsf (17-51%; Tab. 4.3). They show a see-saw variation down the sequence below that depth, with maxima at 190 mbsf (61-70%) and 400-425 mbsf (74-75%), and minima at 243 mbsf (38%) and 440 mbsf (49%; Tab. 4.3). Below 500 mbsf, Q contents show a steady increase, from *c.* 51 to 87%, but values apparently stabilise at *c.* 80-85% from 575 mbsf to the base of the sequence. Feldspar (F) shows a broadly antithetic variation compared with quartz. F contents are relatively high and variable above 100 mbsf (15-42%), becoming essentially constant between 100 and 500 mbsf except for several minor excursions to lower values (less than 15%) at *c.* 190-200, 300-310 and 400-425 mbsf. From 500 mbsf, F contents diminish to *c.* 8-10% at *c.* 570 mbsf, then remain roughly constant to base.

A consequence of the roughly antithetic Q and F variations is that Q/F ratios are essentially constant for a large section of the sequence, only varying between 1.7 and 2.5 between about 250 and 500 mbsf (Fig. 4.7). However, a minimum occurs between 50 and 150 mbsf, and another (less obvious) between 210 and 250 mbsf. By contrast, a striking feature of the Q/F ratios is the presence of several excursions to high Q/F values at 190-200, 290-310, 365-375 and 400-425. They correspond to peaks and troughs observed in the distribution of Q and F values. Finally, Q/F ratios show a remarkable sustained trend to much higher values (reaching 10.4) starting at *c.* 486 mbsf.

Modal data for total pyroxene (P) are very scattered (generally between 6 and 32%), possibly reflecting the low total counts (for 100 grains), but they show an obvious modal peak between 35 and 42 mbsf, corresponding to values of 20-32%. A second peak is defined at *c.* 147 mbsf (22%). 50-m averaged values suggest that P contents fluctuate only slightly downcore, but there is a significant trend to much lower values commencing at *c.* 500-550 mbsf

Tab. 4.3 - Empirical detrital modes of sand grains in CRP-2/2A sediments and sedimentary rocks. The data are based on counts of 100 grains only (excluding matrix and cement), using unstained smear slides, and they are qualitative.

Sample depth (mbsf)	Grain size	Quartz	Feldspar	Pyroxene	Amphibole	Glass	Opaque and lithic grains	Other grains	Matrix (<50) and cement (%)	Notes
8.50	poorly sorted VF SD	36	29	12	2	4	17	0	31	brown & green biotite;?aenigmatite;spicules;garnet;zircon
20.40	silty VF SD	46	26	13	1	0	13	1	38	brown biotite biot;zircon;carbonate;garnet;zeolite;spicules
26.09	poorly sorted VF(-F) SD	30	19	12	2	17	18	2	25	brown biotite;aegirine?;spicules;diatoms;zircon;spene
26.59	F SD	51	28	15	0	1	5	0	12	epidote?
35.85	F SD	34	20	32	2	0	12	0	1	brown biotite
36.36	poorly sorted F(-M) SD	29	24	23	2	10	10	2	18	spicules
40.15	F SD	39	15	28	4	1	12	1	11	kaersutite?;muscovite?;spicules;garnet
41.77	F SD	49	21	24	0	1	5	0	1	kaersutite;epidote;garnet
46.44	F SD	42	32	11	2	5	7	1	2	kaersutite?;garnet;spene/carbonate
54.40	silty VF SD	23	21	17	3	16	19	1	31	brown biotite?;aegirine?;Ti-augite;spicules;diatoms;spene
73.77	silty VFSD	17	23	9	1	31	15	4	30	hypersthene;Ti-augite;brown biotite;diatoms;spicules
79.00	poorly sorted VF SD	35	22	13	3	16	10	1	44	aegirine?;Ti-augite;spicules;diatoms
86.11	silty VF SST	22	42	17	2	7	10	0	47	kaersutite?;brown biotite
92.16	VF SST	25	26	8	1	15	23	2	28	hypersthene;brown&green biotite;garnet;spicules;diatoms;epidote?
111.09	silty VF SST	21	25	8	2	32	10	2	9	augite;spicules;garnet;diatoms;zircon;spene;epidote
133.72	(F-)VF SST	32	24	16	0	15	11	2	12	kaersutite;diatoms;spicules;spene;zircon
146.22	VF-F SST	44	25	21	1	4	5	0	5	kaersutite;spene;diatoms;garnet;zircon
147.63	VF(-F) SST	46	27	22	1	0	4	0	7	Ti-augite;hypersthene;epidote;zircon;garnet
149.75	VF SST	46	34	12	1	3	4	0	11	garnet
152.87	VF SST	53	27	12	2	2	4	0	7	Ti-augite;hypersthene;spene;garnet;zircon
155.91	VF-F SST	44	28	18	2	1	6	1	26	hypersthene;diatoms;garnet;zircon;spene
186.42	well sorted M SST	70	21	6	0	0	3	0	0	hypersthene;spene;zircon;garnet
187.46	well sorted M SST	61	20	11	0	0	6	2	3	hypersthene;garnet
193.46	silty VF SST	48	15	16	1	13	5	2	36	hypersthene;diatoms
200.33	silty VF SST	47	20	17	0	6	7	3	55	brown biotite;garnet;spicules;diatoms
224.46	well sorted VF SST	41	29	6	1	10	13	0	21	brown biotite;garnet;diatoms;spicules
243.44	muddy VF SST	38	23	12	0	15	9	3	43	hypersthene;kaersutite;green&brown biotite;diatoms;spicules
275.03	well sorted F-VF SST	47	27	12	0	8	6	0	7	Ti-augite;hypersthene;green&brown biotite;garnet;diatoms
280.07	well sorted F SST	48	26	7	1	9	9	0	9	brown biotite;garnet;spene
280.32	well sorted F SST	55	21	9	0	3	11	1	4	hypersthene;brown biotite;diatoms;garnet
287.15	well sorted F SST	58	17	14	0	1	10	0	8	hypersthene;garnet;diatoms;spene
295.20	well sorted F SST	52	29	11	1	0	7	0	13	brown biotite;spicules;diatoms
302.51	muddy-silty VF SST	53	22	17	1	0	7	0	40	Ti-augite;brown biotite;garnet
308.28	VF SST	60	15	13	0	0	12	0	10	hypersthene;kaersutite;brown biotite;zircon;garnet
310.10	VF SST	58	13	22	0	0	7	0	12	brown biotite;spicules;diatoms
318.35	well sorted VF SST	52	30	12	0	0	6	0	0	brown biotite;garnet
326.73	well sorted VF SST	62	26	6	0	0	6	0	0	kaersutite;brown biotite
359.00	F SST	61	26	9	0	0	4	0	30	garnet

Sample depth (mbsf)	Grain size	Quartz	Feldspar	Pyroxene	Amphibole	Glass	Opaque and lithic grains	Other grains	Matrix (<50%) and cement (%)	Notes
359.30	F SST	57	23	17	0	0	0	3	0	hypersihene:garnet; carbonate cement
364.22	F SST	67	18	11	0	0	0	4	0	hypersihene:garnet
372.77	(F-)VF SST	63	18	17	0	0	0	2	0	hypersihene:garnet;sphene
381.75	F SST	53	26	15	0	0	0	6	0	hypersihene?:brown biotite:garnet?
389.37	F-VF SST	50	28	21	0	0	0	1	0	Ti-augite:brown biotite:garnet;sphene
394.16	F SST	49	22	24	0	0	0	5	0	hypersihene?:brown biotite;sphene
399.00	VF SST	74	12	8	0	0	0	5	1	sphene
405.00	(F-)M SST	61	24	12	0	0	0	3	0	garnet
409.42	VF-F SST	57	25	10	1	0	0	7	0	brown biotite:spicules:garnet
417.26	F SST	51	28	16	0	0	0	5	0	carbonate cement
424.06	F SST	55	23	13	1	0	0	8	0	artvedsonite?:garnet
426.96	M SST	79	11	6	0	0	0	4	0	hypersihene
435.45	F-M SST	49	27	23	0	0	0	1	0	brown biotite:garnet
475.99	VF SST	59	25	12	1	0	0	2	1	aegirine?:hypersihene?:brown biotite:sphene:garnet
479.18	(VF-)F SST	51	24	17	1	0	0	7	0	hypersihene:garnet
486.13	VF SST	59	15	15	2	0	0	8	1	brown&green biotite:zircon:garnet:calcite cement
495.12	VF SST	63	19	9	0	0	0	9	0	kaersutite?:garnet
503.91	sandy SILTST	49	23	23	0	0	0	5	0	kaersutite?:green biotite:sphene:garnet; abundant gypsum cement
510.07	F SST	73	17	3	0	0	0	7	0	brown biotite?:garnet:zircon: trace gypsum cement
511.42	F SST	64	9	14	0	0	0	13	0	garnet; abundant gypsum cement
516.37	F SST	68	10	11	0	0	0	11	0	garnet; abundant gypsum cement
522.98	F SST	74	12	7	0	0	0	7	0	garnet;sphene; micrite cement
528.18	(M-)F SST	65	10	12	0	0	0	13	0	hypersihene?:garnet
529.00	F SST	60	15	17	0	0	0	8	0	brown biotite
532.70	F-M SST	62	11	16	0	0	0	11	0	brown biotite:garnet; carbonate cement
535.20	VF-F SST	71	7	11	0	0	0	11	0	micrite&calcite cement
545.66	M SST	74	14	6	0	0	0	6	0	brown biotite:diatoms:garnet
552.67	F SST	77	10	4	0	0	0	9	0	garnet
556.68	VF SST	78	12	5	0	0	0	5	0	brown biotite:zircon:diatoms:spicules
570.97	M SST	87	3	3	0	0	0	7	0	garnet
596.28	F SST	71	14	2	0	0	0	13	0	brown biotite; abundant gypsum cement
601.40	F-VF SST	83	11	1	0	0	0	5	0	brown biotite:zircon:garnet; minor gypsum cement
615.74	F SST	83	8	1	0	0	0	8	0	gypsum cement

Note: owing to deformation of samples during sampling and slide preparation, matrix/cement values may be exaggerated.

*Other grains - listed in notes.

Abbreviations - mbsf - metres below sea floor; Tr - trace amount (<<1%); SD - sand; SST - sandstone; SILTST - siltstone; VF - very fine; F - fine; M - medium.

Tab. 4.3 - Continued.

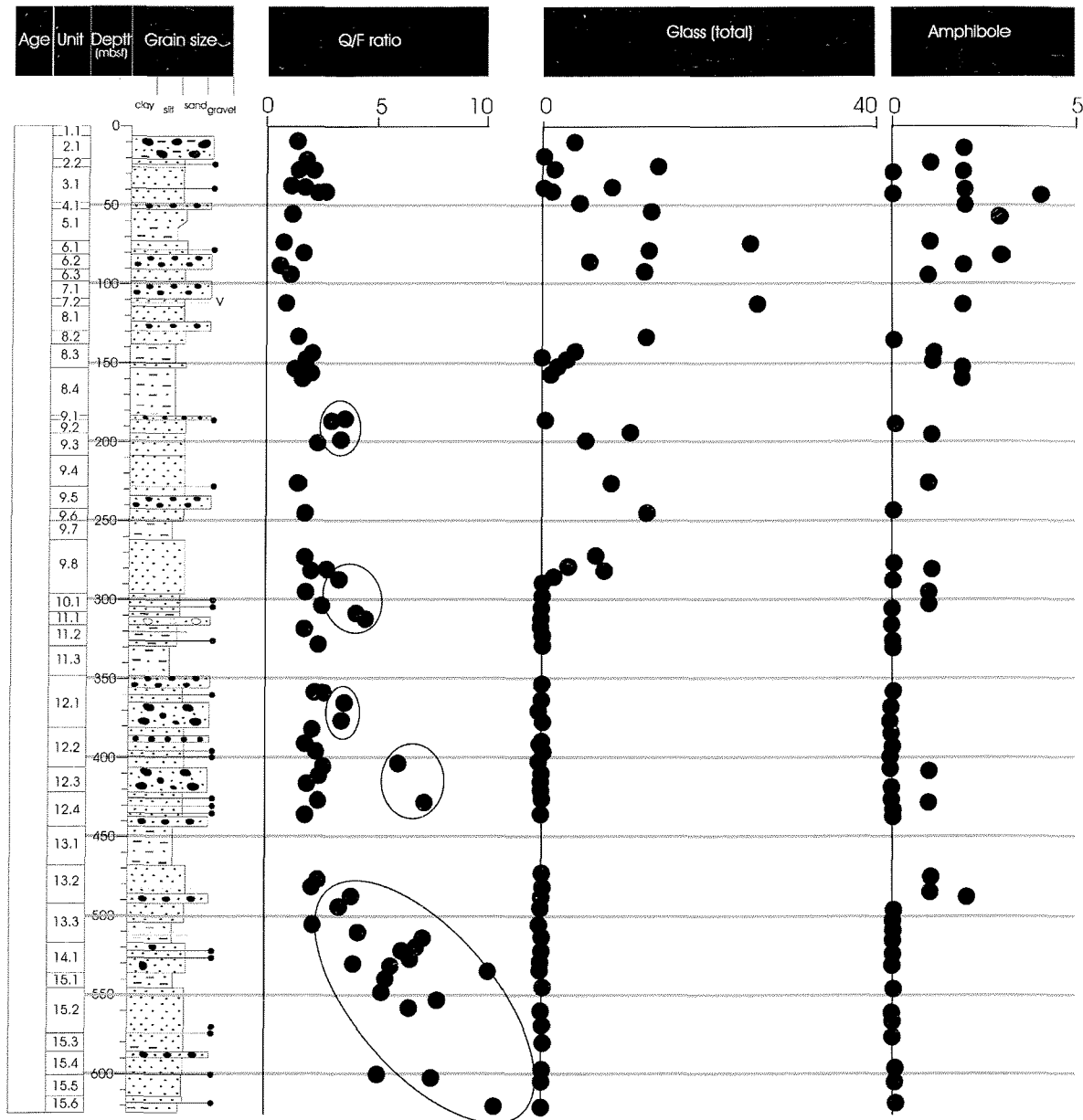


Fig. 4.7 - Summary diagram showing selected 'empirical detrital modes' for sand-grade samples from CRP-2/2A, illustrating variations of major compositional features with depth in the sequence. See text for description. Abbreviations: Q - total quartz; F - total feldspar. Samples with high Q/F ratios, believed to be dominated by Beacon-derived sand grains, are also indicated (encircled).

and decreasing to 1% at the base of the core. By contrast, amphibole shows a simple down-core trend of falling values, from *c.* 4% at 40 mbsf, becoming essentially absent below *c.* 300 mbsf (Fig. 4.7). However, amphibole is present in trace amounts in many samples to the base of the core. Biotite seems to show a similar distribution pattern to amphibole, but there are no quantified modal data since it usually occurs in trace amounts.

Modal data for glass grains show a small but distinct peak corresponding to Pliocene LSU 2.2, and two much broader peaks between 46 and 150 and 200-280 mbsf (Fig. 4.7). Below 280 mbsf, glass is practically absent, occurring only as isolated (one or two) grains in a few samples down to a depth of final appearance at 469 mbsf. Within the broad glass-rich zone at 46-150 mbsf, the glass distribution shows a strong lithofacies control. It is abundant

in beds of sandstone but absent or minor in the sandy matrices of diamictites.

Although modal values for opaque grains are very variable, at least three maxima are evident in the data set, corresponding to depths of 0-134, 200-308 and below 490 mbsf. The two upper maxima correspond closely to the two most prominent zones of peak glass abundances.

PROVENANCE

There are no grain types in the sandstone samples examined that are unique to CRP-2/2A; all are well documented from similar modal studies of samples from cores previously recovered from other sites in McMurdo Sound (MSSTS-1, CIROS-1, CRP-1; Barrett et al., 1986; George, 1989; Smellie, 1998). Similar provenances,

comprising granitoid and (volumetrically minor?) metamorphic 'basement' rocks, predominantly quartzose sandstones of the Beacon Supergroup, Ferrar dolerite and Kirkpatrick basalt, and alkaline lavas and tephra from the McMurdo Volcanic Group, are inferred for all sites.

Variations in the Q/F ratios are a clear indication of an evolving provenance. Between 625 and 500 mbsf, the sequence is characterized by variable but upward-diminishing, high Q/F ratios diagnostic of a source dominated by Beacon Supergroup sandstones (with very high Q/F ratios; Korsch, 1974). The trend to lower Q/F ratios at 500 mbsf, which are then remarkably constant between 500 and c. 280 mbsf (except for the three narrowly-defined Q/F 'peaks', described above; Fig. 4.7), indicates that a different lithological source has contributed to the provenance of the CRP-2/2A sandstones, which the observed grain and clast types indicate were likely 'basement' rocks (mainly granitoids and metamorphic rocks; see also Basement Clasts section). However, the intermittent presence of quartz-rich sandstones with high Q/F ratios (indicated in Fig. 4.7) suggests that Beacon Supergroup detritus temporarily dominated the local sediment supply, and these influxes are also characterised by an increased proportion of Beacon-derived rounded quartz grains (*cf.* Barrett et al., 1986; George, 1989; Smellie, 1998). Above 280 mbsf, the Q/F ratios show two 'dips' to lower ratios, 230. The locations of these features coincide with episodes of enhanced input of volcanic detritus, which diluted quartz but buffered feldspar, thus diminishing the Q/F ratios. At the end of each volcanic episode, Q/F ratios returned to values characteristic of a basement-dominated supply. Broadly comparable results are also shown by XRD analyses (see section on X-Ray Mineralogy), although the F/Q ratios used in that study (Fig. 4.5) do not clearly reproduce the pronounced ratio changes below 500 mbsf demonstrated by the sand grain modes reported here, possibly because of the fewer samples used in the XRD study.

The presence of fresh unabraded volcanic glass and tephra layers (*e.g.* at 112 mbsf; Volcanic Clasts section) is evidence for active volcanism coeval with sedimentation. The periodic influxes of volcanic debris (*e.g.* in Pliocene LSU 2.2, and at 46-150 and 200-280 mbsf) are evidence for significant volcanic episodes (*cf.* Smellie, 1998). As in CRP-1 (Armienti et al., 1998; Smellie, 1998), the volcanism was bimodal (basalt-trachyte) during all three documented episodes. The lack of a correlation between the glass-rich beds in CRP-2/2A and equivalent stratigraphical levels in CRP-1, situated only 800 m away, and the observed lithological control on the distribution of glass in CRP-2/2A indicate that input of the glass is overwhelmingly by sedimentation rather than by pyroclastic processes, which would be expected to yield a much more uniform and widespread distribution. A local volcanic source is likely, and was possibly situated within a few tens of km of the drill site. The prediction by the Cape Roberts Science Team (1998), that the glass detritus and the proportions of the compositional types may be good proxies for volcanism throughout the McMurdo Volcanic Group at any instant, is thus weakened. From the presence of fresh glass grains at 469 mbsf, volcanism was underway in the area during

early Oligocene times, at least. The sparse presence of glass between 469 and 280 mbsf suggests that the volcanic source(s) may have been relatively distant or else any glass-rich sediment bypassed the CRP-2/2A site during that depositional period. Conversely, the sudden volcanic influx at c. 280 mbsf indicates the inception of activity at a local volcano proximal to the drill site in late Oligocene times. It is speculated that the same volcano may have been responsible for the volcanic episode recorded by high glass abundances at 46-150 mbsf, which also probably erupted the multiple pumice layers in LSU 7.2, dated by W.C. McIntosh as 21.4 Ma (Early Miocene; see Volcanic Clasts section).

ORGANIC GEOCHEMISTRY

Some basic organic geochemical measurements were undertaken as part of the initial core characterization effort and to provide preliminary information regarding organic matter provenance, as well as the environments of deposition and early diagenesis. This effort comprised measurements of the C and N contents of 70 whole-rock samples and examination of some solvent-soluble organic matter extracted from one sample.

METHODS

Samples were collected at 5-10 m intervals and were intended to be representative of the major lithologies penetrated by CRP-2/2A. The sampling was biased to sediments and rocks with finer grain-sizes and well-preserved laminations. Although efforts were made to sample only the matrix of the diamictite and conglomerate units, some granule and pebble-sized clasts were included. An "oily overprint" was noted in the core logs at a number of intervals below 500 mbsf. Several of these intervals were sampled and one (CRP-2A-523.45-523.48) was selected for preliminary examination of solvent-soluble organic matter in the Crary Science and Engineering Center at McMurdo Station.

All samples, with the exception of CRP-2A-523.45-523.48, were freeze-dried to remove excess water, ground and homogenized in a Spex 8000 Mixer/Mill, and stored in 15 ml glass vials. All glassware used in sample preparation was cleaned with a commercial detergent followed by sequential rinses with 1% hydrochloric acid, methanol (Baker HPLC Solvent, lot J12293), and dichloromethane (Fisher Scientific, GC Resolv, lot 962656). Three sets of elemental analyses (Tab. 4.4) were performed using a Carlo-Erba NA 1500 analyzer and acetanilide as a standard: 1) total carbon (TC) and total nitrogen (TN) measurements were made on whole-rock samples, 2) total organic carbon (TOC_{LT}) was measured using the low-temperature vapour acidification technique outlined by Hedges & Stern (1984), and 3) total organic carbon (TOC_{HT}) was also measured using a high-temperature vapour acidification technique. The high temperature acidification was performed by placing a known mass of the powdered whole-rock samples in silver capsules. The capsules were then loaded in holes that had been drilled in

Tab. 4.4 - Values of total carbon (TC), total organic carbon determined by low temperature vapour acidification (TOC_{LT}), total organic carbon determined by high temperature vapour acidification (TOC_{HT}), and total nitrogen (TN) measured from samples of the CRP-2 core.

Sample	%TC	% TOC_{LT}	% TOC_{HT}	%TN	$\text{TOC}_{\text{HT}}/\text{TN}$
2-6.00-6.02	0.19±0.02	0.18±0.01	0.092±0.003	0.007±0.001	12
2-9.85-9.87	0.28±0.02	0.21±0.01	0.13±0.01	0.010±0.001	14
2-15.09-15.11	0.18±0.01	0.16±0.01	0.077±0.002	0.008±0.001	10
2-20.02-20.04	0.44±0.04	0.28±0.01	0.19±0.01	0.015±0.002	12
2-24.28-24.30	0.089±0.007	0.12±0.01	0.051±0.002	0.0068±0.0009	7
2-26.55-26.57	0.077±0.006	0.14±0.01	0.0087±0.0002	0.0068±0.0009	1
2-31.41-31.43	0.20±0.02	0.26±0.01	0.17±0.01	0.016±0.002	10
2-37.42-37.44	0.25±0.02	0.22±0.01	0.14±0.01	0.016±0.002	9
2-40.42-40.44	0.21±0.02	0.20±0.01	0.13±0.01	0.012±0.002	11
2-45.04-45.06	0.26±0.02	0.25±0.01	0.30±0.01	0.018±0.002	17
2-50.15-50.17	0.15±0.01	0.16±0.01	0.12±0.01	0.012±0.002	10
2-55.10-55.12	0.29±0.02	0.19±0.01	0.15±0.01	0.014±0.002	10
2A-55.32-55.34	0.20±0.02	0.25±0.01	0.17±0.01	0.019±0.003	9
2A-67.85-67.87	0.22±0.02	0.24±0.01	0.16±0.01	0.018±0.002	9
2A-77.06-77.08	0.11±0.01	0.15±0.01	0.1±0.01	0.009±0.001	11
2A-86.43-86.45	0.11±0.01	0.13±0.01	0.097±0.01	0.010±0.001	10
2A-96.29-96.31	0.22±0.02	0.26±0.01	0.20±0.01	0.021±0.003	10
2A-107.48-107.50	0.18±0.01	0.22±0.01	0.14±0.01	0.018±0.002	8
2A-113.63-113.65	0.26±0.02	0.32±0.02	0.22±0.01	0.035±0.005	6
2A-118.74-118.76	0.19±0.02	0.25±0.01	0.17±0.01	0.017±0.002	10
2A-128.10-128.12	2.90±0.23	0.19±0.01	0.15±0.01	0.010±0.001	15
2A-135.88-135.90	0.16±0.01	0.12±0.01	0.14±0.01	0.014±0.002	10
2A-149.58-149.60	0.37±0.03	0.24±0.01	0.17±0.01	0.015±0.002	12
2A-150.97-150.99	0.77±0.06	0.26±0.01	0.18±0.01	0.016±0.002	12
2A-155.45-155.47	0.093±0.007	0.14±0.01	0.08±0.01	0.0056±0.0008	14
2A-164.95-164.97	0.34±0.03	0.31±0.02	0.24±0.01	0.021±0.003	11
2A-173.32-173.34	0.29±0.02	0.34±0.02	0.27±0.01	0.024±0.003	11
2A-176.75-176.77	0.31±0.02	0.34±0.02	0.28±0.01	0.027±0.004	10
2A-184.45-184.47	0.25±0.02	0.18±0.01	0.12±0.01	0.011±0.002	11
2A-192.44-192.46	0.11±0.01	0.12±0.01	0.075±0.003	0.0069±0.0009	11
2A-198.50-198.52	0.27±0.02	0.18±0.01	0.14±0.01	0.012±0.002	11
2A-206.82-206.84	0.37±0.03	0.22±0.01	0.15±0.01	0.014±0.002	11
2A-221.31-221.33	2.23±0.18	0.32±0.01	0.18±0.01	0.017±0.002	10
2A-226.67-226.69	0.29±0.02	0.30±0.01	0.18±0.01	0.019±0.003	9
2A-238.53-238.55	0.33±0.03	0.39±0.01	0.25±0.01	0.023±0.003	11
2A-245.34-245.36	0.35±0.03	0.38±0.01	0.22±0.01	0.027±0.004	8
2A-255.92-255.94	0.68±0.05	0.70±0.02	0.53±0.02	0.061±0.008	9
2A-270.03-270.05	0.20±0.02	0.31±0.01	0.17±0.01	0.022±0.003	8
2A-277.43-277.45	0.12±0.01	0.21±0.01	0.097±0.003	0.008±0.001	12
2A-287.11-287.13	0.15±0.01	0.23±0.01	0.12±0.01	0.008±0.001	16
2A-295.09-295.11	0.11±0.01	0.23±0.01	0.093±0.003	0.0066±0.0009	14
2A-296.83-296.85	0.93±0.07	0.26±0.01	0.14±0.01	0.015±0.002	9
2A-304.98-305.00	0.37±0.03	0.32±0.01	0.21±0.01	0.013±0.002	16
2A-314.24-314.26	0.65±0.05	0.35±0.01	0.25±0.01	0.017±0.002	15
2A-317.59-317.61	0.65±0.05	0.67±0.02	0.53±0.02	0.041±0.006	13
2A-321.59-321.61	0.58±0.05	0.29±0.01	0.19±0.01	0.010±0.001	19
2A-325.84-325.86	0.53±0.04	0.27±0.01	0.17±0.01	0.008±0.001	21
2A-337.40-337.42	1.02±0.08	0.33±0.01	0.21±0.01	0.016±0.002	13
2A-347.70-347.72	0.98±0.08	0.48±0.02	0.34±0.01	0.027±0.004	13
2A-358.09-358.11	0.58±0.05	0.45±0.01	0.34±0.01	0.024±0.003	14
2A-359.54-359.56	0.64±0.05	0.56±0.02	0.49±0.02	0.018±0.002	27
2A-370.37-370.39	0.72±0.06	0.33±0.01	0.23±0.01	0.012±0.002	19
2A-382.00-382.02	0.34±0.03	0.39±0.01	0.28±0.01	0.017±0.002	16
2A-390.38-390.40	0.47±0.04	0.56±0.02	0.39±0.01	0.026±0.004	15
2A-404.01-404.03	0.34±0.03	0.28±0.01	0.21±0.01	0.008±0.001	26
2A-412.56-412.58	0.42±0.03	0.42±0.01	0.31±0.01	0.018±0.002	17
2A-426.36-426.38	0.28±0.02	0.35±0.01	0.23±0.01	0.009±0.001	26
2A-437.73-437.75	0.49±0.04	0.32±0.01	0.21±0.01	0.015±0.002	14
2A-450.26-450.28	1.10±0.09	0.49±0.02	0.38±0.01	0.029±0.004	13
2A-459.04-459.06	0.61±0.05	0.66±0.02	0.54±0.02	0.045±0.006	12
2A-465.49-465.51	0.59±0.05	0.56±0.02	0.42±0.02	0.041±0.006	10
2A-467.51-467.53	2.02±0.16	0.47±0.02	0.36±0.01	0.027±0.004	13
2A-477.34-477.36	0.46±0.04	0.32±0.01	0.21±0.01	0.017±0.002	13
2A-481.29-481.31	0.58±0.05	0.41±0.01	0.26±0.01	0.020±0.003	13
2A-486.90-486.92	0.47±0.04	0.31±0.01	0.17±0.01	0.014±0.002	12
2A-498.72-498.74	0.072±0.006	0.16±0.01	0.04±0.01	0.008±0.001	5
2A-500.42-500.44	0.18±0.01	0.26±0.01	0.14±0.01	0.009±0.001	16
2A-523.45-523.47	0.75±0.06	0.59±0.04	0.37±0.02	0.021±0.003	18
2A-583.46-583.48	0.56±0.04	0.60±0.04	0.39±0.02	0.026±0.004	15
2A-623.21-623.23	0.62±0.05	0.65±0.04	0.44±0.03	0.023±0.003	19

a 25 mm section of 25 mm teflon rod. Each section of teflon rod could accommodate three capsules. The teflon rod and capsules were placed inside a 15 ml wide-mouth teflon bottle with 1-2 ml of concentrated HCl acid. The teflon containers were sealed with a screw closure, loaded into a stainless steel pressure vessel and placed in an oven at 150°C for 12 hours. The samples were removed after the pressure vessel had cooled and placed in a oven to dry at 55°C.

Only C and N data are reported here. The Carlo-Erba NA1500 did not function properly during the project period and whole-rock C, N and S data from all samples will be reported in the Scientific Results volume.

Sample CRP-2A-523.45-523.48 was crushed in the SPEX 8000 mixer/mill, weighed and placed in a cellulose extraction thimble. The sample was extracted for 24 hours using an azeotropic mixture of toluene (Fisher Scientific Optima, lot 962474) and methanol in a Soxhlet apparatus. The sample was then extracted for an additional 24 hours using dichloromethane. Whereas the methanol/toluene solution changed from colourless to light yellow over the course of the extraction, the dichloromethane remained colourless throughout the 24 hour extraction. The methanol/toluene solution was placed in a separating funnel and a hydrophobic phase was isolated using water that had been purified in a Barnstead 4-stage purification system. The aqueous phase was transferred to another separating funnel where a second hydrophobic phase was isolated using the dichloromethane solution obtained in the second extraction. The hydrophobic phases were evaporated to dryness under partial vacuum using a rotary evaporator. The resulting liquid was transferred to a 1 ml glass vial using dichloromethane and dried to a constant mass. This C_{15+} fraction was analyzed on a Hewlett-Packard 5890 gas chromatograph equipped with a J&W Scientific fused silica capillary column (30 m x 0.32 mm) coated with DB-5 (0.25 Fm film thickness). The flame ionization detector and injector were regulated by thermostat to 300°C, whereas the oven temperature was controlled at 38°C for 3 minutes followed by an increase to 290°C at 4°C/minute and isothermal conditions for an additional 60 minutes.

RESULTS AND DISCUSSION

TOC values obtained from the CRP-2/2A core are low. Only ten of the TOC_{LT} and three of the TOC_{HT} measurements obtained exceed 0.5% (Tab. 4.4). Although the precision of the measurements is quite good there is clearly a slight problem with accuracy: a number of the samples have TOC_{LT} values that exceed the TC values by amounts in excess of the assigned errors. The problem is most pronounced in samples with very low TOC and TC values (Tab. 4.4). Two of intervals with the highest TOC values correspond to zones with abundant biogenic sediment: 1) a zone containing abundant diatoms centred on 250 mbsf, and 2) a zone containing abundant diatoms and calcareous nannofossils centred on 460 mbsf (Fig. 4.8). The correlation between higher TOC values and greater amounts of biogenic debris is not universal, however. A number of zones with abundant biogenic sediment do not exhibit elevated TOC values; most notable among these

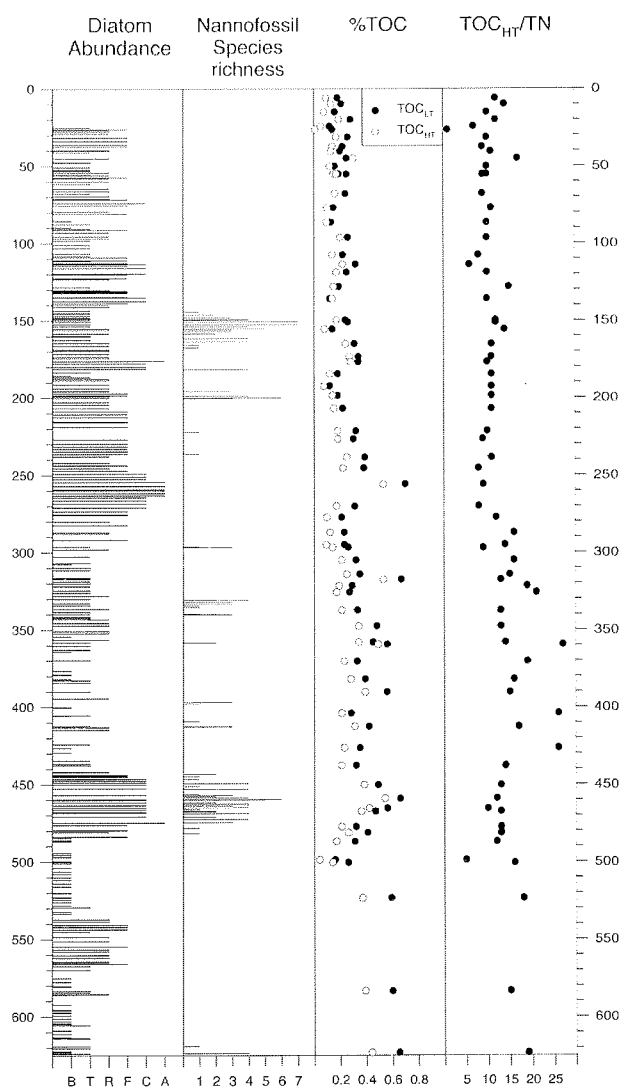


Fig. 4.8 - Comparison of values of total organic carbon determined using low temperature (TOC_{LT}) and high temperature (TOC_{HT}) vapour acidification, and TOC_{HT}/TN compared with the abundance of diatoms, and the nannofossil species richness of the CRP-2/2A core.

are the zones of high diatom abundance in the upper 150 m of CRP-2/2A (Fig. 4.8). Although TOC values of samples obtained from below 300 mbsf are, in general, higher than those obtained at more shallow depths (Tab. 4.4, Fig. 4.8), the slight decrease in TOC values up-section does not correspond to a similar decrease in the amount of biogenic debris.

TOC:TN ratios are high throughout the section. Organic matter with TOC:TN ratios significantly greater than 10 is derived largely from land plants and coals, whereas aquatic organisms have much lower TOC:TN ratios (Bordovskiy, 1965). The high TOC:TN ratios observed in the CRP-2/2A core are strong evidence that the preserved organic matter comprises a mixture of detrital coal and aquatic organic matter. The TOC:TN ratios decrease slightly in the high TOC sections observed at 250 mbsf and 460 mbsf and are interpreted as evidence that the preservation of greater amounts of organic carbon is related to the greater abundances of biogenic debris in these sediments and

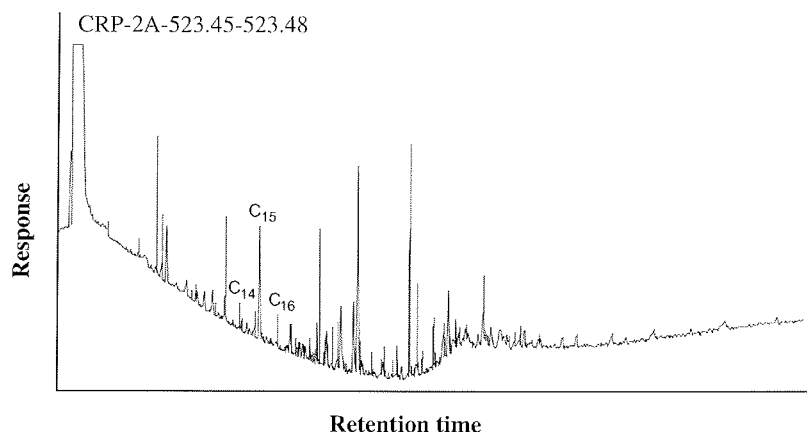


Fig. 4.9 - Chromatogram of solvent-soluble organic matter obtained from Sample CRP-2A-523.45-523.48. The peaks labeled C₁₄, C₁₅, and C₁₆ have been tentatively identified as the alkanes n-tetradecane, n-pentadecane, and n-hexadecane.

rocks. On the other hand, the TOC:TN ratios of samples obtained from below 300 mbsf are elevated slightly relative to those in the upper portion of the core, and are evidence that detrital coal is more abundant in the lower portion of the core than it is from 0 to 300 mbsf.

Two types of TOC measurements were undertaken to assess the contribution of refractory carbonate phases to the carbon content of the rocks. Although the results from the CRP-1 core were imprecise (Cape Roberts Science Team, 1998c; p. 87), no apparent difference between TOC and TC was observed. Later work established the presence of siderite in samples from the CRP-1 core (Baker & Fielding, 1998). Siderite is a refractory carbonate phase that requires months to dissolve when subjected to low temperature acidification (Rosenbaum & Shepard, 1986; p. 1148). The high-temperature vapour acidification technique was developed in an attempt to quantify the abundances of labile carbonate (largely calcite) and refractory carbonate in the CRP-2/2A core. A few samples contain significant amounts of labile carbonate reflecting the presence of the calcite-cemented concretions and layers observed in the core. Examples include CRP-2A-221.31-221.33, a rock that has a TC value of 2.2%, whereas the TOC_{LT} value is only 0.32%. With one exception, the values of TOC_{LT} are significantly higher than the values of TOC_{HT} for identical samples. If the different values of TOC_{LT} and TOC_{HT} are caused by the presence of siderite or other refractory carbonate phases, then one can calculate

the amounts of labile carbonate and refractory carbonate present by difference. The relationship between the TOC_{LT} and TOC_{HT} values is evidence that siderite is present in the CRP-2/2A core and, combined with the low TOC values, is evidence that the diagenetic environment at the drill site was largely post-oxic (Berner, 1981).

Sample CRP-2A-523.45-523.48 did not fluoresce under ultraviolet light. It did, however, yield a small amount of bitumen. That sample, comprising 36.60 g of sand and shale, produced 3.6 mg of bitumen for a bitumen ratio of 27 mg bitumen/g organic carbon. Although the amount of bitumen recovered is small, it is significantly larger than the amounts recovered during processing of CRP-1 core (Kettler, 1998). A chromatogram of the total extract (Fig. 4.9) has a number of large peaks and a relatively small unresolved complex mixture (UCM). Interpretation of the chromatogram is complicated by a tailing solvent peak. The alkane hydrocarbons n-tetradecane (n-C₁₄), n-pentadecane (n-C₁₅), and n-hexadecane (n-C₁₆) are tentatively identified by comparison of retention times with a standard mixture. The small size of the UCM and the abundance of compounds with apparently lower molecular weights than n-C₁₅, are evidence that the bitumen has not been severely degraded by microbial activity or water-washing. The apparent predominance of odd-numbered alkanes over the even-numbered alkanes (Fig. 4.9) is evidence that this bitumen has a low thermal maturity.

5 - Palaeontology

INTRODUCTION

Six groups of fossils were examined during the preliminary investigation of the CRP-2/2A pre-Pliocene sequence: diatoms, calcareous nannofossils, foraminifers, marine palynomorphs, terrestrial palynomorphs, and marine invertebrate macrofossils. Each of these fossil groups provides important biostratigraphical and palaeo-environmental data for the analysis of the recovered sequence. Marine diatoms provide the principal data for biostratigraphically dating the core material. Calcareous nannofossils and marine palynomorphs provide additional biostratigraphical control. Biostratigraphical dating provides age control for the sedimentary rock sequence in CRP-2/2A, allows regional correlation to other sections in the Victoria Land Basin and the Southern Ocean, and helps constrain the calculation of sediment accumulation rates.

All six fossil groups provide valuable information on the palaeoenvironment of the Ross Sea and surrounding continental areas near Cape Roberts. Planktic diatoms and marine palynomorphs are important monitors of neritic or mesotrophic surface water conditions in the geological past, while calcareous nannofossils indicate when oligotrophic oceanic waters invaded the site. In consequence, these planktic microfossil groups provide information on relative water depth, nutrient availability, turbidity, and water temperature. Benthic foraminifers and invertebrate macrofossils indicate past seafloor conditions including temperature and substrate character. Terrestrial palynomorphs yield a record of the vegetation on the continent adjacent to the site of CRP-2/2A, as well as indicate the age of existing sedimentary rocks that are being eroded on the mainland.

Changes in fossil assemblages through time may be the result of evolutionary changes in the organisms, environmental changes that force ecological restructuring of the biota, or shifts in preservational regime. All of these factors are clearly at work in the fossil succession in CRP-2/2A. A sequence of formal or informal zones for each microfossil group is illustrated in figure 5.1, and a brief introduction to the fossil groups is given below.

Diatoms are the most abundant fossil group in CRP-2/2A sediments. In certain intervals, diatoms constitute as much as 30% of the sedimentary rock. However, in most samples, diatom abundance is not more than about 5% of the silt and sand-dominated sediment, and some intervals are barren of diatoms. High sediment accumulation rates and generally good diatom preservation provide the opportunity to develop a detailed biostratigraphy for the late Palaeogene-early Miocene period for the Ross Sea, although several major disconformities are present. CRP-2/2A diatom assemblages are dominated by planktic assemblages, which

are better biostratigraphical markers than benthic taxa. The diatom assemblages, however, are dominated by neritic taxa, rather than open-ocean pelagic taxa, which form the basis of Southern Ocean deep-sea biostratigraphy. Diatoms provide ages of *c.* 20 Ma below the Plio-Pleistocene/Miocene unconformity at *c.* 26 mbsf. The base of the Miocene cannot be confidently identified based on diatoms, but is suggested to be at *c.* 130 mbsf and is associated with an unconformity. Similarly, the upper/lower Oligocene boundary is probably within a barren interval between *c.* 300 and 412 mbsf. Lower Oligocene sediments are recognized, based on diatom assemblages, from *c.* 412 mbsf down to at least *c.* 484 mbsf. Diatom assemblages below 484 mbsf cannot be confidently assigned to either Lower Oligocene or uppermost Eocene at present.

Foraminifera, representing 28 genera and 45 species, occur in 73 of the 135 samples examined from the upper

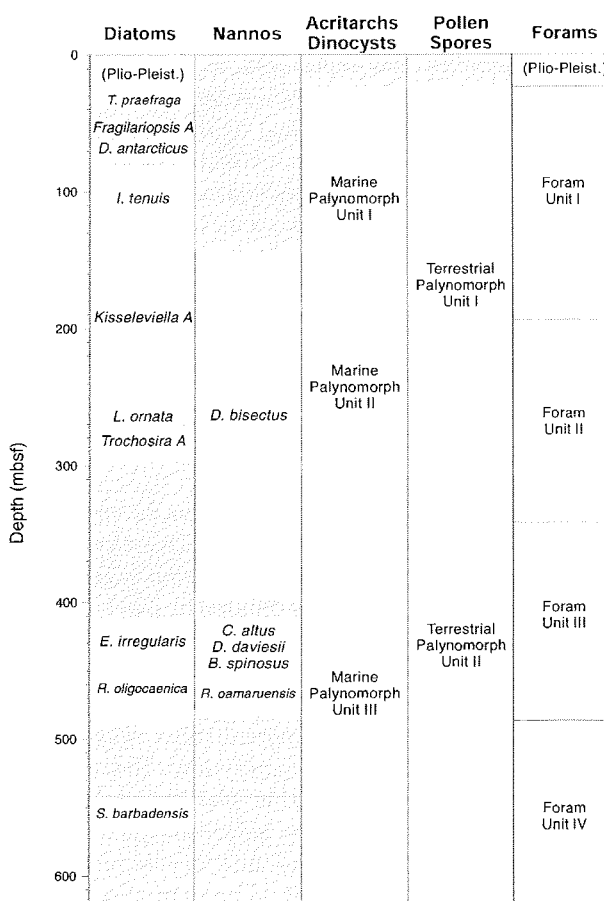


Fig. 5.1 - Summary diagram of tentative CRP-2/2A zonation schemes from diatom, calcareous nannofossil, marine palynomorph, terrestrial palynomorph, and foraminifer stratigraphy. Shaded areas represent intervals of poor preservation, barren samples, or gaps in sample spacing.

Palaeogene through Lower Miocene section of CRP-2/2A from c. 34 to c. 624 mbsf. All assemblages contain only calcareous benthic taxa, and neither planktic nor agglutinated benthic forms were observed. Four major foraminiferal units were delineated for the succession, and ascribed to local biofacies shifts. The units may reflect long-term bathymetric changes from inshore environments in early Oligocene to mid or outer shelf and then outer shelf or upper bathyal in early late Oligocene. Inshore conditions apparently returned during the late Oligocene-early Miocene.

Calcareous nannofossils in the CRP-2A succession record episodes of hemipelagic sedimentation marking times when open oceanic surface waters penetrated into the Victoria Land Basin. One major, and several minor, pulses of oceanic surface water invasion are indicated during the Upper Oligocene *Dictyococcites bisectus* Zone from c. 144 to 397 mbsf. Another episode of oceanic incursion is evidenced by nannofossil assemblages from c. 412 to 481 mbsf, where at least two upper biostratigraphical zones are represented. A long barren interval, from c. 482 to 613 mbsf, overlies two nannofossil-bearing samples just above the base of the hole.

Well-preserved marine palynomorphs were recovered from most samples from the upper Palaeogene through Miocene section. Species richness is moderate to high. The majority of specimens are considered to be *in situ* and many have not been described formally. Three marine palynological units are recognized (Fig. 5.1). Unit I is dominated by prasinophyte algae, mainly *Leiospheres* and *Sigmopollis*, and represents an extension of the assemblage recovered from below 99.01 mbsf. Marine palynomorphs Unit II is marked by the presence of the dinoflagellate *Lejeunecysta* sp. 1. Unit III assemblages are characterized by the acritarch *Leiofusa*, the dinoflagellate *Pyxidinospis* sp. and several species of *Lejeunecysta*. These units probably reflect changes in the palaeoenvironment. The assemblages recovered from CRP-2/2A continue to fill in a gap in the knowledge of marine palynomorph biostratigraphy between the well-established Palaeogene Transantarctic flora and the Recent. Several species of dinoflagellates, notably *Lejeunecysta* spp., may provide several biostratigraphical datums for the Ross Sea area.

Terrestrial palynomorphs are very rare throughout the upper part of the core, above c. 306 mbsf. This is interpreted as the result of both sparse contemporaneous vegetation in the surrounding landscape and dilution by rapid sediment accumulation. The rare spores and pollen reflect a long-lived tundra vegetation that survived in coastal lowlands in harsh periglacial conditions. Below 306 mbsf, palynomorphs are relatively more diverse and common, although total numbers remain very low. They reflect a low diversity woody vegetation that included several species of *Nothofagus* and podocarpaceous conifers, along with other angiosperm taxa and cryptogams. The assemblages in lowermost CRP-2A never reach the species richness and abundance seen in the Eocene sedimentary rocks documented from the lower part of CIROS-1 or the McMurdo Sound erratics. Recycled palynomorphs, of

probable Eocene, Jurassic-Cretaceous, and Permian-Triassic age, are also recognized. Permian-Triassic palynomorphs derived from the Beacon Supergroup are most abundant below 306 mbsf.

SILICEOUS MICROFOSSILS

INTRODUCTION

Diatoms provide one of the primary biostratigraphical and palaeoenvironmental tools for interpreting the CRP-2/2A core. In addition to diatoms, silicoflagellates and ebridians (both siliceous flagellates), and a chrysophyte cyst provide supporting biostratigraphical information. Upper Palaeogene through Lower Miocene diatom assemblages are recognized from c. 28 mbsf to the bottom of the hole at 624.15 mbsf, and this interval is divided into 10 tentative biostratigraphical zones. A large number of taxa in this interval are previously unknown or undescribed, many of which have been informally recognized in Ross Sea cores. Three undescribed, but taxonomically distinct, taxa provide tentative zonal boundaries. The CRP-2/2A core will provide age constraints on these and other taxa for the Ross Sea, which will permit age calibration of previously-drilled Antarctic cores.

METHODS

All samples were prepared for siliceous microfossils as strewn slides of raw sediment, following standard procedures. As necessary, selected samples were reacted in H_2O_2 and/or HCl to help remove organic and carbonate cements, respectively. Additional samples were prepared further by separating the $>10 \mu m$ fraction using nylon screens. Several samples were sieved with $20 \mu m$ and $25 \mu m$ stainless steel mesh sieves, and diatoms in about 15 samples were prepared with density separation techniques, using a sodium polytungstate solution prepared at 2.2 specific gravity. Relative diatom abundance, represented graphically on figure 5.2 and in table 5.1, was determined from strewn slides of unsieved material. Stratigraphical occurrence and abundance data are based on detailed analysis of more than 50 diatom-bearing samples, plus cursory examination of 250 additional samples.

RESULTS

Siliceous microfossils occur in variable abundance through the recovered stratigraphical succession of CRP-2/2A (Fig. 5.2). Diatoms are most abundant in fine-grained lithologies, except in intervals that have undergone significant diagenesis. More than 150 diatom species and species groups, plus 11 silicoflagellates, 7 ebridians, 2 endoskeletal dinoflagellates, and one biostratigraphically-useful chrysophyte cyst are recognized in the initial examination of CRP-2/2A samples. Radiolarians were not observed in the recovered sequence.

CRP-2/2A Initial Report siliceous microfossil data (Fig. 5.3) include many informal taxonomic designations.

Tab. 5.1 - CRP-2/2A relative diatom abundance data.

Top	Bottom	Abund.	Top	Bottom	Abund.	Top	Bottom	Abund.	Top	Bottom	Abund.
25.25	25.26	T	147.07	147.08	T	288.00	288.01	R	468.52	468.53	C
26.48	26.49	F	148.19	148.20	T	292.08	292.10	F	470.79	470.80	C
26.78	26.79	R	148.72	148.73	T	296.39	296.40	T	474.90	474.91	A
27.70	27.71	R	149.65	149.66	T	298.07	298.08	R	476.30	476.31	F
29.06	29.08	R	150.70	150.71	T	302.65	302.66	T	479.71	479.72	F
31.71	31.72	F	152.40	152.41	T	306.95	306.96	T	480.82	480.83	R
33.84	33.85	F	153.70	153.71	T	307.70	307.71	B	483.92	483.93	F
36.24	36.25	F	155.20	155.21	R	309.88	309.89	T	484.55	484.56	B
36.40	36.41	F	156.07	156.08	R	311.56	311.57	T	486.28	486.30	B
37.44	37.45	F	158.50	158.51	R	316.48	316.50	T	486.76	486.77	B
39.82	39.83	R	159.81	159.82	T	317.27	317.28	T	494.38	494.39	B
40.24	40.25	R	160.29	160.30	T	318.85	318.68	T	495.62	495.63	B
41.19	41.20	T	162.42	162.43	T	320.05	320.06	T	496.90	496.91	B
45.12	45.13	R	164.50	164.51	R	322.00	322.01	T	499.65	499.66	B
47.41	47.54	T	166.34	166.35	R	324.54	324.55	T	500.26	500.27	B
47.82	47.83	T	168.79	168.80	R	326.07	326.08	T	501.05	501.06	B
50.82	50.83	T	169.58	169.59	R	328.08	328.09	R	503.90	503.91	B
52.47	52.48	T	171.49	171.50	R	330.08	330.09	T	506.22	506.23	B
54.36	54.37	R	173.46	173.47	R	332.76	332.77	T	507.86	507.88	B
56.10	56.11	R	174.38	174.39	R	334.14	334.15	T	510.13	510.14	B
57.32	57.42	F	176.29	176.30	A	336.51	336.52	R	511.75	511.76	B
CRP-2A			177.89	177.90	C	338.45	338.46	T	514.04	514.05	B
53.19	53.20	T	179.93	179.94	C	339.80	339.82	T	516.08	516.09	B
55.81	55.82	T	181.32	181.33	C	341.72	341.73	T	520.12	520.13	B
58.15	58.16	R	183.58	183.59	T	342.46	342.47	T	523.04	523.05	B
59.96	59.97	R	185.76	185.77	B	343.26	343.27	R	524.39	524.41	B
61.50	61.51	T	186.70	186.71	T	345.58	345.59	R	526.01	526.02	B
64.60	64.61	R	187.67	187.68	R	347.31	347.32	R	528.22	528.23	B
66.24	66.25	R	188.57	188.58	R	350.89	350.90	R	529.33	529.34	T
67.84	67.85	T	191.36	191.37	R	352.15	352.16	R	532.34	532.35	B
69.47	69.48	R	193.99	194.00	R	354.23	354.24	B	533.43	533.44	B
71.13	71.13	R	195.70	195.72	R	356.44	356.45	R	537.25	537.26	R
71.70	71.71	F	197.12	197.13	F	358.22	358.24	T	538.46	538.47	R
73.94	73.95	C	198.52	198.53	F	360.27	360.28	T	540.73	540.74	F
75.52	75.56	F	199.08	199.09	R	362.91	362.92	T	542.04	542.05	F
79.48	79.49	R	200.16	200.17	R	364.27	364.28	B	543.81	543.83	F
80.79	80.80	F	202.85	202.86	R	369.73	369.74	T	545.18	545.19	T
85.57	85.58	B	204.58	204.59	R	376.54	376.55	B	548.57	548.58	R
87.58	87.59	T	206.81	206.82	R	379.03	379.04	B	551.29	551.30	R
89.72	89.73	B	208.76	208.77	F	382.02	382.03	B	554.70	554.71	F
90.77	90.78	T	210.58	210.59	F	382.81	382.82	T	556.60	556.61	R
91.19	91.20	F	212.61	212.62	F	384.28	384.29	T	557.85	557.86	R
93.04	93.05	R	215.33	215.34	F	390.01	390.02	T	560.33	560.34	R
95.61	95.62	R	215.72	215.74	F	390.19	390.21	T	562.31	562.32	R
96.84	96.85	R	218.80	218.81	F	394.48	394.49	R	564.63	564.66	R
98.30	98.31	T	226.94	226.95	F	400.22	400.23	B	565.50	565.51	R
101.17	101.18	T	229.70	229.71	F	405.37	405.38	T	565.98	565.99	F
103.28	103.29	T	231.49	231.50	F	405.58	405.59	B	567.50	567.51	T
106.77	106.78	T	233.00	233.01	F	412.27	412.29	T	570.02	570.03	T
108.18	108.19	T	234.70	234.71	F	413.05	413.06	R	575.15	575.16	B
109.12	109.13	F	236.25	236.26	F	414.79	414.80	R	577.67	577.68	B
111.05	111.06	F	237.87	237.88	R	424.10	424.11	T	580.53	580.54	B
111.53	111.54	T	241.89	241.90	R	426.49	426.50	B	583.51	583.52	T
112.90	112.91	F	243.63	243.64	F	429.38	429.39	B	584.54	584.57	T
113.51	113.52	C	245.54	245.55	R	434.66	434.67	T	585.58	585.59	R
114.43	114.44	F	247.08	247.09	F	436.72	436.73	T	585.84	585.85	T
116.15	116.16	C	249.07	249.08	C	437.68	437.69	T	592.23	592.24	B
119.65	119.66	C	250.93	250.94	C	441.85	441.86	R	595.72	595.73	B
120.33	120.34	F	252.46	252.47	C	443.89	443.90	F	597.44	597.45	B
122.56	122.57	F	254.43	254.44	A	444.25	444.26	F	599.25	599.26	B
123.32	123.33	R	256.91	256.92	A	444.96	444.98	F	601.35	601.36	B
128.52	128.53	T	259.20	259.21	A	446.55	446.56	C	603.14	603.15	B
130.32	130.33	R	260.02	260.04	A	447.68	447.69	C	604.40	604.42	B
130.90	130.93	F	261.60	261.61	A	448.73	448.74	C	604.92	604.93	B
131.67	131.68	F	263.20	263.21	A	450.06	450.07	C	605.66	605.67	T
132.34	132.35	F	264.38	264.39	C	453.19	452.20	C	609.07	609.08	B
134.74	134.75	F	266.38	266.39	C	456.83	456.84	C	611.10	611.11	B
135.09	135.10	C	268.31	268.32	C	459.70	459.71	C	613.35	613.36	B
137.46	137.47	C	271.02	271.04	C	459.90	459.91	C	614.03	614.04	T
138.83	138.84	F	273.50	273.51	F	460.13	460.14	C	619.19	619.20	T
139.90	139.91	R	275.48	275.49	F	461.65	461.66	C	620.50	620.51	T
141.26	141.27	R	275.90	275.91	F	463.53	463.54	C	622.31	622.32	B
143.69	143.70	T	280.12	280.13	R	464.98	465.00	C	623.03	623.04	B
145.14	145.15	T	282.42	282.43	F	466.27	466.28	C	623.76	623.79	B
145.58	145.59	T	287.07	287.08	R	467.85	467.86	C	624.03	624.04	T

Note: all depths are in metres below sea floor (mbsf).

Samples 25.25 through 57.32 mbsf, above the solid line, are from hole CRP-2.

Samples from 53.19 through 624.03 mbsf, below the solid line, are from hole CRP-2A.

"Top" refers to upper depth of sample interval, and "Bottom" refers to lower depth of sample interval (in mbsf).

B = barren, T = trace, R = rare, F = few, C = common, and A = abundant.

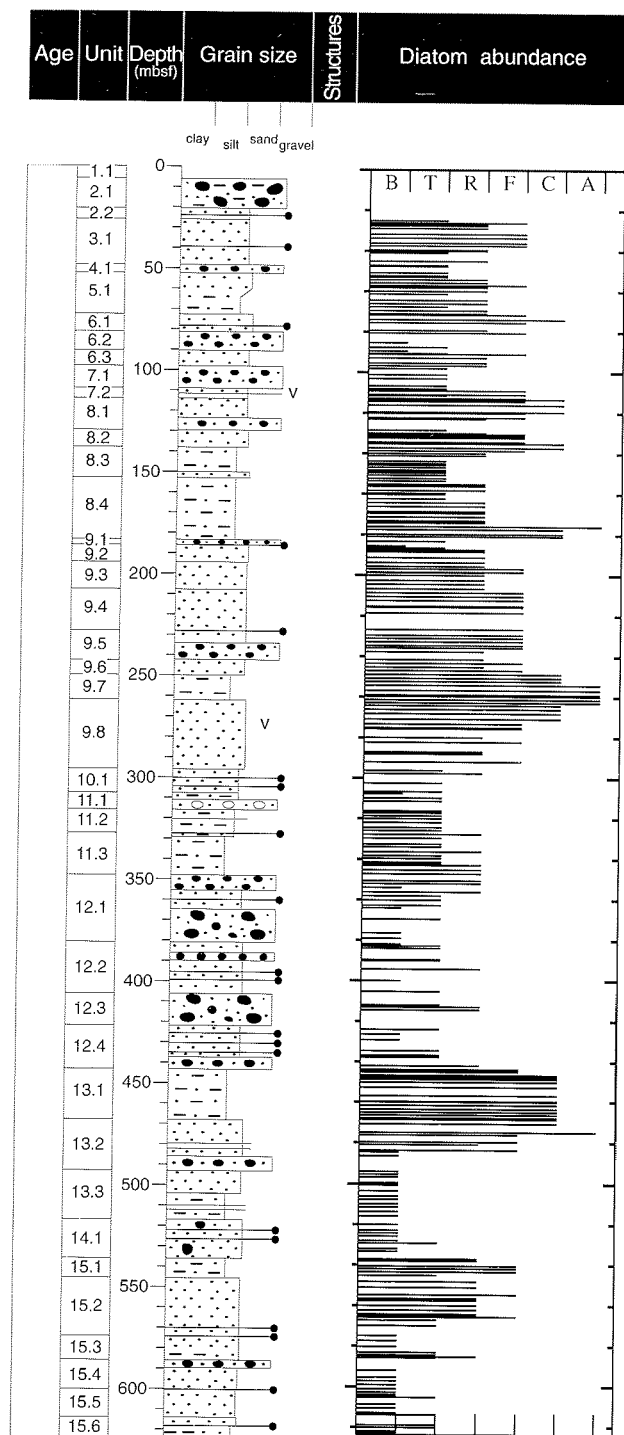


Fig. 5.2 - Diatom abundance in Lower Miocene-upper Palaeogene sediments, CRP-2/2A, plotted against the lithological summary log. Abundance categories (B = barren; T = trace; R = rare; F = few; C = common; A = abundant) are based on analysis of strewn slides of unsieved material. Intervals containing abundant diatoms contain the highest proportion of pelagic species.

These designations are internal to CRP-2/2A unless specific reference is made to published works (e.g. *Hemiaulus* sp. A (MSSTS-1)). Age assignments and diatom taxonomy are based on a large body of literature, but primary sources of information are reports from Southern Ocean drilling, notably Harwood & Maruyama (1992), Baldauf & Barron (1991), Gombos & Ciesielski (1983), Gombos (1977), Hajós (1976), and Schrader (1976). Useful diatom reports

from Antarctic continental shelf drilling and piston coring include Harwood et al. (1998), Harwood et al. (1989b), Harwood (1989), Harwood (1986), Barron & Mahood (1993), and Mahood et al. (1993). Several reports from stratigraphical sections outside of the Antarctic region also contribute useful information, including Yanagisawa & Akiba (1998), Scherer & Koç (1996), Gladenkov & Barron (1995), Akiba et al. (1993), and Schrader & Fenner (1976).

TENTATIVE DIATOM ZONATION

The nearly 600 m of Miocene and upper Palaeogene sediment recovered include significant diatom floral overturn, allowing subdivision into 10 tentative diatom range or partial range biozones, based on first and/or last occurrences of more than 50 taxa (Fig. 5.3, Tab. 5.2). Most other taxa are either long-ranging, or too sporadic in their abundance or distribution for reliable biostratigraphical utility. Biozones proposed in this report are not formally defined and, as such, should not be considered beyond the present context. This working zonal scheme will be updated and formally defined in the CRP-2/2A Scientific Results volume.

The *Thalassiosira praepraga* Zone is a total range zone recognized from the first occurrence (FO) of *T. praepraga* at 36.25 mbsf to the top of the Lower Miocene section at c. 28 mbsf (Tab. 5.2, Fig. 5.3). Diatoms in this interval are moderately preserved, which suggests the FO of *T. praepraga* is not truncated. Harwood et al. (1998) defined this zone in the CRP-1 core based on the total range of *T. praepraga*. The last occurrence (LO) of *T. praepraga*, however, is not represented in CRP-2/2A due to an unconformity at c. 28 mbsf, which separates Lower Miocene and Plio-Pleistocene sediments.

The *Fragilariopsis* sp. A Zone is a partial range zone defined from the FO of *Fragilariopsis* sp. A (at 57.42 mbsf) up to the FO of *Thalassiosira praepraga* (at 36.23 mbsf). This interval is characterized by poor to moderate diatom preservation and low abundance. *Fragilariopsis* sp. A is a relatively common component of diatom assemblages within this zone and continues as a common component of assemblages through the *T. praepraga* Zone. The taxon referred to as *Fragilariopsis* sp. A in the present study has been previously recognized in several Ross Sea cores, but its FO has not been well documented.

We tentatively define the *Dactyliosolen antarcticus* Zone as a partial range zone from the FO of *Dactyliosolen antarcticus* (at 75.56 mbsf) up to the FO of *Fragilariopsis* sp. A (at 57.42 mbsf). Diatoms are common and moderately preserved from 75.56 to 71.13 mbsf but are poorly preserved and rare above this interval to the base of the overlying zone. *Dactyliosolen antarcticus* is a rare to common component of diatom assemblages within this zone and continues as a component of assemblages through the *T. praepraga* Zone. A distinctive taxon in the interval from 75.56 to 71.13 mbsf is a small, previously undescribed *Rhizosolenia* sp., which we refer to as *Rhizosolenia* sp. A.

The *Ikebia tenuis* Zone is a partial range zone defined from the LO of *Kisseleviella* sp. A (at 130.90 mbsf) up to the FO of *Dactyliosolen antarcticus* (at 80.65 mbsf). Diatoms are common and well preserved in this interval.

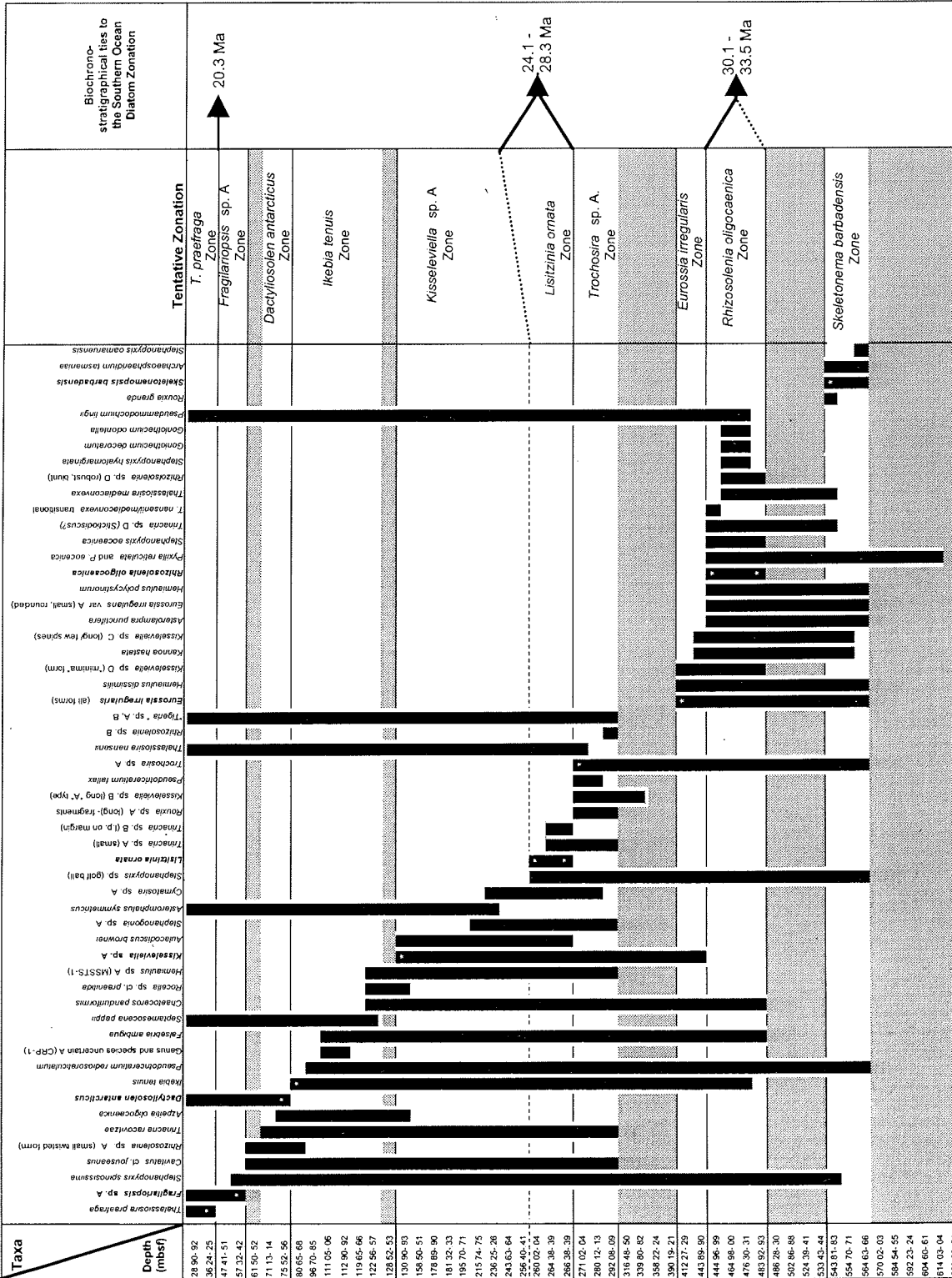


Fig. 5.3 - Stratigraphical ranges of key diatoms and diatom species groups (1) and chrysophyte cysts (1) in CRP-2/2A. The chart is a graphical representation of selected taxa from total taxonomic census data, illustrating the first and/or last consistent occurrences of these taxa within CRP-2/2A. These ranges are the foundation for a tentative zonal scheme, including total range and partial range zones. Shaded areas reflect poor biosiliceous preservation.

Tab. 5.2 - Definition of boundaries for tentative diatom zonation of CRP-2/2A and characteristic taxa of each zone.

Zone	Boundaries	CRP-2/2A depth (mbsf)	Characteristic Taxa
<i>Thalassiosira praeфрага</i> Total Range Zone	Top. LO <i>Thalassiosira praeфрага</i> Base. FO <i>Thalassiosira praeфрага</i>	Not represented 36.25	<i>Dactyliosolen antarcticus</i> <i>Fragilariopsis</i> sp. A <i>Thalassiosira nansenii</i> <i>Thalassiosira praeфрага</i>
<i>Fragilariopsis</i> sp. A Partial Range Zone	Top. FO <i>Thalassiosira praeфрага</i> Base. FO <i>Fragilariopsis</i> sp. A	36.25 57.42	<i>Dactyliosolen antarcticus</i> <i>Fragilariopsis</i> sp. A
<i>Dactyliosolen antarcticus</i> Partial Range Zone	Top. FO <i>Fragilariopsis</i> sp. A Base. FO <i>Dactyliosolen antarcticus</i>	57.42 75.56	<i>Dactyliosolen antarcticus</i> <i>Rhizosolenia</i> sp. A
<i>Ikebia tenuis</i> Partial Range Zone	Top. LO <i>Ikebia tenuis</i> Base. LO <i>Kisseleviella</i> sp. A	80.65 130.90	<i>Azpeitia oligocaenica</i> <i>Ikebia tenuis</i> <i>Rocella</i> sp. cf. <i>praenitida</i>
<i>Kisseleviella</i> sp. A Partial Range Zone	Top. LO <i>Kisseleviella</i> sp. A Base. LO <i>Lisitzinia ornata</i>	130.90 259.21	<i>Aulacodiscus brownei</i> <i>Cymatosira</i> sp. A <i>Kisseleviella</i> sp. A <i>Stephanogonia</i> sp. A
<i>Lisitzinia ornata</i> Total Range Zone	Top. LO <i>Lisitzinia ornata</i> Base. FO <i>Lisitzinia ornata</i>	259.21 266.38	<i>Aulacodiscus brownei</i> <i>Cymatosira</i> sp. A <i>Kisseleviella</i> sp. A <i>Stephanogonia</i> sp. A <i>Trinacria</i> sp. A <i>Trinacria</i> sp. B
<i>Trochosira</i> sp. A Partial Range Zone	Top. LO <i>Trochosira</i> sp. A Base. Not defined.	271.02 -	<i>Cymatosira</i> sp. A <i>Kisseleviella</i> sp. A <i>Kisseleviella</i> sp. B <i>Rouxia</i> sp. A <i>Stephanogonia</i> sp. A <i>Trinacria</i> sp. A <i>Trochosira</i> sp. A
<i>Eurossia irregularis</i> Partial Range Zone	Top. LO <i>Eurossia irregularis</i> Base. LO <i>Rhizosolenia oligocaenica</i>	412.27 444.96	<i>Eurossia irregularis</i> <i>Hemiaulus dissimilis</i> <i>Kannoa hastata</i> <i>Kisseleviella</i> sp. C <i>Kisseleviella</i> sp. D
<i>Rhizosolenia oligocaenica</i> Total Range Zone	Top. LO <i>Rhizosolenia oligocaenica</i> Base. FO <i>Rhizosolenia oligocaenica</i>	444.96 483.93	<i>Asterolampra punctifera</i> <i>Eurossia irregularis</i> <i>Goniothecium decoratum</i> <i>Goniothecium odontella</i> <i>Hemiaulus dissimilis</i> <i>Hemiaulus polycystinorum</i> <i>Kannoa hastata</i> <i>Kisseleviella</i> sp. C <i>Kisseleviella</i> sp. D <i>Rhizosolenia</i> sp. D <i>Pyxilla reticulata</i> <i>Rhizosolenia oligocaenica</i> <i>Stephanopyxis eocenica</i> <i>Thalassiosira nansenii</i> <i>mediaconvexa</i>
<i>Skeletonemopsis barbadensis</i> Partial Range Zone	Top. LO <i>Skeletonemopsis barbadensis</i> Base. Not defined.	543.81 -	<i>Archaeosphaeridium tasmaniae</i> <i>Asterolampra punctifera</i> <i>Eurossia irregularis</i> <i>Hemiaulus dissimilis</i> <i>Hemiaulus polycystinorum</i> <i>Kannoa hastata</i> <i>Kisseleviella</i> sp. C <i>Pyxilla reticulata</i> <i>Rouxia granda</i> <i>Skeletonemopsis barbadensis</i>

Note: FO = first occurrence, and LO = last occurrence.

Ikebia tenuis is not abundant in this interval, but is consistently present through the *Ikebia tenuis* Zone. This stratigraphical interval also contains several, distinct ash beds, of varying thickness. No significant diatom assemblage changes were noted through the ash-bearing section. Diatoms are well-preserved within the volcanic

glass-bearing interval (114.2 to 109.1 mbsf), probably due to the high silica availability in the sediments, which may have buffered pore waters and reduced the dissolution rate of diatom frustules.

The *Kisseleviella* sp. A Zone is a partial range zone defined from the LO of *Lisitzinia ornata* (at 259.21 mbsf)

up to the LO of *Kisseleviella* sp. A (at 130.90 mbsf). The assemblages in this interval are characterized by variable diatom abundance and preservation. *Kisseleviella* sp. A, however, is present in all samples containing rare to abundant diatoms and comprises a significant component of the assemblages. The LO of *Stephanogonia* sp. A is noted within this zone and may provide a datum to further subdivide this zone.

Kisseleviella sp. A is an undescribed taxon which occurs in CRP-2/2A, MSSTS-1, and CIROS-1. Illustrated specimens, designated as *Kisseleviella carina* by Harwood (1986, p. 86, Pl. 6, Figs. 12-15) from several intervals in the MSSTS-1 have a similar lanceolate form to what we have designated as *Kisseleviella* sp. A in this report. We believe that *Kisseleviella* sp. A is taxonomically distinct from morphotypes in the strict definition of *Kisseleviella carina* (see Akiba & Yanagisawa, 1986). A re-examination of several samples from the CIROS-1 core shows that the *Kisseleviella* species above the unconformity at c. 366 mbsf are of the *Kisseleviella* sp. A type (of CRP-2A), whereas another *Kisseleviella* form, more closely related to *K. carina* (*sensu stricto*) occurs in the lowest Oligocene/uppermost Eocene, below the unconformity in CIROS-1.

The *Lisitzinia ornata* Zone is a total range zone that is tentatively defined in the present study from the FO of *Lisitzinia ornata*, at 259.21 mbsf, up to its LO, at 266.38 mbsf. Diatoms are abundant and well-preserved within this short interval, but *Lisitzinia ornata* is rare. Distinctive diatom taxa that also occur in this zone include *Trinacria* sp. A and *Trinacria* sp. B.

The *Lisitzinia ornata* Total Range Zone as defined in the present study differs from the *Lisitzinia ornata* Partial Range Zone proposed by Harwood (1986) and applied in deep-sea sediments on ODP Leg 120 (Harwood & Maruyama, 1992). In these studies, the *Lisitzinia ornata* Partial Range Zone is defined by the FO of *Lisitzinia ornata* at the base and the FO of *Rocella gelida* as the top (Harwood, 1986). *Rocella gelida* was not observed in CRP-2/2A, and, consequently, cannot be used as a zonal marker. We, therefore, use the total range of *L. ornata*.

The top of the *Trochosira* sp. A Partial Range Zone is defined by the LO of *Trochosira* sp. A (at 271.02 mbsf). The base of this zone is not defined due to an underlying thick interval of poor preservation and low diatom abundance from 302.65 to 412.27 mbsf. Distinctive taxa within the *Trochosira* sp. A Zone (271.02 to 292.09 mbsf) include *Kisseleviella* sp. B and *Rouxia* sp. A. The first occurrences of *Hemiaulus* sp. A, *Stephanogonia* sp. A, *Trinacria* sp. A, and "Tigeria" spp. A & B occur at 292.08 mbsf, suggesting the presence of an unconformity at or below this depth in the interval of poor preservation.

The *Eurossia irregularis* Partial Range Zone is tentatively defined from the LO *Rhizosolenia oligocaenica* (at 444.96 mbsf) up to the LO of *Eurossia irregularis* (at 412.27 mbsf). Diatoms in this interval are poor to moderately preserved and present in low abundance. The LOs of *Hemiaulus dissimilis* and *Kisseleviella* sp. D occur at the top of this zone at 412.27 mbsf and provide further support for a significant unconformity between c. 300 and 412 mbsf. The diatom assemblage in this zone is similar to that of the underlying *Rhizosolenia oligocaenica* Zone

(see below) but is distinguished by the absence of *R. oligocaenica*.

The *Rhizosolenia oligocaenica* Total Range Zone is defined from the FO of *Rhizosolenia oligocaenica* (at 483.93 mbsf) up to the LO of *Rhizosolenia oligocaenica* (at 444.96 mbsf). This interval contains common and well-preserved diatoms. The top of this zone marks the LO of several taxa (see Fig. 5.3) which indicate a possible unconformity between 444.99 and 443.90 mbsf. Alternatively, these last occurrences may be a reflection of poorer preservation in the overlying *Eurossia irregularis* Zone. The assemblage composition, however, is significantly different from that above the level of poor preservation at c. 300 mbsf. The bottom of the *Rhizosolenia oligocaenica* Zone is underlain by an interval of poor preservation from 486.28 to 533.44 mbsf, suggesting the FO of *Rhizosolenia oligocaenica* may be truncated. Distinctive taxa that are stratigraphically limited to the *Rhizosolenia oligocaenica* Zone include *Goniothecium odontella*, *Goniothecium decoratum*, *Rhizosolenia* sp. D, and *Thalassiosira nansenii/mediacconvexa* transitional forms.

The *Rhizosolenia oligocaenica* Total Range Zone, as defined in the present study, differs from the *Rhizosolenia oligocaenica* Partial Range Zone, originally proposed by Gombos & Ciesielski (1983) and redefined by Harwood & Maruyama (1992). The *Rhizosolenia oligocaenica* Partial Range Zone is defined by the FO occurrence of *Rhizosolenia oligocaenica* up to the FO of *Cavitatus jouseanus* (Harwood & Maruyama, 1992). The FO of *Cavitatus jouseanus* is not applied as a datum in CRP-2A due to taxonomic uncertainties and discontinuous occurrence.

The top of the *Skeletonemopsis barbadensis* Partial Range Zone is defined by the LO of *Skeletonemopsis barbadensis* at 543.81 mbsf. The base of this zone is not presently defined because of poor preservation below 564.66 mbsf; the lowermost 50 m of core (565.50 to 624.03 mbsf), beneath the *Skeletonemopsis barbadensis* Zone, contains only rare, recrystallized and non-age-diagnostic diatoms. The *Skeletonemopsis barbadensis* zone contains moderately preserved diatoms in low abundance. The assemblage within this interval is of low species richness but is otherwise similar to the that in the *R. oligocaenica* Zone. The assemblage is distinguished by the presence of *Archaeosphaeridium tasmaniae* (a chrysophyte cyst), *Rouxia granda*, and *Skeletonemopsis barbadensis*, which are confined to this interval.

AGE AND STRATIGRAPHICAL CORRELATIONS

Correlation of key taxa in CRP-2/2A with palaeomagnetic chrons, and with occurrences in other McMurdo Sound cores is presented in table 5.3. Most of the taxa present in CRP-2/2A are rare in the deep-sea pelagic record, and most open-ocean taxa common in deep-sea sediments are rare in CRP-2/2A. Consequently, few of the zones proposed above can be confidently tied to the magnetostratigraphically-calibrated Southern Ocean diatom records. However, direct correlation with deep-sea diatom datums (Harwood & Maruyama, 1992) is possible

Tab. 5.3 - Deep-sea ranges of selected Oligocene-early Miocene diatom taxa and occurrence in CRP-2/2A and other McMurdo Sound cores.

Species	Age Range (Ma / Chron)	Occurrence in CRP-2/2A (mbsf)	Occurrence in McMurdo Sound Cores (mbsf)	Sources
<i>Thalassiosira praeфрага</i>	20.3 [†] (FCAD) to 18.3 [‡] (C6r to C5En)	FO at 36.25	FO at 103.39 (CRP-1)	H&M / Y&A / H*
<i>Cavitatus rectus</i>	LO at ~20.5 [†] (C6r)	Not present	LO at 146.79 (CRP-1)	A+ / Y&A
<i>Dactyliosolen antarcticus</i>	26.5 [‡] to present (C8n.2n)	FO at 75.56	Ranges through CRP-1 lower Miocene	H&M / H*
<i>Lisitinia ornata</i>	28.3 [‡] to 24.1 [‡] (C9r to C6Cr)	266.38 to 259.21	Not present in CRP-1 309.38 (CIROS-1) 222.04 to 187.21 (MSSTS-1)	H / H* / B / H&M
<i>Asteromphalus symmetricus</i>	28.7 [‡] to 18.3 [‡] (C10n.2n to C5En)	Lowest confirmed occurrence at 236.25	LO at 84.00 (CRP-1) 179.32 to 149.26 (CIROS-1) 222.58 to 61.52 (MSSTS-1)	H / H* / H&M / H+
<i>Cavitatus jouseanus</i>	30.9 [‡] to 14.6 [‡] (C12n to C5ADr)	292.09 to 71.13	147.69 to 99.02 (CRP-1) 359.63 to 110.26 (CIROS-1) 222.58 to 50.88 (MSSTS-1)	H / H* / B / H&M / Y&A / H+
<i>Asterolampra punctifera</i>	LO at 27.0 [‡] (C9n)	Highest confirmed occurrence at 444.96	500.14 to 382.70 (CIROS-1)	H* / H&M
<i>Pyxilla reticulata</i>	LO at 30.1 [‡] (C11r)	624.79 to 444.96	661.13 to 366.99 (CIROS-1)	H* / H&M
<i>Rhizosolenia oligocaenica</i>	33.5 [‡] to 30.9 [‡] (C13n to C12r)	564.63 to 444.96	428.00 to 382.70 (CIROS-1)	H* / B / H&M

Note: Ages are calibrated to the Berggren et al. (1995) time scale. Ages indicated with ‡ are datums derived from Southern Ocean cores, and those indicated with † are datums derived from North Pacific cores. Information is compiled from the following sources: H = Harwood (1986), H* = Harwood (1989), B = Baldauf & Barron (1991), H&M = Harwood & Maruyama (1992), A+ = Akiba et al. (1993), Y&A = Yanagisawa & Akiba (1998), and H+ = Harwood et al. (1998).

with at least 10 taxa (Tabs. 5.3 & 5.4). Age calibrations are based on correlation with the magnetostratigraphical records of ODP legs 120 (Harwood & Maruyama, 1992), 119 (Baldauf & Barron, 1991), and several North Pacific cores (Yanagisawa & Akiba, 1998). Many stratigraphically-useful neritic taxa are also known from Northern Hemisphere high-latitude records (Schrader & Fenner, 1976; Scherer & Koç, 1996). We have recalibrated the reported ages of the first and last occurrence datums from these ODP legs to the Berggren et al. (1995) timescale.

Diatoms in the upper part of CRP-2/2A can be correlated with the Lower Miocene section of CRP-1, though not completely. The best datum for correlation between CRP-1 and CRP-2/2A is the First Common Appearance Datum (FCAD) of *Thalassiosira praeфрага*, which occurs at 102.24 mbsf in CRP-1 and at 36.24 mbsf in CRP-2. This datum defines the base of the *Thalassiosira praeфрага* Zone (Fig. 5.3, Tab. 5.2). In the North Pacific, this datum occurs at 20.3 Ma, in Chron C6r (Yanagisawa & Akiba, 1998). Proposed correlation points between CRP-1 and CRP-2/2A are presented in table 5.4.

Dactyliosolen antarcticus is an extant species in the Southern Ocean and has a reported first occurrence in Chron C8n, c. 26.5 Ma (Harwood & Maruyama, 1992). This diatom occurs from 118.56 mbsf to the top of the Miocene section of CRP-1, and occurs from 75.52 mbsf to the top of the Miocene section of CRP-2A. The Southern Ocean calibration for the first occurrence of this taxon provides a maximum age for sediments at c. 75 mbsf and above. *Dactyliosolen antarcticus*, however, probably has a younger first occurrence on the continental shelf

The top of the *Cavitatus rectus* Zone in CRP-1 occurs at 147.48 mbsf (Harwood et al., 1998), but this zone is not recognized in CRP-2/2A, suggesting that a relatively short

disconformity may exist in the lower Miocene section of CRP-2/2A, removing this zone. The duration of the *C. rectus* Zone in the Southern Ocean is currently unknown. The absence of *Ikebia tenuis* in the *C. rectus* Zone in CRP-1 (Harwood et al., 1998) suggests that this unconformity is above 80.65 mbsf in CRP-2/2A. Sediments below 80.65 mbsf in CRP2A are, therefore, interpreted as being older than the base of CRP-1.

The ⁴⁰Ar/³⁹Ar dates on the ash (21.44±0.05 Ma) in the interval from 111.58 to 114.03 mbsf help constrain the age of the proposed *Ikebia tenuis* Zone (80.65 to 130.90 mbsf). Calculation of accumulation rates from an age-depth plot in this interval will enable a precise age determination for the LO of *Ikebia tenuis*.

At present, the position of the Miocene/Oligocene boundary in CRP-2/2A cannot be assigned with confidence based on diatoms. A significant change in the diatom assemblage is recognized below 128.52 mbsf, which appears to mark a significant disconformity. *Kisseleviella* sp. A is common in assemblages below 130.90 mbsf and absent in assemblages above 128.52 mbsf. *Kisseleviella* sp. A occurs in MSSTS-1 from 50.88 mbsf to the base of that core at

Tab. 5.4 - Tentative correlation of CRP-2/2A to CRP-1 based on diatom assemblages.

CRP-2/2A (fast-track sample depth in mbsf)	CRP-1 (interval of possible correlation in mbsf)
36.25 to 26.30	102.25 to 59.58 (LSU 5.8 to 5.2)
47.41-47.51 (poor preservation)	?
57.32-57.42	141.80 to 103.39 (LSU 6.3 to 6.1)
75.56 to 71.13	No correlative assemblage present

222.58 mbsf and in CIROS-1 from c. 366 to 145.15 mbsf. The LO of this taxon in CIROS-1 and in CRP-2/2A may provide a good point of correlation, but its LO may be truncated by disconformities in each hole, thereby limiting its usefulness as a time marker between holes.

The *Lisitzinia ornata* Zone in CRP-2A (259.21 to 266.38 mbsf) represents a strong pulse of biosiliceous sedimentation on the continental shelf, which can be seen in diatom abundance data on figure 5.2. The total range of *L. ornata* in the deep sea is calibrated to the palaeomagnetic time scale, ranging from Chrons C9r to C6r (28.3 to 24.1 Ma). The last occurrence of *L. ornata* is confined to C8n (25.8 Ma) in most cores from the Southern Ocean (Harwood & Maruyama, 1992; Baldauf & Barron, 1991).

Lisitzinia ornata is a pelagic species that was probably excluded ecologically from the Antarctic continental shelf, except during intervals of enhanced exchange with pelagic water masses. Consequently, the *L. ornata* Zone in CRP-2A most likely represents only a part of the total range of the taxon in the deep sea. This taxon is known to occur in one sample in CIROS-1 at 309.38 mbsf and may represent a correlative assemblage to that within the *L. ornata* Zone of CRP-2A. *Lisitzinia ornata* also occurs in MSSTS-1, scattered through 100 m of core, from 122.87 to 222.58 mbsf.

The *Trochosira* sp. A Zone is not calibrated with biostratigraphical datums tied to the magnetic polarity time scale. Diatom preservation is poor, and abundance low, in the interval 316.48 mbsf to 390.21 mbsf, preventing biostratigraphical interpretation of the base of the *Trochosira* sp. A Zone and the top of the underlying proposed *Eurossia irregularis* Zone. The *Eurossia irregularis* Zone, which is recognized below 412.27 mbsf, is assigned a stratigraphical position of Lower Oligocene, based on the presence of *Eurossia* spp., *Hemiaulus dissimilis*, and *Kannoa hastata*. These taxa have not been reported in Upper Oligocene sediments in the Southern Ocean.

The Upper/Lower Oligocene boundary cannot be identified with confidence in CRP-2A. The interval between c. 300 and 412 mbsf, which represents a brecciated, microfossil-poor interval. The boundary may lie in the *Trochosira* sp. A Zone or within the underlying diatom-poor interval. A distinct change in lithology at c. 300 mbsf may represent an unconformable boundary between the Upper and Lower Oligocene.

Rhizosolenia oligocaenica occurs in CRP-2/2A from 444.96 to 483.96 mbsf in an interval rich in biosiliceous material. The total range of *R. oligocaenica* is widely recognized in the Southern Ocean, with a reported range from 30.1 to 33.5 Ma, in Chrons C12r to C13n. The Southern Ocean first occurrence of this taxon, however, is not well calibrated due to poor diatom preservation and/or poor palaeomagnetic results in most holes, but is not reported to occur below C13n. The first occurrence of *R. oligocaenica* in the Southern Ocean commonly marks the onset of continuous high diatom productivity in the earliest Oligocene.

The lowermost interval with well-preserved diatom assemblages in CRP-2A occurs between 564.66 and

Tab. 5.5 - Siliceous microfossil taxa with ranges restricted to intervals below the unconformity (at ~366 mbsf) in CIROS-1.

<i>Archaeosphaeridium australensis</i> *	<i>Parebriopsis fallax</i> *
<i>Archaeosphaeridium tasmaniae</i>	<i>Pseudammodochium dictyoides</i> *
<i>Asterolampra punctifera</i>	<i>Pyxidicula</i> sp. A*
<i>Cotyledon fogedi</i>	<i>Pyxilla eocena</i>
<i>Dictyocha deflandrei</i>	<i>Pyxilla reticulata</i>
<i>Ebrinula paradoxa</i> *	<i>Rhizosolenia oligocaenica</i>
<i>Ebriopsis crenulata</i> (loricate)*	<i>Rocella praenitida</i> *
<i>Ebriopsis crenulata</i> *	<i>Rouxia granda</i>
<i>Eurossia</i> spp.	<i>Sceptroneis lingulatus</i>
<i>Hemiaulus characteristicus</i> *	<i>Sphinctolothus pacificus</i> *
<i>Hemiaulus dissimilis</i>	<i>Stephanopyxis oamaruensis</i>
<i>Kannoa hastata</i> †	<i>Stephanopyxis superba</i> *
<i>Kisseleviella carina</i> s.s.‡*	<i>Stictodiscus kittonianus</i> *

Note: taxa indicated with an asterisk were not observed in CRP-2/2A. Reported late Eocene to earliest Oligocene ranges from CIROS-1 are reported in Harwood (1989) and Harwood & Bohaty (in press) and are based on the Wilson et al. (1998) age model.

(†) *Kannoa hastata* was identified as *Ikebia tenuis* in the CIROS-1 core (Harwood, 1989). (‡) *Kisseleviella* forms below 366 mbsf in CIROS-1 (designated as *Kisseleviella carina* by Harwood (1989)) may represent a new species, taxonomically separate from *Kisseleviella carina* Sheshukova-Poretzkaya.

543.83 mbsf and is designated the *Skeletonemopsis barbadensis* Zone. The occurrence of *Rhizosolenia oligocaenica* in this zone is equivocal, due to preservational limitations. *Skeletonemopsis barbadensis* ranges from the Middle Eocene to up to the lower part of the *Rhizosolenia oligocaenica* Zone in the Southern Ocean (Gombos & Ciesielski, 1983). This assemblage is difficult to date biostratigraphically, because of a paucity of well-constrained markers.

The *Rhizosolenia oligocaenica* and *Skeletonemopsis barbadensis* Zones of CRP-2A share some of the floral elements of the diatom assemblage below the unconformity (c. 366 to 500 mbsf) in CIROS-1. However, many taxa characteristic of CIROS-1 (Tab. 5.5; Harwood, 1989) and lowermost Oligocene/uppermost Eocene sediment of Prydz Bay, East Antarctica (Barron & Mahood, 1993) do not occur in CRP-2A. These include, among others, *Hemiaulus characteristicus*, *Sphinctolothus pacificus*, and *Kisseleviella carina* (*sensu* Harwood, 1989, Pl. 4, Figs. 35-37; Barron & Mahood, 1993, Pl. 5, Fig. 11; and Hajós, 1976, Pl. 25, Figs. 5-9). The lowermost assemblages in CRP-2A also lack typical Late Eocene diatoms, such as *Distephanosira architecturalis*. Consequently, we interpret the *R. oligocaenica* Zone in CRP-2A (444.96 to 483.93 mbsf) as Lower Oligocene (Chron C12r), and the *S. barbadensis* Zone (543.81 to 564.66 mbsf) as Lower lower Oligocene or Upper upper Eocene.

PALAEOENVIRONMENTS

Throughout the interval recovered in CRP-2/2A, the diatom record is strongly dominated by neritic planktic diatoms, with *Stephanopyxis* spp. the most abundant taxa. The diatom record of CRP-2/2A indicates deposition well below sea-level, and almost entirely below the photic zone (>~50m water depth), based on the rare occurrence of benthic diatoms. Fragments and rare whole specimens of large, bottom-dwelling diatoms, such as *Isthmia* and

Archnoidiscus, occur throughout the diatom-bearing intervals in low abundance. We consider these to be allochthonous, as are smaller benthic taxa that occur relatively commonly, including *Cocconeis* spp. and *Rhabdonema* spp.

Benthic diatoms may be *in situ* in the interval 110-112 mbsf, in association with volcanic deposits ($^{40}\text{Ar}/^{39}\text{Ar}$ dated as 21.44 Ma). Diatom assemblages in these samples include a very large and distinctive diatom, referred to as "Genus and Species uncertain A" in the lower Miocene section of CRP-1 (Harwood et al., 1998). The low abundance of benthic diatoms in CRP-2/2A contrasts with CRP-1 and CIROS-1, both of which include intervals with significant abundance of benthic diatoms, which typically indicate shallow-water deposition (<50 m) (Harwood, 1989; Harwood et al., 1998). An alternative hypothesis worthy of consideration is the possibility that benthic diatoms are excluded from parts of the stratigraphical section due to high sediment input and turbid waters. A high suspended sediment load would have limited light penetration, and a highly mobile bottom may have limited colonization by many benthic diatom taxa.

SUMMARY

The CRP-2/2A core provides a detailed stratigraphical record for the Antarctic continental shelf, despite numerous disconformities. The diatom assemblages suggest high sediment accumulation rates throughout the recovered successions, especially between *c.* 80 and *c.* 300 mbsf. Several distinct neritic diatom assemblages are identified through the core, and numerous FO and LO datums provide a basis for a detailed diatom biostratigraphical zonation. Major diatom assemblages in CRP-2/2A are confined to distinct stratigraphical intervals and are interpreted as being bounded by unconformities, based on deep-sea ranges of selected taxa. It is not possible to define firm age boundaries at this time, but using the diatom assemblages, we consider the interval from 26.9 mbsf to *c.* 130 mbsf to be Lower Miocene and the interval from *c.* 130 to 300 mbsf to be Upper Oligocene. The interval from *c.* 412 to 483 mbsf is Lower Oligocene, and from 483 mbsf to the base of the hole is considered lowermost Oligocene/Upper Eocene.

FORAMINIFERA

INTRODUCTION

A total of 135 samples, including 32 "Fast-track", 99 routine and 4 macrofossil matrix samples, covering the interval from 34.28 to 623.77 mbsf, were selected for foraminiferal study from CRP-2/2A cores and processed and examined at Crary Science and Engineering Center. Seventy-three were found to contain foraminifers, and yielded a fauna of *c.* 28 genera and *c.* 45 species. Specimen preservation was generally good, with test microstructures only slightly altered by leaching or recrystallization, but ranged from very good to poor.

Miocene and Oligocene strata in CRP-2/2A comprise a *c.* 600 m thick sequence of diamictite, muddy sandstone, sandy or silty mudstone and conglomerate, encompassing the interval from 26.79 mbsf (metres below sea-floor) to 624.15 mbsf (Bottom of Hole). Top of the Miocene is placed at the unconformable contact between LSU 2.2 (Pliocene) and 3.1 (26.79 mbsf in CRP-2; 27.14 mbsf in CRP-2A) of the standard lithostratigraphical classification (see Description of Sequence section, chapter 3) for the drill hole. The Oligocene-Miocene boundary is determined to lie at *c.* 130 m, near the base of LSU 8.1, and the Lower Oligocene-Upper Oligocene boundary is at *c.* 440 m, near the base of LSU 12.4 (see Chronology section, chapter 7). Boundary determinations rest primarily on diatom and nannofossil evidence. The Eocene-Oligocene boundary had not been reached upon termination of drilling.

MATERIAL AND METHODS

Sample selection emphasised fine-grained sediments, mostly sandy or silty mudstones, as the most likely to contain foraminifers. There was no attempt to sample all the lithologies present. Samples, most weighing 50-100 g (undried) and representing *c.* 5 cm of core, were processed using standard techniques, and the resulting residues wet-sieved into >500 μm , >125 μm , >63 μm and <63 μm fractions. After drying, the first three fractions were examined for microfossils, and the last reserved for other non-palaeontological studies. All fossil material, including sponge spicules, diatoms, shell fragments, *etc.*, observed during picking was recorded, but samples lacking foraminifers are referred to here as "non-fossiliferous".

Most foraminifers were found in the 125-500 μm residue, and systematic search therefore focussed on this fraction. Small samples were picked entirely, but for large samples, the >125 μm material was subdivided, using a microsampler, to provide at least two well-covered picking trays (9 x 5 cm; usually 1/4 to 1/8 of total residue) for examination. This defines the minimum criterion for determining a sample to be non-fossiliferous. In addition, all of the >500 μm - 2 mm residue was scanned for large specimens, and a small portion of >63 μm material was searched for minute species. Some large miliolids (see below) were removed by hand from surrounding matrix.

CRP-2 and CRP-2A samples overlap by about 6 m at the top of LSU 5.1, but all contain similar faunas and are included in a single sample suite.

BIOSTRATIGRAPHY

Four characteristic foraminiferal assemblages, defined by their taxonomic composition and overall character, occupy successive parts of the CRP-2/2A sequence, and appear in most cases to show a clear relationship to the boundaries of lithostratigraphical units (see Fig. 5.4). These units are considered to reflect changes in biofacies and lithofacies at the CRP-2/2A site, and therefore to be of only local significance. All assemblages comprise only calcareous benthic taxa; neither planktic nor agglutinated species were recorded in the Oligocene-Miocene section

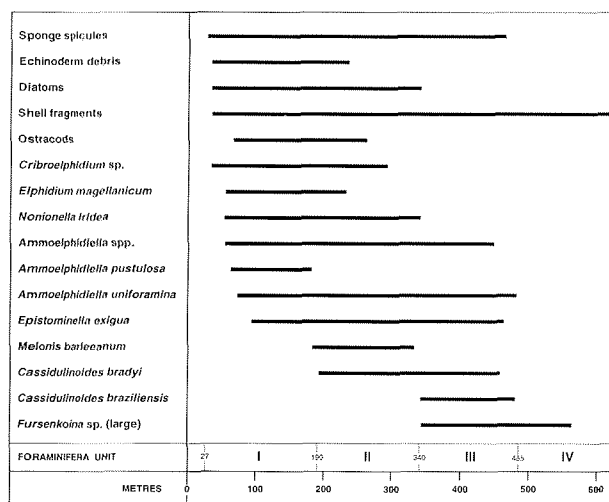


Fig. 5.4 - Distribution of Foraminiferal Units, selected foraminiferal species, and other fossil material in the CRP-2/2A drill hole.

of CRP-2/2A. Figure 5.4 shows the distribution of the faunal units in the CRP-2/2A section, along with the ranges of significant foraminiferal species.

Foraminiferal Unit I (26.91-193.75 mbsf)

Samples from this interval, which includes LSU 3.1 to LSU 9.2, generally contain either sparse, low diversity foraminiferal faunas, or are non-fossiliferous. Seventy samples were examined, and 38 contained foraminifera. *Elphidium magellanicum* and *Cribroelphidium* sp. are the most typical and persistent taxa, and appear in most assemblages. Although richer faunas occur at a few levels, typical assemblages contain five or fewer individuals, and three or fewer species. The maximum observed abundance/diversity was 60 specimens/10 species at 71.13 mbsf. *Nonionella iridea* displays a short interval of persistent occurrence between *c.* 56 and *c.* 76 mbsf; and *Epistominella exigua* has scattered occurrences down hole from *c.* 95 mbsf.

Persistently non-fossiliferous intervals occur at *c.* 36-41 mbsf, (LSU 3.1, medium to fine sandstone), and *c.* 107-123 mbsf (LSU 7.1, 7.2 and 8.1; sandstone, diamicite and lapillistone).

The Miocene - Upper Oligocene boundary occurs within Unit I at *c.* 130 mbsf (see Chronology section, chapter 7), but no significant change in foraminiferal assemblages was noted near this level.

Foraminiferal Unit II (193.95-342.42 mbsf)

The top of Foraminiferal Unit II, which probably coincides with the boundary between lithostratigraphical LSU 9.2 and 9.3, is marked by the highest occurrences of *Cassidulinoides bradyi* (193.95 mbsf), and *Eponides bradyi* (just below at 195.57 mbsf). Both characterize assemblages down to 342.42 mbsf, where the next faunal change occurs. As compared to the overlying unit, foraminiferal abundance and diversity are higher, and samples are more

consistently fossiliferous (23 of 35 samples). Common species within this interval include *Epistominella exigua*, *Melonis barleeanum*, *Ammoelphidiella* spp. and *Cribroelphidium* sp.

Foraminifera are relatively common down to *c.* 260 mbsf, with typical samples yielding 10-50 specimens, representing 4-9 species. The lower part, from *c.* 260 mbsf to *c.* 340 mbsf has sparser assemblages, commonly with only one or two species. There is a substantial barren interval from *c.* 275 to *c.* 320 mbsf. The lower boundary of Unit II lies near the base of LSU 11.3.

Diatom and calcareous nanofossil data indicate that Foraminiferal Unit II is entirely Late Oligocene in age.

Foraminiferal Unit III (342.42 - *c.* 486.19 mbsf)

Highest occurrences of *Cassidulinoides braziliensis* at 342.42 mbsf and a large, unnamed *Fursenkoina* sp., *c.* 3 m below at 345.50 m, mark the top of Foraminiferal Unit III, and the two species are the most common taxa within it. *Epistominella exigua* and *Eponides bradyi* have sporadic occurrences. Eleven of 20 samples contained sparse to moderate foraminiferal assemblages, consisting of three to six species. Isolated, large miliolid individuals were observed in the core at *c.* 345, 460 and 466 mbsf.

The upper part of Foraminiferal Unit III is poorly developed, but more diverse and abundant assemblages occur in its lower third. There is an abrupt increase in abundance and diversity below *c.* 440 mbsf., the level thought to represent the Upper Oligocene-Lower Oligocene boundary (see Chronology section, chapter 7). There is a major barren interval from *c.* 347 to *c.* 435 m, which includes all of LSU 12.1 and 12.2 (diamicite and sandstone). The base of the unit lies *c.* 6 m above the base of LSU 13.2.

Foraminiferal Unit IV: Impoverished (486.19-624.15 mbsf)

The top of Foraminiferal Unit IV is placed at a non-fossiliferous sample *c.* 4 m below the lowest occurrence of *Cassidulinoides braziliensis*. The Unit commences near the base of LSU 13.2 and continues to the base of the drilled section in LSU 15.6. Rocks within the Unit are well-indurated and difficult to disaggregate. Only one (564.58 mbsf) of the eight samples examined yielded foraminifers: a single, moderately preserved, specimen of *Fursenkoina* sp. (of Foraminiferal Unit III). Despite the virtual absence of smaller foraminifera, isolated single specimens of large, apparently well preserved, biloculine miliolids (probably *Pyrgo* spp.) were observed in the core at *c.* 599 and 620 mbsf. Their presence may indicate a specialised, perhaps hypersaline, environment unsuitable for other species.

PALAEOENVIRONMENT

All of the four Foraminiferal Units described above contain calcareous benthic foraminiferal faunas of moderate to very low diversity, and lack both planktic and

agglutinated benthic foraminifera. These factors suggest that all four assemblages reflect various inshore benthic environments, which were isolated from oceanic circulation and affected by various events and processes, e.g. reduced salinity, involving meltwater.

Progressing from Foraminiferal Units IV to II, the faunas suggest a long-term deepening trend, as indicated by increasing foraminiferal abundance and diversity (although with second-order reversals) followed by a return, as reflected by the Unit I fauna, to more inshore environments.

The sparse fauna of Unit IV, with scattered large miliolids, is consistent with a shallow water (hypersaline?) environment, above wave base (c. 50 m?), as suggested by sedimentological evidence (see Facies Analysis section, chapter 3). Foraminiferal Unit III assemblages probably reflect increased, mid- to outer- shelf (100-200 m) water depths, especially from c. 440-485 mbsf. Still further deepening, to perhaps outer-shelf or upper-slope depths (200-300 m), may indicated by the more consistent and diverse faunas of Unit II. Foraminiferal Unit I marks an abrupt return to low diversity, sparse faunas characterized by the shallow water taxa, *Elphidium* and *Criboelphidium*. A near-shore setting is likely, but apparently there is no sedimentological evidence that the site was above wave base.

AGE AND CORRELATION

All foraminifers from CRP-2/2A have either long or poorly known ranges, and no age-diagnostic species were encountered to permit external correlation. Although the CRP-2/2A faunas are less diverse and lack planktic species, they bear a general resemblance to Oligocene and Miocene faunas from lithostratigraphical Unit 2 (especially 2B to 2I) at DSDP Site 270 (Leckie & Webb, 1985). Foraminiferal Units II and III are comparable to the *Globocassidulina-Cassidulinoides-Trochoelphidiella* Assemblage Zone from the lower part of DSDP270, while Foraminiferal Unit I resembles the *Epistominella-Elphidium-Nonionella* Assemblage Zone from the upper part of that drill hole. CRP-2/2A faunas also seem closely related to faunas in Units 5, 7, 8, 9 and 15 in CIROS-1, but significantly, no fauna equivalent to the lowermost CIROS-1 fauna, from Unit 21 (Webb, 1989, p. 105), was encountered in CRP-2/2A.

Only Foraminiferal Unit I assemblages are represented in the nearby CRP-1 drill hole (Cape Roberts Science Team, 1998c).

CALCAREOUS NANNOFOSSILS

INTRODUCTION

Calcareous nannofossils occur throughout the Southern Ocean in pre-Miocene sedimentary rocks deposited in pelagic and hemipelagic settings where the bottom was above the carbonate compensation depth (CCD). Conditions during the Cretaceous through Oligocene were sufficiently different in the Southern Ocean from the

temperate and tropical areas of the world that separate biostratigraphical zonation have been developed. The Southern Ocean biostratigraphical zonation of Wei & Wise (1990) has been adopted to subdivide the Eocene and Oligocene sequence in the Cape Roberts cores. This zonation has the advantage of utilizing several prominent high-latitude species while retaining those biostratigraphical marker species from temperate zonation that penetrate in the high Southern latitudes. Most of the biohorizons used in this zonation have been correlated directly to the palaeomagnetic time scale and, indirectly, to the geochronological time scale.

RESULTS

The entire pre-Pliocene sequence from holes CRP-2/2A was sampled and examined for calcareous nannofossils. Samples were chosen preferentially from fine-grained lithologies or at least from sedimentary rocks with fine-grained matrix material. All samples were examined initially by using smear slides of raw sediment. In most cases, no additional sample preparation was done. A few coarser-grained sediments were processed by a gravitational settling technique in which approximately 0.1 cm³ of sediment was disaggregated and suspended in sufficient purified water to constitute a column of approximately 2 cm height in a small closed vial. This suspension was allowed to settle undisturbed for 60 seconds, at which point an aliquot of the supernatant was withdrawn and mounted on a cover glass. This procedure removed grains larger than approximately 20 microns from the supernatant, and thus concentrated the finer, nannofossil-bearing size fraction.

A total of six samples spanning in the cored interval from 29.70 to 57.32 mbsf in Hole CRP-2 and 179 samples from 54.67 to 624.10 mbsf in CRP-2A drill hole were examined for calcareous nannofossils. All of the pre-Pliocene samples from CRP-2 are barren of calcareous nannofossils. In total, 72 of the 183 samples from CRP-2A contain some nannofossils. This suggests a representation of nannofossils in less than 40% of the cored interval. However, examination of figure 5.5 indicates that the distribution of nannofossil-bearing samples in the section is not uniform, but occur with nannofossiliferous intervals separated by barren intervals. For example, the 25 m from c. 144 to 169 mbsf contains nannofossils in 90% of the samples (18 out of 20), whereas the subjacent 25 m from c. 169 to 194 mbsf contains nannofossils in only 11% of the samples (one out of nine). These intervals of nannofossil-bearing samples define a set of hemipelagic depositional episodes (see below) that punctuate the Oligocene history of the Ross Sea. These fossiliferous intervals occur generally in the finest-grained mudrocks and correspond to those where other palaeontological indicators of deep water have been found (e.g. pteropods).

The highest of these stratigraphical intervals (144.44 to 167.35 mbsf) constitutes an interval of relatively continuous nannofossil occurrence. Excluding the barren samples intercalated within this sequence, the average nannofossil species richness is 3.3 species per sample. The highest richness values occur near the centre of the sequence

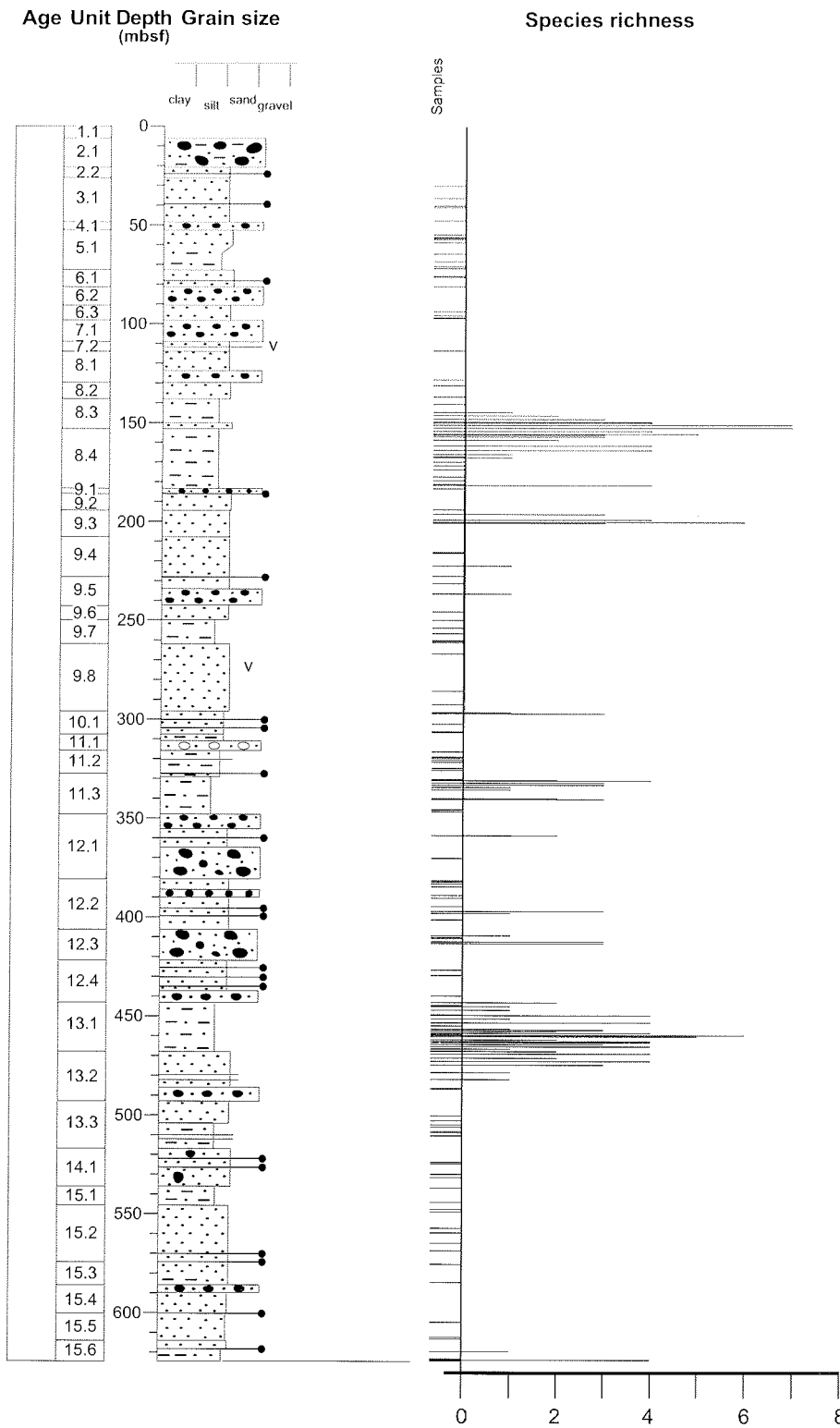


Fig. 5.5 - Species richness of calcareous nannofossil assemblages from CRP-2/2A. Horizontal axis is the number of species identified in a given sample. Those samples with zero (0) species identified are barren samples. Note that the distribution of nannofossil-bearing samples is non-random, defining a set of hemipelagic episodes during deposition of the Oligocene of CRP-2A (see text).

(150.70 to 155.20 mbsf), with two samples having seven species per sample (Tab. 5.6). Specimen abundance and species richness decrease both up-section and down-section from this richness maximum. Taxa present include *Dictyococcites bisectus*, *Dictyococcites productus*, *Reticulofenestra minuta* and *Reticulofenestra minutula*. The presence of *D. bisectus* without *Chiasmolithus altus* is indicative of the *Dictyococcites bisectus* Zone of late

Oligocene age. The last occurrence of *D. bisectus* is well constrained in the Southern Ocean (Wei & Wise, 1992; Berggren et al., 1995) at 23.9 Ma. This datum (identified at 149.28 mbsf) is almost certainly a minimum estimate for the age of this horizon, as this species is only present in this sequence during the interval of highest species richness. The late Oligocene age is corroborated by the presence of *R. minuta*.

Tab. 5.6 - Range chart of calcareous nannofossils identified in samples from CRP-2A.

Sample	Abundance	Preservation	<i>Bicolmnus ovatus</i>	<i>Chiasmolithus altus</i>	<i>Dictyococcites bisectus</i>	<i>Dictyococcites daviesii</i>	<i>Dictyococcites hesslandii</i>	<i>Dictyococcites productus</i>	<i>Isthmolithus recurvus</i>	<i>Reticulofenestra hampdenensis</i>	<i>Reticulofenestra minuta</i>	<i>Reticulofenestra minutula</i>	<i>Reticulofenestra oamaruensis</i>	<i>Reticulofenestra umbilicus</i>	<i>Sphenolithus sp. cf. S. moriformis</i>	<i>Thoracosphaera sp.</i>	<i>Thoracosphaera heimii</i>	<i>Thoracosphaera saxea</i>	sp. Indet. A	<i>Triquetrorhabdulus sp. Indet.</i>	species richness
140.22	B																				0
144.44	VR	P																			1
146.18	VR	P																			2
148.06	R	M																			3
149.28	R	M																			3
149.45	R	P																			4
149.60	R	M																			4
149.66	R	P																			4
150.70	F	G																			7
152.40	F	G																			7
153.70	R	G																			4
155.20	R	M																			5
156.07	R	M																			3
157.06	R	P																			3
158.50	R	P																			2
161.42	R	M																			4
163.50	R	M																			4
165.65	VR	M																			1
167.35	VR	P																			1
169.58	B																				0
180.75	B																				0
181.74	R	M																			4
183.15	B																				0
193.65	B																				0
195.70	R	M																			3
198.83	R	M																			4
200.15	R	M																			6
200.54	R	M																			3
215.52	B																				0
215.75	B																				0
222.25	VR	M																			1
227.34	B																				0
231.03	B																				0
236.25	VR	M																			1
245.50	B																				0

Sample	Abundance	Preservation	<i>Bicolmnus ovatus</i>	<i>Chiasmolithus altus</i>	<i>Dictyococcites bisectus</i>	<i>Dictyococcites daviesii</i>	<i>Dictyococcites hesslandii</i>	<i>Dictyococcites productus</i>	<i>Isthmolithus recurvus</i>	<i>Reticulofenestra hampdenensis</i>	<i>Reticulofenestra minuta</i>	<i>Reticulofenestra minutula</i>	<i>Reticulofenestra oamaruensis</i>	<i>Reticulofenestra umbilicus</i>	<i>Sphenolithus sp. cf. S. moriformis</i>	<i>Thoracosphaera sp.</i>	<i>Thoracosphaera heimii</i>	<i>Thoracosphaera saxea</i>	sp. Indet. A	<i>Triquetrorhabdulus sp. Indet.</i>	species richness
330.26	B																				0
330.69	R	G																			2
330.82	R	G																			4
332.11	R	P																			3
333.26	R	P																			3
334.40	R	M																			3
335.35	R	M																			4
339.80	VR	M																			1
340.00	R	M																			2
340.19	R	P																			3
340.28	B																				0
358.40	B																				0
358.22	VR	P																			1
358.49	C	P																			2
369.85	B																				0
394.15	B																				0
396.98	R	M																			3
397.92	VR	P																			1
401.06	VR	M																			0
409.38	VR	M																			1
410.10	B																				0
410.94	B																				0
412.25	R	M																			3
413.05	R	M																			3
426.49	B																				0
439.82	B																				0
443.18	VR	M																			2
444.38	B																				0
444.78	VR	P																			1
446.70	VR	P																			1
448.92	B																				0
449.35	R	M																			4
451.30	VR	P																			1
453.19	F	P																			4
454.51	B																				0

Sample	Abundance	Preservation	<i>Bicolmnus ovatus</i>	<i>Chiasmolithus altus</i>	<i>Dictyococcites bisectus</i>	<i>Dictyococcites daviesii</i>	<i>Dictyococcites hesslandii</i>	<i>Dictyococcites productus</i>	<i>Isthmolithus recurvus</i>	<i>Reticulofenestra hampdenensis</i>	<i>Reticulofenestra minuta</i>	<i>Reticulofenestra minutula</i>	<i>Reticulofenestra oamaruensis</i>	<i>Reticulofenestra umbilicus</i>	<i>Sphenolithus sp. cf. S. moriformis</i>	<i>Thoracosphaera sp.</i>	<i>Thoracosphaera heimii</i>	<i>Thoracosphaera saxea</i>	sp. Indet. A	<i>Triquetrorhabdulus sp. Indet.</i>	species richness
456.32	R	P																			1
457.00	F	G																			3
457.74	R	P																			2
458.49	F	M																			4
459.10	B																				0
459.52	R	G																			6
460.28	F	G																			5
461.76	R	P																			2
462.55	C	G																			4
463.36	C	M																			4
464.00	F	M																			3
465.00	R	M																			4
466.24	VR	P																			1
467.24	R	M																			2
467.76	R	P																			2
468.73	F	M																			4
471.00	R	P																			2
471.11	R	M																			2
472.66	F	M																			4
474.63	R	M																			3
478.29	R	M																			3
481.69	VR	M																			1
486.30	B																				0
612.97	B																				0
619.11	R	P																			1
623.03	B																				0
623.39	F	M																			0
623.60	B																				4
624.10	B																				0

Note: shaded rows indicate where contiguous barren samples have been removed from this table in order to save space. Distribution of all samples, including barren ones, is illustrated in figure 5.5. The "Abundance" column denotes the abundance of calcareous nannofossils as a sedimentary component, where B = barren, VR = very rare (1-2 specimens per longitudinal traverse of the 40 mm smear slide), R = rare (3-10 specimens per traverse), and F = few (10-100 specimens per traverse). The "Preservation" column denotes the average preservation of the fossils, with P = poor (severely dissolved so that species identification is frequently impaired), M = moderate (species identification only occasionally impaired by diagenesis), and G = good (mild or no diagenesis, species identification not impaired). The abundance of individual species is expressed by the following letters: R = rare (<5 specimens per traverse), F = few (6-10 specimens per traverse), C = common (>11 specimens per traverse).

The interval from 169.58 to 193.65 mbsf is characterized by samples that are largely barren of calcareous nannofossils. Only one sample, at 181.74 mbsf, contains rare, moderately preserved nannofossils. Species present include *D. bisectus*, *Dictyococcites daviesii*, and *R. minuta*. This assemblage is consistent with the *D. bisectus* Zone, although it might also be a depauperate representative of the underlying *Chiasmolithus altus* Zone.

Calcareous nannofossils occur consistently in samples from the short interval of 195.70 to 200.54 mbsf. All four samples taken from this interval contain rare, moderately preserved assemblages consisting of three to six taxa (Tab. 5.6). The most species-rich sample, from 200.15 mbsf, contains the smaller reticulofenestrads (*R. minuta* and *R. minutula*) as well as the larger dictyococcitids (*D. daviesii*, *D. hesslandii*, and *D. productus*), but significantly lacks *D. bisectus*. In addition, it contains *Thoracosphaera saxae*, a calcareous dinoflagellate. The assemblage is consistent with, but not definitive of, the *D. bisectus* Zone of late Oligocene age.

Below this short interval of nannofossiliferous rock, there is a thick (at least 115 m) sequence of strata that is largely devoid of calcareous nannofossils (Fig. 5.5). From 215.52 to 330.26 mbsf, it yielded only four samples (222.25, 236.25, 296.39, and 296.83 mbsf) that contain very rare, generally poorly preserved nannofossils. Because of the very rare occurrence of these specimens in a thick sequence of otherwise barren sedimentary rock, it is entirely probable that the specimens are reworked. None of the depauperate assemblages are age diagnostic. It is notable, however, that they contain the last down-hole occurrence of *R. minuta* (at 296.83 mbsf).

All nine samples taken from the interval 330.69 to 340.19 mbsf contain calcareous nannofossils, although surrounding rocks immediately above and below are barren. The assemblages are similar to others higher up-section, containing *D. bisectus*, *D. daviesii*, and *D. hesslandii*. In addition, thoracosphaerids occur in samples 330.82 and 340.00 mbsf. Below is another thick (c. 70 m) interval of rock that is largely barren of nannofossils. From 340.28 to 410.94 mbsf, only four samples (358.22, 396.98, 397.92, and 409.38 mbsf; Tab. 5.6) contain nannofossils. The assemblages are generally poorly preserved and contain only very rare nannofossils including *D. daviesii* and *D. hesslandii*. In addition, however, a sample at 358.49 mbsf contains common fragments of *Thoracosphaera heimii* and *Thoracosphaera saxea*, mainly as single platelets, representing thoracosphaerid tests that have been broken. No other nannofossils are present. This thoracosphaerid-rich interval is reminiscent of the thoracosphaerid horizons in the Quaternary of CRP-1 (Cape Roberts Science Team, 1998b) and CRP-2A (this volume). Villa & Wise (1998) related the Quaternary occurrences in CRP-1 to relatively warm intervals during an otherwise glacially dominated climatic regime. However, this deduction may not be applicable directly to the mid-Oligocene occurrence.

The identification of calcareous nannofossil assemblages of the late Oligocene *Dictyococcites bisectus* Zone distinguishes this sequence in CRP-2A from others in the Ross Sea. Direct comparison with others in the Ross

Sea is difficult because of the lack of previous work on upper Oligocene nannofossils. Interest in the CIROS-1 core focused on the Lower Oligocene and Upper Eocene. Neither Edwards & Waghorn (1989) nor Wei (1992) sampled above CIROS-1 Lithostratigraphical Unit 18 (highest samples at 385.77 and 380.00 mbsf, respectively). Monechi & Reale (1997) sampled CIROS-1 Lithological Units 11 (four samples between 214.55 and 228.83 mbsf) and 15 (310.45 and 316.34 mbsf), dated by diatoms as late Oligocene in age (Harwood et al., 1989a). However, these samples were barren of nannofossils. The stratigraphically highest sample known to contain nannofossils in CIROS-1 is from Lithological Unit 16, at 334.37 mbsf, with rare, poorly preserved specimens of *Coccolithus pelagicus* and *D. daviesii* (Monechi & Reale, 1997). Although *D. daviesii* is the most common component of Oligocene assemblages from CRP-2A, no definitive specimens of *C. pelagicus* have been identified during our preliminary examination. The sample at 334.37 mbsf, located near the base of the Upper Oligocene, is the only known nannofossil-bearing horizon in the Upper Oligocene at CIROS-1. At CRP-2A, there is more than 100 m of nannofossil-bearing strata in the Upper Oligocene *D. bisectus* Zone. This suggests, by correlation, that nannofossil-bearing strata should occur above Unit 16 in CIROS-1. Similarly, there was no systematic examination of the MSSTS-1 Upper Oligocene for calcareous nannofossils. As a result, it is difficult to judge whether or not the record of late Oligocene calcareous nannoplankton in CRP-2A is unique for the Ross Sea.

There was a significant addition to the calcareous nannofossil assemblage that occurred during the underlying episode of hemipelagic sedimentation. The thin siltstones interbedded with coarser lithotypes from 412.25 to 413.05 mbsf contain *Chiasmolithus altus*, in addition to *D. daviesii*, *D. hesslandii*, and *R. hampdenensis*. The last appearance datum (LAD) of *C. altus* has been well documented elsewhere in Chron C8n at 26.1 Ma (Berggren et al., 1995). The LAD of *C. altus* is used as the upper boundary of the *C. altus* Zone of late early to early late Oligocene age. This species appears to range down to a first appearance in the Lower Oligocene (Perch-Nielsen, 1985; de Kaenel & Villa, 1996), although Wei & Wise (1990) report this taxon significantly lower (upper to middle? Eocene) in the Weddell Sea. This species has been found in only two samples during our preliminary examination of CRP-2A, indicating that a significant part of the zone is missing. Diatom evidence (this volume) suggests that this interval is early Oligocene in age, suggesting that much of the upper part of the zone is missing in a major unconformity.

Samples in the interval from 426.49 to 456.32 mbsf are difficult to date biostratigraphically using calcareous nannofossils. All but three of the 13 samples examined from this interval are either barren or contain such very rare, poorly preserved nannofossils that biostratigraphical classification is impossible. Three samples having somewhat better assemblages still evidently lack any diagnostic species. This interval can be characterized only based on its stratigraphical relationship with the overlying (*C. altus*) and underlying (*R. oamaruensis*) zones, and, on

account of its position it is assigned tentatively to the combined *Dictyococcites daviesii/Blackites spinosus* Zone of early Oligocene age. The two zones have been combined because the biohorizon used to differentiate the two, the LAD of *Isthmolithus recurvus*, was not identified in our preliminary examination. This might suggest that the entire interval should be placed in the *D. daviesii* Zone. However, *I. recurvus* is rare in CRP-2A, having been identified from only one sample (459.52 mbsf) in the underlying zone.

The interval from 457.00 to 474.63 is well-characterized biostratigraphically by well-preserved assemblages containing *Reticulofenestra oamaruensis*. This high southern latitude species has a total range that defines the *R. oamaruensis* Zone of earliest Oligocene to latest Eocene age and is well-documented geochronologically. The FAD of *R. oamaruensis* appears to occur consistently in Chron C16 in the Southern Ocean (Wei & Wise, 1992), with its best placement within C16n.1n (Berggren et al., 1995), yielding an age of 35.4 Ma. The LAD of *R. oamaruensis* has been correlated to Chron 13r, although it may occur at the C13n/C13r boundary based on the record at ODP Site 699 (Wei, 1991; Berggren et al., 1995). Given this placement in C13n, it has been assigned an age of 33.7 Ma by Berggren et al. (1995), which is numerically the age of the Eocene/Oligocene boundary as used by them. However, if the record of ODP Site 699 is correct, the actual age of the LAD of *R. oamaruensis* should be slightly higher. Berggren et al. (1995) date the Chron C13n/C13r boundary at 33.545 Ma. This earliest Oligocene age assignment is appealing as it is more in keeping with the traditional assignment of the zone as straddling the Eocene/Oligocene boundary. Moreover, other palaeontological evidence from CRP-2A suggests that this interval is earliest Oligocene rather than latest Eocene in age. In fact, there is significant evidence from diatoms that suggests *R. oamaruensis* specimens in this interval may be reworked.

There is a thick interval of rock that is barren of calcareous nannofossils from 486.30 to 612.97 mbsf. Nevertheless, near the base of the hole, two samples yielded calcareous nannofossils. At 619.11 mbsf, a rare, poorly preserved assemblage contains only *Dictyococcites hesslandii*. A significantly better assemblage was recovered from the basal "fast track" sample at 623.60 mbsf that includes *Bicolumnus ovatus*, *Dictyococcites bisectus*, and *D. hesslandii*. *Bicolumnus ovatus* was first described from the Upper Eocene and Lower Oligocene of Maud Rise, Weddell Sea, but is also known to occur from the Upper Eocene and Lower Oligocene of the Falkland Plateau and Rio Grande Rise (Wei & Wise, 1990). More recently, it has been reported from as high as the Upper Oligocene (Zone NP 25) of the Iberian Abyssal Plain (de Kaenel & Villa, 1996). Thus, the species present in this assemblage cannot be used to assign an age for the base of CRP-2A.

PALYNOLOGY

INTRODUCTION

183 samples were collected for palynological analysis (Tab. 5.7), of which 122 "fast-track" and regular samples

were processed and studied at CSEC laboratory during the core characterization phase; finest grain size rocks were selected with a target sampling interval of 3 to 6 m. Palynological preparation followed the techniques used for CRP-1 and described by Cape Roberts Science Team (1998a) and Simes & Wrenn (1998), with only minor modification. Between 5 and 12 g of rock were processed for each sample. One tablet of *Lycopodium* spores (Lund University batch # 124961) was added to each sample before processing to enable later estimation of palynomorph concentration per weight of sediment. Microwave digestion in hydrochloric and hydrofluoric acid was followed by 7 minutes oxidation with concentrated nitric acid, decantation using a swirling method and sieving with 125 or 212 μm mesh to remove coarse mineral grains, and heavy liquid separation with sodium polytungstate. Finally, most organic residues were sieved to remove particles less than 6 μm diameter.

Very few modern contaminant pollen grains were seen during microscopic examination of the slides. Autofluorescence characteristics (using a Zeiss epillumination system III-RS with blue-violet excitation) were used as an aid to distinguish different pollen and spore components: modern pollen displayed a white autofluorescence, Cenozoic specimens yellow to orange colours, and Permian and lower Mesozoic pollen and spores dull red to no autofluorescence. The drilling mud used in CRP-2/2A was primarily the same synthetic polymer used in drilling of CRP-1, and had previously been found to contain negligible contamination. Guar gum, a mud additive of vegetable origin, also was used in CRP-2/2A. The residue retained by filtering a diluted suspension of the gum on a 6 μm sieve contained a minor amount of colourless fibres and other cellular material. This displayed white autofluorescence and could easily be distinguished from fossil material.

PALYNOFACIES

A simple visual estimate of relative organic residue volume was made from the number and density of microscope slides produced (all recovered material was mounted), as time available did not permit more accurate estimation using *Lycopodium* spore counts. This value was divided by the weight of sample processed to obtain an approximate measure of the "palynological residue", or coarse organic matter content of the sediments (Fig. 5.6). Excluded from estimation were samples in which significant loss during processing was noted. The estimate may not reflect total sediment organic content, as organic residue particles less than 6 μm were removed by sieving. Amorphous organic matter in particular will have been removed by sieving and by nitric acid oxidation.

In general, total residue is not abundant above 306 mbsf, although there are peaks at about 230 and 260 mbsf. Below 306 mbsf residue is distinctly more abundant, with the exception of low values at 531.65 mbsf and 594.90-601.34 mbsf. The principal residue component consists of redeposited coal fragments. The dominance of these is partly controlled by hydrodynamic factors: the low values are probably due to current sorting in the sandstones at those levels.

Tab. 5.7 - Palynology sampling during core characterization.

Hole	Top	Base	Lab. #	Wt (g)	Lithology	Unit	Hole	Top	Base	Lab. #	Wt (g)	Lithology	Unit
2	13.31	13.32	62	7.50	sandy diamicton	2.1	2A	256.03	256.04	135	4.50	mudstone	9.4
2	15.74	15.75	60	8.00	muddy sand (diamicton)	2.1	2A	260.00	260.02	123	11.50	sandy mudstone	9.4
2	15.75	15.76	61	6.50	sandstone clast	2.1	2A	261.68	261.69			mudstone	9.4
2	21.02	21.03	63	6.50	sand (diamicton)	2.1	2A	266.03	266.04			v.f. sandstone	9.5
2	21.18	21.19	71	6.50	sand (diamicton)	2.1	2A	270.94	270.95	134	8.50	muddy f. sandstone	9.5
2	22.33	22.34	72	6.50	m. sand	2.2	2A	275.91	275.92			muddy f. sandstone	9.5
2	24.41	24.42	73	7.00	sandy diamicton	2.2	2A	285.57	285.58	137	10.50	clay bed in f. sand	9.5
2	25.44	25.45	74	6.50	sandy diamicton	2.2	2A	287.99	288.00			v.f. sand	9.5
2	25.86	25.87	75	9.00	sandy diamicton	2.2	2A	292.31	292.32	126	11.50	muddy f. sand	9.5
2	26.29	26.30	76	9.50	fine sand	2.2	2A	292.31	292.32	180*	10.00	muddy f. sand	9.5
2	26.36	26.37	77	11.00	fine sand	2.2	2A	296.32	296.33	138	10.50	sandy mudstone	10.1
2	26.79	26.80	78	10.50	muddy fine sand	3.1	2A	302.84	302.85			v.f. sandstone	11.1
2	26.89	26.90	80	11.00	muddy fine sand	3.1	2A	307.12	307.13	139	6.00	silty claystone	11.1
2	27.88	27.89	64	8.50	muddy v.f. sandstone	3.1	2A	309.98	309.99			v.f. sandstone	11.1
2	29.00	29.02	59	5.50	v.f. silty sand	3.1	2A	316.50	316.52	129	12.00	mudstone	11.2
2	32.75	32.76	79	9.50	muddy m. sandstone	3.1	2A	317.59	317.60	141	5.50	mudstone	11.2
2	34.38	34.39	65	6.00	muddy m. sandstone	3.1	2A	321.82	321.83			mudstone	11.2
2	36.24	36.28	56	5.50	m. sand	3.1	2A	325.66	325.67	142	8.00	siltstone	11.2
2	40.54	40.55	66	6.50	muddy fine sand	3.1	2A	330.86	330.87			mudstone	11.3
2	44.08	44.09	67	7.00	muddy fine sand	3.1	2A	335.29	335.30	143	9.00	mudstone	11.3
2	47.41	47.54	57	6.00	muddy fine sand	3.1	2A	339.80	339.82	128	9.50	mudstone	11.3
2	48.63	48.64	68	6.50	muddy sand (diamicton)	4.1	2A	339.80	339.82	181*	10.50	mudstone	11.3
2	51.96	51.97	69	9.00	v.f. sandy mudstone	4.1	2A	342.14	342.15			mudstone	11.3
2	54.17	54.18	70	6.00	muddy v.f. sandstone	5.1	2A	346.12	346.13	144	8.50	sandy mudstone	11.3
2A	52.96	52.97	84	11.00	muddy v.f. sandstone	5.1	2A	349.21	349.22			muddy f. sandstone (diamictite)	12.1
2A	55.80	55.81	85	9.50	muddy v.f. sandstone	5.1	2A	353.61	353.62	145	9.00	sandy diamicite	12.1
2	57.32	57.42	58	6.50	sandy mudstone	5.1	2A	358.20	358.22	133	8.50	mudstone	12.1
2A	59.97	59.98	86	11.50	mudstone	5.1	2A	360.00	360.01			siltstone	12.1
2A	63.28	63.29	87	7.50	mudstone	5.1	2A	361.33	361.34			sandy diamicite	12.1
2A	67.63	67.64	89	9.00	mudstone	5.1	2A	363.00	363.01	147	8.00	mudstone	12.1
2A	70.79	70.80	90	7.00	mudstone	5.1	2A	369.85	369.86	148	10.50	muddy f. sandstone	12.1
2A	71.20	71.21	82	10.00	mudstone	5.1	2A	376.54	376.55			muddy f. sandstone	12.1
2A	75.59	75.60	81	7.00	muddy fine sandstone	6.1	2A	382.25	382.26	149	11.00	muddy v.f. sandstone	12.1
2A	76.12	76.13	91	8.50	v.f. sandy mudstone	6.1	2A	384.37	384.38			muddy f. sand	12.1
2A	79.44	79.45	93	6.50	v.f. sandy mudstone	6.1	2A	390.17	390.19	136	10.50	mudstone	12.1
2A	83.73	83.74	94	11.00	muddy f. sandstone (diamictite)	6.2	2A	396.65	396.66			mudstone	12.1
2A	89.52	89.53	95	9.50	fine sandstone (diamictite)	6.2	2A	401.05	401.06	152	10.00	muddy f. sandstone	12.2
2A	90.46	90.48	96	14.00	muddy v.f. sandstone	6.2	2A	405.57	405.58			sandy mudstone	12.2
2A	93.76	93.77	97	11.00	muddy v.f. sandstone	6.3	2A	412.25	412.27	140	11.50	muddy f. sandstone	12.2
2A	96.77	96.78	83	10.50	muddy v.f. sandstone	6.3	2A	416.95	416.96	153	12.00	muddy f. sandstone	12.2
2A	101.10	101.11	98	11.50	muddy v.f. sandstone (diamictite)	7.1	2A	423.87	423.88			m. sandstone	12.2
2A	103.62	103.63	101	7.50	sandy diamicite	7.1	2A	429.32	429.33	157	11.00	v.f. sandy mudstone	12.2
2A	106.00	106.01	103	8.00	sandy diamicite	7.1	2A	437.69	437.70	158	12.50	mudstone	12.2
2A	109.13	109.14	102	9.00	f. sandstone	7.2	2A	443.17	443.18			mudstone	13.1
2A	111.06	111.07	104	11.00	f. sand	7.2	2A	444.76	444.78	146	10.50	mudstone	13.1
2A	113.50	113.51	105	8.50	mudstone	7.2	2A	449.22	449.23			mudstone	13.1
2A	114.23	114.24	106	12.50	v.f. sandstone	8.1	2A	453.26	453.27	159	11.50	sandy mudstone	13.1
2A	114.71	114.72	107	12.00	v.f. sandstone	8.1	2A	458.52	458.53			sandy mudstone	13.1
2A	118.88	118.89	108	11.00	muddy v.f. sandstone	8.1	2A	463.54	463.55			sandy mudstone	13.1
2A	122.55	122.56	109	10.00	muddy v.f. sandstone	8.1	2A	464.98	465.18	151	11.50	sandy mudstone	13.1
2A	123.50	123.51	110	11.00	muddy v.f. sandstone	8.1	2A	467.90	467.91			sandy mudstone	13.1
2A	128.09	128.10	111	10.50	muddy v.f. sandstone	8.1	2A	471.07	471.08			sandy mudstone	13.1
2A	130.90	130.92	88	11.50	muddy f. sandstone	8.2	2A	473.97	473.98			muddy f. sandstone	13.1
2A	132.14	132.15	112	11.50	f. sandstone	8.2	2A	474.97	474.98	165	10.50	muddy f. sandstone	13.1
2A	135.08	135.09			v.f. sand	8.2	2A	480.81	480.82	160	11.00	sandy mudstone	13.1
2A	139.91	139.92	115	10.50	v.f. sandy mudstone	8.3	2A	484.54	484.55			v.f. sandy mudstone	13.1
2A	141.27	141.28			v.f. sandy mudstone	8.3	2A	486.32	486.34	150	8.50	v.f. sandy mudstone	13.1
2A	145.59	145.60			v.f. sandy mudstone	8.3	2A	494.10	494.11	166	9.50	laminated v.f. sandstone	13.1
2A	147.53	147.54	116	6.00	v.f. sandy mudstone	8.3	2A	499.02	499.03			f. sandstone	13.1
2A	149.55	149.57			v.f. sandy mudstone	8.3	2A	502.55	502.56	167	11.00	mudstone	13.1
2A	150.77	150.78			v.f. sandy mudstone	8.3	2A	502.56	502.57			lam. siltstone/v.f. sandstone	13.1
2A	154.47	154.48	117	11.50	v.f. sandy mudstone	8.4	2A	507.77	507.79	156	11.00	siltstone	13.1
2A	157.09	157.10			mudstone	8.4	2A	509.80	509.81			lam. mudstone/v.f. sandstone	13.1
2A	158.51	158.53	92	10.50	v.f. sandy mudstone	8.4	2A	515.82	515.83	168	12.00	muddy v.f. sandstone (intraclast)	13.1
2A	161.74	161.75			v.f. sandy mudstone	8.4	2A	523.36	523.37			muddy v.f. sandstone	13.1
2A	165.89	165.90	118	7.00	v.f. sandy mudstone	8.4	2A	524.46	524.48	155	11.00	v.f. sandstone	13.1
2A	168.94	168.95			v.f. sandy mudstone	8.4	2A	531.65	531.66	169	12.50	green m. sandstone	14.1
2A	171.74	171.75			v.f. sandy mudstone	8.4	2A	536.50	536.51	171	12.50	mudstone	15.1
2A	173.44	173.46	119	11.00	v.f. sandy mudstone	8.4	2A	540.90	540.91			muddy v.f. sandstone	15.1
2A	176.18	176.19			v.f. sandy mudstone	8.4	2A	543.81	543.83	154	10.50	siltstone	15.1
2A	177.75	177.76	120	7.50	v.f. sandy mudstone	8.4	2A	548.46	548.47	172	12.00	siltstone	15.2
2A	177.90	177.92	100	11.50	v.f. sandy mudstone	8.4	2A	556.06	556.07	173	13.00	muddy v.f. sandstone	15.2
2A	178.85	178.86			v.f. sandy mudstone	8.4	2A	561.31	561.32			muddy v.f. sandstone	15.2
2A	181.73	181.74	121	8.00	v.f. sandy mudstone	8.4	2A	563.97	563.98			muddy f. sandstone	15.2
2A	185.24	185.25			muddy v.f. sand	9.1	2A	564.68	564.70	162	9.50	v.f. sandy mudstone	15.2
2A	187.45	187.46	122	8.00	f. sandstone	9.2	2A	569.77	569.78			sandy diamicite	15.2
2A	193.96	193.97			muddy f. sandstone (diamictite)	9.3	2A	575.36	575.37	174	11.00	mudstone	15.3
2A	195.70	195.72	99	12.50	v.f. sandstone (diamictite)	9.3	2A	579.04	579.05			siltstone	15.3
2A	199.09	199.10	125	10.00	muddy f. sandstone (diamictite)	9.3	2A	583.41	583.42			muddy v.f. sandstone	15.3
2A	202.34	202.35			muddy f. sandstone	9.3	2A	584.59	584.61	161	9.50	v.f. sandy mudstone	15.3
2A	207.21	207.22	127	5.00	muddy f. sandstone	9.3	2A	588.13	588.14			f. sandstone	15.4
2A	211.25	211.26			muddy v.f. sandstone	9.3	2A	594.90	594.91	175	8.50	muddy f. sandstone	15.4
2A	215.24	215.25	130	7.00	muddy f. sandstone	9.3	2A	601.34	601.35	176	11.00	muddy f. sandstone	15.4
2A	215.49	215.52	113	10.00	muddy f. sandstone	9.3	2A	603.06	603.07			lam. v.f. sandstone/siltstone	15.5
2A	218.17	218.18			muddy v.f. sandstone	9.3	2A	604.44	604.46	164	12.50	sandy mudstone	15.5
2A	220.52	220.53			muddy f. sandstone	9.3	2A	608.25	608.27	170	-	coal pebble	15.5
2A	227.01	227.02	131	6.00	muddy f. sandstone	9.3	2A	608.33	608.34			lam. v.f. sandstone/siltstone	15.5
2A	232.90	232.91			muddy f. sandstone	9.3	2A	612.60	612.61	177	11.00	muddy f. sandstone	15.5
2A	236.34	236.35	114	11.50	muddy v.f. sandstone	9.3	2A	620.21	620.22	179	12.00	v.f. sandy mudstone	15.6
2A	242.82	242.83			muddy v.f. sandstone	9.3	2A	623.77	623.79	163	10.50	sandy mudstone	15.6
2A	245.49	245.50	132	5.50	mudstone	9.3	2A	624.14	624.15	178	12.00	v.f. sandy mudstone	15.6
2A	251.20	251.21			mudstone	9.4							

Note: blank laboratory numbers = reserved samples; * = reprocessed sample.

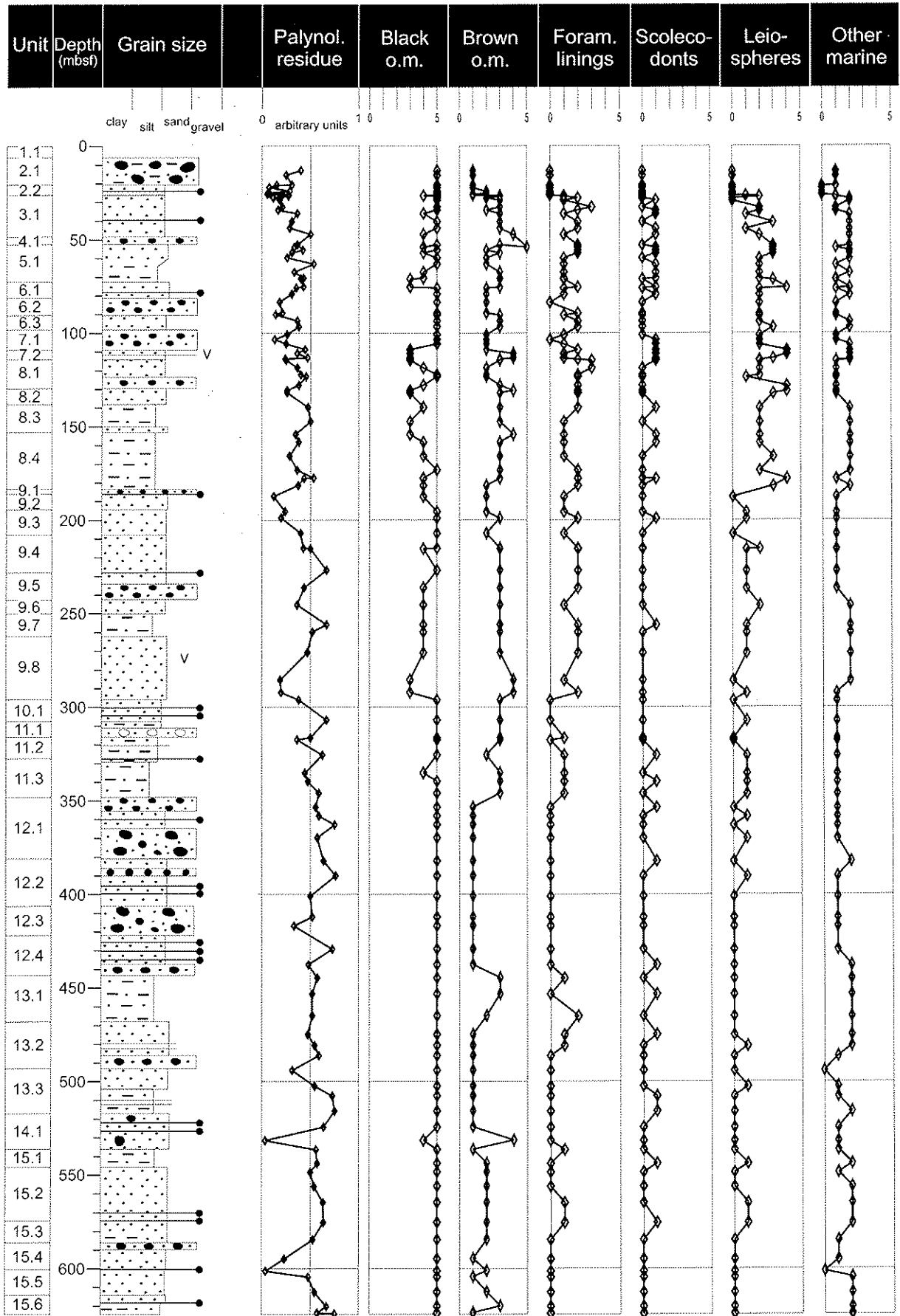


Fig. 5.6 - Palynofacies: relative abundance of organic particulate material (palynological residue) per unit weight of sediment; and relative abundance of major components of the organic matter classed according to a semi-quantitative scale by visual estimation: 0 - absent; 1 - rare, one to a few specimens per sample; 2 - sparse, moderate numbers of specimens per sample; 3 - common, very many specimens per sample; 4 - abundant, major component of organic residue; 5 - prolific, dominant component of residue.

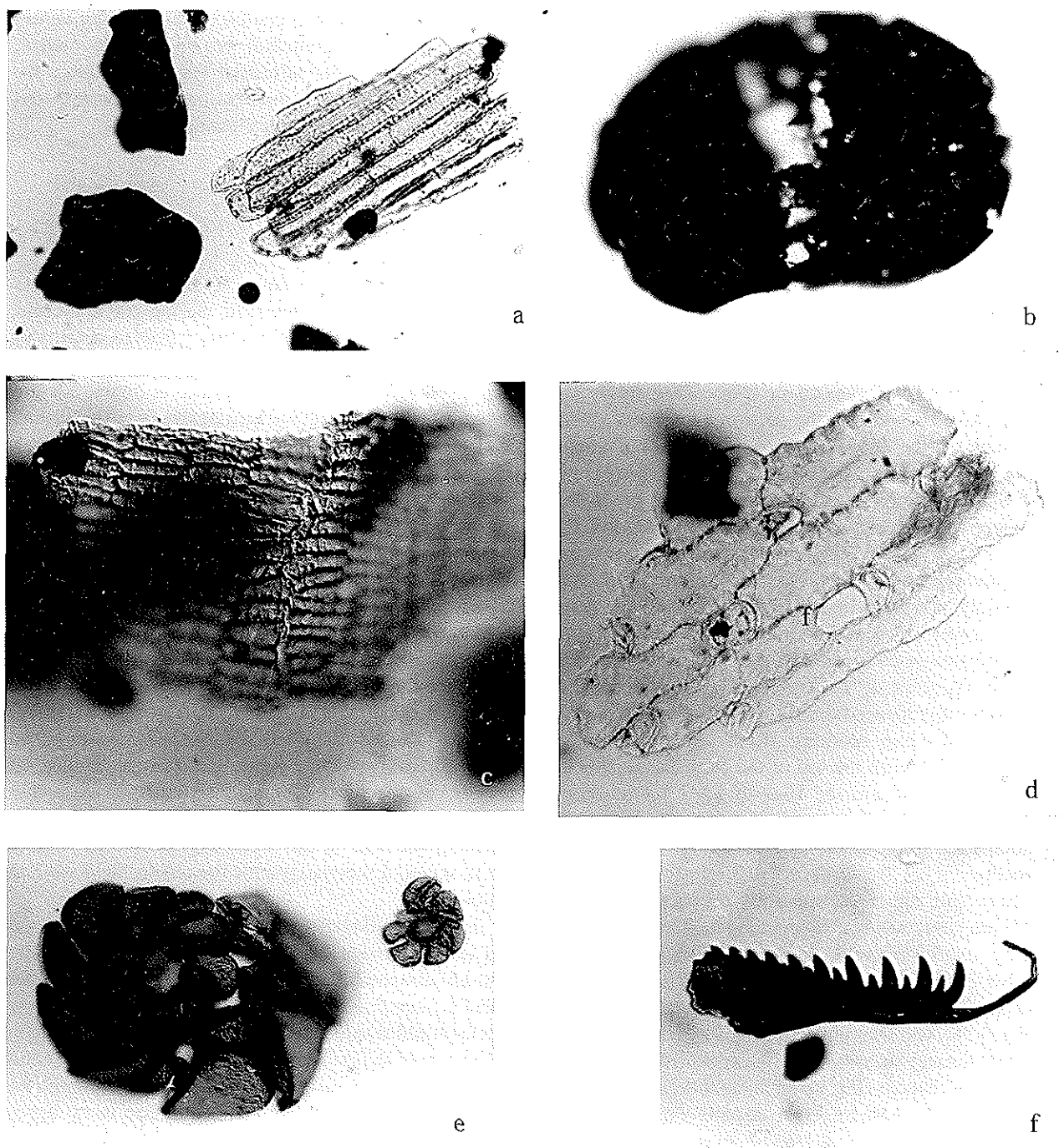


Fig. 5.7 - Palynofacies: photomicrographs of selected organic material and palynomorphs found in CRP-2/2A samples. *a*) light-coloured woody phytoclast and black recycled coaly fragments: depth 620.21-620.22 mbsf, slide number P179/2, England Finder coordinates O40/0, magnification x200; *b*) black thermally metamorphosed recycled taeniate bisaccate pollen: 531.65-531.66 mbsf, P169/1, V41/0, x1000; *c*) plant tissue of undetermined affinity: 524.46-524.48 mbsf, P155/3, V39/4, x250; *d*) plant cuticle with stomata, of undetermined affinity: 335.29-335.30 mbsf, P143/2, E47/4, x1000; *e*) microforaminiferal linings: 44.08-44.09 mbsf, P67/1, H50/1, x250; *f*) jaw apparatus of polychaete annelid (scolecodont): 474.97-474.98 mbsf, P165/2, F36/3, x250.

Relative proportions of components of the palynological material (Batten, 1996), excluding amorphous organic matter, were classed by visual inspection of the microscope slides using a 5-part scale (Fig. 5.6). The major components include:

- black organic matter: opaque angular, more or less equidimensional particles of c. 10-120 μm diameter, a range determined by the mesh of sieves used in

preparation (Fig. 5.7a); these are regarded as detrital coal which, from the identified provenance of macroscopic sediment clasts (see Sedimentology chapter) and the occurrence of recycled Permian and Triassic pollen and spores (e.g. Figs. 5.7b & 5.11j, l & m), is certainly derived from the Beacon Supergroup; the component dominates the palynological material in almost all samples, except a few in the upper part of

the section in which the total amount of residue is small and in which brown organic matter and foraminiferal linings assume a greater relative proportion;

- brown organic matter: translucent brown, structured organic matter; probably mostly phytoclasts, *i.e.* derived from plants, and including mainly wood but also some cuticle and other resistant tissue (Fig. 5.7a, c & d); moderate values prevail in the section above 350 mbsf, except for low values in Plio-Pleistocene LSU 2.1 and 2.2, but below 350 mbsf there are relatively low values except for peaks around 450 mbsf in LSU 13.1, at 531.65 mbsf in the well-sorted sandstone of LSU 14.1, and near the base of the section in LSU 15.6;
- foraminiferal linings: the "chitinous" test linings of mainly benthic foraminifera (Fig. 5.7e); these are relatively abundant in the section above 306 mbsf, except for the Plio-Pleistocene interval, but attain similar values in only a few parts of the section below 306 mbsf - peaks in relative abundance in the lower section reflect relatively finer-grained intervals in LSU 13.1, 13.2, and 15.1-15.3, in which conditions were apparently more favourable for foraminifera, and possibly intervals where sediment accumulation rates were lower with less of a dilution effect;
- leiospheres: smooth-walled cysts or cell walls of marine algae (species of *Leiosphaeridia*, Fig. 5.9i, and *Sigmopollis*) of uncertain affinity, classed as Acritarcha (see succeeding section); these are clearly most abundant between the top of the Miocene section at about 27 mbsf and the base of LSU 8.4 at about 180 mbsf, a distribution consistent with their high abundance in the lower part of the CRP-1 Miocene section.

Minor but either conspicuous or palynologically significant components also recorded include:

- other marine microplankton, including spinose and other Acritarcha (Fig. 5.9c-e & h), Prasinophyceae (*e.g.* *Tasmanites*, Fig. 5.9g; *Cymatiosphaera*, Fig. 5.9h), and Dinophyceae (*e.g.* Fig. 5.8a-i); rare to sparse throughout the section; their detailed distribution and significance is discussed in the following section;
- scolecodonts: these are dispersed parts of the mandibles and maxillary apparatus (feeding organs) of polychaete annelid worms (Szaniawski, 1996), but the component may also include superficially similar arthropod and mollusc parts (Fig. 5.7j); rare throughout the sequence but more consistently present in the section above about 200 mbsf; commonly associated with intervals rich in foraminiferal test linings;
- pellets: approximately ellipsoidal aggregates of amorphous and fine particulate organic matter were recorded only in LSU 7.2 and 8.1 in the interval 111.06-118.88 mbsf, where they are rare to sparse; they are probably fecal pellets of marine invertebrates such as copepods, crustaceans, or polychaetes;
- pollen and spores (*e.g.* Fig. 5.10a-m): these are rare almost throughout the section, attaining moderate numbers between 40.54 and 47.41 mbsf in the lower part of LSU 3.1 and in a number of samples below 306 mbsf, in LSU 11.3, 13.1, 14.1, 15.1, 15.2, and 15.3

(there may be an association of these higher values with relatively abundant brown organic matter, reflecting a similar terrestrial vegetation source for this material; detailed distribution of various taxa and groups is discussed in a following section).

MARINE PALYNOFORMS

Assemblage Details

The marine palynomorph contents of 116 samples were examined. Well-preserved marine palynomorphs were recovered, often in high numbers, from most samples examined (Tab. 5.8). Many marine palynomorphs mentioned in this report are illustrated in figures 5.8 and 5.9. Most species not figured here are illustrated in Hannah et al. (1998). The marine palynomorphs from CRP-1 (Hannah et al., 1998; Wrenn et al., 1998) represent a new early Miocene assemblage that had not previously been recorded. Core from CRP-2/2A extends this new *in situ* assemblage down into the Oligocene and then adds additional new *in situ* early Oligocene material at its base. Together, the two wells bridge a significant gap in the Antarctic marine palynomorph record between the older group of largely Palaeogene species referred to as the Transantarctic flora (Wrenn & Hart, 1988) first described by Wilson (1967), and recent material (see McMinn, 1995, for a discussion of this supposed gap). Many of the taxa recorded here are new and are referred to in open nomenclature. A more comprehensive study of the flora is planned for the Science Results Volume on CRP-2/2A, which should lead to the establishment of a potentially useful series of biostratigraphic datums for the Ross Sea region.

In situ dinoflagellate cysts (dinocysts) are common and are dominated by protoperidinioid taxa including *Phelodinium* and *Batiacasphaera*. Of particular note is the genus *Lejeunecysta* which is represented by up to six new species in addition to *Lejeunecysta cowiei* and the common *Lejeunecysta fallax*. Acritarchs, mainly *Sigmopollis* and several species of *Leiosphaeridia* are common throughout the drill hole but dominate the assemblage in the upper 160 m of the Oligo-Miocene section. The phycocyst of prasinophyte green algae are present throughout the drill hole (*Pterospermella* and several species of *Cymatiosphaera*).

Several species of the Palaeogene Transantarctic flora were recovered. *Vozzhennikovia apertura* is the most common form, but *Enneadocysta partridgei* (Fig. 5.8f), *Deflandrea antarctica*, *Spinidinium macmurdoense* (Fig. 5.8h), *Turbiosphaera filosa* (Fig. 5.7h) and *Arachnodinium antarcticum* (Fig. 5.8d) were also recorded. With the possible exception of specimens from the bottom of the core, all are considered reworked. The presence of *Enneadocysta partridgei* within the Plio-Pleistocene section (26.29-26.30 mbsf) is the highest recorded appearance of this flora in the drill hole. Four species were recorded in a single sample at 40.54-40.55 mbsf. This sudden burst of reworking is probably due to the processing of a clast of Eocene material. Below about 122 mbsf,

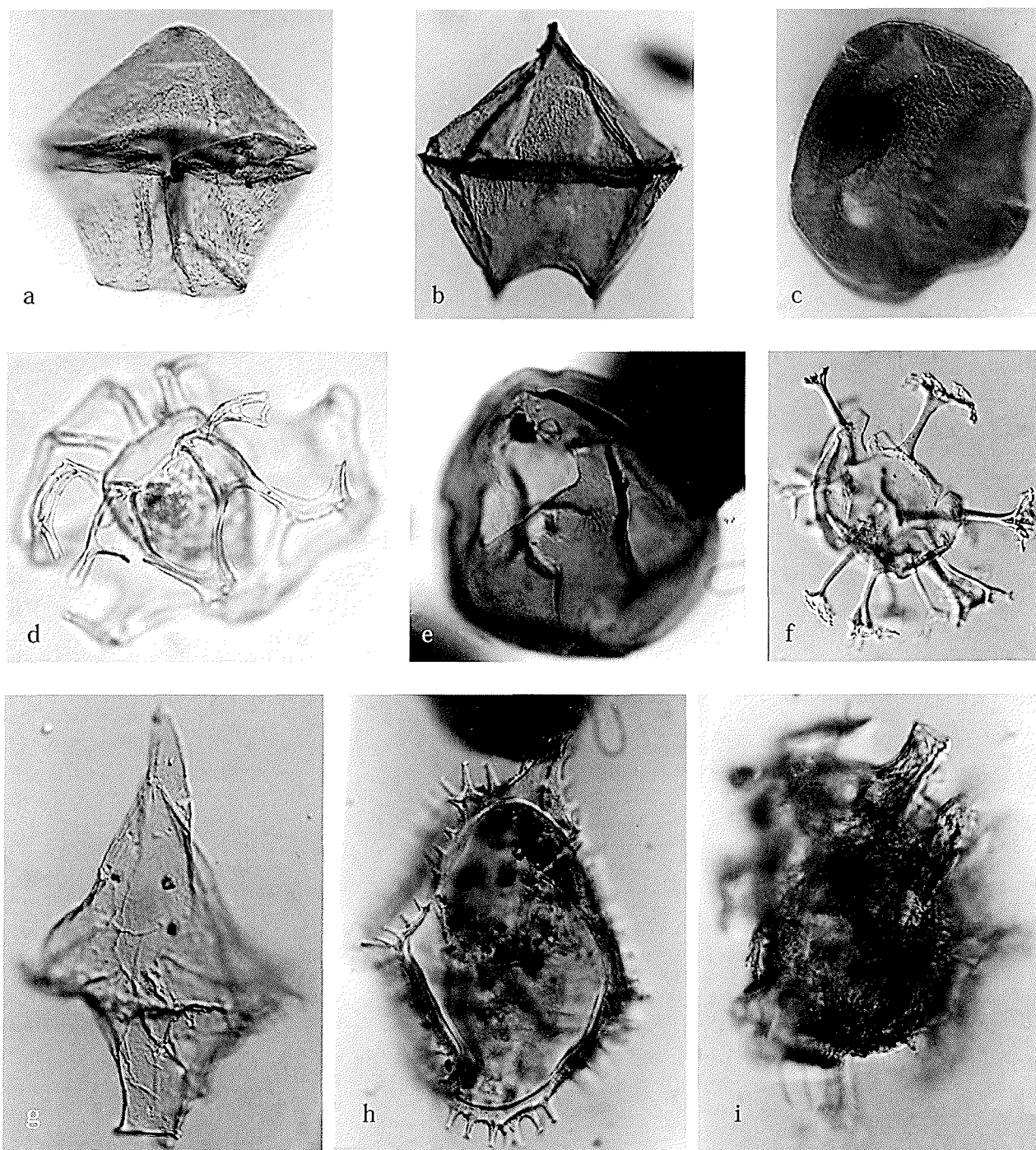


Fig. 5.8 - Selected marine palynomorphs from CRP-2/2A. a) *Lejeunecysta* sp.1: depth = 256.03-256.04 mbsf, slide number = P135/2, England finder co ordinates = N38/4, length = 80 μm ; b) *Lejeunecysta* sp.6: 486.32-486.34 mbsf, P150/3, length = 110 μm ; c) *Lejeunecysta* sp.5: 215.49-215.52 mbsf, P113/1, Q42/1, length = 99 μm ; d) *Arachnodinium antarcticum*: 125.09-125.10 mbsf, single grain mount 001, width of central body = 39 μm ; e) ?*Brigantedinium* sp: 515.82-515.83 mbsf, P168/3, D55, width of central body = 47 μm ; f) *Enneadocysta partridgei*: 346.12-346.13 mbsf, P144/1, V41, length=55 μm ; g) *Lejeunecysta* sp.7: 495.02-495.04 mbsf, P151/2, M38, length = 70 μm ; h) *Spinidinium macmurdoense* : 316.50-316.52 mbsf, P129/3, P45/4, length = 70 μm ; i) *Turbiosphaera filosa*: 346.12-346.13 mbsf, P144/1, W39/4, width of central body = 61 μm .

reworking becomes more persistent. It is particularly intense between samples at 464.98-454.18 and 444.76-444.78 mbsf.

The Oligo-Miocene *in situ* marine palynomorph assemblage can be subdivided into three informal units:
 - *Marine Palynomorph Unit I*: 26.89-26.90 to 181.73-181.74 mbsf. Samples from Unit I yielded some of the richest marine palynomorph floras in the drill hole. Assemblages are commonly dominated by high

numbers of the acritarchs *Leiosphaeridia* and *Sigmopollis*. The base of this interval is marked by the last down-hole occurrence of *Sigmopollis* and the dinocysts *Paralecaniella indentata* and *Lejeunecysta fallax*, which are restricted to this interval. At approximately the same level there is a gradual change down-hole to significantly lower numbers of *Leiosphaeridia*. The three species of *Leiosphaeridia* previously recognised in CRP-1 (Hannah et al., 1998)

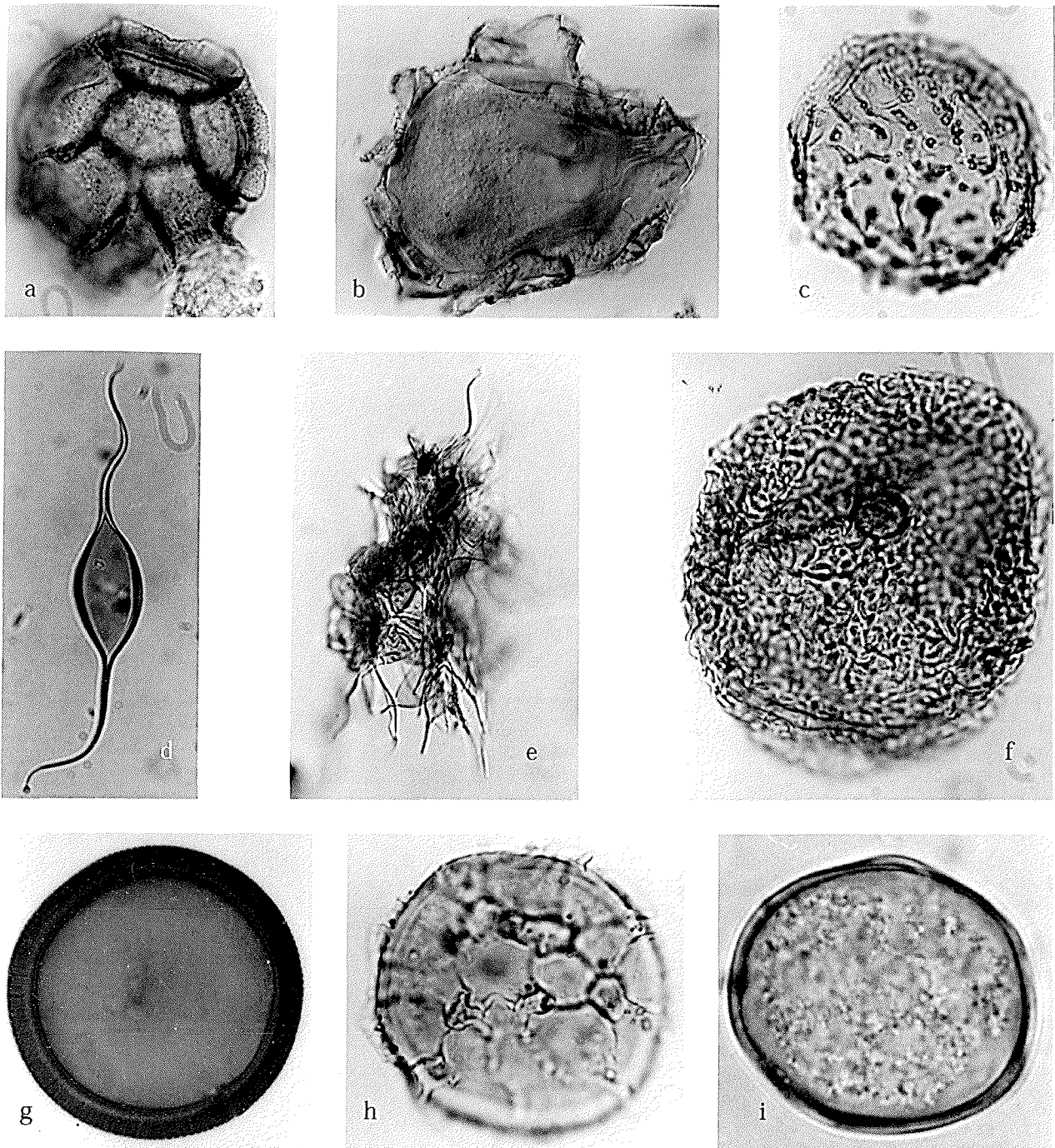


Fig. 5.9 - Selected marine palynomorphs from CRP-2/2A. a) *Impagidinium cf elegans*: depth = 536.50-536.51 mbsf, slide number = 171/4 England finder co ordinates = C46/2, length = 94 μm ; b) *Glaphrocysta* sp.: 256.03-256.04 mbsf, P135/1, P40/1, width = 77 μm ; c) *Micrhystridium* sp.: 464.98-465.18 mbsf, P155/1, P40/1, width = 29 μm ; d) *Leiofusa* sp.: 316.50-316.52 mbsf, P129/2, S38, length = 72 μm ; e) *Leiofusa* ?colony: 307.12-307.13 mbsf, P139/1, S38, length = 115 μm ; f) *Pysidinopsis* sp.: 453.26-453.27 mbsf, P159/1, O54/3, width = 50 μm ; g) *Tasmanites* sp.: 260.00-260.02 mbsf, P123/1, N37/2, width = 100 μm ; h) *Cymatiosphaera* sp.: 453.26-453.27 mbsf, P159/1, E46/4, width = 29 μm ; i) *Leiosphaeridia* sp.: 75.59-75.60 mbsf, P81/1, U38/4, width = 27 μm .

are all present in this unit and additional forms have been recognized, particularly in the two lower units. Several species of *Cymatiosphaera* and *Pterospermella* make up a small proportion of assemblages.

In Unit I both the number and diversity of spinose acritarchs is very low and the assemblage very similar to that recorded from between 99.01 mbsf and the bottom of the hole in CRP-1. The similarity between the assemblages documented in Unit I of CRP-2/2A

and the basal part of CRP-1 is underscored by the presence of the dinocyst *Phelodinium cranwelliae* in the upper part of Unit I. This species occurs persistently below 112.44 mbsf in CRP-1, although it does have a patchy distribution up to 82.18 mbsf. Other distinctive protoperidinioid dinocysts described from CRP-1 (*Batiacasphaera cooperi*, *Brigantedinium pynei*, and *Lejeunecysta cowiei*) are also found in the upper part of Unit I.

- *Marine Palynomorph Unit II: 187.45-187.46 to 296.32-296.33 mbsf.* This interval is bounded above by the first appearance datum (FAD) of *Sigmopollis*, *Paralecaniella indentata* and *Lejeunecysta fallax*, coupled with a decrease in number and diversity in leiospheres. Its base is placed at the FAD of the dinocyst *Lejeunecysta* sp.1 (a distinctive compact form, Fig. 5.7a), and the first appearance datum (FAD) of *?Pyxidinospis* (Fig. 5.9f) together with the incoming of the fusiform acritarch *Leiofusa* (Fig. 5.9d). Assemblages from this interval are generally sparse with low acritarch and prasinophyte numbers. *Lejeunecysta* sp.1 is present in all but one sample from Unit II.
- *Marine Palynomorph Unit III: 307.12-307.13 to bottom of hole.* The top of this interval is placed at the FAD of *Lejeunecysta* sp.1, and the LADs of *?Pyxidinospis* sp. and the fusiform acritarch *Leiofusa*. The interval continues to the bottom of the hole. A sharp increase in coaly fragments accompanies the dinocyst and acritarch changes.

In some samples, *Leiofusa* is abundant. Although usually occurring as single grains in two samples (at 307.12-307.13 and 480.81-480.82 mbsf, Fig. 5.9d), clumps consisting of numerous individuals were located which are interpreted as colonies (Fig. 5.9e). The significance of these forms in large numbers at the base of the hole is unclear.

Lejeunecysta sp.6 (Fig. 5.8c) is another distinctive protoperidinioid dinocyst with two prominent antapical horns and an elongate apical horn. It is one of several new species of *Lejeunecysta* which dominate the dinocyst assemblages in this interval.

?Pyxidinospis sp. (Fig. 5.8f) is a moderate to large dinocyst with a variably rugulose wall texture. Some specimens clearly show a precingular archaeopyle and can be confidently assigned to this genus. However, on some individuals an apical archaeopyle may be present. In addition, the variation in the wall texture suggests that further work may subdivide this into several species.

The appearance of distinctive species of *Lejeunecysta* and *Impagidinium* cf. *elegans* (Fig. 5.9a) at 453.26-453.27 mbsf offers the possibility that Unit III may be subdivided further.

Age and Environmental Significance

Since most of the *in situ* marine palynomorph assemblage is either undescribed or reworked, little can be added to the age determination of CRP-2/2A provided by other microfossil groups. Because the elements of the Transantarctic flora present in Unit III are still most likely reworked, it appears that the drill hole did not reach the earliest Oligocene/Eocene dinoflagellate assemblage recorded in CIROS-1 (Hannah, 1997; Wilson, 1967). The presence of *Lejeunecysta fallax* suggests an age of no younger than middle Miocene for the section below 29.00-29.02 mbsf

Wrenn et al. (1998) recognized two distinct sections in the Miocene part of CRP-1, reflecting differing environmental conditions at the time of deposition. The

section above 99.01 mbsf in CRP-1 is characterized by abundant acanthomorph acritarchs. It was suggested that high acanthomorph numbers were linked to the presence of seasonal sea-ice during deposition. The section below 99.01 mbsf is dominated by leiospheres and *Sigmopollis*, and a lack of acanthomorphs indicating perhaps a lack of seasonal sea-ice.

Acanthomorph acritarchs are relatively uncommon in CRP-2/2A, and they never reach the frequency and abundance recorded in CRP-1, with the possible exception of the sample at 36.24-36.27 mbsf which does contain a modest number. If the tentative linkage made by Wrenn et al. (1998) were to be substantiated, this would suggest that seasonal sea-ice was not common or did not exist during the deposition of most of the Oligo-Miocene interval of CRP-2/2A. Alternately, the absence of acanthomorphs may be a result of other, perhaps evolutionary reasons.

There is no analogous section in CRP-1 to Unit III. This interval is characterized by protoperidinioid cysts, persistent occurrence of *Cymatiosphaera* (but not the other common prasinophyte algae *Pterospermella*, which is largely restricted to Units I & II), and the presence of the fusiform acritarch *Leiofusa*. The palaeoenvironmental significance of this interval is unclear.

TERRESTRIAL PALYNOMORPHS

Distribution

A total of 123 samples was examined. A great scarcity of terrestrial palynomorphs (spores and pollen) and a lack of any major change down-hole characterizes CRP-2/2A (Tab. 5.9). Both presumed contemporaneous and recycled components can be recognized, the latter including Cenozoic forms (most likely Eocene) and Permian to Mesozoic components.

The terrestrial succession is subdivided into two broad units. Although total numbers of recovered taxa and specimens remain very low, there is a significant increase in species diversity and spore and pollen abundance below approximately 300 mbsf. Recycled assemblages occur in intervals or individual samples and include what are interpreted as recycled Eocene, Jurassic-Cretaceous, and Permian-Triassic specimens. A significant increase in Permian-Triassic palynomorphs is also noted below 300 mbsf.

Preservation of the Cenozoic palynomorphs, including presumed contemporaneous and recycled specimens, is generally good to very good. There are some poor specimens, however, that are broken and torn, or have mineral scarring from pyritization, particularly in the lower part of the hole. The Cenozoic specimens are mostly light yellow to yellow in colour, although some have a darker (orange) tinge and most of these are presumed to be recycled from older Cenozoic rocks (see below). The recycled Jurassic-Cretaceous and Permian-Triassic palynomorphs are generally less well-preserved, although a few very good specimens were encountered. Exinal colors are darker, ranging from orange and brown to black, with a few yellow-orange specimens obviously much less affected by thermal metamorphism.

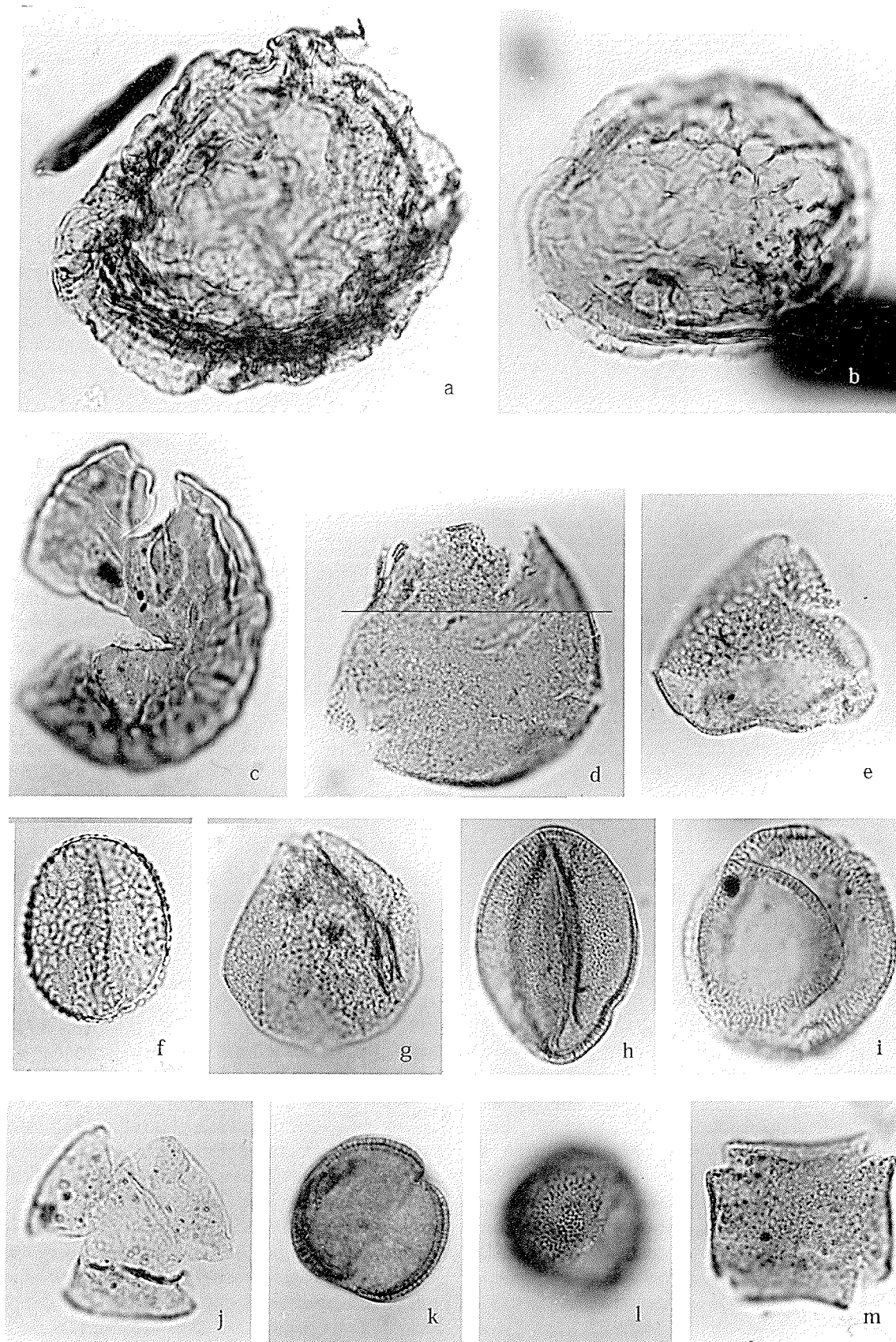


Fig. 5.10 - Photomicrographs of selected spores and pollen from CRP-2/2A, all at magnification approximately x1000. All are Cenozoic taxa. a) Marchantiaceae, depth 123.50-123.51 mbsf, P110/2, England Finder coordinates C45/0, maximum dimension 78 μ m; b) *Ricciaesporites* sp., 575.36-575.37 mbsf, P174/2, M42/0, 67 μ m; c) *Coptospora* sp., 260.00-260.02 mbsf, P123/1, X36/4, 78 μ m; d) *Assamiapollenites incognitus* Pocknall & Mildenhall, 215.49-215.52 mbsf, P113/2, K43/2, 44 μ m; e) *Phormium* sp., 346.12-346.13 mbsf, P144/1, P43/3, 34 μ m; f) *Liliacidites variegatus* Couper, 536.50-536.51 mbsf, P171/1, E38/0, 36 μ m; g) ?*Cyperaceapollis* sp., 444.76-444.78 mbsf, P146/2, O35/1, 39 μ m; h) *Tricolpites* sp.a, 21.02-21.03 mbsf, P63/1, N52/3, 45 μ m; i) *Tricolpites* sp.a, irregularly syncolpate specimen, 113.50-113.51 mbsf, P105/2, N43/2, 44 μ m; j) *Tricolpites* sp.b, 453.26-453.27 mbsf, P159/3, G36/0, 32 μ m; k, l) *Tricolpites* sp.c, different focus levels, 27.88-7.89 mbsf, P64/1, E51/2, 29 μ m; m) ?*Styliidiaceae*, 47.41-47.54 mbsf, P57/1, W50/0, 31 μ m.

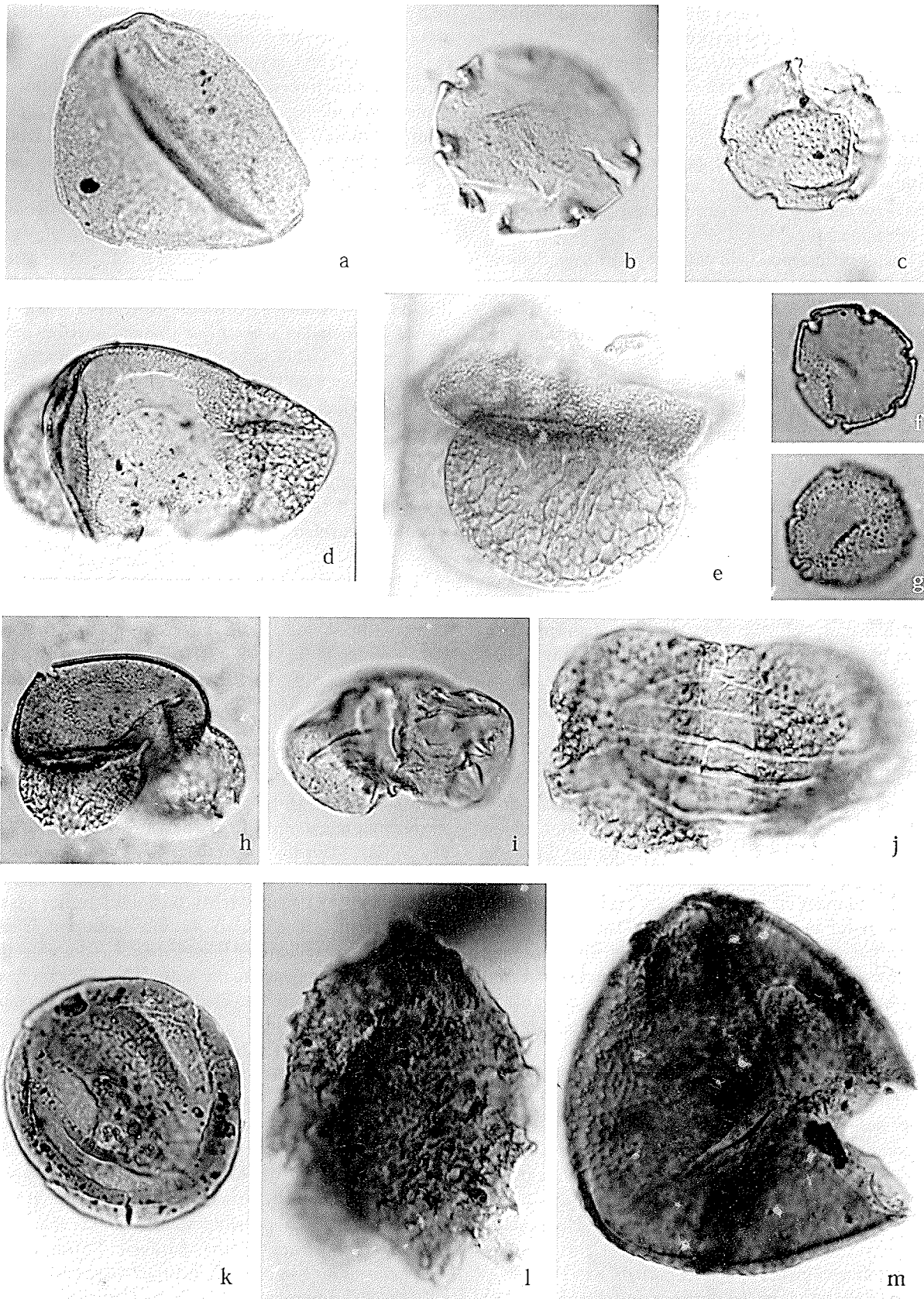


Fig. 5.11 - Photomicrographs of selected spores and pollen from CRP-2/2A, all at magnification approximately $\times 1000$. Figures a) to g) are Cenozoic taxa, figures j, l, m are recycled Permian-Triassic taxa, figure k) is a recycled Jurassic-Cretaceous taxon. a) *Triporopolienites* sp., 256.03-256.04 mbsf, P135/1, O35/0, 42 μm ; b) *Nothofagidites flemingii* (Couper) Potonié, 40.54-40.55 mbsf, P66/1, Q36/4, 37 μm ; c) *Nothofagidites lachlaniae* (Couper) Pocknall & Mildenhall, 584.59-584.61 mbsf, P161/2, H42/4, 30 μm ; d) *Podocarpidites* sp.a, 548.46-548.47 mbsf, P172/2, P43/4, 59 μm ; e) *Podocarpidites* sp.b, 22.33-22.34 mbsf, P72/1, F56/2; f, g) *Nothofagidites* sp. (*fusca* group), different focus levels, 594.90-594.91 mbsf, P175/1, T55/0, 23 μm ; h) *Podocarpidites* sp.a, 390.17-390.19, P136/1, M51/2; i) *Podocarpidites* cf. *exiguus* Harris, 353.61-353.62 mbsf, P145/1, Y58/1, 41 μm ; j) *Protohaploxylinus* sp., 44.08-44.09 mbsf, P67/1, E40/2, 63 μm ; k) *Corollina* sp., 480.81-480.82 mbsf, P160/single mount, 45 μm ; l) *Aratrisporites parvispinosus* Leschik em. Playford, 474.97-474.98 mbsf, P165/1, U40/0, 66 μm ; m) *Pseudoreticulatispora pseudoreticulata* (Balme & Hennelly) Bharadwaj & Srivastava, 57.32-57.42, P58/1, E48/2, 69 μm .

Cape Roberts Science Team, 1998c, p. 106, and Raine, 1998, for comments on this species).

Terrestrial palynomorph Unit II, ~306 to 624.15 mbsf.

This interval includes an increased diversity and abundance of palynomorphs, particularly *Nothofagidites* spp. (including *N. flemingii*, *N. cf. flemingii* - a smaller form, *N. lachlaniae* [Fig. 5.11c], *N. spp.* [undifferentiated *fusca* group, e.g. Fig. 5.11f-g]), and various species of *Podocarpidites* spp. Numbers increase again at about 437 mbsf and below.

Notable occurrences and possibly significant datums in this interval include the LAD of *Podocarpidites* sp.a at 316.50-316.52 mbsf; the First Appearance Datum (FAD) of Marchantiaceae at 339.80-339.82 mbsf; and occurrence of *Phormium* sp. at 346.12-346.13, ?*Cyperaceae* sp. at 444.76-444.78, and ?Ranunculaceae at 488.32-488.34 mbsf.

The conifer pollen species *Podocarpidites* sp.a (Fig. 5.11d, h) occurs throughout most of the lower interval, together with other species of *Podocarpidites*. These, along with taxa such as *Phormium* sp. (Fig. 5.10e), ?*Cyperaceae* sp. (Fig. 5.10g) and ?Ranunculaceae, may prove useful age indicators in the future, although the single occurrences of the latter three in no way can reflect their total ranges. In New Zealand, examples of *Phormium* sp. with a morphology similar to that of the modern species of the genus have an FAD in the Late Eocene or Oligocene (Raine, unpublished data).

Palaeoenvironmental Significance

The rare and extremely low number of species of terrestrial palynomorphs preserved in the CRP-2/2A drill hole provides a picture of a very sparse vegetation which survived essentially unchanged for much of the Oligocene and Miocene. Both sparseness of vegetation and dilution by rapid sediment accumulation rate contributed to the rarity of spores and pollen in the core. The total numbers of presumed contemporaneous terrestrial palynomorphs are so low that they probably do not adequately reflect the local (or regional) vegetation. Even so, it is possible to reconstruct at least part of the vegetation in the sampled Oligocene to Miocene section.

Prior to deposition of the basal sediments of CRP-2/2A, the relatively rich Antarctic Eocene vegetation had disappeared, presumably in response to major cooling and glaciation of the landscape near the end of the Eocene. In New Zealand a major vegetational change, also in response to cooling, occurred near the top of the Upper Eocene Kaiatan Stage (~36-35 Ma) (Pocknall, 1989; Hollis et al., 1997).

Assemblages in the lowermost part of CRP-2/2A never reach the richness in species diversity and abundance seen in the Eocene McMurdo Sound erratics (Wilson, 1967; Askin, unpubl. data) or in the Eocene lower part of CIROS-1 where a great variety of angiosperm taxa, including Proteaceae and representatives of other families not encountered here, were recorded (Mildenhall, 1989). Instead, the Lower Oligocene assemblages found in the lower part of the core suggest a low diversity woody

vegetation which included several species of *Nothofagus* and podocarpaceous conifers, several other angiosperm families, and few cryptogams except for bryophytes (mosses and liverworts). Many of the important components of the prior Eocene flora are missing, for example several species of Proteaceae, various other angiosperms, gymnosperms and cryptogams.

Further deterioration of conditions in this part of Antarctica resulted in additional loss of various components from the land flora. Unglaciating parts of the Late Oligocene to Miocene landscape supported a much reduced flora, probably a low-growing sparse tundra vegetation, as discussed by Raine (1998) for the CRP-1 core. The vegetation included at least one (though possibly more) species of *Nothofagus*, at least one species of podocarpaceous conifer, and a few other angiosperms and cryptogams including mosses. Physiognomically similar vegetation occurs today in the northern Arctic region. Elements of the Antarctic Neogene flora survive in the modern Subantarctic and southern alpine floras.

Possible Recycled Cenozoic Palynomorphs

It is likely that some or many of the Cenozoic spores and pollen are recycled from older Cenozoic rocks. Particularly obvious is the interval with three samples (40.54-40.55, 44.08-44.09, 47.41-47.54 mbsf) in the Lower Miocene (Tab. 5.9). These samples contain significantly increased numbers of palynomorphs, mainly *Nothofagidites* spp. Some of these specimens have a slightly darker exinal colour, suggestive of a greater burial history, but many are indistinguishable from presumed in-place specimens. Most of these species (which have ranges throughout much of the Cenozoic of New Zealand) were also observed in the Quaternary and Miocene parts of CRP-1 (Cape Roberts Science Team, 1998b, 1998c; Raine, 1998) and in the Eocene McMurdo Sound erratics (Askin, unpubl. data). The 40 to 48 mbsf interval is also characterized by abundant recycled Eocene dinoflagellate cysts, lending credence to the notion that these spore and pollen specimens are recycled from Eocene sediments.

Recycled Jurassic-Cretaceous Palynomorphs

Sporadic single occurrences of spore and pollen taxa typical of Jurassic-Lower Cretaceous strata (such as *Corollina* spp., Fig. 5.11k; *Callialasporites segmentatus*) were noted in the drill hole, the highest occurrence being at 93.76-93.77 mbsf. None of the taxa recorded has a restricted range. A possible source of this material is sedimentary strata of the Jurassic Ferrar Group. Palyniferous Jurassic sedimentary rocks have been reported (Tasch & Lammons, 1977) from Carapace Nunatak, upstream of and slightly to the north of Mackay Glacier.

Recycled Permian-Triassic Palynomorphs

Well-preserved yellow-orange specimens to barely recognizable black corroded remnants of Permian-Triassic spores and pollen occur sporadically throughout most of

the drill hole (e.g. Figs. 5.7b & 5.11j, l, m). There is a significant increase in the frequency of these occurrences below ~306 mbsf. As identified in table 5.9, some of these taxa have restricted Permian or Triassic ranges in the Transantarctic Mountains and elsewhere. The provenance of these specimens is the Permian-Triassic Victoria Group of the Beacon Supergroup. Much of the organic material recovered in the palynology samples comprises black coaly fragments interpreted as derived from the Beacon Supergroup (see section on Palynofacies above). Judging from the greater abundance of Beacon palynomorphs below ~306 mbsf, erosion and redeposition of Beacon Supergroup strata were greater during that part of the Oligocene represented by this lower section of the drill hole. At some levels above this, occurrences may represent short intervals of down-cutting into Beacon strata. These are sometimes recognizable immediately above erosion surfaces (such as in 26.29-26.30 and 26.36-26.37 mbsf). Other occurrences may simply result from incorporation of a Beacon microclast into the sediment. The sample at 130.90-130.93 mbsf contains several specimens of varying ages (Permian and Triassic) and varying states of preservation and thermal alteration (from orange specimens to black skeletal remnants), suggestive of erosion from different parts of the Beacon Supergroup and from different areas. At 531.65-531.66 mbsf, an unconsolidated green sand with coaly granules yielded an assemblage composed entirely of black corroded specimens (e.g. Fig. 5.7b). Most of these are recognizable as bisaccate and taeniate bisaccate pollen and are probably of Permian age, suggestive of erosion of the Permian Weller Coal Measures. This is also the likely source of the high rank coal pebble at 608.25-608.27 mbsf, from which no palynomorphs could be extracted.

MACROPALAEONTOLOGY

INTRODUCTION

Macrofossils visible in the half of the core available for sampling (and locally in the archive half) were all recorded (Fig. 5.12, Tab. 5.10). Potential macrofossil-bearing core intervals were, in some cases, specifically searched for less obvious body fossils and moulds through the inspection of fractured surfaces. A few macrofossils were also identified within micropalaeontological (foraminifera) residues. Macrofossils are locally abundant throughout the CRP-2/2A core in both lithified and semi-lithified sediment, and within concretions, although not in all lithostratigraphical units.

Preservation is highly variable. Pristine shells are relatively common in fine-grained sediments, especially in association with mudstone lithologies in LSU 8.4, 9.3 and 9.4. In most cases, however, diagenetic processes have affected the calcareous skeletal parts resulting in a variety of preservation of macrofossils, ranging from slightly chalky to complete dissolution of the shell. Aragonitic fossils (e.g. corals and gastropods) are seldom preserved and never in good condition; corals typically display a sugar-like texture, whereas gastropods are

normally completely leached and preserved as moulds; in some rare cases, shells show advanced stages of decalcification and deposition of secondary cements. Concretion development is also common at specific levels of the core CRP-2/2A core, resulting in semi-indurated sediment up to fossiliferous "limestones" (LSU 9.4, 9.7 and 15.1, Fig. 5.13). Pyritization is rare and in most cases not advanced; e.g. pyritized infillings of serpulid tubes (178.89 mbsf) and bivalves (182.17 mbsf).

Thus far, 324 macrofossil-bearing horizons have been identified in the CRP-2/2a core. In consideration of the preliminary character of the present report, most taxonomic nomenclature is left open and suitable for revision. The preliminary list of macrofossils is reported in appendix 1.

TAXONOMIC REMARKS

Various groups of marine invertebrates are represented in the CRP-2/2A core. These are: Mollusca, Annelida, Cnidaria, Echinodermata, Bryozoa and Porifera, while the possible occurrence of Brachiopoda (161.52 mbsf) awaits confirmation. Vertebrates are represented by the rare occurrence of fish scales (166.64 mbsf) and teeth.

Relatively few fossils are sufficiently well-preserved to be discussed in detail regarding their taxonomic position and only some general and very preliminary comments are provided here.

Mollusca

Mollusca are by far the dominant taxonomic group in the macrofossil assemblages documented in the CRP-2/2A core. This phylum includes representatives of Bivalvia (with a minimum of seven species recognized so far, but possibly in excess of ten), Gastropoda (four-five species at least) and Scaphopoda (one species, uncertain).

Class Bivalvia. Fragmented or whole bivalves are widespread throughout the core, with the exception of LSU 4.1, 10.1, 11.1, 11.2, 13.3, 14.1, 15.3, 15.5, and 15.6, which appear barren of macrofossils; they are also the most common of the macrofossils.

- 1- Large protobranchs have been positively recognized in LSU 9.7. Material ranges from fresh to highly decalcified. Unfortunately, no complete fresh shells are available for inspection. Preliminary determination is based on the very few specimens showing some diagnostic features. A very decalcified and incomplete specimen (210.10 mbsf; Fig. 5.14a) shows evidence of a taxodont hinge; the best preserved specimen is a left valve from 260.83 mbsf whose shell is reminiscent of *Yoldia* (Fig. 5.14b).
- 2 - Pectinids (scallop) are rare and mostly occur as incomplete and/or abraded fragments in LSU 2.1 to 6.3, and 8.4. The best specimen is an incomplete shell (broken during drilling and lacking most of the diagnostic shell parts) tentatively assigned to *Adamussium*.
- 3 - Mytilids (mussels) dominate the macrofossil assemblages in LSU 12.4, 13.1, 13.2 and 15.4

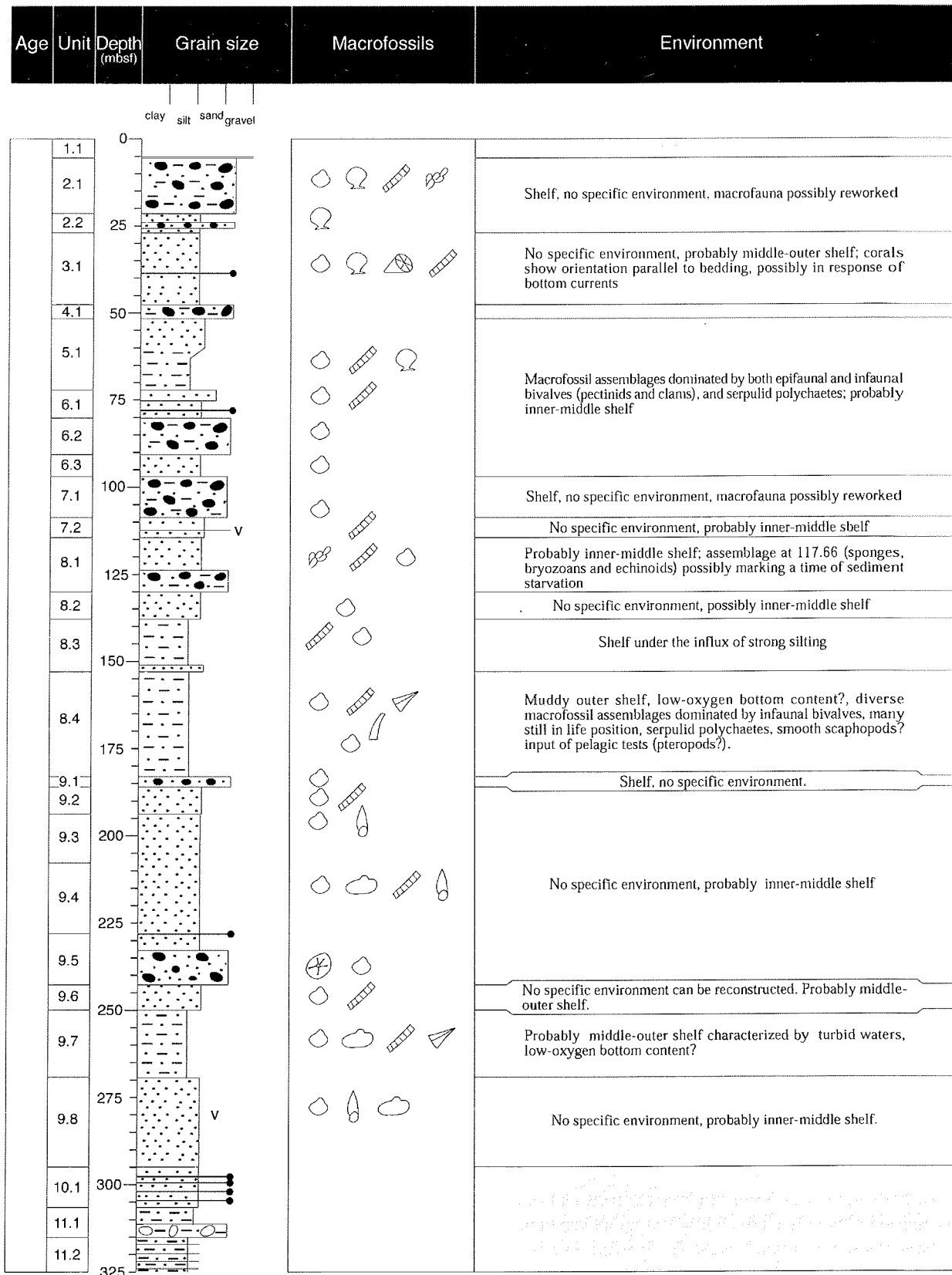


Fig. 5.12 - Lithostratigraphical summary of CRP-2/2A drill hole showing position and composition of the major macrofossil assemblages and their palaeoenvironmental significance.

(Fig. 5.14c). Mytilids apparently belong to a single species of a modioloid mussel (probably *Modiolus*). Most specimens appear to be still articulated and some are in life position. *Modiolus* is known from Early Tertiary deposits on Seymour Island, Antarctic

Pensinsula (Stilwell & Zinsmeister, 1992) but it is unknown from younger beds in Antarctica.
 4 - Veneracean? clams occur in LSU 8.4 and 9.3. The only relatively well-preserved specimen shows concentric grooves on the external surface.

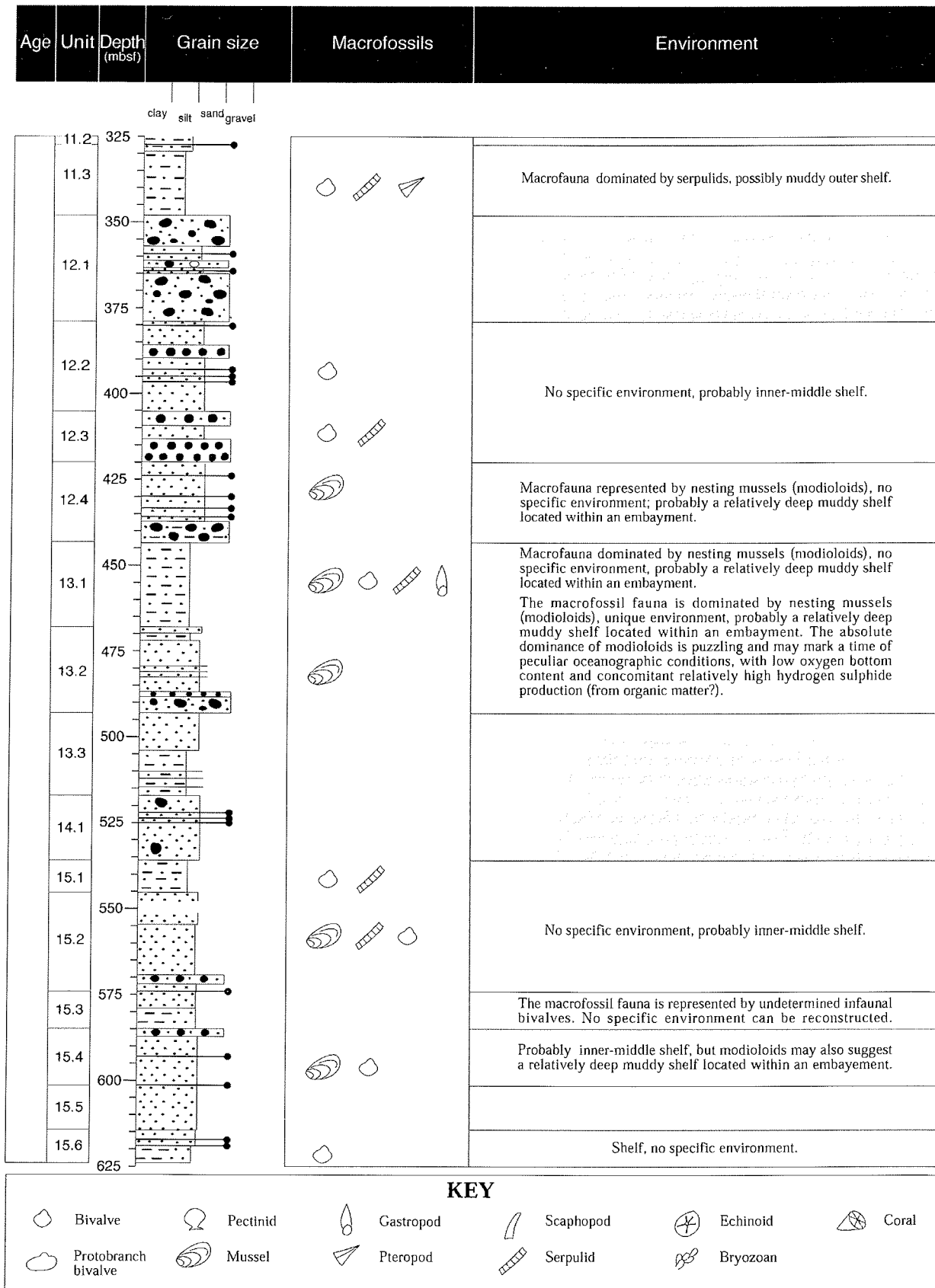


Fig. 5.12 - Continued.

5 - A square-shaped, shell shows some resemblance to species belonging to the nesting bivalve genus *Hiatella* (Fig. 5.14d) the advanced decalcification of the shell prevents any further taxonomic speculation at present.

Class Gastropoda. Gastropods are rare and are represented by a few decalcified specimens and moulds. Remarkable is the discovery of possible holoplanktic mollusca (thecosomatous pteropods). A few broken shells from LSU 8.4 (still retaining some original shell material),

Table 5.10 - Inventory of CRP-2/2A macrofossils.

LSU 2.1	96.71-96.76 mbsf: pectinid and other bivalve fragments
6.95-7.02 mbsf: unidentified macrofossil fragment	96.79-96.84 mbsf: unidentified macrofossil fragment
9.13-9.14 mbsf: unidentified macrofossil	
10.12-10.13 mbsf: unidentified mollusc fragment	LSU 7.1
10.14-10.15 mbsf: unidentified bivalve fragment	100.59-100.60 mbsf: unidentified small bivalve (decalcified)
10.28-10.29 mbsf: unidentified bivalve fragment	100.60 mbsf: unidentified small bivalve
10.46-10.47 mbsf: unidentified bivalve fragment	
15.15-15.16 mbsf: unidentified bivalve (pectinid?) fragment	LSU 7.2
15.76-15.86 mbsf: unidentified bivalve fragment	114.00-114.01 mbsf: serpulid polychaete tubes
16.30-16.38 mbsf: bryozoan and bivalve fragment, echinoid spines	
19.84-19.90 mbsf: serpulid polychaete tube fragment, echinoid spines	LSU 8.1
	116.00-116.01 mbsf: serpulid polychaete tubes
LSU 2.2	117.32-117.34 mbsf: unidentified small bivalve (decalcified)
20.50-20.51 mbsf: unidentified bivalve fragment	117.66-117.72 mbsf: bryozoans (aligned), sponge-spicule mats?, echinoid theca? (fragments)
22.05-22.06 mbsf: bivalve (pectinid?) fragment	117.75-117.76 mbsf: unidentified bivalve (decalcified), serpulid polychaete tubes?
22.12-22.13 mbsf: pectinid (" <i>Chlamys</i> ") fragment	118.20-118.21 mbsf: serpulid polychaete tube (decalcified)
23.90-23.19 mbsf: bivalve (pectinid?) fragment	119.30-119.31 mbsf: unidentified bivalve (<i>Hiatella</i> ?) (decalcified)
24.49-24.51 mbsf: bivalve (pectinid?) fragment	119.64-119.66 mbsf: unidentified thin shelled bivalve
	119.77-119.80 mbsf: unidentified thin shelled bivalve
LSU 3.1	121.43-121.45 mbsf: unidentified bivalve (decalcified)
33.38-33.39 mbsf: bivalve fragment	121.54-121.56 mbsf: unidentified small bivalve (decalcified)
33.74-33.75 mbsf: bivalve fragment	126.55-126.56 mbsf: bivalve fragments (pectinid), polychaete serpulid tube
34.62-34.63 mbsf: unidentified macrofossil fragment	
34.77-34.78 mbsf: unidentified macrofossil fragment	LSU 8.2
35.94-35.96 mbsf: bivalve fragment	133.72-133.74 mbsf: unidentified bivalve
36.01-36.05 mbsf: solitary coral? fragment (sugar-like texture)	135.48-135.51 mbsf: unidentified macrofossil
36.21-36.22 mbsf: pectinid and solitary coral? fragment (sugar-like texture)	137.74-137.75 mbsf: concretion with unidentified thin shelled bivalves
36.24-36.27 mbsf: solitary coral?	
36.29-36.30 mbsf: bivalve (pectinid) fragment	LSU 8.3
36.50-36.51 mbsf: solitary coral? (sugar-like texture)	138.39-138.41 mbsf: unidentified thin shelled ?bivalve
37.17-37.18 mbsf: serpulid polychaete tube	138.43-138.45 mbsf: serpulid polychaete tubes
39.91-39.92 mbsf: unidentified macrofossil (bivalve?, coral?) fragment	141.74-141.78 mbsf: bunch of serpulid polychaete tubes (recrystallized)
40.12-40.13 mbsf: unidentified bivalve fragment (very small)	
	LSU 8.4
LSU 5.1	158.38-158.48 mbsf: serpulid polychaete tube (only mold)
54.11-54.14 mbsf: undet thin shelled bivalve (pectinid)	161.52-161.54 mbsf: unidentified ribbed clam or brachiopod
54.23-54.26 mbsf: undet thin shelled bivalve (pectinid?)	162.98-163.06 mbsf: serpulid polychaete tube fragment
54.28-54.26 mbsf: pectinid (" <i>Adamussium</i> ") fragment	163.41-163.42 mbsf: serpulid polychaete tube, scaphopod?
54.32-54.33 mbsf: undet thin shelled bivalve	163.56-163.58 mbsf: serpulid polychaete tube or scaphopod?
54.61-54.64 mbsf: concretion with undet thin-shelled bivalve	163.87-163.88 mbsf: articulated bivalve (decalcified)
54.83-54.84 mbsf: undet bivalve, serpulid polychaete tube? fragment	165.41-165.42 mbsf: unidentified scaphopod?
54.94-54.98 mbsf: undet thin shelled bivalve (pectinid?)	165.48-165.50 mbsf: articulated bivalve (veneracean?)
55.79-55.80 mbsf: undet bivalve fragment	165.79-165.80 mbsf: articulated bivalve (veneracean?)
55.87-55.88 mbsf: unidentified macrofossil (serpulid?bivalve?) concreted	166.64-166.65 mbsf: unidentified macrofossils, fish scale
56.00-56.01 mbsf: undet bivalve (<i>Hiatella</i> ?) fragment	168.17-168.20 mbsf: unidentified large bivalve
56.03-56.04 mbsf: serpulid polychaete tube	167.83-167.84 mbsf: unidentified tubular macrofossil
56.19-56.20 mbsf: serpulid polychaete tube?	168.17-168.20 mbsf: relatively large, thin shelled bivalve
56.48-56.51 mbsf: serpulid polychaete tubes?	169.38-169.40 mbsf: fresh unidentified macrofossil (broken during preparation) most probably an articulated small bivalve
57.32-57.42 mbsf: serpulid polychaete tube	170.92-170.94 mbsf: concretion with thecosomatous pteropod?
63.69-63.71 mbsf: serpulid polychaete tube (fragment)	176.30-176.33 mbsf: large thin shelled bivalve (pectinid?) almost encased in semi-endurated mudstone
71.42-71.47 mbsf: well preserved (but broken by drilling) pectinid (" <i>Adamussium</i> ")	176.74-176.75 mbsf: scaphopod (fresh, but incomplete shell) or perhaps a thecosomatous pteropod
	178.11-178.13 mbsf: unidentified thin shelled bivalve
LSU 6.1	178.89-178.91 mbsf: serpulid polychaete tubes (pyritized)
75.60-75.67 mbsf: serpulid polychaete tube	179.25-179.27 mbsf: unidentified thin shelled macrofossil.
80.10-80.13 mbsf: concretion with unidentified bivalves	180.08-180.10 mbsf: thecosomatous pteropod? (fresh)
80.55-80.58 mbsf: serpulid polychaete tube	180.17-180.22 mbsf: unidentified articulated bivalve (veneracean?), pectinid (<i>Adamussium</i> ?)
80.65-80.68 mbsf: serpulid polychaete tubes (well preserved); bivalves (<i>Hiatella</i> ?; articulated but decalcified)	182.17-182.22 mbsf: unidentified articulated bivalve (pyritized), serpulid polychaete tube
LSU 6.2	LSU 9.1
86.42-86.43 mbsf: unidentified macrofossil	184.14-184.16 mbsf: unidentified thin shelled bivalve
90.49-90.51 mbsf: bivalve (? pectinid) fragment	184.29-184.31 mbsf: unidentified thin bivalve fragment
91.36-91.38 mbsf: bivalve (?pectinid) fragment	184.96-184.98 mbsf: unidentified thin bivalve fragment
LSU 6.3	LSU 9.2
91.46-91.47 mbsf: unidentified bivalve fragment	191.18-191.19 mbsf: unidentified large and articulated thin shelled bivalve
91.56-91.57 mbsf: unidentified bivalve (decalcified)	191.24-191.25 mbsf: unidentified macrofossil
91.88-91.89 mbsf: small unidentified macrofossil fragment	
93.16-93.17 mbsf: unidentified bivalve (decalcified)	
95.30-95.42 mbsf: concretion with unidentified thin shelled bivalves	
95.51 mbsf: mbsf: unidentified thin shelled bivalve	

Table 5.10 - Continued.

192.41-192.42 mbsf: unidentified large thin shelled bivalve	226.85-226.89 mbsf: relat. large unidentified turritiform, high-spire gastropod (recrystallized)
192.65-192.66 mbsf: unidentified small macrofossil fragment	227.27-227.33 mbsf: unidentified bivalve (<i>Yoldia?</i>)
193.40-193.42 mbsf: unidentified thin shelled bivalve	
193.43-193.44 mbsf: unidentified thin shelled bivalve	
193.48-193.49 mbsf: unidentified macrofossil fragment	
LSU 9.3	LSU 9.5
193.73-193.75 mbsf: unidentified tiny bivalve fragments	227.39-227.42 mbsf: unidentified ribbed bivalve, juvenile unidentified articulated bivalve
193.81-193.83 mbsf: unidentified relatively large thin shelled bivalve	228.94-228.96 mbsf: unidentified thin costate articulated bivalve
194.87-194.91 mbsf: unidentified small articulated bivalves, serpulid polychaete tube	230.22-230.25 mbsf: echinoid
195.29-195.32 mbsf: unidentified thin shelled bivalve	231.16-231.19 mbsf: unidentified thin shelled bivalve fragment
195.36-195.37 mbsf: unidentified thin shelled, articulated and costate bivalve	232.47-232.49 mbsf: unidentified thin costate bivalve fragment
195.44-195.48 mbsf: unidentified articulated bivalve (veneracean?, decalcified)	232.98-233.00 mbsf: unidentified thin shelled articulated bivalve
195.51-195.52 mbsf: unidentified tiny bivalve fragments	233.43-233.47 mbsf: unidentified bivalve? fragment
195.75-195.78 mbsf: unidentified thin shelled bivalve	234.99-235.03 mbsf: unidentified articulated bivalve
196.21-196.23 mbsf: unidentified relatively large thin shelled bivalve	236.54-236.55 mbsf: unidentified bivalve fragment
196.63-196.66 mbsf: unidentified thin shelled bivalve	236.61-236.64 mbsf: unidentified macrofossil (echinoid?)
197.02-198.03 mbsf: unidentified thin shelled bivalve (decalcified)	238.60-238.62 mbsf: unidentified bivalve fragment
197.00-198.04 mbsf: unidentified thin shelled bivalve	240.13-240.14 mbsf: unidentified bivalve fragment
197.14-198.15 mbsf: unidentified bivalve fragments	
197.24-197.25 mbsf: unidentified thin shelled bivalve	LSU 9.6
197.55-197.57 mbsf: unidentified macrofossil fragment	244.80-244.83 mbsf: unidentified bivalve fragment
197.67-197.72 mbsf: unidentified tiny bivalve fragment	246.97-247.00 mbsf: unidentified articulated bivalve (protobranch?)
197.96-197.98 mbsf: unidentified thin shelled bivalve	247.09-247.12 mbsf: unidentified thin shelled bivalve
198.02-198.04 mbsf: unidentified articulated bivalve (decalcified)	247.67-247.71 mbsf: serpulid polychaete attached on unidentified bivalve shell fragment
198.04-198.05 mbsf: unidentified thin shelled bivalve	249.65-249.69 mbsf: concretion with numerous unidentified bivalves, many still articulated (coquina)
198.07-198.08 mbsf: unidentified thin shelled bivalve	
198.08-198.12 mbsf: unidentified thin shelled bivalve	LSU 9.7
198.52-198.53 mbsf: unidentified bivalve	250.96-250.97 mbsf: unidentified macrofossil
198.73-198.74 mbsf: unidentified thin shelled bivalve	251.32-251.36 mbsf: unidentified bivalve fragment
198.93-198.94 mbsf: unidentified macrofossil.	254.99-255.03 mbsf: unidentified bivalve (<i>Yoldia?</i>)
199.56-199.59 mbsf: low-spined, globose gastropod, turritiform high-spined gastropod, ribbed articulated bivalve	255.27-255.30 mbsf: thecosomatous pteropod?
199.72-199.75 mbsf: unidentified bivalve (decalcified)	256.04-256.05 mbsf: serpulid polychaete tube
199.82-199.85 mbsf: unidentified bivalve (decalcified)	256.40-256.43 mbsf: unidentified articulated bivalve (protobranch?)
199.91-199.93 mbsf: unidentified macrofossil (decalcified)	256.58-256.59 mbsf: unidentified thin shelled bivalves
200.97-200.99 mbsf: unidentified articulated bivalve	257.60-257.63 mbsf: unidentified articulated bivalve
205.39-205.42 mbsf: unidentified bivalve (decalcified)	258.65-258.68 mbsf: unidentified articulated bivalve
	259.16-259.20 mbsf: many serpulid polychaete tubes
LSU 9.4	259.21-259.25 mbsf: serpulid polychaete tubes
208.58-208.60 mbsf: unidentified bivalve	259.49-259.61 mbsf: unidentified bivalve (<i>Yoldia?</i>)
209.19-209.22 mbsf: unidentified bivalves (decalcified)	260.83-260.87 mbsf: unidentified bivalve (<i>Yoldia?</i>)
209.33-209.35 mbsf: protobranch? bivalve	262.02-262.12 mbsf: unidentified articulated ribbed bivalve (or brachiopod?)
209.45-209.49 mbsf: unidentified articulated bivalve (decalcified)	262.21-262.24 mbsf: unidentified articulated bivalve (<i>Yoldia?</i>)
210.10-210.14 mbsf: large protobranch bivalve	262.67-262.69 mbsf: unidentified articulated bivalve
210.20-210.27 mbsf: unidentified bivalve fragment	
210.24-210.30 mbsf: concretion with globose low-spined and turritiform, high-spined gastropods (two species), serpulid polychaete tubes, articulated costate bivalve (mostly decalcified)	LSU 9.8
214.07-214.10 mbsf: unidentified macrofossil	263.16-263.20 mbsf: unidentified bivalve (<i>Yoldia?</i>), serpulid polychaete tube
215.24-215.26 mbsf: unidentified thin shelled bivalve	263.98-264.01 mbsf: unidentified bivalve? fragment
214.34-214.36 mbsf: unidentified bivalve (decalcified)	285.15-285.93 mbsf: turritiform, high-spined gastropod
215.60-215.68 mbsf: unidentified bivalve	285.65-285.68 mbsf: unidentified articulated bivalve
216.35-216.38 mbsf: serpulid polychaete tube? unidentified bivalve fragment	291.95-292.03 mbsf: unidentified articulated bivalve
216.93-216.96 mbsf: unidentified thin shelled bivalve	294.07-294.13 mbsf: unidentified large bivalve (mould)
217.75-217.78 mbsf: unidentified thin shelled bivalve	
218.09-218.12 mbsf: unidentified thin shelled bivalve	LSU 11.3
219.18-219.21 mbsf: unidentified thin shelled bivalve	328.73-328.76 mbsf: serpulid polychaete tube
219.53-219.56 mbsf: unidentified thin shelled bivalve	338.75-338.79 mbsf: serpulid polychaete tube
220.45-220.47 mbsf: unidentified thin shelled bivalve	341.79-341.87 mbsf: many serpulid polychaete tubes
220.97-220.99 mbsf: unidentified thin shelled bivalve	342.07-342.15 mbsf: many serpulid polychaete tubes, most parallel to bedding
222.35-222.38 mbsf: unidentified bivalve fragments	342.26-342.30 mbsf: unidentified tubular macrofossil
223.13-223.15 mbsf: unidentified thin shelled bivalves	344.35-344.38 mbsf: thecosomatous pteropod, unidentified bivalve?
224.03-224.06 mbsf: unidentified macrofossil fragment	
224.17-224.20 mbsf: unidentified articulated bivalve (protobranch?)	LSU 12.2
224.30-224.32 mbsf: unidentified thin shelled bivalve fragment	403.30-403.32 mbsf: unidentified macrofossil fragments
224.41-224.47 mbsf: unidentified articulated bivalve	403.36-403.38 mbsf: unidentified bivalve fragments
224.54-224.57 mbsf: unidentified bivalve (<i>Yoldia?</i>)	403.40-403.41 mbsf: unidentified macrofossil fragments
224.84-224.88 mbsf: unidentified articulated bivalve	403.54-403.55 mbsf: unidentified macrofossil fragments
225.58-225.61 mbsf: unidentified bivalve	404.85-404.86 mbsf: unidentified macrofossil fragments
225.96-226.00 mbsf: unidentified bivalve fragment	
	LSU 12.3
	406.08-406.09 mbsf: unidentified bivalve fragments
	411.32-411.36 mbsf: unidentified bivalve fragments
	413.19-413.22 mbsf: serpulid polychaete tube

Table 5.10 - Continued.

LSU 12.4	469.87-469.93 mbsf: articulated modioloid bivalves
441.59-441.62 mbsf: articulated bivalve (modioloid?)	482.91-482.93 mbsf: modioloid bivalve
	483.15-483.18 mbsf: modioloid? bivalve
LSU 13.1	LSU 15.1
443.10-443.12 mbsf: unidentified thin shelled bivalve	539.37-539.38 mbsf: unidentified macrofossil fragment
443.50-443.56 mbsf: articulated modioloid bivalves	540.00-540.01 mbsf: unidentified macrofossil fragment
443.91-443.93 mbsf: unidentified articulated bivalve	540.53-540.54 mbsf: unidentified macrofossil fragment
444.09-444.12 mbsf: unidentified gastropod	540.58-540.60 mbsf: unidentified macrofossil fragments
444.31-444.33 mbsf: serpulid polychaete tube	540.61-540.62 mbsf: serpulid polychaete tube?
444.62-444.64 mbsf: articulated modioloid bivalve	541.35-541.36 mbsf: unidentified bivalve fragment
444.72-444.76 mbsf: unidentified marine plant?	544.23-544.24 mbsf: unidentified macrofossil fragment
445.05-445.07 mbsf: unidentified articulated bivalve	544.72-544.73 mbsf: unidentified macrofossil fragment
445.11-445.15 mbsf: articulated juvenile modioloid bivalves	544.80-544.82 mbsf: unidentified bivalve fragment
446.33-446.38 mbsf: unidentified articulated bivalve	
446.65-446.67 mbsf: articulated modioloid bivalve	LSU 15.2
446.59-446.63 mbsf: unidentified bivalve	556.03-556.04 mbsf: unidentified articulated bivalve?
447.24-447.26 mbsf: serpulid polychaete tube	558.74-558.75 mbsf: serpulid polychaete tube?
447.43-447.48 mbsf: articulated modioloid bivalves	559.04-559.07 mbsf: serpulid polychaete tube
447.69-447.81 mbsf: articulated modioloid bivalve	559.71-559.72 mbsf: serpulid polychaete tube?
448.02-448.04 mbsf: modioloid bivalve	560.43-560.44 mbsf: unidentified macrofossil fragment
448.17-448.19 mbsf: serpulid polychaete tube	560.67-560.68 mbsf: undetermined macrofossil fragment
448.58-448.61 mbsf: depressed-spined gastropod	560.95-560.96 mbsf: undetermined macrofossil fragment
449.31-449.35 mbsf: articulated modioloid bivalve	560.98-560.99 mbsf: unidentified bivalve fragment
449.64-449.69 mbsf: articulated modioloid bivalves	561.08-561.09 mbsf: unidentified macrofossil fragment
450.68-450.73 mbsf: articulated modioloid bivalves	561.54-561.55 mbsf: unidentified macrofossil fragment
452.55-452.57 mbsf: unidentified articulated bivalve (decalcified)	563.61-563.62 mbsf: serpulid polychaete tube?
454.45-454.49 mbsf: turriform, high-spined gastropod, modioloid bivalves	564.95-564.97 mbsf: unidentified bivalve fragment
456.61-456.63 mbsf: modioloid? bivalve	565.48-565.49 mbsf: unidentified articulated bivalves (decalcified)
457.00-457.02 mbsf: unidentified small articulated bivalve	565.93-565.94 mbsf: unidentified bivalve fragment
459.15-459.19 mbsf: articulated modioloid bivalve	566.08-566.09 mbsf: unidentified bivalve fragment
459.28-459.32 mbsf: unidentified bivalve	567.27-567.29 mbsf: unidentified bivalve fragment
460.50-460.58 mbsf: articulated modioloid bivalves	567.81-567.82 mbsf: unidentified bivalve fragment
460.64-460.67 mbsf: two modioloid bivalves	567.87-567.89 mbsf: unidentified thin bivalve fragment
460.76-460.78 mbsf: modioloid bivalve	
461.53-461.57 mbsf: articulated modioloid bivalve and gastropod	LSU 15.4
462.47-462.50 mbsf: unidentified gastropod	585.24-585.25 mbsf: unidentified macrofossil fragment
462.58-462.65 mbsf: articulated modioloid bivalves	592.33-592.34 mbsf: unidentified bivalve fragment
461.65-461.69 mbsf: juvenile modioloid bivalves	594.75-594.76 mbsf: unidentified bivalve? fragment
461.80-461.83 mbsf: modioloid bivalve	595.90-595.91 mbsf: unidentified bivalve? fragment
463.36-463.38 mbsf: articulated modioloid bivalve	596.28-526.29 mbsf: unidentified macrofossil fragment
463.57-463.62 mbsf: juvenile modioloid bivalves, unidentified gastropod	596.52-596.53 mbsf: unidentified macrofossil fragment
463.98-464.00 mbsf: two articulated modioloid bivalves	596.87-596.88 mbsf: unidentified macrofossil fragment
464.40-464.42 mbsf: serpulid polychaete tube	597.28-597.30 mbsf: unidentified macrofossil fragment
464.44-464.47 mbsf: articulated modioloid bivalve	598.19-598.25 mbsf: unidentified bivalves (some articulated)
464.78-464.82 mbsf: three articulated modioloid bivalves	599.01-599.02 mbsf: unidentified bivalve fragment
464.85-464.87 mbsf: articulated (modioloid?) bivalve	599.04-599.05 mbsf: unidentified bivalve fragments
465.22-465.26 mbsf: articulated modioloid bivalve	599.16-599.21 mbsf: unidentified bivalves (pectinid?)
467.16-467.18 mbsf: serpulid polychaete tubes	599.21-599.24 mbsf: concretion with unidentified articulated bivalves
467.20-467.22 mbsf: unidentified small articulated bivalve	599.27-599.35 mbsf: concretion with unidentified bivalves (parallel to bedding, mostly dissolved)
467.34-467.40 mbsf: articulated modioloid bivalves	599.89-599.91 mbsf: concretion with unidentified bivalve
467.41-467.44 mbsf: unidentified bivalve (decalcified)	599.97-600.01 mbsf: large modioloid valve
467.71-467.75 mbsf: serpulid polychaete tubes (recrystallized)	
LSU 13.2	LSU 15.6
469.87-469.93 mbsf: modioloid bivalve	614.57-614.60 mbsf: concretion with unidentified bivalve
471.05-471.07 mbsf: modioloid bivalve	
482.60-482.64 mbsf: articulated modioloid bivalves	

9.7 and 11.3 (decalcified mould) have been tentatively ascribed to this group of pelagic gastropods previously unreported from the pre-Quaternary Antarctica. Benthic gastropods include at least four species. In particular, high-spined, turriform shells occur in LSU 9.3 (199.56 mbsf), 9.4 (210.20 and 226.85 mbsf; Fig. 5.14e), 9.8 (285.15 mbsf), and 13.1 (454.45 mbsf); more than one taxon may be represented. Low-spined, subglobose shells possibly a naticid occur in LSU 9.3 (199.56 mbsf) and 9.4 (210.24 mbsf). Low-spined, small-sized gastropods occur in LSU 12.4 (444.09 mbsf), and 13.1 (448.51, 461.56, and 463.57 mbsf).

Class Scaphopoda. Smooth, tubular, thin, slightly angular shells occurring in LSU 8.4 may be scaphopods, but additional study of the sparse and fragmentary material available is needed to confirm this preliminary identification (Fig. 5.14f).

Annelida

Annelida follow in order of abundance (two species at least) and are widely distributed in the core from top to bottom. The material comprises a number of calcareous tubes belonging to serpulid polychaetes. Serpulid tubes in

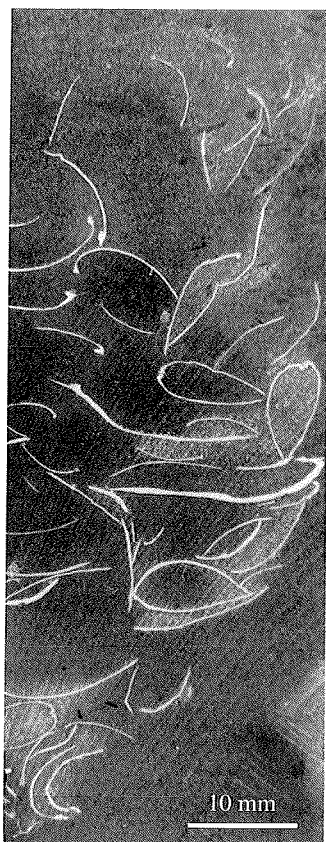


Fig. 5.13 - Fossiliferous "limestone" (coquina) from LSU 9.7 (249.65 mbsf). Note the great abundance of thin shelled bivalves, many still articulated; the assemblage is considered to be largely *in situ*.

various states of preservation occur in LSU 2.1, 3.1., 5.1, 6.1, 6.2, 7.2, 8.1, 8.3, 8.4, 9.2, 9.4, 9.6, 9.7, 11.3, 12.3, 12.4, 13.1, 15.1, and 15.2. Concentrations of serpulid polychaete tubes were observed at 114.00, 138.43, 141.74, 341.79, 342.07, and 467.71 mbsf. The most common serpulid is a simple, slender tube with annular ornamentation found almost ubiquitously in both the Miocene and Oligocene sections of the core. It strongly resembles the lower Miocene taxon reported from CRP-1 core (Jonkers & Taviani, 1998). The best preserved specimen shows a slightly arched shell (Fig. 5.14g). On shell characters alone, it is difficult to establish whether a single species of serpulid is involved from top to bottom of core CRP-2/2A. Another serpulid polychaete, characterized by a coiled and apparently smooth shell, has been observed attached to a bivalve fragment at 247.67 mbsf. The high level of bioturbation and a number of traces observed at specific levels of the CRP-2/2A core is probably linked to the action of soft-bodied worms which left no skeletal fossils.

Bryozoa

Bryozoa are represented by only two occurrences (16.30 and 117.66 mbsf).

Cnidaria

Cnidaria are represented by one species of coral s.l. (36.01, 36.21, 36.24, 36.50, and 739.91 mbsf). It appears to have been a solitary species living on mixed sand-silty bottoms (Fig. 5.14h).

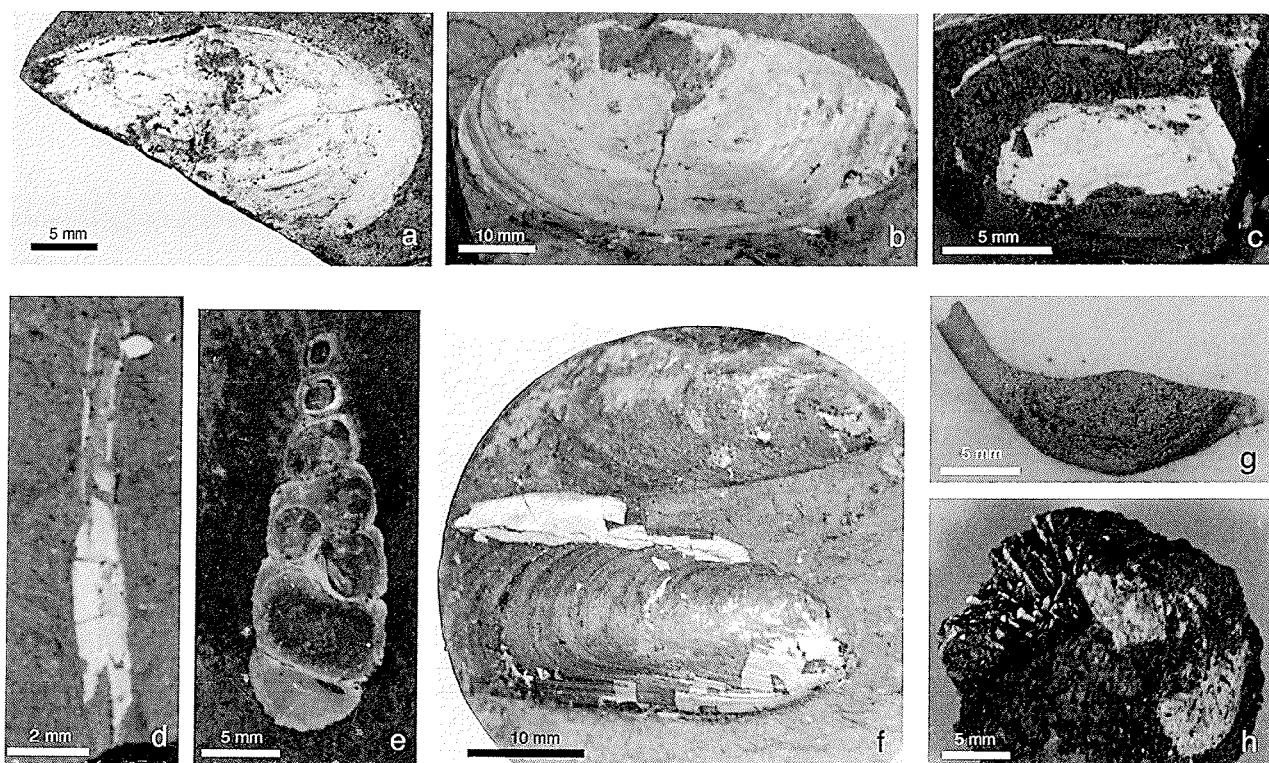


Fig. 5.14 - a) Relatively large protobranch bivalve (right valve) from LSU 9.4 (210.10 mbsf) showing an advanced state of decalcification. b) Protobranch bivalve (*Yoldia?* sp., left valve) from LSU 9.7 (260.83 mbsf). c) Imprint of a relatively large modioid mussel from LSU 13.1 (447.43 mbsf). Note the presence of some original shell material and details of the external valve ornamentation (growth stages). d) Articulated bivalve (*Hiatella?* sp.) from LSU 6.2 (80.65 mbsf). Note the advanced state of decalcification. e) Unidentified turritiform, high-spired gastropod in a calcareous concretion from LSU 9.4 (226.85 mbsf). f) Fragmented shell of a thin and smooth scaphopod? from LSU 8.4 (165.41 mbsf). g) Well-preserved tube (partly embedded in matrix) of a serpulid polychaete from LSU 6.2 (80.65 mbsf). h) Solitary coral (s.l.) from LSU 3.1. (36.24 mbsf).

Echinodermata

Echinodermata are represented by the rare occurrence of spines (16.30 and 19.84 mbsf) and fragmented tests (117.66, 230.22 and? 236.61 mbsf).

Porifera

Porifera are documented by the recurrent presence of sponge spicules (see under Foraminifera) and by coherent spicule mats at 117.66 mbsf.

BIOSTRATIGRAPHICAL AND PALAEOENVIRONMENTAL REMARKS

No precise age assessment can be derived from macrofossils identified in the CRP-2/2A core. Only some general and preliminary remarks are given here.

Most macrofossils appear to be taxa not encountered in other Oligo-Miocene records of Antarctica (*e.g.* Dell & Fleming, 1975; Beu & Dell R, 1989; Jonkers & Taviani,

1998). A possible exception is the common serpulid polychaete recovered throughout the CRP-2/2A core which appears to be very close to serpulids identified in the lower Miocene section of the CRP-1 drill hole (Jonkers & Taviani, 1998). Pectinids, which appear to be of some stratigraphical value (*e.g.* Jonkers & Taviani, 1998), are unfortunately rare in CRP-2/2A and only represented by incomplete valves that are difficult to interpret at present.

The occurrence of modioloid mussels in lower Oligocene sediments in CRP-2/2A is significant since the youngest documentation of similar bivalves in the Tertiary of Antarctica, is that from the Upper Eocene deposits of Seymour Island (Stilwell & Zinsmeister, 1992). These conspicuous bivalves have not been documented from sediments, presumed to be coeval with CRP-2/2A, in the CIROS-1 core.

All recognized macrofossils in CRP-2/2A are marine invertebrates and a preliminary interpretation of their possible palaeoenvironmental significance is summarized in figure 5.12.

6 - Palaeomagnetism

INTRODUCTION

The goal of the palaeomagnetic investigations was to develop a magnetic polarity zonation for CRP-2/2A. The magnetostratigraphy for the Pliocene-Quaternary interval is described above (see Introduction chapter). The present discussion is restricted to the pre-Pliocene sequence below 26.79 mbsf.

Coarse-grained lithologies, such as diamicts, sands and sandy diamicts are common in CRP-2/2A (see Lithostratigraphy and Sedimentology chapter). Such lithologies are usually not suitable for palaeomagnetic analysis. However, in previous palaeomagnetic studies of sedimentary units from the Victoria Land Basin, strong and stable magnetizations have been recorded and even coarse-grained units have proved suitable for palaeomagnetic analysis (Wilson et al., 1998; Roberts et al., 1998). We attribute the stability of the magnetizations to the presence of fine magnetite particles within the fine-grained sediment matrix in these otherwise coarse-grained units (*cf.* Sagnotti et al., 1998a, 1998b; Wilson et al., 1998; Roberts et al., 1998). The success of previous palaeomagnetic work in the Victoria Land Basin suggests that further studies will provide valuable information for dating and correlating cores from the Cape Roberts Project.

METHODS

The majority of the sediments in CRP-2/2A are sufficiently consolidated to allow drilling of conventional cylindrical palaeomagnetic samples with a modified drill press. These samples were analysed in the palaeomagnetic laboratory at the Crary Science and Engineering Center, McMurdo Station, Antarctica. The sampling techniques, laboratory facilities and equipment used in this study are the same as those described by the Cape Roberts Science Team (1998a). Unconsolidated sediments were sampled with plastic cubes (6.25 cm³) and were analysed in the palaeomagnetic laboratory at the University of California, Davis. The unconsolidated samples were measured on an automated, pass-through cryogenic magnetometer and were subjected to in-line stepwise alternating field (AF) demagnetization up to peak fields of 60 mT.

Information was collected at the drill site to enable azimuthal orientation of the core. However, these constraints were not available at the time of data analysis and no effort has been made to re-orient the core. Lack of azimuthal orientation does not pose a problem for magnetostratigraphical studies because the geomagnetic field has a steep inclination at the high latitude of the CRP-2 site (77°S). As a consequence, the palaeomagnetic inclination, which is determined from linear fits to characteristic

remanence components on vector demagnetization plots, is sufficient to determine polarity uniquely (*i.e.* negative (upward) magnetizations correspond to normal polarity; positive (downward) magnetizations correspond to reversed polarity).

Where possible, the CRP-2/2A core was sampled at 0.5 m intervals. This strategy was adopted to avoid missing any short polarity intervals due to inadequate sampling. Lower sampling resolution was achieved in intervals where the lithology was unsuitable. However, sediment accumulation rates appear to have been sufficiently high (*c.* 10 m/My), for much of the core, that it is unlikely that short polarity intervals were missed due to inadequate sampling resolution. It is more likely that significant time is missing in the numerous disconformities in the core.

Diamictites and other coarse-grained sediments are common in CRP-2/2A. Whenever possible, samples were selected from fine-grained horizons. However, there was often no alternative but to sample diamictites or sandstone-dominated lithofacies. The diamictite matrix is often silt-sized and is, therefore, potentially useful for palaeomagnetic study. However, very coarse sand grains, granules and pebbles within samples from diamictites pose a problem because the deposition of such large particles would be controlled by gravitational rather than magnetic forces. Thus, their orientation could not be expected to represent the geomagnetic field at or near the time of deposition. This problem would be most severe for strongly magnetic basic igneous material, which is a common clast constituent in CRP-2/2A (see Petrology chapter). The presence of such grains means that care should be taken in interpreting palaeomagnetic data from coarse-grained intervals. The possible presence of clasts was taken into account by adopting a conservative interpretive approach within coarse-grained lithologies. After magnetic measurements were completed, such samples were examined to determine the presence of clasts. Results from such samples are considered reliable only if no clasts were visible, if the palaeomagnetic inclinations are consistently steep throughout coarse-grained intervals, and if the results from these intervals are consistent with results from surrounding finer-grained intervals.

One thousand and eleven samples were collected from CRP-2/2A (including the 25 samples from the Pliocene-Quaternary interval). Forty-four pairs of samples, each separated stratigraphically by a few cm, were collected at 5-10 m intervals from varying lithofacies throughout the core. These samples were used for a pilot study, which was aimed at determining the most suitable demagnetization technique for routine treatment of the samples. The pilot study was conducted by subjecting one sample from each pair to stepwise AF demagnetization, while the corresponding sample was subjected to thermal de-

magnetization. After measurement of the natural remanent magnetization (NRM), AF demagnetization was conducted at successive peak fields of 5, 10, 15, 20, 25, 30, 40, 50 and 60 mT and thermal demagnetization was conducted at temperatures of 120, 180, 240, 300, 350, 400, 450, 500, 550, and 600°C. Magnetic susceptibility was measured after each thermal demagnetization step to monitor for thermal alteration. Seven hundred and twenty five samples (including the Pliocene - Quaternary ones) were subjected to detailed stepwise demagnetization. Time constraints limited the number of samples that could be measured. Almost all samples from between 7 and 350 mbsf were measured; the spacing between measured samples was increased below 350 mbsf to enable preliminary assessment of the magnetic polarity stratigraphy to the bottom of CRP-2/2A.

Mineral magnetic studies were conducted on 18 samples after they had been subjected to stepwise AF demagnetization. These samples were given an isothermal remanent magnetization (IRM) with inducing fields of 0.05, 0.15, 0.2, 0.3, 0.4, 0.5, 0.75 and 1 T. The IRM (at 1 T) was then demagnetized by inverting the sample and applying fields of 10, 20, 30, 40, 50, 60, 80, 100, and 300 mT. IRM acquisition and back-field demagnetization studies were performed to determine the coercivity of

remnance (B_{cr}) and a parameter known as the S-ratio ($-IRM_{0.3T}/IRM_{1T}$). These parameters provide information about the bulk coercivity of the magnetic assemblage and are therefore useful in understanding the magnetic mineralogy (*e.g.* King & Channell, 1991; Verosub & Roberts, 1995). The IRM at 1 T (IRM_{1T}) and the low-field magnetic susceptibility are useful indicators of magnetic mineral concentration. Magnetic susceptibility was measured for 973 samples and the data were compared with the whole-core susceptibility log that was obtained at the Cape Roberts drill site.

RESULTS

PILOT STUDY

Results of the pilot study indicate that thermal and AF demagnetization are equally efficient in removing secondary remanence components and in isolating characteristic remanence components for both normal and reversed polarity samples (Fig. 6.1). The efficiency of the two techniques did not vary among intervals of relatively high and low coercivity. AF demagnetization was adopted for routine treatment of samples for the entire core because

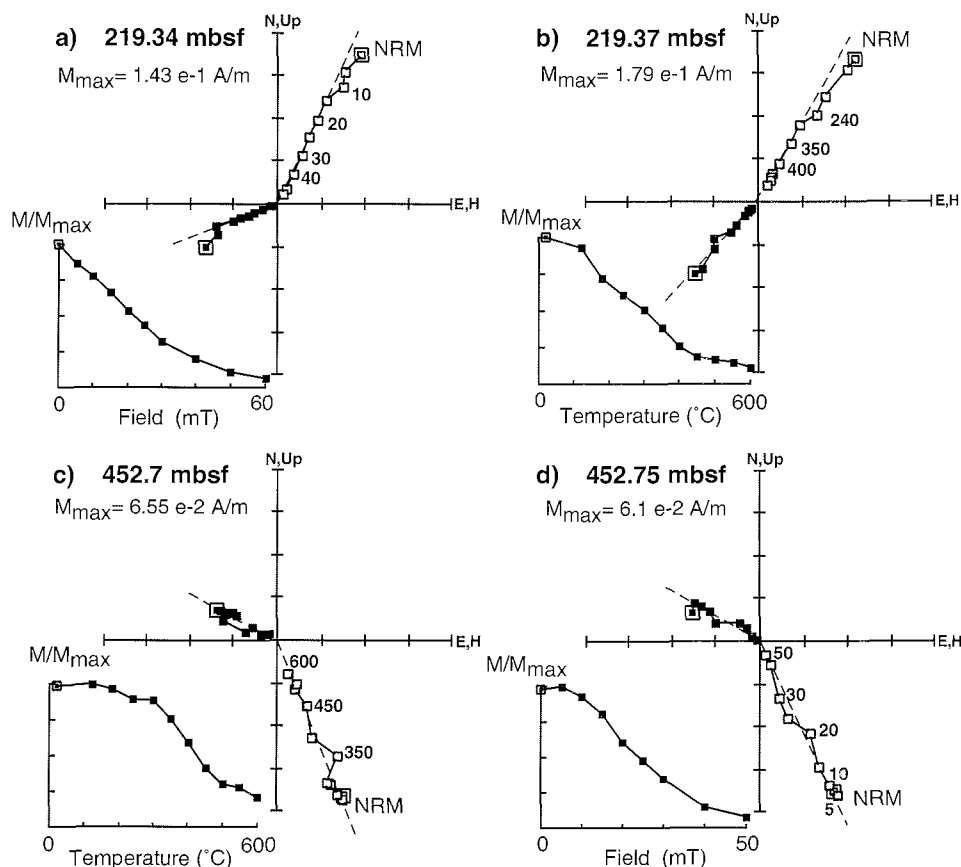


Fig. 6.1 - Vector component diagrams (with normalized intensity decay plots) of demagnetization behaviour of representative samples from the pilot study of CRP-2/2A: (a) and (b) comparison of AF and thermal demagnetization of normal polarity samples from 219.34 and 219.37 mbsf, respectively; (c) and (d) comparison of thermal and AF demagnetization of reversed polarity samples from 452.7 and 452.75 mbsf, respectively. Open (closed) symbols represent projections onto the vertical (horizontal) plane. The dashed lines represent linear regression fits which indicate the characteristic remanence component for each sample. The core is not azimuthally oriented, therefore declination values are not meaningful. The results indicate that thermal and AF demagnetization are equally efficient at removing secondary overprints and isolating characteristic remanence components for both normal and reversed polarity samples.

it is less time-consuming than thermal demagnetization and it also avoids thermal alteration.

PALAEOMAGNETIC BEHAVIOUR

Many of the analysed samples display a low coercivity, near-vertical, normal polarity component that is interpreted as representing a drilling-induced overprint. In most cases, this component was removed with peak AFs of less than 20 mT. In some cases, the drilling-induced overprint and the original remanence had completely overlapping coercivity spectra. In these situations, it was not possible to isolate the two components (e.g. Fig. 6.2a). Such samples were excluded from subsequent magnetostratigraphic interpretations. In some cases, particularly in dominantly sandy lithologies between 199.64 and

212.10 mbsf, another overprint is present. This overprint has a nearly horizontal inclination and a southward-directed declination (e.g. Fig. 6.2b). We attribute this overprint to contamination introduced by cutting the samples (after drilling) because the overprint is always perpendicular to the cut face of the sample (i.e. in sample coordinates, the overprint is entirely in the x-z plane, with y = 0). Rotation of the saw blade produces a measurable magnetic induction perpendicular to the blade. In most cases, the overprint produced by this field was easily removed by application of peak AFs of 10 mT. Where present, this overprint is usually stronger than the drilling-induced overprint. The saw-overprint is only sporadically present below 212.10 mbsf (mainly in sandy lithologies).

Many of the samples are from intervals where clasts may dominate the magnetic properties of the sample and

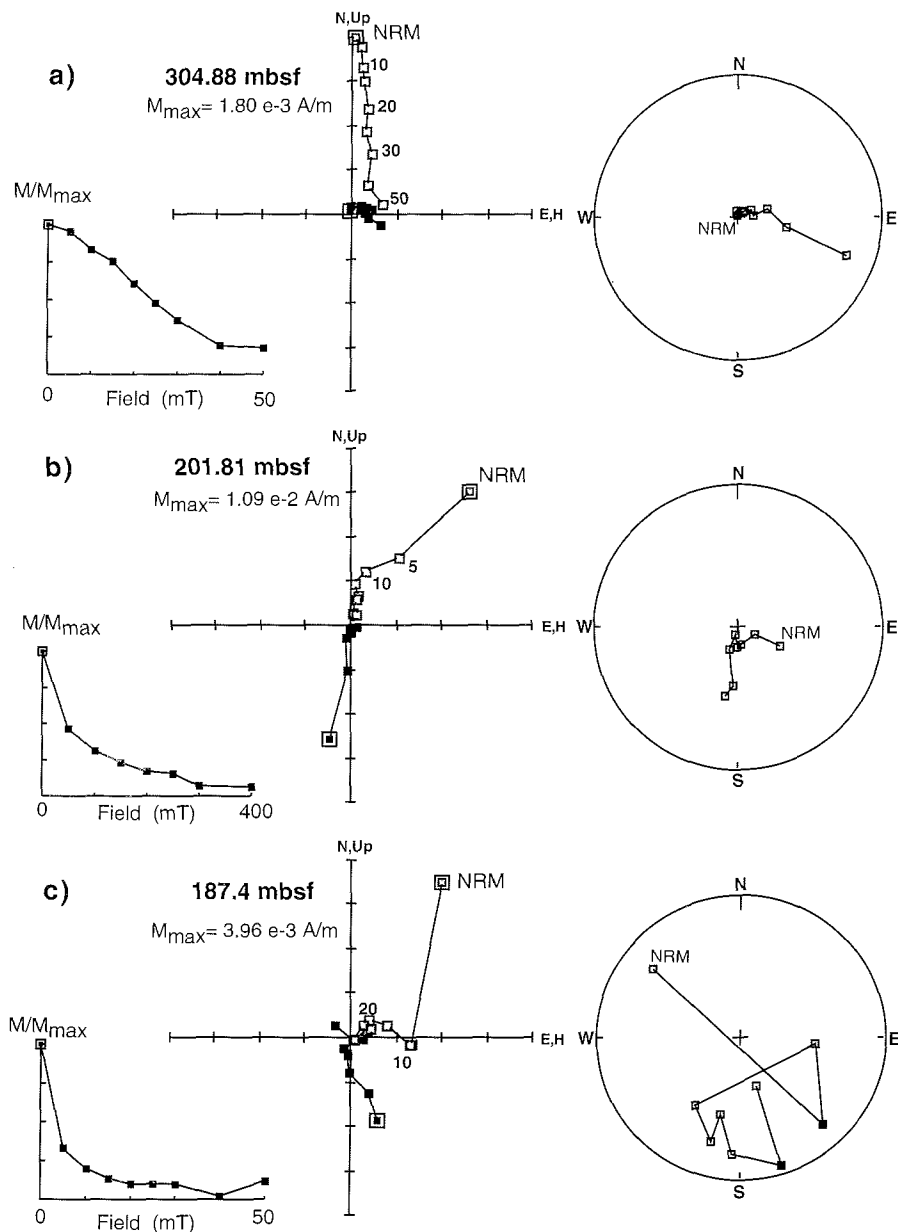


Fig. 6.2 - Vector component diagrams (with normalized intensity decay plots) for CRP-2/2A samples that illustrate: (a) a dominant drilling-induced overprint (304.88 mbsf), (b) a low coercivity saw overprint (201.81 mbsf), and (c) low coercivity and random behaviour in a sample that contains pebbles (187.4 mbsf). The conventions are the same as in figure 6.1. The stereoplots are equal area projections, with open (closed) symbols indicating upper (lower) hemisphere projections.

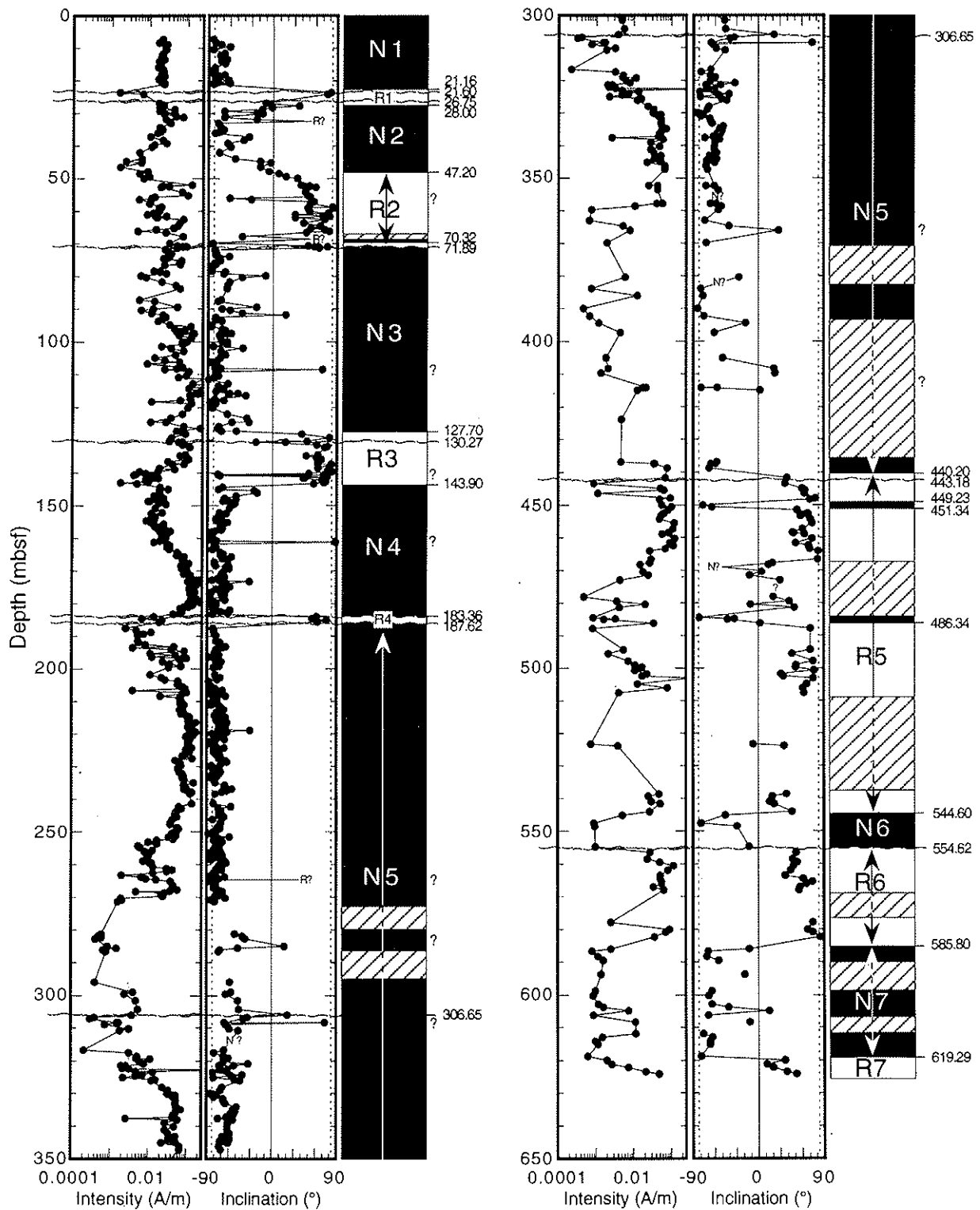


Fig. 6.3 - Plot of NRM intensity and inclination of the characteristic remanence component (identified from best-fit lines through data from multiple demagnetization steps, as shown in Fig. 6.1) with respect to depth for CRP-2/2A. Polarity is shown on the log to the right (black (white) = normal (reversed) polarity; cross-hatching indicates uncertain polarity), with magnetozones labelled from top to bottom (N1 to R7). The depths of polarity boundaries and major disconformities are also indicated. Dashed lines on the inclination plot indicate the expected inclination ($\pm 83.4^\circ$) at the site latitude (77°S).

produce a magnetization that does not represent the geomagnetic field orientation at or near the time of deposition. Samples that contain such clasts usually display abnormal palaeomagnetic behaviour and are readily detected (e.g. Fig. 6.2c). Such samples were excluded from subsequent magnetostratigraphical interpretations.

Stable palaeomagnetic behaviour was evident from the vector component plots of 612 of the 700 demagnetized samples (87%). In most cases, the characteristic remanence direction was determined using a best-fit line that was constrained through the origin of the vector component diagram (e.g. Fig. 6.1). In some cases, the best-fit lines

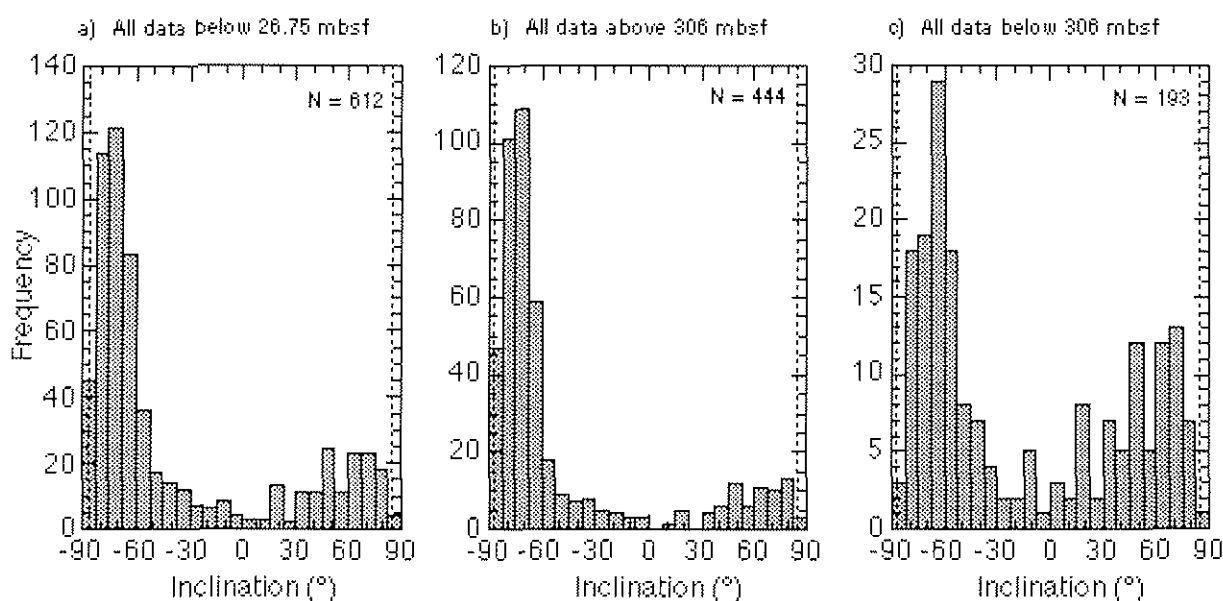


Fig. 6.4 - Histograms of palaeomagnetic inclinations for CRP-2/2A (from Fig. 6.3). (a) All data below 26.75 mbsf, (b) all data above 306 mbsf (including the Pliocene - Quaternary), (c) all data below 306 mbsf. In all cases, the inclinations are shallower than expected ($\pm 83.4^\circ$; shown by dashed lines) for the site latitude. The inclinations appear to be shallower for the interval below 306 mbsf, which indicates that the discontinuity at c. 306 mbsf probably represents an angular unconformity.

were not constrained through the origin of the plots. In other cases, the polarity of the characteristic remanence component was clear, but because of a low signal/noise ratio or incomplete removal of secondary components, the final direction of magnetization could not be precisely determined. In these cases, the sample is represented on figure 6.3 by either an N? or an R?

The inclinations of the characteristic remanence directions have a clear bimodal distribution that demonstrates the dominance of the two stable polarity states (Fig. 6.4a). Steep normal and reversed polarity directions, as would be expected at high latitudes, are clearly dominant. In conjunction with evidence from vector component diagrams (e.g. Fig. 6.1), this indicates that secondary remanence components have been successfully removed. The distribution of inclinations is strongly biased toward normal polarity. This is because of a combination of relatively high sedimentation rates (see discussion below), possible stratigraphical breaks that juxtapose more than one normal polarity zone, and a high measurement density. Furthermore, intervals in the lower part of the core, in which reversed polarity was dominant, were not analysed in such detail because of time constraints. It should therefore not be assumed that this polarity bias is cause for concern about the reliability of the palaeomagnetic signal from CRP-2/2A.

In addition, it appears that the palaeomagnetic inclinations below the discontinuity at 306.65 mbsf are shallower than those above the discontinuity (Fig. 6.4b, c). While more data (particularly reversed polarity data) are needed to demonstrate this possibility rigorously, the palaeomagnetic data may indicate that the discontinuity at 306.65 mbsf represents an angular unconformity. This hypothesis needs to be tested with structural analyses of the core. This observation will also be more easy to quantify when a more complete palaeomagnetic data set is obtained after the drilling season.

Overall, both normal and reversed polarity directions are up to 15° shallower than expected ($\pm 83.4^\circ$) for the site latitude (77°S ; Fig. 6.4). There are two plausible explanations for this observation. First, tectonic tilting will cause rotation of the magnetic vector with the rock unit and, if the tilting was in an appropriate direction, it would cause shallowing of the palaeomagnetic vector for both normal and reversed polarity samples. Second, inclination error is commonly observed in sedimentary environments where bioturbation is not widespread, such as seems to be the case for some lithostratigraphical units in CRP-2/2A. In environments where bioturbation is widespread, magnetic particles have freedom to rotate and to follow the geomagnetic field in water-saturated shallow sediments. Thus, when the remanence is locked in, the magnetization of bioturbated sediments can provide an accurate record of the geomagnetic field. On the other hand, in sediments where bioturbation is absent, magnetic grains can roll as they settle onto the substrate and the resultant inclination can be retained in the absence of bioturbation (Verosub, 1977). In addition, sediment compaction has been interpreted as being responsible for inclination errors (e.g. Anson & Kodama, 1987; Arason & Levi, 1990). At present, we cannot distinguish between these possibilities. From core observations and seismic reflection studies, it seems likely that the sequence is tilted, but it is unlikely to be tilted by as much as 15° (Henry et al., 1994; Core Properties and Down-Hole Geophysics chapter). It is therefore likely that the shallow palaeomagnetic inclinations result from a combination of these effects.

In addition to the dominantly steep normal and reversed polarity directions, a significant number of samples display behaviour that is transitional between normal and reversed polarity (e.g. Figs. 6.3 & 6.4). Most of these samples display stable palaeomagnetic behaviour and are not obviously affected by the presence of clasts. It is not

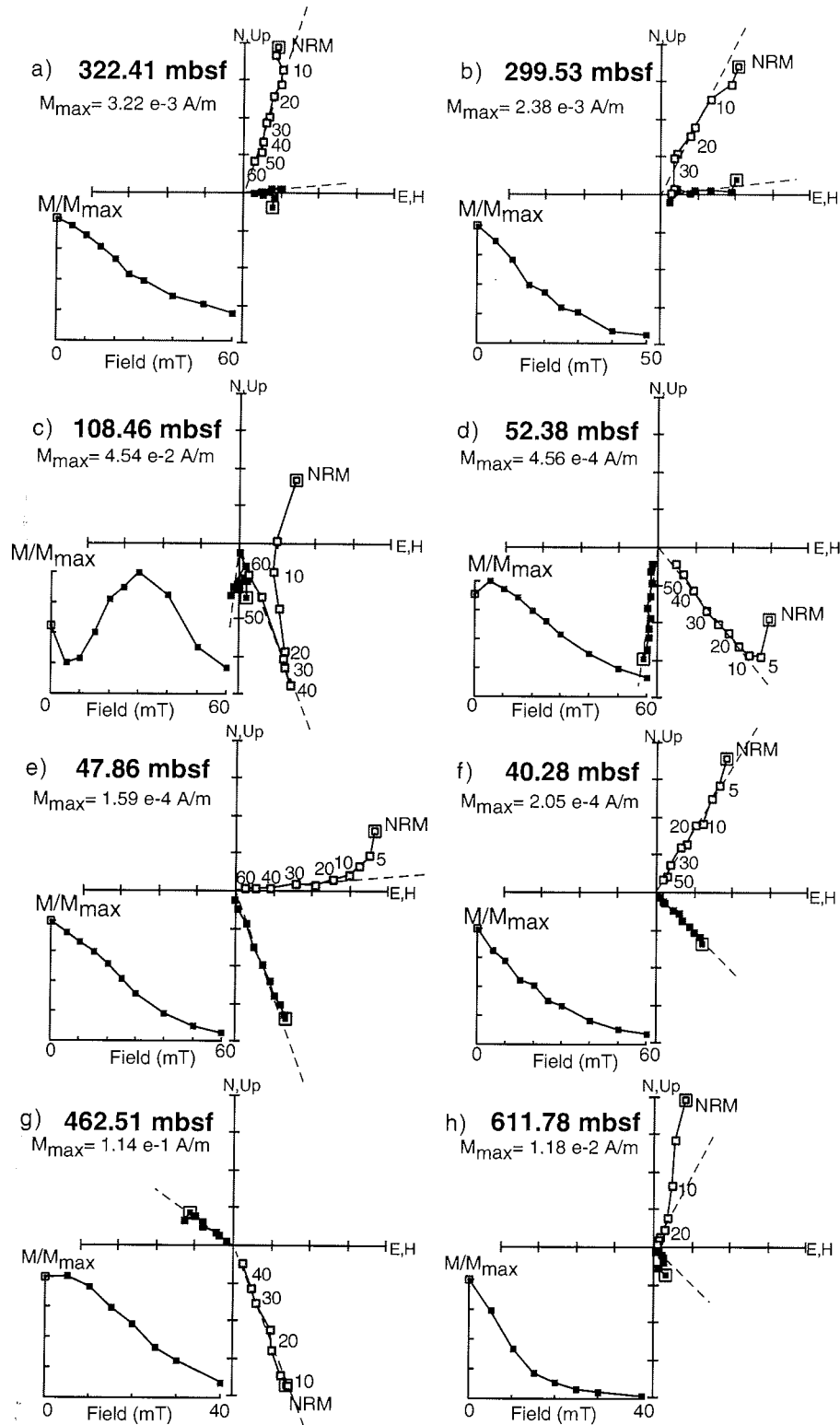


Fig. 6.5 - Vector component diagrams (with normalized intensity decay plots) for selected samples from CRP-2/2A: (a) a relatively high coercivity sample (322.41 mbsf), (b) a relatively low coercivity sample (299.53 mbsf), (c) a stable, but anomalous, reversed polarity sample from magnetozone N3 (108.46 mbsf), (d) a reversed polarity sample from magnetozone R2, below the detailed polarity transition (52.38 mbsf), (e) a sample from the polarity transition between magnetozones R2 and N2 (47.86 mbsf), (f) a normal polarity sample from magnetozone N2, above the detailed polarity transition (40.28 mbsf), (g) a stable reversed polarity sample from the lower part of the core (462.51 mbsf), (h) a normal polarity sample, from the lower part of the core, with behaviour that is difficult to interpret (611.78 mbsf). The conventions are the same as in figure 6.1. See text for discussion.

surprising that transitional directions are recorded in parts of the record that were rapidly deposited: there is a higher probability of reordering deposition during geomagnetic polarity transitions in such intervals (see below).

Data from 88 demagnetized samples were not included in the magnetostratigraphic interpretation (Fig. 6.3). In total, 9% of the samples were unstably magnetized (*i.e.* the demagnetization behaviour was either incoherent or the

samples had low coercivity), 2% of the samples had coercivity spectra that did not permit discrimination between a drill-string overprint and a stable characteristic remanence direction (e.g. Fig. 6.2a), and 2% of the samples were dominated by the effects of pebbles (e.g. Fig. 6.2c).

The quality of palaeomagnetic data does not seem to depend on whether the samples have high or low coercivity (unless the median destructive field is less than about 15 mT and the samples are clearly dominated by magnetically unstable multi-domain grains). Relatively high coercivities are observed in samples from 306.5 to 328 mbsf (about 25% of the NRM intensity remains after AF demagnetization to 60 mT; Fig. 6.5a). High coercivity is also observed in some samples between 297 and 306.5 mbsf, but here they alternate with low coercivity samples (fully demagnetized after AF treatment at 40-50 mT; Fig. 6.5b). Preliminary rock magnetic measurements indicate that there are significant concentrations of high coercivity minerals in samples from much of the core. Plots of IRM acquisition have steep slopes at low magnetic inductions. However, saturation is not usually achieved until above 300 mT (Fig. 6.6). This indicates that a fraction of high coercivity particles is present. S-ratios vary between 0.89 and 0.99 (Fig. 6.7). S-ratios of 0.98-1.00 indicate a dominance of low coercivity minerals. The S-ratio is highly non-linear and ratios of 0.95 can indicate the presence of substantial quantities of high coercivity minerals (e.g. Bloemendal et al., 1992). The observed range of S-ratios therefore indicates the presence of significant concentrations of high coercivity phases. The lack of significant differences in the relative efficiency of AF and thermal demagnetization in isolating characteristic remanence components indicates that, despite the presence of high coercivity particles, AF demagnetization is suitable for routine sample treatment.

Palaeomagnetic stability appears to be stratigraphically controlled, with data from zones of high remanence intensity being of better quality than those from zones of low intensity. In the upper c. 270 m of CRP-2/2A, the palaeomagnetic behaviour is of consistently high quality (Fig. 6.3). Below c. 270 mbsf, the palaeomagnetic behaviour is more variable because zones of low remanence intensity are more common. The lower quality of palaeomagnetic data in the lower part of CRP-2/2A, coupled with the lower measurement density, makes it difficult to interpret the magnetic polarity stratigraphy (see discussion below).

MAGNETIC SUSCEPTIBILITY

Previous studies of the CIROS-1 and CRP-1 cores demonstrated that the magnetic susceptibility (κ) signal is representative of changes in the concentration of pseudo-single domain magnetite and that these changes are environmentally (probably palaeoclimatically) controlled (Sagnotti et al., 1998a, 1998b). While it is impossible to interpret the κ signal from CRP-2/2A directly in terms of environment until more detailed rock magnetic investigations are carried out, some preliminary observations are relevant to the present discussion of the magnetostratigraphy.

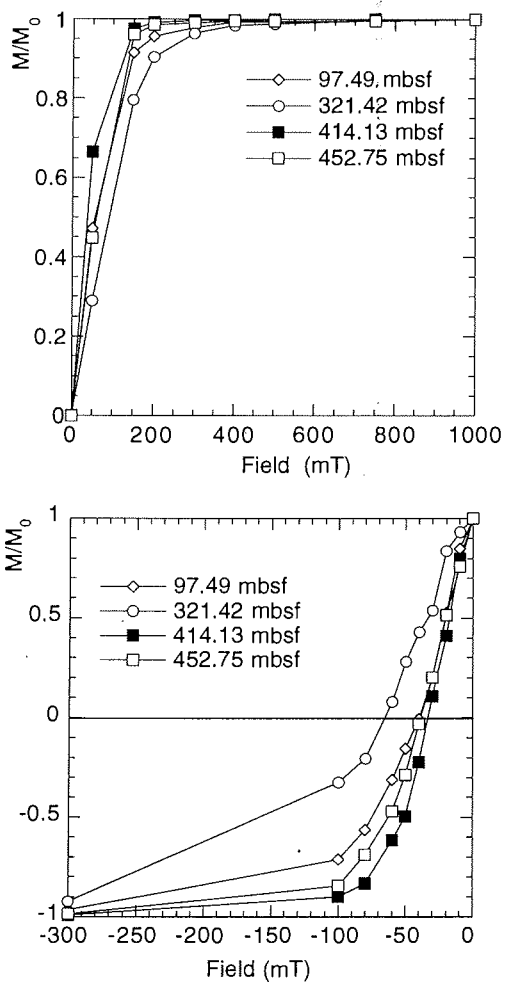


Fig. 6.6 - Plot of IRM acquisition and DC demagnetization of four representative samples from CRP-2/2A. Some samples have low coercivity (B_{cr} of about 40 mT) and saturate rapidly (below 300 mT), while other samples have high coercivity (B_{cr} of about 60 mT) and saturate above 300 mT, which indicates the presence of significant amounts of high coercivity phases.

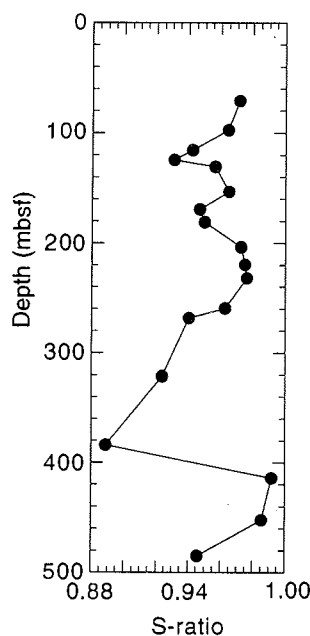


Fig. 6.7 - Plot of S-ratio (see text for definition) for 18 pilot samples with respect to depth for CRP-2/2A. S-ratios below about 0.97 indicate a significant high coercivity content.

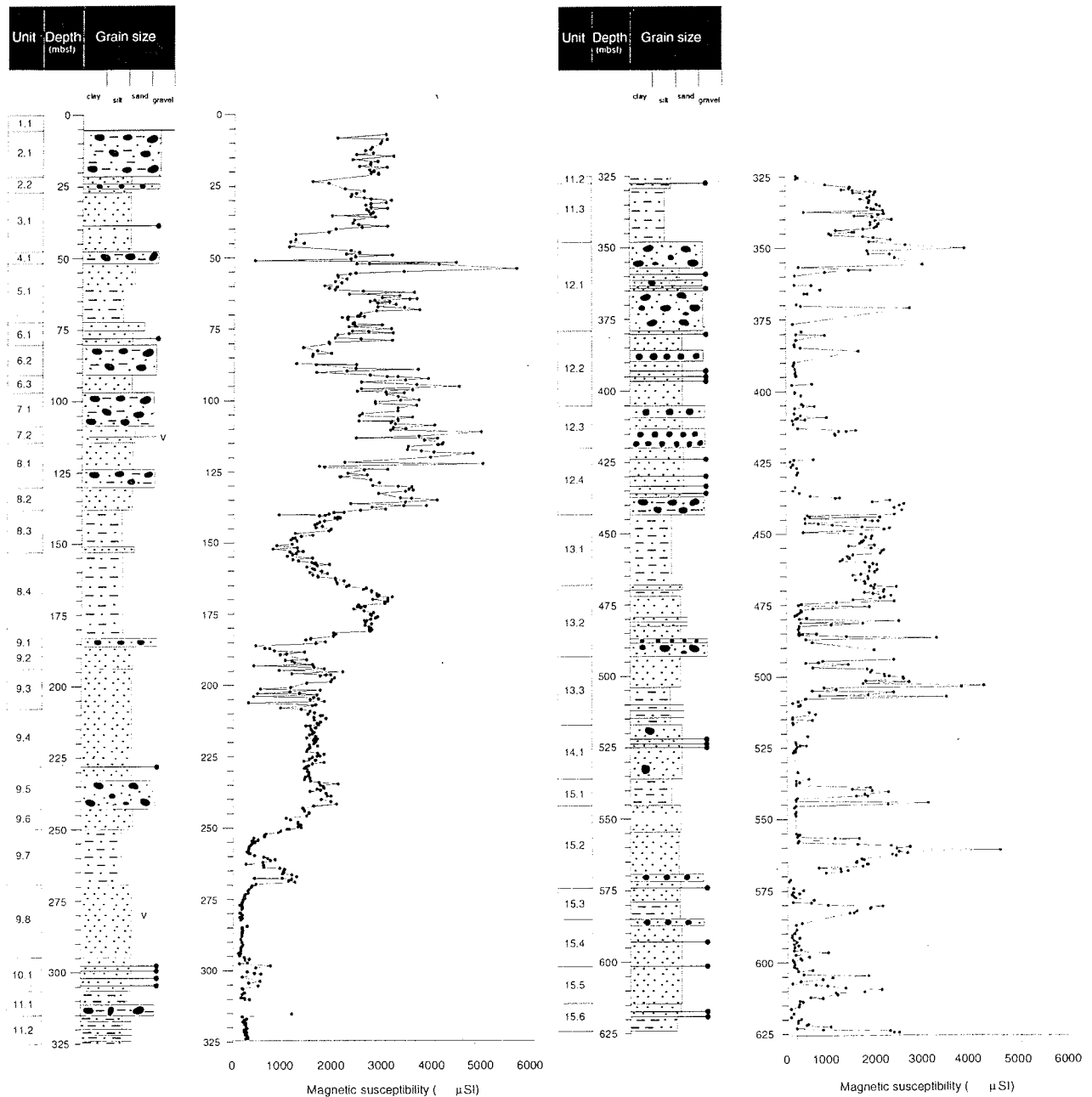


Fig. 6.8 - Magnetic susceptibility (in μSI) and lithostratigraphical variations for CRP-2/2A from discrete samples. The susceptibility record from discrete samples is similar to the whole-core record obtained at the drill site, except in conglomerate and diamictite units. In these lithologies, the whole-core record is affected by the presence of large clasts. The discrete sample record represents a better estimate of the magnetic susceptibility of the fine sediment matrix, although samples from some intervals contain pebbles and have more erratic susceptibility variations.

Volume susceptibility values include the contribution of all the minerals present in the sediment, in proportion to their intrinsic susceptibility and abundance. For susceptibilities larger than $300 \mu\text{SI}$, it is generally assumed that the ferrimagnetic component dominates the paramagnetic and diamagnetic components (*cf.* Tarling & Hrouda, 1993). A paramagnetic "base level" susceptibility of *c.* $235 \mu\text{SI}$ was estimated for the CRP-1 core (Sagnotti et al., 1998b). The similar range of κ values in the many low κ zones (*c.* $150\text{--}250 \mu\text{SI}$) below *c.* 270 mbsf (Fig. 6.8) suggests that the magnetic susceptibility in these zones is dominated by paramagnetic phases. It therefore seems likely that in the stably magnetized high-susceptibility zones (which dominate the upper part of CRP-2/2A), the

contribution from ferrimagnetic grains overwhelms that of the paramagnetic matrix. In the weakly magnetized low-susceptibility zones (which are more common in the lower part of CRP-2/2A), the contribution of the paramagnetic grains may be comparable or even larger than that of the ferrimagnetic grains. The low values of remanence intensity in the low-susceptibility zones (Figs. 6.3 & 6.8) probably indicate that ferrimagnetic grains occur in low abundances in the low κ zones. These observations may account for the comparatively poor quality of palaeomagnetic behaviour in the lower part of CRP-2/2A.

It is evident, with respect to the sequence stratigraphical interpretation (see Sequence Stratigraphical Interpretation

section), that some of the sequence boundaries correspond to sharp susceptibility changes. The relevant boundaries are at 21.6 mbsf (sequences 1-2), 51.94 mbsf (sequences 4-5), 185.94 mbsf (sequences 9-10), 356.83 mbsf (sequences 13-14), 420.53 mbsf (sequences 17-18), 443.18 mbsf (sequences 18-19) and 494.08 mbsf (sequences 19-20). Two sharp increases in κ are evident at c. 183.5 and 186 mbsf (Fig. 6.8). These sharp increases in κ correspond to the upper and lower boundaries of a magnetic polarity zone (Fig. 6.3) and coincide with the position of disconformities at 183.36 and 185.94 mbsf, respectively.

The discrete sample κ record agrees well with the whole-core κ record for most of CRP-2/2A. Careful selection of samples that represent only the matrix in diamictite units allows recovery of a susceptibility signal that is free from the influence of extraformational pebbles. As a consequence, the susceptibility record from discrete samples is more representative of the sediment matrix than the whole-core susceptibility log (see Physical Properties from On-Site Core Measurement section) for the intervals that are dominated by diamictites and/or dropstones. The discrete sample κ record from CRP-2/2A is still partially affected by the presence of extraformational pebbles, but such samples can be removed. This procedure produced a remarkable improvement of the susceptibility log in CRP-1 (compare Cape Roberts Science Team (1998c) with Sagnotti et al. (1998b)) and will be repeated for the CRP-2/2A core after the drilling season.

MAGNETIC POLARITY STRATIGRAPHY

The magnetic polarity stratigraphy shown in figure 6.3 is tentatively divided into 14 magnetozones: 7 of dominantly normal polarity and 7 of dominantly reversed polarity. The uppermost two magnetozones (N1 and R1) are of Quaternary and Pliocene age, respectively, and are discussed in the Pliocene-Quaternary Strata section. Here, we will only discuss the polarity zonation from N2 to R7, with implicit reference to figure 6.3. Also, any references to sequence stratigraphical interpretations refer to the Sequence Stratigraphical Interpretation section. It should be noted that the magnetic polarity zonation described below is preliminary and awaits refinement after measurement of further samples from the lower part of the record. It is unlikely, however, that further measurements will result in refinement of the zonation for the upper 350 m of CRP-2/2A (except, perhaps, for the sandy intervals from 273.5 to 281 mbsf and from 286.7 to 291.5 mbsf).

In many of the polarity zones, there are sporadic samples that display opposite polarities to those of the surrounding rocks (*e.g.* Fig. 6.5c). In each case, the palaeomagnetic behaviour is stable and the presence of a steep normal polarity drill-string overprint suggests that the samples have not been inadvertently inverted. In the following discussion, no interpretations are based on results from single samples because such samples could be anomalous.

Normal polarity dominates the interval from c. 28 to 47.20 mbsf. The transition from R2 to N2 is gradual and occurs across a lithostratigraphical boundary between

LSU 4.1 (diamiction) and 3.1 (sands). Facies analysis indicates that the sands were rapidly deposited in a shore-face or deeper environment after glacial retreat (see Facies Analysis section). It is expected that time would be missing between the diamiction and the sands because the contact is sharp and not gradational. Stable palaeomagnetic directions are observed within both of the lithostratigraphical units below, within, and above the polarity transition (Fig. 6.5d-f). The diamiction and the sands have a significant mud content, which we presume is responsible for the strong and stable magnetizations. Transitional directions are recorded over a stratigraphical interval of about 6 m (Fig. 6.9). The upper part of the diamiction could have been disturbed by ice movement, which could have produced anomalous palaeomagnetic directions. However, all of the observed lithostratigraphical units are marine and it is possible that the entire sequence was water-lain (see Facies Analysis section). It is well-known that the process of polarity reversal occurs over periods of about 5-10 ky (Jacobs, 1994). If it is assumed that this interval represents a high-resolution polarity transition record, it is possible to directly estimate a sedimentation rate for the interval (*c.* 0.5-1 m/ky). This is a minimum estimate because the amount of missing time at the contact between LSU 4.1 and 3.1 is unknown. Given the thickness of the polarity transition, and the apparently continuously varying palaeomagnetic directions, it is likely that the sand, and possibly the underlying diamiction, were deposited relatively continuously rather than as discrete events (because the geomagnetic field usually varies slowly). Furthermore, this record suggests that little time is missing in the disconformity between LSU 4.1 and 3.1 (probably less than 1 ky). Our preliminary interpretation is that the boundary between magnetozones R2 and N2 is represented by a high-resolution polarity transition in rapidly deposited sediments. If this suggestion is verified by further work, it could provide valuable insights into rates of glacial processes. Such rapid deposition is likely to have occurred only over restricted time intervals because estimates of longer-term sediment accumulation rates for CRP-2/2A are much lower (*c.* 10 cm/ky; see below).

The boundary between magnetozones N3 and R2 occurs at a stratigraphical contact (71.89 mbsf) that is not interpreted as representing a sequence stratigraphical boundary. The boundaries between magnetozones N4 and R3 and between R3 and N3 do not appear to occur at disconformities, although several disconformities and sequence stratigraphical boundaries occur within these magnetozones. Magnetozone R4 is about 4.3 m thick and is restricted to the diamictite that comprises LSU 9.1. R4 is truncated by disconformities at the lower and upper surfaces of the diamictite. The lower disconformity is interpreted as a sequence stratigraphical boundary, but the upper disconformity is not.

N5 is a thick zone of normal polarity with several zones in which the polarity is uncertain. The intervals from *c.* 273.5 to 281 mbsf and from *c.* 286.7 to 291.5 mbsf are dominated by poorly consolidated sands. These intervals were sampled, but, because of the friable nature of the samples, it was not possible to analyse them on the high-

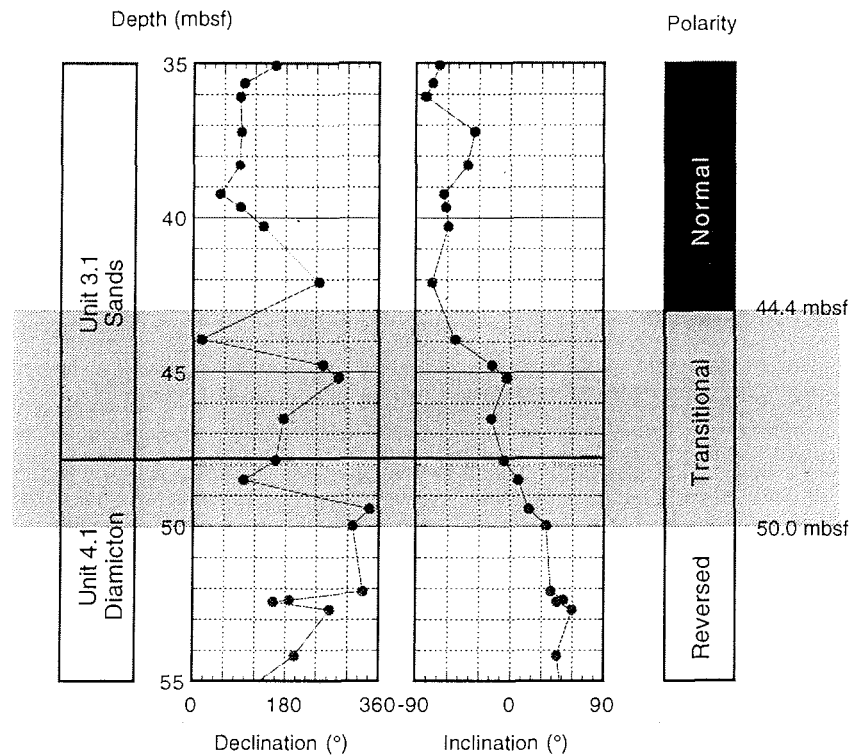


Fig. 6.9 - Variations in palaeomagnetic declination and inclination (identified from best-fit lines through data from multiple demagnetization steps) through the inferred geomagnetic polarity transition (shaded) between magnetozones R2 and N2. The core is not azimuthally oriented, therefore declination values are not meaningful. The transition crosses the contact between LSU 4.1 and 3.1. A minimum sedimentation rate can be estimated for the interval. This can help to quantify rates of glacial processes.

speed (89.2 revolutions per second) spinner magnetometer used at McMurdo Station. These samples will be analysed after the drilling season. It was not possible to collect samples from the following intervals because either the lithology was unsuitable or because the sediment was too deformed: *c.* 371-379, 401.5-404.5, 415.4-423.8 and 429.2-433.6 mbsf. In addition, significant parts of the two cross-hatched intervals in the lower part of N5 (Fig. 6.3) are unstably magnetized and, at present, reliable interpretations cannot be made for these intervals. Analysis of the remaining samples from these intervals may resolve the uncertainty.

Significant intervals of the lower part of CRP-2/2A are dominated by reversed polarity. A major disconformity occurs in the upper part of R5 at 443.18 mbsf. This disconformity is interpreted as a sequence stratigraphical boundary (between LSU 13.1 and 12.4); significant breaks have also been noted in sediment provenance and palaeontology at this level (see Petrology and Palaeontology chapters). One reversed polarity sample is recorded above this disconformity. It is therefore possible that R5, like other magnetozones that contain significant stratigraphical breaks, represents a composite magnetozone of more than one period of reversed polarity. Many of the reversed polarity zones in the lower part of CRP-2/2A have strong remanence intensities, whereas several zones of unstable magnetic behaviour, including some normal polarity zones, occur in intervals of weak remanence intensity. The reversed polarity samples are clearly

interpretable (Fig. 6.5g), whereas the normal polarity samples can be difficult to interpret (Fig. 6.5h). There are two zones of normal polarity within R5. The upper zone (449.23 to 451.34 mbsf) is thin, but has strong and stable magnetizations, whereas the lower normal polarity zone has weaker magnetizations with erratic palaeomagnetic directions that are difficult to interpret. In addition, there are two zones in R5 from which samples were not collected due to a lack of suitable material for sampling: 516.3-520.7 and 548.5-554.7 mbsf.

Samples from magnetozone N6 are weakly magnetized and have scattered characteristic remanence component directions. The lower boundary of N6 occurs at a disconformity at 554.62 mbsf which represents a sequence stratigraphical boundary within LSU 15.2. R6 is a zone of stable reversed polarity which includes an interval with weak and unstable magnetizations that cannot be interpreted. Magnetozones N7 and R7 are relatively poorly defined: N7 contains numerous scattered normal polarity directions and R7 is defined by only a few reversed polarity samples at the base of CRP-2/2A.

The common occurrence of magnetozone boundaries at disconformities that do not coincide with interpreted sequence stratigraphical boundaries, as well as at sequence stratigraphical boundaries, suggests that there is a significant amount of time missing and that this missing time could be distributed throughout the record. It is clear that such a record requires independent constraints before a useful chronostratigraphical scheme can be developed.

Furthermore, because of the relatively poorly constrained magnetic polarity zonation for the lower part of CRP-2/2A, it is only possible, at this stage, to propose tentative correlations to the magnetic polarity timescale (MPTS) for this part of the core.

DISCUSSION

A preliminary correlation of the polarity of CRP-2/2A to the MPTS is plotted against lithology in figure 7.1, and includes constraints from available biostratigraphical data. The resulting age model and its construction are discussed in the Chronology section. Using the age model, it is possible to reach some preliminary conclusions about the CRP-2/2A record. Most of the record (*c.* 500 m) is Oligocene in age, with sedimentation rates of *c.* 100 m/My. This sedimentation rate suggests that only *c.* 5 My of the Oligocene has been recorded in CRP-2/2A, whereas the

chronological constraints indicate that the record covers a span of about 14-16 My.

ADDITIONAL WORK

The above-reported initial characterization studies have served to identify several areas that warrant additional work. The magnetostratigraphy of CRP-2/2A clearly needs to be refined, particularly in the lower part of the record. This could have significant implications for the chronostratigraphical interpretation. The present interpretation is preliminary and should be used with caution. Although high quality palaeomagnetic results have been obtained from many of the CRP-2/2A samples, it is still important to characterize the mineral magnetic properties of different parts of the core. The mineral magnetic measurements will provide the basis for studies of the environmental magnetic record of CRP-2/2A.

7 - Summary of Results

INTRODUCTION

In this final chapter of the Initial Report, the major geological outcomes of CRP-2/2A are summarised, conclusions are drawn and plans for the final drilling season are set out. Although the Initial Report as a document is focussed primarily on core characterization, a number of important conclusions can already be drawn from the geological and geophysical analyses carried out during and immediately following the drilling season at Cape Roberts and McMurdo Station. This chapter contains four substantive sections, which deal with the major outcomes of CRP-2/2A in terms of geochronology, climatic and depositional history, and volcanic-tectonic history, followed by some conclusions and plans for the future.

Current chronological interpretations of the strata penetrated by CRP-2/2A are based on biostratigraphy (principally utilising marine diatoms and, to a lesser extent, calcareous nannofossils), palaeomagnetic studies and $^{40}\text{Ar}/^{39}\text{Ar}$ dates from the volcanic tephra unit at 109-114 mbsf. The distribution of microfossils recovered from the core is irregular. This, together with the abundance of coarse-grained lithologies, the numerous disconformities recorded in the core, and variable palaeoenvironmental conditions, have complicated interpretation of the distribution of key fossil taxa in CRP-2/2A. In addition, some microfossil groups are either previously undescribed or are known to be endemic to the region, further frustrating efforts to compile an integrated biostratigraphical framework for the hole.

The initial magnetic polarity stratigraphy for CRP-2/2A is divided into 14 magnetozones, of which 12 are pre-Pliocene in age. Several key diatoms and nannofossils, together with the $^{40}\text{Ar}/^{39}\text{Ar}$ age determination at 113 mbsf (21.44 ± 0.05 Ma), constrain correlation of these magnetozones to the magnetic polarity time scale, allowing construction of a preliminary, integrated age-depth plot. The current interpretation for the cored succession places Quaternary strata from the sea floor to 21.20 mbsf, a thin Pliocene interval from 21.20 to 26.80 mbsf, early Miocene strata from 26.80 to 130.27 mbsf, late Oligocene strata from 130.27 to 306.65 mbsf, and early Oligocene (with possibly some latest Eocene) strata from 306.65 mbsf to the base of the hole at 624.15 mbsf.

On the basis of the facies analysis reported in chapter 3, the core has been interpreted in terms of an array of glacimarine and open coastal/shelf depositional environments, involving repeated advance and retreat of floating and grounded ice across the shelf. The facies assemblage is considered to be typical of cool, but not cold, climate, polythermal glaciers with considerable melt-water discharge in the Oligocene, but with less melt-water

influence in the Miocene. Palynological investigations also suggest that, even in the oldest strata recovered from CRP-2/2A, climatic conditions were not fully temperate.

The abundant and extensive deformational features preserved in the core may partially reflect glacial over-riding of the drill-site at various times. If subglacial over-riding and deposition is recorded in the core, the glaciers responsible were probably grounded on the continental shelf. Twenty-four vertically stacked, erosionally-based, cyclic facies successions (sequences) are interpreted as recording cycles of glacier advance and retreat across the area, and broad variations in shelfal water depths of the order of 50-100 m. The uppermost two sequences are amalgamated, recording a cryptic and incomplete Quaternary and Pliocene record that accumulated during a period of low net accommodation. The early Miocene and Oligocene record, on the other hand, is relatively more complete with 6 and 16 sequences, respectively, recognized. The controlling factors on this cyclicity cannot yet be fully evaluated.

Sediments preserved in CRP-2/2A were derived from a variety of rock types, all of which crop out in the area landward of Cape Roberts, suggesting a relatively local provenance. A major change in sediment provenance is recorded in the core at about 310 mbsf (close to the preferred location for a Late/Early Oligocene unconformity), from detritus derived predominantly from Jurassic dolerites, lavas and Beacon Supergroup sedimentary rocks, to detritus containing additional abundant basement granitoid material. Up-hole changes in the relative abundances of different extraformational sediment types are interpreted as recording the progressive unroofing of the Transantarctic Mountains. This may have been a consequence of earlier, or continuing, uplift in a period when climate was warmer and allowed greater amounts of fluvial sediment transport than at present.

Superimposed on this pattern is a contemporaneous record of volcanic activity. Petrographical evidence suggests that volcanic activity associated with the McMurdo Volcanic Group was active as far back as the Early Oligocene, which confirms a longer history of McMurdo Volcanic Group activity than that known from onshore. The sources for this volcanic material, including a spectacular, tephra-rich interval dated as early Miocene in age, may have been local to the Cape Roberts area, though the possibility of a more distant source remains.

The implications of CRP-2/2A for basin history cannot yet be fully assessed. Cyclical variation in the thickness of depositional sequences may indicate changes in subsidence regime through time, and the extensive deformation preserved in the core may in part record tectonic activity. Furthermore, initial correlation of the core with seismic

records and the near doubling of sonic velocity of strata below 300 mbsf indicate that tectonic dips are twice that which had been inferred previously (Barrett et al., 1995; Bartek et al., 1996). Dips are interpreted as increasing with depth, and truncations indicate angular discordances. Such features may be related to discrete episodes of rifting associated with the evolution of the Victoria Land Basin. Testing of these ideas must await further research.

CHRONOLOGY

The biostratigraphical framework for the pre-Pliocene section of CRP-2/2A is provided primarily by marine diatoms and, to a lesser extent, by calcareous nannofossils. There is considerable variation in distribution and abundance of these microfossils throughout the core (see chapter 5) and representation by open-ocean pelagic diatom or nannofossil taxa, which provide direct correlations to Southern Ocean and global bio- and chronostratigraphies, is limited.

As in CRP-1 (Harwood et al., 1998), marine diatoms are the most abundant and age-diagnostic forms recovered in CRP-2/2A. The diatom floras constrain the age of several intervals of CRP-2/2A by comparison with Southern Ocean Deep Sea Drilling Project (DSDP) and Ocean Drilling Program (ODP) drill holes. Assemblages are compared, for correlation purposes, with the CIROS-1, MSSTS-1, and CRP-1 cores from the Ross Sea. Calcareous nannofossils also provide important constraints on the age of CRP-2/2A by correlation to DSDP and ODP drill holes, and to CIROS-1. Foraminifera and marine palynomorphs have biostratigraphical potential. However, the foraminifera found in the core are all benthic forms; planktic age-diagnostic taxa are entirely absent. Marine palynomorphs (dinoflagellate cysts and acritarchs) are abundant and varied, but the floras are endemic, with many new species, and cannot currently provide biostratigraphical control for the Miocene and Oligocene. Radiometric dates ($^{40}\text{Ar}/^{39}\text{Ar}$) on two volcanic ash layers,

together with magnetostratigraphy, provide additional chronological constraints. Seven pre-Pliocene magnetozones are defined above 350 mbsf (N2 to the upper part of N5; Fig. 7.1). Below 350 mbsf, 6 magnetozones are defined (the lower part of N5 to R7). These lower magnetozones are poorly defined and further analyses are necessary to improve the magnetostratigraphy. A preliminary age-depth plot and correlation to the magnetic polarity timescale (MPTS) is presented in figure 7.1. The correlation is discussed below.

Sporadic fossil occurrences, coarse lithofacies, numerous disconformities and variable palaeo-environmental conditions all make it difficult to establish the complete distribution of key fossils in the pre-Pliocene interval of CRP-2/2A (26.75-624.15 mbsf). There are numerous stratigraphical breaks (disconformities) that divide the CRP-2/2A record into discrete packages of strata. The most significant breaks occur at three of the major sequence boundaries: c. 130, 307 and 443 mbsf (see chapter 3). These disconformities define four stratigraphical intervals, which are discussed below.

The uppermost interval, from 26.75 to c. 130 mbsf, is geochronologically well constrained by the first common occurrence of *Thalassiosira praeфрага* at 36.25 mbsf (D3; Tab. 7.1 and Fig. 7.1), which ranges from the upper part of Chron C6r through Chron C6n (Gersonde & Burckle, 1990; Baldauf & Barron, 1991; Harwood & Maruyama, 1992). In CRP-2/2A, this datum occurs near the base of a normal polarity interval (magnetozone N2) that we correlate with Chron C6n. The interval from 36.25 to c. 130 mbsf is confined to the middle lower Miocene by a volcanic ash at c. 113 mbsf that is dated at 21.44 ± 0.05 Ma by the $^{40}\text{Ar}/^{39}\text{Ar}$ method (A9 in Fig. 7.1). Chron C6Ar (21.32-21.77 Ma; Cande & Kent, 1995; Berggren et al., 1995) spans the age of the ash (including the uncertainty on the age determination). The ash, however, lies within a thick normal polarity magnetozone (N3, 71.89-127.70 mbsf; Fig. 7.1). It is unlikely that the ash was reworked significantly (see Volcanic Clasts section). Our preferred explanation for this discrepancy is that, given uncertainties

Tab. 7.1 - Biostratigraphical datum events in CRP-2/2A.

Event	Datum	CRP-2/2A Depth (mbsf)	Age (Ma) / Chron
D3	FO <i>Thalassiosira praeфрага</i> complex [‡]	36.25	20.3 (C6r)
D7	FO <i>Dactyliosolen antarcticus</i>	75.56	26.5 (C8n.2n)
D8	FO <i>Asteromphalus symmetricus</i>	236.25*	28.7 (C10n.2n)
D9	LO <i>Lisitzinia ornata</i> [‡]	259.21	24.2 (C6Cr)
D10	FO <i>Lisitzinia ornata</i> [‡]	266.38	28.2 (C9r)
D11	FO <i>Cavitatus jouseanus</i>	292.09*	30.9 (C12n)
D12	LO <i>Asterolampra punctifera</i>	444.96**	27.0 (C9n)
D13	LO <i>Pyxilla reticulata</i>	444.96**	30.1 (C11r)
D14	LO <i>Rhizosolenia oligocaenica</i>	444.96**	31.0 (C12r)
D15	FO <i>Rhizosolenia oligocaenica</i>	483.96*	33.5 (C13n) or older?
N1	LO <i>Dictyococcites bisectus</i>	144.44	23.9 (C6Cn.2r)
N2	LO <i>Isthmolithus recurvus</i>	459.52	31.8 (C12r)
N3	LO <i>Reticulofenestra oamaruensis</i>	458.40	33.7 (C13r)
A9	Ash	111.58 to 114.15	21.44 ± 0.05
A10	Ash	280.03 to 280.12	24.22 ± 0.06

Note: * = lowest confirmed occurrence in CRP-2/2A; ** = highest confirmed occurrence in CRP-2/2A; † = age-depth interpretations of CRP-1 place datum in C6r to C5En (Roberts et al., 1998); ‡ = total range of taxon is most likely more restricted on Antarctic shelf than in deep-sea.

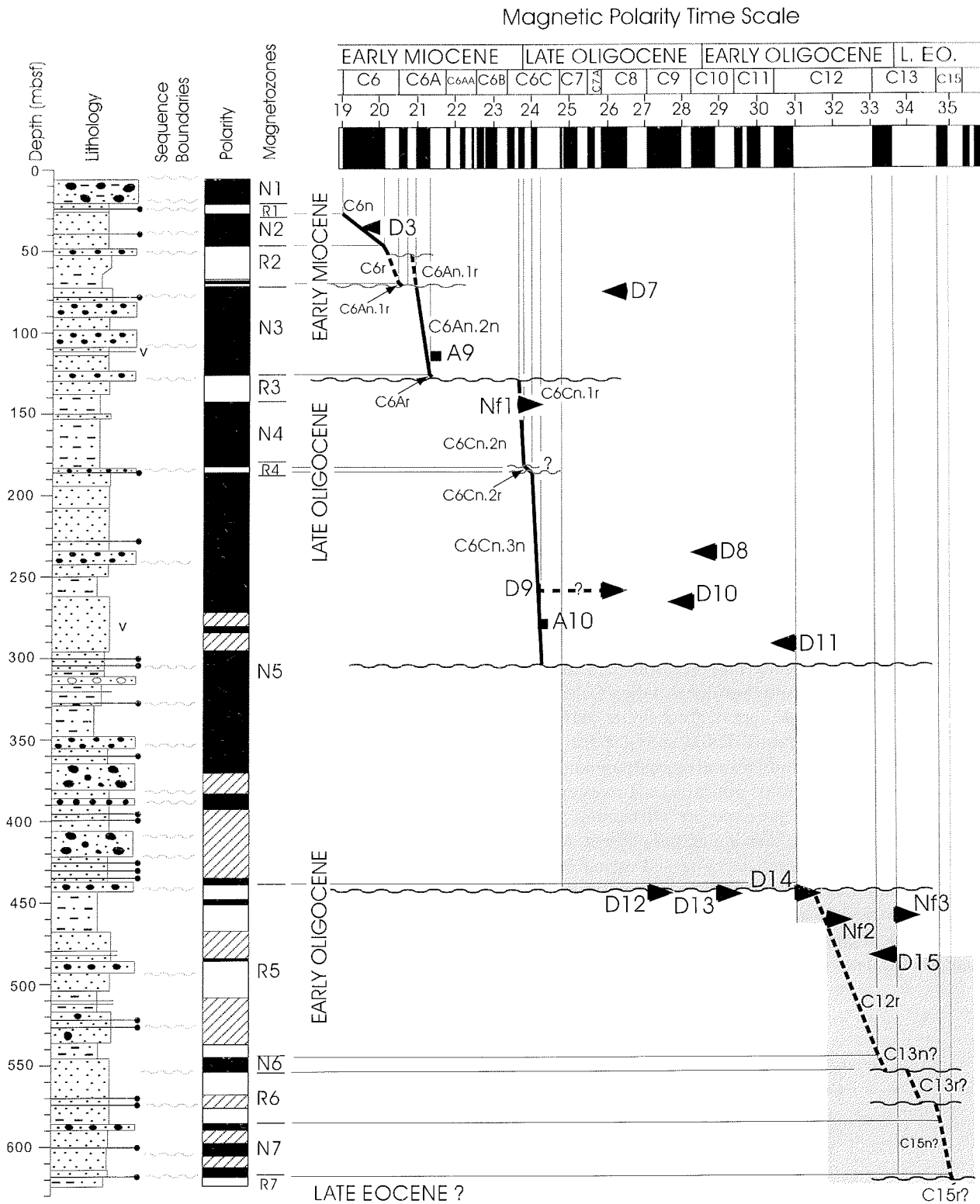


Fig. 7.1 - Correlation of CRP-2/2A with the MPTS of Cande & Kent (1995) and Berggren et al. (1995) using the preliminary magnetic polarity zonation (black = normal polarity, white = reversed polarity, hatched = unresolved) defined in chapter 6 (Palaeomagnetism), palaeontological datum events (chapter 5), and two radiometric ages described in chapter 4 (Volcanic Clasts section) and in the note following this section. The tip of the arrow marking each datum indicates its stratigraphical position and the base of the arrow is aligned with its age on the MPTS. Major unconformities are defined both by lithological sequence boundaries (see chapter 3, Sequence Stratigraphical Interpretation section) and by palaeontological datums. Other unconformities that coincide with lithostratigraphical breaks (see chapter 3, Description of Sequence section) are defined by the magnetic polarity stratigraphy (see chapter 6). Palaeontological and radiometric datums are defined in table 7.1. The datums are numbered according to the designations given by Roberts et al. (1998): diatom datums not reported in CRP-1 are given higher numbers, starting with D7. The shaded area below 307 mbsf defines the envelope of other possible correlations that are consistent with the data. Stepwise appearances are defined by the datums and do not imply the presence of additional disconformities in the sequence. A tentative interpretation is presented for the interval below 443 mbsf.

in numerical ages assigned to $^{40}\text{Ar}/^{39}\text{Ar}$ standards (Renne et al., 1998) and uncertainties in calibration of the MPTS in the early Miocene, the ash actually fell within the nearest normal polarity chron (C6An.2n). We correlate the thin reversed polarity interval directly above magnetozone N3 with C6An.1r. In this interpretation, magnetozone N3 is truncated by an inferred disconformity (at c. 70 mbsf) in which we interpret little time as having been lost. The normal polarity zone below the ash bed (c. 113 mbsf) is interpreted as part of C6An.2n and the transition from reversed to normal polarity (magnetozone R3 to N3) immediately above the disconformity at c. 130 mbsf is interpreted as representing the boundary between Chrons C6Ar and C6An.2n (middle early Miocene). There is no independent evidence for the inferred disconformity at c. 70 mbsf (which occurs in a high-stand systems tract) and a second interpretation is possible in this interval. In this interpretation, there is no time missing in a disconformity at c. 70 mbsf, magnetozone R2 would represent Chron C6An.1r, and the single normal polarity sample at the base of magnetozone R2 would have no correlative in the MPTS. The sequence boundary at c. 52 mbsf would therefore represent a disconformity (with c. 500 kyr missing) and the polarity transition from Chron C6r to C6n would lie immediately above the disconformity. This second interpretation only differs from the first interpretation in the interval between 52 and c. 70 mbsf (Fig. 7.1). At this stage, we cannot discriminate between these two possible interpretations.

A second stratigraphical interval is defined by the disconformities at c. 130 and 307 mbsf. There is a major change in the diatom flora at c. 130 mbsf, but poor age calibration prevents direct assessment of the hiatus. However, the calcareous nannofossil assemblage that accompanies *Dictyococcites bisectus* at 144.44 mbsf (Nf1, 23.9 Ma; Tab. 7.1 and Fig. 7.1) and an $^{40}\text{Ar}/^{39}\text{Ar}$ date on a second ash layer (A10; Fig. 7.1) at 280 mbsf (24.22 ± 0.06 Ma) suggest a hiatus of at least 2 m.y. at c. 130 mbsf. Normal polarity is dominant between 143.90 and c. 307 mbsf. A sequence stratigraphical boundary at c. 188 mbsf marks the base of a thin interval of reversed polarity (magnetozone R4) which separates magnetozones N4 and N5 (Fig. 7.1). Given these constraints, it is most likely that the interval defined by the lower part of magnetozone R3, and by magnetozones N4, R4, and the upper part of N5 correlate with C6Cn.1r, C6Cn.2n, C6Cn.2r, and C6Cn.3n, respectively. The ash itself should lie within Chron C6Cr, but given the same level of chronological uncertainty as explained for the ash at c. 113 mbsf, the apparently rapid sedimentation (c. 300 m/My), and the lack of physical evidence for a hiatus, it is more likely that the ash occurs within the lower part of C6Cn.3n. This correlation is broadly consistent with the biostratigraphical datums. There is a slight discrepancy with the range of the diatom *Lisitzinia ornata* (D9-D10, 259.21-266.4 mbsf, 24.2-28.2 Ma). In addition, a biostratigraphical break is recognized between c. 266 and 271 mbsf, where the ranges of six taxa are truncated, which suggests that the base of the range of *L. ornata* may be truncated. This palaeontologically defined break was not recognized during

lithological description and is not shown in the correlation discussed above (Fig. 7.1). Further work is needed to understand these discrepancies, but, based on the above chronological interpretation, it seems unlikely that this break represents a significant hiatus.

The third disconformity-bounded interval (c. 307 to 443 mbsf) is poorly defined on the basis of biostratigraphy. Throughout most of its thickness (c. 314 to 411 mbsf), this interval is devoid of age-diagnostic siliceous or calcareous microfossil assemblages. Normal polarity is dominant in the upper part of the interval, which must therefore correlate with C7n or with older periods of normal polarity. This suggests that at least Chron C6Cr (24.12-24.73 Ma) was lost in the hiatus at c. 307 mbsf. The lower Oligocene diatom assemblages from c. 412 through 443 mbsf contain neither *Cavitatus jouseanus* nor *Rhizosolenia oligocaenica*. This suggests that the age of the base of the interval is younger than 31 Ma, and that the base of magnetozone N5 could lie within C12n (Fig. 7.1). However, palaeoecological exclusion of either taxon is possible and there are indications that the disconformity at c. 443 mbsf is significant (*i.e.* the biostratigraphical ranges of nine diatom taxa are truncated at this horizon). In addition, the interval between c. 307 and 412 mbsf contains several possible unconformities (see chapter 3, Sequence Stratigraphical Interpretation section), and time may be distributed through several normal subchrons (C7n-C12n) in this interval. The uncertainty in chronological interpretation of this interval is indicated by the shading on figure 7.1.

The lowermost stratigraphical interval (c. 443 to 624.15 mbsf) is biostratigraphically well constrained only in the upper 40 m. The presence of *R. oligocaenica* indicates an age of between 31.0 and 33.5 Ma. A single specimen of the calcareous nannofossil *Isthmolithus recurvus* (at 459.52 mbsf) is consistent with this age assignment (Nf2, Tab. 7.1, Fig. 7.1), which suggests correlation of magnetozone R5 with Chron C12r. However, the calcareous nannofossil *Reticulofenestra oamaruensis* occurs up to 458.12 mbsf (Nf3; Tab. 7.1 and Fig. 7.1). The LO of *R. oamaruensis* is well documented in C13r (Berggren et al., 1995), and not C12r, as shown on the preliminary correlation in figure 7.1. It is possible that *R. oamaruensis* is reworked in CRP-2/2A because other floral and faunal evidence suggests that this interval is of early Oligocene age (see Palaeontology chapter). An increased abundance of reworked Eocene dinoflagellate cysts between c. 437 and 475 mbsf (see chapter 5, Palynology section) supports this possibility.

The c. 50 m interval below 484 mbsf is barren of age-diagnostic siliceous or calcareous microfossils. Taxa that are not age-diagnostic are found in intervals from c. 544 to 565 mbsf and from c. 565 mbsf to the bottom of the hole (624 mbsf). Microfossils are poorly preserved in the lowermost interval. A similar interval of poor siliceous microfossil preservation was recovered below 500 mbsf in CIROS-1. The absence of the diatom *Distephanosira architecturalis*, a widespread Southern Ocean taxon with a well-calibrated LO at 36.5 Ma (Harwood & Maruyama, 1992), suggests a likely maximum age for this interval. This absence, however, may be a purely diagenetic phenomenon.

Correlation of magnetozones N6, R6, N7, and R7 to the MPTS is ambiguous. Microfossil evidence suggests that the base of the hole is no older than latest Eocene in age (also, see note below on recognition of the Eocene-Oligocene boundary). The magnetic polarity zonation at the base of CRP-2/2A is uncertain. However, the biostratigraphical constraints, in conjunction with the presence of considerable thicknesses of reversed polarity, suggest that the base of the hole may range in age between Chron C13r and C15r (c. 33.5-35 Ma). A tentative correlation, which will be tested by further work, is shown (Fig. 7.1).

The above-described age model implies that the pre-Pliocene portion of CRP-2/2A spans an interval of 14-16 m.y. from the early Miocene (19 Ma) at 27 mbsf to the early Oligocene (or possibly latest Eocene, 33.5-35 Ma) at the base (624.15 mbsf). The age model is well defined down to 307 mbsf (c. 24 Ma), and indicates sediment accumulation rates that range between 30 and 300 m/My, with a 2 My hiatus at c. 130 mbsf. Below 307 mbsf, the age model is poorly constrained, although a significant time break is inferred at 443 mbsf, as suggested by the truncation of several diatom datums.

RECOGNITION OF THE EOCENE-OLIGOCENE BOUNDARY

A key issue for the lowermost part of CRP-2/2A is the question of what constitutes a late Eocene assemblage. The faunally and floristically rich assemblages which characterize all major groups of marine microfossils and the terrestrial palynomorphs in the Eocene do not extend to the very end of the epoch, as currently defined by Berggren et al. (1995). This is, in part, a result of repositioning of the boundary at a later level by those authors, and it also reflects a major environmental and biotic turnover that began before the end of the Eocene, as previously defined. The Antarctic floras and faunas that are preserved tend to be highly endemic, specialized polar associations, and they are often restricted to currently non-diagnostic benthic and regional neritic biotas (see chapter 5). The degree of possible diachroneity in first or last appearances for many of the Antarctic fossil taxa is still uncertain. Thus, unambiguous recognition of the Eocene is problematical, especially given the apparent lack of incursions of global oceanic waters during the time represented by the basal part of the core and the resulting lack of global ocean microfossil assemblages.

⁴⁰Ar/³⁹Ar AGE FOR PUMICE AT 280 MBSF (NOTE ADDED IN PROOF)

Feldspar crystals from a pumice-rich layer at 280 mbsf in CRP-2A provide a precise ⁴⁰Ar/³⁹Ar age of 24.22 ± 0.06 Ma. A total of fifty-five 1 to 2 mm diameter potassium-feldspar phenocrysts were extracted from pumice lapilli sampled from a pumice concentration zone near 280 m in CRP-2A. Following neutron irradiation at Texas A & M Nuclear Science Center, samples were analyzed by the ⁴⁰Ar/³⁹Ar single-crystal laser fusion method in the New

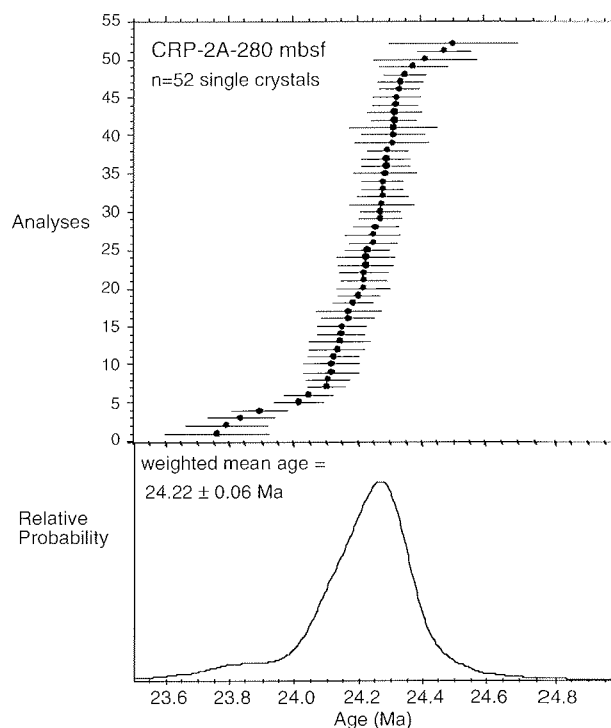


Fig. 7.2 - Probability distribution diagram of single-crystal laser-fusion analyses from CRP-2A-280 m feldspars. Upper panel shows individual analyses with ± 1 sigma error bars; lower panel shows cumulative probability distribution curve.

Mexico Geochronology Research Laboratory at New Mexico Institute of Mining and Technology, using procedures similar to those described in McIntosh & Chamberlin (1984). All ages were determined relative to the inter-laboratory standard Fish Canyon Tuff sanidine with an assigned age of 27.84 Ma (Deino & Potts, 1990). After rejecting data from two crystals that gave poor data, ages from 52 crystals form a tight group with a nearly perfect Gaussian probability distribution (Fig. 7.2). The weighted mean age of 24.22 ± 0.06 Ma (2 sigma error) is considered to be an accurate age for the eruption that produced the pumice-rich layer at 280 mbsf. The high concentration of pumice at 280 mbsf and the complete lack of older contaminant feldspar grains indicate that this age accurately represents the depositional age of the sampled horizon.

CLIMATIC AND DEPOSITIONAL HISTORY

The history of growth and decay of the Antarctic ice sheet and its links with climatically-driven global sea-level change were two of the questions that the Cape Roberts Project was designed to address. Sedimentological analysis of the core has shown that it can address these questions, at least in part, at this early stage of data analysis and synthesis. High-resolution lithological description of the core and facies analysis were carried out on a bed-by-bed basis to establish vertical changes in depositional environments, and sequence stratigraphic analysis was

used to establish broader trends related to base level fluctuations through the vertical succession.

The section represented in CRP-2/2A can be rationalized into 12 recurrent lithofacies which are: 1) mudstone, 2) interstratified sandstone and mudstone, 3) poorly sorted (muddy) very fine to coarse sandstone, 4) moderate to well sorted stratified fine sandstone, 5) moderately sorted stratified or massive medium to coarse sandstone, 6) stratified diamictite, 7) massive diamictite, 8) rhythmically interstratified sandstone and siltstone, 9) clast-supported conglomerate, 10) matrix-supported conglomerate, 11) mudstone breccia, and 12) volcanoclastic sediment. These facies are interpreted in terms of deposition in glacimarine and open coastal/shelf environments by a combination of tractional currents, fall-out from suspension, sediment gravity flows, rain-out from floating glacial ice and perhaps deposition and redeposition in subglacial positions (see chapter 3, Facies Analysis section). The facies analysis indicates that, by comparison with modern glacimarine settings, the substantial amount of melt-water associated with the glaciers in Oligocene times declined in the early Miocene. In addition, the range of glacimarine facies represented in CRP-2/2A core reflect high rates of sediment discharge by a variety of glacial processes. Such facies do not occur in the present day polar glacial regime of Victoria Land, and are characteristic of polythermal glaciation under warmer climatic conditions. For example, the early Miocene strata of CRP-2/2A have the same features as those of CRP-1, where the setting is most comparable with that of polythermal glaciers in the sub-Arctic (Powell et al., 1998). However, even the oldest strata cored do not indicate the high meltwater flows associated with temperate glaciation, as found in Alaska and Chile. This assessment is consistent with the sparse terrestrial palynomorph assemblage (see chapter 5).

The marine shelf setting is indicated by a number of facies, including mudstone (Facies 1), which is indicative of hemipelagic sedimentation; sandstone and mudstone (Facies 2), which are indicative of either waves and marine currents or sediment gravity flows; poorly sorted sandstones (Facies 3) which were deposited by sediment gravity flows or settling from turbid plumes; stratified fine sandstones (Facies 4), with possible hummocky cross-stratification, which are indicative of wave-base settings; planar to cross-stratified medium to coarse sandstone (Facies 5), which is indicative of shoreface and delta-front environments; rhythmic sandstones and siltstones (Facies 8), which are interpreted as cyclopsams and cyclopels from highly sediment-charged glacial streams in the sea; and volcanoclastic-rich sediment. Furthermore, the gradational contacts of the diamictites (Facies 6 and 7) and the interbedding of some diamict intervals with other marine facies is indicative of proximal glacimarine redeposition and rain-out processes.

The shallow marine settings appear to have varied from the shoreface to below wave base and included deltaic and/or grounding-line fan settings with large fluvial discharges. These produced glacial facies such as conglomerates, cyclopels and cyclopsams as well as the

associated delta/fan front and prodeltaic/fan sediment gravity flow deposits. The fan setting, and perhaps also the deltaic setting, are associated with ice-contact and ice-proximal environments. Grounding-line fan systems commonly include debris flow diamictites and associated penecontemporaneous sediment deformation. However, the deformation in the sequence may also result from glacial over-riding or local tectonically-induced brecciation and intrusion. Fabric analyses thus far indicate no strong sub-glacial till fabric, but it remains for further analysis to determine if some diamictites were subglacially deposited.

In the overall context of a shallow marine succession, if sub-glacial erosion, over-riding and deposition has occurred, the ice margin must have grounded offshore. The relatively flat shoreface and shelf during phases of glacial retreat may have had relief in the form of morainal banks produced by grounding-line deposits during advance periods. Relief of this type was probably sufficient to produce mass flow and sediment redeposition in the shelf setting. Some macrofossil assemblages and the darker Facies 1 mudstones of distal glacimarine and paraglacial conditions may have formed when isolated banks created restricted circulation conditions on their shoreward margins. Nearby volcanic eruptions contributed volcanic ash of variable composition into the sea, and most of it subsequently was reworked there.

The recognition of vertically-stacked cyclical facies successions bounded by sharp erosion surfaces has allowed the cored interval to be subdivided readily into sequences. It is suggested here that sequence boundaries coincide with glacial surfaces of erosion that record periods of glacier ice advancing across the sea-floor. In many cases, these advances have occurred in concert with sea-level fall. Sequence boundaries may have formed by two processes: (1) direct grounding of glacier ice onto the sea floor, or (2) erosion from debris-flow diamictites spilling off the front of proglacial grounding-line fans. In the latter case, subsequent ice-contact erosion may remove any evidence of the grounding-line fan. The constituent facies assemblage of each sequence has been interpreted as representing an ice-proximal record of glacial advance and retreat followed by a period of relatively ice-free paraglacial or open marine sedimentation. Sequences display a characteristic vertical organisation of lithofacies that have been subdivided into systems tracts, and include the following elements in ascending stratigraphical order (Fig. 7.3):

- 1 - LST-TST: a sharp-based, poorly sorted, coarse-grained unit comprising diamict and/or conglomerate, which is interpreted as ice-proximal and ice-contact glacimarine sedimentation during the advance and retreat of glacier ice into a shallow marine setting;
- 2 - TST: a fining-upwards interval of muddy sandstone which passes up-section into fine sandy mudstone, and is interpreted as the distal marine record of glacier retreat during sea-level rise;
- 3 - HST: a mudstone that passes gradationally upwards into a muddy sandstone/sandstone facies assemblage, which is interpreted as shoaling from mid/outer shelf to inner shelf water depths under a sea-level highstand;

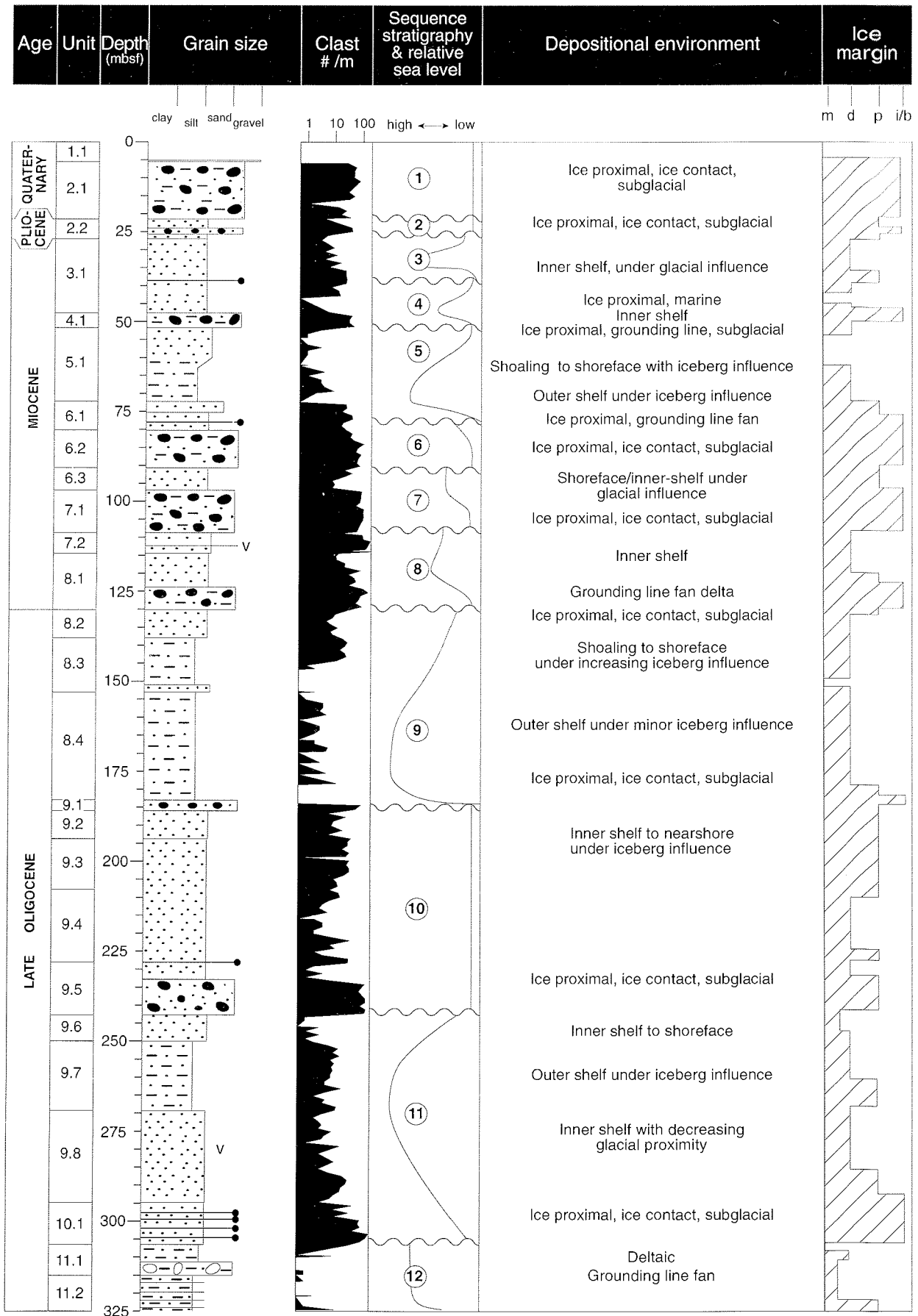


Fig. 7.3 - Stratigraphical summary and interpretation of the CRP-2/2A core.

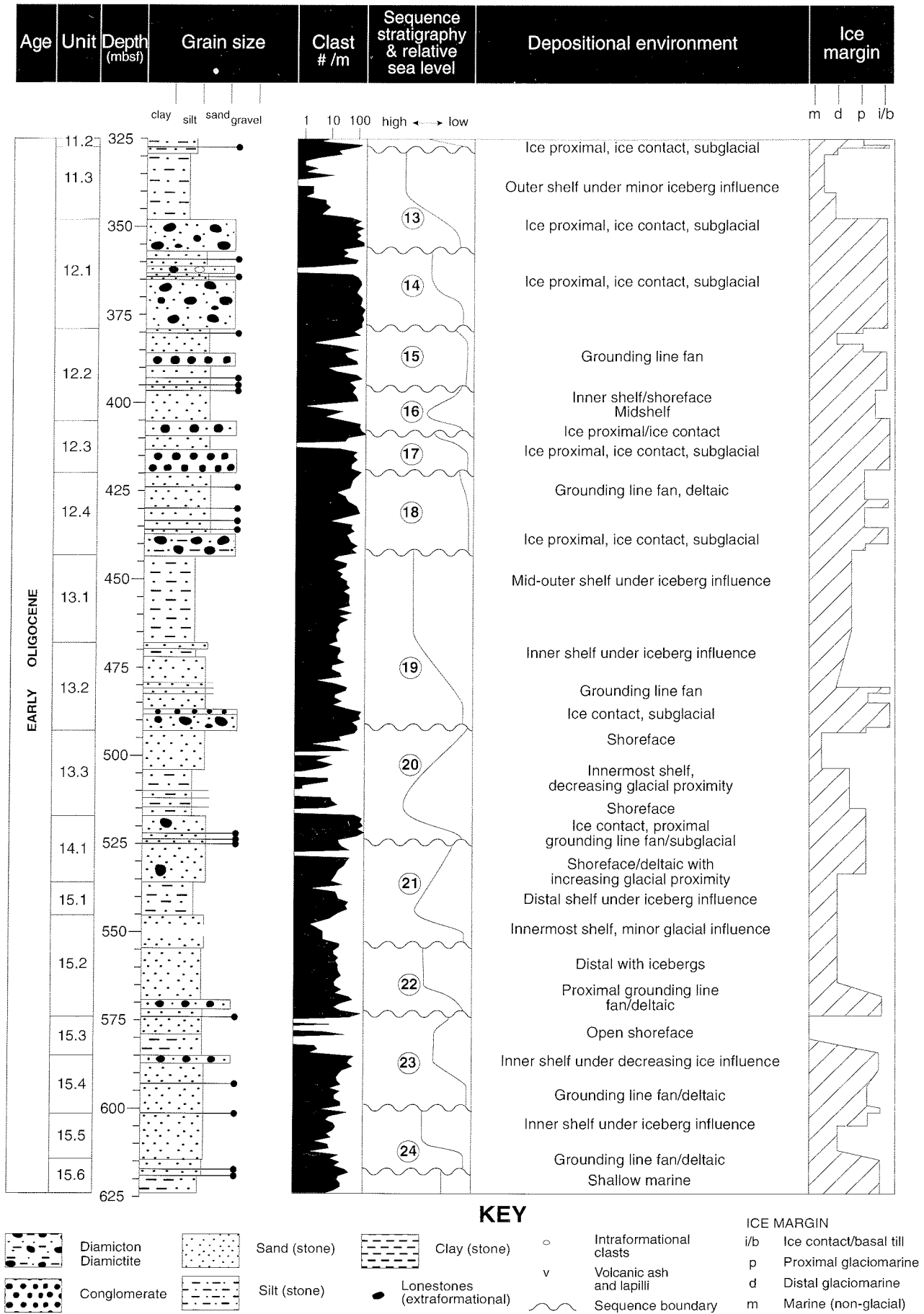


Fig. 7.3 - Continued.

4 - RST: a sharp-based, well-sorted, massive to cross-bedded sandstone, which is interpreted as a regressive facies assemblage forming in a proglacial deltaic depositional environment seaward of the advancing ice front.

Twenty-four cycles of local advance and retreat of glacier ice during the Oligocene to Quaternary can be identified on the basis of the preliminary facies and sequence stratigraphical analysis of the CRP-2/2A core. The Quaternary and Pliocene intervals, Sequences 1 and 2, respectively, are probably an amalgamated series of sequences recording a cryptic and incomplete glacial history of the last 5 Ma. That the Quaternary record lies within a normal polarity interval interpreted as representing Bruhnes Chron suggests that high-amplitude climatic variations characteristic of the last 700 ky may have driven major glacial episodes, destroying much of the earlier Plio-Pleistocene stratigraphical record. The recognition of a thin interval of Pliocene glacial/interglacial stratigraphy in CRP-2/2A is important, as significant fluctuations in the size of the Antarctic ice sheet have been inferred from studies of the on-land "Pliocene" Sirius Formation (Webb & Harwood, 1991; Wilson, 1995). Although punctuated by significant unconformities, the Oligocene-early Miocene section of the core is relatively more complete with 6 sequences preserved in the early Miocene and 16 sequences representing the Oligocene.

Broad constraints on the amplitudes of palaeobathymetric fluctuations reveal cyclical changes in water depth from shoreline-inner shelf to outer shelf water depths, perhaps of 50 to 100 m magnitude. These water depth changes are likely to result from the combined influence of eustasy, local tectonism, and sediment supply factors. The isolation of the eustatic sea-level component from a continental-margin sedimentary succession is inherently difficult to achieve. At this stage it has not been possible to estimate the amplitude of any glacio-eustatic component, but the inferred changes in water depth that are illustrated in figure 7.3 are consistent with the magnitude of eustatic water depth changes inferred for the Oligo-Miocene from seismic records (Haq et al., 1988), and deep ocean oxygen isotope records (Vitor & Anderson, 1998).

A preliminary chronology presented in this volume for CRP-2/2A indicates a thick interval of normal polarity in the late Oligocene which may span up to nine sequences. This implies that individual depositional sequences in certain parts of the core may correspond to Milankovitch orbital frequencies (eccentricity). Such an interpretation has several important implications, notably: (1) that the cored interval contains an incomplete record of the Oligocene-Quaternary of western Ross Sea with large periods of time represented at sequence-bounding unconformities, and (2) where sequences are preserved they may represent an important ice-proximal record of orbital control on the dynamics of the Antarctic ice sheet, which has significant implications for understanding the origin of variations in global eustatic sea-level in late Paleogene and Neogene times.

Alternatively, the frequency of sequence cyclicity may be of a longer duration, similar to that of the 3rd order

(0.5-2 Ma) eustatic cyclicity reported on the Haq et al. (1988) sea-level curve, and the composite Cenozoic oxygen isotope curve of Vitor & Anderson (1998). Of importance is that many of the characteristics of this glacial marine succession can be explained in terms of local glacial processes. Identifying the relative roles of eustasy, tectonism, and local glacial processes on controlling the depositional architecture of this important Antarctic record is one of the future challenges facing the Cape Roberts Team.

VOLCANIC AND TECTONIC HISTORY

VOLCANISM

Volcanic-derived clasts and grains occur throughout the entire CRP-2/2A core. Reworked basalt fragments are particularly common below 310 mbsf, but their mineralogy and textural characteristics indicate that they were derived by weathering from the Jurassic Kirkpatrick basalt. Evidence for active coeval volcanism is restricted to depths above 469 mbsf, which indicates that volcanism was active in Early Oligocene times, at least, and confirms a history of volcanism in the McMurdo Volcanic Group that is longer than that currently exposed onshore (less than 19 My; Kyle, 1990; cf. George, 1989). Volcanic glass occurs only in trace amounts up to 280 mbsf, where a layer of evolved pumice lapilli marks the base of a volcanic-rich interval that continues up to 200 mbsf. This indicates a significant period of volcanism during the Late Oligocene. A second volcanic-rich interval is present between 150 and 46 mbsf, marking a Late Oligocene/Early Miocene episode, and a third (Pliocene) episode is recorded in LSU 2.2 (21.1-26.8 mbsf). The volcanism was bimodal (basaltic/?trachytic) in each case and was probably alkaline, which is characteristic of continental rift settings. The glass was probably derived mainly by rapid reworking from local sources and was deposited by sedimentary rather than pyroclastic processes, and therefore does not provide a complete record of volcanic activity in the region (cf. Cape Roberts Science Team, 1998).

Evolved (trachytic?) pumice lapilli are common in LSU 7.1 and 7.2 (c. 97-114 mbsf), and LSU 7.2 includes a prominent trachytic tephra layer 1.2 m thick. The thickness and coarse grain-size of the 1.2 m-thick tephra layer indicates derivation from a volcano possibly situated only a few tens of km from the CRP-2/2A drill site. This is consistent with the interpretation of a local source for the glass in the associated sediments. Possible locations of the Oligocene/Lower Miocene volcanic source(s) are uncertain, but may include two small, but prominent, magnetic anomalies of likely volcanic origin identified c. 6 km west of CRP-2/2A, and larger anomalies situated c. 12 km to the northwest, near Granite Harbour (called the 'Barrett anomaly'), and c. 80 km to the ENE (the 'Kyle anomaly') (Behrendt et al., 1987; Behrendt, 1990). The origin of the 1.2 m-thick tephra deposit in LSU 7.2 is uncertain. Whilst deposition by air fall and settling through water are possible, other origins, including secondary thickening and redeposition are being tested.

PROVENANCE AND TRANSANTARCTIC MOUNTAINS UPLIFT

The clast and sand grain assemblages can be divided into three contrasting types: an upper assemblage (0 to 280 mbsf) with a multi-component source (granitoids, sediments, dolerite and abundant contemporary volcanic detritus), a middle assemblage (280-310 mbsf) which is similar to the upper assemblage but essentially lacking a volcanic component, and a lower assemblage (*c.* 310-625 mbsf) which contains numerous fine-grained Jurassic dolerite and basalt fragments and (?)Beacon sedimentary detritus, and in which the proportion of granitoids diminishes markedly toward the base (Fig. 7.4; and see chapter 4, Basement Clasts). In addition, below *c.* 310 mbsf, hornblende and biotite, which are common granitoid minerals, become scarce, reworked Jurassic basalts become abundant, and there is a significant increase in the proportion of Beacon-derived coal debris and rounded quartz grains. This is also reflected (from *c.* 350 mbsf) in lower feldspar/quartz ratios in the sediments. Thus, 310 mbsf marks a major petrological transition which represents a fundamental change in provenance, reflecting an upward change from detritus derived predominantly from Jurassic dolerites, lavas and Beacon sedimentary rocks, to detritus containing additional abundant basement granitoid material.

The provenance change records erosion down through the Beacon Supergroup and Ferrar Group sequence above the Kukri Erosion Surface to expose the sub-Kukri basement complex. This may represent progressive uplift of the Transantarctic Mountains (the likely provenance) or it may be climate-related. Other features in nearby levels of the CRP-2/2A core, including an unconformity at *c.* 307 mbsf, a thick intraformational breccia at *c.* 311 to 315 mbsf, and a possible change in stratal dip at *c.* 296 mbsf, are possibly attributable to tectonism and could be interpreted as an indication of faulting that affected the basin margin. If these features prove to be of tectonic origin, the change in provenance may coincide with an episode of faulting and uplift in the Transantarctic Mountains beginning at *c.* 30 Ma.

DEFORMATION

Brecciation, soft-sediment deformation (folding, convolute bedding, shear zones) and sedimentary dykes are common in the CRP-2/2A core. It is clear that more than one phase of deformation occurred, and these phases may reflect glacitectonic, mass movement, and/or tectonic activity (see chapter 3, Deformation section). An intraformational breccia between *c.* 311 and 315 mbsf contains angular to subrounded clasts and possibly resulted from slope failure, perhaps in response to tectonic instability within the basin. Microfaults and sedimentary intrusions are also abundant in the interval from *c.* 309 to 325 mbsf, which could be another indicator of tectonic instability. There is an intriguing association of these features with an unconformity at *c.* 307 mbsf, which is inferred to mark the Early to Late Oligocene boundary, and an interpreted angular discordance in seismic reflectors at *c.* 296 mbsf.

Brittle fractures, abundant throughout CRP-2/2A, are consistent with the structural setting of the site in proximity to the Transantarctic Mountains - Victoria Land Basin boundary. Natural fracture types include brittle microfaults, veins and clastic dykes. Most faults, including sediment- and vein-filled varieties, have normal-sense offset of bedding and in some cases have clear conjugate fault geometry. The geometry and kinematics of these fault arrays is characteristic of a rift environment and most likely records rift-related tectonic deformation in the Cape Roberts area. When fault orientation patterns can be determined from oriented core, it will be possible to compare the trends of faults in the core with seismically mapped faults in the Cape Roberts area to help to constrain the timing and kinematics of regional faulting. Drilling-induced and coring-induced fractures are also abundant in CRP-2/2A core, and preliminary analysis of oriented borehole televiewer imagery of the borehole walls suggests that there may be a consistent northeast-southwest orientation of the steeply-dipping induced fractures. If borne out by detailed analysis, this would indicate that the contemporary maximum horizontal compressive stress has a NE-SW orientation, oblique to the Transantarctic Mountains Front.

BASIN HISTORY

The pre-Pliocene strata of CRP-2/2A span the time interval from *c.* 19 to 33 Ma and accumulated at an average rate of 100 m/My. Subsidence along the margin of the Victoria Land Basin must have accommodated this substantial accumulation of Miocene and Oligocene strata. Sequence stratigraphical analysis has revealed cycles with marked thickness changes and, if the timing of the cycles is relatively uniform, this may reflect tectonically-driven changes in basin subsidence rate and/or sediment supply from the Transantarctic Mountains. An upward change from relatively thin to thick cycles occurs across the inferred Early to Late Oligocene unconformity at *c.* 307 mbsf (28-30 Ma), which possibly marks an increased subsidence rate. There is a change from thick to thinner cycles across an Early Oligocene unconformity at *c.* 443 mbsf, which possibly indicates a decreased subsidence rate in that part of the record.

CRP-2/2A results provide new age constraints for seismic reflectors in the Victoria Land Basin. There are two possible alternatives for the major V3/V4 seismic boundary, at *c.* 80 and 183 mbsf with *c.* 21 Ma (Early Miocene) and 26-27 Ma (Late Oligocene) ages, respectively. Additional reflectors in the sequence are all of Oligocene age. Because these reflectors can be tied to the regional seismic stratigraphy of the Victoria Land Basin, these new age data will provide a means to improve our understanding of the evolution of the Victoria Land Basin and the timing of rift episodes that shaped it.

Velocity data measured from CRP-2/2A core (see chapter 2, Core Physical Properties section) show relatively high seismic velocities for the sedimentary section. Conversion of seismic travel times to depth using the physical properties data yields higher dips for the seismic

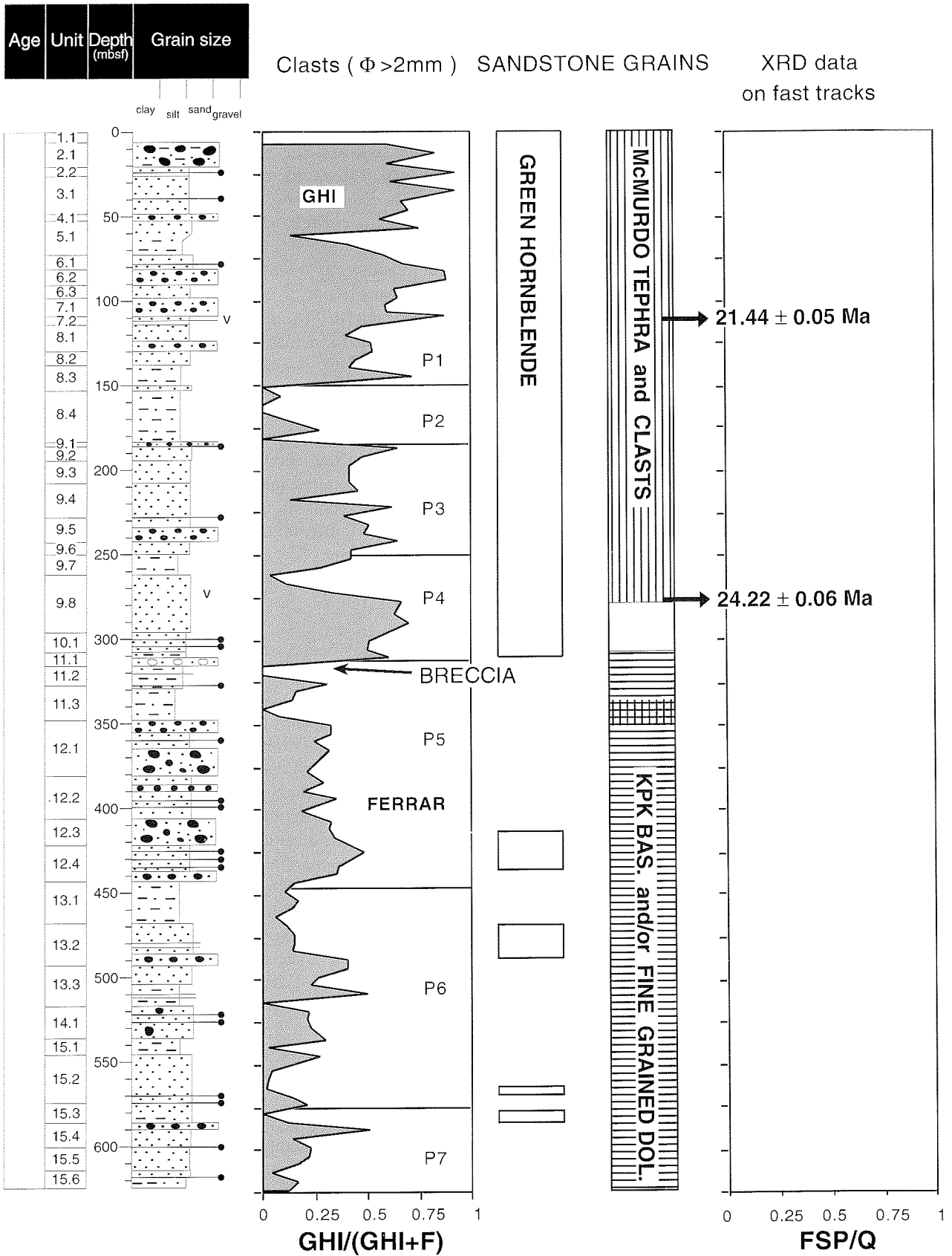


Fig. 7.4 - Summary diagram showing major petrological changes in the CRP2/2A sequence. GHI: Granite Harbour Intrusives; F: Ferrar; KPK BAS.: Kirkpatrick basalt; DOL.: dolerite.

reflectors than was previously interpreted (see Fig. 1.4). Reflector dips define a fan between c. 183 mbsf (possibly the V3/V4 boundary) and the major reflector at c. 296 mbsf. Dips beneath the reflector at c. 296 mbsf steepen from c. 5

to 10°. The relatively steep dips are maintained below this depth, including the V4/V5 boundary. The increase in dip documents basinward tilting of the strata. If the fan-shaped arrangement of the reflectors is real, it indicates a

gradual increase in the tilt of older strata through the sequence. If an angular unconformity is present, this suggests distinct phases of tilting that may document discrete rift episodes. More detailed analysis of seismic dips and possible onlap and/or downlap relations of the reflectors may constrain the timing of episodes of tilting, and therefore of faulting events, that affected the basin margin.

When correlations in age, lithostratigraphy, physical properties, and provenance trends are established between CRP-2/2A and CIROS-1, it will be possible to evaluate key issues regarding the tectonic evolution of the Transantarctic Mountains and Victoria Land Basin in the McMurdo Sound area. Detailed comparison of provenance history may reveal either regionally consistent uplift patterns or different uplift histories for discrete crustal blocks along the range, *i.e.* for the Convoy Range, McMurdo Dry Valleys and Royal Society Range blocks, which are divided by structures lying along or close to Mackay Glacier and Ferrar Glacier, respectively (Fitzgerald, 1992; Fitzgerald & Baldwin, 1997). Comparison of age, thickness, and dips of lithostratigraphical sequences between CRP-2/2A and CIROS-1, as well as correlation of seismic reflectors parallel and transverse to the coastline, will constrain models for the subsidence history of the Victoria Land Basin margin and its relationship to faulting along the Transantarctic Mountains Front.

CONCLUSIONS AND FUTURE PLANS

Drilling at CRP-2/2A has yielded more or less continuous core recovery (95%) through about 600 m of strata that have recorded climatic and tectonic history on the margin of the Victoria Land Basin from *c.* 19 to *c.* 33 Ma. The strata have proved to be significantly younger than expected, and cover about the same time interval as the CIROS-1 drill hole 70 km to the south. While this has meant further delay in sampling strata representing earlier climatic and tectonic events, two features give CRP-2/2A special significance in advancing the main goals of the project through offering the prospect of a dramatic improvement in dating strata on the Antarctic continental shelf.

The first feature is the biota being recovered from the core. Although some facies are unproductive, many have well-preserved assemblages, notably of diatoms and marine palynomorphs, some of which include taxa not yet described. These assemblages show progressive changes through the sequence that can provide the basis for a much better circum-Antarctic biostratigraphy. For reasons that we do not understand, the microfossil assemblages in CRP-2/2A are significantly more varied and better preserved than in CIROS-1.

The second feature is the occurrence of volcanic debris and shell fragments throughout most of the core. These materials provide a way of dating a number of stratigraphical levels independent of each other and of the few biostratigraphical datums that can be recognized from lower latitude taxa. The most striking is the volcanic ash layer at 112 mbsf, for which an age of 21.44 ± 0.05 Ma has

already been obtained (see chapter 4, Volcanic Clasts section). A further ash at 280 mbsf has been sampled for dating, and has provided another reference point for building a chronology for the Cape Roberts sequence. A number of volcanic clasts have also been collected in order to provide maximum ages for the levels from which they have been sampled.

The volcanic material extends down only to 469 mbsf, but shell fragments, from which ages can be estimated from the isotopic composition of strontium, were found throughout the length of the core. Although the accuracy of this approach is an order of magnitude lower (0.5 Ma vs 0.05 Ma), the wider distribution of the material will make the results from this work invaluable. In addition to these features, the intensive palaeomagnetic measurements carried out on the full length of the core are providing a reversal stratigraphy that, once calibrated, will enhance further the chronology for CRP-2/2A. When this has been integrated with the biostratigraphical datums yet to be established from the assemblages now being described for the first time, biostratigraphical schemes comparable with that of middle and low latitudes should be achievable for correlation of shelf sequences around the Antarctic margin and into lower latitudes.

One of the main goals of the project is to seek a record of climate and sea level from the climatically sensitive Antarctic margin. Preliminary assessment of the sequence cored in CRP-2/2A indicates that the sequence is entirely marine, but varies from nearshore to offshore, with sedimentation keeping pace with subsidence over the 14 million years spanned by the core. The preliminary age model also suggests two significant gaps in the record, from 21 to 26 Ma and from 28 to 30 Ma, but, of the strata preserved, 22 depositional sequences are recognized, each representing part of a cycle of glacial advance and retreat, and, in some cases, associated with falling and rising sea level. The cycles vary in thickness and time span but average *c.* 30 m and 300 000 years. Features in the core indicate that the climate was much warmer than today and perhaps comparable with that of the margins of the Quaternary ice sheets in the Northern Hemisphere. If the preliminary chronology is accurate, then this suggests that the Antarctic ice sheet in a warmer climatic regime may have a naturally longer period than the northern ice sheets of the Quaternary with their 40 and 100 ka cycles. A significant opportunity that the core is providing is for the analysis of various properties for cyclicity with the three main Milankovitch frequencies. Early results suggest that there are cyclicities on Milankovitch frequencies, but that these are much shorter than the cycles of ice advance and retreat.

The other principal goal of the project, to elucidate the early tectonic history of the Victoria Land Basin and the adjacent Transantarctic Mountains, has also been advanced significantly with the record of progressive erosion through the mountains being recorded in the clasts and minerals in the core. The shift from Beacon and Ferrar rocks, including Kirkpatrick basalt, which caps the Beacon Supergroup at the head of the Mackay Glacier 100 km from the coast, in the lower part of the core, to largely basement-derived clasts above 300 mbsf, plainly records the stripping of the

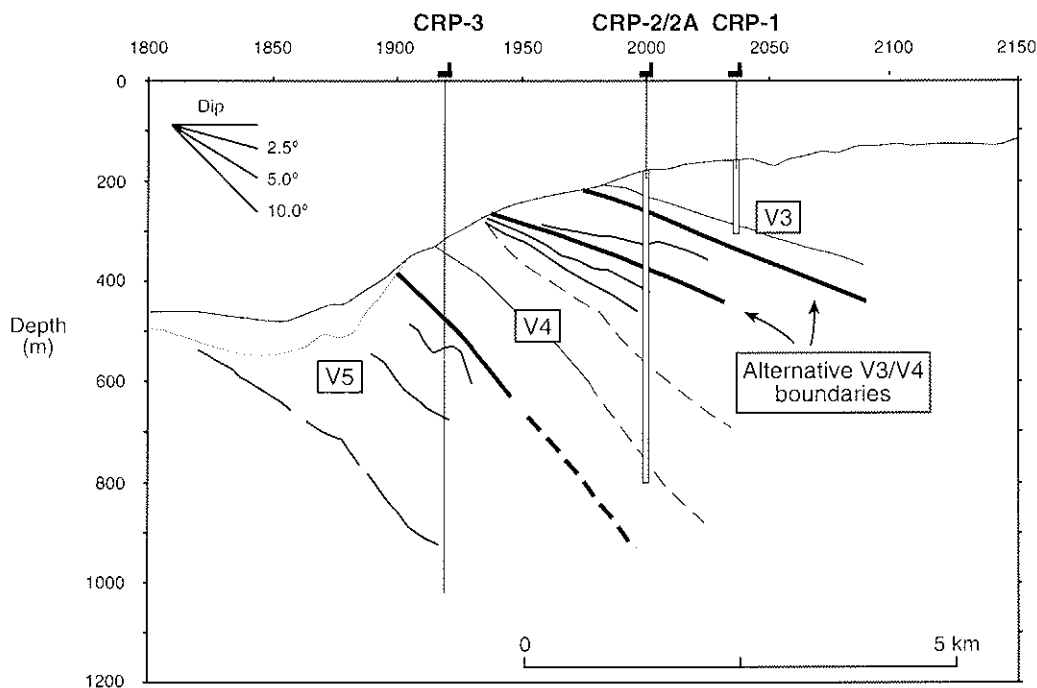


Fig. 7.5 - Depth section from seismic line NBP9601-89, showing the location for CRP-3 in the next drilling season.

landscape through the Devonian-Jurassic “cover beds”. Whether this represents contemporaneous middle Cenozoic uplift, or erosion responding to an earlier rapid uplift event is not yet clear. Work on old and new fracture patterns in the core will yield results for a Neogene stress history for the area. Whatever the changes in stress regime, however, the slow subsidence at this point of the margin of the Victoria Land Basin (around 40 m/Ma net) suggests that the margin of the West Antarctic Rift System has not been tectonically very active in Neogene times.

The drilling in 1998 has completed coring of a little over half of the 1 200 m of strata that were originally targetted, though we have yet to reach strata old enough to record the changes in climate and tectonics in the region that are the primary target of the project. The age of the oldest strata cored this year takes us close to the widely accepted transition period, from *c.* 36 to 34 Ma, from “green-house” to “ice-house”. In the next and final drilling season, we expect to core down through this period.

CRP-3 will be sited to core the lower 50 m of CRP-2A to ensure that the two cored sequences can be linked precisely by correlation using a range of techniques, including down-hole logging, core properties,

lithostratigraphy and biostratigraphy. Water depth at the site will be a little over 300 m and the target depth will be 700 mbsf. This will take us deep into seismic sequence V5, which lies just 120 m below the bottom of CRP-2/2A and the oldest sequence in the Victoria Land Basin (Fig. 7.5).

Some aspects of the drilling operation in 1999 will be easier and others will be more difficult. The experience this year with the new sea riser should help speed the deployment process, and coring through older and harder strata should make for few drilling problems. However, the riser will be set in much deeper water, and there will undoubtedly be fresh problems to be overcome.

Drilling supplies have already been ordered for shipment to Antarctica in January 1999, in preparation for transporting by sledge to Cape Roberts in the early spring. We are hoping that ice conditions will allow us to proceed as planned, and this will be evident from satellite imagery in June 1999. If conditions are marginal, then drilling will be postponed a further season. In the meantime, the focus for the Cape Roberts Science Team is on the more than 5 000 samples and 600 m of logs to be studied for contributions to the Scientific Results volume, due for the workshop in Wellington on 28 June 1999.

REFERENCES

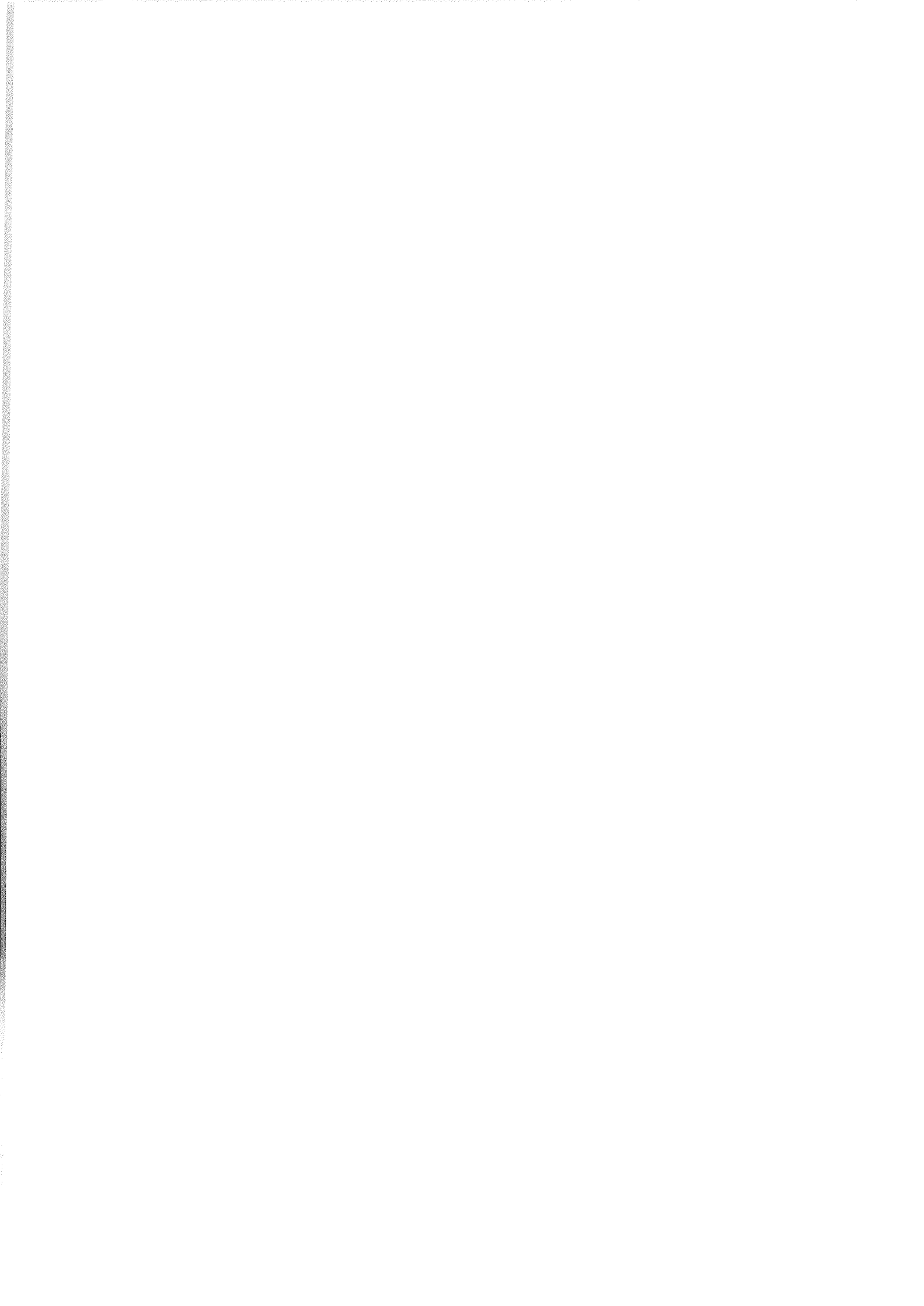
- Akiba F., Hiramoto C. & Yanagisawa Y., 1993. A Cenozoic diatom genus *Cavitatus* Williams; an emended description and two new biostratigraphically useful species, *C. lanceolatus* and *C. rectus* from Japan. *Bull. Natn. Sci. Mus., Tokyo*, Ser. C, **19**(1), 11-39.
- Akiba F. & Yanagisawa Y., 1986. Taxonomy, morphology and phylogeny of the Neogene diatom zonal marker species in the middle-to-high latitudes of the North Pacific. In: Kagami H., Karig D.E., Caultbourn W.T. et al. (eds.), *Initial Reports of the Deep Sea Drilling Project*, Washington. U.S. Government Printing Office, **87**, 483-544.
- Alley R., 1997. How glaciers entrain and transport basal sediment: physical constraints. *Quaternary Science Reviews*, **16**, 1017-1038.
- Allibone A.H., 1992. Low pressure/high temperature metamorphism of Koettlitz Group schists in the Taylor Valley and Ferrar Glacier regions. *New Zealand Journal of Geology and Geophysics*, **35**, 115-127.
- Allibone A.H., Cox S.C., Graham I.J., Smillie R.W., Johnstone R.D., Ellery S.G. & Palmer K., 1993b. Granitoids of the Dry Valleys area, southern Victoria Land, Antarctica: field relationships, and isotopic dating. *New Zealand Journal of Geology and Geophysics*, **36**, 281-291.
- Allibone A.H., Cox S.C. & Smillie R.W., 1993a. Granitoids of the Dry Valleys area, southern Victoria Land: geochemistry and evolution along the early Paleozoic Antarctic Craton margin. *New Zealand Journal of Geology and Geophysics*, **36**, 299-316.
- Anson G.L. & Kodama K.P., 1987. Compaction-induced shallowing of the post-depositional remanent magnetization in a synthetic sediment. *Geophysical Journal of the Royal Astronomical Society*, **88**, 673-692.
- Arai K., Sakai H. & Konishi K., 1996. High-resolution rock-magnetic variability in shallow marine sediment: a sensitive paleoclimatic metronome. *Sedimentary Geology*, **110**, 7-23.
- Arason P. & Levi S., 1990. Compaction and inclination shallowing in deep sea sediments from the Pacific Ocean. *Journal of Geophysical Research*, **95**, 4501-4510.
- Armenti P., Macedonio G. & Pareschi M.T., 1988. A numerical model for the simulation of tephra transport and deposition: applications to May 18, 1980 Mt. St. Helens eruption. *J. Geoph. Res.*, **93**, 6463-6476.
- Armenti P., Messiga B. & Vannucci R., 1998. Sand Provenance from Major and trace Element Analyses of Bulk Rock and Sand Grains. *Terra Antarctica*, **5**(1), 589-599.
- Askin R.A. & Ashworth A., 1998. Palynomorphs from peat and lacustrine beds in the Sirius Group of the Transantarctic Mountains. North-Central Section. *GSA Annual Meeting*, Columbus, Ohio, March 1998, *Abstracts with Programs*, **30**(2), A-3.
- Askin R.A. & Markgraf V., 1986. Palynomorphs from the Sirius Formation, Dominion Range, Antarctica. *Antarctic Journal of the United States*, **21**, 34-35.
- Baker J.C. & Fielding C.R., 1998. Diagenesis of Glacimarine Miocene Strata in CRP-1, Antarctica. *Terra Antarctica*, **5**(3), 647-653.
- Baldauf J.G. & Barron J.A., 1991. Diatom biostratigraphy: Kerguelen Plateau and Prydz Bay regions of the Southern Ocean. *Proceedings of the Ocean Drilling Program, Scientific Results*, **119**, College Station, TX, 547-598.
- Bankwitz P. & Bankwitz E., 1995. Fractographic features on joints of KTB drill cores (Bavaria, Germany). In: Ameen M.S. (ed.), *Fractography: fracture topography as a tool in fracture mechanics and stress analysis*, Geological Society Special Publication, **92**, 39-58.
- Barrett P.J., 1980. The shape of rock particles, a critical review. *Sedimentology*, **27**, 291-303.
- Barrett P.J. (ed.), 1986. Antarctic Cenozoic history from MSSTS-1 drill hole, McMurdo Sound. *DSIR Bulletin*, **237**, Science Information Publishing Centre, Wellington, 174 p.
- Barrett P.J. (ed.), 1989. Antarctic Cenozoic history from CIROS-1 drill hole, McMurdo Sound. *DSIR Bulletin*, **245**, Science Information Publishing Centre, Wellington, 254 p.
- Barrett P.J. & Davey F.J., 1992. Cape Roberts Project Workshop Report. *Royal Society of New Zealand, Miscellaneous Series*, **23**, 38 p.
- Barrett P.J., Henrys S., Bartek L.R., Brancolini G., Busetti M., Davey F.J., Hannah M.J. & Pyne A.R., 1995. Geology of the margin of the Victoria Land basin off Cape Roberts, southwest Ross Sea. In: Cooper A.K., Barker P.F. & Brancolini G. (eds.), *Geology and Seismic Stratigraphy of the Antarctic Margin*, *Antarctic Research Series*, **68**, AGU, Washington, 183-208.
- Barrett P.J., McKelvey B.C. & Walker B.C., 1986. Sand provenance. *DSIR Bulletin*, **237**, 137-144.
- Barrett P.J., Pyne A.R. & Ward B.L., 1981. Modern sedimentation in McMurdo Sound, Antarctica. In: Oliver R.L., James P.R. & Jago J.B. (eds.), *Antarctic Earth Science*, *Australian Academy of Science*, Canberra, 550-555.
- Barron J.A. & Mahood A.D., 1993. Exceptionally well-preserved early Oligocene diatoms from glacial sediments of Prydz Bay, East Antarctica. *Micropaleontology*, **39**(1), 29-45.
- Bartek L.R., Henrys S.A., Anderson J.B. & Barrett P.J., 1996. Seismic stratigraphy in McMurdo Sound: implications for glacially influenced early Cenozoic eustatic change. *Marine Geology*, **130**, 79-98.
- Barton C., Tessler L. & Zoback M., 1991. Interactive analysis of borehole televiewer data. In: Palaz I. & Sengupta S. (eds.), *Automated pattern analysis in petroleum exploration*, Springer-Verlag, 217-242.
- Batten D., 1996. Palynofacies and environmental interpretation. In: Jansonius J. & McGregor D.C. (eds.), *Palynology: principles and applications*, American Association of Stratigraphic Palynologists Foundation, **3**, 1011-1064.
- Behrendt J.C., 1990. Ross Sea. In: LeMasurier W.E. & Thomson J.W. (eds.), *Volcanoes of the Antarctic Plate and Southern Oceans*, *American Geophysical Union, Antarctic Research Series*, **48**, 89-90.
- Behrendt J.C., Blankenship D.D., Damaske D. & Cooper A.K., 1995. Glacial removal of Late Cenozoic subglacially emplaced volcanic edifices by the West Antarctic Ice Sheet. *Geology*, **23**, 1111-1114.
- Behrendt J.C., Blankenship D.D., Finn C.A., Bell R.E., Sweeney R.E., Hodge S.R. & Brozena J.M., 1994. Evidence for Late Cenozoic flood basalts (?) in the West Antarctic Rift System revealed by the CASERTZ aeromagnetic survey. *Geology*, **22**, 527-530.
- Behrendt J.C., Cooper A.K. & Yuan A., 1987. Interpretation of marine magnetic gradiometer and multichannel seismic-reflection observations over the western Ross Seashelf, Antarctica. In: Cooper A.K. & Davey F.J. (eds.), *The Antarctic Continental Margin: Geology and Geophysics of the Western Ross Sea*, *Circum-Pacific Council for Energy and Natural Resources, Earth Science Series*, **5B**, 155-177.
- Bell J.S., 1996. In situ stresses in sedimentary rocks (Part 1): Measurement techniques. *Geoscience Canada*, **23**, 85-100.
- Bellanca A., Neri R. & Palumbo B., 1998. Provenance of CRP-1 Drillhole Fine-Grained Sediments, McMurdo Sound, Antarctica: Evidence from Geochemical Signals. *Terra Antarctica*, **5**(1), 639-643.
- Berger A., 1984. Accuracy and frequency stability of the earth's orbital elements during the Quaternary. In: Berger A.L., Imbrie J., Hays J., Kukla G. & Saltzman B. (eds.), *Milankovitch and Climate, Part 1*, Reidel Publ. Co., Dordrecht, 3-39.
- Berger A. & Loutre M.F., 1994. Astronomical forcing through geological time. In: de Boer P.L. & Smith D.G. (eds.), *Orbital forcing and cyclic sequences*, IAS Special Publication, **19**, 15-24.
- Berggren W.A., Kent D.V., Swisher C.C. & Aubry M.-P., 1995. A revised Cenozoic geochronology and chronostratigraphy. In: Berggren W.A., Kent D.V., Aubry M.-P. & Hardenbol J. (eds.), *Geochronology, Time Scales and Global Stratigraphic Correlation*, Soc. Econ. Paleontol. Mineral. Spec. Publ., **54**, 129-212.
- Bergman L., 1982. Clastic dykes in the Aland Islands, SW Finland and their origin. *Geological Survey of Finland Bulletin*, **317**, 33 p.
- Berner R.A., 1981. A new geochemical classification of sedimentary environments. *Journal of Sedimentary Petrology*, **51**, 359-365.
- Berner R.A., 1984. Sedimentary pyrite formation: An update. *Geochimica et Cosmochimica Acta*, **48**, 605-615.
- Beu A.G. & Dell R.K., 1989. Mollusca. In: Barrett P.J. (ed.), *Antarctic Cenozoic history from the CIROS-1 drillhole, McMurdo Sound*, *DSIR Bulletin*, **245**, 135-141.
- Biscaye P.E., 1965. Mineralogy and sedimentation of recent deep-sea clay in the Atlantic Ocean and adjacent seas and oceans. *Geol. Soc. Am. Bull.*, **76**, 803-832.

- Blackman R.B. & Tuley J.W., 1958. *The measurement of power spectra from the point of view of communication engineering*. Dover Publications, New York, 190 p.
- Blatt H., 1992. *Sedimentary Petrology*. W.H. Freeman (ed.), 2nd ed., New York.
- Bloemendal J., King J.W., Hall F.R. & Doh S.-J., 1992. Rock magnetism of late Neogene and Pleistocene deep-sea sediments: relationship to sediment source, diagenetic processes, and sediment lithology. *Journal of Geophysical Research*, **97**, 4361-4375.
- Bordovskiy O.K., 1965. Accumulation and transformation of organic substance in marine sediments. *Marine Geology*, **3**, 3-114.
- Boulton G.S., 1996. Theory of glacial erosion, transport and deposition as a consequence of subglacial sediment deformation. *Journal of Glaciology*, **42**(140), 43-62.
- Bozzo E., Damaske D., Caneva G., Chiappini M., Ferraccioli F., Gambetta M. & Meloni A., 1997. A High Resolution Aeromagnetic Survey over Proposed Drill Sites Off Shore of Cape Roberts in the Southwestern Ross Sea (Antarctica). In: Ricci C.A. (ed.), *The Antarctic Region: Geological Evolution and Processes*, Terra Antarctica Publication, Siena, 1129-1134.
- Bridle I.M. & Robinson P.A., 1990 Diagenesis. In: Barrett P.J. (ed.), *Antarctic Cenozoic history from the CIROS-1 drillhole McMurdo Sound, DSIR Bulletin*, **245**, 201-207.
- Bullard E.C., 1947. The time necessary for a borehole to attain temperature equilibrium. *Monthly Notices Roy. Astr. Soc. Geophys. Suppl.*, **5**, 127-130.
- Cande S.C. & Kent D.V., 1995. Revised calibration of the geomagnetic polarity time scale for the Late Cretaceous and Cenozoic. *Journal of Geophysical Research*, **100**, 6093-6095.
- Cape Roberts Science Team, 1998. Initial Report on CRP-1, Cape Roberts Project, Antarctica. *Terra Antarctica*, **5**(1), 187 p.
- Cape Roberts Science Team, 1998a. Background to CRP-1, Cape Roberts Project, Antarctica. *Terra Antarctica*, **5**(1), 1-30.
- Cape Roberts Science Team, 1998b. Quaternary Strata in CRP-1, Cape Roberts Project, Antarctica. *Terra Antarctica*, **5**(1), 31-61.
- Cape Roberts Science Team, 1998c. Miocene Strata in CRP-1, Cape Roberts Project, Antarctica. *Terra Antarctica*, **5**(1), 63-124.
- Cape Roberts Science Team, 1998d. Summary of Results from CRP-1, Cape Roberts Project, Antarctica. *Terra Antarctica*, **5**(1), 125-137.
- Chamley H., 1989. *Clay Sedimentology*. Springer, Berlin, 623 p.
- Claps M. & Aghib F.S., 1998. Carbonate Diagenesis in Miocene Sediments from CRP-1, Victoria Land Basin, Antarctica. *Terra Antarctica*, **5**(3), 655-660.
- Claps M. & Masetti D., 1994. Milankovitch periodicities recorded in Cretaceous deep-sea sequences from Southern Alps (Northern Italy). In: de Boer P.L. & Smith D.G. (eds.), *Orbital forcing and cyclic sequences*, IAS Special Publication, **19**, 99-107.
- Cooper A.K. & Davey F.J., 1985. Episodic rifting of Phanerozoic rocks in the Victoria Land basin, western Ross Sea, Antarctica. *Science*, **229**, 1085-1087.
- Cooper A.K. & Davey F.J. (eds.), 1987. The Antarctic Continental Margin: Geology & Geophysics of the Western Ross Sea. Circum-Pacific Council for Energy & Mineral Resources. *Earth Sciences Series*, **5B**, Houston, Tex.
- Cooper A.K., Davey F.J. & Hinz K., 1991. Crustal extension and the origin of sedimentary basins beneath the Ross Sea and Ross Ice Shelf, Antarctica. In: Thomson M.R.A., Crame J.A. & Thomson J.W. (eds.), *Geological Evolution of Antarctica*, Cambridge University Press, Cambridge, 285-291.
- Cowan E.A., Cai J., Powell R.D., Clark J.D. & Pitcher J.N., 1997. Temperate glacial marine varves from Disenchantment Bay, Alaska. *Journal of Sedimentary Research*, **67**, 536-549.
- de Boer P.L. & Smith D.G., 1994. Orbital forcing and cyclic sequences. In: de Boer P.L. & Smith D.G. (eds.), *Orbital forcing and cyclic sequences*, IAS Special Publication, **19**, 1-14.
- De Kaenel E. & Villa G., 1996. Oligocene/Miocene calcareous nanofossil biostratigraphy and paleoecology from the Iberia Abyssal Plain, Northeastern Atlantic. *ODP Sc. Results*, **149**, 79-145.
- Deino A. & Potts R., 1990. Age probability spectra for examination of single-crystal ⁴⁰Ar/³⁹Ar dating results: examples from Ologesailie Formation, Southern Kenya Rift. *Quaternary International*, **13/14**, 47-53.
- Dell R.K. & Fleming C.A., 1975. Oligocene-Miocene bivalve Mollusca and other macrofossils from Sites 270 and 272 (Ross Sea), DSDP Leg 28. *Initial Reports of the Deep-Sea Drilling Project*, **28**, 693-703.
- Dickinson W.R., 1970. Interpreting detrital modes of graywacke and arkose. *J. Sed. Petrol.*, **40**, 695-707.
- Diggle P.J., 1990. *Time series. A Biostatistical Introduction*. Oxford University Press, London, 257 p.
- Domack E.W. & Lawson D.E., 1985. Pebble fabric in an ice-rafted diamict. *Journal of Geology*, **93**, 577-591.
- Dowdeswell J.A., Hambrey M.J. & Ruitang Wu., 1985. A comparison of clast fabric and shape in Late Precambrian and modern glacial sediments. *Journal of Sedimentary Petrology*, **55**, 691-704.
- Edwards A.R. & Waghorn D.B., 1989. Calcareous nanofossils. In: Barrett P.J. (ed.), *Antarctic Cenozoic history from the CIROS-1 drillhole, McMurdo Sound, DSIR Bulletin*, **245**, 145-149.
- Ehrmann W.U., 1997. Smectite Concentrations and Crystallinities: Indications for Eocene Age of Glaciomarine Sediments in the CIROS-1 Drill Hole, McMurdo Sound, Antarctica. In: Ricci C.A. (ed.), *The Antarctic Region: Geological Evolution and Processes*, Terra Antarctica Publications, Siena, 771-780.
- Ehrmann W., 1998a. Implications of late Eocene to early Miocene clay mineral assemblages in McMurdo Sound (Ross Sea, Antarctica) on paleoclimate and ice dynamics. *Palaeogeogr., Palaeoclimatol., Palaeoecol.*, **139**, 213-231.
- Ehrmann W., 1998b. Lower Miocene and Quaternary Clay Mineral Assemblages from CRP-1. *Terra Antarctica*, **5**(3), 613-619.
- Ehrmann W.U. & Mackensen A., 1992. Sedimentological evidence for the formation of an East Antarctic ice sheet in Eocene/Oligocene time. *Palaeogeogr., Palaeoclimatol., Palaeoecol.*, **93**, 85-112.
- Ehrmann W.U., Melles M., Kuhn G. & Grobe H., 1992. Significance of clay mineral assemblages in the Antarctic Ocean. *Mar. Geol.*, **107**, 249-273.
- Fielding C.R., Woolfe K.J., Howe J.A. & Lavelle M., 1998. Sequence Stratigraphic Analysis of CRP-1, Cape Roberts Project, McMurdo Sound, Antarctica. *Terra Antarctica*, **5**(3), 353-361.
- Findlay R.H., Skinner D.N.B. & Craw D., 1984. Lithostratigraphy and structure of the Koettlitz Group, McMurdo Sound, Antarctica. *New Zealand Journal of Geology and Geophysics*, **27**, 513-536.
- Fischer A.G. & Bottjer D.J., 1991. Orbital forcing and sedimentary sequences. *Journal of Sedimentary Petrology*, **61**, 1063-1069.
- Fischer A.G., de Boer P.L. & Premoli Silva I., 1990. Cyclostratigraphy. In: Ginsburg R.N. & Beaudoin B. (eds.), *Cretaceous Resources, Events and Rhythms - Background and Plans for Research*, Kluwer Academic Publ., Dordrecht, 139-172.
- Fitzgerald P.G., 1992. The Transantarctic Mountains of southern Victoria Land: The application of apatite fission track analysis to a rift shoulder uplift. *Tectonics*, **11**, 634-662.
- Fitzgerald P.G. & Baldwin S., 1997. Detachment fault model for the evolution of the Ross Embayment. In: Ricci C.A. (ed.), *The Antarctic Region: Geological Evolution and Processes*, Terra Antarctica Publication, Siena, 555-564.
- Francis J.E. & Hill R.S., 1996. Fossil plants from the Pliocene Sirius Group, Transantarctic Mountains: Evidence for climate from growth rings and fossil leaves. *Palaios*, **11**, 389-396.
- Gazdzicki A. & Webb P.N., 1996. Foraminifera from the Pecten Conglomerate (Pliocene) of Cockburn Island, Antarctic Peninsula. *Palaeontologica Polonica*, **55**, 147-174.
- George A., 1989. Sand provenance. *DSIR Bulletin*, **245**, 159-167.
- Gersonde R. & Burckle L.H., 1990. Neogene biostratigraphy of ODP Leg 113, Weddell Sea (Antarctic Ocean). *Proceedings of the Ocean Drilling Program, Scientific Results*, **113**, 761-789.
- Gladenkov A.Y. & Barron J.A., 1995. Oligocene and early middle Miocene diatom biostratigraphy of Hole 884B. In: Rea D.K., Basov I.A., Scholl D.W. & Allan J.F. (eds.), *Proceedings of the Ocean Drilling Program, Scientific Results*, College Station, TX, Ocean Drilling Program, **145**, 21-41.
- Gombos A.M., 1977. Paleogene and Neogene diatoms from the Falkland Plateau and Malvinas Outer Basin. In: Barker P.F., Dalziel I.W.D. et al. (eds.), *Initial Reports of the Deep Sea Drilling Project*, Washington, U.S. Government Printing Office, **36**, 575-687.
- Gombos A.M. & Ciesielski P.F., 1983. Late Eocene to early Miocene diatoms from the southwest Atlantic. In: Ludwig W.J., Krasheninnikov V.A. et al. (eds.), *Initial Reports of the Deep Sea Drilling Project*, Washington, U.S. Government Printing Office, **71**, 583-634.
- Griffin J.J., Windom H. & Goldberg E.D., 1968. The distribution of clay minerals in the World Ocean. *Deep-Sea Res.*, **15**, 433-459.
- Grindley G.W. & Warren G., 1964. Stratigraphic nomenclature and correlation in the western Ross Sea region, Antarctica. In: Adie R.J.

- (ed.), *Antarctic Geology*, North Holland Publishing Company, Amsterdam, 206-219.
- Gunn B.M. & Warren G., 1962. Geology of Victoria Land between the Mawson and Mulock Glaciers, Antarctica. *New Zealand Geological Survey Bulletin*, **71**, 157 p.
- Hajós M., 1976. Upper Eocene and lower Oligocene diatomaceae, archaecomonadaceae, and silicoflagellatae in southwestern Pacific sediments, DSDP Leg 29. In: Hollister C.D., Craddock C. et al. (eds.), *Initial Reports of the Deep Sea Drilling Project*, Washington, U.S. Government Printing Office, **35**, 817-884.
- Hambrey M.J., Barrett P.J. & Robinson P.H., 1989. Stratigraphy. In: Barrett P.J. (ed.), *Antarctic Cenozoic history from the CIROS-1 drillhole, McMurdo Sound, DSIR Bulletin*, **245**, 23-48.
- Hambrey M.J. & Wise S.W. (eds.), 1998. Scientific Report on CRP-1, Cape Roberts Project, Antarctica. *Terra Antarctica*, **5**(3), 713 p.
- Hamilton R.J., Sorlien C.C., Luyendyk B.P., Bartek L.R. & Henrys S.A., 1998. Tectonic Regimes and Structural Trends Off Cape Roberts, Antarctica. *Terra Antarctica*, **5**(3), 261-272.
- Hannah M.J., 1997. Climate Controlled Dinoflagellate Distribution in Late Eocene/Earliest Oligocene Strata from the CIROS-1 Drillhole, McMurdo Sound, Antarctica. *Terra Antarctica*, **4**, 73-78.
- Hannah M.J., Wrenn J.H. & Wilson G.J., 1998. Early Miocene and Quaternary Marine Palynomorphs from Cape Roberts Project CRP-1, McMurdo Sound, Antarctica. *Terra Antarctica*, **5**(3), 527-538.
- Haq B.U., Hardenbol J. & Vail P.R., 1988. Mesozoic and Cenozoic chronostratigraphy and eustatic cycles. In: Wilgus et al. (eds.), *Sea-level changes: an integrated approach*, Society of Economic Paleontologists and Mineralogists, **42**, 70-108.
- Harwood D.M., 1986. Diatoms. In: Barrett P.J. (ed.), *Antarctic Cenozoic History from the MSSTS-1 Drillhole, McMurdo Sound, DSIR Bulletin*, **237**, 69-107.
- Harwood D.M., 1989. Siliceous microfossils. In: Barrett P.J. (ed.), *Antarctic Cenozoic History from the CIROS-1 Drillhole, McMurdo Sound, DSIR Bulletin*, **245**, 67-97.
- Harwood D.M., Barrett P.J., Edwards A.R., Rieck H.J. & Webb P.-N., 1989a. Biostratigraphy and chronology. In: Barrett P.J. (ed.), *Antarctic Cenozoic History from the CIROS-1 Drillhole, McMurdo Sound, DSIR Bulletin*, **245**, 231-239.
- Harwood D.M. & Bohaty S.M., in press. Ebridians and silicoflagellates from McMurdo Sound glacial erratics and the southern Kerguelen Plateau. *Antarctic Research Series*, AGU.
- Harwood D.M., Bohaty S.M. & Scherer R.P., 1998. Lower Miocene Diatom Biostratigraphy of the CRP-1 Drillcore, McMurdo Sound, Antarctica. *Terra Antarctica*, **5**(3), 499-514.
- Harwood D.M. & Maruyama T., 1992. Middle Eocene to Pleistocene diatom biostratigraphy of Southern Ocean sediments from the Kerguelen Plateau, Leg 120. In: Wise S.W. Jr., Schlich R. et al. (eds.), *Proceedings of the Ocean Drilling Program, Scientific Results*, College Station, TX, Ocean Drilling Program, **120**(2), 683-733.
- Harwood D.M., Scherer R.P. & Webb P.-N., 1989b. Multiple Miocene productivity events in West Antarctica as recorded in upper Miocene sediments beneath the Ross Ice Shelf (Site J-9). *Marine Micropaleontology*, **15**, 91-115.
- Hedges J.I. & Stern J.H., 1984. Carbon and nitrogen determinations of carbonate-containing solids. *Limnology and Oceanography*, **29**, 657-663.
- Henrys S.A., Bartek L.R., Brancolini G., Luyendyk B.P., Hamilton R.J., Sorlien C.C. & Davey F.J., 1998. Seismic Stratigraphy of the Pre-Quaternary Strata Off Cape Roberts and their Correlation with Strata Cored in the CIROS-1 Drillhole, McMurdo Sound. *Terra Antarctica*, **5**(3), 273-279.
- Henrys S.A., Bartek L.R., Anderson J.B. & Barrett P.J., 1994. Seismic Stratigraphy in McMurdo Sound: Correlation of High Resolution Data Sets. *Terra Antarctica*, **1**, 373-374.
- Hinnov L.A. & Goldhammer R.K., 1991. Spectral analysis of the Middle Triassic Latemar Limestone. *Journal of Sedimentary Petrology*, **61**, 1173-1193.
- Hollis C.J., Waghorn D.B., Strong C.P. & Crouch E.M., 1997. Integrated Paleogene biostratigraphy of DSDP site 277 (Leg 29): foraminifera, calcareous nannofossils, Radiolaria, and palynomorphs. *Institute of Geological & Nuclear Sciences, Science Report 97/07*, 73 p.
- Houtz R.E. & Davey F.J., 1973. Seismic profiler and sonobuoy measurements in the Ross Sea, Antarctica. *J. Geophys. Res.*, **78**, 3448-3468.
- Ingersoll R.V., Bullard T.F., Ford R.L., Grimm J.P., Pickle J.D. & Sares S.W., 1984. The effects of grain size on detrital modes: a test of the Gazzi-Dickinson point-counting method. *J. Sed. Petrol.*, **54**, 103-116.
- International Steering Committee, 1994. Cape Roberts Project - coring for Antarctic tectonic and climatic history. *EOS*, **75**(1), 2-3.
- Ishman S.E. & Rieck H.J., 1992. A late Neogene Antarctic glacio-eustatic record, Victoria Land Basin margin. In: Kennett J.P. & Barron J.A. (eds.), *The Antarctic Paleoenvironment: a perspective on global change*, Antarctic Research Series, **56**(1), 327-347.
- Jacobs J.A., 1994. *Reversals of the Earth's Magnetic Field*. 2nd ed., Cambridge University Press, 346 p.
- Jonkers H.A. & Taviani M., 1998. Lower Miocene Macrofossils from CRP-1 Drillhole, Cape Roberts (Victoria Land Basin, Antarctica). *Terra Antarctica*, **5**(3), 493-498.
- Kettler R.M., 1998. Preliminary Results of Bitumen and Kerogen Analyses of the CRP-1 Core. *Terra Antarctica*, **5**(3), 669-672.
- King J.W. & Channell J.E.T., 1991. Sedimentary magnetism, environmental magnetism, and magnetostratigraphy. *U.S. National Report to the International Union of Geodesy and Geophysics 1987-1990, Reviews of Geophysics*, **29**, 358-370.
- Korsch R.J., 1974. Petrographic comparison of the Taylor and Victoria Groups (Devonian to Triassic) in south Victoria Land, Antarctica. *NZ J. Geol. Geophys.*, **17**, 523-541.
- Kuhn G., Melles M., Ehrmann W.U., Hambrey M.J. & Schmiedl G., 1993. Character of clasts in glaciomarine sediments as an indicator of transport and depositional processes, Weddell and Lazarev seas, Antarctica. *J. Sedimentary Geology*, **63**(3), 477-487.
- Kulander B.R., Dean S.L. & Ward B.J. Jr., 1990. Fractured Core Analysis: Interpretation, Logging, and Use of Natural and Induced Fractures in Core. *American Association of Petroleum Geologists Methods in Exploration Series*, **8**, 88 p.
- Kyle P.R., 1990. McMurdo Volcanic Group, western Ross embayment. In: LeMasurier W.E. & Thomson J.W. (eds.), *Volcanoes of the Antarctic Plate and Southern Oceans*, AGU, Antarctic Research Series, **48**, 19-25.
- Kyle P.R., 1990. McMurdo Volcanic Group, western Ross embayment. In: LeMasurier W.E. & Thomson J.W. (eds.), *Volcanoes of the Antarctic Plate and Southern Oceans, American Geophysical Union, Antarctic Research Series*, **48**, 19-25.
- LaPrade K.E., 1982. Petrology and petrography of the Beacon Supergroup, Shackleton Glacier area, Queen Maud Range, Transantarctic Mountains, Antarctica. In: Craddock C. (ed.), *Antarctic Geoscience*, International Union of Geological Sciences, Series B, **4**, Wisconsin, 581-589.
- Lamothe M., Hillaire-Marcel C. & Page P., 1983. Decouverte de concrections calcaires dans le till de Gentilly, basses-terres du Saint-Laurent, Quebec. *Canadian Journal of Earth Sciences*, **20**, 500-505.
- Larsen E. & Mangerud J., 1992. Subglacially formed clastic dykes. *Sveriges Geologiska Undersökning*, **81**, 163-170.
- Lavelle M., 1998. Strontium Isotope Stratigraphy of the CRP-1 Drillhole, Ross Sea, Antarctica. *Terra Antarctica*, **5**(3), 691-696.
- Leckie M.A. & Webb P.N., 1985. Late Paleogene and early Neogene foraminifers of Deep Sea Drilling Project Site 270, Ross Sea, Antarctica. In: Kennett J.P., Von der Broch C.C. et al. (eds.), *Initial Reports of the Deep Sea Drilling Project* XC, 1093-1142.
- Li Y. & Schmitt R., 1997. Well-bore bottom stress concentration and induced core fractures. *American Association of Petroleum Geologists Bulletin*, **81**, 1909-1925.
- Lorenz J.C., Finley S.J. & Warpinski N.R., 1990. Significance of coring-induced fractures in Mesaverde core, northwestern Colorado. *American Association of Petroleum Geologists Bulletin*, **74**, 1017-1029.
- Mackiewicz N.E., Powell R.D., Carlson P.R. & Molnia B.F., 1984. Interlaminated ice-proximal glaciomarine sediments in Muir Inlet, Alaska. *Marine Geology*, **57**, 113-147.
- Mahood A.D., Barron J.A. & Sims P.A., 1993. A study of some unusual, well-preserved Oligocene diatoms from Antarctica. *Nova Hedwigia, Beiheft*, **106**, 243-267.
- Mark D.M., 1973. Analysis of axial orientation data, including till fabrics. *Geol. Soc. America Bull.*, **84**, 1369-1374.
- McIntosh W.C., 1998. ⁴⁰Ar/³⁹Ar Geochronology of Volcanic Clasts and Pumice in CRP-1 Core, Cape Roberts, Antarctica. *Terra Antarctica*, **5**(3), 683-690.
- McIntosh W.C. & Chamberlin R.M., 1994. ⁴⁰Ar/³⁹Ar geochronology of Middle to Late Cenozoic ignimbrites, mafic lavas, and volcanoclastic

- rocks in the Quemado Region, New Mexico. *New Mexico Geological Society Guidebook*, **45**, 165-185.
- McMinn A., 1995. Why are there no post-Paleogene dinoflagellate cysts in the Southern Ocean? *Micropaleontology*, **41**, 383-386.
- Mildenhall D.C., 1989. Terrestrial palynology. In: Barrett P.J. (ed.), *Antarctic Cenozoic history from the CIROS-1 drillhole, McMurdo Sound*. *DSIR Bulletin*, **245**, 119-127.
- Mildenhall D.C. & Pocknall D.T., 1989. Miocene-Pleistocene spores and pollen from central Otago, South Island, New Zealand. *New Zealand Geological Survey Paleontological Bulletin*, **59**, 128 p.
- Monochi S. & Reale V., 1997. Calcareous nannofossil assemblages of the CIROS-1 core (Ross Sea): further assessments on age. *Terra Antarctica*, **4**(2), 89-102.
- Naish T.R. & Kamp P.J.J., 1997. Sequence stratigraphy of 6th order (41 k.y.) Pliocene-Pleistocene cyclothems, Wanganui Basin, New Zealand: A case for the regressive systems tract. *Geological Society of America Bulletin*, **109**, 979-999.
- Nelson R.A., Lenox L.C. & Ward B.J. Jr., 1987. Oriented core: Its use, error, and uncertainty. *American Association of Petroleum Geologists Bulletin*, **71**, 357-367.
- Niessen F. & Jarrard R.D., 1998. Velocity and Porosity of Sediments from CRP-1 Drillhole, Core, Ross Sea, Antarctica. *Terra Antarctica*, **5**(3), 311-317.
- Niessen F., Jarrard R.D. & Bucker C., 1998. Log-Based Physical Properties of the CRP-1 Core, Ross Sea, Antarctica. *Terra Antarctica*, **5**(3), 299-310.
- Paillard D., Labeyrie L. & Yiou P., 1996. Macintosh program performs time-series analysis. *Eos Trans. AGU*, **77**, 379 p.
- Passchier S., Wilson T.J. & Paulsen T.S., 1998. Origin of Breccias in the CRP-1 Core. *Terra Antarctica*, **5**(3), 401-409.
- Paulsen T. & Wilson G., 1998. Orientation of CRP-1 Core. *Terra Antarctica*, **5**(3), 319-325.
- Perch-Nielsen K., 1985. Cenozoic calcareous nannofossils. In: Bolli H.M., Saunders J.B. & Perch-Nielsen K. (eds.), *Plankton Stratigraphy*, Cambridge England, Cambridge University Press, 427-554.
- Pestiaux P. & Berger A., 1984. An optimal approach to the spectral characteristics of deep-sea climatic records. In: Berger A.L., Imbrie J., Hays J., Kukla G. & Saltzman B. (eds.), *Milankovitch and Climate, Part 1*, Reidel Publ. Co., Dordrecht, 417-445.
- Plint A.G., 1988. Sharp-based shoreface sequences and "Offshore Bars" in the Cardium Formation of Alberta: Their relationship to relative changes in sea-level. In: Wilgus C.K. et al. (eds), *Sea-level changes: an integrated approach*, Society of Economic Paleontologists and Mineralogists, **42**, 357-370.
- Plumb R.A. & Cox J.W., 1987. Stress directions in eastern North America determined to 4.5 km from borehole elongation measurements. *Journal of Geophysical Research*, **92**, 4805-4816.
- Pocknall D.T., 1989. Late Eocene to Early Miocene vegetation and climate history of New Zealand. *Journal of the Royal Society of New Zealand*, **19**, 1-18.
- Pocknall D.T. & Mildenhall D.C., 1984. Late Oligocene-early Miocene spores and pollen from Southland, New Zealand. *New Zealand Geological Survey Paleontological Bulletin*, **51**, 66 p.
- Posamentier H.W., Jervey M.T. & Vail P.R., 1988. Eustatic controls on clastic deposition 1 - Conceptual Framework. In: Wilgus C.K. et al. (eds), *Sea-level changes: an integrated approach*, Society of Economic Paleontologists and Mineralogists, **42**, 109-124.
- Powell R.D., Hambrey M.J. & Kriisek L.A., 1998. Quaternary and Miocene Glacial and Climatic History of the Cape Roberts Drillsite Region, Antarctica. *Terra Antarctica*, **5**(3), 341-351.
- Press W.H., Flannery B.P., Teukolsky S.A. & Vetterling W.T., 1989. *Numerical recipes in Pascal: the art of scientific computing*. Cambridge University Press, Cambridge, 759 p.
- Pyne A.R., 1986. Sea-ice operations: McMurdo Sound-Granite Harbour. *NZ Antarctic Record*, **7**, 5-13.
- Raine J.I., 1998. Terrestrial Palynomorphs from Cape Roberts Project Drillhole CRP-1, Ross Sea, Antarctica. *Terra Antarctica*, **5**(3), 539-548.
- Reijmer J.J.G., Sprenger A., Ten Kate W.G.H.Z., Schlager W. & Krystyn L., 1994. Periodicities in the composition of Late Triassic calciturbidites (Eastern Alps, Austria). In: de Boer P.L. & Smith D.G. (eds.), *Orbital forcing and cyclic sequences*, IAS Special Publication, **19**, 323-343.
- Renne P.R., Swisher C.C., Deino A.L., Karner D.B., Owens T.L. & DePaolo D.J., 1998. Intercalibration of Standards, Absolute Ages and Uncertainties in ⁴⁰Ar/³⁹Ar Dating. *Chemical Geology*, **149**, 259.
- Rider M., 1996. *The geologic interpretation of well-logs*. Whittles Publishing, 288 p.
- Roberts A.P., Wilson G.S., Florindo F., Sagnotti L., Verosub K.L. & Harwood D.M., 1998. Magnetostratigraphy of Lower Miocene Strata from the CRP-1 core, McMurdo Sound, Ross Sea, Antarctica. *Terra Antarctica*, **5**(3), 703-713.
- Rosenbaum J. & Sheppard S.M.F., 1986. An isotopic study of siderites, dolomites, and ankerites at high temperatures. *Geochimica et Cosmochimica Acta*, **50**, 1147-1150.
- Sagnotti L., Florindo F., Verosub K.L., Wilson G.S. & Roberts A.P., 1998a. Environmental magnetic record of Antarctic palaeoclimate from Eocene-Oligocene glaciomarine sediments, Victoria Land Margin. *Geophysical Journal International*, **134**, 653-662.
- Sagnotti L., Florindo F., Wilson G.S., Roberts A.P. & Verosub K.L., 1998b. Environmental Magnetism of Lower Miocene Strata from the CRP-1 core, McMurdo Sound, Antarctica. *Terra Antarctica*, **5**(3), 66-667.
- Scherer R.P. & Koç N., 1996. Late Paleogene diatom biostratigraphy and paleoenvironments of the northern Norwegian-Greenland Sea. In: Thiede J., Myhre A.M., Firth J.V., Johnson G.L. & Ruddiman W.F. (eds.), *Proceedings of the Ocean Drilling Program, Scientific Results*, College Station, TX, Ocean Drilling Program, **151**, 75-99.
- Schmitz D., Hirschmann G., Kessels W., Kohl J., Rohr C. & Dietrich H.-G., 1989. Core orientation in the KTB pilot well. *Scientific Drilling*, **1**, 150-155.
- Schrader H.-J., 1976. Cenozoic planktonic diatom biostratigraphy of the Southern Pacific Ocean. In: Hollister C.D., Craddock C. et al. (eds.), *Initial Reports of the Deep Sea Drilling Project*, Washington, U.S. Government Printing Office, **35**, 605-672.
- Schrader H.-J. & Fenner J., 1976. Norwegian Sea Cenozoic diatom biostratigraphy and taxonomy. In: Talwani M., Udintsev G. et al. (eds.), *Initial Reports of the Deep Sea Drilling Project*, Washington, U.S. Government Printing Office, **38**, 921-1099.
- Serra O., 1984. Fundamentals of well-log interpretation. Vol. 1: The acquisition of logging data. *Developments in Petroleum Science*, **15A**, Elsevier, Amsterdam, 440 p.
- Simes J. & Wrenn J.H., 1998. Palynologic Processing in Antarctica. *Terra Antarctica*, **5**(3), 549-552.
- Smellie J.L., 1998. Sand Grain Detrital Modes in CRP-1: Provenance Variations and Influence of Miocene Eruptions on the Marine Record in the McMurdo Sound Region. *Terra Antarctica*, **5**(3), 579-587.
- Stilwell J.D. & Zinsmeister W.J., 1992. Molluscan Systematics and Biostratigraphy. Lower Tertiary La Meseta Formation, Seymour Island, Antarctic Peninsula. *Antarctic Research Series*, American Geophysical Union, **55**, 192 p.
- Szaniewski H., 1996. Scolecodonts. In: Jansonius J. & McGregor D.C. (eds), *Palynology: principles and applications*, American Association of Stratigraphic Palynologists Foundation, **1**, 337-354.
- Talarico F. & Sandroni S., 1998. Petrography, Mineral Chemistry and Provenance of Basement Clasts in the CRP-1 Drillcore (Victoria Land Basin, Antarctica). *Terra Antarctica*, **5**(3), 601-610.
- Tarling D.H. & Hrouda F., 1993. *The Magnetic Anisotropy of Rocks*. Chapman and Hall, London, 217 p.
- Tasch P. & Lammons J.M., 1977. Palynology of some lacustrine interbeds of the Antarctic Jurassic. *Palinologia*, **1**.
- Taviani M., Beu A. & Lombardo C., 1998. Pleistocene Macrofossils from CRP-1 Drillhole, Victoria Land Basin, Antarctica. *Terra Antarctica*, **5**(3), 485-491.
- Vail P., 1987. Seismic stratigraphy interpretation using sequence stratigraphy, part 1: seismic stratigraphy interpretation procedure. In: Bally A.W. (ed.), *Atlas of Seismic Stratigraphy*, AAPG, Tulsa, Oklahoma, **27**, 1-10.
- van der Meer J.J.M., 1993. Microscopic evidence of subglacial deformation. *Quaternary Science Reviews*, **12**, 553-587.
- Van Wagoner J.C., Mitchum R.M., Campion K.M., & Rahmanian V.D., 1990. Siliciclastic Sequence Stratigraphy in Well Logs, Cores, and Outcrops. *Concepts for High-Resolution Correlation of Time and Facies*. AAPG Methods in Exploration, **7**, 55 p.
- Van Wagoner J.C., Posamentier H.W., Mitchum R.M., Vail P.R., Sarg, J.F., Loutit T.S., & Hardenbol J., 1988. An overview of sequence stratigraphy and key definitions. In: Wilgus C.K. et al. (eds), *Sea-*

- Level Changes: An Integrated Approach*, Society of Economic Paleontologists and Mineralogists, Special Publication, **42**, 39-40.
- Verosub K.L., 1977. Depositional and postdepositional processes in the magnetization of sediments. *Reviews of Geophysics and Space Physics*, **15**, 129-143.
- Verosub K.L. & Roberts A.P., 1995. Environmental magnetism: past, present, and future. *Journal of Geophysical Research*, **100**, 2175-2192.
- Villa G. & Wise S.W., Jr., 1998. Quaternary calcareous nannofossils from the Antarctic Region. *Terra Antarctica*, **5**(3), 479-484.
- Vitor S.A. & Anderson J.B., 1998. Glacial eustasy during the Cenozoic: Sequence stratigraphic implications. *Bulletin of the American Association of Petroleum Geologists*, **82**, 1385-1400.
- Von Brunn V. & Talbot C.J., 1986. Formation and deformation of subglacial intrusive clastic sheets in the Dwyka formation of northern Natal, South Africa. *Journal of Sedimentary Petrology*, **56**(1), 35-44.
- von Rad U. & Botz R., 1983. Authigenic Fe-Mn carbonates in Cretaceous and Tertiary sediments of the Continental Rise off eastern North America. Leg 603 Deep Sea Drilling Project. *Initial Reports of the Deep Sea Drilling Project*, **603**, 1061-1077.
- Webb P.N., 1974. Micropaleontology, palaeoecology, and correlation of the Pecten Gravels, Wright Valley, Antarctica, and description of *Trichoelphidiella onyx* n.gen et n. sp. *Journal of Foraminiferal Research*, **4**, 184-199.
- Webb P.N., 1989. Benthic foraminifera. In: Barrett P.J. (ed.), *Antarctic Cenozoic history from the CIROS-1 drillhole, McMurdo Sound*, *DSIR Bulletin*, **245**, 99-118.
- Webb P.N. & Harwood D.M., 1991. Late Cenozoic glacial history of the Ross Embayment, Antarctica. *Quaternary Science Reviews*, **10**, 215-223.
- Webb P.N. & Strong C.P., 1998a. Occurrence, Stratigraphic Distribution and Palaeoecology of Quaternary Foraminifera from CRP-1. *Terra Antarctica*, **5**(3), 455-472.
- Webb P.N. & Strong C.P., 1998b. Recycled Pliocene Foraminifera from the CRP-1 Quaternary Succession. *Terra Antarctica*, **5**(3), 473-478.
- Weber H., 1994. Analyse geologischer Strukturen mit einem Bohrkernscanner [Analysis of geological structures using the DMT Corescan® machine]. *Felsbau*, **12**(6), 401-403.
- Weber M.E., Niessen F., Kuhn G. & Wiedicke M., 1997. Calibration and application of marine sedimentary physical properties using a multi-sensor core logger. *Marine Geology*, **136**, 151-172.
- Wei W., 1991. Middle Eocene-lower Miocene calcareous nannofossil magnetobiochronology of ODP Holes 699A and 703A in the subantarctic South Atlantic. *Marine Micropaleontology*, **18**, 143-165.
- Wei W., 1992. Updated nannofossil stratigraphy of the CIROS-1 core from McMurdo Sound (Ross Sea). *Proc. ODP Sc. Results*, **120**, 1105-1117.
- Wei W. & Wise S.W., 1990. Middle Eocene to Pleistocene calcareous nannofossils recovered by Ocean Drilling Program Leg 113 in the Weddell Sea. *Proc. Ocean Drilling Program Sc. Results*, **113**, 639-666.
- Wei W. & Wise S.W., 1992. Oligocene-Pleistocene calcareous nannofossils from Southern Ocean Sites 747, 748, and 751. *Proc. ODP Sc. Results*, **120**, 509-521.
- Wilson G.J., 1967. Some new species of lower Tertiary dinoflagellates from McMurdo Sound, Antarctica. *New Zealand Journal of Botany*, **5**, 57-83.
- Wilson G.J., 1989. Marine palynology. In: Barrett P.J. (ed.), *Antarctic Cenozoic history from the CIROS-1 drillhole, McMurdo Sound*, *DSIR Bulletin*, **245**, 129-134.
- Wilson G.S., 1995. The Neogene East Antarctic Ice Sheet: A dynamic or stable feature? *Quaternary Science Reviews*, **14**, 101-123.
- Wilson G.S., Harwood D.M., Askin R.A. & Levy R.H., in press. Late Neogene Sirius Group strata in Reedy Valley, Antarctica: a multiple-resolution record of climate, ice-sheet and sea-level events. *Journal of Glaciology*.
- Wilson G.S., Roberts A.P., Verosub K.L., Florindo F. & Sagnotti L., 1998. Magnetobiostratigraphic chronology of the Eocene-Oligocene transition in the CIROS-1 core, Victoria Land Margin, Antarctica: Implications for Antarctic glacial history. *Geological Society of America Bulletin*, **110**(1), 35-47.
- Wilson T.J., 1995. Cenozoic transtension along the Transantarctic Mountains-West Antarctica rift boundary, southern Victoria Land, Antarctica. *Tectonics*, **14**, 531-545.
- Windom H.L., 1976. Lithogenous material in marine sediments. In: Riley J.P. & Chester R. (eds.), *Chemical Oceanography*, **5**, Academic Press, New York, 103-135.
- Wrenn J.H., Hannah M.J. & Raine J.I., 1998. Diversity and Palaeoenvironmental Significance of Late Cainozoic Marine Palynomorphs from the CRP-1 Core, Ross Sea, Antarctica. *Terra Antarctica*, **5**(3), 553-570.
- Wrenn J.H. & Hart G.F., 1988. Paleogene dinoflagellate cyst biostratigraphy of Seymour Island, Antarctica. In: Feldmann R.M. & Woodburne M.O. (eds.), *Geology and Palaeontology of Seymour Island, Antarctic Peninsula*, *Geological Society of America Memoir*, **169**, 321-447.
- Yanagisawa Y. & Akiba F., 1998. Refined Neogene diatom biostratigraphy for the northwest Pacific around Japan, with an introduction of code numbers for selected diatom biohorizons. *The Journal of the Geological Society of Japan*, **104**(6), 395-414.
- Zemanek J., Glenn E.E.J., Norton L.J. & Caldwell R.L., 1970. Formation evaluation by inspection with the borehole televiwer. *Geophysics*, **35**, 254-269.



TERRA ANTARTICA

Università di Siena
Museo Nazionale dell'Antartide
Sezione Scienze della Terra

Direttore Responsabile:
Maurizio Boldrini

Direttore Scientifico:
Carlo Alberto Ricci

Autorizzazione del Tribunale di Siena
n. 633 del 18 Luglio 1996

